

Technical Report Documentation Page

1. Report No. FHWA/TX-12/0-6348-2		2. Government Accession No.		3. Recipient's Catalog No.	
4. Title and Subtitle Bridge Deck Reinforcement and PCP Cracking: Final Report				5. Report Date October 2012; Revised March 2013 Published April 2013	
				6. Performing Organization Code	
7. Author(s) Oguzhan Bayrak, Shih-Ho Chao, James O. Jirsa, Richard E. Klingner, Umid Azimov, James Foreman, Stephen Foster, Netra Karki, Ki Yeon Kwon, and Aaron Woods				8. Performing Organization Report No. 0-6348-2	
9. Performing Organization Name and Address Center for Transportation Research The University of Texas at Austin 1616 Guadalupe Street, Suite 4.202 Austin, TX 78701 University of Texas at Arlington 701 South Nedderman Drive Arlington, TX 76019-9800				10. Work Unit No. (TR AIS)	
				11. Contract or Grant No. 0-6348	
12. Sponsoring Agency Name and Address Texas Department of Transportation Research and Technology Implementation Office P.O. Box 5080 Austin, TX 78763-5080				13. Type of Report and Period Covered Technical Report September 1, 2008–August 31, 2012	
				14. Sponsoring Agency Code	
15. Supplementary Notes Project performed in cooperation with the Texas Department of Transportation and the Federal Highway Administration.					
16. Abstract Bridge decks composed of precast, prestressed panels (PCPs) overlain by cast-in-place (CIP) are popular in many states, including Texas. Optimization of top-mat reinforcement and reduction of collinear panel cracking were addressed in this project. Longitudinal top-mat reinforcement was found to be already optimized. Further optimization of transverse top-mat reinforcement is possible by slightly reducing the area of deformed reinforcement or by using welded-wire reinforcement. Collinear panel cracking can be reduced by reducing lowering the initial prestress or by placing additional transverse reinforcement at panel ends. Measured prestress losses in PCPs were at most 25 ksi, much less than the 45 ksi currently assumed by TxDOT. The comparative efficiency of different types of high-performance steel fibers was examined. Double-punch testing, appropriately standardized as proposed in this report, is a reliable and repeatable measure of the comparative efficiency of high-performance steel fibers.					
17. Key Words bridge decks, double-punch test, fiber-reinforced concrete, panels, prestress, prestress losses, reinforcement			18. Distribution Statement No restrictions. This document is available to the public through the National Technical Information Service, Springfield, Virginia 22161; www.ntis.gov.		
19. Security Classif. (of report) Unclassified		20. Security Classif. (of this page) Unclassified		21. No. of pages 356	22. Price



Bridge Deck Reinforcement and PCP Cracking: Final Report

Oguzhan Bayrak
Shih-Ho Chao
James O. Jirsa
Richard E. Klingner
Umid Azimov
James Foreman
Stephen Foster
Netra Karki
Ki Yeon Kwon
Aaron Woods

Technical Report:	0-6348-2
Report Date:	October 2012; Revised March 2013
Project:	0-6348
Project Title:	Controlling Cracking in Prestressed Concrete Panels and Optimizing Bridge Deck Reinforcing Steel
Sponsoring Agency:	Texas Department of Transportation
Performing Agency:	Center for Transportation Research at The University of Texas at Austin The University of Texas at Arlington

Project performed in cooperation with the Texas Department of Transportation and the Federal Highway Administration.

Center for Transportation Research
The University of Texas at Austin
1616 Guadalupe, Suite 4.202
Austin, TX 78701

www.utexas.edu/research/ctr

Copyright (c) 2012
Center for Transportation Research
The University of Texas at Austin

All rights reserved
Printed in the United States of America

Disclaimers

Author's Disclaimer: The contents of this report reflect the views of the authors, who are responsible for the facts and the accuracy of the data presented herein. The contents do not necessarily reflect the official view or policies of the Federal Highway Administration or the Texas Department of Transportation (TxDOT). This report does not constitute a standard, specification, or regulation.

Patent Disclaimer: There was no invention or discovery conceived or first actually reduced to practice in the course of or under this contract, including any art, method, process, machine manufacture, design or composition of matter, or any new useful improvement thereof, or any variety of plant, which is or may be patentable under the patent laws of the United States of America or any foreign country.

Engineering Disclaimer

NOT INTENDED FOR CONSTRUCTION, BIDDING, OR PERMIT PURPOSES.

Project Engineer: Richard E. Klingner
Professional Engineer License State and Number: Texas No. 42483
P. E. Designation: Research Supervisor

Acknowledgments

The authors express appreciation to the TxDOT Project Director, Manuel (Bernie) Carrasco, P.E. (Bridge Division). We also acknowledge the contributions of the Project Advisors: Graham Bettis, P.E. (Construction Division); Robert Cochrane, P.E. (Bryan District); David Hohmann, P.E. (Bridge Division); John Holt, PE (Bridge Division); Kirk Krause (Waco District); John Vogel, P.E. (Houston District); and Wade Odell, P.E. (Research and Technology Implementation Office). We are grateful to the management and personnel of the precast plants who furnished panels for field studies, and to the laboratory personnel at Ferguson Lab (UT Austin) and UT Arlington. We acknowledge the fieldwork contributions of Jae-Sung Cho and Regina Waweru, Graduate Research Assistants at UT Arlington.

Table of Contents

Chapter 1. Introduction.....	1
1.1 Background of Project 0-6348.....	1
1.2 Background on Precast, Prestressed Panels.....	2
1.3 Issues Addressed in Study 6348.....	3
Chapter 2. Literature Review.....	7
2.1 Introduction to CIP-PCP Bridge Decks.....	7
2.2 Issues in CIP-PCP Bridge Decks.....	8
2.3 Studies Conducted under TxDOT Projects 0-4098 and 0-6348.....	15
2.4 Fiber-Reinforced Concrete (FRC).....	21
Chapter 3. Optimization of Reinforcement in CIP Slabs: Field Application.....	27
3.1 Introduction.....	27
3.2 Wharton-Weems Overpass.....	27
3.3 Lampasas River Bridge.....	51
3.4 Calculations of Construction Cost of Various Top-Mat Reinforcement Options.....	85
3.5 Conclusions from Field Instrumentation.....	86
Chapter 4. Optimization of Reinforcement in CIP Slabs: Restrained-Shrinkage Test.....	87
4.1 Introduction.....	87
4.2 Test Specimens for Restrained-Shrinkage Test.....	88
4.3 Results and Conclusions, Restrained-Shrinkage Test.....	104
Chapter 5. Double-Punch Testing.....	111
5.1 Introduction to Double-Punch Testing.....	111
5.2 Extension of the Double-Punch Test to Evaluate the Mechanical Properties of FRC.....	114
5.3 Summary of Advantages of Double-Punch Test.....	119
5.4 Summary of Results from Double-Punch Tests at UT Arlington.....	119
5.5 Double-Punch Testing at the University of Texas at Austin.....	122
Chapter 6. Control of Cracking in Precast, Prestressed Concrete Panels.....	131
6.1 Introduction.....	131
6.2 Fabrication of Panels.....	131
6.3 Monitoring of Strains in PCPs.....	134
6.4 Prestress Loss Monitoring.....	137
6.5 Results from Monitoring of Panel Strains.....	143
6.6 Conclusions of Study on Control of Cracking in PCPs.....	149
Chapter 7. Summary, Conclusions, and Recommendations.....	151
7.1 Summary and Conclusions on Top-Mat Reinforcement and PCP Cracking.....	151
7.2 Recommendations on Top-Mat Reinforcement and PCP Cracking.....	152
7.3 Summary and Conclusions on Double-Punch Test.....	152
7.4 Conclusions regarding DPT.....	152
7.5 Recommendations regarding Double-Punch Test.....	156
References.....	157
Appendix A. Development Length Calculation.....	163

Appendix B. Sample Restraint Moment Calculation Using P-method Wharton-Weems Overpass	169
Appendix C. Sample Restraint Moment Calculation Using the P-method Restrained Shrinkage Test.....	177
Appendix D. Model for Prestress Loss in PC Panels.....	181
Appendix E. Standard Test Methods for Fiber-Reinforced Concrete.....	201
Appendix F. Details of Double-Punch Testing	221
Appendix G. Statistical Evaluation of DPT Results At UT Austin	305
Appendix H. ASTM Draft Ballot for Standardization of Double-Punch Test.....	325

List of Figures

Figure 1-1: CIP-PCP bridge deck (adapted from Buth et al. (1972))	2
Figure 1-2: CIP-PCP bridge deck (section view)	2
Figure 1-3: Criteria for rejection of precast panel	4
Figure 1-4: Schematic of Double-Punch Test (Chen, 1970)	5
Figure 2-1: Arching Action in Concrete Slabs (adopted from (Foster 2010))	9
Figure 2-2 Reflected cracking in top surface of CIP-PCP bridge deck (Folliard et al. 2003)	9
Figure 2-3: “Poor-boy” Joint (adapted from Roberts et al. 1993)	11
Figure 2-4: Force acting on a strand after release	12
Figure 2-5: Gradient of prestress in strand after releasing	13
Figure 2-6: The force acting in the surrounding concrete	13
Figure 2-7: Poisson’s effect	14
Figure 2-8: Forces on strand due to “wedge” created by Hoyer effect	14
Figure 2-9: Restrained-shrinkage test setup of TxDOT Project 0-4098 (Folliard et al. 2003)	16
Figure 2-10: Constant bending moment test setup (Foster 2010)	17
Figure 2-11: Concentrated-load test setup (Foster 2010)	17
Figure 2-12: Direct tensile test using composite specimen (Foster 2010)	18
Figure 2-13: Delamination during direct tensile test (Foster 2010)	18
Figure 2-14: Direct tensile test using non-composite specimen (Foster 2010)	19
Figure 2-15: Long-term monitoring of prestress loss in PCPs	20
Figure 2-16: Knife-edge test (Foreman 2010)	20
Figure 2-17: Schematic of (a) Stand Alone, (b) Combination, and (c) Repair Applications for HPFRCC (Ramakrishnan, 1987)	22
Figure 2-18: Graphical Comparison of Specimen Weights for Current FRC Testing Procedures	24
Figure 3-1: Plan view, Wharton-Weems Overpass	28
Figure 3-2: Section view, Wharton-Weems Overpass	28
Figure 3-3: CIP deck reinforcement options, Wharton-Weems Overpass	29
Figure 3-4: Details of longitudinal splices, Wharton-Weems Overpass	30
Figure 3-5: Section showing details of longitudinal splices, Wharton-Weems Overpass (Joint 1)	30
Figure 3-6: Section showing details of longitudinal splices, Wharton-Weems Overpass (Joint 2)	31
Figure 3-7: Details of transverse splices, Wharton-Weems Overpass	31
Figure 3-8: Details of transverse splices, Wharton-Weems Overpass (Section A-A)	32
Figure 3-9: Details of transverse splices, Wharton-Weems Overpass (Section B-B)	32

Figure 3-10: Details of transverse splices, Wharton-Weems Overpass (Section C-C)	32
Figure 3-11: Typical VWG as installed on the reinforcement.....	33
Figure 3-12: Gage layout for longitudinal bars, Wharton-Weems Overpass	34
Figure 3-13: Gage layout for transverse bars, Wharton-Weems Overpass	34
Figure 3-14: Solar-powered data-acquisition system, Wharton-Weems Overpass	35
Figure 3-15: Location of data-acquisition box, Wharton-Weems Overpass	35
Figure 3-16: Bracket for solar panel, Wharton-Weems Overpass	36
Figure 3-17: Gage instrumentation, Wharton-Weems Overpass.....	37
Figure 3-18: Threading wires through holes in bedding strip, Wharton-Weems Overpass.....	37
Figure 3-19: Data-acquisition box after connection, Wharton-Weems Overpass	38
Figure 3-20: Mounting solar panel beside bent cap, Wharton-Weems Overpass.....	38
Figure 3-21: Construction sequence for CIP deck, Wharton-Weems Overpass.....	39
Figure 3-22: Spraying water on bridge deck for cracking inspection, Wharton-Weems Overpass.....	40
Figure 3-23: Results of first cracking inspection, Wharton-Weems Overpass.....	41
Figure 3-24: Results of second cracking inspection, Wharton-Weems Overpass	41
Figure 3-25: Stresses in Current TxDOT Standard Reinforcement, Wharton-Weems Overpass (longitudinal direction)	43
Figure 3-26: Stresses in Reduced Deformed-Bar Reinforcement, Wharton-Weems Overpass (longitudinal direction)	43
Figure 3-27: Stresses in Current TxDOT Standard Reinforcement, Wharton-Weems Overpass (transverse direction).....	44
Figure 3-28: Stresses in Reduced Deformed-Bar Reinforcement, Wharton-Weems Overpass (transverse direction).....	44
Figure 3-29: The area for the calculation of longitudinal restraint moment of Wharton- Weems Overpass.....	47
Figure 3-30: Simplified Section T-T.....	47
Figure 3-31: Longitudinal restraint moment and cracking moment, Wharton-Weems Overpass.....	48
Figure 3-32: Area for calculation of transverse restraint moment, Wharton-Weems Overpass.....	49
Figure 3-33: Simplified Section L-L, Wharton-Weems Overpass	50
Figure 3-34: Transverse restraint moment and cracking moment, Wharton-Weems Overpass.....	50
Figure 3-35: Plan view of Lampasas River Bridge (Spans 1 to 3)	52
Figure 3-36: Plan view of Lampasas River Bridge (Spans 4 to 5)	53
Figure 3-37: Section view of Lampasas River Bridge (Spans 1 to 3)	54
Figure 3-38: Section view of Lampasas River Bridge (Spans 4 to 5)	55
Figure 3-39: Reinforcement options, Lampasas River Bridge	56
Figure 3-40: Details of longitudinal splices, Lampasas River Bridge (Span 1 and Span 2).....	57

Figure 3-41: Details of longitudinal splices, Lampasas River Bridge (Span 4 and Span 5).....	58
Figure 3-42: Details of longitudinal splices, Lampasas River Bridge (Sections A-A and G-G)	58
Figure 3-43: Details of longitudinal splices, Lampasas River Bridge (Sections B-B and H-H)	58
Figure 3-44: Details of longitudinal splices, Lampasas River Bridge (Sections C-C and I-I)	59
Figure 3-45: Details of longitudinal splices, Lampasas River Bridge (Section D-D)	59
Figure 3-46: Details of longitudinal splices, Lampasas River Bridge (Section E-E)	59
Figure 3-47: Details of longitudinal splices, Lampasas River Bridge (Section F-F).....	59
Figure 3-48: Details of longitudinal splices, Lampasas River Bridge (Section J-J).....	60
Figure 3-49: Details of longitudinal splices, Lampasas River Bridge (Section K-K)	60
Figure 3-50: Details of longitudinal splices, Lampasas River Bridge (Section L-L)	60
Figure 3-51: Details of transverse splices, Lampasas River Bridge (Span 1 and Span 2).....	61
Figure 3-52: Details of transverse splices, Lampasas River Bridge (Span 4 and Span 5).....	61
Figure 3-53: Details of transverse splice, Lampasas River Bridge (Section M-M).....	61
Figure 3-54: Details of transverse splice, Lampasas River Bridge (Section N-N).....	62
Figure 3-55: Details of transverse splice, Lampasas River Bridge (Section O-O).....	62
Figure 3-56: Details of transverse splice, Lampasas River Bridge (Section P-P)	62
Figure 3-57: Details of transverse splice, Lampasas River Bridge (Section Q-Q).....	62
Figure 3-58: Details of transverse splice, Lampasas River Bridge (Section R-R)	63
Figure 3-59: Gage layout for longitudinal bars, Lampasas River Bridge.....	64
Figure 3-60: Gage layout for transverse bars, Lampasas River Bridge.....	64
Figure 3-61: Location of data-acquisition system, Lampasas River Bridge.....	65
Figure 3-62: View of top-mat reinforcement from south end, Lampasas River Bridge.....	65
Figure 3-63: Test area for Current TxDOT Standard Reinforcement, Lampasas River Bridge.....	66
Figure 3-64: Typical placement of Current TxDOT Standard Reinforcement, Lampasas River Bridge.....	66
Figure 3-65: Test area for Reduced Welded-Wire Reinforcement, Lampasas River Bridge	67
Figure 3-66: Typical placement of Reduced Welded-Wire Reinforcement, Lampasas River Bridge.....	67
Figure 3-67: Test area for Reduced Deformed-Bar Reinforcement, Lampasas River Bridge.....	68
Figure 3-68: Typical placement of Reduced Deformed-Bar Reinforcement, Lampasas River Bridge.....	68
Figure 3-69: Armor joint between Spans 2 and 3, Lampasas River Bridge	69
Figure 3-70: Side view of Lampasas River Bridge from north end.....	70
Figure 3-71: Side view of Lampasas River Bridge from south end	70
Figure 3-72: Typical field installation of VWG, Lampasas River Bridge.....	71

Figure 3-73: Making holes in bedding strip, Lampasas River Bridge	71
Figure 3-74: Checking gage before threading wire through the holes in bedding strip, Lampasas River Bridge.....	72
Figure 3-75: Sealing holes in bedding strip (Spans 1 and 2), Lampasas River Bridge	72
Figure 3-76: Split tube covering exposed parts of wires, Lampasas River Bridge.....	73
Figure 3-77: Data-acquisition box between Spans 1 and 2, Lampasas River Bridge.....	74
Figure 3-78: Data-acquisition box between Spans 4 and 5, Lampasas River Bridge.....	74
Figure 3-79: Scaffolding for accessing bent cap between Spans 4 and 5, Lampasas River Bridge.....	75
Figure 3-80: Inside of data-acquisition box placed on the bent between Spans 1 and 2, Lampasas River Bridge.....	75
Figure 3-81: Drilling holes on the side face of the bent caps for anchor bolts, Lampasas River Bridge.....	76
Figure 3-82: Mounting bracket for solar panel, Lampasas River Bridge	76
Figure 3-83: Solar panel mounted on side face of bent between Span 1 and 2, Lampasas River Bridge.....	77
Figure 3-84: Back side of the bracket showing wireless antenna, Lampasas River Bridge	77
Figure 3-85: Construction sequence for deck, Lampasas River Bridge	79
Figure 3-86: Result of cracking inspection of Lampasas River Bridge.....	80
Figure 3-87: Exposure of crack former, Lampasas River Bridge.....	80
Figure 3-88: Stresses in Current TxDOT Standard Reinforcement, Lampasas River Bridge (longitudinal direction)	81
Figure 3-89: Stresses in Reduced Deformed-Bar Reinforcement, Lampasas River Bridge (longitudinal direction)	82
Figure 3-90: Stresses in Reduced Welded-Wire Reinforcement, Lampasas River Bridge (longitudinal direction)	82
Figure 3-91: Stresses in Current TxDOT Standard Reinforcement, Lampasas River Bridge (transverse direction).....	83
Figure 3-92: Stresses in Reduced Deformed-Bar Reinforcement, Lampasas River Bridge (transverse direction)	83
Figure 3-93: Stresses in Reduced Welded-Wire Reinforcement, Lampasas River Bridge (transverse direction)	84
Figure 3-94: The area for calculation of longitudinal restraint moment, Lampasas River Bridge.....	85
Figure 3-95: The area for calculation of transverse restraint moment, Lampasas River Bridge.....	85
Figure 4-1: Region of the bridge deck simulated in the restrained-shrinkage test	87
Figure 4-2: Dimensions of restrained-shrinkage specimen	89
Figure 4-3: Terminology for restrained-shrinkage specimen	89
Figure 4-4: Mechanism of restrained shrinkage test.....	90
Figure 4-5: Components of restrained-shrinkage specimen	90

Figure 4-6: Attaching steel tube to back-to-back channels.....	91
Figure 4-7: Half-size precast, prestressed concrete panels (strands cut on one side).....	92
Figure 4-8: Wooden side forms with anchors, restrained-shrinkage test.....	92
Figure 4-9: Complete assembly of first bay, restrained-shrinkage test	93
Figure 4-10: Space between precast, prestressed panels, restrained-shrinkage test	93
Figure 4-11: Installing restraining rods, restrained-shrinkage test	94
Figure 4-12: Arrangement of Current TxDOT Standard Reinforcement, restrained-shrinkage test	95
Figure 4-13: Arrangement of Reduced Deformed-Bar Reinforcement, restrained-shrinkage test	95
Figure 4-14: Arrangement of reduced welded-wire reinforcement, restrained-shrinkage test.....	96
Figure 4-15: Gage layout for restrained-shrinkage test	97
Figure 4-16: Location of outlets for gage wires, restrained-shrinkage test	98
Figure 4-17: Complete gage installation for one bay of restrained-shrinkage test.....	98
Figure 4-18: Installation sequence for foil gages, restrained-shrinkage test	100
Figure 4-19: Gage instrumentation (foil gage and vibrating-wire gage).....	101
Figure 4-20: Deck-construction sequence, restrained-shrinkage test	103
Figure 4-21: Compressive strength from 4- \times 8-in. cylinder tests, restrained-shrinkage specimen	104
Figure 4-22: Long-term monitoring results from vibrating-wire gage, restrained-shrinkage test	105
Figure 4-23: Long-term monitoring results from foil gage, restrained-shrinkage test	105
Figure 4-24: Dimensions of the specimen for calculation	106
Figure 4-25: Restraint moment and cracking moment of the test frame	108
Figure 5-1: Apparatus (Chen, 1970) and Loading Schematic (Marti, 1989) for the Double-Punch Test.....	111
Figure 5-2: Modified Mohr-Coulomb Criterion for Concrete (W. Chen 1970)	112
Figure 5-3: Bearing Capacity of a Double-Punch Test (Chen, 1970).....	113
Figure 5-4: Two Possible DPT Collapse Mechanisms with (a) Three and (b) Four Radial Fracture Planes (Pros, Diez, & Molins, 2010)	115
Figure 5-5: Damage Profiles for (a) Split-Cylinder Test and (b) Double-Punch Test Loading on Plain Concrete Cylinders (Pros, Diez, & Molins, 2010)	116
Figure 5-6: Comparison of Test Specimen Weights for Current FRC Testing Procedures vs. Double-Punch Test.....	119
Figure 5-7: Combined Results - Selected DPT Performance Curves showing Effect of Fiber Type and Volume Fraction at 0.75% Fiber Content.....	123
Figure 5-8: Combined Results - Selected DPT Performance Curves showing Effect of Fiber Type and Volume Fraction at 1.00% Fiber Content.....	123

Figure 5-9: Combined Results - Selected DPT Performance Curves showing Effect of Fiber Type and Volume Fraction at 1.50% Fiber Content.....	124
Figure 5-10: Effect of Fiber Type and Volume Fraction on Crack Widths and Cracking Pattern	125
Figure 5-11: Effect of Misaligned Steel Punches in DPT shown (a) Schematically and (b) for Trial Specimen	126
Figure 5-12: Steel Punch Centering Guide and Masking Tape Used to Secure Against Eccentric Loading Effects.....	126
Figure 5-13: Schematic of Shakedown Procedure for DPT Experiments	127
Figure 5-14: Typical DPT Performance Curve Showing Key Test Parameters	129
Figure 6-1: Gage layout for Current TxDOT initial prestressed panel from Plant A (Foreman 2010).....	132
Figure 6-2: Gage layout for Current TxDOT initial prestressed panel from Plant B (Foreman 2010).....	133
Figure 6-3: Gage layout for Reduced initial prestressed panel from Plants A and B (Azimov 2012).....	134
Figure 6-4: Stacking panels at Ferguson Laboratory (Azimov 2012)	135
Figure 6-5: Stacked panels at Ferguson Laboratory	135
Figure 6-6: Campbell Scientific CR 5000 data logger.....	136
Figure 6-7: Steel box for data logger	136
Figure 6-8: Wooden box for data logger.....	137
Figure 6-9: Hand-held reader for VWGs (Model GK-404, Geokon)	137
Figure 6-10: Long-term monitoring results, Current TxDOT initial prestress	138
Figure 6-11: Long-term monitoring results, Reduced initial prestress	139
Figure 6-12: Typical long-term monitoring data	140
Figure 6-13: Prestress losses during first month after casting	141
Figure 6-14: Calculations of prestress losses using AASHTO and TxDOT procedures.....	143
Figure 6-15: Measured tensile strains in all test panels in transverse direction (Foreman 2010, Azimov 2012)	144
Figure 6-16: Strain variation in Current TxDOT initial prestressed panel during first week after release	146
Figure 6-17: Strain variation in Reduced initial prestressed panel during first week after release	146
Figure 6-18: Long-term prestress in the Current TxDOT initial prestressed panels	147
Figure 6-19: Long-term prestress losses in the Reduced initial prestressed panels.....	148
Figure 6-20: Long-term monitoring results of the Current TxDOT and the Reduced initial prestressed panels	149
Figure B-1: Longitudinal restraint moment due to M_s	172
Figure B-2: Longitudinal restraint moment due to M_d	172
Figure B-3: Transverse restraint moment due to M_p	175

Figure B-4: Transverse restraint moment due to M_s	175
Figure B-5: Transverse restraint moment due to M_d	176
Figure D-1: Flow chart for proposing new equation for predicting prestress loss in PCPs.....	187
Figure D-2: Curve fitting result for Plant A	191
Figure D-3: Curve fitting result for Plant B.....	191
Figure D-4: Measured and predicted prestress losses, Current TxDOT initial prestress, Plant A	193
Figure D-5: Measured and predicted prestress losses, Current TxDOT initial prestress, Plant B.....	194
Figure D-6: Measured and predicted prestress losses, Reduced initial prestress, Plant A	194
Figure D-7: Measured and predicted prestress losses, Reduced initial prestress, Plant B.....	195
Figure E-1: Test Specimen Positioned in (a) Jig for Aligning Cylinder and Bearing Strips and in Testing Machine for Determination of Splitting Tensile Strength (ASTM C496 2011).....	202
Figure E-2: Beam with Three-Point Loading Test Setup (ASTM C1609 2010).....	204
Figure E-3: Schematic of Japanese Yoke Loading System (Chen and Mindess 1995).....	204
Figure E-4: Test Arrangement to Obtain Net Deflection via Japanese Yoke Loading System (ASTM C1609 2010)	204
Figure E-5: Variability of ASTM C1609 for Replicate Specimens in the (a) Load vs. Deflection Curves and (b) Location of Major Cracks (S.-H. Chao 2011).....	207
Figure E-6: Schematic of Apparatus with Stainless Steel Plate and Suitable Support Frame (ASTM C1399 2010).....	208
Figure E-7: Typical Load-Deflection Curve (ASTM C1399 2010)	209
Figure E-8: Schematic of Specimen Cross Sections to Indicate Permitted Flexural Tensile Surfaces during Testing (ASTM C1399 2010).....	210
Figure E-9: Effect of Steel Plate on Determining Performance Immediately After First Crack – adapted from (ASTM C1399 2010)	211
Figure E-10: Testing Arrangement using Suggested Round Panel Support Fixture (ASTM C1550 2010).....	212
Figure E-11: Rolling Steel Form after Molded Specimen Has Gained Sufficient Strength (ASTM C1550 2010)	213
Figure E-12: Manual Spraying of Shotcrete Panels (ASTM C1550 2010)	213
Figure E-13: (a) Profile and (b) Plan Views of Suggested Method of Deflection Measurement to Exclude Load-Train Deformations Using an LVDT (ASTM C1550 2010).....	214
Figure E-14: View from (a) Below and (b) Above Tested Round Panel Specimen Showing Location of Major Cracks (S.-H. Chao 2011)	215
Figure E-15: View of Underside of ASTM C1550 Test Specimen showing Crack Width vs. LVDT Probe Width at Location of LVDT (S.-H. Chao 2011)	215
Figure E-16: Setup for EFNARC Panel Test (EFNARC 1996)	216
Figure E-17: Uniaxial Direct Tensile Test Specimen Dimensions (S.-H. Chao 2011)	217

Figure E-18: Uniaxial Direct Tensile Test (a) Mold and (b) Testing Arrangement (S.-H. Chao 2011).....	218
Figure E-19: Replicate Specimen Results for Uniaxial Direct Tensile Test (S.-H. Chao 2011)	218
Figure E-20: Variability of Uniaxial Tensile Test in Location of Major Cracks for Four Replicate Specimens with 1.5% Fiber Content (S.-H. Chao 2011)	219
Figure F-1: Types of fiber used in first phase of study for DPT: (a) Type 1 (royal, single-bend hooked at end); (b) Type 2 (Bekaert short, double-bend hooked at end); (c) Type 3 (Bekaert long, double-bend hooked at end).....	222
Figure F-2: Typical procedure for mixing concrete: (a) batching of materials; (b) gradual addition of water to prepare workable paste	223
Figure F-3: Typical procedure for mixing concrete (continued): (c) adding coarse aggregate; (d) adding steel fibers.....	224
Figure F-4: Preparation of Phase 1 specimens at UT Arlington.....	226
Figure F-5: Preparation of 6-in. × 6-in. DPT specimens, Phase 1 at UT Arlington	227
Figure F-6: Setup for DPT, Phase 1 at UT Arlington.....	228
Figure F-7: Typical stages of testing for Phase 1 at UT Arlington (DPT and compressive-strength tests)	229
Figure F-8: Examples of mixing difficulties in Phase 1 with high fiber-volume fractions	230
Figure F-9: Steel molds used to prepare specimens in Phase 3 at UT Arlington	232
Figure F-10: Helix (twisted fiber) added in Phase 4 at UT Arlington	233
Figure F-11: Test setup used for Phase 4 testing at UT Arlington	235
Figure F-12: Typical test specimens with various fiber volume fractions (Phase 4, UT Arlington).....	236
Figure F-13: Steel fibers used in Phase 5 at UT Arlington.....	238
Figure F-14: Equivalent tensile strengths from Phase 1 DPT at UT Arlington.....	243
Figure F-15: Selection of 0.1-in deformation to determine residual strength.....	245
Figure F-16: Comparison of residual strengths at 0.1-in. deformation, Phase 1 of DPT at UT Arlington.....	247
Figure F-17: Average DPT curves for plain concrete versus SFRC specimens, Phase 1 of DPT at UT Arlington: (a) SFRC-R, (b) SFRC-BS, and (c) SFRC-BL.....	248
Figure F-18: Average load-deformation curves for DPT for plain concrete versus SFRC specimens, Phase 1 of DPT at UT Arlington: volume fraction of (a) 0.50%, (b) 0.75%, (c) 1.0%, and (d) 1.5%	249
Figure F-19: Comparison of Equivalent Tensile Strengths, Phase 2 of DPT, UT Arlington	250
Figure F-20: Comparison of residual strengths at 0.1-in. deformation, Phase 2, UT Arlington.....	251
Figure F-21: Average load-deformation curves for plain concrete and SFRC specimens, Phase 2, UT Arlington: (a) SFRC-R, (b) SFRC-BS, and (c) SFRC-BL.....	253
Figure F-22: Average load-deformation curves for plain concrete and SFRC specimens, Phase 2, UT Arlington: (a) 0.75%, (b) 1.0%, and (c) 1.50%	254

Figure F-23: Typical cracking patterns, DPT, Phase 2, UT Arlington	255
Figure F-24: Peak equivalent tensile strengths, Phase 3, UT Arlington.....	257
Figure F-25: Residual strengths at 0.1-in. deformation, Phase 3, UT Arlington.....	258
Figure F-26: Load-deformation curves for plain concrete and SFRC specimens with different types of fibers, Phase 3, UT Arlington: (a) SFRC-R, (b) SFRC-BS, and (c) SFRC-BL.....	259
Figure F-27: Load-deformation curves for plain concrete and SFRC specimens with different volume fractions of fibers, Phase 3, UT Arlington: (a) 0.50%, (b) 0.75%, (c) 1.0%, and (d) 1.50%	260
Figure F-28: Load-deformation curves for (a) Phase 1 with SFRC-R-075 (Type 1 fiber 0.75%) and (b) Phase 3 with SFRC-R-075 (Type 1 fiber 0.75%)	261
Figure F-29: Peak equivalent tensile strengths, Phase 4, UT Arlington.....	262
Figure F-30: Comparison of residual strengths at 0.1-in. deformation for different fiber types, Phase 4, UT Arlington.....	263
Figure F-31: Comparisons of plain concrete and SFRC specimens with different types of fibers, Phase 4, UT Arlington: (a) SFRC-R, (b) SFRC-BS, (c) SFRC-BL, and (d) SFRC-H.....	265
Figure F-32: Comparisons of plain concrete and SFRC specimens with different volume fractions, Phase 4, UT Arlington: (a) 0.50%, (b) 0.75 %, (c) 1.0%, (d) 1.5%, and (e) 2.0%.....	266
Figure F-33: Photographs of typical double-punch specimens, Phase 4, UT Arlington	268
Figure F-34: Other material test setups for SFRC	269
Figure F-35: Load-deformation curves from DPT.....	272
Figure F-36: Load-deflection curves from third-point bending test (ASTM C1609).....	273
Figure F-37: Load-deflection curves from direct tension test	274
Figure F-38: Comparative strengths of three test methods (DPT, bending, DTT).....	276
Figure F-39: Load-deflection curves for top versus bottom portions of cylinders used in DPTs, UT Arlington.....	277
Figure F-40: Load-deformation curves from DPT with HYB1, UT Arlington	278
Figure F-41: Comparison of load-deformation curves for two SFRC specimens: (a) Hybrid (0.75% Type 5 fiber + 0.75 Type 6 fiber) and (b) HYB2 (0.50% Type 5 fiber +1% Type 6 fiber) (Phase 5, UT Arlington)	279
Figure F-42: Comparison of load-deformation curves for two hybrid specimens with the same type of steel fibers and the same volume fraction, but different concrete mixtures: (a) HYB3 and (b) HYB4 (Phase 5, UT Arlington).....	279
Figure F-43: Comparison of load-deflection curves for two specimens with the same concrete mix but with different methods of preparation: (a) ML-075(1) and (b) +ML-075(2) (Phase 5, UT Arlington)	280
Figure F-44: Comparison of stiffness between different concrete mixtures with different types of fibers (Phase 5, UT Arlington).....	281
Figure F-45: Comparison of average total crack widths at different deformations for different DPT specimens (Phase 5, UT Arlington).....	282

Figure F-46: Load-deflection curve for hybrid mortar specimens (2% Type 6 and 1% Type 7 Steel Fibers) (Phase 5, UT Arlington)	283
Figure F-47: Testing matrix for DPT research and testing program	287
Figure F-48: Nomenclature used to identify specimens for DPT research and testing program.....	287
Figure F-49: Royal™ steel fibers	288
Figure F-50: Bekaert Dramix® steel fibers	288
Figure F-51: Royal vs. Bekaert fiber type	289
Figure F-52: SFRC mixing sequence, Step 2	290
Figure F-53: SFRC mixing sequence, Step 3	290
Figure F-54: SFRC mixing sequence, Step 4	291
Figure F-55: SFRC mixing sequence, Step 5	291
Figure F-56: Example of “clumping” and “balling” of fibers observed during mixing	291
Figure F-57: SFRC mixing sequence, Step 6	292
Figure F-58: SFRC mixing sequence, Step 7	292
Figure F-59: SFRC mixing sequence, Step 8	293
Figure F-60: Using wet-saw to cut 6 x 12-in. cylinder in half.....	294
Figure F-61: Schematic showing surface roughness on top and bottom surfaces of cylinder due to mold	295
Figure F-62: Surface-grinding (SG) uneven faces of test specimens	296
Figure F-63: Process of applying hydro-stone to rough faces of test specimen	297
Figure F-64: Schematic of DPT arrangement on 60-kip Baldwin UTM (hydraulic)	298
Figure F-65: DPT setup on 60-kip Baldwin UTM (hydraulic).....	299
Figure F-66: Schematic of DPT arrangement on 120-kip Olsen UTM (screw-type).....	299
Figure F-67: DPT setup on 120-kip Olsen UTM (screw-type).....	300
Figure F-68: Effect of misaligned steel punches in DPT shown (a) schematically and (b) for trial specimen	301
Figure F-69: Steel punch centering guide and masking tape used to secure against eccentric loading effects	301
Figure F-70: Schematic of shakedown procedure for DPT experiments.....	302
Figure F-71: Typical DPT performance curve showing key test parameters	304
Figure G-1: Effect of fiber type and volume fraction on (a) coefficient of variation and (b) average value of initial slope.....	306
Figure G-2: Effect of fiber type and volume fraction on (a) coefficient of variation and (b) average value of peak load	307
Figure G-3: Effect of fiber type and volume fraction on (a) coefficient of variation and (b) average value of residual strength.....	308
Figure G-4: Effect of surface preparation on (a) coefficient of variation and (b) average value of initial slope for royal fiber type	310

Figure G-5: Effect of surface preparation on (a) coefficient of variation and (b) average value of peak load for royal fiber type.....	311
Figure G-6: Effect of surface preparation on (a) coefficient of variation and (b) average value of residual strength for royal fiber type.....	312
Figure G-7: DPT performance curves showing effect of surface preparation on initial slope parameter	313
Figure G-8: Effect of test machine on (a) coefficient of variation and (b) average value of initial slope for Bekaert fiber type	314
Figure G-9: Effect of test machine on (a) coefficient of variation and (b) average value of peak load for Bekaert fiber type.....	315
Figure G-10: Effect of test machine on (a) coefficient of variation and (b) average value of residual strength for Bekaert fiber type	316
Figure G-11: Calibration setup for Baldwin (left) and Olsen (right) UTMs	317
Figure G-12: Tangent stiffness calibration curves.....	318
Figure G-13: Effect of cylinder portion (casting) on (a) coefficient of variation and (b) average value of initial slope for Bekaert fiber type.....	320
Figure G-14: Effect of cylinder portion (casting) on (a) coefficient of variation and (b) average value of peak load for Bekaert fiber type	321
Figure G-15: Effect of cylinder portion (casting) on (a) coefficient of variation and (b) average value of residual strength for Bekaert fiber type	322
Figure G-16: Effect of casting on (a) the fiber distribution and (b) the number of fibers crossing crack planes in top and bottom test specimens.....	323

List of Tables

Table 1-1: Research Team for Project 0-6348.....	1
Table 1-2: Project Monitoring Committee (PMC) for Project 0-6348	1
Table 2-1: Use of CIP-PCP bridge decks by state (Sneed et al. 2010).....	8
Table 2-2: Test Specimens Required for Current FRC Testing Procedures	24
Table 2-3: Simplicity, Reliability, and Reproducibility of Current FRC Testing Procedures.....	25
Table 3-1: Properties of top-mat reinforcement, Lampasas River Bridge.....	65
Table 3-2: Material costs of each top-mat option	85
Table 4-1: Reinforcement options for restrained-shrinkage test.....	88
Table 4-2: Concrete mixture proportions (by weight), restrained-shrinkage test.....	101
Table 4-3: Details of top-mat reinforcement for restraint-moment calculation.....	107
Table 5-1: Tensile Strength Computed from Double-Punch Tests on Plain Concrete Cylinders – modified from (Chen, 1970).....	114
Table 5-2: Comparison of the Specific Failure Surface of Test Specimens for Current FRC Test Methods vs. Double-Punch Test.....	118
Table 6-1: Summary of fabrication of panels	131
Table 6-2: Summary of results from prestress-loss monitoring.....	138
Table 6-3: Average environmental conditions of both plants during the first month after casting	141
Table 6-4: Calculated prestress losses - AASHTO 2004.....	142
Table 6-5: Calculated prestress losses - AASHTO 2008.....	142
Table 6-6: Typical tensile strengths and corresponding strains using two different tensile test methods	143
Table 6-7: Average measured tensile strain and stress depending on existence of additional transverse edge bar and type of coarse aggregate.....	145
Table 7-1: Simplicity, Reliability, and Reproducibility of Current FRC Testing Procedures vs. Double-Punch Test	155
Table D-1: Resultant values for constants CSH and CCR.....	192
Table D-2: Constant values and parameters for Equation 5-45	192
Table D-3: Comparative accuracy by residual method.....	198
Table D-4: Summary of statistical analysis results for accuracy	199
Table F-1: Properties of steel fibers used in Phase 1 at UT Arlington	221
Table F-2: Mixture proportions by weight used in Phase 1 at UT Arlington.....	222
Table F-3: Specimens for Phase 1 at UT Arlington.....	225
Table F-4: Phase 2 specimens tested at UT Arlington.....	230
Table F-5: Mixture proportions by weight for Phase 3 at UT Arlington.....	231

Table F-6: Specimens tested in Phase 3 at UT Arlington.....	232
Table F-7: Mixture proportions used in Phase 4 at UT Arlington.....	233
Table F-8: Properties of Helix fiber added in Phase 4 at UT Arlington.....	233
Table F-9: Phase 4 specimens tested at UT Arlington.....	234
Table F-10: Steel fibers used in Phase 5 at UT Arlington.....	239
Table F-11: Mixture proportions by weight used in Phase 5 at UT Arlington (comparison of test methods).....	239
Table F-12: Mixture proportions by weight used for Phase 5 at UT Arlington (post-cracking behavior and strain-hardening).....	240
Table F-13: Specimens in Phase 5 of DPT (UT Arlington).....	240
Table F-14: Hybrid-fiber specimens in Phase 5 of DPT (UT Arlington).....	241
Table F-15: Mixture proportions by weight used for mortar specimens in Phase 5 of DPT (UT Arlington).....	242
Table F-16: Results from Phase 1 of DPT at UT Arlington.....	243
Table F-17: Peak strength of specimens using Type 3 fibers (SFRC-BL) versus specimens using Type 1 fibers (SFRC-R) and specimens using Type 2 fiber (SFRC-BS) (First Phase).....	244
Table F-18: Residual strengths at 0.1-in. deformation, Phase 1 of DPT at UT Arlington.....	246
Table F-19: Comparison of residual strengths at 0.1-in. deformation for specimens with Type 3 fibers (SFRC-BL) and specimens with Type 2 fibers (SFRC-BS), Phase 1 of DPT, UT Arlington.....	247
Table F-20: Average peak load and equivalent tensile strength, Phase 2 of DPT, UT Arlington.....	250
Table F-21: Peak strengths of specimens with Type 3 fiber versus specimens with Type 1 and Type 2 fiber, Phase 2, UT Arlington.....	250
Table F-22: Residual strength at 0.1-in. deformation, Phase 2, UT Arlington.....	251
Table F-23: Residual strength of specimens with Type 3 fibers versus specimens with Type 1 and Type 2 fibers, Phase 2, UT Arlington.....	252
Table F-24: Average peak load and equivalent tensile strength, Phase 3, UT Arlington.....	256
Table F-25: Peak strengths of specimens with Type 3 fibers and specimens with Type 1 or Type 2 fibers, Phase 3, UT Arlington.....	257
Table F-26: Residual strengths at 0.1-in. deformation, Phase 3, UT Arlington.....	258
Table F-27: Residual strengths of specimens with Type 3 fibers versus specimens with Type 1 or Type 2 fibers, Phase 3, UT Arlington.....	258
Table F-28: Average peak load and equivalent tensile strength, Phase 4, UT Arlington.....	262
Table F-29: Peak strengths of SFRC specimens with Type 3 fibers versus specimens with Type 1, Type 2, or Type 4 (Helix) fibers, Phase 4, UT Arlington.....	263
Table F-30: Comparisons of residual strength at 0.1-in. deformation, Phase 4, UT Arlington.....	264
Table F-31: Comparison of residual strengths of specimens with Type 3 fibers versus specimens with Type 1, 2, or 4 fibers, Phase 4, UT Arlington.....	264

Table F-32: Average toughness at 0.10-in. deformation, Phase 4, UT Arlington	267
Table F-33: Comparison of peak loads and COVs between DPT and other material test methods for SFRC.....	270
Table F-34: Comparison of residual strengths and toughnesses (and corresponding COVs) for DPT versus other material test methods for SFRC.....	271
Table F-35: Residual strengths for third-point bending test (ASTM C1609) as per ACI 318-11	275
Table F-36: Summary results for Phase 5 (post-cracking evaluation of DPT), UT Arlington.....	278
Table F-37: Summary of results from additional DPTs (Phase 5, UT Arlington).....	283
Table F-38: Comparison of average COVs for Phases 1 through 4 of DPT (UT Arlington)	284
Table F-39: Comparison of average COVs for DPT, bending test, and DTT (UT Arlington).....	285
Table F-40: Verification of average residual strengths to meet requirements of ACI 318-11 for use of steel fibers for shear resistance	285
Table F-41: Concrete mixture proportions	289
Table F-42: (a) Batch quantities and (b) fresh and hardened concrete properties of SFRC mixtures used in DPT experiments	293
Table G-1: Comparison between initial slopes from DPT and calibration test	317

Chapter 1. Introduction

1.1 Background of Project 0-6348

Texas Department of Transportation (TxDOT) Project 0-6348, “Controlling Cracking in Prestressed Concrete Panels and Optimizing Bridge Deck Reinforcing Steel,” began September 1, 2008 and ended August 31, 2012. The objectives of Project 0-6348 are as follows. Each objective is discussed further in subsequent sections of this report.

- 1) Optimize reinforcement in the cast-in-place (CIP) concrete placed on bridge decks; and
- 2) Identify ways of controlling cracking in precast, prestressed bridge deck panels.

The project was also tasked with developing test methods for comparing the behavior of different types of high-performance steel fibers in concrete elements, including bridge decks.

As shown in Table 1-1, the research team for Project 0-6348 consisted of Profs. Richard Klingner, Oguzhan Bayrak, and James Jirsa from The University of Texas at Austin (Center for Transportation Research) and Prof. Shih-ho (Simon) Chao from the University of Texas at Arlington.

Table 1-1: Research team for Project 0-6348

Name	Agency	Duty
Richard E. Klingner	UT Austin / CTR	Research Supervisor
Oguzhan Bayrak.	UT Austin / CTR	Researcher
James O. Jirsa	UT Austin / CTR	Researcher
Shih-Ho (Simon) Chao	UT Arlington	Researcher

The Project Monitoring Committee (PMC) for Project 0-6348 is shown in Table 1-2.

Table 1-2: Project Monitoring Committee (PMC) for Project 0-6348

Name	Agency	Duty
Manuel (Bernie) Carrasco, PE	Bridge Division (BRG)	Project Director
Graham Bettis, PE	Construction Division (CST)	Project Advisor
Robert Cochrane, PE	Bryan District (BRY)	Project Advisor
David Hohmann, PE	Bridge Division (BRG)	Project Advisor
John Holt, PE	Bridge Division (BRG)	Project Advisor
Kirk Krause	Waco District (WAC)	Project Advisor
John Vogel, PE	Houston District (HOU)	Project Advisor
Wade Odell, PE	Research Technology and Implementation Office (RTI)	Research Engineer

1.2 Background on Precast, Prestressed Panels

Since a CIP bridge deck on Precast, prestressed concrete panels (PCPs) was first used in a bridge on the Illinois Tollway project in the 1950s (Barker 1975), this system has been used world-wide (Goldberg 1987). The Texas Department of Transportation (TxDOT) uses it for approximately 85% of the bridges in Texas (Merrill 2002).

In this system, shown in Figure 1-1 and Figure 1-2, PCPs span between the adjacent girders and serve as stay-in-place forms for the CIP concrete slabs. Panels, 4-in. thick and 8-ft wide with lengths that vary according to girder spacing are commonly used in Texas. Dimensions of the panels differ from state to state (Sneed *et al.* 2010). In Texas, PCPs have 16 strands spaced at 6 in. on centers and located at mid-depth of the panels. After the PCPs are placed on the top flange of adjoining girders, the top mat reinforcement is placed and a CIP concrete slab is cast to produce an 8-in. thick deck.

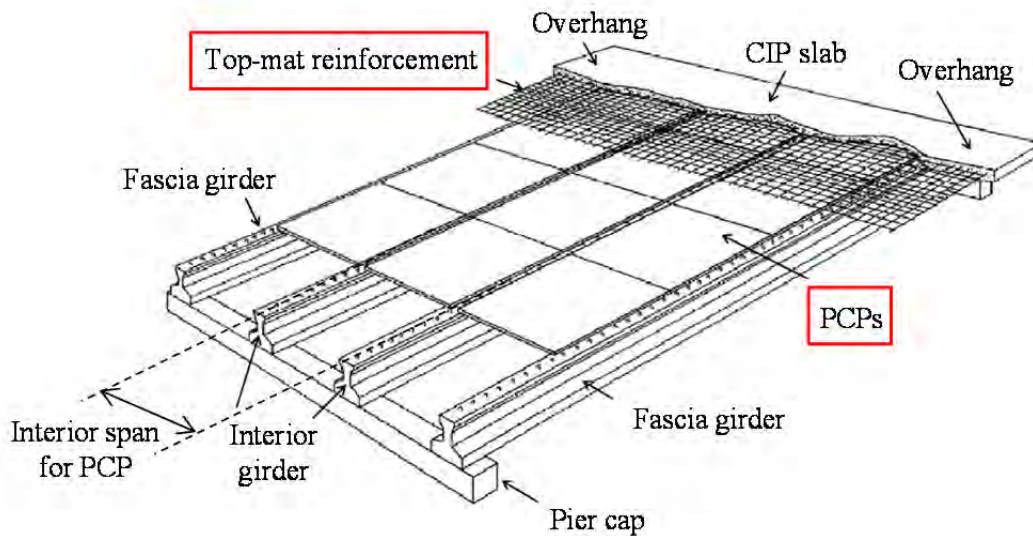


Figure 1-1: CIP-PCP bridge deck (adapted from Buth et al. (1972))

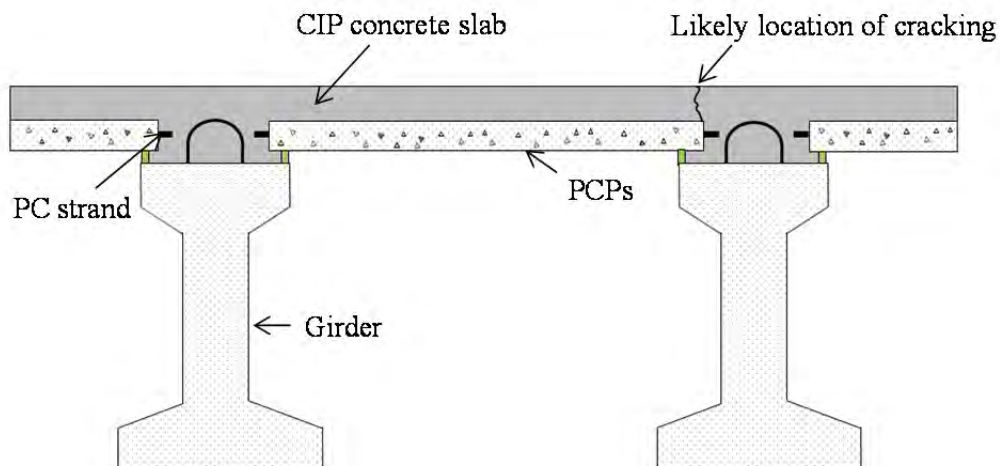


Figure 1-2: CIP-PCP bridge deck (section view)

CIP-PCP bridge decks have many advantages compared to decks which use only CIP concrete. The CIP-PCP system requires significantly less formwork, which reduces cost and time for construction. Increasing construction speed reduces the time that workers are exposed to construction hazards. Moreover, CIP-PCP bridge decks are suitable for bridges constructed in sensitive sites such as sites over water or sites with limited construction access.

1.3 Issues Addressed in Study 6348

The design recommendations of this study are intended to contribute to more cost-effective design of CIP-PCP bridge decks by reducing the amount of steel in CIP concrete, and by decreasing the number of rejected panels. They also permit TxDOT to compare the effectiveness of different types of high-performance steel fibers.

1.3.1 Cracking of Bridge Decks

Bridge decks tend to crack at the interface between PCPs or at the PCP-to-CIP transition over the girder (Figure 1-2). The cracks at panel joints are caused by shrinkage in the CIP portion of the deck and creep in the PCPs (Merrill 2002). The cracks do not affect the strength of the bridge decks, but can cause serviceability problems such as corrosion of reinforcement due to ingress of deicing agents or damage due to freeze-thaw cycles (Sprinkel 1985; Goldberg 1987). To eliminate serviceability problems in CIP concrete slabs, TxDOT requires a minimum amount of reinforcement in both directions. Coselli (2004) indicates that current CIP slabs, especially for interior span, have much higher strength due to arching action than the strength determined in the design stage. No serious serviceability problems should develop under service loads. Therefore, it is possible that current reinforcement details can be optimized by reducing the amount of reinforcing steel in the CIP slabs (Coselli 2004). Current reinforcement requirements in Texas for CIP slabs are No. 4 bars spaced 9 in. on center in the longitudinal direction and No. 5 bars spaced 6 in. on centers in the transverse direction.

In previous research in Project 6348 (Foster 2010), the following issues are verified: i) the longitudinal reinforcement currently required by TxDOT cannot be reduced; ii) transverse reinforcement can be further optimized; and iii) to determine an optimized reinforcement detail in the transverse direction, CIP-PCP interaction must simulate as closely as possible the boundary conditions in actual bridges.

To optimize reinforcement details in the transverse direction considering CIP-PCP interaction, bridge decks under construction were instrumented and large-scale restrained-shrinkage tests were conducted. Several reinforcement options, including welded-wire reinforcement (WWR), were selected based on the test results from previous research in Project 6348 (Foster 2010). The selected options were installed in bridges near Houston and Belton. Their behavior after construction was monitored, and was evaluated by comparing observed strains to calculated cracking strains. The width and pattern of cracking in the instrumented bridges were inspected periodically. To evaluate the behavior of various reinforcement options, large-scale restrained-shrinkage tests were also conducted.

1.3.2 Collinear Cracking of Precast, Prestressed Panels

Significant numbers of PCPs are rejected due to cracking that occurs during fabrication and transportation. The cracks usually form as shown in Figure 1-3. To be accepted by TxDOT, the following conditions should be satisfied (TxDOT 2004):

- i) any cracks parallel to strands should not occur within 1 in. of the strand and their length should be less than $1/3$ of the total length of the embedded strands
- ii) any transverse cracks should not cross two adjacent strands

If the rejection rate of PCPs is reduced, construction cost and time for fabricating additional PCPs can be reduced.

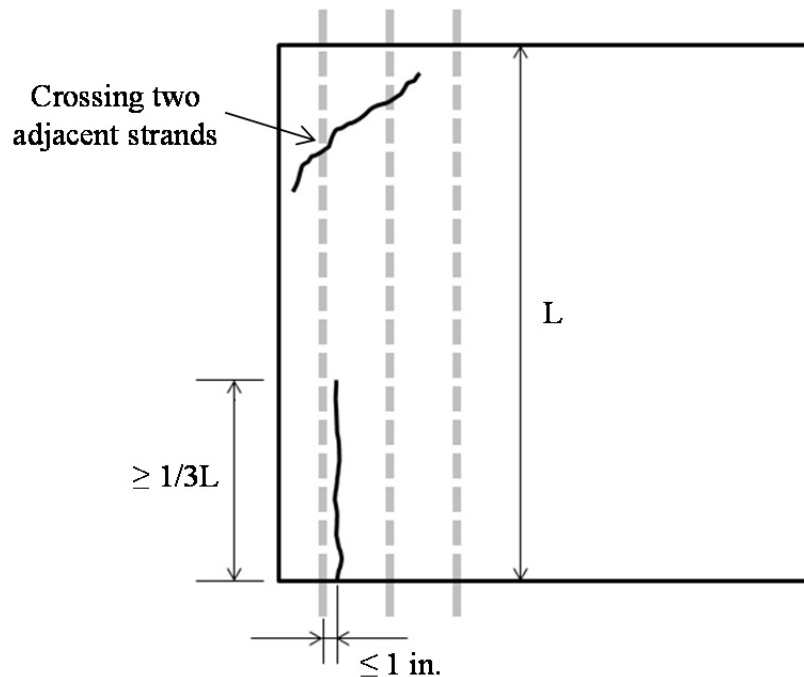


Figure 1-3: Criteria for rejection of precast panel

In previous research conducted as part of Project 6348 (Foreman 2010; Azimov 2012), design options were suggested to control cracking in PCPs. One option was to reduce initial prestress force, and the other was to place additional transverse reinforcement at the edges of the panels.

Long-term prestress loss in PCPs with different levels of initial prestress was measured and the results were compared with losses predicted using models that were developed based on the test results of prestressed beams and girders. Some of the equations in codes may give reasonable results for PCPs because they were developed from the test results that exhibited wide scatter. However, they do not consider characteristics of PCPs, so they may not be accurate for all cases. Therefore, the available data on PCPs was analyzed and a model for losses in PCPs was developed.

1.3.3 Validation of Test Methods for Comparing the Effectiveness of High-Performance Steel Fibers

A series of material tests on steel fiber-reinforced concrete (SFRC) specimens were proposed by UT Austin and UT Arlington to determine the feasibility of using SFRC in bridge deck applications. The purpose was to quantify the mix compositions, fiber types, and fiber dosages that could be used to enhance the durability and extend the service life of bridge decks by controlling cracking.

However, in order to quantify steel fiber-reinforced concrete mixtures for both CIP and PCP bridge deck applications, a material test capable of predicting the performance of SFRC for field loading conditions is first necessary. Following an extensive literature review of test methods used for concrete, it was determined that the Double-Punch Test (DPT), originally introduced by Chen in 1970 for *plain concrete*, could be extended to evaluate the behavior of *fiber-reinforced concrete* composites. As shown in Figure 1-4, in the DPT, a concrete cylinder is placed vertically between the loading platens of the test machine and compressed by two steel punches located concentrically on the top and bottom surfaces of the cylinder (Chen, 1970). The DPT loading results in indirect tension along radial planes of the cylinder specimen.

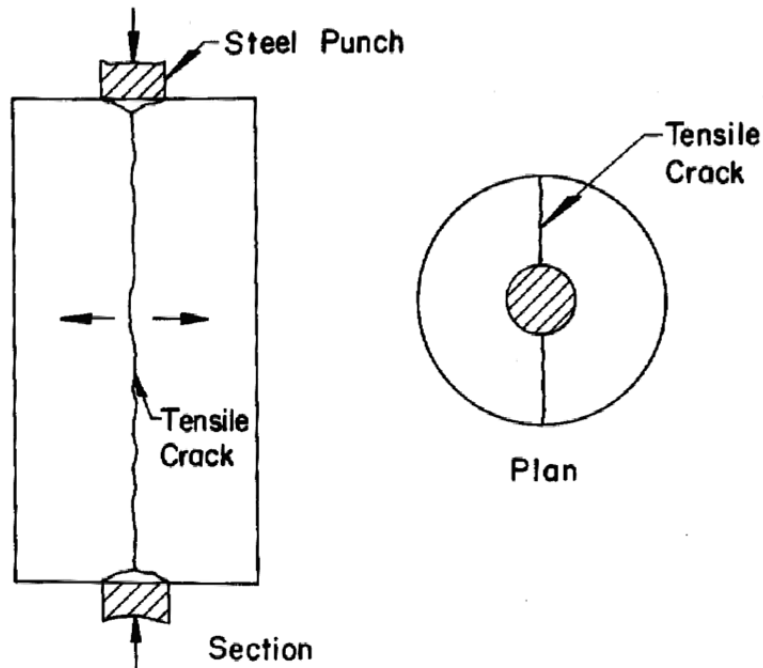


Figure 1-4: Schematic of DPT (Chen, 1970)

Chapter 2. Literature Review

2.1 Introduction to CIP-PCP Bridge Decks

A CIP-PCP bridge deck consists of precast, prestressed concrete panels (PCPs) and a cast-in-place (CIP) concrete deck. As shown in Table 2-1, it has been used in many states (Sneed *et al.* 2010).

The thickness of PCPs ranges from 3 to 6 in., with the most common thickness being 3.5 in. Specified compressive strengths of concrete for PCPs are generally greater than those of the CIP topping. Specified concrete strengths of PCPs range from 4,000 to 10,000 psi; those of the CIP topping range from 3,500 to 5,800 psi. The trend for PCPs is towards higher compressive strength and reduced panel thickness.

Six states have been using CIP-PCP bridge decks for fewer than 20 years; three states have been using the system for 20 to 30 years; and three states have been using the system for 30 to 40 years.

The CIP-PCP bridge decks have following advantages:

- i) Fast construction;
- ii) Less formwork;
- iii) Easy construction at sensitive sites; and
- iv) Better durability

Table 2-1: Use of CIP-PCP bridge decks by state (Sneed et al. 2010)

State	PCPs			CIP topping		Ages (year)
	Thickness (in.)	Reinforcement type	f_c' (psi)	Curing method	f_c' (psi)	
Arkansas	-	EC	5,800	MC	5,800	-
Colorado	-	PR, MR	5,000	LM, WC	5,000	16
Florida	-	PR, EC	-	-	-	40
Georgia	6	PR, MR	5,000	MC, WC	3,500	28
Hawaii	3.5	PR, MR	6,000	MC, LM	4,000	14
Iowa	3.5	PR, EC, MR	10,000	WC	3,500	25
Kansas	3-3.5	PR, EC	4,000	MC	4,000	20
Kentucky	-	PR, EC		MC	5,000	10
Michigan	-	EC	4,000	MC	4,000	-
Minnesota	3.5	PR, EC, WWR	6,000	MC	4,000	8
Missouri	3	PR	6,000	MC, LM	4,000	35
Oklahoma	4	PR	5,000	MC	4,000	15
Tennessee	3.5-4	PR	4,000	MC, LM	4,000	33
Texas	4	PR	5,000	MC, WC	4,000	25

PR=Prestressing reinforcement, EC=Epoxy-coated reinforcement, WWR=Welded-wire reinforcement, MR=Uncoated mild reinforcement, MC=Moisture curing, WC=Water-proof curing, LM=Liquid membrane curing

2.2 Issues in CIP-PCP Bridge Decks

To identify key aspects of the behavior of CIP-PCP bridge decks, in-depth literature reviews were conducted as part of Project 6348 by Foster (2010), Foreman (2010), Azimov (2012), and Kwon (2012). In this report, those reviews are combined.

2.2.1 Issues in CIP Slabs

Arching action in bridge decks

Most bridge decks have greater flexural strength than is customarily assumed in design, because of arching action. Arching action increases strength because of the in-plane restraint in a deck from surrounding portions of the deck. This horizontal restraint results in compressive membrane action. This phenomenon was defined by Ockleston (1958), and has been studied by many researchers. The effects of the compressive membrane forces on flexural strength of deck are negligible before cracking, but the compressive membrane force could cause considerable increase of flexural strength of the deck after cracking (Fang *et al.* 1986; Fang *et al.* 1990; Klingner *et al.* 1990; Kim *et al.* 1994; Graddy *et al.* 1995; Graddy *et al.* 2002). Figure 2-1 shows arching action in concrete slabs.

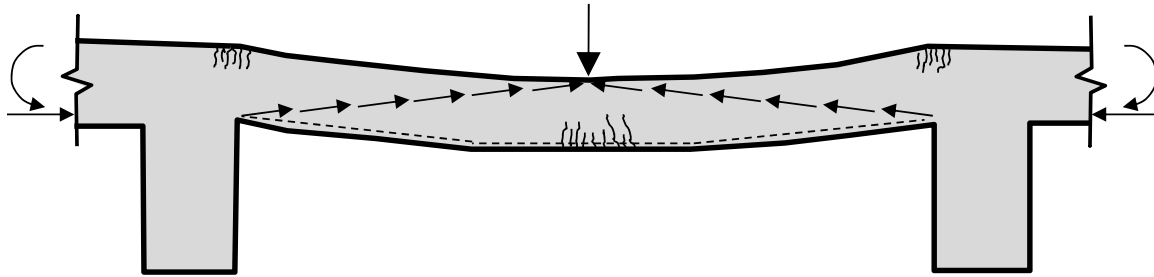


Figure 2-1: Arching action in concrete slabs (adopted from (Foster 2010))

Conservatism in bridge deck design

Significant reserve strength of bridge decks has been confirmed by recent studies (Coselli 2004; Coselli, Griffith *et al.* 2006). Through tests conducted by Coselli in 2004 using a full-scale CIP-PCP bridge deck, it was observed that decks tested could carry 3 times the HS-25 design load on an overhang and more than 5 times the design load on interior spans. This reserve strength is due partially to arching action of the bridge deck and also to the conservative nature of design standards. As a result, it may be possible to reduce reinforcement in some bridge decks. A deck without any reinforcement can resist twice its design load (Batchelor and Hewitt 1976).

Typical cracking in CIP-PCP bridge deck: reflected cracks

To optimize top-mat reinforcement, it is important to understand the cracking pattern in CIP-PCP bridge decks. The main role of top-mat reinforcement is to control the widths of cracks in a bridge deck.

Figure 2-2 shows typical cracking in a CIP-PCP bridge deck. The cracks lie along the edges of the panels, and reflect the discontinuity between the PCPs and between the PCPs and CIP concrete. The cracks that run parallel to the direction of traffic are labeled longitudinal cracks, and the cracks perpendicular to the direction of traffic are labeled transverse cracks.

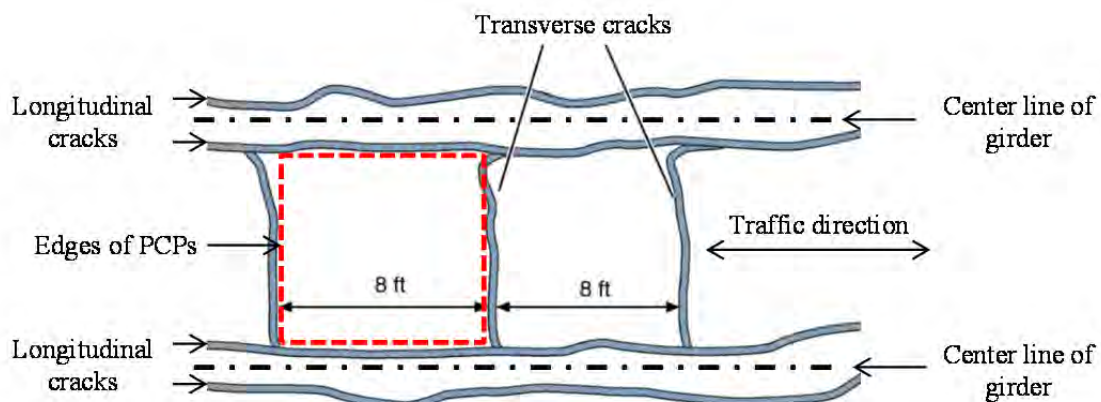


Figure 2-2 Reflected cracking in top surface of CIP-PCP bridge deck (Folliard *et al.* 2003)

Transverse cracking in bridge decks is caused by creep and shrinkage deformations in CIP slabs and PCPs. In most case, the deformations in the PCPs are smaller than that in the CIP

slabs, because old PCPs are generally used, in which most deformation due to creep and shrinkage has already occurred. Shrinkage deformation in the CIP slabs is restrained at the supports, and causes tensile stress throughout the CIP deck. Because old PCPs experience less shrinkage than the deck overlying the panels, they restrain the shrinkage of that deck. Because of the discontinuities at panel edges, cracks tend to form along the joints. If new PCPs are used, their shrinkage and creep produce tensile stresses in the deck at panel edges, exacerbating deck cracking. Because most transverse cracks develop before the bridge deck is opened to traffic, traffic load is not a main cause of transverse cracking. However, it can widen existing cracks. The type of girder supporting the panels does not affect cracking in the transverse direction (Krauss and Rogalla 1996).

Longitudinal cracks develop in the negative-moment regions of the CIP deck, over the girder. Their occurrence is affected by the type of girder. A bridge with steel girders is more susceptible to longitudinal cracking than a bridge with concrete girders because of smaller stiffness of steel girders (Krauss and Rogalla 1996). Longitudinal cracks usually do not occur before a bridge is opened to traffic. Loads on the bridge before opening the bridge to traffic are not large enough to crack the concrete. The main causes of longitudinal cracks are shrinkage deformation of the CIP deck and (with new PCPs) shrinkage and creep deformations of PCPs. Although the stress induced by creep and shrinkage may be large enough to crack the deck, the cracks will generally be quite narrow.

Restrained thermal deformation of concrete may cause cracking in both directions in the deck. Because the level of restraint is generally higher in the longitudinal direction than the transverse direction of a bridge deck, cracking due to restrained thermal deformations is more likely to occur in the transverse direction than in the longitudinal direction of the deck.

The coefficient of thermal expansion (CTE) is usually a function of the coarse aggregate type; river gravel has a higher CTE than limestone (Lukefahr and Du 2010). In studying means of controlling thermal cracking in concrete at early ages, Riding *et al.* (2009) conclude that thermal cracking can be reduced by replacing aggregates with a high CTE by aggregates with a low CTE, and by casting the deck at cooler times of the day.

“Texas poor-boy” joint

The “Texas poor-boy joint,” commonly used in Texas, is made by casting a continuous concrete slab over the girders, with reinforcement placed in the continuous slab to control crack widths over the joint (Figure 2-3).

No closure strip is cast and no construction joints are used at the ends of the girders. Cracks form in the deck at the ends of the girders due to negative moment and long-term shrinkage of the deck. Because no special attention is given to the slabs over the ends of the girders, the cost of construction and maintenance of joints between girders can be reduced.

Roberts *et al.* (1993) note that the poor-boy joint behaves very similarly to a joint where the space between the girders is filled with concrete. In bridge design, however, the poor-boy joint region is treated as simply supported, implicitly accounting for possible yielding over time of the reinforcement crossing the joint.

The bridges instrumented in this study (Chapter 3) included the “Texas poor-boy joint.” Tests were conducted to determine whether the amount of top-mat reinforcement crossing the poor-boy joint could be reduced. In addition, the bridges were instrumented with gages to monitor cracking at the poor-boy joint and cracks were monitored following completion of the bridge decks.

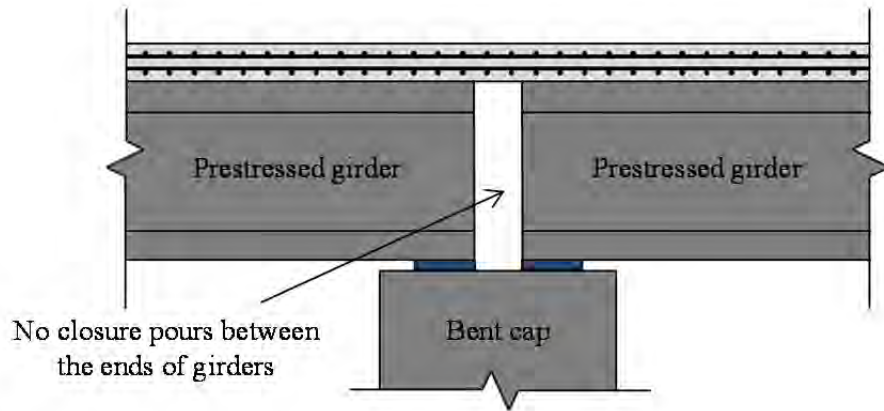


Figure 2-3: “Poor-boy” joint (adapted from Roberts et al. 1993)

Welded-wire reinforcement

Welded-wire reinforcement is a possible design option for top-mat reinforcement of bridge decks due to its high strength, bonding characteristics, and ease of placement. Welded-wire reinforcement is prefabricated, so construction time, labor, and field errors can be reduced (Bernold *et al.* 1989).

Ayyub *et al.* (1994) tested ultimate strength and ductility of various types of welded-wire reinforcement from different countries (United States, Germany, and Canada) to encourage engineers to use welded-wire reinforcement in field. They conclude that US welded-wire reinforcement has mechanical properties appropriate for use in bridge decks. They note that tempering wire and coating it with epoxy might decrease its strength, but also increase its ductility (Ayyub *et al.* 1994).

Russo (1999) focused on differences in behavior of concrete slabs depending on ductility of welded-wire reinforcement. Two prestressed double-T concrete slabs were tested; one was reinforced with high-ductility welded-wire reinforcement, and the other with normal welded-wire reinforcement. The slab reinforced with high-ductility welded-wire reinforcement had higher maximum moment and larger curvature at failure (Russo 1999).

Soltani *et al.* (2004) studied effects of arrangement of wire on ductility, cracking, and post-cracking performance, using RC membrane elements subjected to in-plane stress. They observed that specimens reinforced with welded-wire reinforcement have smaller crack spacing and narrower crack width than specimens reinforced with standard deformed bars, because welded-wire reinforcement has higher anchorage strength than normal deformed bars. They also found that crack spacing was not determined by the spacing of wire when that spacing is less than 20 times the wire diameter. The effect of tension stiffening was much greater with welded-wire reinforcement than with conventional deformed bars (Soltani *et al.* 2004).

Gilbert and Sakka (2007) studied failures of concrete slabs reinforced with low-ductility, welded-wire reinforcement. The slabs failed in a brittle manner with little plastic deformation and little stress redistribution. Based on the test results, they suggest that strength reduction should be considered when engineers design the slab with low-ductility welded-wire reinforcement (Gilbert and Sakka 2007).

2.2.2 Issues in PCPs as Used in Texas

Collinear cracking in PCPs

Figure 2-4 shows the forces acting on a prestressing strand in a PCP after release. An unrestrained strand would shorten; because the strand is restrained by the surrounding concrete, forces are created that act inward on the concrete, away from the ends of the member, and outward on the strand, toward the ends of the member. The bond force acts on the circumferential surface of the strand. The magnitude of the bond force increases toward the ends of the strand. The reason is that bond force is proportional to the gradient of stress in the strand. The maximum gradient of the prestress occurs at the ends, and the value decreases as the distance from the ends increases (Figure 2-5).

The strand has reduced diameter before release due to initial applied prestress. After release, the strand at the ends tends to regain its original diameter and expand circumferentially because the prestress force is zero at the ends (Figure 2-5). This radial expansion is due to Poisson's effect and this expansion is restrained by surrounding concrete. Therefore, radial force toward the strand develops and acts on the strand. The magnitude of the radial force at the ends is larger than that at the center, because radial deformation of the strand at the ends is bigger than that at the center. These two forces in the axial and radial directions result inclined force acting toward the strand.

Figure 2-6 shows the force acting in the surrounding concrete when the strand is released. To resist the force acting on the strand shown in Figure 2-4, an inclined force acts on the concrete. The direction of the inclined force in concrete is opposite to the direction of the force acting on the strand. The inclined force in the concrete produces circumference tensile stress and if its value is greater than the tensile strength of concrete, crack forms along the strand. This crack is called a collinear crack.

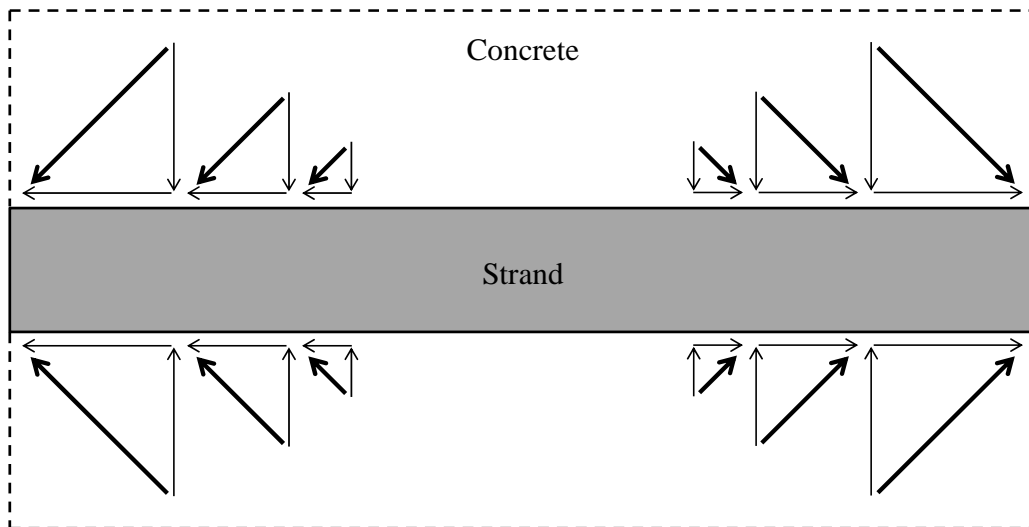


Figure 2-4: Force acting on a strand after release

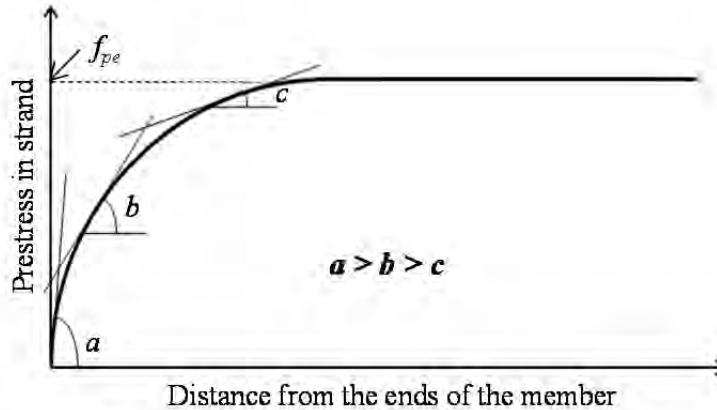


Figure 2-5: Gradient of prestress in strand after releasing

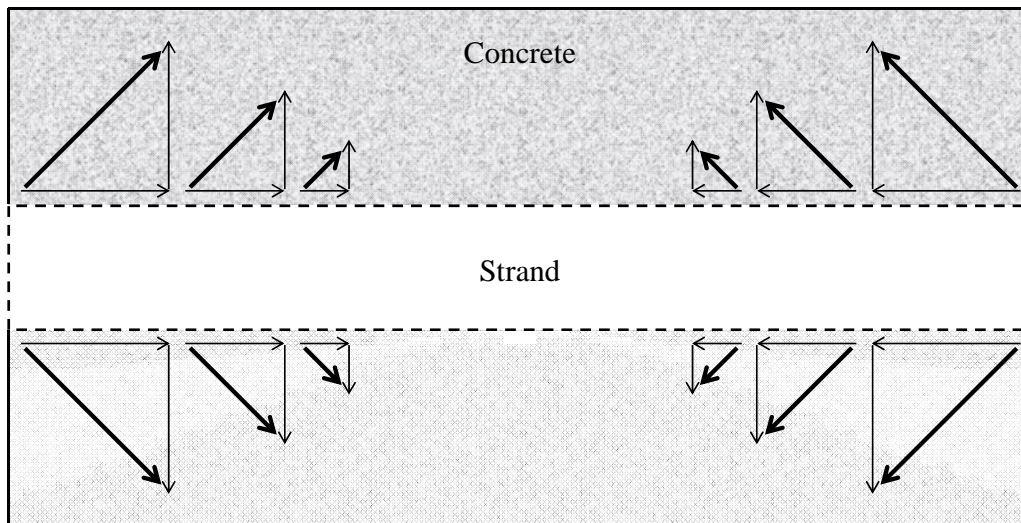


Figure 2-6: The force acting in the surrounding concrete

Collinear cracking usually starts at the edge of the panels and extends toward the center. The potential for collinear cracking increases if prestress force in the strand is released suddenly, or if the strand has insufficient transfer length (Sneed *et al.* 2010).

Circumferential stresses are also created in the concrete surrounding the strand due to Poisson's effect (Figure 2-7). In the figure, the red block represents the original shape before applying loading. The blue block represents the deformed shape after loading. When a material is loaded in one direction, the material usually deforms perpendicular to the loading direction. This phenomenon is called Poisson's effect. Poisson's effect can be quantified by calculating Poisson's ratio. Poisson's ratio is obtained by dividing the strain in loading direction by the strain normal to the loading direction. The ratio ranges from 0.0 to 0.5. Generally, Poisson's ratio for steel is 0.3 before yield and 0.5 after yield.

When releasing the strands, the stress at both ends of the strands becomes zero. Due to the zero stress at both ends after release, the length of the strands is reduced, and the diameter of the strands increases due to Poisson's effect. This radial expansion causes circumferential tensile stress in the surrounding concrete (Hoyer effect). If the tensile stress is larger than the tensile strength of the surrounding concrete, it may cause cracks in PCPs. However, if the strength of

concrete and depth of clear cover are large enough to resist this expansion, a wedge may be created by the Hoyer effect as shown in Figure 2-8 (Collins and Mitchell 1991). This wedge effect helps transfer prestress from strand to concrete (Krishnamurthy 1971; Krishnamurthy 1973).

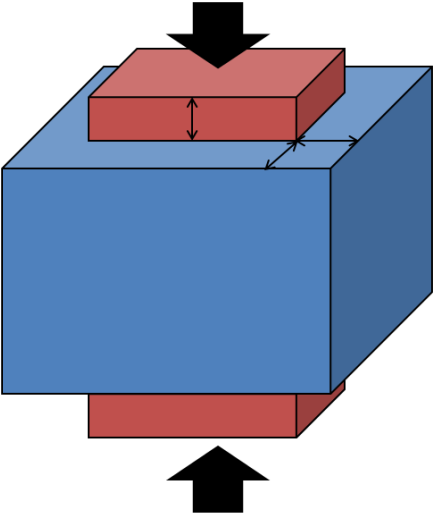


Figure 2-7: Poisson's effect

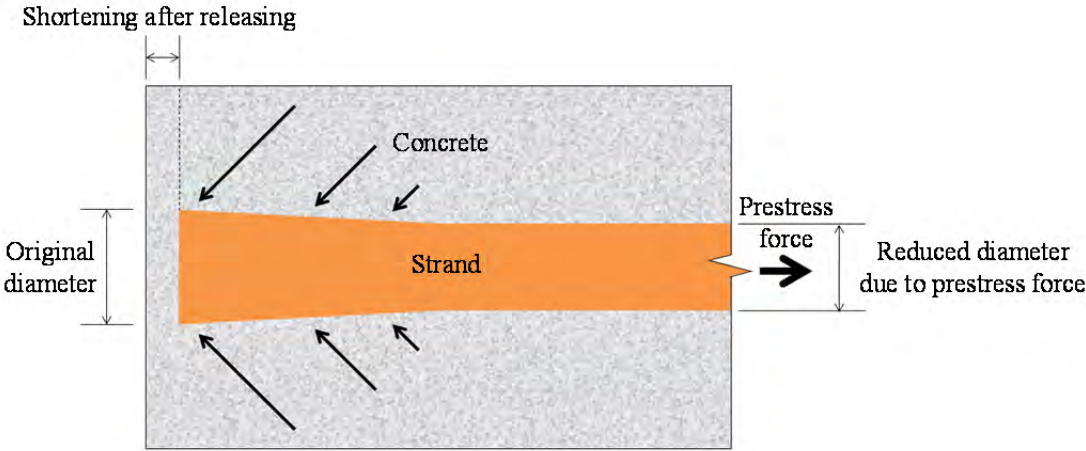


Figure 2-8: Forces on strand due to “wedge” created by Hoyer effect

Ageing and creep coefficients for computing prestress losses

To determine the rate of loss of initial prestress, the first step is to evaluate time-dependent deformation, using reliable creep and ageing coefficients. The creep coefficient is the ratio of creep strain to elastic strain under constant load, and is designated as ' ϕ ' in most references. The ageing coefficient, developed to account for changes in load over time, is generally expressed as ' χ '. For example, if the specimen is subjected to constant stress from time t' to time t , the creep deformation can be calculated by multiplying elastic strain by $\phi(t, t')$.

However, if the load changes with time, the creep deformation can be calculated by multiplying elastic strain by $\chi(t, t')$ and $\phi(t, t')$ (Neville *et al.* 1983).

Several researchers (Bazant 1972; Tadros, Ghali *et al.* 1975; Dilger 1982) suggest that a reasonable range for the creep coefficient is 0.6 to 0.8. Creep and ageing coefficients under specific environmental conditions have been studied by Shrestha and Chen (2011).

ACI 209 (1997) provides options for determining creep and shrinkage effects. In Chapter 5, prestress losses are discussed in more detail.

2.3 Studies Conducted under TxDOT Projects 0-4098 and 0-6348

In TxDOT 0-4098, restrained creep and shrinkage were studied and the procedure used was adopted in this study (Chapter 4). Foster (2010), Foreman (2010), and Azimov (2012) reported on studies conducted under project TxDOT 0-6348, and their results are data is used in this report. Therefore, those studies are summarized here.

2.3.1 TxDOT Project 0-4098

The objective of TxDOT Project 0-4908 was to find the most promising concrete mixtures for preventing or minimizing cracking due to drying shrinkage. Based on a literature review, the researchers selected several concrete mixtures and tested them using small- and large-scale laboratory tests. Several inspections of cracking in bridge decks were also conducted to evaluate characteristics of drying-shrinkage cracks in the field. In Figure 2-9, the test setup for the large-scale laboratory tests in Project 0-4098 is shown.

Shear studs and threaded reinforcing bars were firmly attached to the restraining frame and two PC panels were used for each specimen. Shear studs, reinforcing bars at end regions and PC panels restrain the CIP portion and result in cracking at the middle of the specimens. To force a crack to form at the middle of the CIP slab, no reinforcement was placed in the CIP slab across the joint between precast panels. No shear stud was installed in middle portion of the frame.

Based on test results from project 0-4098, it was concluded that drying-shrinkage cracking can be controlled by adding shrinkage-reducing admixture, fibers, calcium-sulfoaluminate admixture, or a high volume of fly ash to the concrete mixture.

The test setup for the restrained-shrinkage test in Chapter 4 was built using the test setup of the large-scale laboratory tests in Project 0-4098.

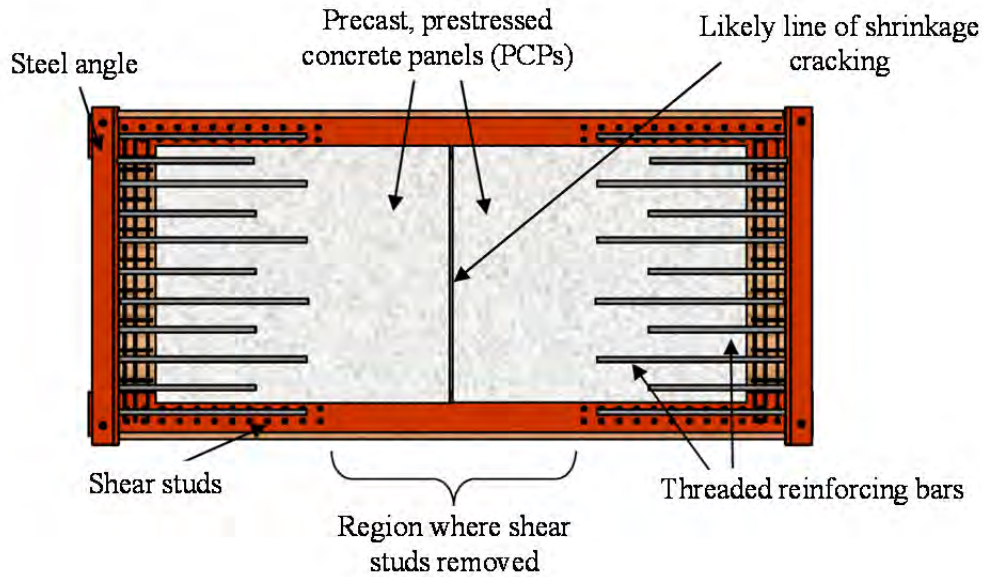


Figure 2-9: Restrained-shrinkage test setup of TxDOT Project 0-4098 (Folliard et al. 2003)

2.3.2 TxDOT Project 0-6348: Foster (2010)

The objectives of this research were to optimize top-mat reinforcement in a CIP-PCP bridge deck considering the effects of PC panels on cracking in CIP slabs. Foster reviewed several different formulas for crack width calculations and suggested possible design options for top-mat reinforcement (Foster 2010). The selected reinforcement options were tested in the lab using bending tests and direct tensile tests (DTT).

Figures 2-10 and 2-11 show two different bending test setups. In the bending moment tests, composite specimens consisting of CIP slab and PCPs were used to consider the effects of the PC panel on cracking in CIP slabs. However, the cracking pattern of the test specimens did not match the pattern shown in Figure 2-2. In the bending tests, multiple cracks occurred in the uniform moment region and delamination between the CIP deck and the PCPs was observed. The loading condition in the tests did not simulate the shrinkage conditions in a real bridge deck.

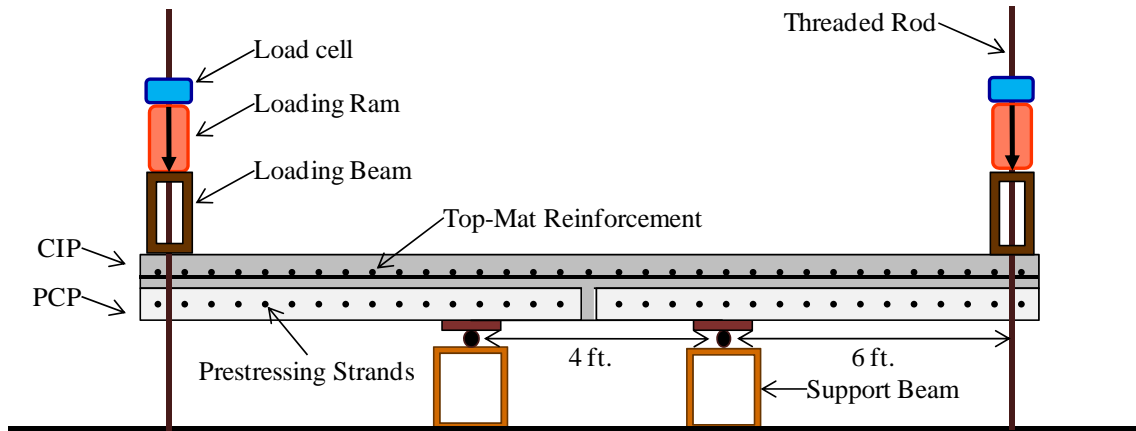


Figure 2-10: Constant bending moment test setup (Foster 2010)

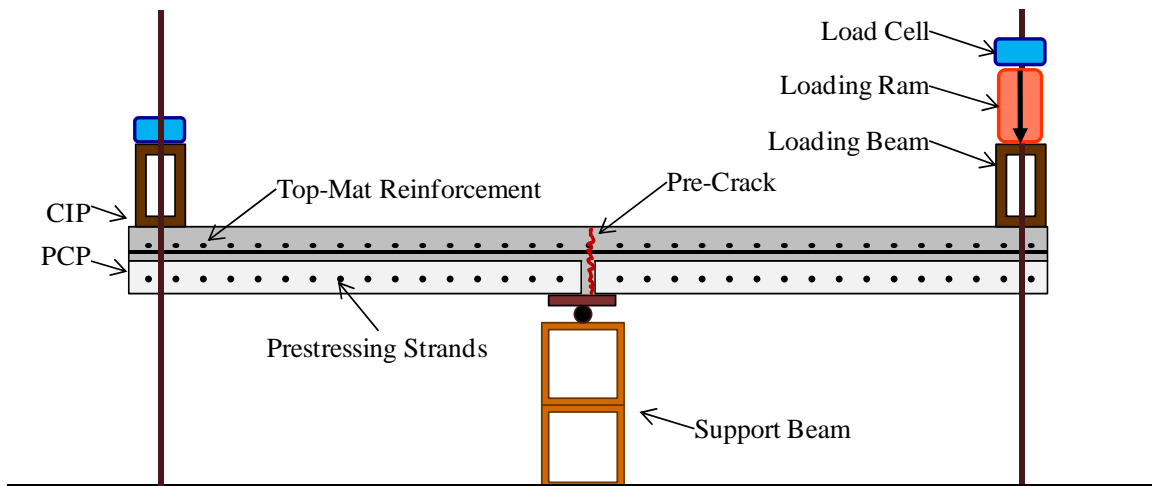


Figure 2-11: Concentrated-load test setup (Foster 2010)

To overcome these problems, Foster applied direct tension to composite specimens (Figure 2-12). Tensile load was applied through the reinforcement in the CIP portion. In this test, delamination was still observed due to eccentricities of geometry between the geometry of the specimen and the loading (Figure 2-13).

Finally, Foster used a DTT of the CIP portion of the bridge deck (Figure 2-14). To force the first crack to form at the mid-height of the specimen and to minimize geometrical eccentricity of the specimen, a saw cut was made on both sides of the specimens. While the test provided information on the relationship between crack width and steel stress, CIP-PCP interaction was not included. Longitudinal cracks, which are controlled by transverse reinforcement, occur due to restrained shrinkage of CIP slabs and creep of PC panels neither of which was reflected in the test specimens.

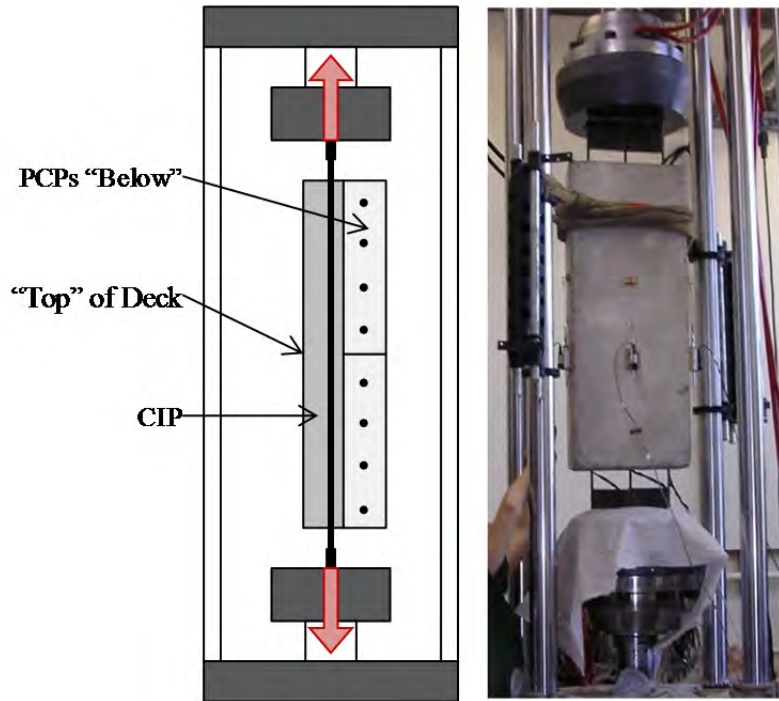


Figure 2-12: DTT using composite specimen (Foster 2010)



Figure 2-13: Delamination during DTT (Foster 2010)

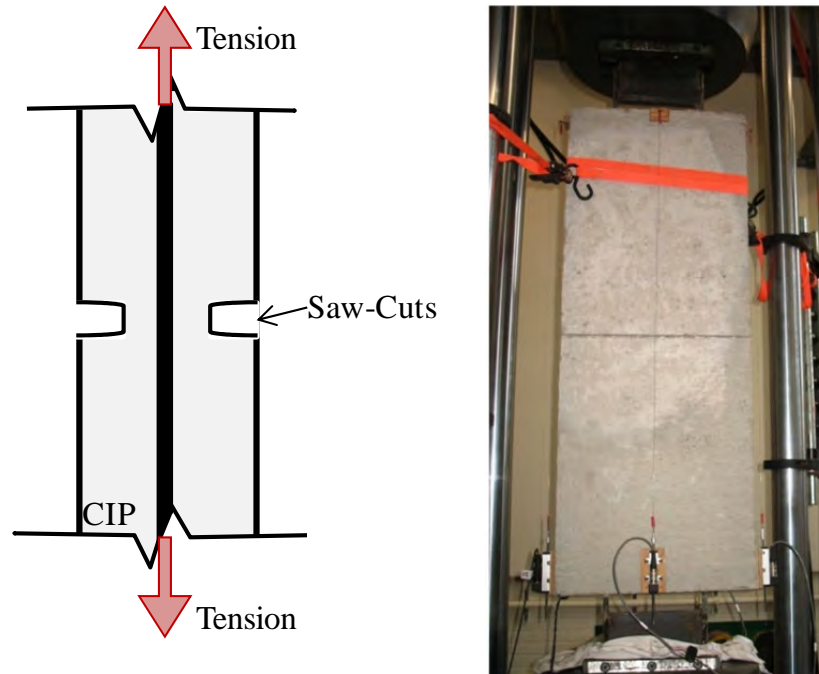


Figure 2-14: DTT using non-composite specimen (Foster 2010)

Based on the test results, Foster found that current top-mat reinforcement in the longitudinal direction (No. 4 bar @ 9 in.) is already optimized, but further reduction may be possible for the reinforcement in the transverse direction. Smaller-diameter reinforcement or welded-wire reinforcement were recommended as possible design options for the transverse direction.

2.3.3 TxDOT Project 0-6348: Foreman (2010) & Azimov (2012)

The goal of both studies was to reduce collinear cracking in PCPs. Two possible design approaches were proposed. The first is to reduce the initial prestress force from 16.1 kips per strand to 14.4 kips per strand. The second is to place additional transverse reinforcement at the ends of the panel perpendicular to prestressing strands. To verify effects of both recommendations, long-term prestress loss was monitored using PCPs with different levels of initial prestress (Figure 2-15), and knife-edge tests were conducted (Figure 2-16). Detailed information about the long-term monitoring is given in Chapter 5.



Figure 2-15: Long-term monitoring of prestress loss in PCPs

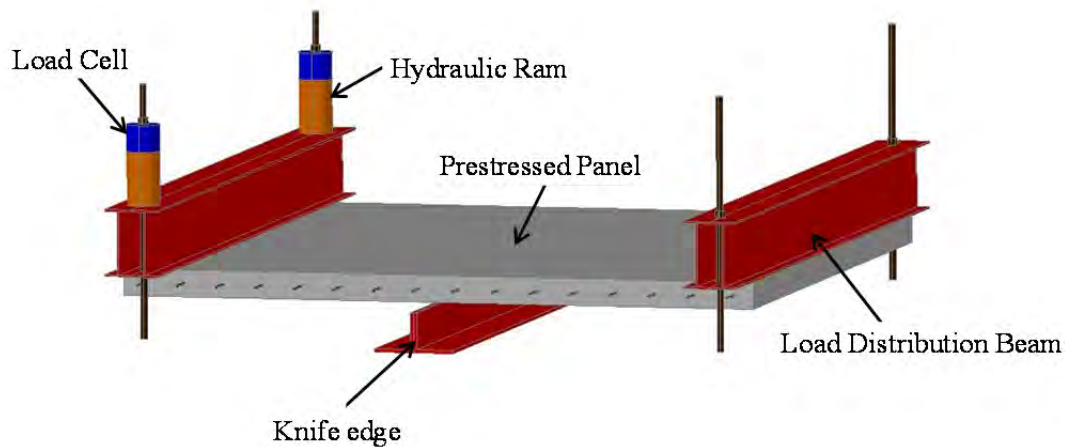


Figure 2-16: Knife-edge test (Foreman 2010)

The objectives of the knife-edge test (Figure 2-16) were to find the effects of additional transverse bars on control of collinear cracking, and the relation between prestress loss and crack width. The test panel was positioned so that a prestressing strand was located directly over the knife edge. All strands were parallel to the knife edge. Negative bending moment was applied on the panel using two hydraulic rams. The highest bending moment occurred along the knife edge, and cracks formed along the strands. Through the knife-edge test, two conclusions were derived:

- i) Placing additional transverse bars at ends of PC panels helped control collinear cracking in the panels; and
- ii) Slip of prestressing strands did not start until collinear cracks become very wide.

2.4 Fiber-Reinforced Concrete (FRC)

2.4.1 Overview of FRC

Material in this section is taken from Woods (2012). Additional information is also given in Cho (2012), Karki (2012), and Waweru (2012). Existing tests for FRC are discussed in detail in Appendix E. Fiber-reinforced concrete is made with hydraulic cement and aggregates of various sizes, incorporating discrete, discontinuous fibers. Fibers are not as efficient as deformed reinforcing bars or prestressing strands at withstanding tensile stresses, because the required volume of fibers and their orientation cannot be guaranteed to coincide with the location and orientation of the expected tensile stresses. However, since the fibers tend to be more closely spaced than conventional reinforcing bars, they are better at controlling crack widths (Stroeven & Shah, 1978).

2.4.2 Applications of FRC

Since its introduction into the marketplace in the late 1960s, the use of fiber-reinforced concrete has increased steadily. Based on data from 2001, approximately 80 million cubic meters of FRC are produced annually, with the principal applications being slabs on grade (60%), fiber-shotcrete (25%), and precast members (5%), with the remainder of the production distributed among a number of other specialty products and structural forms (Bentur & Mindess, 2007). A number of non-structural, structural, and repair applications exist.

Non-Structural Applications of FRC

Fibers are used extensively in thin members such as bridge deck overlays, floor slabs, thin shells, and tunnel linings to reduce cracking and improve fatigue strength. In an evaluation of alternative materials to control drying shrinkage cracking in concrete bridge decks, fibers were effective in delaying early age cracking and limiting crack width (Folliard, Smith, & Breen, 2003). The fibers behave as a second line of defense to limit crack propagation because they help to distribute the stresses in the concrete around existing cracks so that the cracks stay relatively small. It was also shown that polypropylene fibers can eliminate plastic shrinkage. Thus, the addition of fibers improves concrete durability by preventing the ingress of harmful substances such as water, sulfates, and chlorides (Folliard, Smith, & Breen, 2003).

Structural Applications of FRC

Although HPFRCCs have occasionally been used in stand-alone applications, fiber reinforcement is generally not a *substitute* for conventional reinforcement. Fibers and steel reinforcing bars play different roles in modern concrete technology, and there are many applications in which fibers and continuous reinforcing bars can be used together. Fibers have been used in this way to improve the static flexural strength, flexural fatigue strength, and post-cracking energy absorption capacity of structural members (Ramakrishnan, 1987). Figure 2-17 provides some basic schematics of (a) stand-alone, (b) combined, and (c) repair applications for HPFRCC.

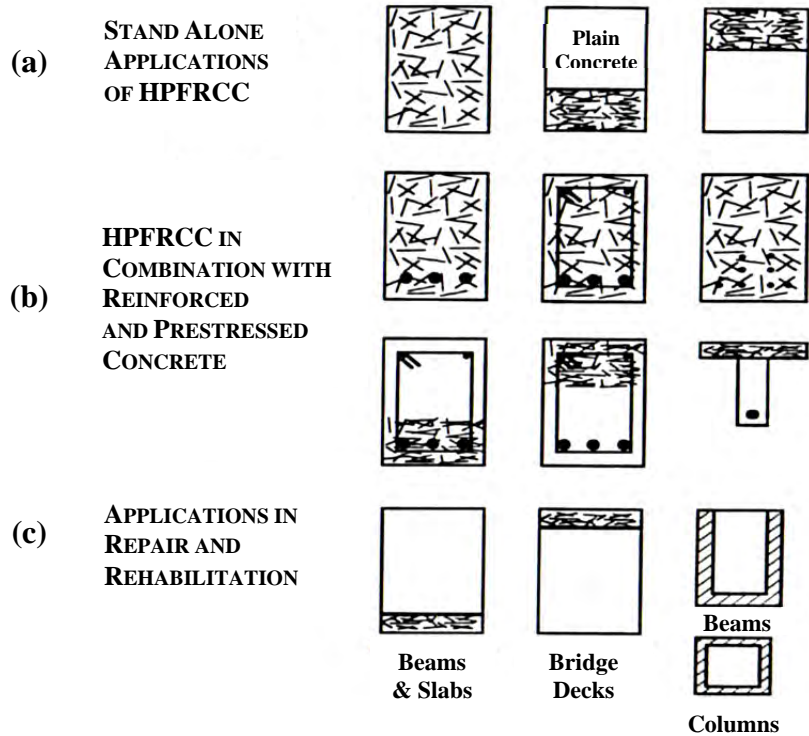


Figure 2-17: Schematic of (a) stand alone, (b) combination, and (c) repair applications for HPFRCC (Ramakrishnan, 1987)

2.4.3 Limitations of Existing Test Methods for FRC

Fibers are still rarely used in purely structural concrete applications, despite their effectiveness under static and dynamic loading, their ability to control crack widths, and improved toughness behavior. This is due largely to the fact that fibers have yet to be widely integrated into structural design codes such as ACI 318 (ACI, 2011). Part of the hesitation to implementing FRC into codes is due to the lack of a widely agreed upon body of standards for testing and quality control of FRC.

Many test methods can evaluate the performance of fibers with respect to plastic shrinkage, anchorage, and pull-out strength. However, test methods used to evaluate the composite properties of FRC that are of structural significance (such as toughness and residual strength) are inadequate and inconsistent (Bentur & Mindess, 2007). This is unfortunate since research shows fiber-reinforced concrete has the potential to be used more commonly for structural purposes. Before FRC can be used extensively in practice, it is critical that simple, accurate, and consistent testing procedures be developed to evaluate the behavior of FRC composites.

Although many test methods are available for evaluating the properties of FRC, none is sufficiently simple, reliable, and reproducible. All current test methods fail to meet one or more of the recommended criteria for testing of FRC listed earlier in this chapter (Bentur & Mindess, 2007). Each of the current test methods can be found wanting with respect to one or more of the following basic criteria: simplicity, reliability, and reproducibility.

Simplicity

Many existing test methods require test specimens that are difficult to fabricate or handle due to specialized formwork, size, weight (Figure 2-18), or curing regimen. In addition, some test methods require an intricate test arrangement for specimen support fixtures or electronic gauge mountings. Adding to the complexity is the need for a servo-controlled test machine, a rare commodity in many laboratories. Finally, elaborate test procedures, data corrections, and calculations drive other test methods away from simplicity.

Reliability

The theoretical basis for evaluating the results of a test method should be consistent with the actual behavior of the test specimen under load. However, this is not the case for some tests, which use elastic theory to evaluate plastic behavior. Furthermore, the high within-batch, single-operator coefficients of variation for key test parameters, which are common to many of the current test methods, suggests the need for more reliable methods.

Also, it is essential to understand that a failure mechanism restricted to a *single major crack* in a *well-defined* plane is disadvantageous. Because fibers are randomly distributed and oriented, the effects that they produce are not well represented by a test in which the failure location is constrained in this way. This disadvantage is amplified if the crack location also varies between tests. Unfortunately, failures of this type are common to many of the current test methods and result in unreliable data since the load-deflection curves may not adequately describe composite behavior.

Reproducibility

An ideal test method should be reproducible from laboratory to laboratory. Most existing FRC test methods, however, have high or undetermined inter-laboratory, multiple-operator coefficients of variation for key test parameters. In addition, specimen construction and handling as well as test procedures are often time consuming, making it strenuous or uneconomical to test a large number of specimens and obtain sufficient data for inter-laboratory studies.

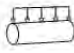
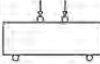
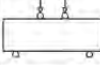
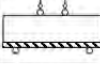

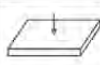

2.4.4 Side-by-Side Comparison of Current Test Methods

As shown in Figure 2-18, over half of the current testing procedures require specimens heavier than 25 lb. Such specimens are difficult to carry and place in position for testing without the use of dollies, cranes, or other special equipment. Manageable specimens are particularly desirable when testing multiple samples.

The test characteristics and factors that affect the simplicity, reliability, and reproducibility of current tests methods for FRC are compared side-by-side in Table 2-2 and Table 2-3.

Each of the current standardized and non-standardized test methods suffers from one or more limitations that make it impractical, unreliable, or inconsistent for evaluating the performance of FRC composites. This has negatively affected the acceptance of FRC applications into structural design codes. A more practical, reliable, and consistent test method is needed for evaluating the characteristics of FRC with different fiber types, fiber volume fractions, and mixture designs.

Table 2-2: Test specimens required for current FRC testing procedures

TEST INFORMATION ¹		TEST SPECIMENS ²			
Designation	Layout	Geometry	Dimensions (in.)	Volume (in. ³)	Weight (lb)
ASTM C496		Cylinder	4" ϕ x 8	101	9
ASTM C1609		Rectangular Prism	6 x 6 x 20	720	63
ASTM C1609		Rectangular Prism	4 x 4 x 14	224	19
ASTM C1399		Rectangular Prism	4 x 4 x 14	224	19
ASTM C1550		Circular Panel	31.5" ϕ x 3	2338	203
EFNARC Panel Test		Square Panel	24 x 24 x 4	2304	200
Uniaxial Direct Tensile Test		Dog-bone	Various	524	45

¹ Test layouts modified from (Molins, 2006).

² Weight of test specimen calculated using average unit weight of FRC = 150 lb/ft³.

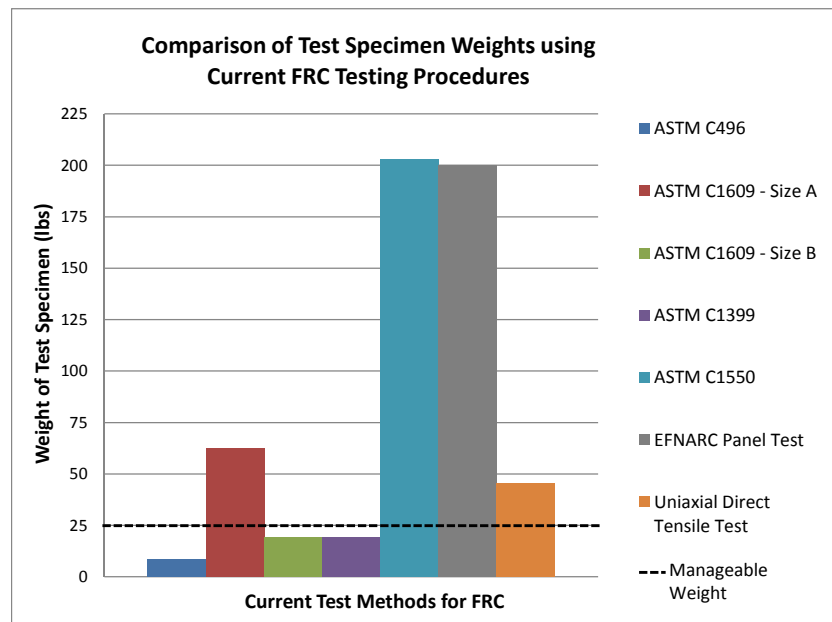
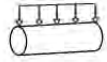
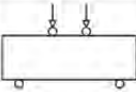
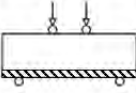
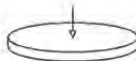
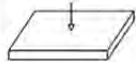
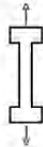


Figure 2-18: Graphical comparison of specimen weights for current FRC testing procedures

Table 2-3: Simplicity, reliability, and reproducibility of current FRC testing procedures

TEST INFORMATION ¹		SIMPLICITY ²				RELIABILITY ³		REPRODUCIBILITY ³
Designation	Layout	Specimen Fabrication & Handling	Test Setup & Support Fixtures	Test Procedure	Test Machine	Failure Mechanism	Within-Batch Precision (COV)	Inter-Laboratory Precision (COV)
ASTM C496		Easy	Easy	Easy	Standard	Single Major Crack	± 5% PL	Not Available
ASTM C1609		Moderate	Difficult	Moderate	Closed-Loop	Single Major Crack	± 8% PL ± 20% RS	Not Available
ASTM C1399		Moderate	Difficult	Difficult	Standard	Single Major Crack	± 20% RS	± 40% RS
ASTM C1550		Difficult	Difficult	Difficult	Closed-Loop	Multiple Cracks	± 6% PL ± 10% RS	± 9% PL ± 9% RS
EFNARC Panel Test		Difficult	Difficult	Moderate	Closed-Loop	Multiple Cracks	Not Available	Not Available
Uniaxial Direct Tensile Test		Difficult	Moderate	Moderate	Closed-Loop	Single Major Crack	Not Available	Not Available

¹ Test layouts modified from (Molins, 2006).

² Complexity levels assigned based on literature and personal communication with researchers who conducted these and other similar tests (Chao S., Assistant Professor in Structural Engineering, 2012).

³ Reliability and reproducibility data obtained from industry standards and research literature (ASTM C496 2011, ASTM C1609 2010, ASTM C1550 2010, ASTM C1399 2010, S.-H. Chao 2011, Bernard 2002). COVs for peak load and residual strength (toughness) are denoted (PL) and (RS), respectively.

Chapter 3. Optimization of Reinforcement in CIP Slabs: Field Application

3.1 Introduction

The objective of the field studies is to compare the behavior of selected top-mat reinforcement options and to suggest optimized reinforcement layouts for CIP slabs. Field instrumentation provides a means of obtaining data that cannot be obtained in the laboratory, where the CIP-PCP interface and boundary conditions of CIP-PCP bridge decks are difficult to simulate. Two structures were investigated: the Wharton-Weems Overpass near Houston (Texas), and the Lampasas River Bridge near Waco (Texas).

3.2 Wharton-Weems Overpass

3.2.1 Description

The Wharton-Weems Overpass is located in the Houston District, at the intersection of Choate Road and Shoreacres Boulevard. The overpass consists of three identical spans, each of which has 9 girders. The overpass has a very slight skew. The CIP concrete slabs and the PCPs are both 4-in. thick, producing an 8-in. composite deck slab. In Figure 3-1 and Figure 3-2, overall views of the Wharton-Weems Overpass are presented.

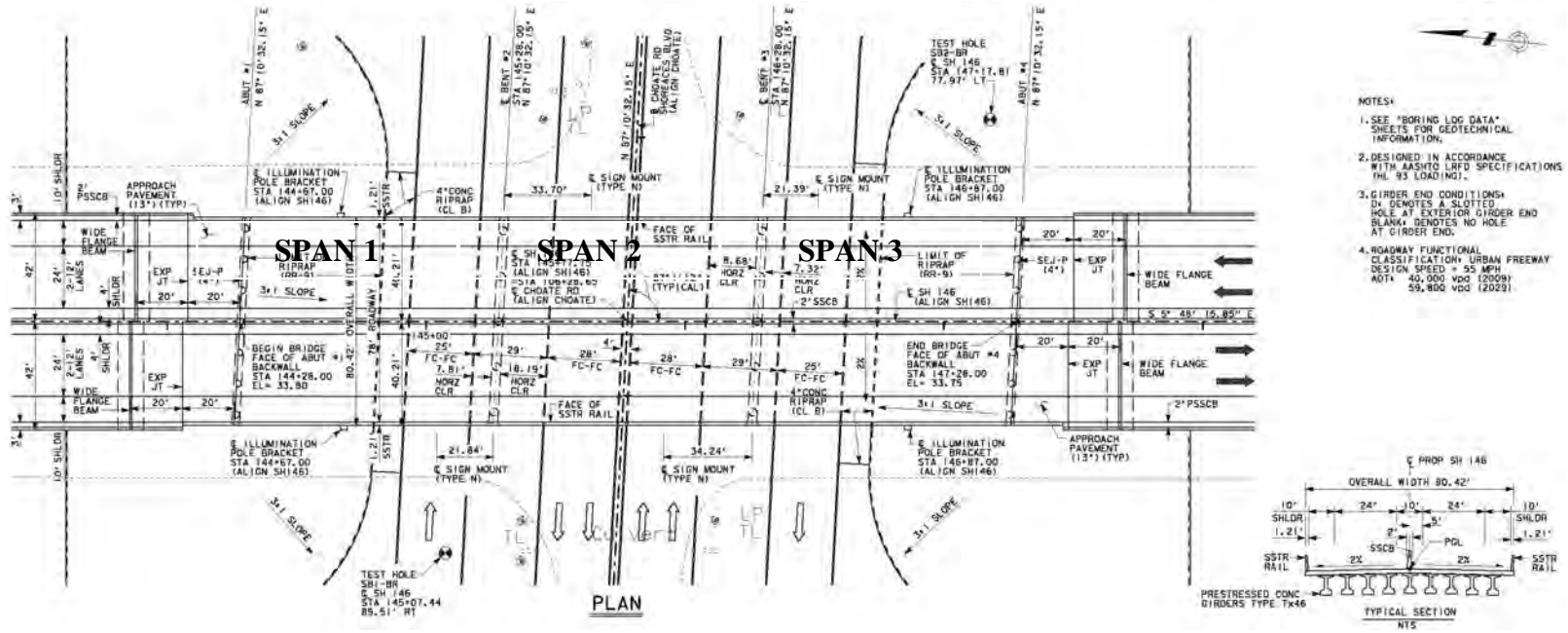


Figure 3-1: Plan view, Wharton-Weems Overpass

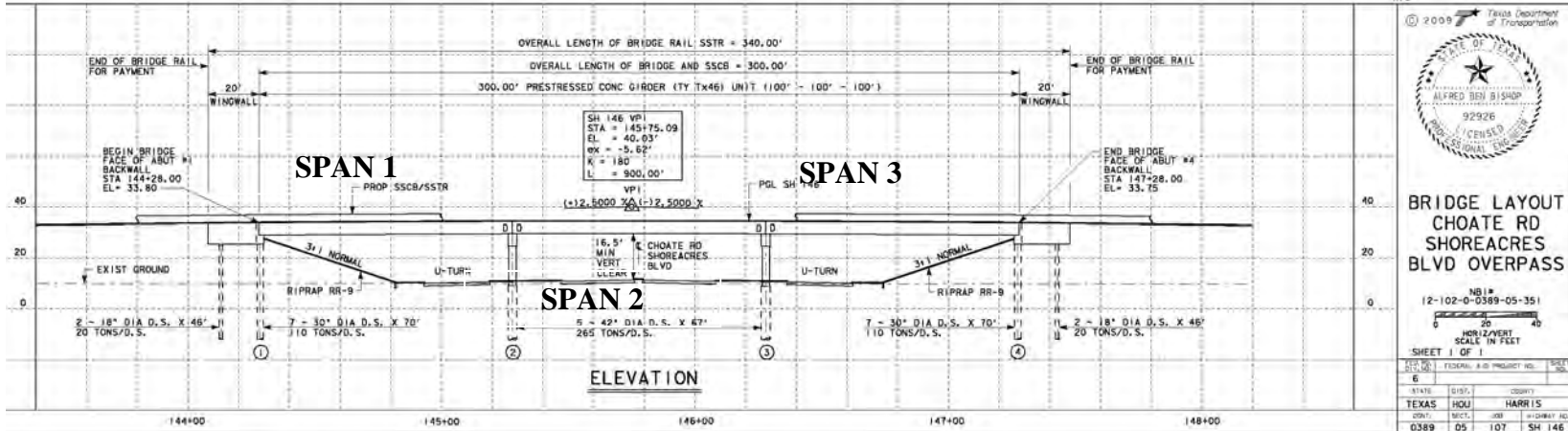


Figure 3-2: Section view, Wharton-Weems Overpass

3.2.2 Top-mat Reinforcement Options for Wharton-Weems Overpass

The top-mat reinforcement options for the Wharton-Weems Overpass are shown in Figure 3-3. As shown in the figure, two spans contained Current TxDOT Standard Reinforcement and one span contained Reduced Deformed-Bar Reinforcement. In the Reduced Deformed-Bar Reinforcement option, the reinforcement layout for the longitudinal direction is the same as the Current TxDOT Standard Design (No. 4 @ 9 in.); for the transverse direction, however, the diameter of the bar is reduced.

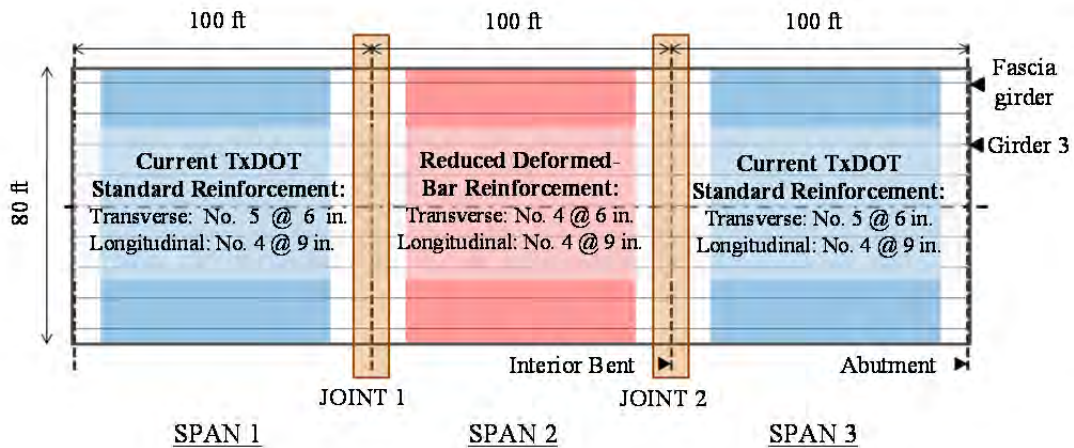


Figure 3-3: CIP deck reinforcement options, Wharton-Weems Overpass

3.2.3 Splice Details

Longitudinal splices

Details of the longitudinal splices are shown in Figure 3-4 to Figure 3-6. Splices were located away from joints, and the longitudinal splice length was calculated using Equation 3-1 (Equation 12-1 of ACI 318 (2011)). Red lines represent the reinforcement in the Reduced Deformed-Bar Reinforcement option and blue lines represent the reinforcement in the Current TxDOT Standard Design. Detailed calculations of splice length are shown in Appendix A.

$$\frac{l_d}{d_b} = \frac{3}{40} \frac{f_y}{\lambda \times \sqrt{f_c'}} \frac{\psi_t \times \psi_e \times \psi_s}{\left(\frac{c_b + K_{tr}}{d_b}\right)}$$

Equation 3-1
(Eq. 12-1, ACI 318-11)

- Where,
- l_d = development length in tension, in.
 - d_b = nominal diameter of bar, in.
 - f_y = specified yield strength of reinforcement, psi
 - f_c' = specified compressive strength of concrete, psi
 - ψ_t = factor used to modify development length based on reinforcement location
 - ψ_e = factor used to modify development length based on reinforcement coating
 - ψ_s = factor used to modify development length based on reinforcement size
 - λ = modification factor related to unit weight of concrete
 - c_b = smaller of (a) the distance from center of bar to nearest concrete surface, and (b) one-half the concrete center-to-center spacing of bars or wires being developed, in.
 - K_{tr} = transverse reinforcement index

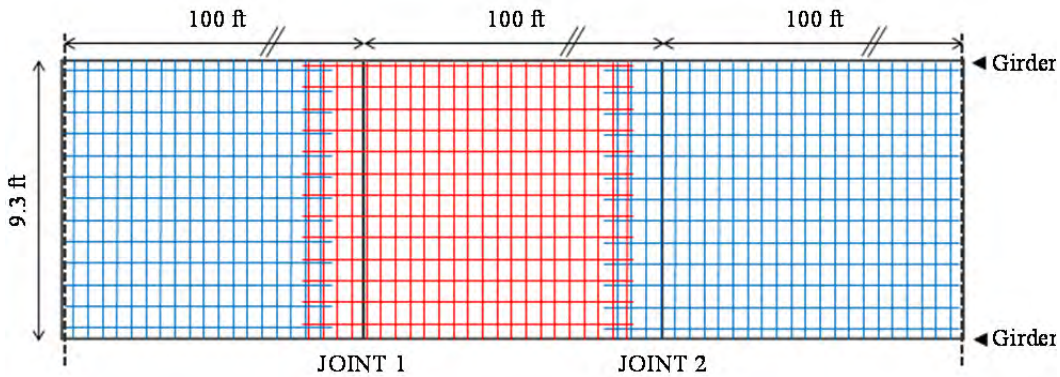


Figure 3-4: Details of longitudinal splices, Wharton-Weems Overpass

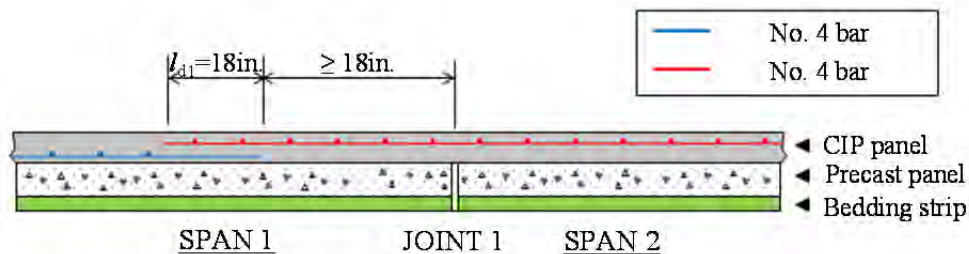


Figure 3-5: Section showing details of longitudinal splices, Wharton-Weems Overpass (Joint 1)

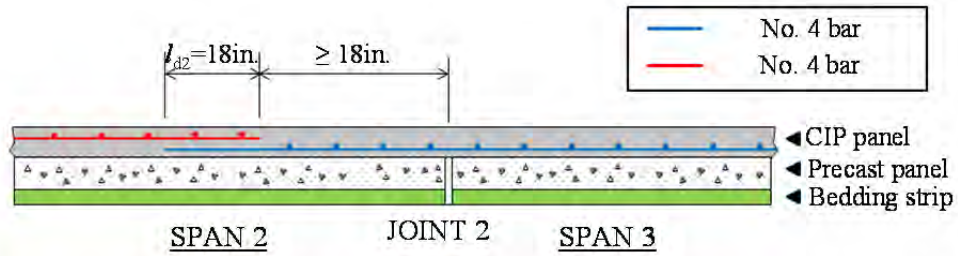


Figure 3-6: Section showing details of longitudinal splices, Wharton-Weems Overpass (Joint 2)

Transverse splices

Details of transverse splices are shown in Figure 3-7 to Figure 3-10. Splice lengths are calculated using the same equation used in the longitudinal direction (Equation 3-1), and detailed calculations are shown in Appendix A.

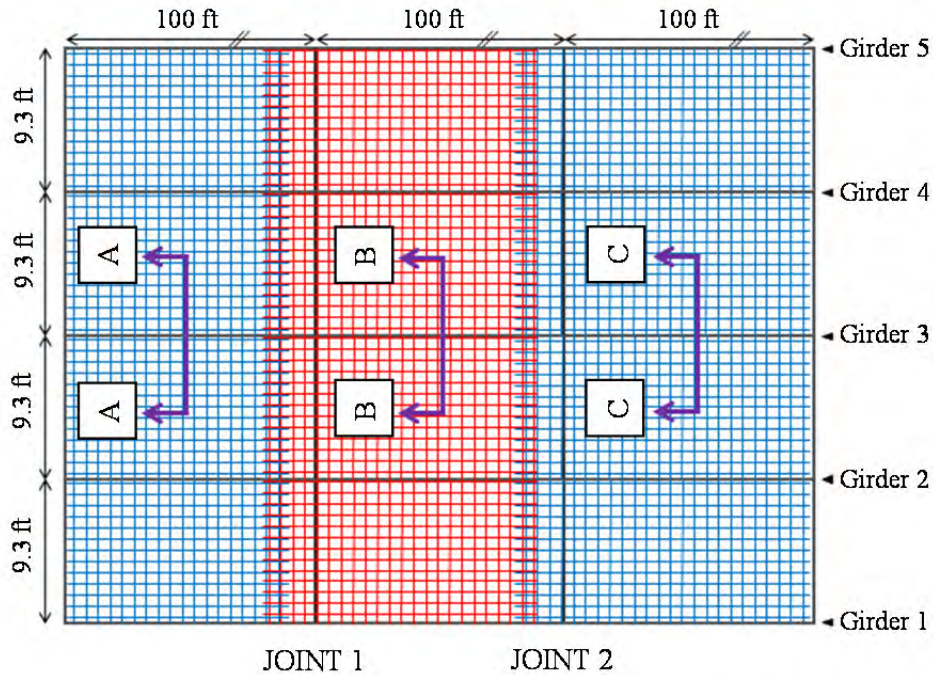


Figure 3-7: Details of transverse splices, Wharton-Weems Overpass

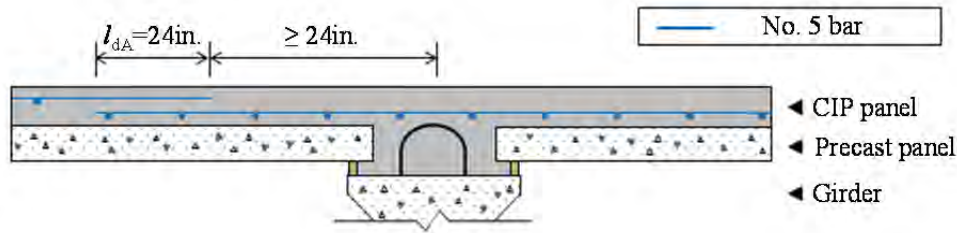


Figure 3-8: Details of transverse splices, Wharton-Weems Overpass (Section A-A)

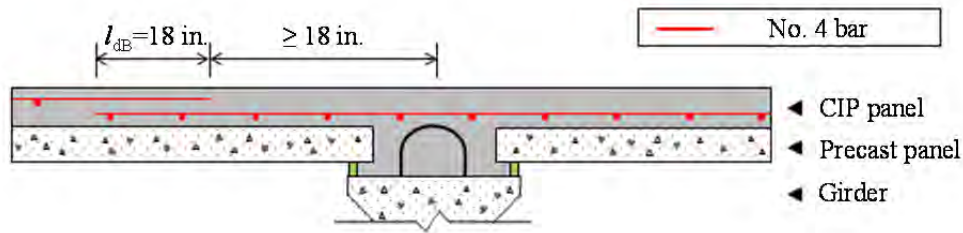


Figure 3-9: Details of transverse splices, Wharton-Weems Overpass (Section B-B)

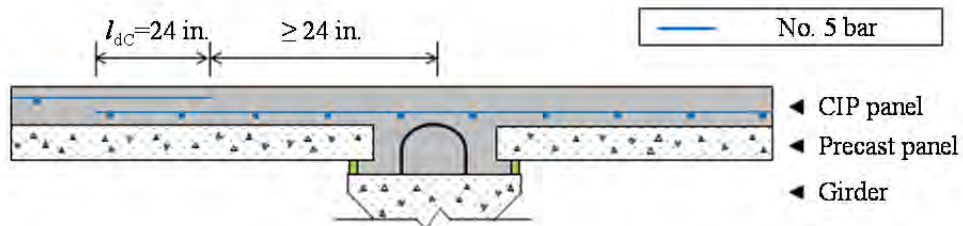


Figure 3-10: Details of transverse splices, Wharton-Weems Overpass (Section C-C)

3.2.4 Instrumentation of Wharton-Weems Overpass

Vibrating-wire gages

Geokon Vibrating-Wire Gages (VWGs), Model VCE-4200, were installed to measure strains in the CIP deck of the Wharton-Weems Overpass. VWGs were attached to top mat reinforcement. The strain values from VWGs represent the strain in the concrete at the same level as that of the bars, assuming perfect bond between reinforcement and concrete. Field installation of a typical VWG is illustrated in Figure 3-11. Each gage was attached to the reinforcement using two wood blocks and plastic zip-ties. The gages should be aligned with the reinforcement, and this orientation should not change during casting. It is also important not to apply bending moment to the gages during installation because it can cause inaccurate measurement. Bending moment can be applied to the gages during installation when the heights of wood blocks are not the same or the two plastic zip-ties have different tensions.

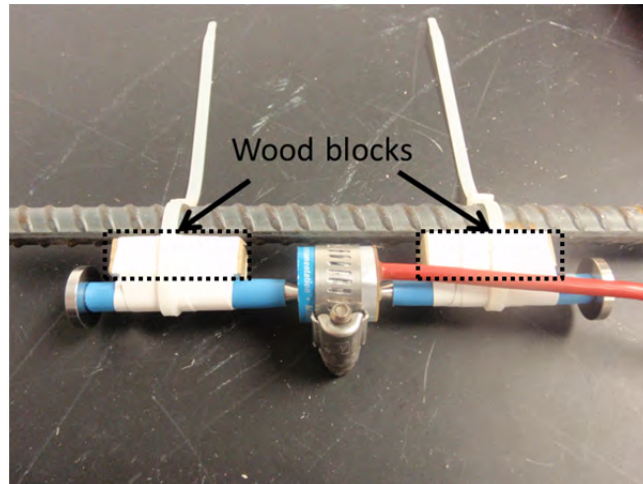


Figure 3-11: Typical VWG as installed on the reinforcement

Gage location and identification

The gage designations are as follows:

- i) Longitudinal gages are denoted as “Lxx.” Odd-numbered gages are located over the fascia girder. Even-numbered gages are placed over Girder 3.
- ii) Transverse gages are denoted as “Txx.” Gages T03 to T06 are located at 25 feet from Joint 2, and T01, T02 and T07, T08 are located 75-ft away from Joint 2. Odd-numbered gages are placed along Girder 2, and even-numbered gages are placed along the centerline of the bridge.

Figure 3-12 and Figure 3-13 show the gage layout for longitudinal bars and for transverse bars, respectively. The brown star in these figures indicates the location of data-acquisition equipment.

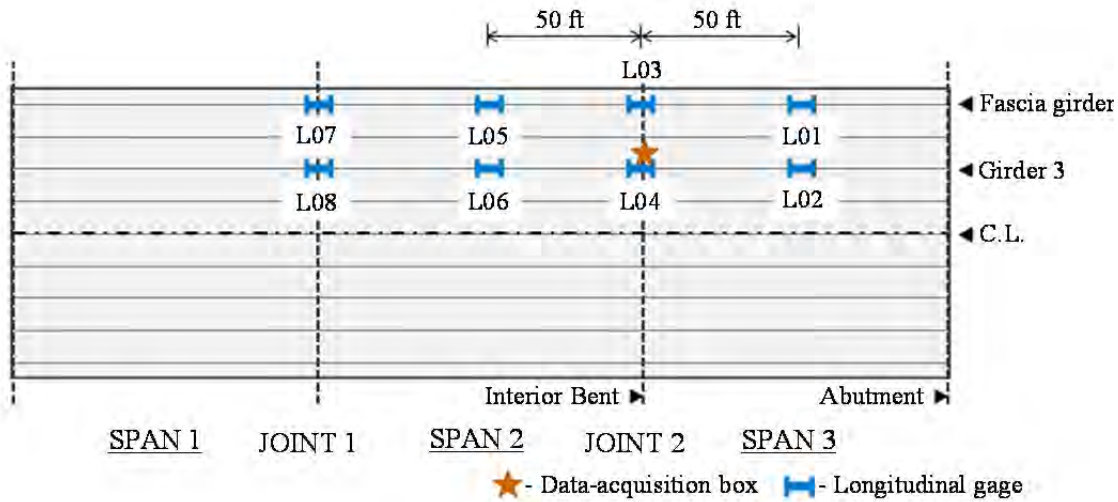


Figure 3-12: Gage layout for longitudinal bars, Wharton-Weems Overpass

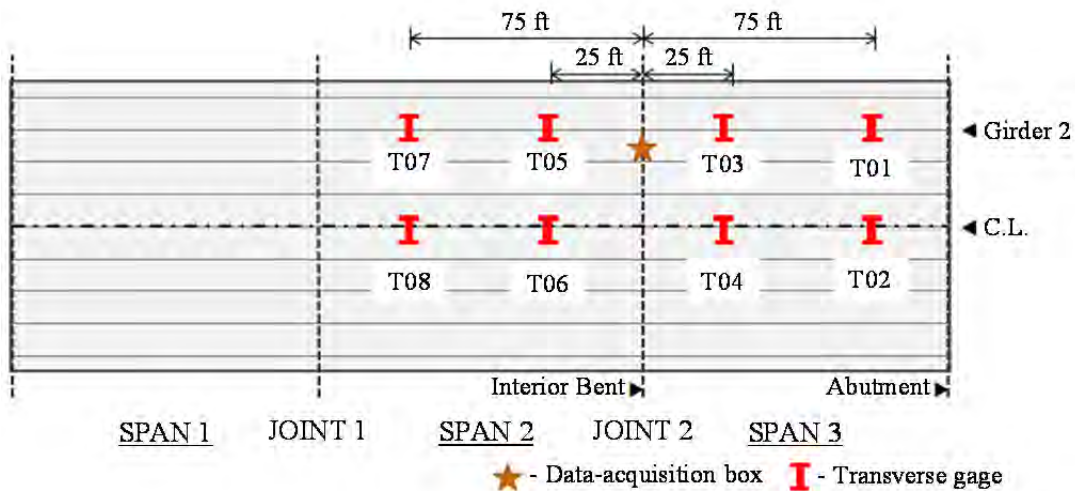


Figure 3-13: Gage layout for transverse bars, Wharton-Weems Overpass

Data-acquisition equipment

Data are recorded automatically and monitored using a wireless connection. Data-acquisition system for the Wharton-Weems Overpass is shown in Figure 3-14, consists of a data logger, a multiplexer, an analyzer, a modem, a battery, and a charge regulator. All components were placed in a stainless-steel box fastened to the bent between Girder 2 and 3 (Figure 3-15), because several wood braces were still in place between Girder 1 and 2.

The data-acquisition system is powered by a solar panel whose size was determined based on the number of vibrating-wire gages and the highest designed scanning rate. The south-facing solar panel was installed on the side face of the bent cap using anchor bolts. If the voltage from the solar panel exceeds a set level, the charge regulator makes an adjustment to avoid malfunction of the system. The battery provides a secondary power source when sunlight is insufficient to operate the system.

Before going to the field, all components of the instrumentation system were tested in the laboratory. The bracket for the solar panel, shown in Figure 3-16, was fabricated to permit the solar panel to face south and to prevent shading from the deck.

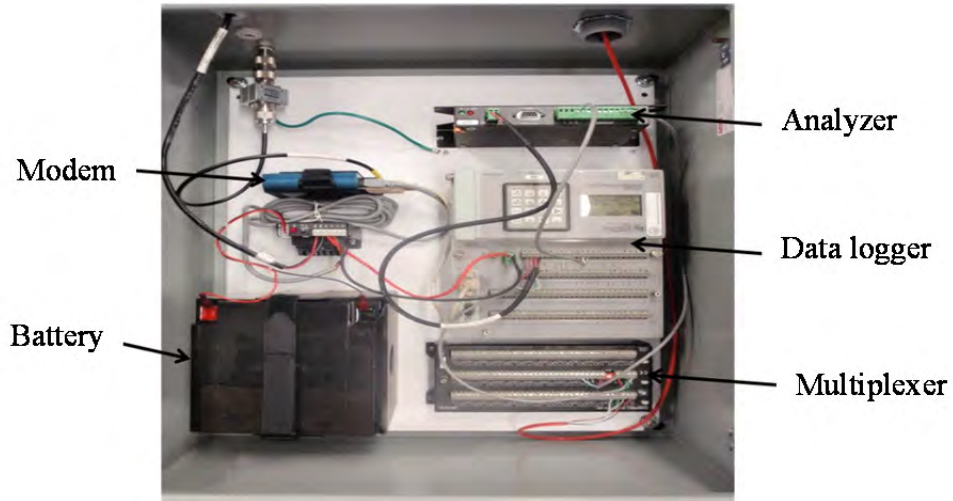


Figure 3-14: Solar-powered data-acquisition system, Wharton-Weems Overpass

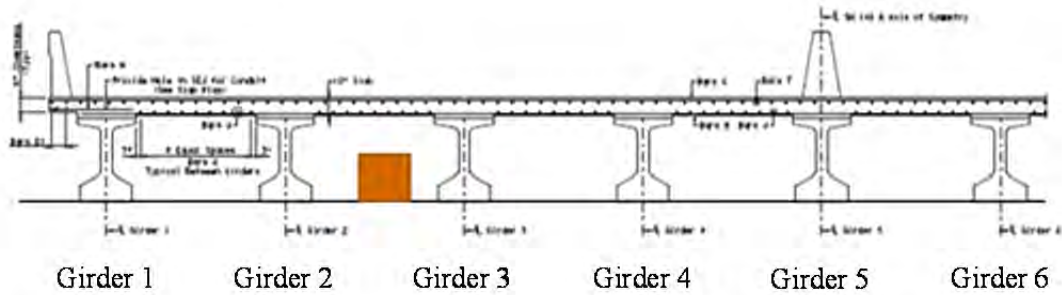


Figure 3-15: Location of data-acquisition box, Wharton-Weems Overpass



Figure 3-16: Bracket for solar panel, Wharton-Weems Overpass

3.2.5 Field instrumentation of Wharton-Weems Overpass

The Wharton-Weems Overpass was instrumented on July 25, 2011 after the contractor had placed all PCPs and the reinforcement for the CIP slab.

Installing vibrating-wire gages

Sixteen vibrating-wire gages were located as shown in Figure 3-17 and Figure 3-18. To identify the locations for gage installation easily, orange and yellow paint were sprayed over reinforcement at gage locations (Figure 3-17). Orange paint was used to mark locations for longitudinal gages, and yellow paint was used for transverse gages. All gage wires were routed under top-mat reinforcement to holes in the bedding strip under the PCPs (Figure 3-18). Before threading wires through the holes, gages were checked using a hand-held reader. After confirming proper connection between data logger and gages, gage wires were neatly arranged with zip-ties, and the holes in bedding strip were sealed with spray foam. During installation, the detection interval of the gages was 2 min. to make sure that connection between the data logger and the gages was maintained. Before casting, the interval was changed to 30 min. to save power and memory space in the data logger. The 30-min. interval was maintained for the next three months.



Figure 3-17: Gage instrumentation, Wharton-Weems Overpass

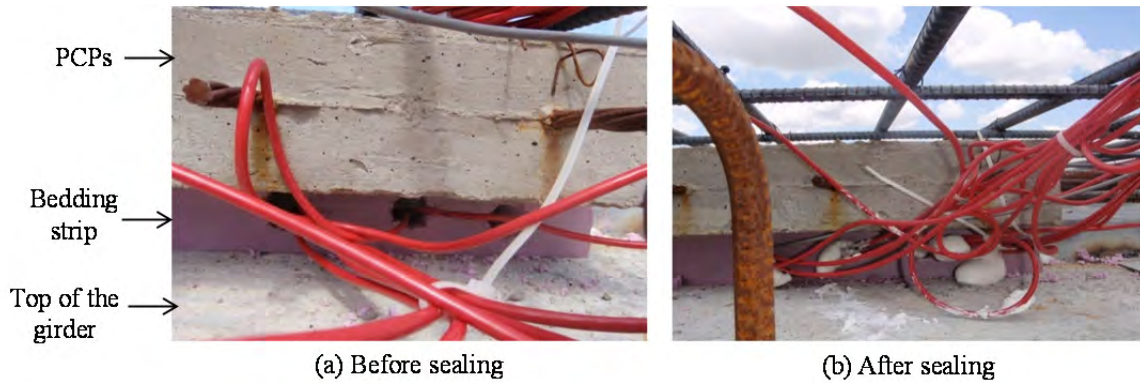


Figure 3-18: Threading wires through holes in bedding strip, Wharton-Weems Overpass

Placing data-acquisition box

The data acquisition-box was placed between Girder 2 and 3 on an interior bent. The box was anchored to the bent. Two bags of desiccant were placed in the box to protect the equipment from moisture. After connection, the hole for gage wires into the box was sealed using spray foam. See Figure 3-19.

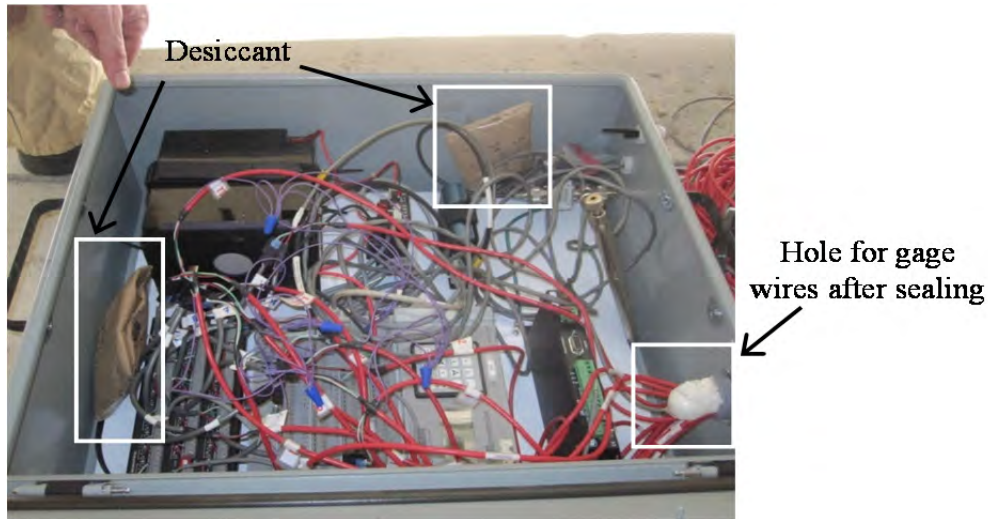


Figure 3-19: Data-acquisition box after connection, Wharton-Weems Overpass

Mounting solar panel

After mounting the solar panel and antenna to the bracket, the pre-fabricated bracket was installed on the side face of bent cap between Spans 2 and 3 after mounting the solar panel and antenna to the bracket. Power cables for the solar panel and antenna were routed to the data-acquisition box. See Figure 3-20.



Figure 3-20: Mounting solar panel beside bent cap, Wharton-Weems Overpass

Casting concrete deck, Wharton-Weems Overpass

The concrete deck was cast on July 28, 2011 during a 9-hour period, using concrete with a specified compressive strength of 4000 psi. Two concrete pump trucks were used. The casting sequence is shown in chronologically in Figure 3-21. Water was sprayed on the surface of the precast panels (Figure 3-21 a) to avoid excessive early-age shrinkage of the CIP portion. The

concrete was distributed over the deck by moving the hose from the concrete pump truck (Figure 3-21 b). The distributed concrete was consolidated with hand-held vibrators (Figure 3-21 c) and the surface was finished smoothly using a motorized trowel after screeding (Figure 3-21 d). Crack formers (“zip-strips”) were inserted along the transverse joints between spans (Figure 3-21 e) and curing compound was sprayed on the surface after bleed water had evaporated (Figure 3-21 f).



(a) Spraying water on panels



(b) Placing concrete



(c) Consolidating concrete



(d) Finishing surface



(e) Inserting crack former



(f) Spraying curing compound on deck surface

Figure 3-21: Construction sequence for CIP deck, Wharton-Weems Overpass

3.2.6 Results from Field Instrumentation of Wharton-Weems Overpass

Cracking inspection

The Wharton-Weems Overpass was inspected twice before it was opened to traffic on April 21, 2012. To observe cracks more clearly, water was sprayed on the surface. Because water in cracks evaporates more slowly than water on a sound surface, this procedure highlights cracks (Figure 3-22).



Figure 3-22: Spraying water on bridge deck for cracking inspection, Wharton-Weems Overpass

The first cracking inspection was conducted on September 12, 2011, and the result is shown in Figure 3-23. Yellow boxes in the figure refer to expected cracking locations based on readings from the vibrating-wire gages. Two transverse cracks along panel joints were expected, because strains measured by the gages which were instrumented along the joints were much higher than the theoretical cracking strain. The theoretical cracking strain was calculated by dividing the expected cracking stress of the topping slab concrete by the elastic modulus of the concrete.

Two transverse cracks were located at the construction joints over the bents. The average crack width over Joint 1 was 0.013 in., and the average crack width over Joint 2 was 0.007 in. No longitudinal cracks were observed.

The second cracking inspection was conducted on April 5, 2012, and the result is shown in Figure 3-24. Middle and side barriers were installed one to two weeks before the second cracking inspection. Cracking was inspected only in the half-width of the bridge where gages had been installed.

The center line of the bridge is highly susceptible to longitudinal cracking due to negative moment from self-weight and traffic loads. However, any cracking along the center line of the bridge could not be seen because the middle barrier was on the centerline of the bridge. As in the

first cracking inspection, two transverse cracks located along construction joints were observed, and no longitudinal cracks were found. The average crack widths along Joint 1 and Joint 2 were 0.010 in. Crack-width values at the locations where plastic crack formers were exposed were not considered for calculating average crack width. The reason is that in those locations, the concrete over the plastic crack former spalled off and accurate crack widths could not be obtained. The measured widths of both cracks do not show significant changes from the first to the second inspection.

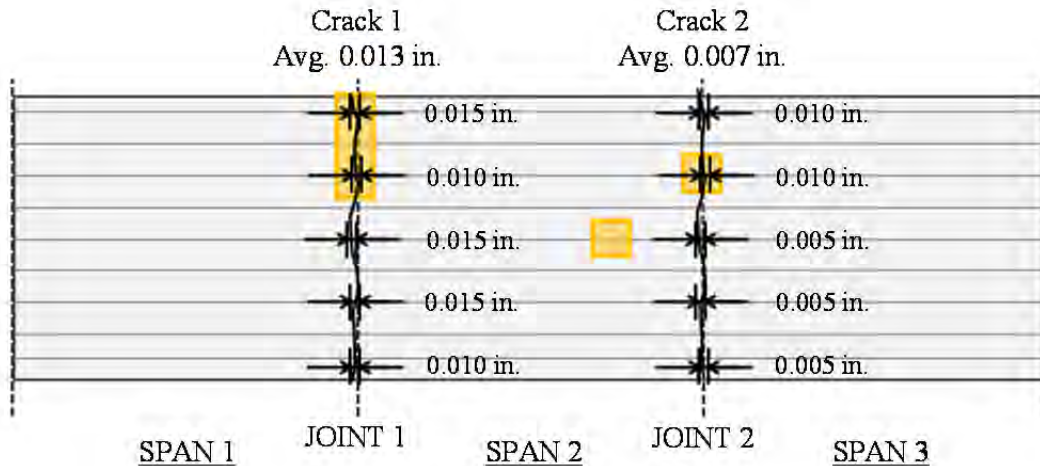


Figure 3-23: Results of first cracking inspection, Wharton-Weems Overpass

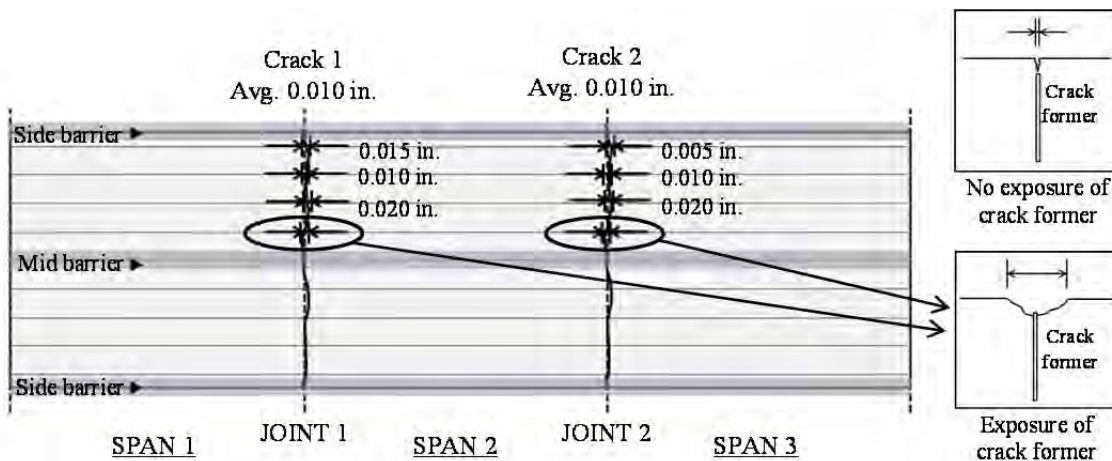


Figure 3-24: Results of second cracking inspection, Wharton-Weems Overpass

Long-term monitoring, Wharton-Weems Overpass

About a year's worth of data has been collected since the casting date (July 28, 2011), and the results are shown in Figures 3-25 to 3-28. In the figures, the x-axis represents the age of the deck from the casting date, and the y-axis represents stress in the concrete. Positive y-axis values indicate tensile stress, and negative values indicate compressive stress.

Figure 3-25 and Figure 3-26 show the results of long-term monitoring in the longitudinal direction of two testing areas in the Wharton-Weems Overpass. In both figures, the readings from the gages along the construction joints increased rapidly and reached the theoretical cracking value within a week after casting. The values started to stabilize about a month after casting. Other gages, located 50 ft from each joint, did not show significant changes in their readings during the entire monitoring period and their highest values were close to theoretical cracking stress.

The Wharton-Weems Overpass was opened to traffic on April 21, 2012, about 270 days after casting. That date is indicated by the black dashed vertical lines in Figure 3-25 to Figure 3-28. In the longitudinal direction, significant increases in steel stresses at the construction joints were observed. The largest measured strains in two testing areas were near the specified yield stress of the top-mat reinforcement. Other longitudinal gages did not show any significant changes.

All gages in the transverse direction showed similar behavior during the monitoring period, as shown in Figure 3-27 and Figure 3-28. High stress values are monitored during cold weather and low stress values are measured during hot weather. The concrete deck expands when the temperature increases, but this expansion is restrained by girders or adjacent decks; compressive stress occurred in bridge deck and it offsets tensile stress in the decks due to restrained creep and shrinkage. Therefore, the tensile stress values measured in hot weather are smaller than the values measured in cold weather. In Figure 3-28, the reading values of T08 are not included. Unrealistic values of strain were monitored in T08 on March 28, 2012, 245 days after casting. The date coincided with installation of the middle barrier. There are two possible reasons for this change in T08. First, a drill bit may have hit the gage while drilling the holes for the barrier. Second, heavy trucks or equipment used during installation of the middle barrier might have caused cracking and large strain measurement.

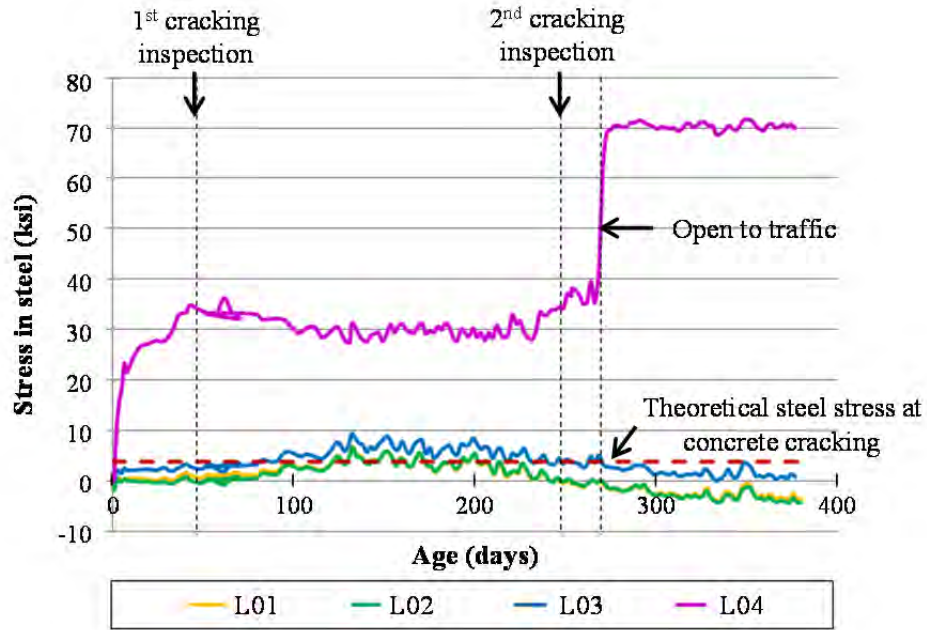


Figure 3-25: Stresses in current TxDOT standard reinforcement, Wharton-Weems Overpass (longitudinal direction)

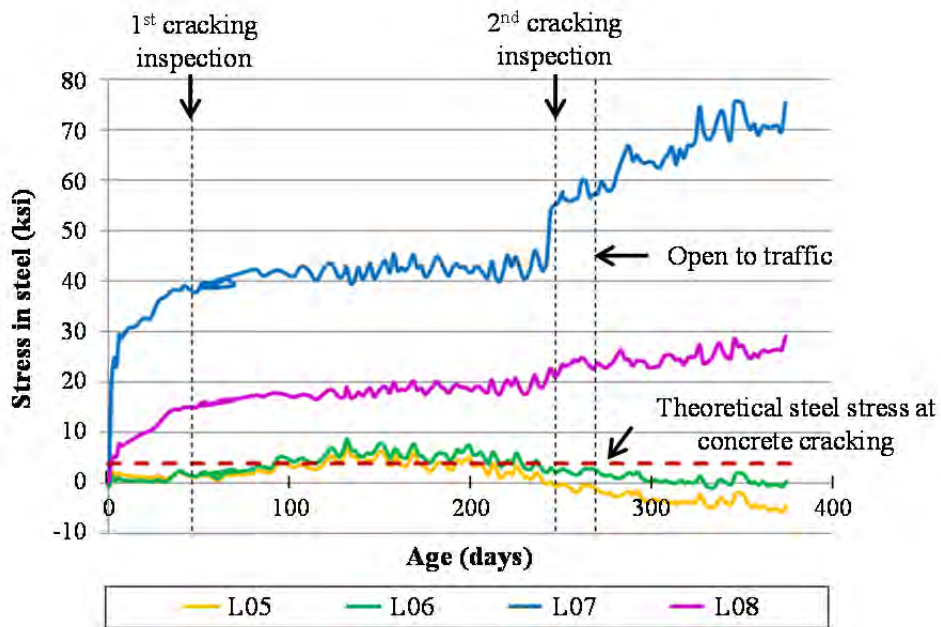


Figure 3-26: Stresses in reduced deformed-bar reinforcement, Wharton-Weems Overpass (longitudinal direction)

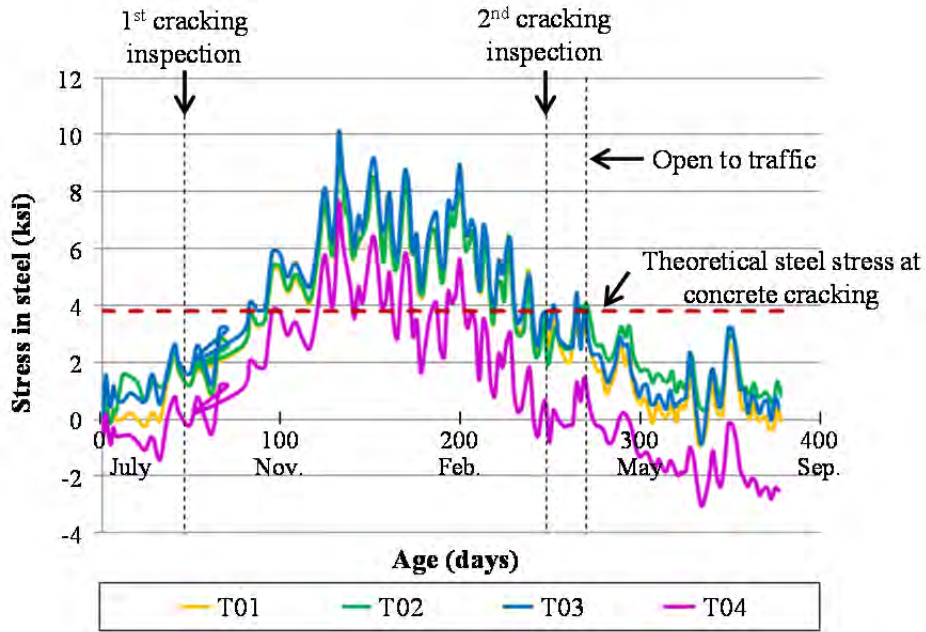


Figure 3-27: Stresses in current TxDOT standard reinforcement, Wharton-Weems Overpass (transverse direction)

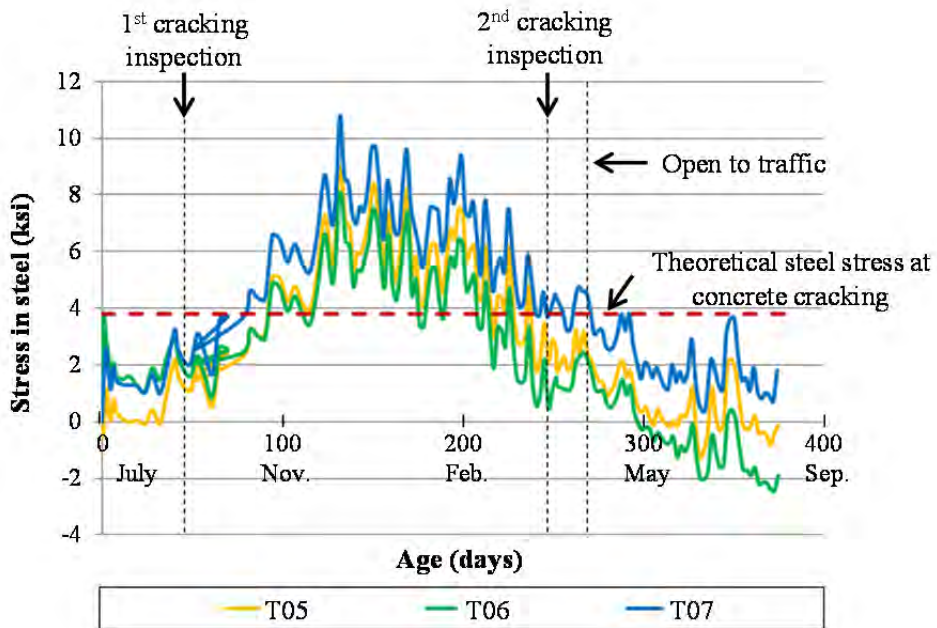


Figure 3-28: Stresses in reduced deformed-bar reinforcement, Wharton-Weems Overpass (transverse direction)

Use of P-method to predict cracking in CIP-PCP bridge decks

Description of P-method

Peterman and Ramirez (1998) propose a technique, called the “P-method,” to determine when cracks are likely to form in CIP-PCP bridge decks. The P-method takes into account the following items: i) the length and stiffness of diaphragm region; ii) the different initiation time for creep of PCPs and CIP slabs; and iii) restraining effects of PCPs and top-mat reinforcement in CIP slabs on shrinkage of CIP slabs. In the P-method, the diaphragm region indicates the area between interior supports subjected to negative moment, and it is assumed that the cracks due to restraint moment will form on the top surface of the diaphragm region and these cracks will reduce the stiffness of the diaphragm region. Moreover, it is also assumed that the cracks due to restraint moment will not form in the main span regions, so the stiffness of the main span does not change after cracking.

Using the P-method, the restraint moment (M_r) at a critical section of the deck can be calculated using Equation 3-2.

$$M_r = \left[\frac{3}{2} \alpha M_p - \alpha (M_d)_{precast} \right] \times [\Delta(1 - e^{-\phi_1})] - \alpha (M_d)_{CIP} \times (1 - e^{-\phi_2}) - \frac{3}{2} \alpha M_s \left(\frac{1 - e^{-\phi_2}}{\phi_2} \right) \quad \text{Equation 3-2}$$

- Where,
- α = coefficient that accounts for the relative stiffness of the diaphragm region and main spans
 - M_p = moment caused by prestressing force about centroid of composite member
 - M_s = differential shrinkage moment, adjusted for restraint of precast panels and steel reinforcement
 - $(M_d)_{precast}$ = mid-span moment due to dead load of precast panels
 - $(M_d)_{CIP}$ = mid-span moment due to dead load of CIP topping
 - ϕ_1 = creep coefficient for creep effects initiating when prestress force is transferred to precast panels
 - ϕ_2 = creep coefficient for creep effects initiating when CIP topping is cast
 - $\Delta(1 - e^{-\phi_1})$ = change in expression $(1 - e^{-\phi_1})$ occurring from time CIP topping is cast to time corresponding to restraint moment calculation

In Equation 3-2, the coefficient α was obtained using moment distribution method. M_p , M_s , $(M_d)_{precast}$, and $(M_d)_{CIP}$ can be assumed to act uniformly over the length of members. If uniform moment is applied over entire length of the member with fixed ends, fixed-end moments occur at both ends, equal in magnitude to the applied uniform moment. Therefore, the restraint moment due to uniform moment can be calculated by applying the fixed-end moment at the ends and distributing them according to the stiffness of the member by moment distribution method (Peterman and Ramirez 1998). Moreover, the different shrinkage moment (M_s) in Equation 3-2 was estimated by Equation 3-3.

$$M_s = \varepsilon_s E_d A_d \left(e_c + \frac{h}{2} \right) \left[\frac{I}{1 + \frac{E_p A_p}{E_d A_d}} \right] \left[\frac{I}{1 + \frac{E_s A_s}{E_d A_d}} \right] \quad \text{Equation 3-3}$$

Where,

E_p	= modulus of elasticity of precast panels
A_p	= area of precast panels
E_s	= modulus of elasticity of steel reinforcement in CIP deck
A_s	= area of steel reinforcement in CIP deck
E_d	= modulus of elasticity of CIP deck
A_d	= area of CIP deck

Application of P-method to Wharton-Weems Overpass

In this section, the restraint moments in the Wharton-Weems Overpass were calculated using the P-method to estimate the likelihood of deck cracking, and the probable time for the development of that cracking. The results of the calculation are also compared with the results of the cracking inspection to determine whether or not the P-method can accurately predict bridge-deck cracking.

Longitudinal restraint moment - Transverse crack

Figure 3-29 shows the area considered in the calculation for longitudinal restraint moment in the Wharton-Weems Overpass. The width of the section was 9.3 ft, equal to the space between two adjacent girders. The section consisted of PCPs and CIP slabs, with a thickness of 4 in.; therefore, the entire thickness of the section was 8 in. Section T-T in Figure 3-29 can be simplified as in Figure 3-30. The length of the main-span region (L_m) was 600 in., and the length of diaphragm (L_d) was 1 in., a space between PCPs in the bridge.

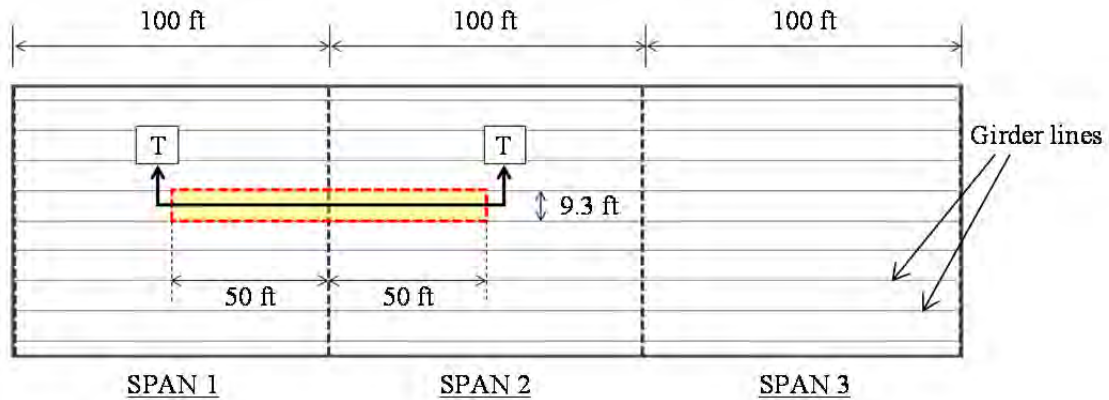


Figure 3-29: The area for the calculation of longitudinal restraint moment of Wharton-Weems Overpass

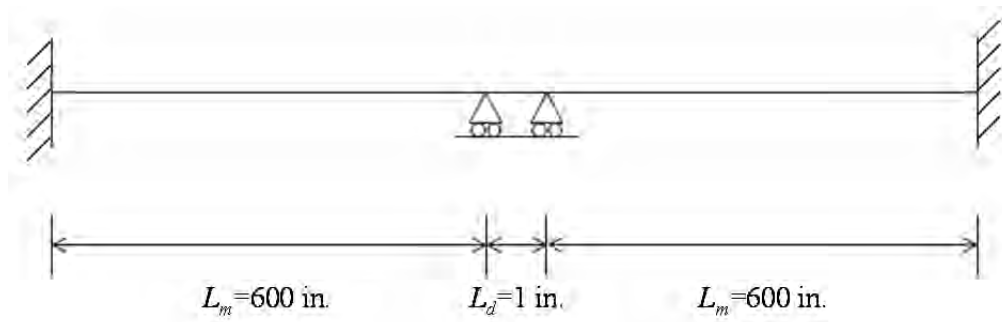


Figure 3-30: Simplified section T-T

The moment due to prestressing strand was ignored because the strands were placed perpendicular to the girder lines. Much of information required for the calculation was unknown, so the following values were assumed. Only the Current TxDOT Standard Reinforcement was considered as top-mat reinforcement, because the change of the top-mat reinforcement in this study is not big enough to change the calculations using the P-method.

- i) Specified concrete strength of PCPs: 9,000 psi
- ii) specified concrete strength of CIP slabs: 4,000 psi
- iii) Age of PCPs when CIP topping was cast: 55 days
- iv) Average humidity: 60%
- v) Prestressing strands of PCPs: 3/8 in. seven-wire strands at 6 in.
- vi) Remaining prestress in strand during first month after the casting: 175 ksi
- vii) Elastic modulus of reinforcement: 29,000 ksi.
- viii) Top-mat reinforcement
 No. 4 bar at 9 in. (longitudinal direction)
 No. 5 bar at 6 in. (transverse direction)

Using the assumed information and ACI 209, ultimate creep coefficients and shrinkage strains of PCPs and CIP slabs were calculated and the resultant values are shown in below:

- i) Ultimate creep coefficient of PCPs: 3.42
- ii) Ultimate creep coefficient of CIP slabs: 3.40
- iii) Ultimate shrinkage strain of PCPs: 600×10^{-6}
- iv) Ultimate shrinkage strain of CIP slabs: 613×10^{-6}

Creep and shrinkage strain at time t can be obtained by multiplying their ultimate values by R (Equation 3-4), a time-dependent creep and shrinkage coefficient (Corley and Sozen, 1966):

$$R = 0.13 \times \ln(t+1) \quad \text{Equation 3-4}$$

Section properties were also evaluated by transforming the PCP section into a section which has the same compressive strength as the CIP slabs. The compressive strength of the PCPs was taken as 9,000 psi regardless of age, because the compressive strength of concrete does not change significantly 28 days after casting. The compressive strength of the CIP slabs did change with time, and was expressed as Equation 3-5 adapted from ACI 209. The detailed procedure for calculating restraint moment is shown in Appendix B.

$$f_c(t) = f_c(28) \times \left(\frac{t}{2.3 + 0.92 \times t} \right) \quad \text{Equation 3-5}$$

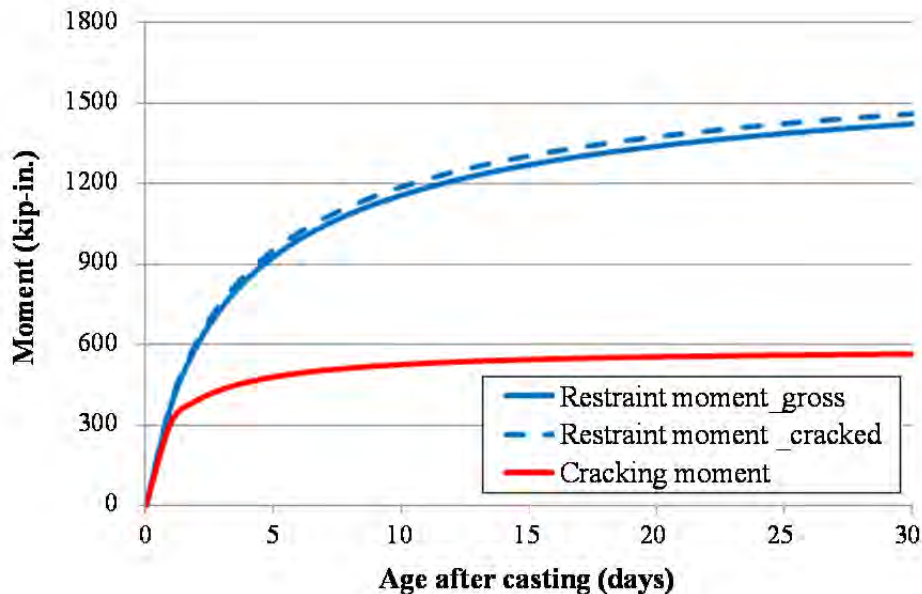


Figure 3-31: Longitudinal restraint moment and cracking moment, Wharton-Weems Overpass

In Figure 3-31, restraint moments calculated using the P-method, and calculated cracking moment using modulus of rupture of the CIP topping concrete are plotted together. In the calculation for the longitudinal restraint moment, M_p is zero because the strands were placed perpendicular to girder lines, so the effect of the prestressing force on the longitudinal restraint moment can be ignored.

In that figure, the blue solid line represents the calculated restraint moment of the uncracked section, and the blue dashed line represents the calculated restraint moment of cracked section. The same values of gross section moment of inertias were used for the diaphragm and main span region for the calculation of un-cracked section. In calculating restraint moment in a cracked specimen, however, the cracked moment of inertia was used for the diaphragm region, and the gross moment of inertia for the main-span region. The red line represents cracking moment calculated using the modulus of rupture of the CIP concrete. If the restraint moment is greater than the cracking moment, it may be concluded that cracks have developed in the specimen.

As shown in Figure 3-31, the restraint moment of the uncracked and the cracked section were almost same in this case, because the length of the diaphragm region was very small compared to the length of the main-span region. Moreover, the restraint moment became greater than the cracking moment within a day after CIP slab casting implying that the bridge may have transverse cracks on the deck within a day after casting. Actually, transverse cracks are expected to occur around 2-3 days after casting based on the measured strain values.

Transverse restraint moment - Longitudinal crack

The area considered in the calculation for transverse restraint moment of Wharton-Weems Overpass is shown in Figure 3-32. Transverse restraint moment can cause longitudinal cracks on the bridge deck. Section L-L in Figure 3-32 can be simplified as shown in Figure 3-33. The width of the section was 100 ft, equal to the span length of the bridge. The length of main span region (L_m) was 92 in., and the length of the diaphragm region (L_d) was 36 in., equal to the length of top flange of a Tx 46 I-girder used in Wharton-Weems Overpass.

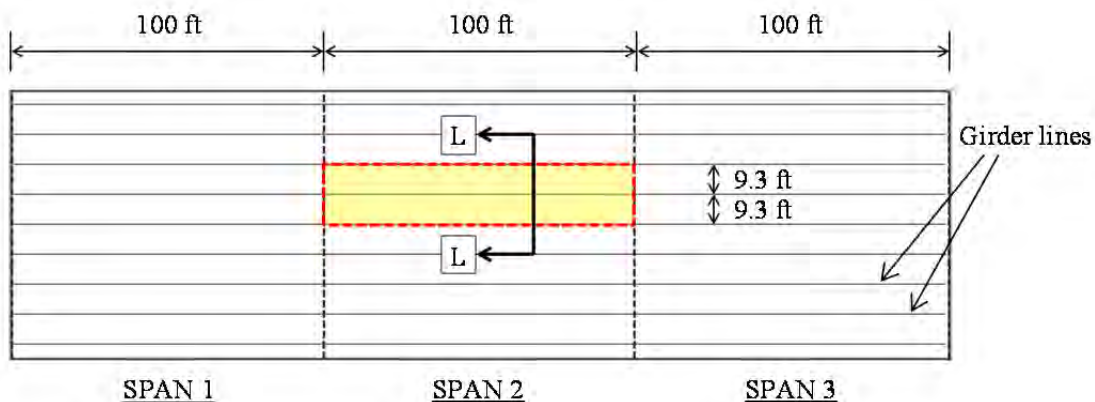


Figure 3-32: Area for calculation of transverse restraint moment, Wharton-Weems Overpass

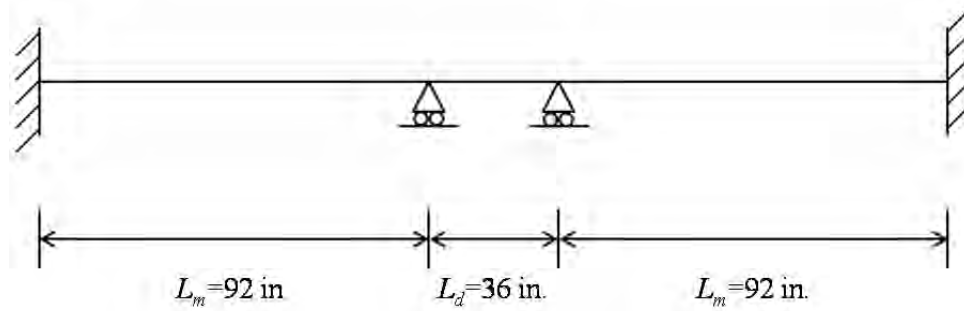


Figure 3-33: Simplified section L-L, Wharton-Weems Overpass

In Figure 3-34, calculated transverse restraint moments using the P-method, and calculated cracking moment using the modulus of rupture of the CIP topping concrete are shown. In the figure, the blue line represents the calculated restraint moment by P-method assuming that the specimen is not cracked. The values on this blue line were obtained by using the same moment of inertia for diaphragm and main-span regions as stated in previous section. The red represents the cracking, calculated using the modulus of rupture of the CIP concrete.

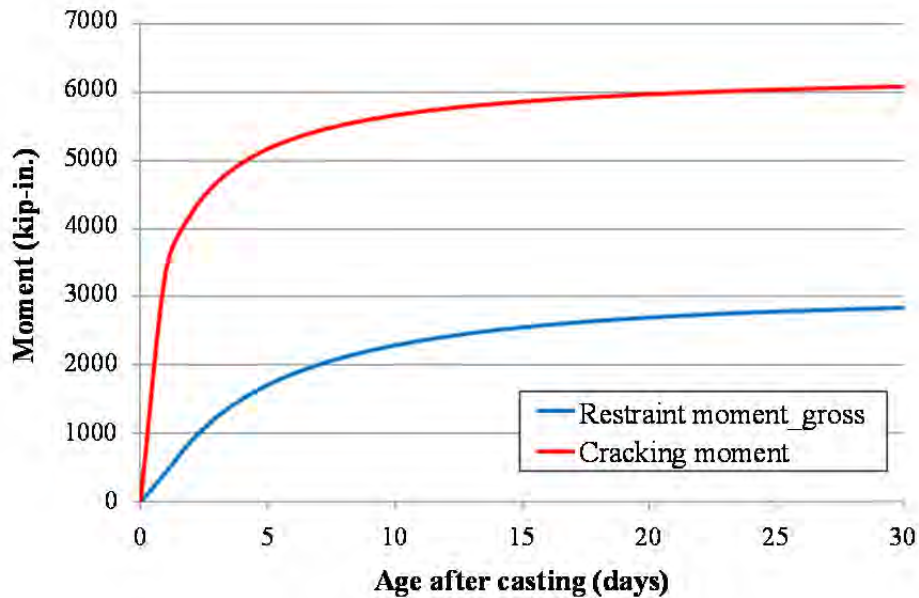


Figure 3-34: Transverse restraint moment and cracking moment, Wharton-Weems Overpass

As shown in Figure 3-34, the values on the blue line are smaller than the value on the red line at the same age. It means that the restraint moment in the bridge was not large enough to cause cracking in the longitudinal direction. This result matches well with the result of cracking inspection

3.3 Lampasas River Bridge

3.3.1 Description

The Lampasas River Bridge is, located near Belton on US IH-35. The bridge consists of 5 spans with different lengths and different numbers of girders. Spans 1 and 2 are 100-ft long and have 4 girders. Span 3 is 120-ft long and has 5 girders. Spans 4 and 5 are 80 ft. long and have 4 girders. The bridge has a 15-degree skew. The bridge was constructed using the CIP-PCP bridge deck system. The CIP concrete slabs and PCPs are 4-in. thick. In Figure 3-35 to Figure 3-38, plan and section views of the Lampasas River Bridge are shown.

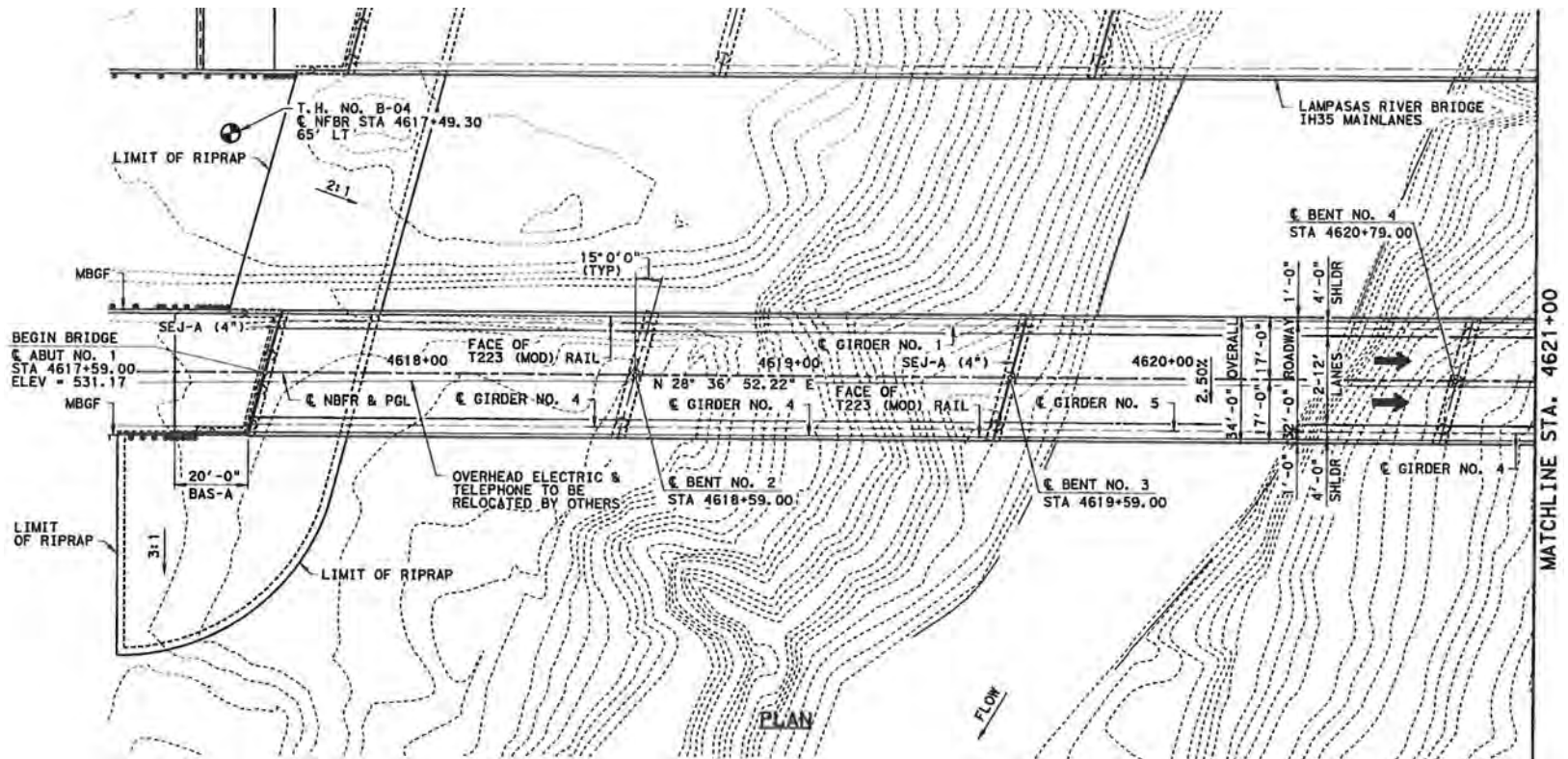


Figure 3-35: Plan view of Lampasas River Bridge (Spans 1 to 3)

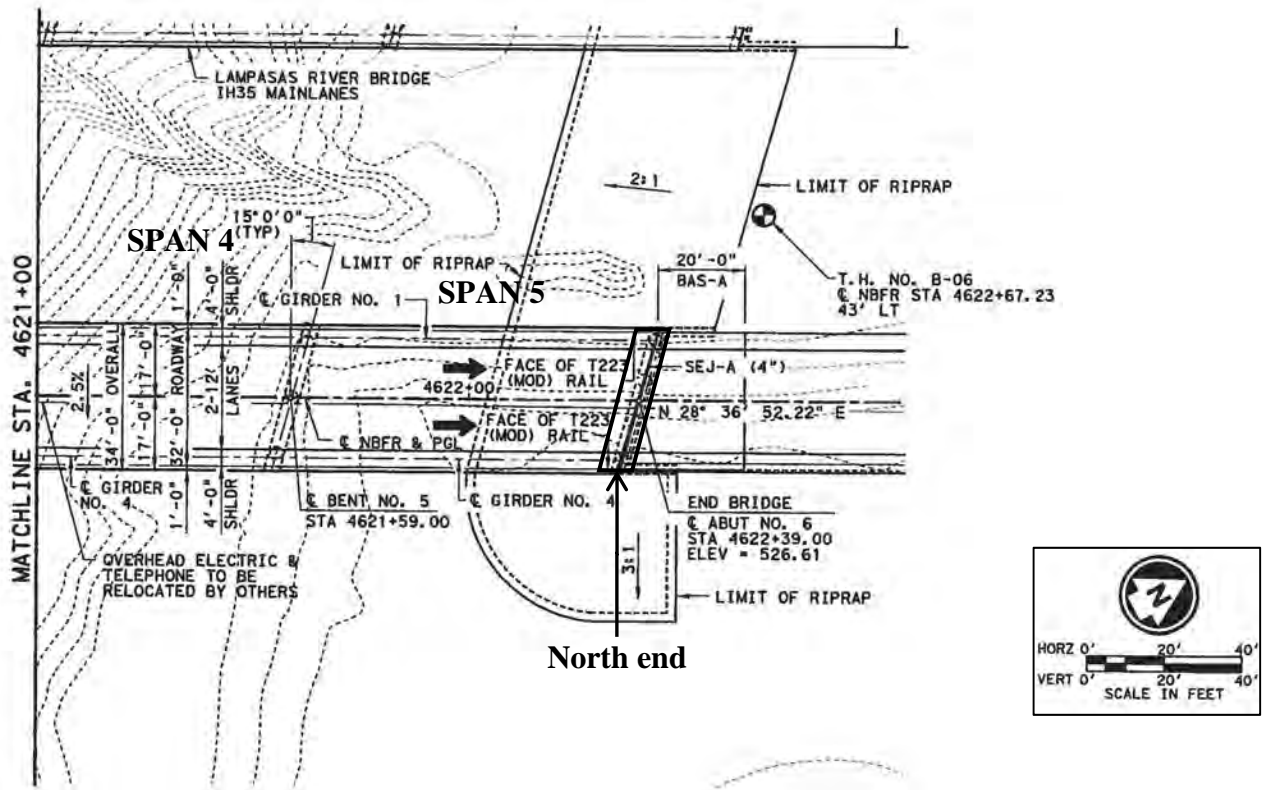


Figure 3-36: Plan view of Lampasas River Bridge (Spans 4 to 5)

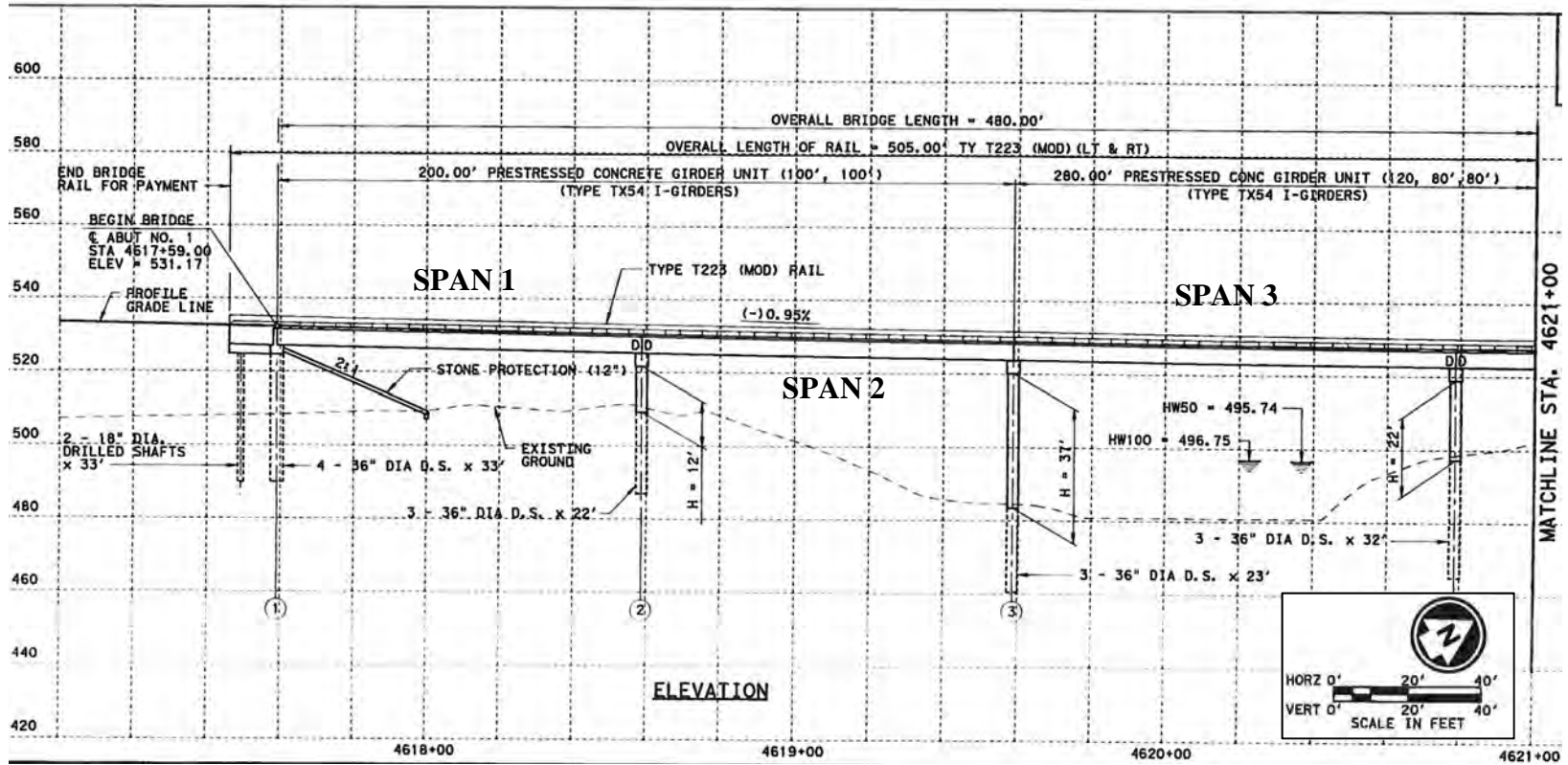


Figure 3-37: Section view of Lampasas River Bridge (Spans 1 to 3)

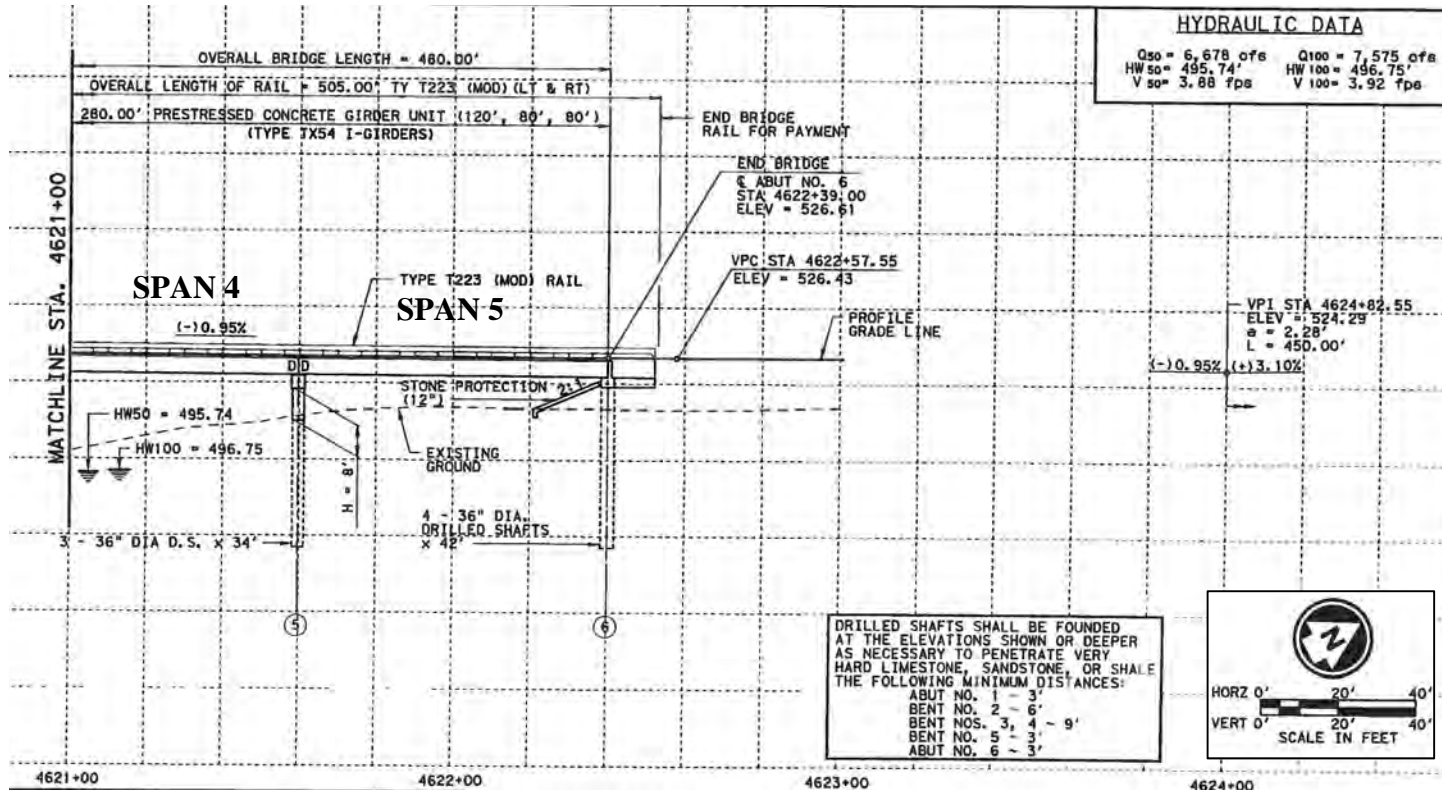


Figure 3-38: Section view of Lampasas River Bridge (Spans 4 to 5)

3.3.2 Top-mat Reinforcement Options, Lampasas River Bridge

In Figure 3-39 are shown the top-mat transverse reinforcement options for the Lampasas River Bridge. Three reinforcement options were included; Current TxDOT Standard Design (No. 5 bars at 6 in.); Reduced Deformed-Bar Reinforcement (No. 4 bars at 6 in.); and Reduced Welded-Wire Reinforcement (D20 wires at 6 in.). To obtain similar testing areas for each option, the testing areas are divided as shown in Figure 3-39. SPAN 3 has a different number of girders compared to other spans, so SPAN 3 was not instrumented. A D20 wire has the same area as a No. 4 bar.

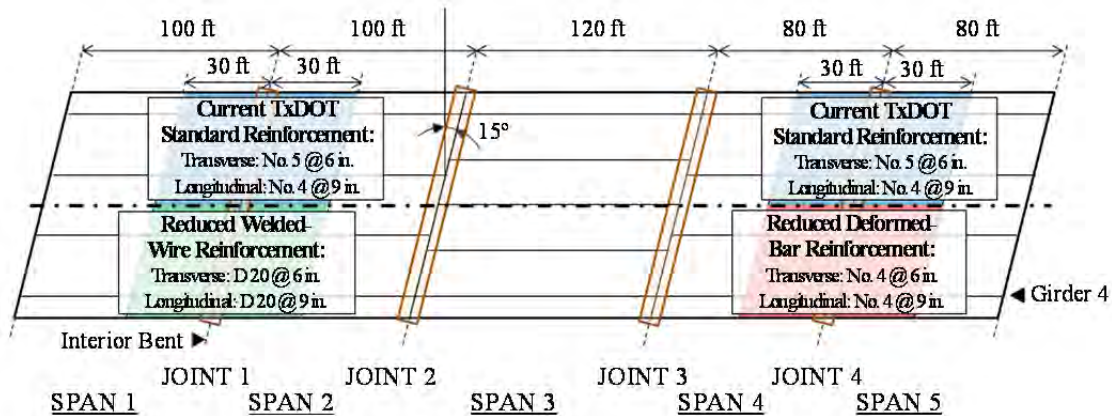


Figure 3-39: Reinforcement options, Lampasas River Bridge

3.3.3 Splice Details, Lampasas River Bridge

Longitudinal splices

Figure 3-40 to Figure 3-50 shows the details of the longitudinal bar splices. As with the Wharton-Weems Overpass, splices were located away from joints. Reinforcement splice lengths for standard deformed bars were calculated using Equation 3-1 (Equation 12-1 of ACI 318 (2011)); and splice lengths for welded wire reinforcement using Equation 3-6. The welded deformed-wire factor (ψ_w) in Equation 3-6 was adopted from Section 12.7.2 of ACI 318 (2011). Blue lines refer to the Current TxDOT Standard Design option; green lines refer to the Reduced Welded-Wire Reinforcement option; and red lines indicate the Reduced Deformed-Bar Reinforcement option. Black lines represent the reinforcement in non-test areas. Detailed calculations for required splice length are shown in Appendix A.

$$\frac{l_d}{d_b} = \psi_w \times \frac{3}{40} \times \frac{f_y}{\lambda \times \sqrt{f'_c}} \times \frac{\psi_t \times \psi_e \times \psi_s}{\left(\frac{c_b + K_{tr}}{d_b}\right)} \quad \text{Equation 3-6}$$

Where, ψ_w = welded deformed-wire reinforcement factor, Section 12.7.2 in ACI 318-11

- l_d = development length in tension, in.
- d_b = nominal diameter of bar, in.
- f_y = specified yield strength of reinforcement, psi
- λ = modification factor related to unit weight of concrete
- f'_c = specified compressive strength of concrete, psi
- ψ_t = factor used to modify development length based on reinforcement location
- ψ_e = factor used to modify development length based on reinforcement coating
- ψ_s = factor used to modify development length based on reinforcement size
- c_b = smaller of (a) the distance from center of bar or wire to nearest concrete surface, and (b) one-half the concrete center-to-center spacing of bars or wires being developed, in.
- K_{tr} = transverse reinforcement index

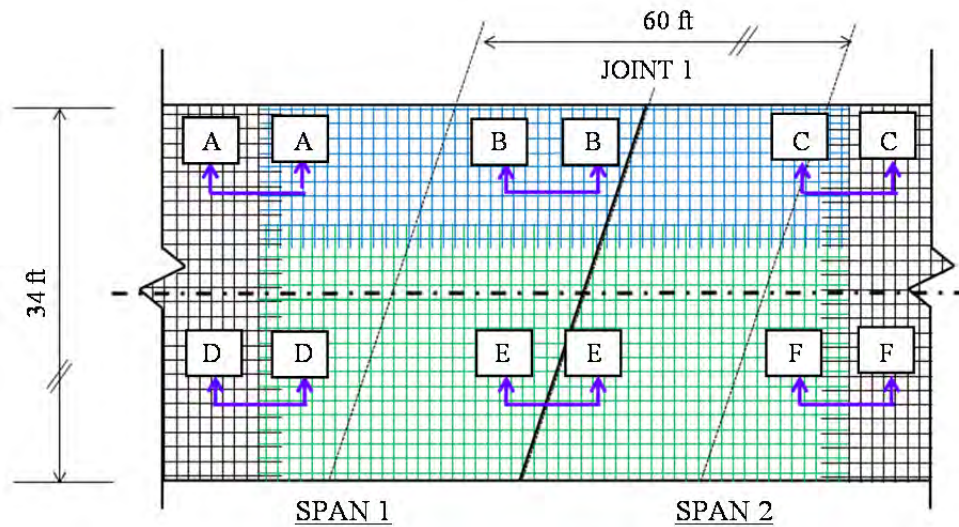


Figure 3-40: Details of longitudinal splices, Lampasas River Bridge (Span 1 and Span 2)

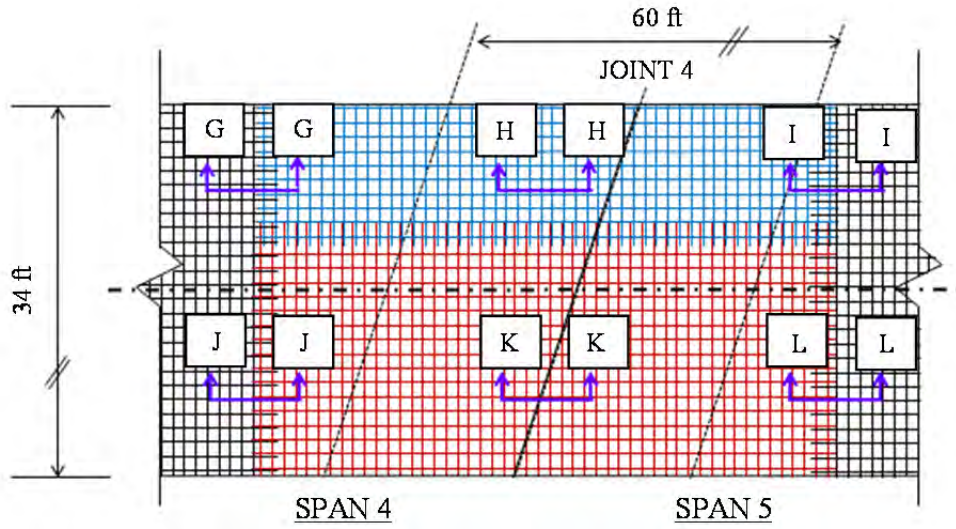


Figure 3-41: Details of longitudinal splices, Lampasas River Bridge (Span 4 and Span 5)

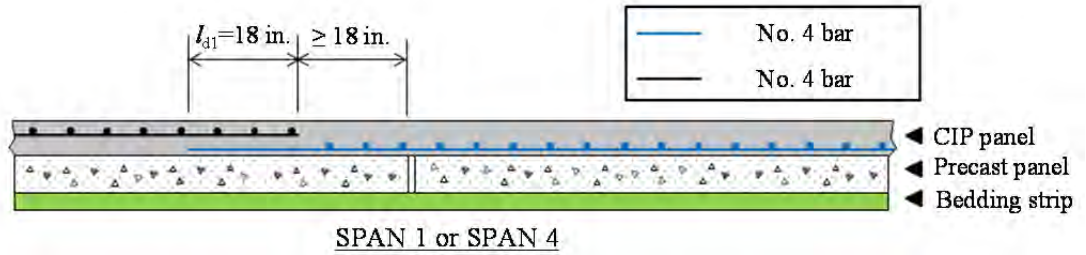


Figure 3-42: Details of longitudinal splices, Lampasas River Bridge (Sections A-A and G-G)

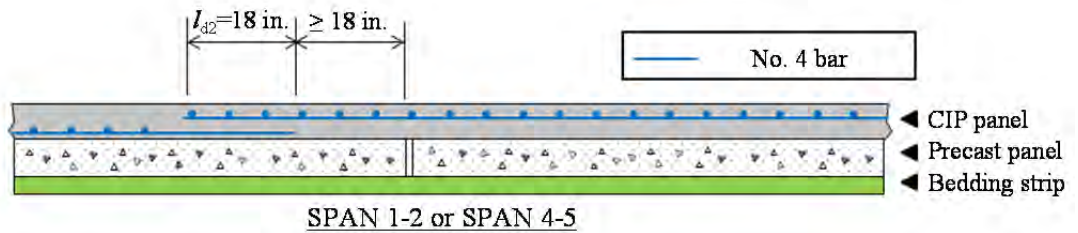


Figure 3-43: Details of longitudinal splices, Lampasas River Bridge (Sections B-B and H-H)

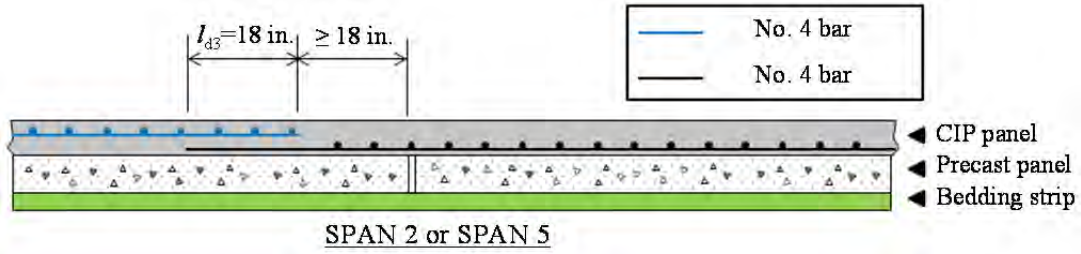


Figure 3-44: Details of longitudinal splices, Lampasas River Bridge (Sections C-C and I-I)

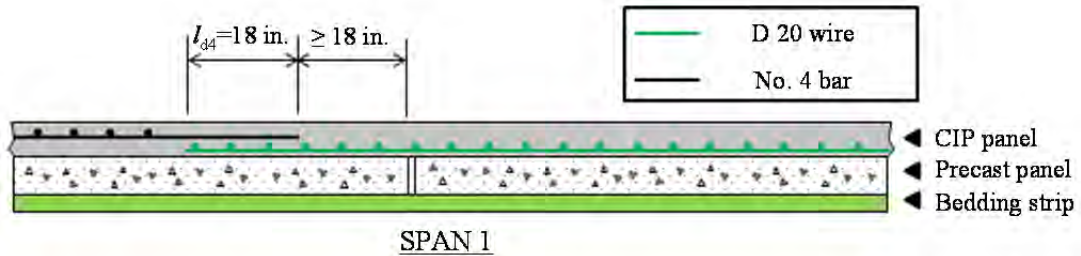


Figure 3-45: Details of longitudinal splices, Lampasas River Bridge (Section D-D)

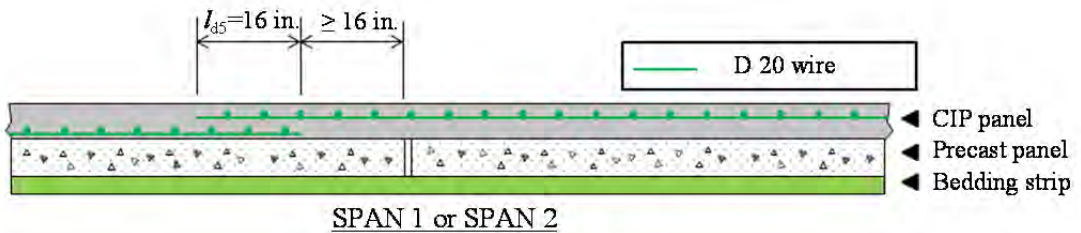


Figure 3-46: Details of longitudinal splices, Lampasas River Bridge (Section E-E)

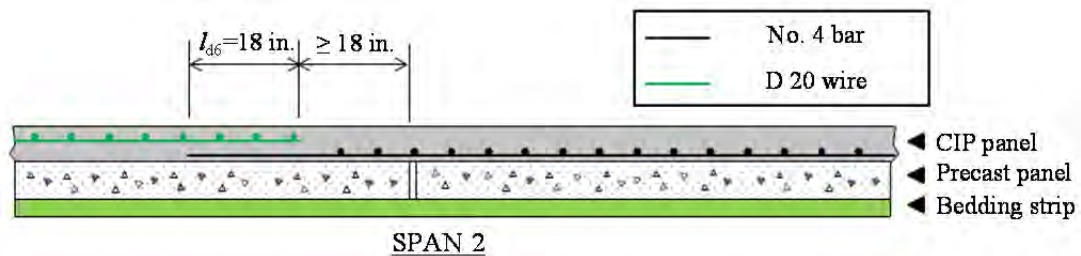


Figure 3-47: Details of longitudinal splices, Lampasas River Bridge (Section F-F)

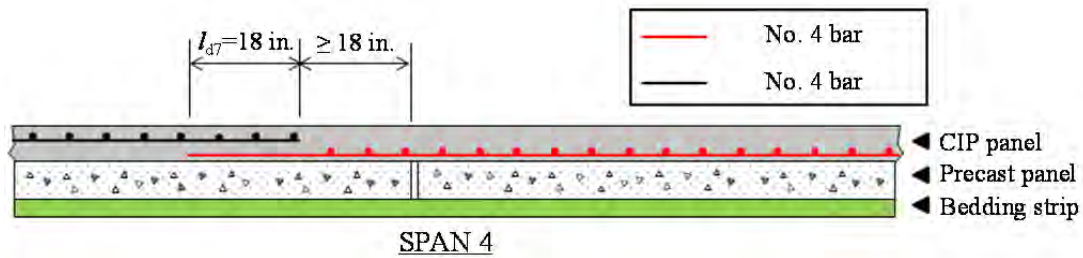


Figure 3-48: Details of longitudinal splices, Lampasas River Bridge (Section J-J)

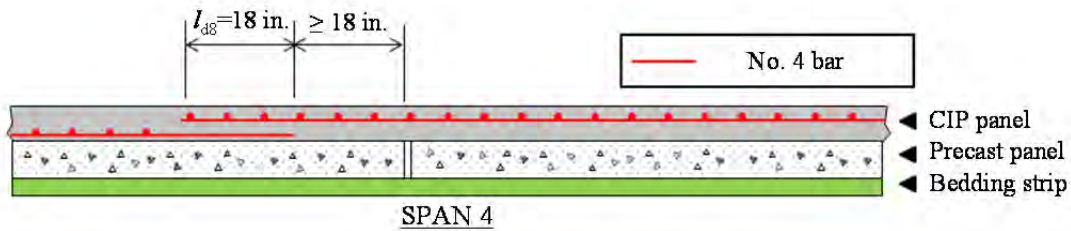


Figure 3-49: Details of longitudinal splices, Lampasas River Bridge (Section K-K)

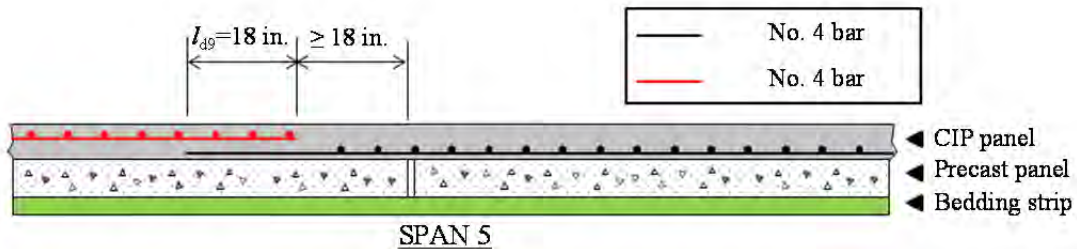


Figure 3-50: Details of longitudinal splices, Lampasas River Bridge (Section L-L)

Transverse splices

In Figure 3-51 to Figure 3-58 are shown details of the transverse bar splices. The calculations are shown in Appendix A.

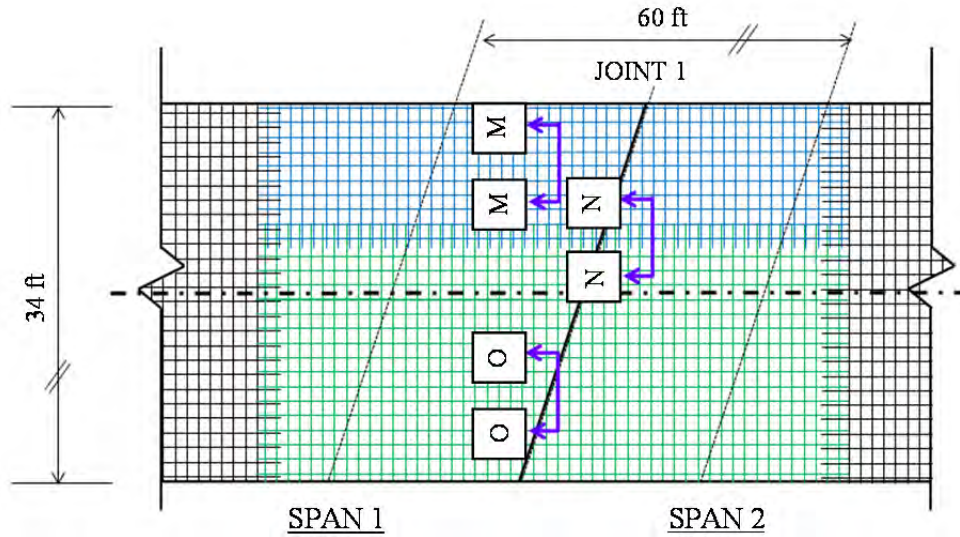


Figure 3-51: Details of transverse splices, Lampasas River Bridge (Span 1 and Span 2)

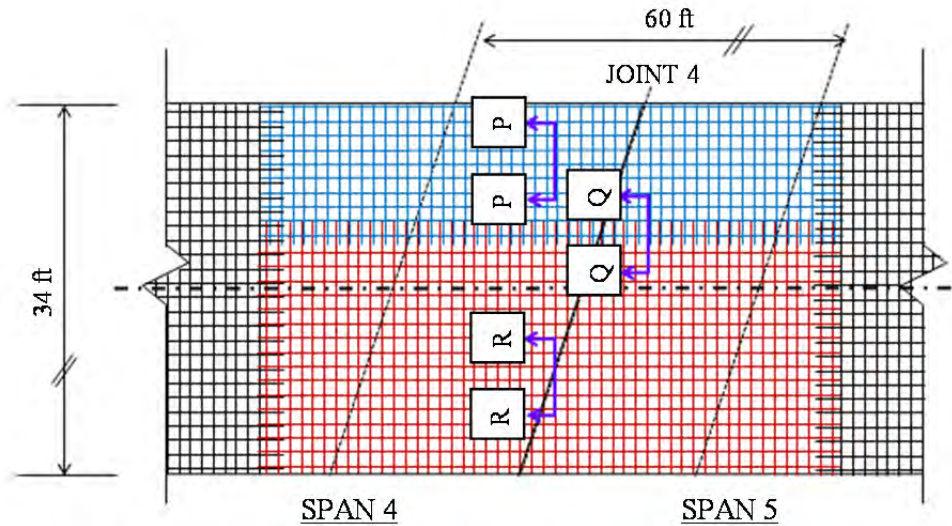


Figure 3-52: Details of transverse splices, Lampasas River Bridge (Span 4 and Span 5)

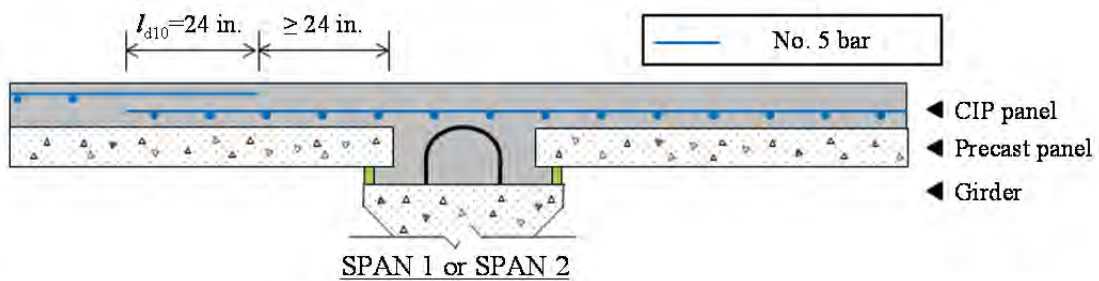


Figure 3-53: Details of transverse splice, Lampasas River Bridge (Section M-M)

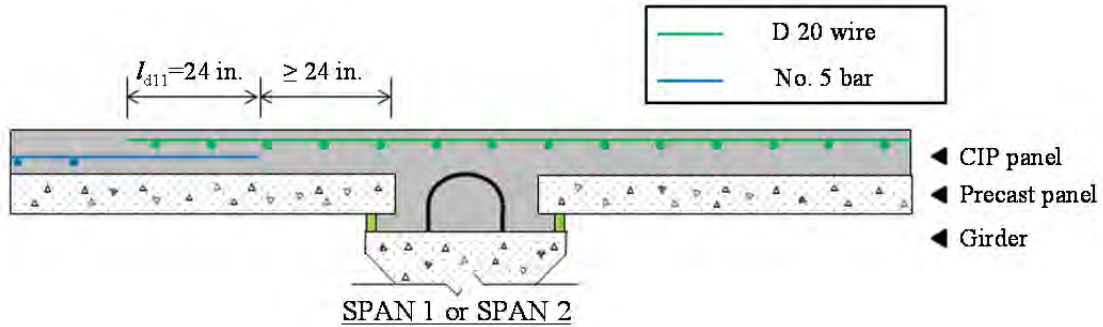


Figure 3-54: Details of transverse splice, Lampasas River Bridge (Section N-N)

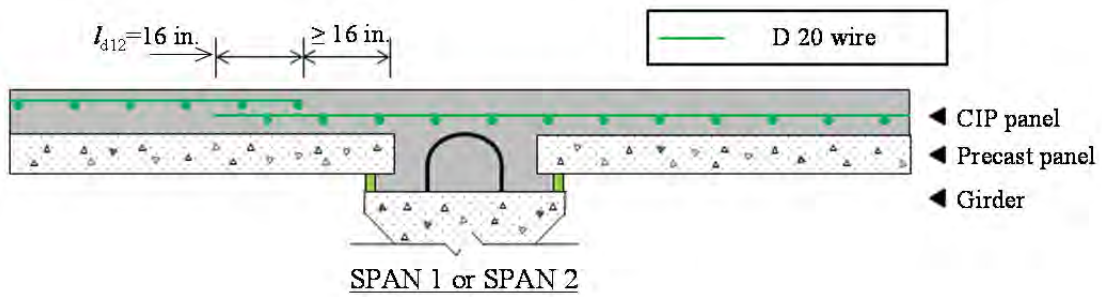


Figure 3-55: Details of transverse splice, Lampasas River Bridge (Section O-O)

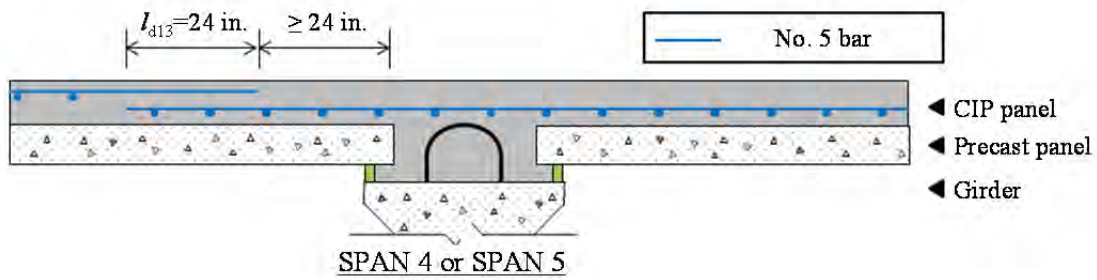


Figure 3-56: Details of transverse splice, Lampasas River Bridge (Section P-P)

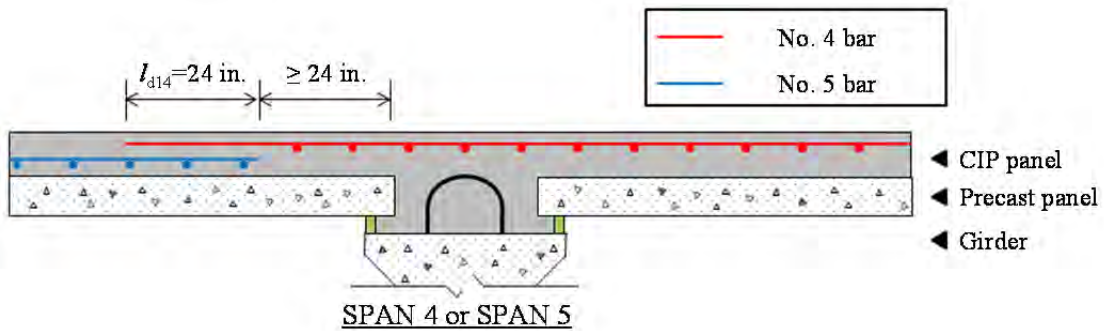


Figure 3-57: Details of transverse splice, Lampasas River Bridge (Section Q-Q)

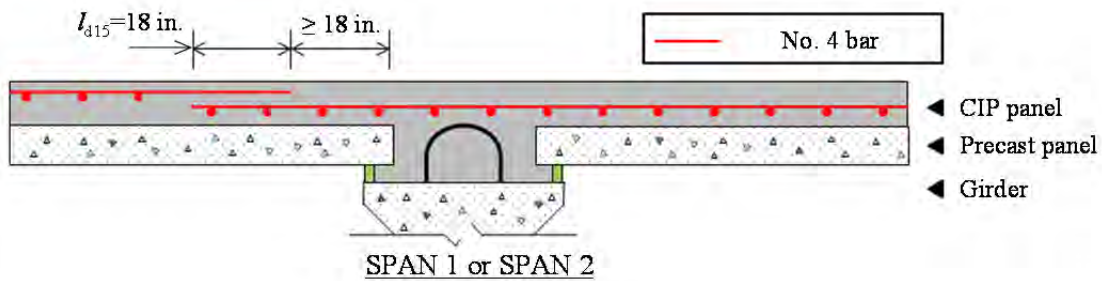


Figure 3-58: Details of transverse splice, Lampasas River Bridge (Section R-R)

3.3.4 Instrumentation of Lampasas River Bridge

Gage location and identification

The gages used in the Lampasas River Bridge are the same as the gages used in the Wharton-Weems Overpass (Section 3.2.4).

Figure 3-59 and Figure 3-60 indicate gage layouts for longitudinal bars and for transverse bars. Brown stars indicate the location of the data-acquisition equipment. Because the number of girders in Span 3 is not equal to the number of girders in other spans, Span 3 was not used as a test area. The following designation system is used:

- i) Longitudinal gages are denoted as “Lxx.” Odd-numbered gages are located over Girder 1 or 4, and even-numbered gages over Girder 2 or 3. Gages on the longitudinal bars are located at the joint and at 25 ft on each side of the joint.
- ii) Transverse gages are denoted as “Txx.” Odd-numbered gages are located over Girder 1 or 4, and even-numbered gages over Girder 2 or 3. All transverse gages are located 20 ft from Joint 1 or Joint 4

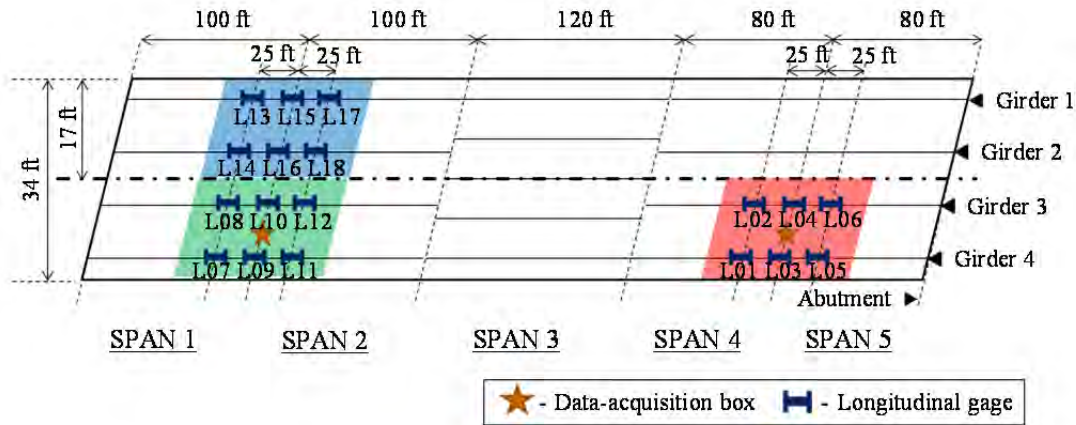


Figure 3-59: Gage layout for longitudinal bars, Lampasas River Bridge

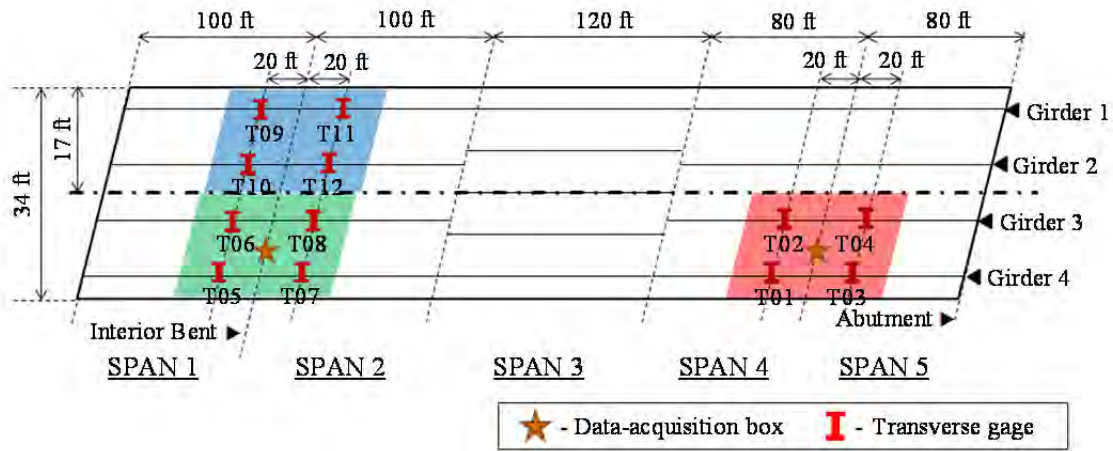


Figure 3-60: Gage layout for transverse bars, Lampasas River Bridge

Data-acquisition equipment

Because the testing areas for the Reduced Welded-Wire Reinforcement and the Reduced Deformed-Bar Reinforcement are 300 ft apart, two data-acquisition boxes were installed. The first box consists of one data logger, two multiplexers, one analyzer, one modem, one battery, and one charge regulator. The boxes were mounted on the interior bents between Girder 3 and 4. The first box was located at Joint 1 and the second box was located at Joint 4. The solar panel was installed on the side of the bent cap at Joint 1, as shown in Figure 3-61.

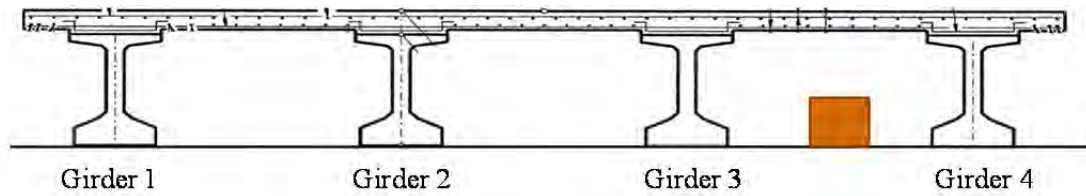


Figure 3-61: Location of data-acquisition system, Lampasas River Bridge

3.3.5 Placement of Top-Mat Reinforcement, Lampasas River Bridge

Top-mat reinforcement was placed over the precast, prestressed concrete panels on May 7 and May 8, 2012. Figure 3-62 shows a view of the top-mat reinforcement. In Figure 3-63 to Figure 3-68 are shown details of the test area and placement of reinforcement for each top-mat option. The test area for Current TxDOT Standard Reinforcement is located on the east side of the bridge over Spans 1 and 2 (Figure 3-63); and the test area for Reduced Welded-Wire Reinforcement is located on the west side over Spans 1 and 2 (Figure 3-64). The test area for Reduced Deformed-Bar Reinforcement is located on the west side of the bridge over Spans 4 and 5 (Figure 3-67). The location of all bars and splices was checked. An armor joint was located between Spans 2 and 3, shown in Figure 3-69. Properties of top-mat reinforcement are presented in Table 3-1.

Table 3-1: Properties of top-mat reinforcement, Lampasas River Bridge

	Yield strength	Tensile strength
No. 4	63.8 ksi	104.5 ksi
No. 5	64.4 ksi	104.6 ksi
D 20	-	94.9 ksi



Figure 3-62: View of top-mat reinforcement from south end, Lampasas River Bridge

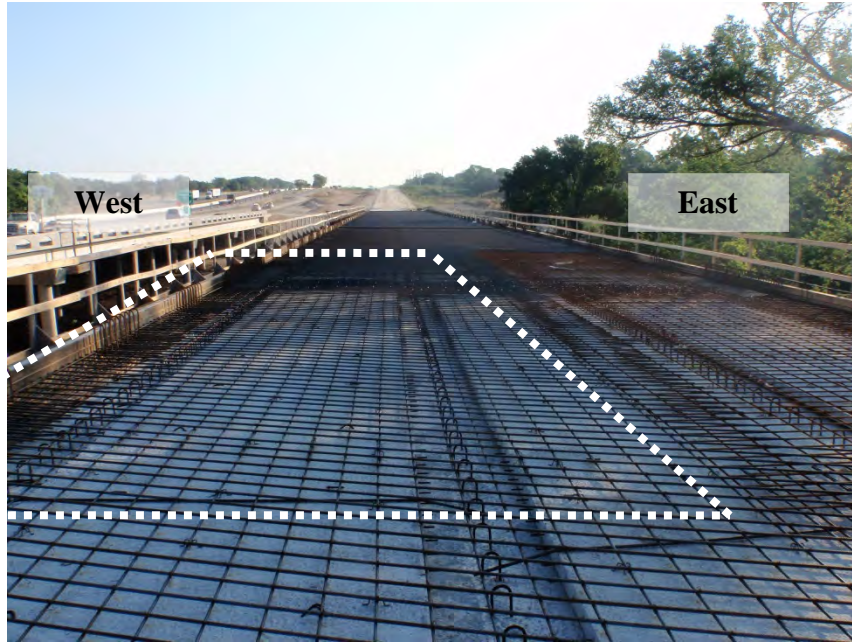


Figure 3-63: Test area for current TxDOT standard reinforcement, Lampapas River Bridge

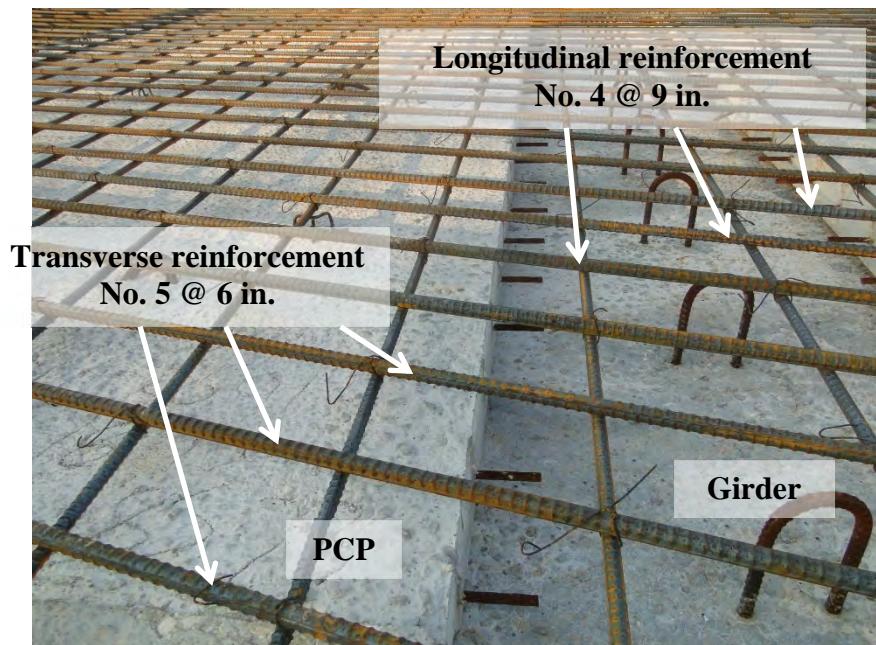


Figure 3-64: Typical placement of current TxDOT standard reinforcement, Lampapas River Bridge



Figure 3-65: Test area for reduced welded-wire reinforcement, Lampasas River Bridge

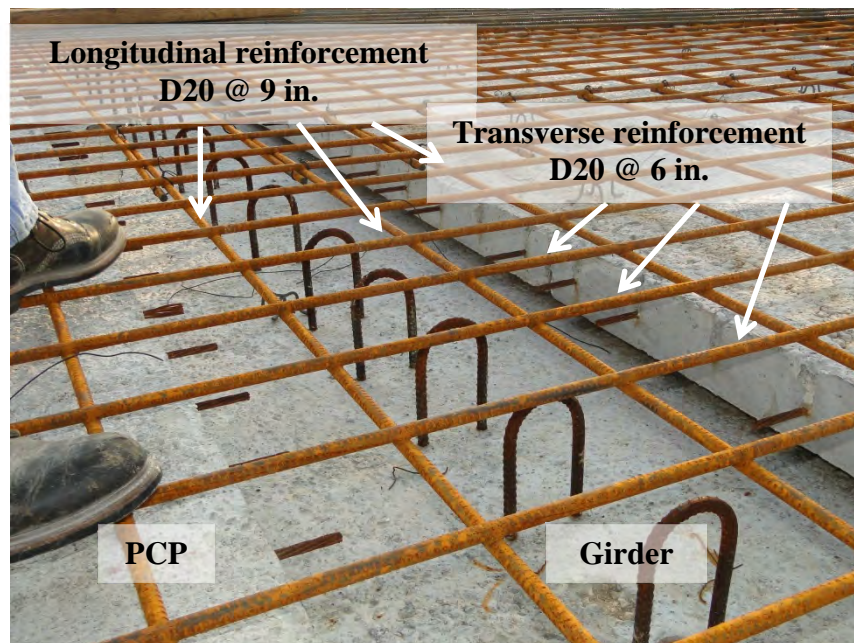


Figure 3-66: Typical placement of reduced welded-wire reinforcement, Lampasas River Bridge

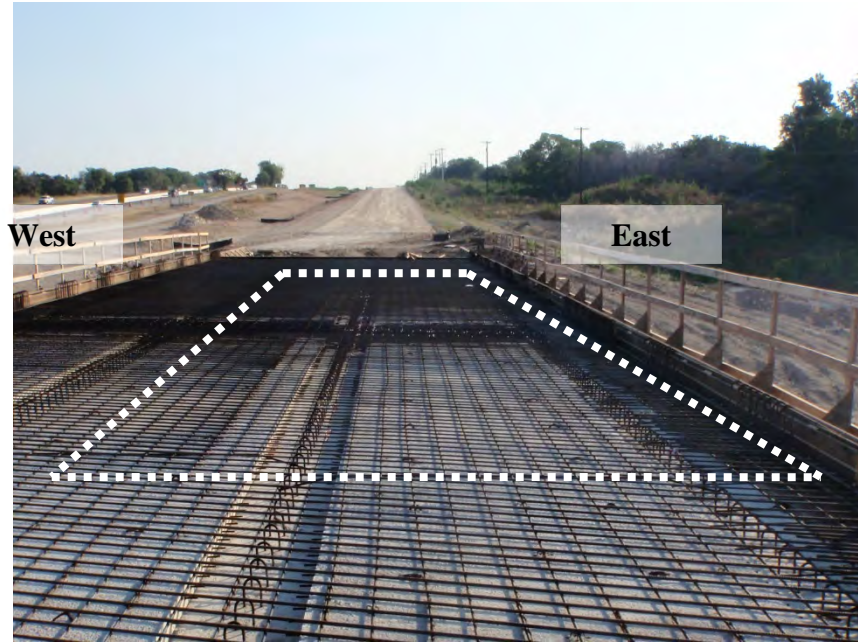


Figure 3-67: Test area for reduced deformed-bar reinforcement, Lampasas River Bridge

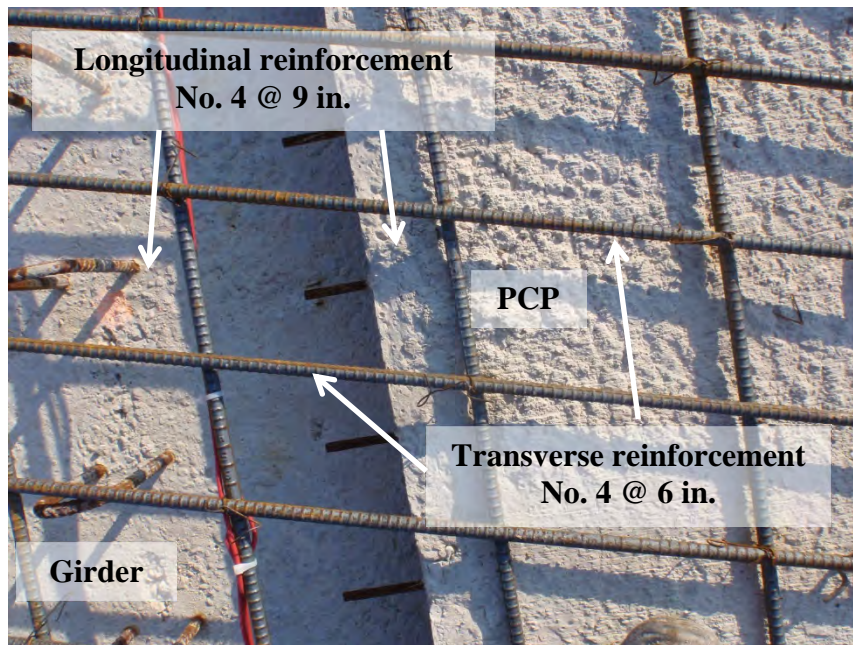


Figure 3-68: Typical placement of reduced deformed-bar reinforcement, Lampasas River Bridge



Figure 3-69: Armor joint between Spans 2 and 3, Lampasas River Bridge

3.3.6 Field Instrumentation of Lampasas River Bridge

The first day for field installation of the instrumentation for the Lampasas River Bridge was May 10, 2012. Work started at 7:30 A.M. and stopped at 1:00 P.M. because of rain. During the first day, all gages were placed and wires located on the deck. The two data-acquisition boxes were placed on bent caps. The solar panel was attached to the pre-fabricated bracket, and the assembly was installed on the east face of the bent cap between Spans 1 and 2.

Field installation was completed on May 17, 2012. Wires for gages were fastened to reinforcement with plastic zip-ties, and electrical connections were finished. Each gage was connected to a port in the data-acquisition boxes, and the antenna was also connected for wireless monitoring. In Figure 3-70 and Figure 3-71 are shown side views of the bridge from both ends.



Figure 3-70: Side view of Lampasas River Bridge from north end



Figure 3-71: Side view of Lampasas River Bridge from south end

Installing vibrating-wire gages

Thirty vibrating-wire gages were installed as shown in Figure 3-72. Yellow and orange paint were used to mark gage locations. All gage wires were routed to holes made in the bedding strip, using an electric drill with a long bit (Figure 3-73). Before feeding wires in the holes, gages were tested using hand-held reader (Figure 3-74). After checking connections between the data

logger and the gages, all wires were arranged neatly with plastic zip-ties. Holes in bedding strips and on data-acquisition boxes were sealed with spray foam as shown in Figure 3-75. The exposed portions of the wires were further protected with split tubing (Figure 3-76).



Figure 3-72: Typical field installation of VWG, Lampasas River Bridge

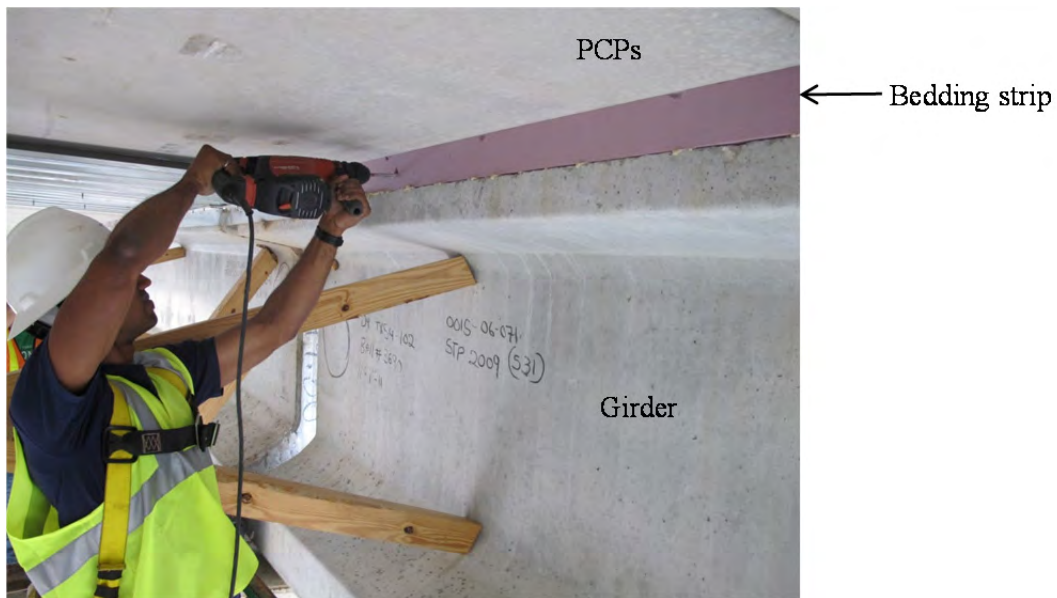


Figure 3-73: Making holes in bedding strip, Lampasas River Bridge



Figure 3-74: Checking gage before threading wire through the holes in bedding strip, Lampasas River Bridge

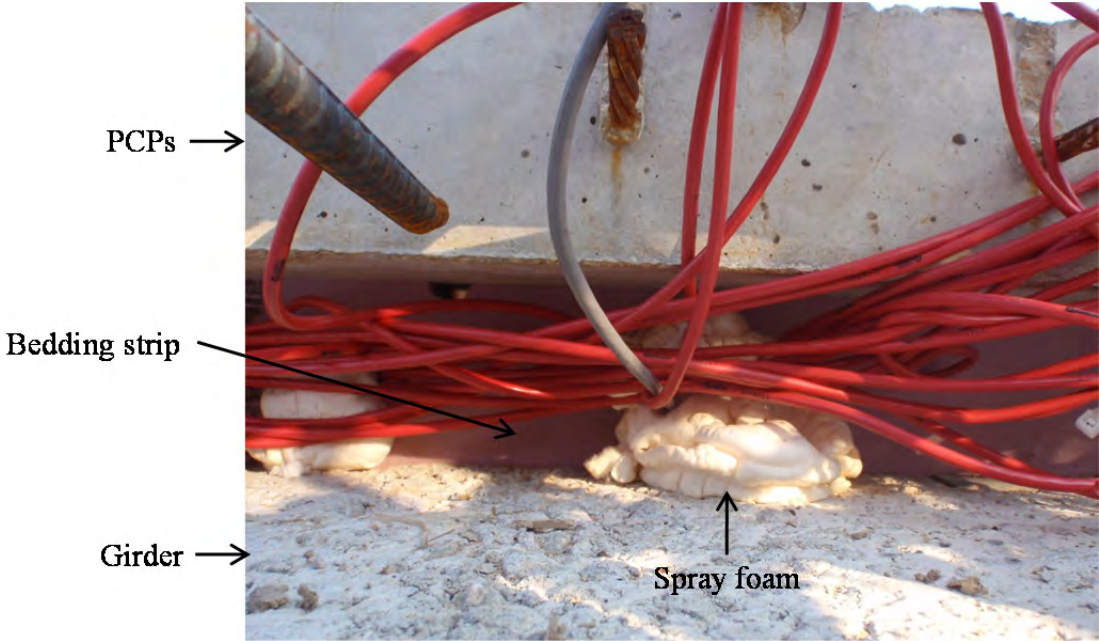


Figure 3-75: Sealing holes in bedding strip (Spans 1 and 2), Lampasas River Bridge

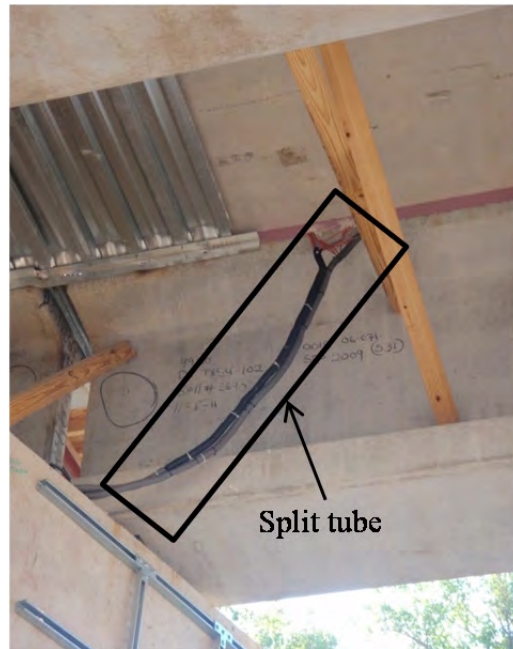


Figure 3-76: Split tube covering exposed parts of wires, Lampasas River Bridge

Placing data-acquisition box, Lampasas River Bridge

Two data-acquisition boxes were attached on the bent cap between Girder 3 and 4. The large data-acquisition box was placed on the bent between Spans 1 and 2 (Figure 3-77), and the small data-acquisition box was placed on the bent between Spans 4 and 5 (Figure 3-78). Both boxes were anchored to the bent caps, and one or two bags of desiccant were placed in each box. Because the top face of the bent cap between Spans 4 and 5 is about 8 feet above ground, two layers of scaffolding were used to access the bent cap (Figure 3-79). The height of the bent cap between Spans 1 and 2 is almost 20 feet, so a man-lift was used.

As with the Wharton-Weems Overpass, all holes of the boxes for wires were sealed with spray foam, and the boxes were locked after finishing electrical connection. Figure 3-80 shows the inside of the data-acquisition box placed on the bent between Spans 1 and 2.



Figure 3-77: Data-acquisition box between Spans 1 and 2, Lampasas River Bridge



Figure 3-78: Data-acquisition box between Spans 4 and 5, Lampasas River Bridge



Figure 3-79: Scaffolding for accessing bent cap between Spans 4 and 5, Lampasas River Bridge

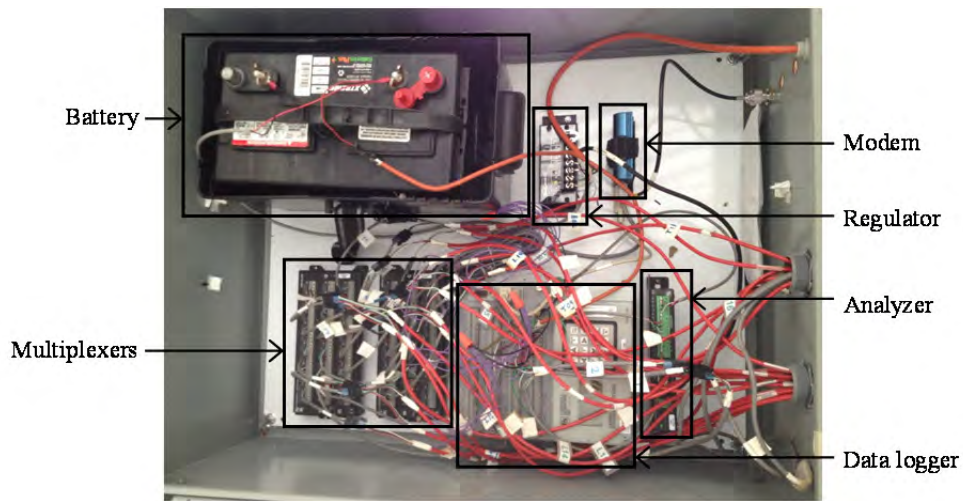


Figure 3-80: Inside of data-acquisition box placed on the bent between Spans 1 and 2, Lampasas River Bridge

Mounting solar panel

The solar panel and bracket were installed on side of the bent cap between Spans 1 and 2. Figure 3-81 and Figure 3-82 show the mounting procedure, and Figure 3-83 shows the bracket and the solar panel after mounting. An antenna was attached to the back side of the bracket (Figure 3-84), and power cables for the antenna and the solar panel were routed to the data-acquisition box. For optimum performance, the south-facing solar panel was tilted 30° from the horizontal (Figure 3-84).



Figure 3-81: Drilling holes on the side face of the bent caps for anchor bolts, Lampasas River Bridge



Figure 3-82: Mounting bracket for solar panel, Lampasas River Bridge



Figure 3-83: Solar panel mounted on side face of bent between Span 1 and 2, Lampasas River Bridge

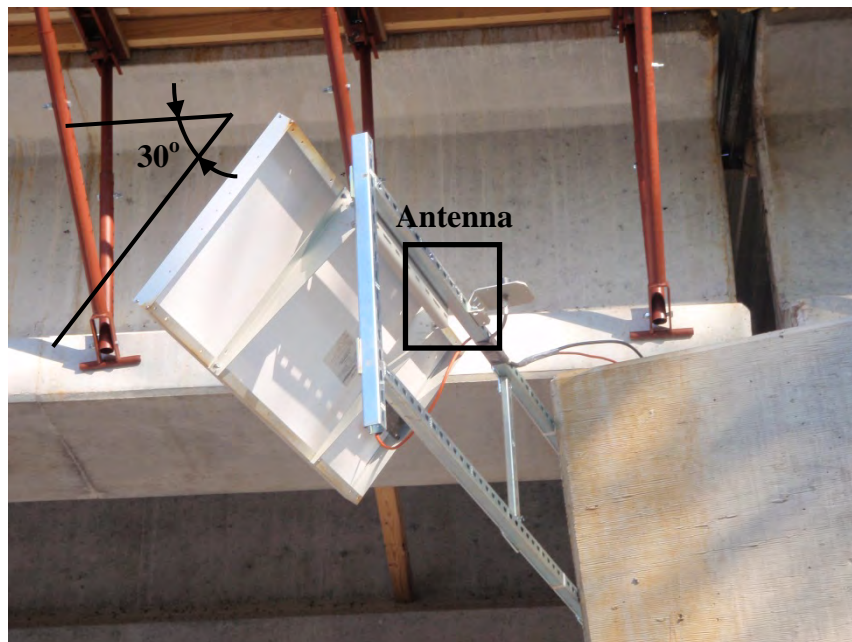


Figure 3-84: Back side of the bracket showing wireless antenna, Lampasas River Bridge

Casting concrete deck, Lampasas River Bridge

The deck was cast on June 1, 2012 starting at 1:30 A.M., and took about 6 hours to complete. The casting time was chosen to avoid high temperature the following day and thereby reduce plastic shrinkage cracking. Two concrete pump trucks were used. Class S concrete mix

was used, with specified compressive strength of 4,000 psi. The mixture proportions of the concrete were as follows:

- 413 lb of cement (Type I/II)
- 138 lb of fly ash (Class F)
- 1,851 lb of coarse aggregates (limestone)
- 1,271 lb of fine aggregates (natural sand)
- 247.4 lb of water
- 78.4 – 784.1 oz of water reducer (Type A&F)
- 19.6 – 117.6 oz of air entrainment (ASTM C260)
- 78.4 – 313.6 oz of retarder (Type B&D)

The casting sequence of the Lampasas River Bridge is the same as for the Wharton-Weems Overpass, and is shown chronological order in Figure 3-85. Before concrete is placed over the precast panels, water was sprayed on the surface (Figure 3-85 a). One or two workers hold the hose of the concrete pump truck to distribute concrete (Figure 3-85 b), and then the concrete was consolidated with hand-held vibrators (Figure 3-85 c). Uneven surfaces were raked (Figure 3-85 d), and the surface was finished using a screeding machine and hand tools. After that, crack formers were inserted over the joints (Figure 3-85 e).

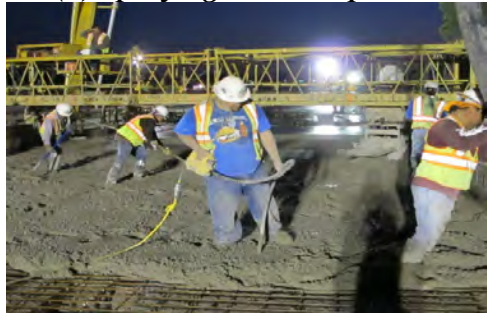
The portions of the deck, where the screeding machine could not reach, were finished using a wood screed (Figure 3-85 g). Curing compound was sprayed on the surface of the deck right after removing moisture from the surface.



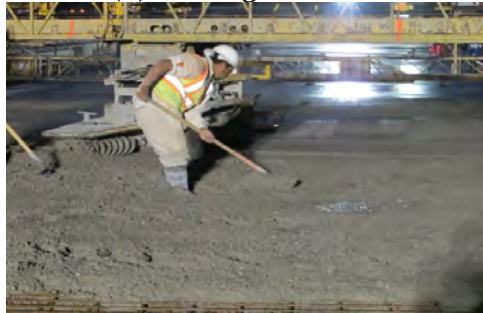
(a) Spraying water on panels



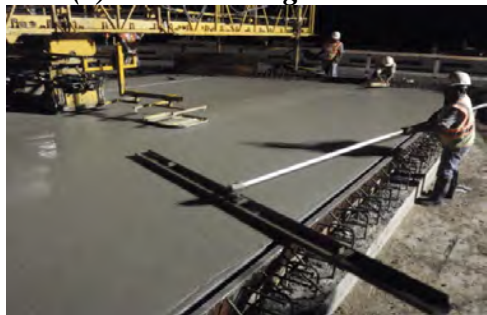
(b) Placing concrete



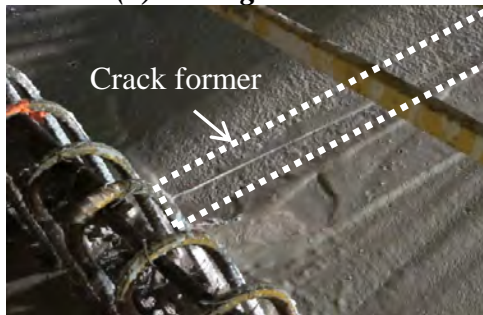
(c) Consolidating concrete



(d) Raking concrete



(e) Finishing surface



(f) Inserting crack former



(g) Hand screeding of portion of deck

Figure 3-85: Construction sequence for deck, Lampasas River Bridge

3.3.7 Results from Field Instrumentation, Lampasas River Bridge

Cracking inspection

The deck of the Lampasas River Bridge was inspected for cracking on August 16, 2012 (75 days after casting). The result of the inspection is shown in Figure 3-86. Two transverse

cracks were expected because the gages installed along joints indicated much higher stresses than the theoretical cracking value.

The two transverse cracks, located at Joint 1 and Joint 4 had an average widths of 0.008 in. At some locations, part of the crack former was exposed as shown in Figure 3-87. The width at those locations was 0.050 in., but could not be accurately read, so the value was not used for calculating average width of crack. No longitudinal cracks were found.

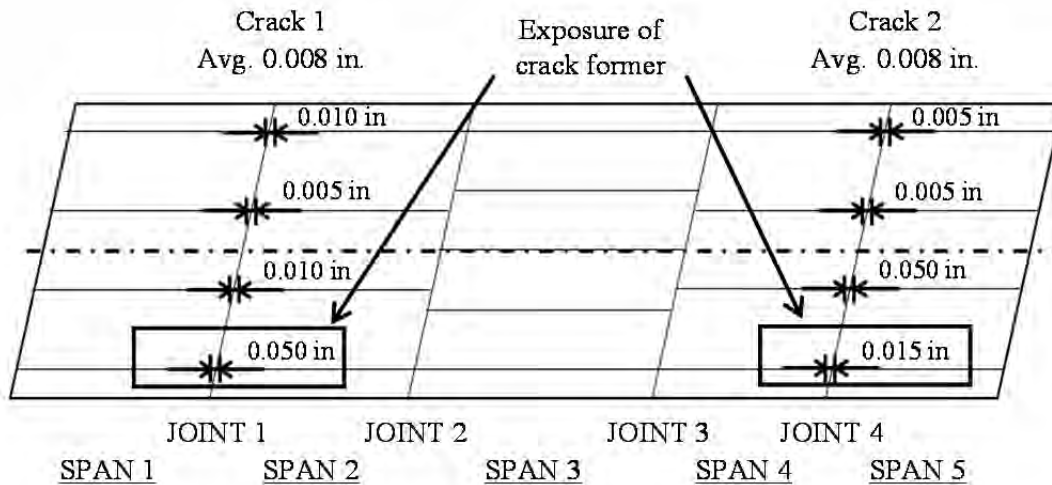


Figure 3-86: Result of cracking inspection of Lampasas River Bridge

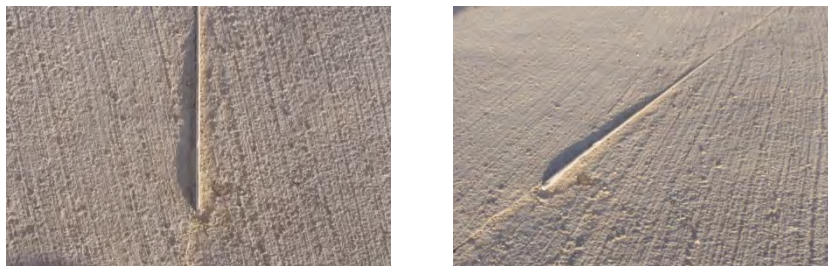


Figure 3-87: Exposure of crack former, Lampasas River Bridge

Long-term monitoring, Lampasas River Bridge

Long-term monitoring data from the Lampasas River Bridge is quite similar to that of the Wharton-Weems Overpass. The entire monitoring period to date is about two months, and the data logger did not work well during the second month because of problems with the cables between two data acquisition boxes. The long-term monitoring results in both directions are shown in Figure 3-88 through Figure 3-93. In the figures, positive sign indicates tensile stress, and negative sign indicates compressive stress.

In the longitudinal direction (Figure 3-88 to Figure 3-90), the stresses in reinforcement based on strains from gages located over the construction joints increased rapidly, and reached values corresponding to cracking of concrete within a week after casting. Other longitudinal gages away from the joints showed strain values less than the cracking value during entire monitoring period.

In the transverse direction (Figure 3-91 to Figure 3-93), the steel stresses based on strains from gages did not change much and were smaller than the theoretical concrete cracking values. The low stresses may be the result of high temperature, because the compressive stress due to restrained thermal expansion of concrete would be greater in hot weather. The similar patterns can be found in long-term monitoring results from the Wharton-Weems Overpass. The measured tensile strains in the transverse direction of the Wharton-Weems Overpass decreased as ambient temperature increased. The data from all three testing areas were similar. The bridge has not been opened to traffic. The crossing marks in Figure 3-89 and Figure 3-92 represent the stresses measured by hand-held reader.

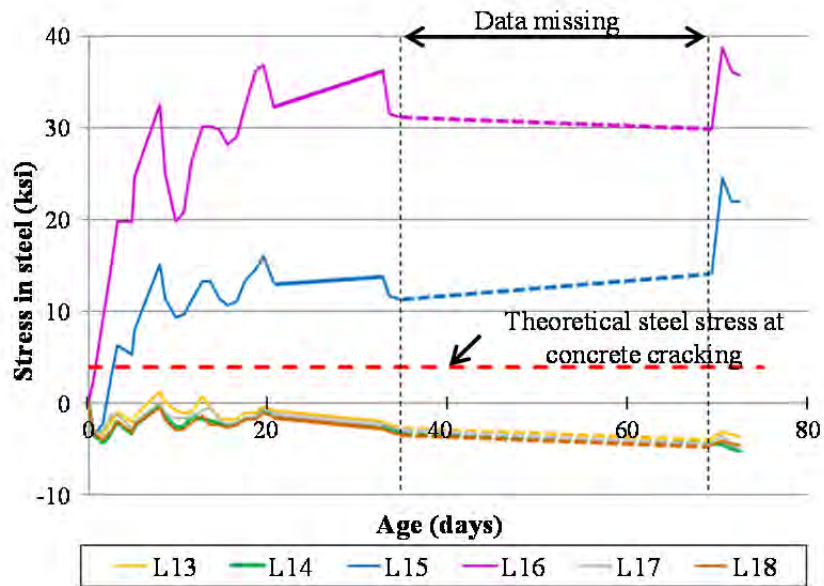


Figure 3-88: Stresses in current TxDOT standard reinforcement, Lampasas River Bridge (longitudinal direction)

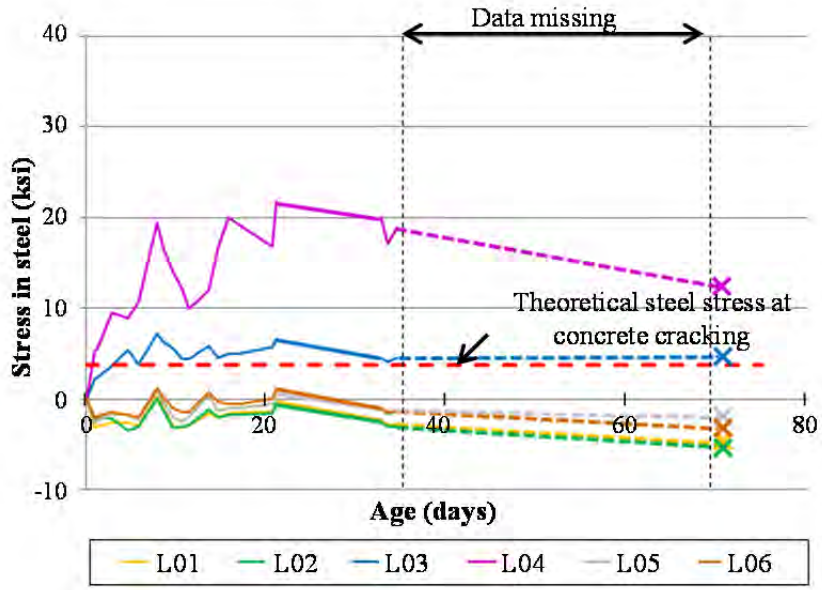


Figure 3-89: Stresses in reduced deformed-bar reinforcement, Lampasas River Bridge (longitudinal direction)

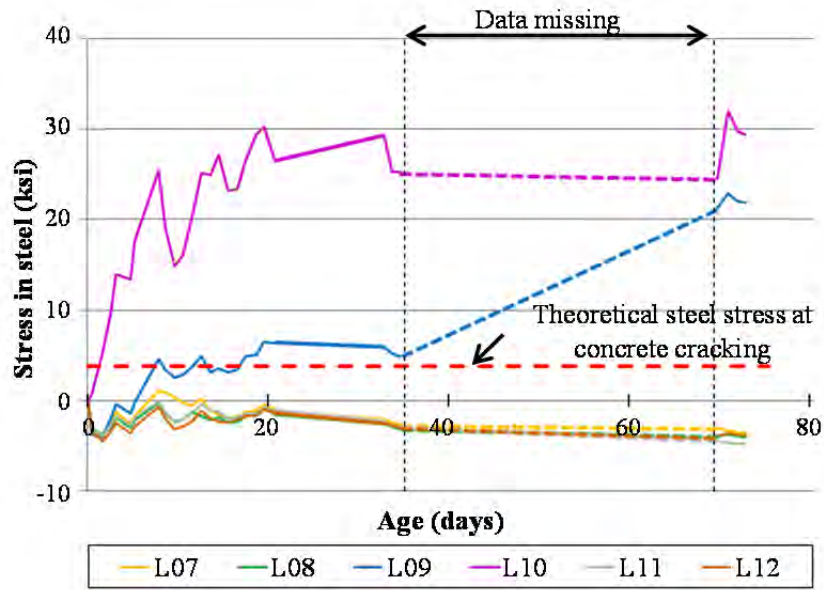


Figure 3-90: Stresses in reduced welded-wire reinforcement, Lampasas River Bridge (longitudinal direction)

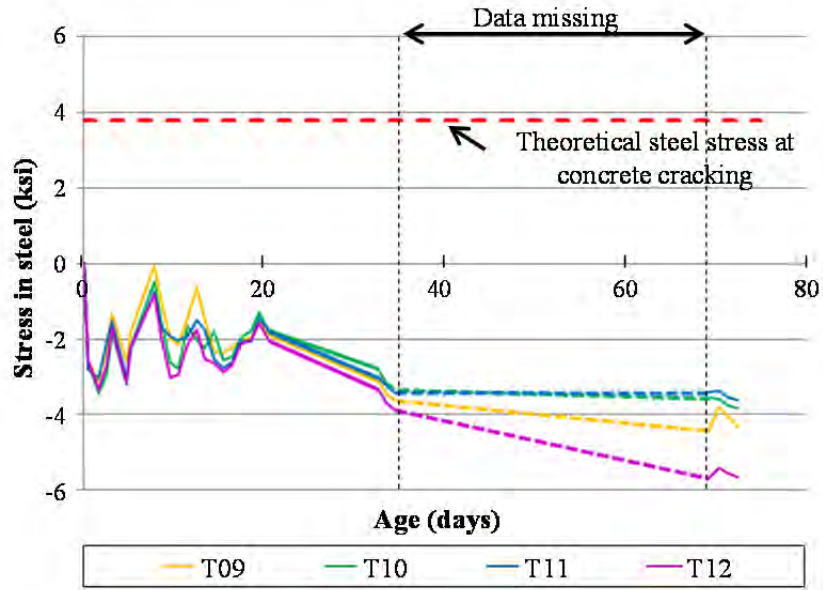


Figure 3-91: Stresses in current TxDOT standard reinforcement, Lampasas River Bridge (transverse direction)

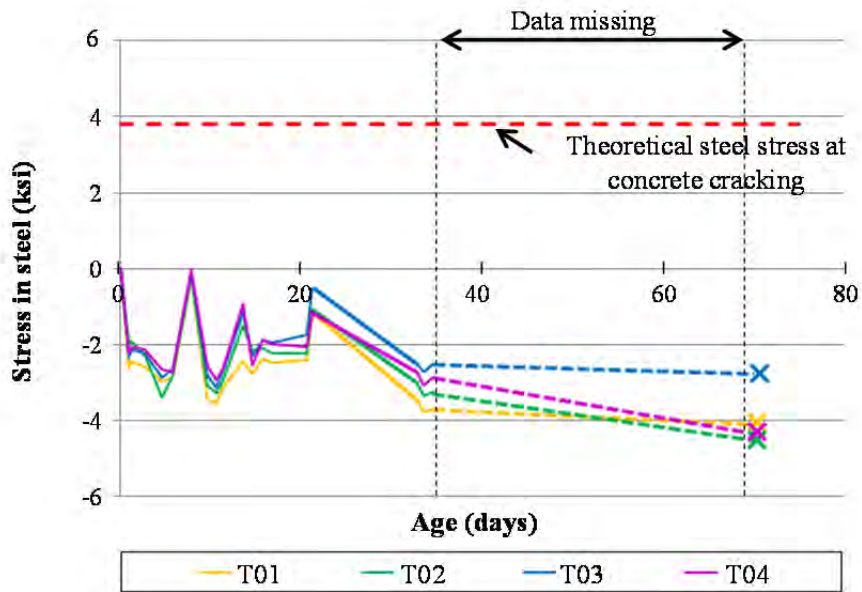


Figure 3-92: Stresses in reduced deformed-bar reinforcement, Lampasas River Bridge (transverse direction)

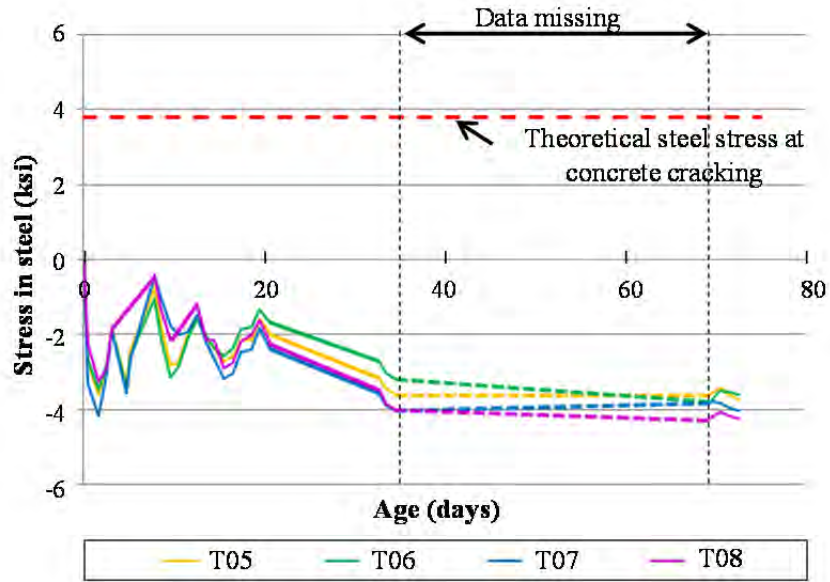


Figure 3-93: Stresses in reduced welded-wire reinforcement, Lampasas River Bridge (transverse direction)

Calculation of restraint moment using P-method, Lampasas River Bridge

Restraint moment of the Lampasas River Bridge can be calculated using the P-method introduced in Section 3.2.6.3. The areas for the calculation of restraint moment of Lampasas River Bridge in both directions are shown in Figure 3-94 and Figure 3-95. Span 1-2 and Span 4-5 were the testing areas of the Lampasas River Bridge, but only span 1-2 was used for the calculation because it was the worst case; so the worst case was considered. Restraint moment increases as length of span increases

The dimensions and conditions of those areas of the Lampasas River Bridge are very similar to those of the Wharton-Weems Overpass (Figure 3-29 and Figure 3-32) except that there was a slight skew in the Lampasas River Bridge. In the P-method, there is no term to address skew; therefore the calculation results of the Lampasas River Bridge will be the same as the calculation results of the Wharton-Weems Overpass (Figure 3-31 and Figure 3-34). Similar to the Wharton-Weems Overpass, transverse cracks opened over the joints within a week after CIP slab casting, and no longitudinal crack occurred in the Lampasas River Bridge based on the first month of measured strain values. Therefore, it can be concluded the calculated and the measured results match well in the Lampasas River Bridge also.

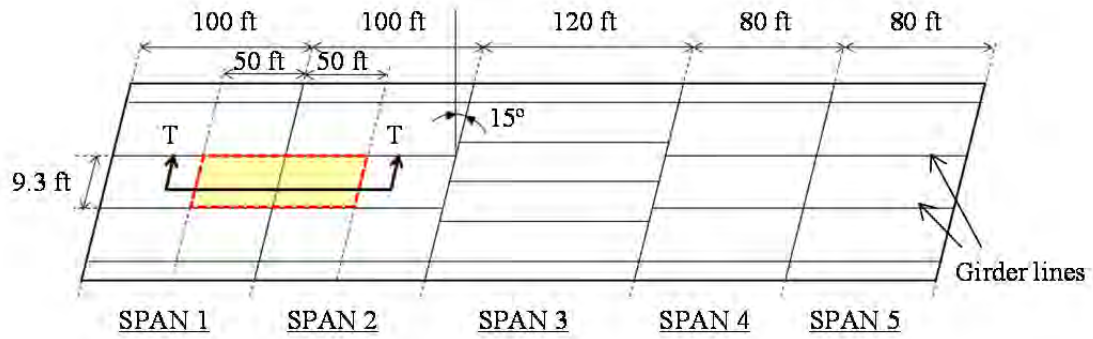


Figure 3-94: The area for calculation of longitudinal restraint moment, Lampasas River Bridge

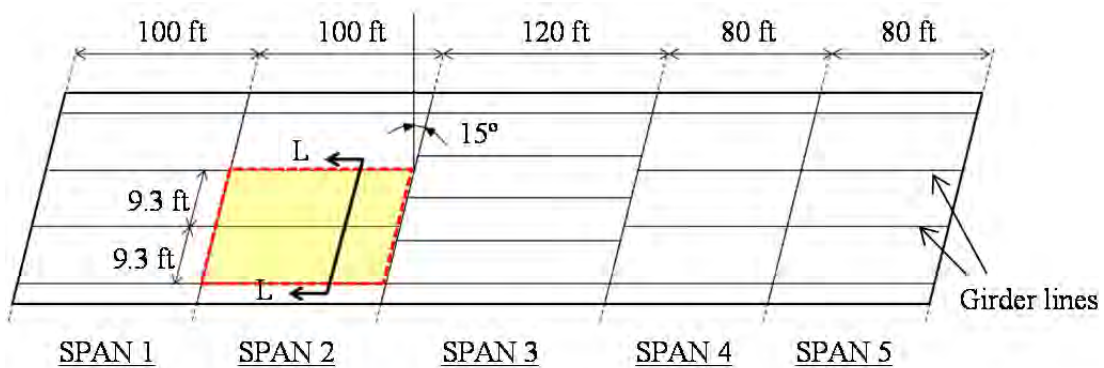


Figure 3-95: The area for calculation of transverse restraint moment, Lampasas River Bridge

3.4 Calculations of Construction Cost of Various Top-Mat Reinforcement Options

According to the results in Table 3-2, material cost can be reduced by 25% by changing the top-mat option from the Current TxDOT Standard Reinforcement to the Reduced Deformed-Bar Reinforcement option. Material cost can be reduced by 5% by changing to the Reduced Welded-Wire Reinforcement option.

Table 3-2: Material costs of each top-mat option

	Current TxDOT Standard Reinforcement	Reduced Deformed-Bar Reinforcement	Reduced Welded-Wire Reinforcement
Cost per unit weight of reinforcement	\$0.30/lb	\$0.30/lb	\$0.38/lb
Weight per unit area of deck	2.977 lb/ft ²	2.227 lb/ft ²	2.227 lb/ft ²
Cost per unit area of deck	\$0.89/ft ²	\$0.67/ft ²	\$0.85/ft ²

By using welded-wire reinforcement, further savings in construction cost can be realized due to savings in labor. Welded-wire reinforcement can be placed more quickly and economically than deformed-bar reinforcement, arranging and tying top-mat reinforcement is eliminated. Based on the comparison of estimated construction cost (considering labor, time, and handling) between welded-wire reinforcement and standard deformed bar shown in the Purdue web site, an average reduction in construction cost of 20% can be realized if welded-wire reinforcement is used. In this regard, the contractor of the Lampasas River Bridge told study researchers that he preferred to welded-wire reinforcement due to a considerable saving in construction time.

3.5 Conclusions from Field Instrumentation

Two bridge decks were instrumented to monitor optimized top-mat reinforcement layouts for the cast-in-place (CIP) concrete slabs. The field applications provide data based on actual CIP-PCP interaction, boundary conditions, environmental conditions, and loading conditions.

During the monitoring period, the selected top-mat options behaved similarly. The longitudinal reinforcement placed according to current design specifications almost reached yield strain at crack locations over the joints between spans, and the cracks were very narrow. Based on the monitoring results, top-mat reinforcement in the longitudinal direction cannot be reduced. Transverse reinforcement, in contrast, exhibited very low strains, even though the sectional area of the transverse reinforcement was reduced. Because the strains in the transverse direction are nearly the same for all reinforcement options, the data are not conclusive. However, it is highly likely that the Reduced Deformed-Bar Reinforcement (No. 4 @ 6 in.), and the Reduced Welded-Wire Reinforcement (D 20 @ 6 in.) will be acceptable design alternatives for the transverse top-mat reinforcement. Continued monitoring of these bridge decks is needed to confirm the performance of the selected top-mat options.

Chapter 4. Optimization of Reinforcement in CIP Slabs: Restrained-Shrinkage Test

4.1 Introduction

The large-scale restrained shrinkage test was planned to provide additional data regarding the comparative behavior of the top-mat reinforcement options, and to supplement data from field studies. Because access to construction sites that would permit installation of instrumentation was limited, it was decided to study the design options, especially welded-wire reinforcement, in a controlled laboratory setting. The intent was to simulate the CIP-PCP interface in the transverse direction of a bridge deck more closely than had been possible in the small-scale lab tests conducted early in the project (the DTTs and the deck segments loaded in flexure).

In Figure 4-1 is shown the region of a bridge that was simulated in the restrained-shrinkage test. Because longitudinal reinforcement has already been optimized through previous tests (Foster 2010), the restrained-shrinkage tests in this chapter are focused on transverse reinforcement, which acts to control crack widths in the longitudinal direction (parallel to girder lines in the bridge).

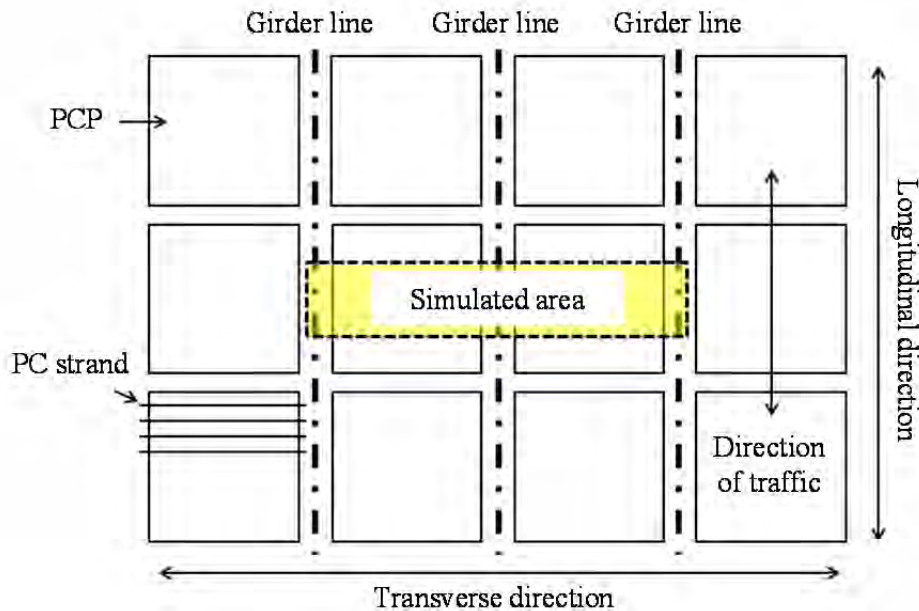


Figure 4-1: Region of the bridge deck simulated in the restrained-shrinkage test

The specimens developed in TxDOT Project 0-4098 (Figure 2-9) were used to establish the test programs described in the next section.

4.2 Test Specimens for Restrained-Shrinkage Test

4.2.1 Reinforcement Options for Restrained-Shrinkage Test

The three reinforcement options for the restrained-shrinkage test are listed in Table 4-1. All options have the same reinforcement ratio in the longitudinal direction, but the ratio in the transverse direction for the Reduced Deformed-Bar Reinforcement and the Reduced Welded-Wire Reinforcement is 35% smaller than the ratio for the Current TxDOT Standard Reinforcement. A No. 4 bar and a D 20 wire have the same cross-sectional area.

Table 4-1: Reinforcement options for restrained-shrinkage test

	Current TxDOT Standard Reinforcement		Reduced Deformed-Bar Reinforcement		Reduced Welded-Wire Reinforcement	
	size & spacing	ratio	size & spacing	ratio	size & spacing	ratio
Transverse	No. 5 @ 6 in.	0.008 6	No. 4 @ 6 in.	0.0056	D 20 @ 6 in.	0.005 6
Longitudinal	No. 4 @ 9 in.	0.002 8	No. 4 @ 9 in.	0.0028	D 20 @ 9 in.	0.002 8

4.2.2 Specimen Configurations for Restrained-Shrinkage Test

Six test specimens were constructed, each 18-ft long and 4-ft wide. The specimens were cast in a stiff steel frame that was designed to provide end restraint (to not shorten in-plane under the loads associated with restrained shrinkage of the concrete). The short direction of the specimens represents the longitudinal direction in a bridge deck, and the long direction of the specimens represents the transverse direction. Figures 4-2 and 4-3 show the restrained-shrinkage specimen.

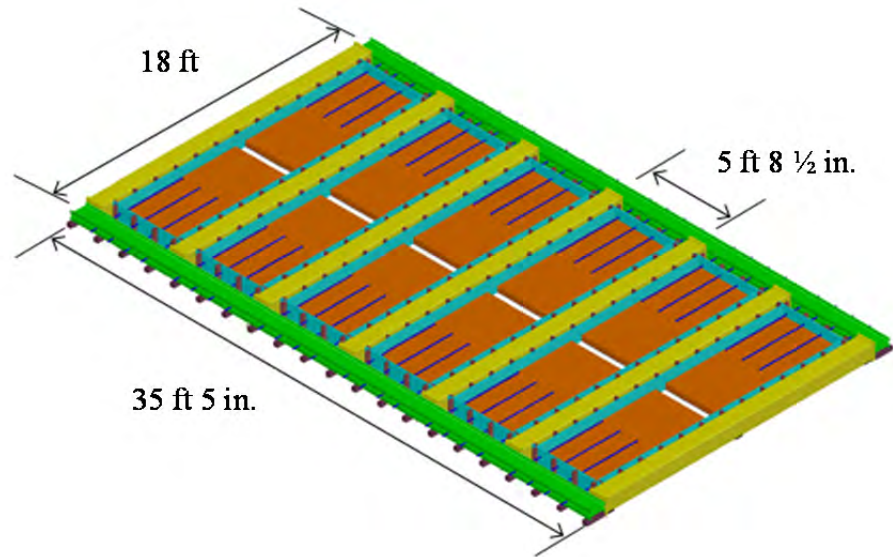


Figure 4-2: Dimensions of restrained-shrinkage specimen

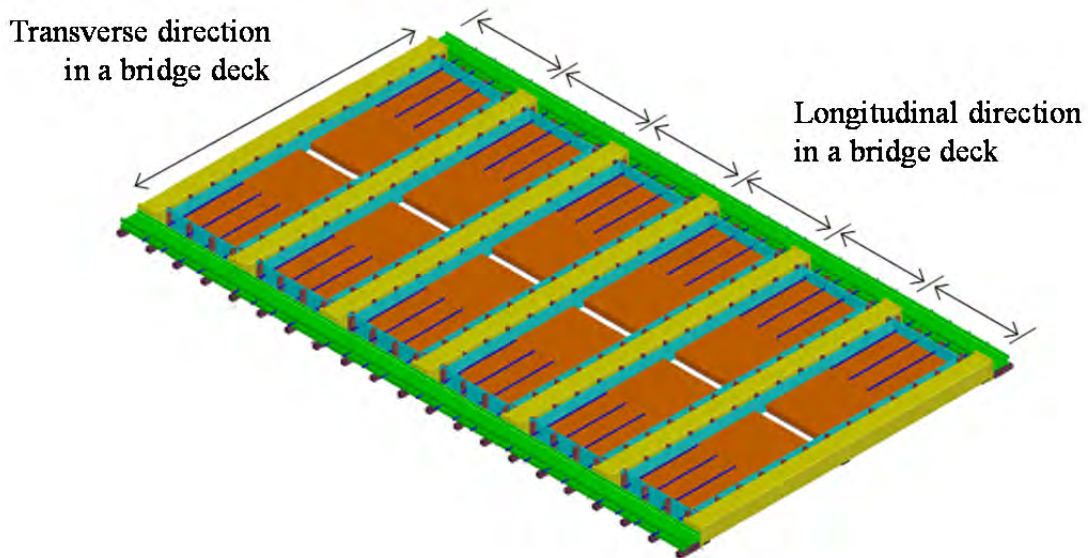


Figure 4-3: Terminology for restrained-shrinkage specimen

4.2.3 Construction of Restraining Frame for Restrained-Shrinkage Test

In the test setup, the concrete specimen was cast in the restraining frame so that shrinkage of the CIP deck and creep of the PCPs was restrained by bars inserted at both ends of the specimens. This restraint should result in tensile stress in the CIP concrete and cracking in the middle of the specimen where the PCPs are supported on a girder. The cracks usually start at the boundary between the PCP and the CIP concrete (Figure 4-4). The cracking pattern is similar to longitudinal cracking of an actual bridge which generally follows girder lines. Therefore, the

behavior of top-mat reinforcement options can be compared. The components of the frame are shown in Figure 4-5.

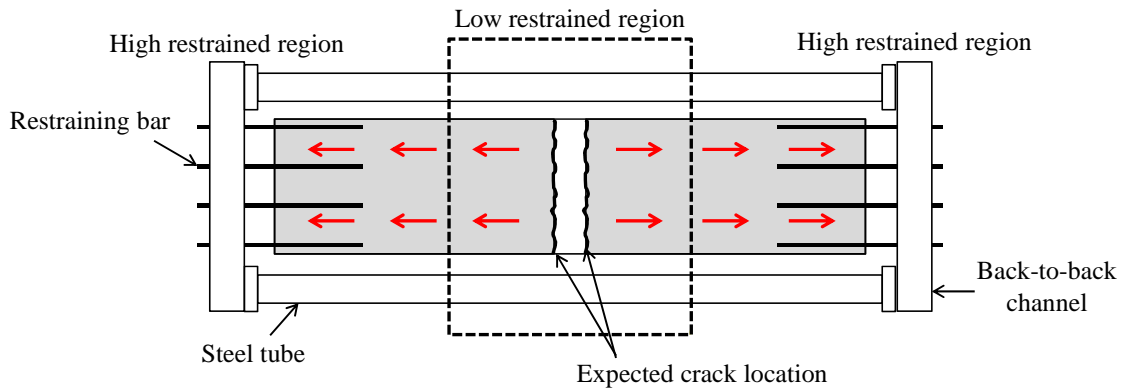


Figure 4-4: Mechanism of restrained shrinkage test

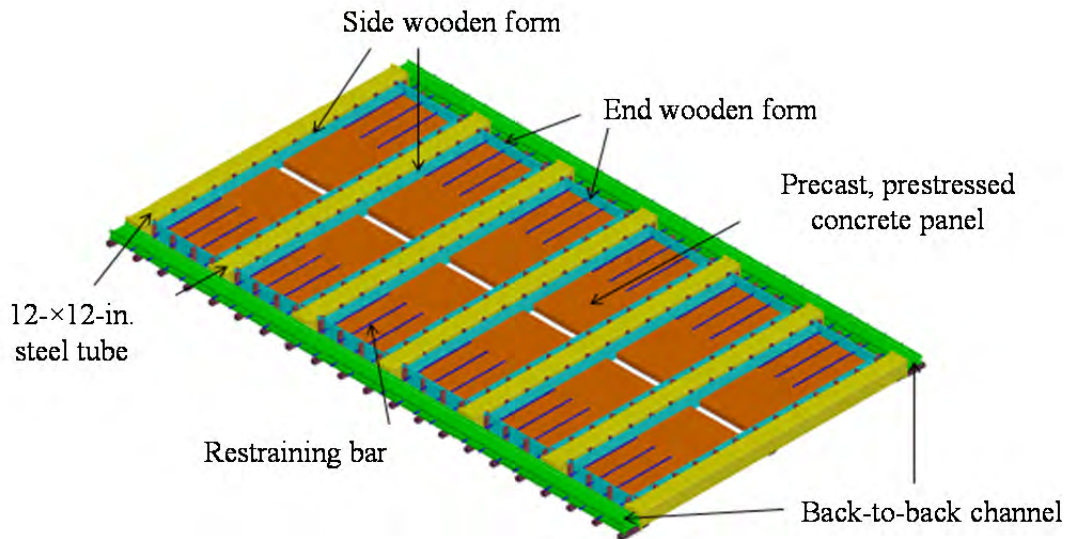


Figure 4-5: Components of restrained-shrinkage specimen

Two back-to-back channels were made using four C10×20 channels, 40-ft long. Small steel plates were welded about 14-in. apart to keep the spacing between two C10×20 channels constant at 1.5 in. The channels were supported on wooden blocks.

Seven 12-×12-in. steel tubes 17.5-ft long were placed between the test specimens to restrain the channels attached to the ends of the specimens. Plates were welded at both ends. Holes in the steel tubes and plates were used to attach the tubes to the back-to-back channels as shown in Figure 4-6.



Figure 4-6: Attaching steel tube to back-to-back channels

4.2.4 Construction of Restrained Shrinkage Specimens

Four PCPs were cast on September 13, 2011 and were shipped to FSEL on September 27, 2011. Each panel had 8 strands, which protruded from both ends of the panels when they were delivered. The projecting strands on one end were cut using a saw (Figure 4-7) to create a smooth face so that the panels could be placed against the wooden end forms. The panels were cut in half to form 4 × 8-ft panels that constituted the base for the CIP deck.

Wooden forms were used to contain the deck concrete. The side form (Figure 4-8) was shimmed against the steel tubes so that they were in contact with the PCPs. The end forms were placed between the back-to-back channels and the PCP ends where the protruding strands had been removed. In Figure 4-9 are shown the PCP and the side and end forms in place. A space was left between the PCPs (Figure 4-10) to simulate the deck over a girder where the CIP concrete would be used to complete the deck. The end wooden forms had four 1 ¼ in. diameter holes, placed 12-in. apart to position the restraining bars (Figure 4-5) at the middle depth of the CIP deck.

The restraining bars are used to create large tensile forces in the concrete panels of the specimen by resisting the shrinkage deformation of the panels.. The restraining bars were No. 9 Dywidag bars meeting the requirements of A615 Grade 75. Their yield and ultimate strength were 87.1 ksi and 121.8 ksi, respectively. Each bar was inserted through the space between the back-to-back channels and holes in the wooden end forms (Figure 4-11). All bars protruded about 4 ft over the precast, prestressed concrete panels. Using hex nuts, each bar was attached firmly to the channel, and chair supports were used to position the bars.



Figure 4-7: Half-size precast, prestressed concrete panels (strands cut on one side)





Figure 4-9: Complete assembly of first bay, restrained-shrinkage test



Figure 4-10: Space between PCPs, restrained-shrinkage test

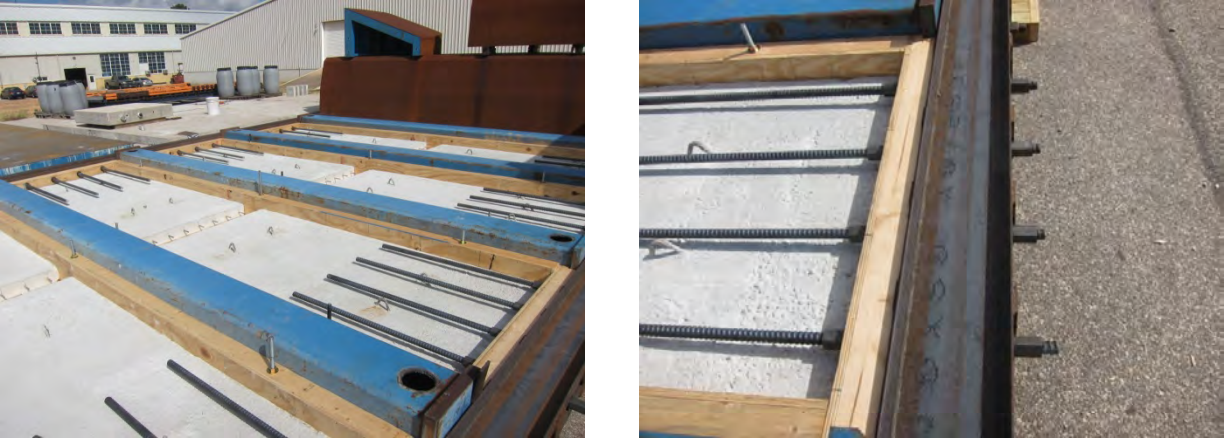


Figure 4-11: Installing restraining rods, restrained-shrinkage test

4.2.5 Placing Top-Mat Reinforcement, Restrained-Shrinkage Test

Standard deformed-bars and welded-wire reinforcement were placed on the PCPs and supported on steel chairs as shown in Figure 4-12 to Figure 4-14. Reinforcement in the longitudinal direction of the bridge was supported on the chairs, and reinforcement in the transverse direction was placed over the longitudinal reinforcement. The bars were tied with steel wires to form a mat of reinforcement. As shown in Figure 4-12 and Figure 4-13, two transverse bars were omitted because those bars were instrumented with foil gages and placed before the deck was cast.

Welded-wire mats were cut to size when fabricated. The time for placing the welded-wire reinforcement was about one-fifth of that for standard deformed-bar reinforcement.

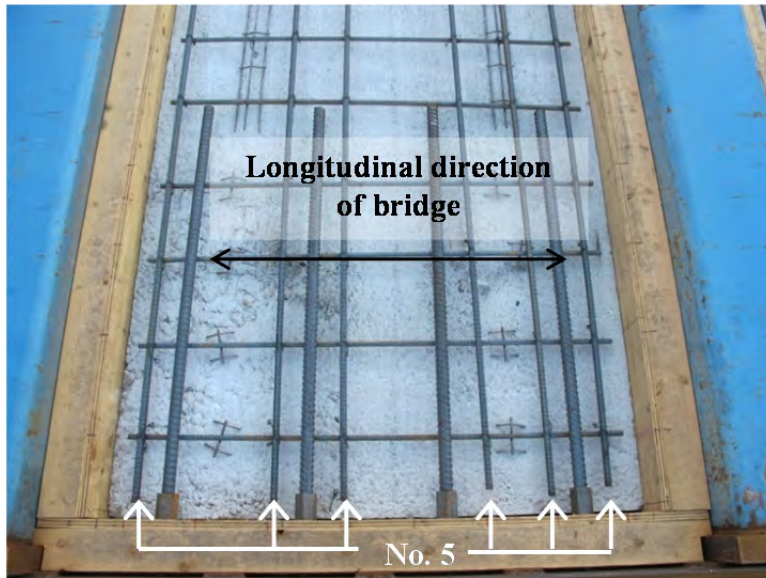


Figure 4-12: Arrangement of current TxDOT standard reinforcement, restrained-shrinkage test

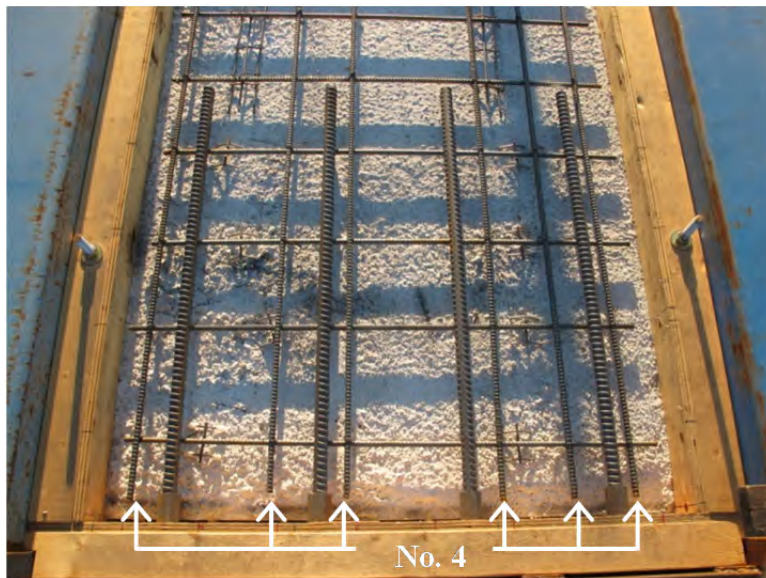


Figure 4-13: Arrangement of reduced deformed-bar reinforcement, restrained-shrinkage test

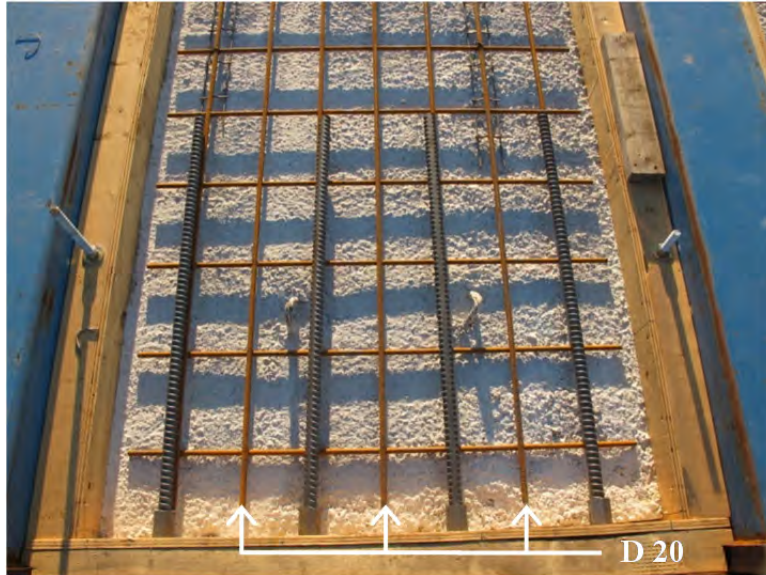


Figure 4-14: Arrangement of reduced welded-wire reinforcement, restrained-shrinkage test

4.2.6 Gage Instrumentation, Restrained-Shrinkage Test

Twenty-four foil gage and twenty-four vibrating-wire gages were installed in the restrained-shrinkage specimen. Four foil gage and four vibrating-wire gage were instrumented in each bay. Figure 4-15 shows gage layout and gage numbering; with F designates a foil gage and V a vibrating-wire gages. Gage wires were arranged neatly using zip-ties and routed to a common point in each test specimen (Figure 4-16).

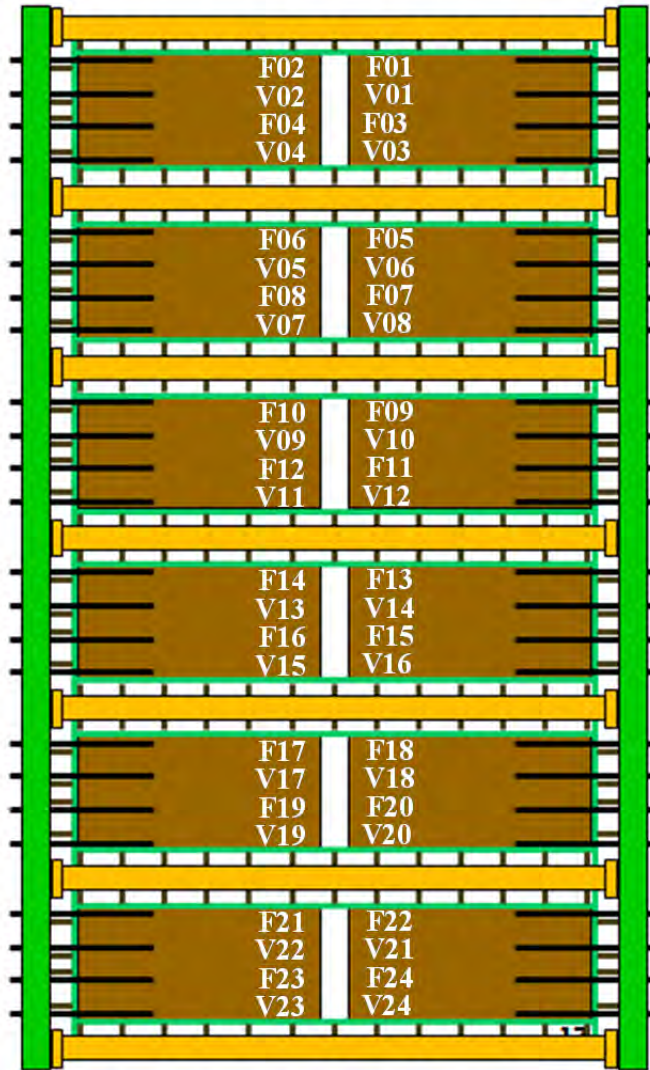


Figure 4-15: Gage layout for restrained-shrinkage test

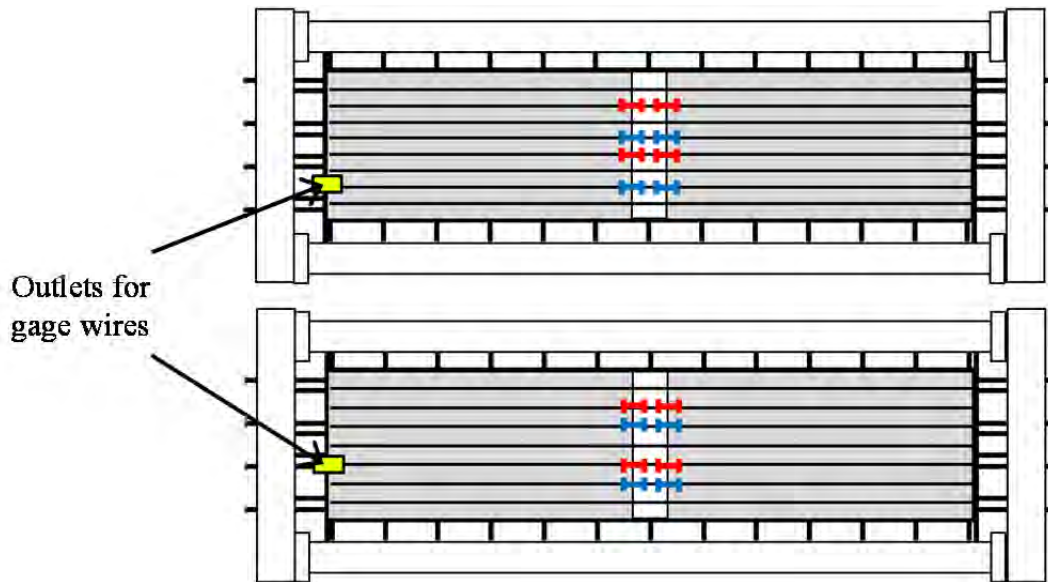


Figure 4-16: Location of outlets for gage wires, restrained-shrinkage test

Both types of gages were instrumented along the edge line of the PCPs, because it were expected that cracks would form at the PCP edge over the simulated girder region (Figure 4-17). Both edges were instrumented since there was no way to determine which edge would crack first.



Figure 4-17: Complete gage installation for one bay of restrained-shrinkage test

The foil gages for the specimen with Current TxDOT Standard Reinforcement and the Reduced Deformed-Bar Reinforcement options were installed before the bars were tied in mats and placed in the forms. The gages on the welded-wire mats were installed after the mats were placed in the forms. The adhesive for foil gage is cyanoacrylate, and it requires 20~60 second for curing under room temperature. The mounting procedure for foil gages is described in Figure 4-18 a-f and summarized below:

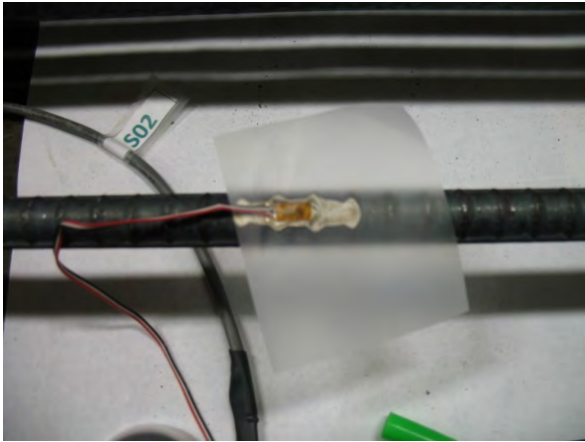
- a) Grind a 7/8 inch long portion of the surfaces of the standard deformed bars
- b) Clean the region using acetone
- c) Apply adhesive and place the gage
- d) Attach waterproof mastic sealing tape on the gage
- e) Wrap gage position with foil tape to protect against abrasion during casting
- f) Installation completed on deformed bars



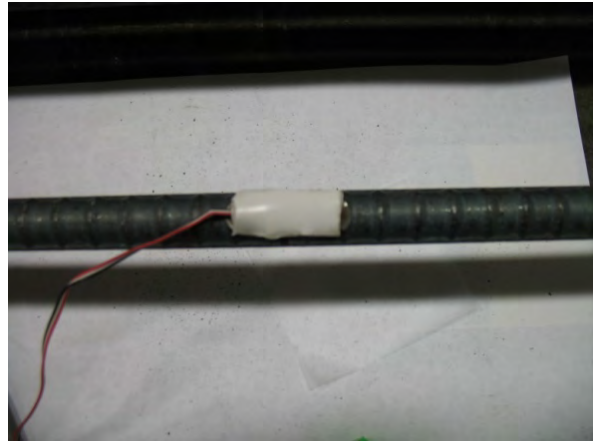
(a) Grind surface of reinforcing bar



(b) Polish with acetone



(c) Place foil gage



(d) Attach waterproof sealing mastic tape



(e) Wrap with foil tape



(f) Completed installation

Figure 4-18: Installation sequence for foil gages, restrained-shrinkage test

A typical foil gage as installed is shown in Figure 4-19 a. The vibrating-wire gages were tied to the sides of the transverse reinforcing bars with plastic zip-ties and Styrofoam spacers as shown in Figure 4-19 b. The gages should be tied firmly so as not to change their orientation during casting. Care was also taken to avoid damage of the vibrating-wire gages during installation.



(a) foil gage



(b) vibrating-wire gage

Figure 4-19: Gage instrumentation (foil gage and vibrating-wire gage)

4.2.7 Casting of Deck Concrete, Restrained-Shrinkage Test

Concrete for the CIP slab of the restrained-shrinkage test was cast on November 7, 2011. The specified compressive strength was 4,000 psi and the concrete mixture proportions are shown in Table 4-2. The mixture used a maximum coarse aggregate size of 1.0 in., and Class F-Fly-Ash, 9.20 oz/yd³ of retarder, and 30.93 oz/yd³ of water reducer.

A slump test was conducted before casting, and water was added to reach the required slump of 6 in. The added water is included in the concrete mixture proportions shown in Table 4-2.

Table 4-2: Concrete mixture proportions (by weight), restrained-shrinkage test

Cement	Water	Coarse agg.	Fine agg.	Fly Ash	Total
1.00	0.38	4.44	2.74	0.39	8.95

In Figure 4-20 a-f is shown the casting sequence for the restrained-shrinkage specimens. Each step is explained below:

- a) To prevent plastic shrinkage cracking and delamination of the CIP deck, water was sprayed on the precast, prestressed concrete panels
- b) About one cubic yard of concrete was placed in the center of each specimen, and spread using shovels.

- c) The concrete was consolidated using two hand-held vibrators.
- d) The surface was screeded with 2 × 4 boards.
- e) Curing compound was sprayed on the surface to simulate field curing conditions. It was applied to the surface as soon as the bleed water disappeared.
- f) One side form was removed in each bay, so that the specimen was not restrained by the forms.



(a) Spray water on panels



(b) Place concrete



(c) Consolidate with hand-held vibrator



(d) Scream



(e) Spray curing compound



(f) Strip wooden form on one side

Figure 4-20: Deck-construction sequence, restrained-shrinkage test

4.2.8 Concrete Compressive Strength, Restrained-Shrinkage Test

Sixteen 4- \times 8-in. cylinders were tested to determine concrete compressive strength at 3, 7, and 28 days. Plastic molds were stripped 1 day after casting and all cylinders were placed near the specimens. No moisture curing or curing compounds were used. Figure 4-21 shows compressive strength with age. Measured compressive strength was equal to design strength. It is expected that the actual compressive strength of the specimen might be greater than the cylinder strength, because the specimen has a smaller surface to volume ratio than the cylinder and the surface of concrete of the specimen was covered with curing compound to minimize loss of water from the surface.

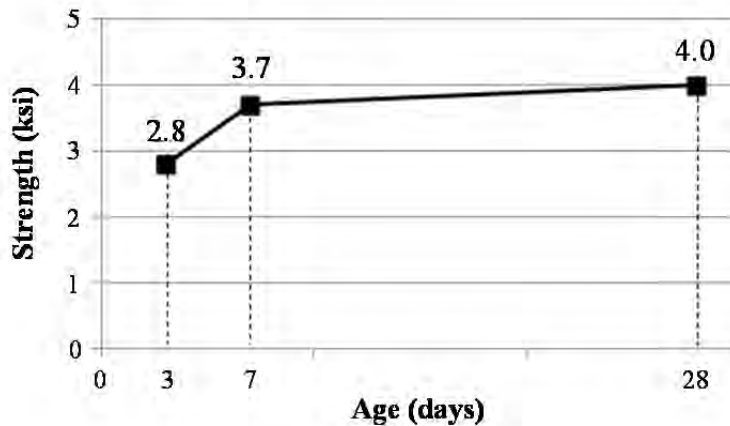


Figure 4-21: Compressive strength from 4- \times 8-in. cylinder tests, restrained-shrinkage specimen

4.3 Results and Conclusions, Restrained-Shrinkage Test

4.3.1 Results of Restrained-Shrinkage Test

Long-term monitoring

Figure 4-22 and Figure 4-23 show long-term monitoring results from the restrained-shrinkage test. Figure 4-22 shows the results from vibrating-wire gage, and Figure 4-23 shows the results from foil gages. Detection intervals are 10 minutes for the first week, 30 minutes for the next 4 months, and 4 hours thereafter. The data from only one gage on each reinforcement option was plotted because other gages gave the same results. Moreover, strains at different gages at the same PCP and CIP edges were essentially the same.

Both gage types gave consistent results, and all design options showed similar behavior during the entire monitoring period. No cracks have been detected.

The stress increased during the first month, because most deformation due to shrinkage and creep usually occurs at early ages. After that, the values stabilized for about 3 months at strains that would indicate the concrete is near cracking. About 4 months after casting the tensile strain readings decreased slowly because outside temperature increased and specimens expanded.

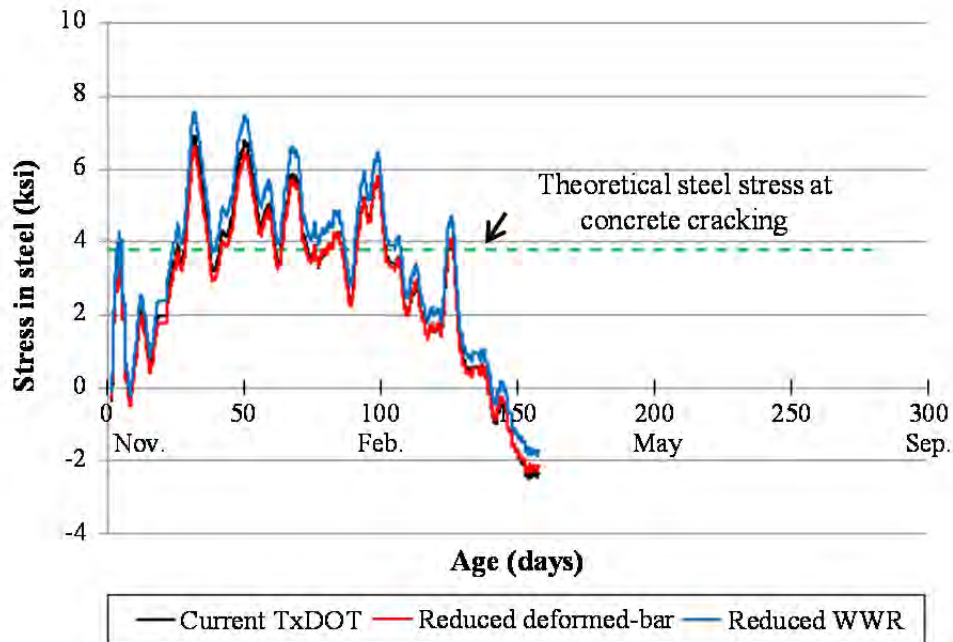


Figure 4-22: Long-term monitoring results from vibrating-wire gage, restrained-shrinkage test

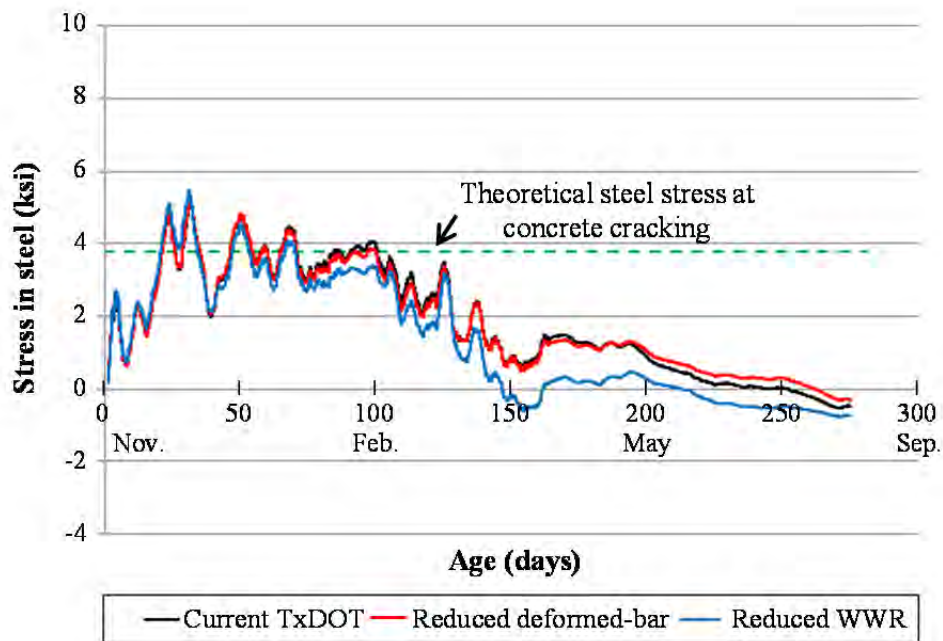


Figure 4-23: Long-term monitoring results from foil gage, restrained-shrinkage test

Calculation of restraint moment

The restraint moments of the restrained-shrinkage test were calculated using the P-method. The calculation results were used to predict the likelihood of cracking and time of occurrence of cracks in the restrained-shrinkage specimen. The calculation results were also

compared with the monitoring results to determine whether or not the P-method could be used for predicting cracking in the restrained-shrinkage specimen.

The differences in length and stiffness between diaphragm region and main span were considered using a coefficient α and it was calculated using the Equation 4-1 for this case. The result obtained by Equation 4-1 is the same to the result by moment distribution method used in Chapter 3 for two-span continuous beam with the same span length. Before cracking, I_d and I_m in Equation 4-1 have the same values and their values are gross section moment of inertia. After cracking, I_m is changed to cracked section moment of inertia to consider reduced stiffness of diaphragm region, but I_d is not changed keeping its value as gross section moment of inertia.

$$\alpha = \frac{\frac{2I_d}{L_d}}{\frac{2I_d}{L_d} + \frac{3I_m}{L_m}} \quad \text{Equation 4-1}$$

Where, I_d = moment of inertia of diaphragm region
 L_d = length of diaphragm region
 I_m = moment of inertia of main spans
 L_m = length of main spans

One bay of the test specimen can be assumed as a two-span continuous bridge as shown in Figure 4-24. Each span consisted of one precast panel 8-ft long, 4-ft wide and 4-in. thick topped with 4-in. thick CIP slab. Two precast panels were used for one bay of test specimen and the spacing between the panels was 10 in (Figure 4-10). This spacing was used as a length of the diaphragm region of the test specimen.

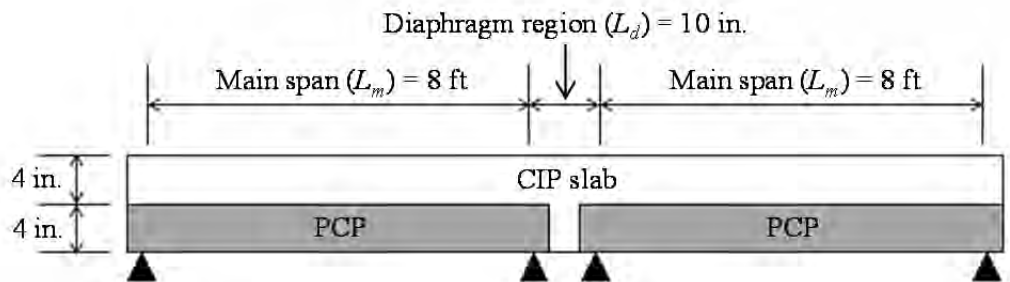


Figure 4-24: Dimensions of the specimen for calculation

Material properties, construction conditions were explained in following several paragraphs, and they were almost the same that in Section 3.2.6.3.

The design strength of concrete for the PCPs was 9,000 psi and the strength of the CIP slabs was 4,000 psi. The design strength for PCPs was determined based on the material test reports from fabrication plant, and the strength for CIP slabs was based on concrete cylinder test in Ferguson laboratory 28 days after casting. CIP topping concrete was cast when the age of the PCP was 55 days. Average relative humidity during the first month after casting was 60 %.

Each precast panel had eight 3/8 in. strands at 6 in. Initial applied prestress was 189.4 ksi per strand and the remaining prestress in the strands after the first month following casting of CIP topping was assumed as 175 ksi.

The details of top-mat reinforcement are shown in Table 4-3. This table only includes the reinforcement details in the transverse direction because to find optimized transverse top-mat reinforcement is the main focus of this test. Size and type of top-mat reinforcement in the transverse direction were varied depending on design options, but the spacing of bars in all options was 6 in. It was assumed that the values of elastic modulus of deformed bars and welded-wires were 29,000 ksi.

Longitudinal top-mat reinforcement details were the same in the Current TxDOT Standard and the Reduced Deformed-Bar Reinforcement, No. 4 bars at 9 in. The longitudinal top-mat reinforcement of the Reduced Welded-Wire Reinforcement was D 20 wire at 9 in. A D 20 wire and a No. 4 bar have the same sectional area. As stated before, longitudinal reinforcement details are not included in Table 4-3.

Table 4-3: Details of top-mat reinforcement for restraint-moment calculation

Current TxDOT Standard Reinforcement	Reduced Deformed-Bar Reinforcement	Reduced Welded- Wire Reinforcement
No. 5 bar @ 6 in.	No. 4 bar @ 6 in.	D 20 wire @ 6 in.

Using the information stated above, ultimate creep coefficients and shrinkage strains for the PCPs and the CIP slabs were calculated using ACI 209:

- i) Ultimate creep coefficient of the PCPs: 3.42
- ii) Ultimate creep coefficient of the CIP slabs: 3.40
- iii) Ultimate shrinkage strain of PCPs: 600×10^{-6}
- iv) Ultimate shrinkage strain of CIP slabs: 613×10^{-6}

Creep and shrinkage strain at time t can be obtained by multiplying ultimate values by R and the compressive strength of the CIP slabs did changed with time as shown in Section 3.2.6.3. A calculation sample of the restraint moment of the restrained-shrinkage test using the P-method is shown in Appendix C.

Figure 4-25 shows calculated restraint moments using the P-method, and calculated cracking moment using modulus of rupture of the CIP topping concrete. The top-mat reinforcement of the specimen was No. 5 bars at 6 in. In the figure, the blue dashed line represents the calculated restraint moment by P-method assuming that the specimen is not cracked. The values on this line were obtained by using the same moment of inertia for the diaphragm and main-span regions. The green dashed line represents the calculated restraint moment of the cracked section. The values on that line were obtained by using the cracked-section moment of inertia for the diaphragm region, and the gross-section moment of inertia for the main-span region.

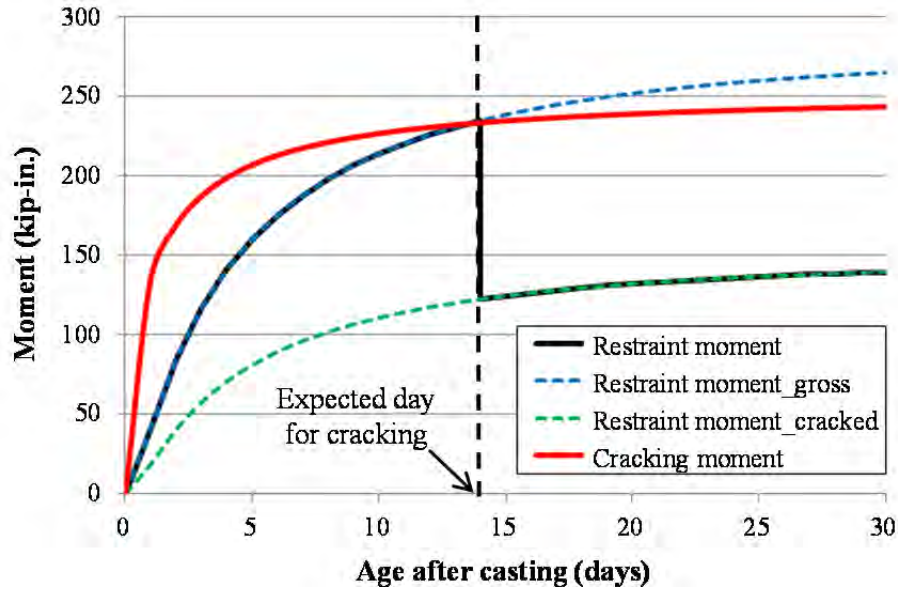


Figure 4-25: Restraint moment and cracking moment of the test frame

Formation of cracks was determined by comparing the calculated restraint moment of the uncracked section (blue dashed line) to the cracking moment (red solid line). The cracking moment was calculated using the modulus of rupture of the CIP deck concrete. If the restraint moment is greater than the cracking moment, it may be concluded that cracks have been developed in the specimen.

Before cracking the restraint moment in the specimen will follow the blue dashed line; after cracking, it will drop (the black solid line) and then follow the green dashed line.

As shown in Figure 4-25, it is possible to predict that cracks will form about 2 weeks after casting. However, no crack has been observed in the test specimens. The reasons for this disparity between the test results and the predictions by P-method may be differences of geometrical and boundary conditions between specimens of this research and the specimens of Peterman and Ramirez. Moreover, in their study, the specimens were placed on the supports that consisted of plates and rollers. However, in this study, the specimen was placed over thin wooden plates, and one continuous wooden plate was used to support entire diaphragm region. Side wooden forms used in this study may have influenced the result by restraining creep and shrinkage deformation.

4.3.2 Conclusions from Restrained-Shrinkage Test

The restrained-shrinkage test was planned to help determine optimized top-mat reinforcement in the transverse direction by comparing the performance of various top-mat reinforcement options. The restrained-shrinkage test has many advantages compared to other tests which were discussed previously in Section 2.3.2. The specimens consist of CIP slabs and precast, prestressed concrete panels (PCPs) constructed in the same manner as they would be constructed in the field. Welded-wire reinforcement, one of the test variables in this research, has been much less widely used in the field than deformed-bar reinforcement, so it is so hard to find the bridge using welded-wire reinforcement as top-mat reinforcement option.

No cracks have been observed, and all specimens have shown similar strain values. Based on the monitoring results to date, the behavior of the restrained-shrinkage specimen is consistent with that of the two bridge decks instrumented in the field.

Chapter 5. Double-Punch Testing

5.1 Introduction to Double-Punch Testing

As discussed in Chapter 2, the tensile strength and toughness of fiber-reinforced concrete can be determined from indirect tensile tests on cylinders (ASTM C496, 2011), flexural tests on beams (ASTM C1609, 2010; ASTM C1399, 2010), centrally load-tested panels (ASTM C1550, 2010; EFNARC, 1996), or direct pull tests on dog-bone specimens (Chao, 2011). Unfortunately, each of these tests suffers from a lack of simplicity, reliability, or reproducibility (alone or in combination). A better test method is needed. That need may be satisfied by the DPT, originally proposed by Chen in 1970.

At the time of its introduction, the DPT was recommended as an alternative to the splitting tensile test for determining the tensile strength of *plain concrete*: As shown in Figure 5-1, in the DPT, a concrete cylinder is placed vertically between the loading platens of the test machine and compressed by two steel punches located concentrically on the top and bottom surfaces of the cylinder (Chen, 1970). It is hypothesized that the simplicity, procedure, and fracture mechanics of this test method make it a prime candidate for evaluating the tensile strength and inelastic behavior of *fiber-reinforced concrete*.

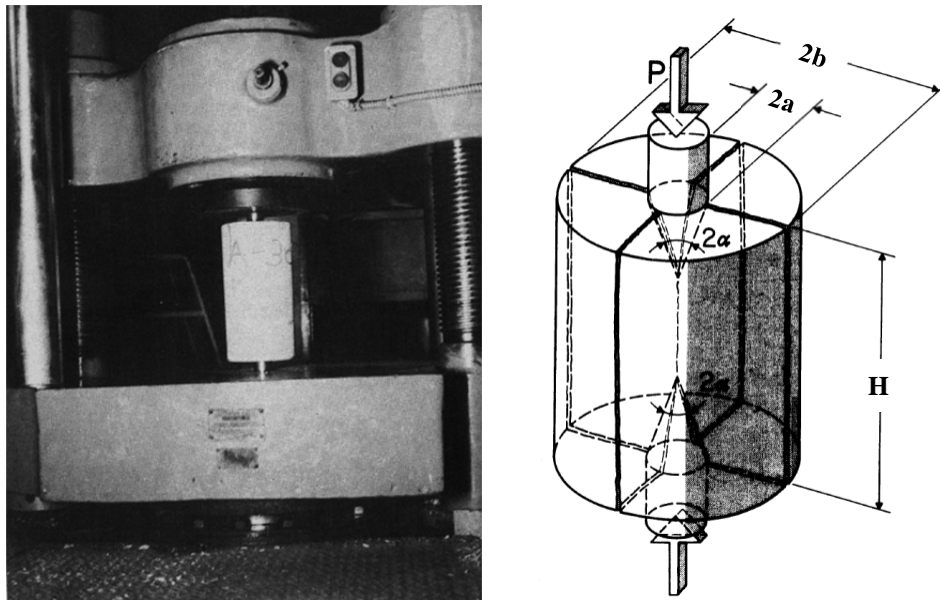


Figure 5-1: Apparatus (Chen, 1970) and loading schematic (Marti, 1989) for the DPT

5.1.1 Theory and Mechanics of the Double-Punch Test

The fundamental theory and mechanics of the DPT are based on the bearing capacity of concrete blocks (W. Chen 1969). A formula for computing the tensile strength of indirect tensile tests was obtained from the theory of linear elasticity and combined with a plasticity approach for concrete. This approach was based on the assumption that sufficient local deformability of concrete in tension and in compression existed such that generalized theorems of limit analysis could be applied to concrete idealized as a perfectly plastic material (W. Chen 1970). As shown

in Figure 5-2, a Mohr-Coulomb failure surface in compression and a small but non-zero tension cut-off was used. Here f'_c and f'_t denote the simple compression and simple tension strength respectively, c is cohesion, and ϕ is the symbol of internal friction of the concrete.

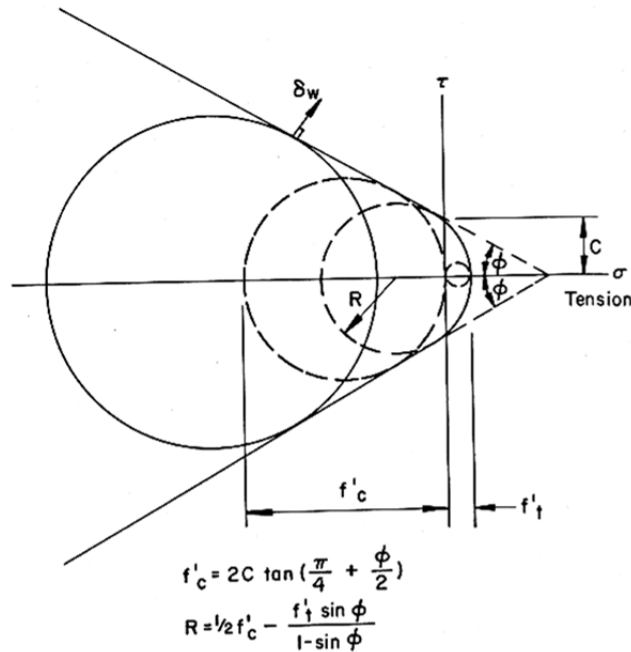


Figure 5-2: Modified Mohr-Coulomb criterion for concrete (W. Chen 1970)

Figure 5-3 shows a schematic of an ideal failure mechanism for a DPT on a cylinder specimen. It consists of many simple, radially oriented tension cracks and two conical rupture surfaces, each located directly beneath a steel punch. The conical shapes defined by those rupture surfaces move towards each other as rigid bodies, displacing the surrounding material radially. The relative velocity vector δw at each point along the conical rupture surface is inclined at an angle ϕ to the surface of the cylinder (W. Chen 1970, Bortolotti 1988).

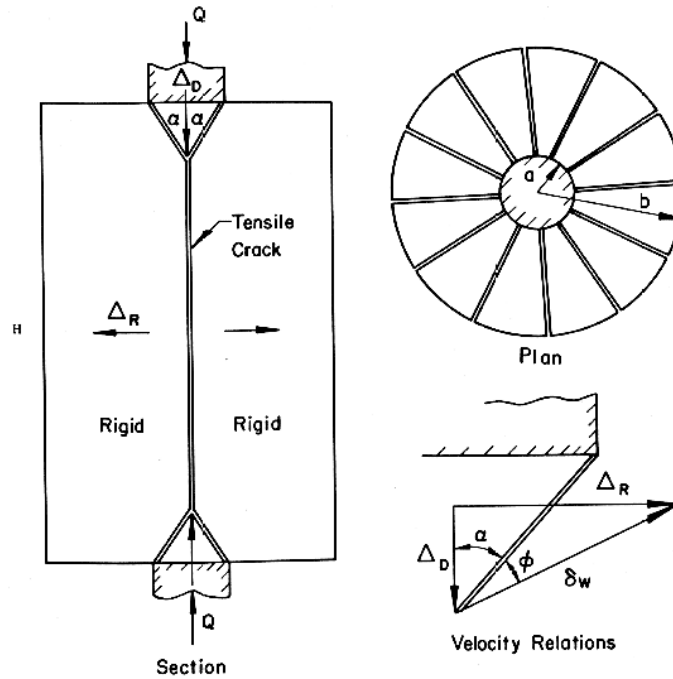


Figure 5-3: Bearing capacity of a DPT (Chen, 1970)

Because the behavior of a concrete block during a bearing capacity test is closely related to the behavior of a DPT, the formula for the DPT was obtained directly from a simple modification of results reported for concrete blocks (Chen, 1969; Bortolotti, 1988). The working formula for computing the tensile strength in a DPT was given by (Chen, 1970):

$$f_t' = \frac{Q}{\pi(1.20 bH - a^2)} \quad \text{Equation 5-1}$$

Where:

- f_t' = tensile strength, psi [kgf/cm²]
- Q = ultimate load, lb. [kg]
- H = cylinder height, in [cm]
- b = cylinder radius, in [cm]
- a = punch radius, in [cm]

It is important to note that earlier bearing capacity tests indicate that when the ratio $\frac{b}{a}$ or $\frac{H}{2a}$ is greater than approximately 4, the local deformability of concrete in tension is not sufficient to permit the application of limit analysis (Chen, 1969). Consequently, for any ratio $\frac{b}{a} > 4$ or $\frac{H}{2a} > 4$, the limiting value $b = 4a$ or $H = 8a$ should be used in Equation 2-1 for the computation of the tensile strength in a DPT. Equation 2-1 is also valid for the case of circular punches on a *square block* specimen. However, the restrictions on the limiting value of the ratio $\frac{b}{a} = 4$ (specimen width/punch diameter) or $\frac{H}{2a} = 4$ should be taken into account in a similar manner (Chen, 1970).

The following example shows a typical DPT calculation for the tensile strength of a plain concrete cylinder specimen: Q = 26,500-lb [12-kg], 2a = 1.5-in. [3.80-cm], 2b = 6-in. [15.30-cm], and H = 6-in. [15.30-cm].

$$f_t' = \frac{26,500}{\pi[1.20 \times 3 \times 6 - (0.75)^2]} = 402 \text{ psi } (\approx \frac{1}{11} f_c')$$

Table 5-1 shows the tensile strength computed from the results of a several DPTs on 6-in. [15.30-cm] plain concrete cylinders with 1.5-in. [3.80-cm] diameter punches.

Table 5-1: Tensile strength computed from DPTs on plain concrete cylinders—modified from Chen, 1970

Set	Make	Cylinder Height H, in. (cm)	Ultimate Load Q, kip (kg)	Tensile Strength f_t' , psi (kgf/cm ²)	$\frac{f_c'}{f_t'}$
1	Concrete	12 (30.60)	36.5 (16.6)	553 (38.8)	11.6
2		12 (30.60)	30.6 (13.9)	464 (32.5)	12.0
3		6 (15.30)	32.2 (14.6)	487 (34.1)	13.2
4		6 (15.30)	29.8 (13.5)	452 (31.7)	12.3
5		4 (10.2)	27.0 (12.3)	620 (43.4)	10.4
6		4 (10.2)	25.3 (11.5)	582 (40.8)	9.6

5.2 Extension of the Double-Punch Test to Evaluate the Mechanical Properties of FRC

The extension of the DPT for testing of FRC is a novel application of this test method. At the time of writing, the earliest use of DPT for FRC was reported in 2007 by Molins *et al.* in Barcelona, Spain. Previous research showed that the DPT resulted in lower coefficients of variation compared to beam tests on FRC (Molins & Aguado, 2009). However, further experimental and theoretical work was recommended to determine the extent of this test to the characterization of tensile properties of fiber-reinforced concrete.

The DPT is thought to be easily applied and advantageous to testing FRC based on the following test characteristics:

1. Test Setup & Procedure
2. Cracking Pattern & Damage
3. Correlation with FRC Structure

Each of these will be discussed separately in the following sections.

5.2.1 Test Setup and Procedure

One of the primary reasons the DPT was thought to be a reasonable substitution for the split-cylinder test was its simple testing arrangement and procedure. Indirect tensile tests enable similar specimens and the same testing machine to be used for both tensile and compressive strength tests. Many of the drawbacks of direct pull tests, such as the difficulty in eliminating eccentricity and complicated gripping devices, are overcome by loading the specimen in compression. In addition, indirect tensile tests give more consistent results with the measured strengths lying between those measured using bending and DTTs (Chen, 1970).

Many of the current test methods for FRC require specialized formwork, heavy specimens, or intricate testing supports and arrangements. Moreover, a closed-loop, servo-controlled testing machine is often necessary. The DPT is conducted using an easily handled 6 x 6-in. [15.30 x 15.30-cm] cylinder specimen weighing about 15-lb [6.80-kg]. Since specimens are tested in compression (indirect tension), any universal testing machine (UTM) can be used to facilitate the test: UTMs of some type (screw-gear or hydraulic) are available at most, if not all, testing laboratories. Simple mounting of LVDTs of appropriate gauge lengths on the UTM is sufficient for recording deflection measurements. The simplified testing arrangement and straightforward procedure of the DPT makes this method attractive for testing of fiber-reinforced concrete.

5.2.2 Cracking and Damage

Similar to the split-cylinder test, the DPT is an indirect tension test but does not confine failure to a predetermined plane (Pros, Diez, & Molins, 2010; Chen, 1970). Typically, three to four radial cracks occur as indicated in Figure 5-4. The applied load gives rise to an almost uniform tensile stress over the planes containing the cylinder axis, and the specimen splits across these planes similar to the split-cylinder test. Ultimately, an average mechanical behavior is obtained due to the multiple crack surfaces that develop from the DPT.

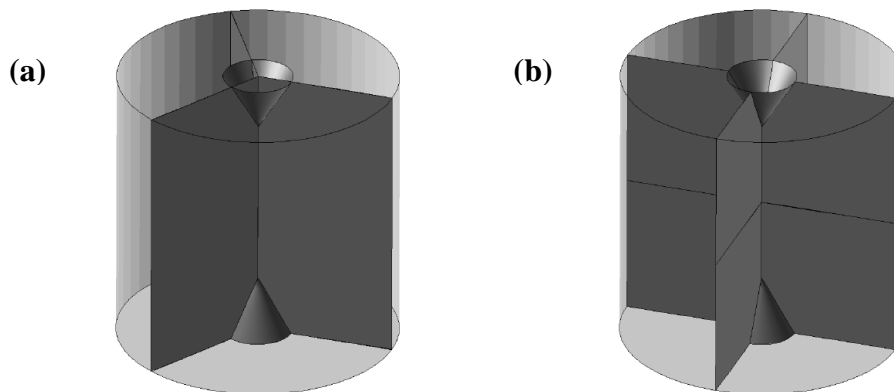
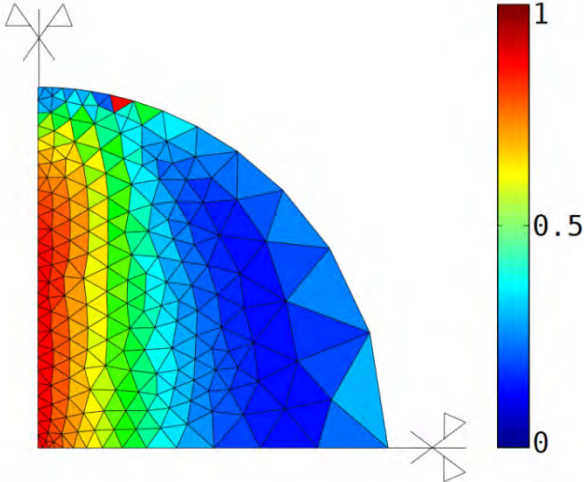


Figure 5-4: Two possible DPT collapse mechanisms with (a) three and (b) four radial fracture planes (Pros, Diez, & Molins, 2010)

The difference between a *single major crack* and the *multiple cracking* pattern of the DPT can be seen in Figure 5-5 (a) and (b) which compare the damage profiles for split-cylinder and double-punch loading on plain concrete cylinders, respectively. The damage profile of the split-cylinder test is similar to current test methods for FRC that result in a single plane of failure. In the damage scale, for $D = 0$, the material is considered healthy and if $D = 1$, the

material is completely damaged (Pros, Diez, & Molins, 2010). It is clear that the DPT results in intense damage at discrete locations.

(a) Split-Cylinder Test



(b) Double-Punch Test

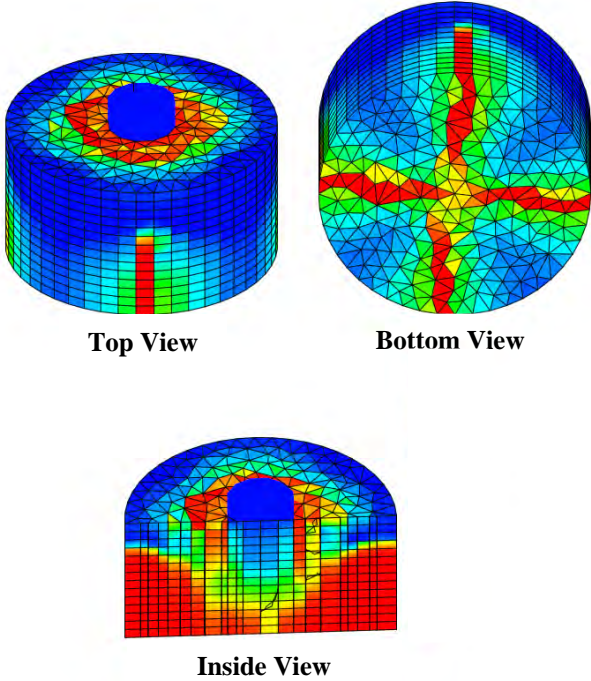



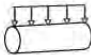
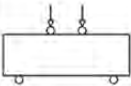
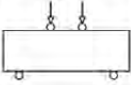
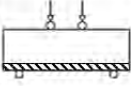
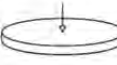
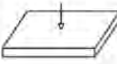

Figure 5-5: Damage profiles for (a) split-cylinder test and (b) DPT loading on plain concrete cylinders (Pros, Diez, & Molins, 2010)

5.2.3 Correlation with FRC Structures

The cracking pattern of the DPT is preferred over a *single crack* in a *well-defined* plane which is common to many of the current testing methods for FRC. Since the fiber dispersion and orientation is random, increasing the number of fracture planes, and more importantly the specific failure surface of a test specimen, increases the probability that fibers will indeed intersect crack planes. Thus, the effect of the fiber-reinforcement, which distinguishes FRC from other concrete mixtures, is more likely to be captured.

The specific failure surface β can be defined as the total failure surface area per unit volume of a test specimen. Numerically, it represents the fractured plane or planes that manifest when a specimen reaches failure for a given test method. As shown in Table 5-2, a specimen tested using the DPT has a higher specific failure surface (β) than specimens tested by any other test method for FRC. The ratio $\beta_{\text{DPT}}/\beta_{\text{TEST}}$ is provided in the last column of Table 5-2 to compare the specific failure surface of the DPT to that of current testing procedures. It is shown that the DPT can result in a specific failure surface up to an order of magnitude higher than other test methods. This data supports the idea that the failure mechanism of the DPT should result in reliable data for fiber-reinforced concrete specimens, particularly in the post-cracking region where fiber performance dominates the composite behavior.

Table 5-2: Comparison of the specific failure surface of test specimens for current FRC test methods vs. DPT

TEST INFORMATION ¹		TEST SPECIMENS				
Designation	Layout	Volume (in. ³)	Number of Failure Planes	Failure Surface Area (in. ²)	Specific Failure Surface, β	$\beta_{DPT} / \beta_{TEST}$
Double-Punch Test		170	3	54.0	0.318	1
ASTM C496		101	1	12.6	0.125	3
ASTM C1609		720	1	36.0	0.050	6
ASTM C1609		224	1	16.0	0.071	4
ASTM C1399		224	1	16.0	0.071	4
ASTM C1550		2338	3	141.8	0.061	5
EFNARC Panel Test		2304	3	144.0	0.063	5
Uniaxial Direct Tensile Test		524	1	16.0	0.031	10

¹ Test layouts modified from (Molins C. , 2006).

In addition to the fact that the DPT produces a higher specific failure surface area than any of the current test methods for FRC, the weight of the specimen required to conduct the test is manageable. As shown in Figure 5-6, the 6 x 6 in. DPT cylinder specimen weighs less than all of the specimens required for current test methods for FRC. It very similar to the cylinder specimen required for the Split Cylinder Test (ASTM C496).

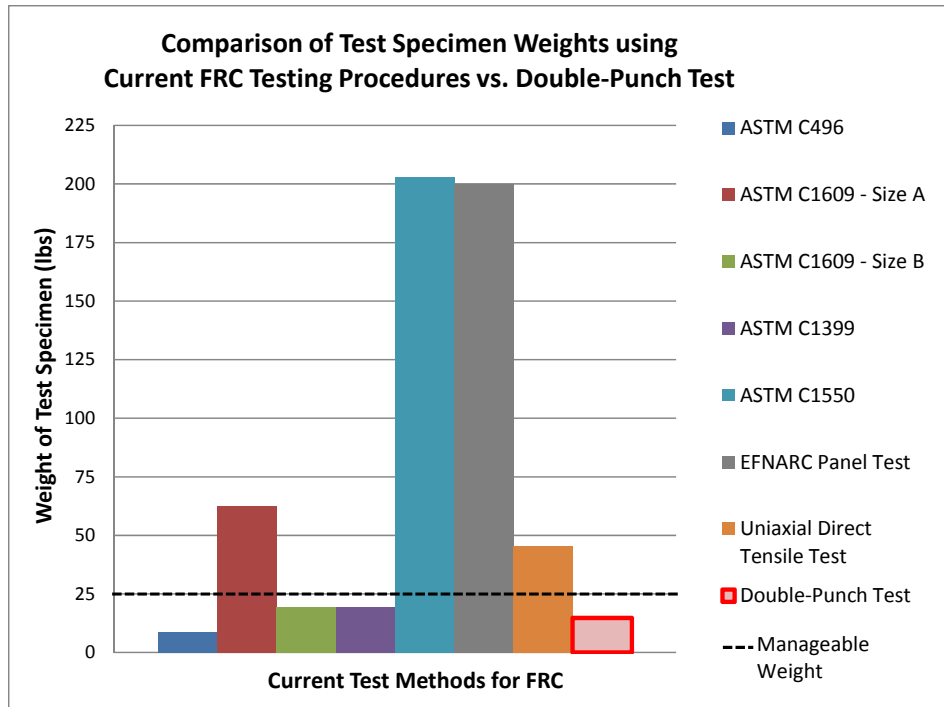


Figure 5-6: Comparison of test specimen weights for current FRC testing procedures vs. DPT

5.3 Summary of Advantages of Double-Punch Test

Based on previous research on both plain and fiber-reinforced concrete, the test arrangement, procedure, specimen size and cracking pattern of the DPT method clearly indicate that the test should be useful for evaluating the elastic and plastic behavior of FRC. The DPT will, by nature, result in a large failure surface area which correlates better with the random distribution and orientation of fibers in FRC composites. Furthermore, it is speculated that the DPT may prove to be more convenient and reliable than current test methods for fiber-reinforced concrete. In order to confirm these hypotheses, the DPT Research and Testing Program was organized at the University of Texas at Austin to determine the effectiveness of the double-punch method for evaluating the mechanical properties of FRC.

5.4 Summary of Results from Double-Punch Tests at UT Arlington

In this section, results from DPTs at UT Arlington are summarized. Details of test procedures and results are provided in Appendix F. Additional information is also given in Cho (2012), Karki (2012), and Waweru (2012).

In the first three phases of double-punch testing at UT Arlington, peak and residual loads and average load-deformation curves for specimens with different types of high-performance steel fibers in different volume fractions were compared with those of plain concrete. Specimens with higher volume fractions showed higher equivalent tensile strength and slight hardening behavior after first cracking. Steel fibers with double-bend hooks at ends of the fibers and greater length gave higher peak strength and higher residual strengths. Strength ratios for Type1 (Royal with single hook at end), Type 2 (Baekert short, double hooks at end and Type 3 (Baekert long,

double hooks at end) fibers were 1.94: 1.44: 1.0. Evidently, the DPT can distinguish among the performances of different FRC mixtures at early ages. Because coefficients of variation are low for peak and residual loads, small numbers replicate specimens can be used. From the fourth phase of double-punch testing at UT Arlington, DPT can show the properties of FRC at 28 days, including peak and residual strengths, toughness at 0.1-in. deformation, and strain-hardening properties.

From the fifth phase of double-punch testing at UT Arlington, results clearly show that peak strength obtained from DPT has a coefficient of variation of about 5%, in contrast to COVs for peak strengths from bending and DTTs, which have COVs of 17% and 18%, respectively. Though COVs for residual strength and toughness from DPT are more than 10% in some cases, these values were still very much lower than COVs for residual strength and toughness from bending and DTTs.

Load-deflection curves for the DPT show much lower scatter than those from third-point bending test (ASTM C1609) and DTT. The COV for toughness is less than 9% for the DPT, and as high as 24–26 % for ASTM beams and DTT. The DPT also has much less variation in post-cracking behavior than ASTM C1609.

The DPT requires only a universal testing machine, while the bending test (ASTM C1609) and DTT require a closed-loop displacement-controlled machine. Finally, DPT specimens are much more convenient to prepare than are those of the other two methods.

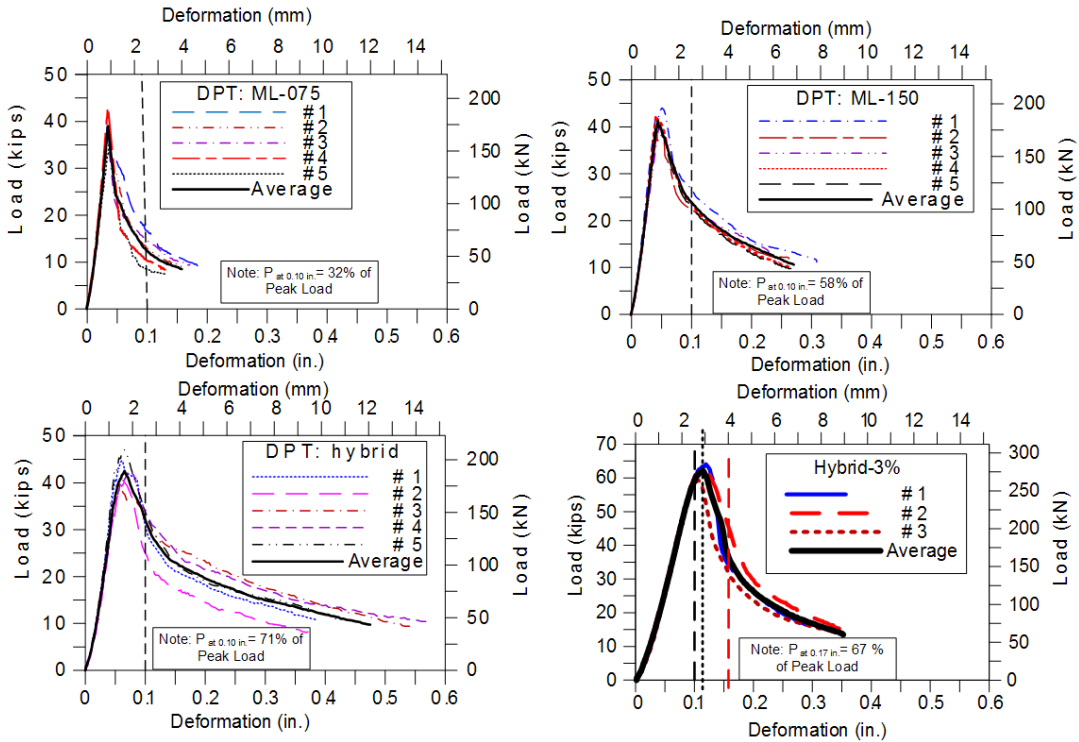
5.4.1 Conclusions from Double-Punch Testing at UT Arlington

1. DPT method can be used to distinguish the peak strength, residual strength, toughness, stiffness, strain-hardening or strain-softening, mix quality of different SFRC mixtures.
2. DPT method showed much less scattered results as compared to that of the third-point bending beam test (ASTM C1609) and direct tensile test (DTT).
3. DPT does not need a closed-loop, servo-controlled machine, a simple small-capacity compression machine is sufficient.
4. Compared to other types of specimens, it is relatively easier to prepare the DPT specimens by just cutting in half the 6×12 in. regular cylinders.
5. Less number of samples is required for DPT due to the low variability in the test results. It was shown that four specimens or two 6×12 in. cylinders are generally sufficient.
6. Unlike specimens for the ASTM C1609 bending test and DTT where the performance is typically governed by one or two major cracks, multiple cracks developed in DPT specimens and thus give a more averaged results which in turn reduces the variability.
7. As load versus deformation curves from DPT show that individual curves are not very much scattered from the average curve, the average curves can be used to compare between different FRC mixes.
8. Finite element analysis indicates that tensile stresses were uniform in most part of the DPT specimens. Test results show that the equivalent tensile strength calculated by Equation 1 (Chen, 1970) is very close to that obtained from DTT and within 15% difference.

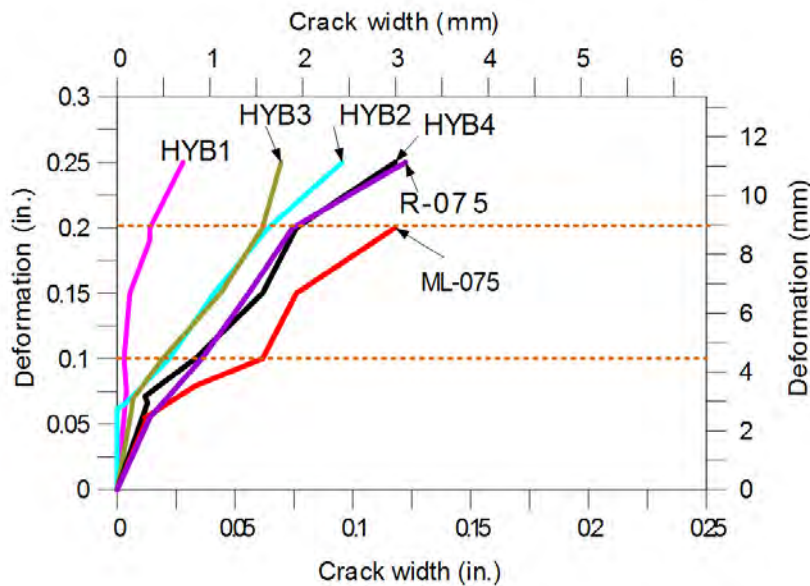
5.4.2 Suggested Evaluation Criteria for DPT Results

Two performance criteria are proposed when an FRC mixture was evaluated by DPT:

- Two critical points: peak strength and residual strength at 0.1-in. deformation (or 0.5-in. from the peak strength if FRC mixtures have high peak strength). A lower bound value of residual strength at 0.1-in. deformation can be specified (see figure below).



- Limits in average crack widths at specified deformation values:



5.5 Double-Punch Testing at the University of Texas at Austin

The main objectives of *this portion* of Study 6348, previously stated in Chapter 1, include the following:

1. Quantify the influence of mix compositions, fiber types, and fiber volume fractions on the mechanical characteristics of FRC;
2. Develop test protocols for comparing the effectiveness of steel fiber-reinforced concrete mixtures with different fiber types and volume fractions;
3. Supply intra- and inter-laboratory data and observations useful for comparing the DPT with current test methods for FRC.

Again, the central focus of the DPT Research and Testing Program at UT Austin is to produce sufficient within-batch, intra-laboratory data to make conclusions and recommendations regarding the simplicity, reliability, and reproducibility of the DPT when applied to steel fiber-reinforced concrete. The testing program and results are presented in detail in Appendix D.

5.5.1 Overview of Results from DPT at UT Austin

The goal of the DPT Research and Testing Program was to produce sufficient within-laboratory data to make conclusions and recommendations regarding the DPT for evaluating FRC. In this chapter, the results of 120 tests on steel fiber-reinforced concrete specimens are summarized. *Selected* DPT Performance Curves from experiments will be presented to show the range of behavior observed during testing. *Typical* statistical analysis results will also be provided to explain the effects of test variables on DPT results. The complete set of (120) DPT Performance Curves as well as Phase 1 and 2 statistical analysis results are available in Appendix A and B, respectively.

Selected performance curves for both Phase 1 and Phase 2 specimens tested on the Baldwin machine are provided in Figure 5-7, Figure 5-8, and Figure 5-9, which compare Royal and Bekaert fibers at 0.75%, 1.00%, and 1.50% volume fractions, respectively.

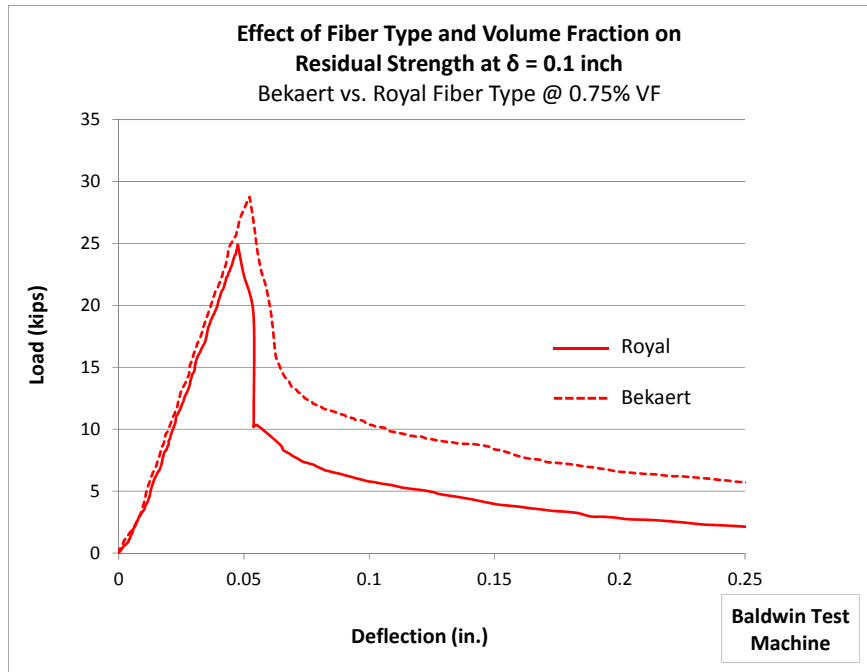


Figure 5-7: Combined results—selected DPT Performance curves showing effect of fiber type and volume fraction at 0.75% fiber content

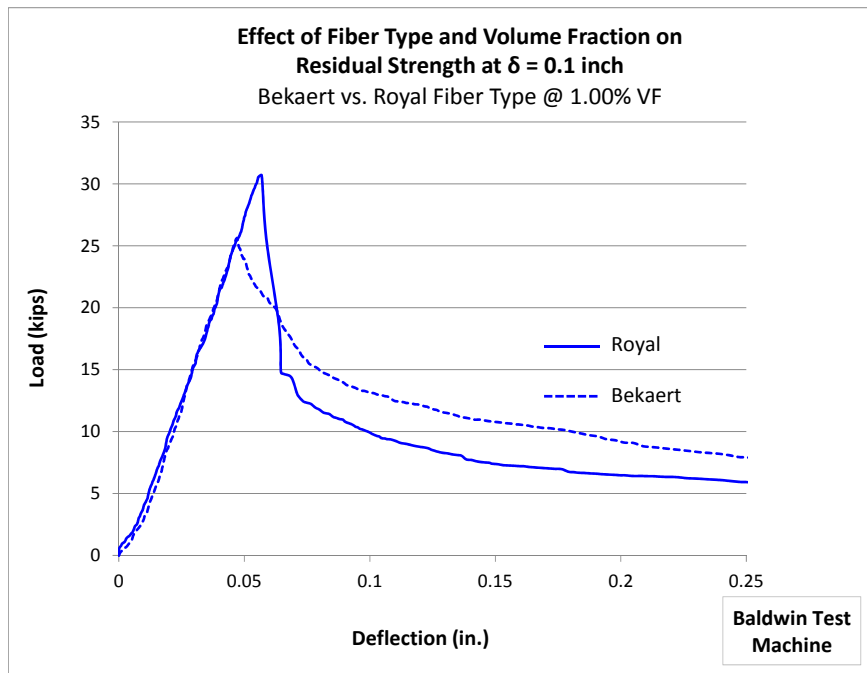


Figure 5-8: Combined results—selected DPT performance curves showing effect of fiber type and volume fraction at 1.00% fiber content

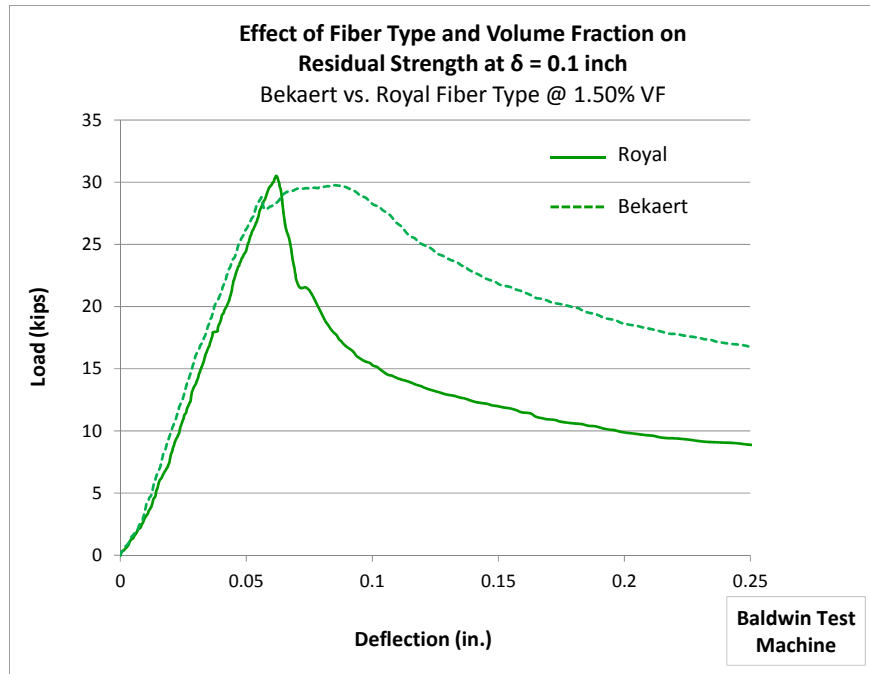


Figure 5-9: Combined results—selected DPT performance curves showing effect of fiber type and volume fraction at 1.50% fiber content

The performance of DPT specimens with different fiber types and volume fractions was also observed in the cracking pattern of test specimens. This comparison is provided in Figure 5-10.

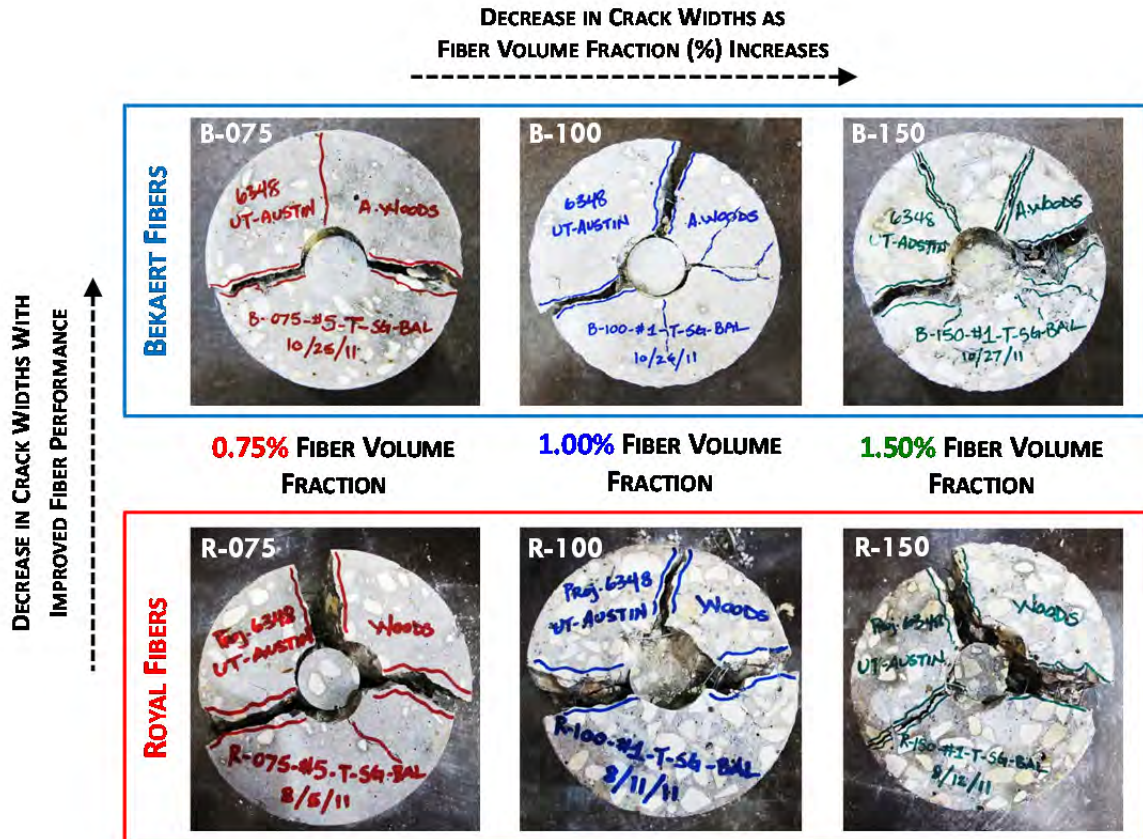


Figure 5-10: Effect of fiber type and volume fraction on crack widths and cracking pattern

Discussion of Combined Results from DPT at UT Austin

The combined selected performance curves for Phase 1 and Phase 2 show that it is possible to compare different fiber types and volume fractions using the load-deflection curves obtained from the DPT. The performance of different mixtures can also be compared using the cracked specimen. As shown in Figure 5-10, cracks were smaller for Bekaert specimens than for Royal specimens, indicating that the Bekaert fibers did not deform as much as the Royal fibers. As expected, crack widths also decreased as the fiber volume fraction increased.

Testing Procedure for DPT at UT Austin

In the DPT, a 6- x 6-in. cylindrical concrete specimen is placed vertically between the loading platens of the test machine and compressed by two steel punches located concentrically on the top and bottom surfaces of the specimen. This loading produces radial transverse tension in the specimen. Although the DPT is simple, centering and seating of the steel punches prior to taking load-deflection measurements is critical. Centering of the punches is necessary to avoid placing a moment on the specimen due to eccentric load. As shown in Figure 5-11, if the punches are misaligned, the specimen can topple during loading due to the overturning force. Results obtained under these conditions are meaningless, and are disregarded.

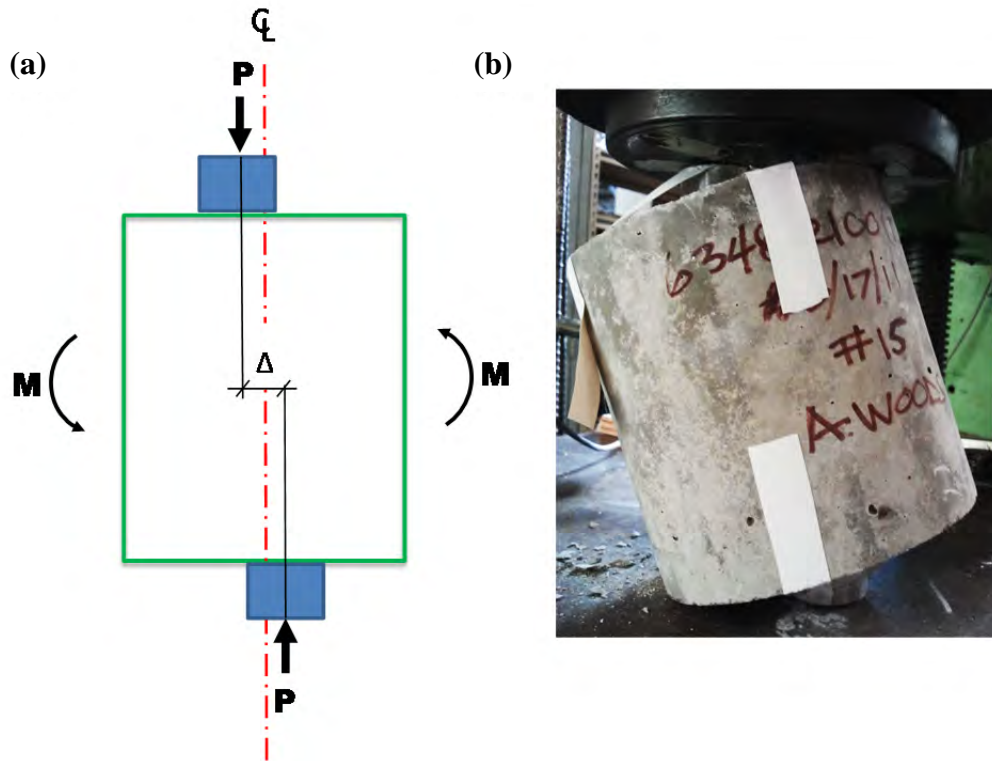


Figure 5-11: Effect of misaligned steel punches in DPT shown (a) schematically and (b) for trial specimen

Even a small degree of misalignment can result in this behavior, and simple measures were used to guard against the effects of eccentric loading. For one, a punch centering guide (Figure 5-12) was constructed to ensure adequate placement of the punches on the DPT specimen. Secondly, the punches were strapped to the specimen using masking tape for additional security against slipping or sliding of the steel punches during placement and loading. Finally, a spherical loading head was used to compensate for any unevenness of the DPT specimen produced from cutting, grinding, or Hydro-Stone.



Figure 5-12: Steel punch centering guide and masking tape used to secure against eccentric loading effects

In addition to alignment, the steel punches must be seated into the specimen. As shown in Figure 5-13, during the initial loading stage, the effect of the steel punches seating into the concrete can be seen in the curved ascending branch of the load-deflection plot. This initial non-linearity indicates the *seating process*. To correct for the seating of the punches, a “shakedown” loading sequence was employed: DPT specimens were loaded up to 10 kips, unloaded, and then reloaded to failure. In this way, the steel punches are set into the concrete and the appropriate *linear-elastic* behavior up to first crack was obtained by using a corrected zero reading corresponding to the end of the shakedown.

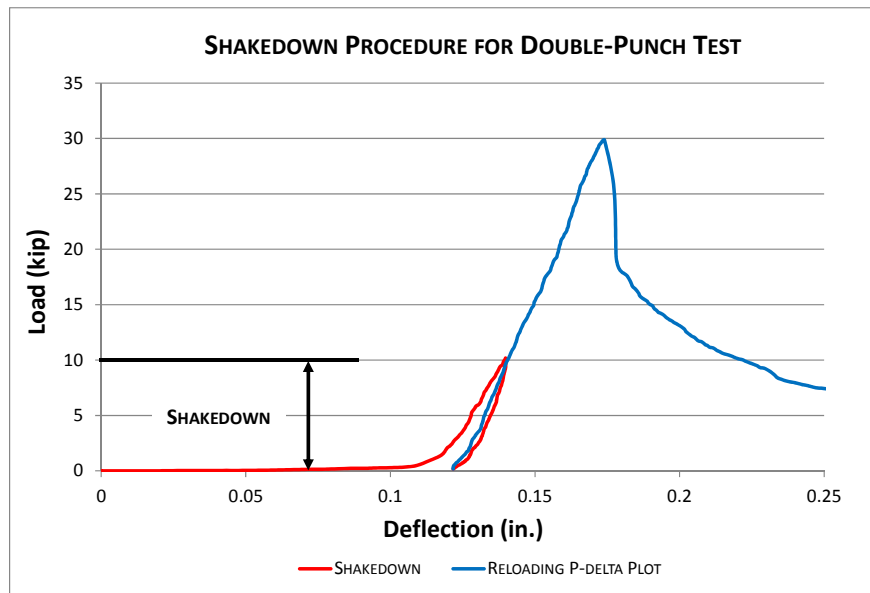


Figure 5-13: Schematic of shakedown procedure for DPT experiments

All specimens were carefully prepared and placed into the loading apparatus. Once positioned, each DPT specimen was tested according to the following sequence:

- 1) *Shakedown (Initial Loading and Unloading to Seat Punches)*
 - Load the specimen at a rate of 100 lb/sec [445 N/sec] \pm 25 lb/sec [\pm 111 N/sec] up to a load of 10 kips [44.5 kN].
 - Unload the specimen at a rate between 100 and 300 lb/sec [445 and 1334 N/sec] to a load between 100 lb [445 N] and 200 lb [890 N].
 - The deflection at that final load is termed the “initial deflection offset.”
- 2) *Reloading*
 - Load the specimen at a rate of 100 lb/sec [445 N/sec] \pm 25 lb/sec [\pm 111 N/sec].
 - Note the corresponding rate of applied deformation.
 - Load at that deformation rate until the first radial crack appears in the top or bottom face of the specimen.

3) *End Point*

- Continue loading at a rate between 1.0 and 3.0 times the pre-cracking deformation rate until the deformation reaches or exceeds 0.5 in. [13 mm], or the steel punches are almost fully penetrated into the specimen.
- Do not permit the loading head of the testing machine to contact the specimen.

4) *Data Recording*

- Record the applied load and the deflection of the loading head at approximately 1-second time intervals.

Calculation of Key Test Parameters for DPT at UT Austin

The corrected load-deflection plot was obtained, and key test parameters were assigned in order to determine how the fiber type, volume fraction, surface preparation, and test machine affect the DPT results. This was done by the following process:

1) *Correct Deflections*

- Subtract the “initial deflection offset” from each deflection reading during the reloading phase. The resulting deflections are termed “corrected deflections.”

2) *Calculate Key Test Parameters*

Using the recorded loads and the corrected deflections, calculate and report the initial slope, peak load, and residual strength, as follows:

- **Initial Slope:** Evaluate the initial slope as the slope between applied loads of approximately 5 kips [22 kN] and 15 kips [67 kN].
- **Peak Load:** Evaluate the maximum load directly.
- **Residual Strength:** Evaluate the residual load at a corrected deflection of 0.1 in. ± 0.01 in. [2.5 mm \pm 0.025 mm].

The key parameters are shown graphically in Figure 5-14: (1) initial slope, (2) peak load, and (3) the residual strength at a deflection of 0.1 in. With these values, the elastic modulus, ultimate tensile strength, and toughness can be calculated, respectively, and the performance of mixtures with different fiber types and volume fractions can be compared. Ultimately, these parameters summarize the behavior of steel fiber-reinforced concrete.

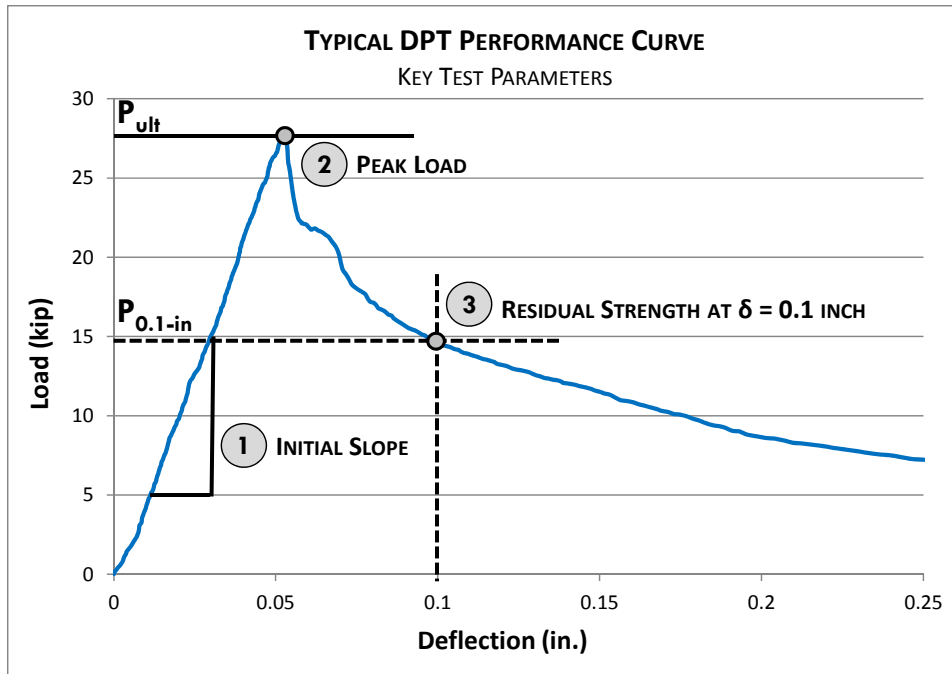


Figure 5-14: Typical DPT performance curve showing key test parameters

The initial slope was calculated between 5 and 15 kips because this range represents the most stable portion of the ascending branch. It was very difficult to control the rate of loading up to 5 kips and beyond about 20 kips due to sensitive dials on the testing equipment. The initial slope represents a tangent stiffness, and was taken in the specified region to avoid potential errors introduced by variations in loading rate.

The key test parameters were evaluated statistically to assess the reliability and reproducibility of the DPT, as well as its ability to accurately describe the performance of steel fiber-reinforced concrete. This information is presented in Appendix G.

Chapter 6. Control of Cracking in Precast, Prestressed Concrete Panels

6.1 Introduction

The objectives of the panel monitoring conducted in this study are to evaluate the effects of initial prestress and additional transverse reinforcement on the formation and propagation of collinear cracks. To this end, twenty-three precast, prestressed panels (PCPs) were fabricated at two plants, designated Plant A and Plant B. Plant A used limestone aggregate, and Plant B used river-gravel aggregate. One set of panels was fabricated using “winter” concrete mixture proportions, and the other set using “summer” concrete. Two different levels of initial prestress were used: the current TxDOT initial prestress (189.4 ksi); and a reduced initial prestress (169.4 ksi).

6.2 Fabrication of Panels

In Table 6-1, panel details are presented. The panels with higher initial prestress level are designated as Current TxDOT initial prestressed panels; all were cast in winter. The panels with lower initial prestress were designated as Reduced initial prestressed panels; all were cast in summer.

Strands were released one day after fabrication, and panels were delivered to Ferguson Lab one or two weeks later. Plant A and Plant B used the same welded-wire mats as a transverse reinforcement. However, the location of the mat differs at each plant. In Plant A, the mats were placed over the prestressed strands; in Plant B, they were placed below the strands. The specific 28-day concrete strength was 10,000 psi.

Table 6-1: Summary of fabrication of panels

Plant	Current TxDOT		Reduced	
	Plant A	Plant B	Plant A	Plant B
Coarse aggregate	Limestone	River gravel	Limestone	River gravel
Initial prestress stress	189.4 ksi per strand		169.4 ksi per strand	
Fabrication date	2/18/2009	2/18/2010	7/20/2010	9/21/2010
Releasing date	2/19/2009	2/19/2010	7/21/2010	9/22/2010
Transportation date	2/26/2009	3/1/2010	7/30/2010	10/5/2010
Reinforcement	Transverse dir.: D 7.5 wires at 4 in. Longitudinal dir.: D 3.5 wires at 18 in.			
Concrete strength	11,015 psi	10,640 psi	10,240 psi	8,810 psi

Instrumentation details are shown in Figure 6-1 to Figure 6-3. In the figures, red stars refer to the foil gages; green I shapes refer to the embedment gages; and red I shapes refer to the vibrating-wire gages. In Figure 6-1, numbers in dashed-line boxes refer to channel numbers of foil gages, and numbers in solid-lined boxes refer to the number of embedment gages. In Figure 6-2, and Figure 6-3, numbers in solid-lined boxes refer to channel number of embedment and vibrating-wire gages. Foil gages (FLA-6-350-11-8LT, Tokyo Sokki Kenkyujo Company) were

0.25-in. long. Embedment gages (PMFL-60-8L, Sokki Kenkyujo Company) had a 2.5-in. gage length. Vibrating-wire gages (VCE-4200, Geokon) had a 6-in. gage length.

The pattern of gages for the summer panels was modified based on data from the winter panels. Foil gages were not used in the summer panels because they were easily damaged during fabrication and transportation. Moreover, vibrating-wire gages (VWGs) showed stable long-term monitoring performance in the winter panels, so the number of vibrating-wire gage was increased in the summer panels. The total number of gages was reduced because it was shown that fewer gages would provide the required data based on the monitoring results of the winter. More detailed information is given in Foreman (2010) and Azimov (2012).

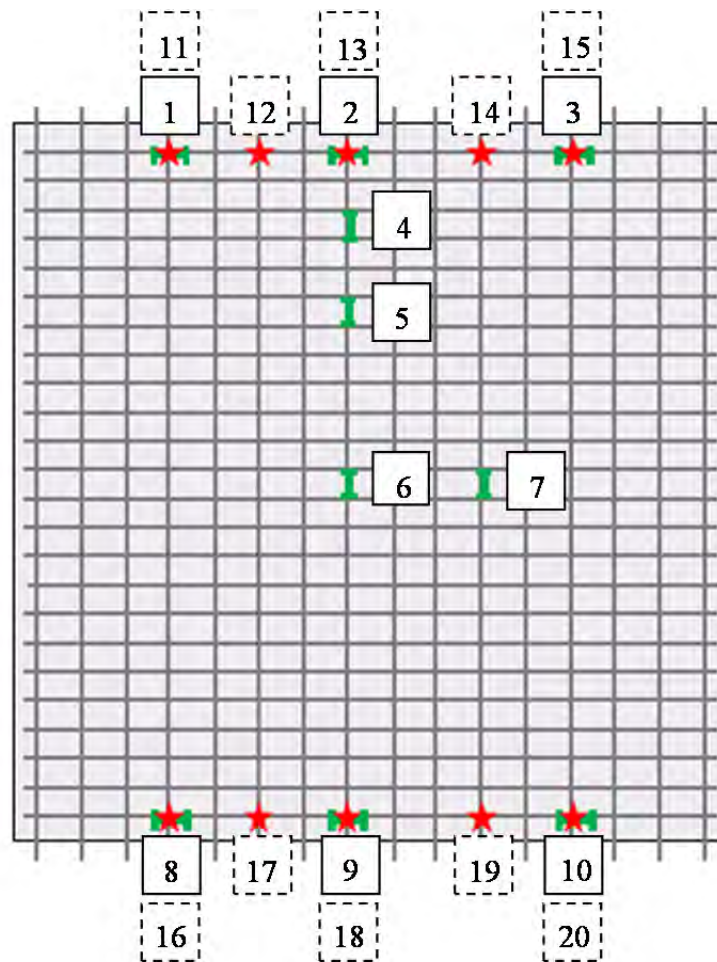


Figure 6-1: Gage layout for current TxDOT initial prestressed panel from Plant A (Foreman 2010)

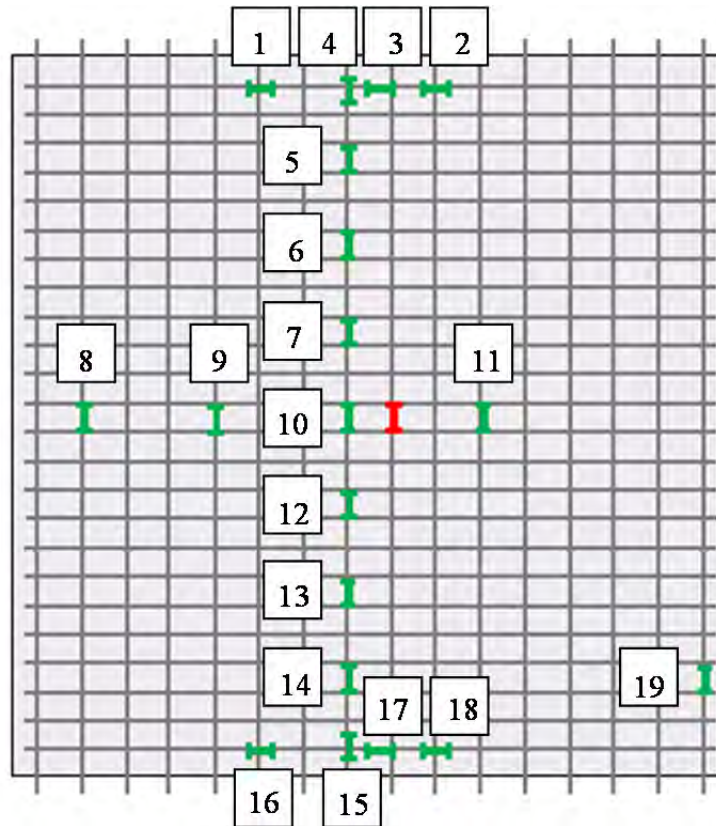


Figure 6-2: Gage layout for current TxDOT initial prestressed panel from Plant B (Foreman 2010)

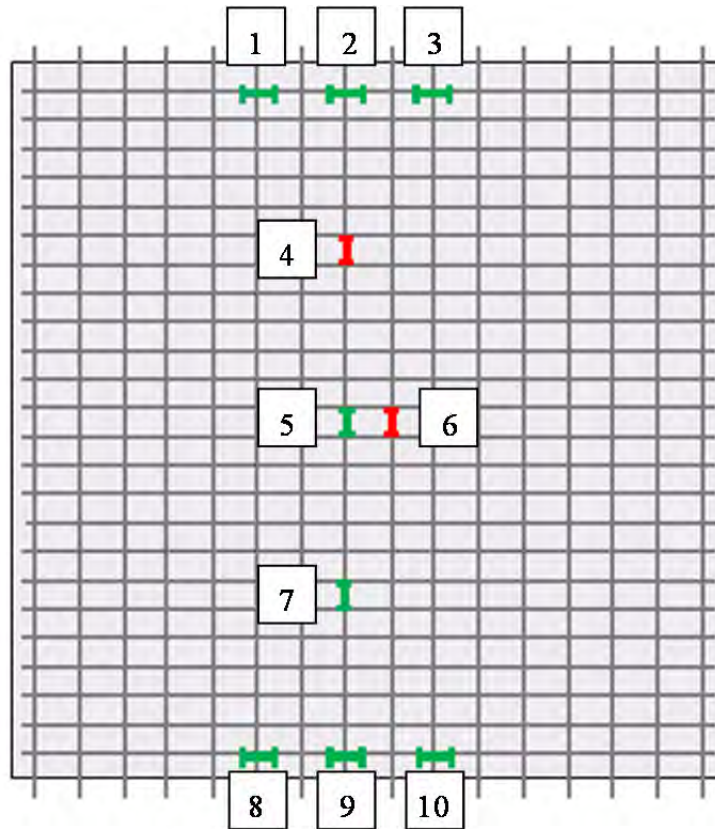


Figure 6-3: Gage layout for reduced initial prestressed panel from Plants A and B (Azimov 2012)

6.3 Monitoring of Strains in PCPs

After the panels arrived at Ferguson Laboratory, they were stacked in the same way they would be stored at a typical bridge site (Figure 6-4 and Figure 6-5). The monitoring procedures were simple. The data loggers, shown in Figure 6-6, store the data in memories allowing occasional download of the data. If the prestress losses show very slight changes, the scanning interval can be increased. The data logger was put in the steel box (Figure 6-7) and the steel box was put in orange wooden box as shown in Figure 6-8 to protect the loggers from moisture and impact. The wooden boxes were painted bright orange so that plant workers would be aware of their importance. The strains from VWGs were measured using a hand-held reader as shown in Figure 6-9.



Figure 6-4: Stacking panels at Ferguson Laboratory (Azimov 2012)



Figure 6-5: Stacked panels at Ferguson Laboratory



Figure 6-6: Campbell Scientific CR 5000 data logger



Figure 6-7: Steel box for data logger



Figure 6-8: Wooden box for data logger



Figure 6-9: Hand-held reader for VWGs (Model GK-404, Geokon)

6.4 Prestress Loss Monitoring

6.4.1 Measured Prestress Losses

Observed prestress losses are summarized in Table 6-2. The monitoring period is 22 to 42 months. The values in the table were obtained by calculating the average prestress losses for each set of panels with the same initial prestress level and made in the same plant. In Table 6-2, the numbers in the brackets were measured by vibrating-wire gages, and other numbers were measured by embedment gages. More detailed information about monitoring is given in Foreman (2010), and Azimov (2012).

Short-term prestress losses, which were measured during the first day after release, did not change much with initial prestress level, but did change with aggregate types. The panels with limestone (Plant A) showed larger short-term prestress losses than the panels with river-

gravel aggregate (Plant B). Long-term prestress loss, which were measured during over a year, decreases as initial prestress decreases, but the difference is not significant. As with the trend of short-term prestress losses, panels with limestone aggregate showed larger long-term prestress losses than panels with river-gravel aggregate.

Table 6-2: Summary of results from prestress-loss monitoring

	Current TxDOT initial ($f_{pi}=189.4$ ksi)		Reduced initial ($f_{pi}=169.4$ ksi)	
	Plant A (limestone)	Plant B (river gravel)	Plant A (limestone)	Plant B (river gravel)
Short-term loss (ksi)	3.5	3.2 (3.1)	4.4 (4.3)	3.6 (3.1)
Long-term loss (ksi)	24.4	12.4 (11.6)	13.8 (15.3)	11.1 (11.6)

Long-term prestress losses with the current TxDOT and the Reduced initial prestressed panels are plotted in Figure 6-10 and Figure 6-11. The values in both figures were detected by the gages placed along strands. Among the gages in a panel, the gage which showed the biggest prestress loss was chosen, and its values were plotted in both figures. The gages installed at the center of the panels generally showed the biggest prestress losses. The panels which had the same initial prestress level and were cast in the same plant showed similar patterns of prestress loss, so only one panel is presented for each group.

In both figure, red lines indicate prestress losses in the panel made in Plant A, and blue lines indicate the panels made in Plant B. Dashed lines represent a period when data logger did not function properly. Purple vertical line indicates the age at which the losses began to stabilize.

As shown in both figures, the prestress losses in the panels cast in Plant A are bigger than those in the panels cast in Plant B regardless of initial prestress level. The difference in prestress losses between two plants increases as the initial prestress increases.

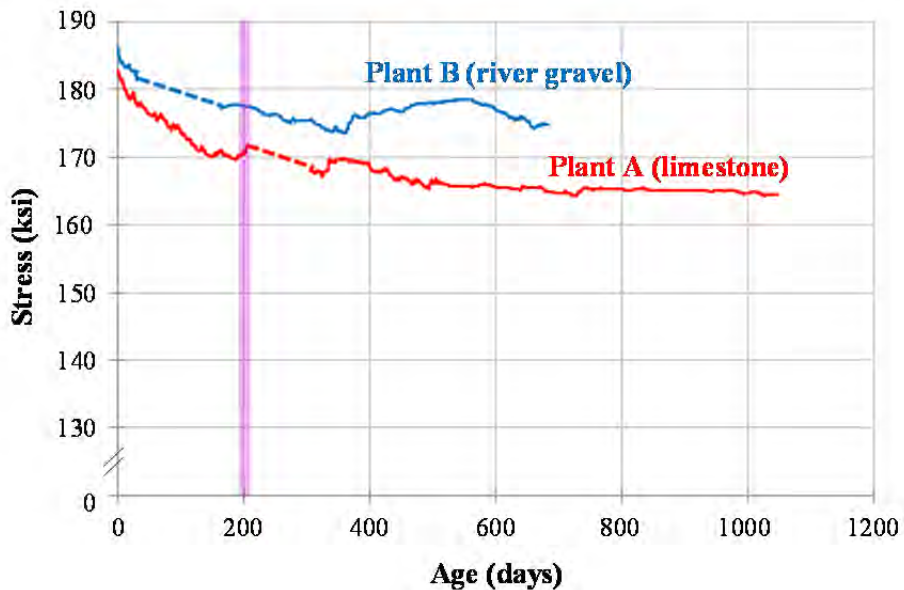


Figure 6-10: Long-term monitoring results, current TxDOT initial prestress

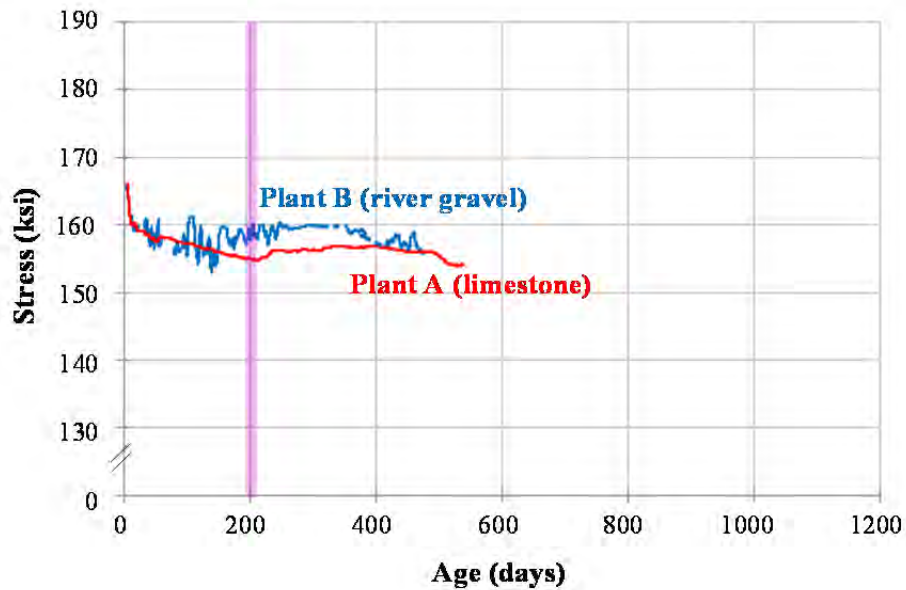


Figure 6-11: Long-term monitoring results, reduced initial prestress

6.4.2 Effects of Gage Type

Figure 6-12 shows typical long-term monitoring data. The black line refers to readings from embedment gages, and red crosses refer to readings from vibrating-wire gages. The strains detected by vibrating-wire gages were occasionally measured by hand-held reader (Figure 6-9), so continuous monitoring was not conducted. For this reason, the red crosses are not connected with a line, and indicate discontinuous monitoring. The black dashed line refers to a period of time when the data logger did not work. Figure 6-12 shows the long-term monitoring data from the panels with Current TxDOT initial prestress and cast in Plant B. The data from both types of gages matched well, and the same trend is found in all panels regardless of initial prestress levels and fabrication plants. Based on this fact, it can be concluded that vibrating-wire gages can be used to back up data missing when the data logger did not work.

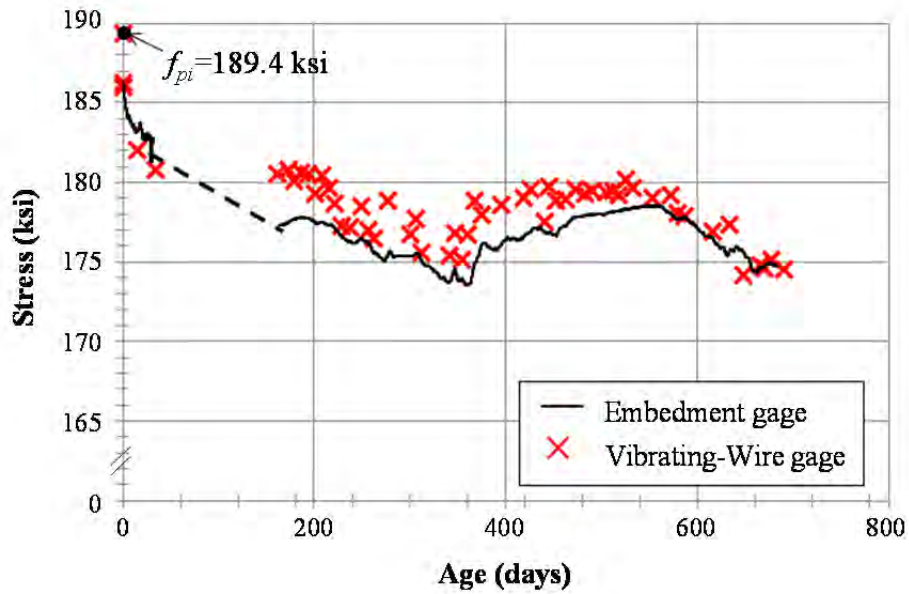


Figure 6-12: Typical long-term monitoring data

6.4.3 Effects of Aggregate Type and Environmental Conditions on Prestress Loss

In Table 6-3 are shown the average environmental conditions during the first month after release in both plants. The magnitude of prestress loss can vary during the entire life of panels, depending on material properties and environmental conditions. Because most prestress loss occurred within the first month, effects of material properties and environmental conditions on prestress loss can be observed by focusing on prestress loss during that time.

In this section, coarse aggregate type and three environmental factors (temperature, humidity, and wind velocity) were considered. Generally, the deformations of concrete due to creep and shrinkage increase as temperature increases, humidity decreases, and wind velocity increases. Prestress losses increase as creep and shrinkage deformations increase. After they were wet-cured, the panels were exposed to air. Therefore, the temperature of the panels can be assumed to be the same as ambient temperature after the curing period.

Under the same initial prestress level, average values of temperature and humidity in both plants were almost same, but the average wind velocity at Plant A was greater than that at Plant B (Table 6-3). Therefore, it can be expected that the creep and shrinkage deformation of the panels at Plant A may be larger than those at Plant B.

In Figure 6-13 are shown measured prestress losses for the first month after casting. The prestress loss of the panels cast at Plant B (blue lines) was less than that of panels cast at Plant A (red lines). The possible reason is that creep and shrinkage deformations of the panels from Plant B might be less than that of the panels from Plant A because of their aggregate type and environmental conditions.

Finally, it may be concluded that prestress loss during the first month can be reduced by using river-gravel aggregate instead of limestone aggregate, or by stacking the panels in a controlled environment so that shrinkage and creep can be reduced. However, prestress losses in panels from both plants were less than those currently assumed by TxDOT, and also less than those predicted by many current design provisions.

Table 6-3: Average environmental conditions of both plants during the first month after casting

	Plant	Temperature [°F]	Humidity [%]	Wind velocity [mph]
Current TxDOT ($f_{pi}=189.4$ ksi)	A	63	51	9
	B	59	72	7
Reduced ($f_{pi}=169.4$ ksi)	A	87	65	8
	B	75	64	3

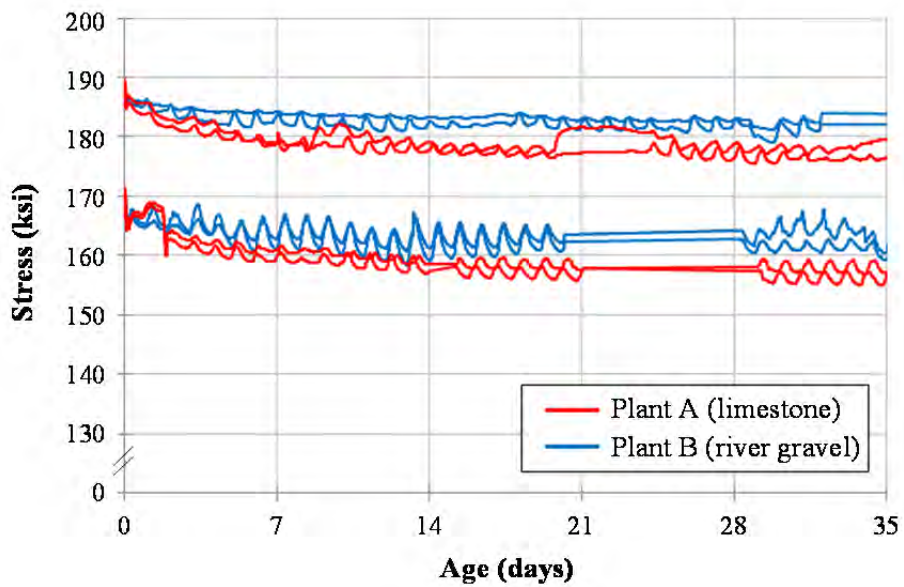


Figure 6-13: Prestress losses during first month after casting

6.4.4 Estimated Prestress Loss Using Design Specification

To compare observed prestress losses with estimated losses, estimated prestresses losses were calculated using AASHTO 2004, AASHTO 2008 and TxDOT design specifications (TxDOT 2004). TxDOT uses the AASHTO 2004 specifications when bridges are designed. Therefore, the AASHTO 2004 specifications are included in this section even though they are older than AASHTO 2008.

In AASHTO 2004 and 2008, the total prestress loss is calculated by adding the followed four elements: i) elastic shortening; ii) creep; iii) shrinkage; and iv) relaxation. The prestress loss due to the elastic shortening is the short-term prestress loss, and the prestress loss due to the other three elements is the long-term prestress loss. The long-term prestress loss is time-dependent, so the age of panel at service load must be assumed to obtain the ultimate value of prestress loss at that time. The prestress loss at 100,000 days is treated as the ultimate prestress loss.

Calculated prestress losses - AASHTO 2004

For the prestress loss calculation using AASHTO 2004, the concrete strength at release was assumed to be 4,000 psi and the 28-day concrete strength was assumed as 5,000 psi. Unit concrete weight was taken as 147.5 lb/ft³. The initial jacking stress is equal to applied initial prestress (189.4 ksi for the Current TxDOT initial prestressed panels and 169.4 ksi for the Reduced initial prestressed panels).

The calculated prestress losses are listed in Table 6-4. As shown in the table, the calculation results are the same because the initial prestress is not considered in the prestress-loss calculations of AASHTO 2004.

Table 6-4: Calculated prestress losses–AASHTO 2004

	Current TxDOT	Reduced
Elastic shortening	5.1 ksi	5.1 ksi
Shrinkage	6.5 ksi	6.5 ksi
Creep	8.0 ksi	8.0 ksi
Relaxation	4.5 ksi	4.5 ksi
Total	24.1 ksi	24.1 ksi

Calculated prestress losses - AASHTO 2008

Table 6-5 shows the results of prestress losses calculations using AASHTO 2008. In AASHTO 2008, prestress losses due to elastic shortening, creep, and relaxation have different values because initial prestress is considered in the calculations.

Table 6-5: Calculated prestress losses–AASHTO 2008

	Current TxDOT	Reduced
Elastic shortening	5.0 ksi	4.5 ksi
Shrinkage	15.8 ksi	15.8 ksi
Creep	10.7 ksi	9.6 ksi
Relaxation	2.6 ksi	1.4 ksi
Total	34.1 ksi	31.3 ksi

Calculated prestress losses - TxDOT design specifications

TxDOT design specifications give only a lump-sum ultimate prestress loss, equal to 45 ksi. In Figure 6-14 are shown the calculated prestress losses using AASHTO 2004, AASHTO 2008 and TxDOT procedures. AASHTO 2004 and 2008 predict similar values of the prestress losses due to the elastic shortening. However, the predicted prestress losses due to shrinkage from AASHTO 2008 are almost twice those of AASHTO 2004. TxDOT design specifications give only a lump-sum value, independent of the initial prestress level.

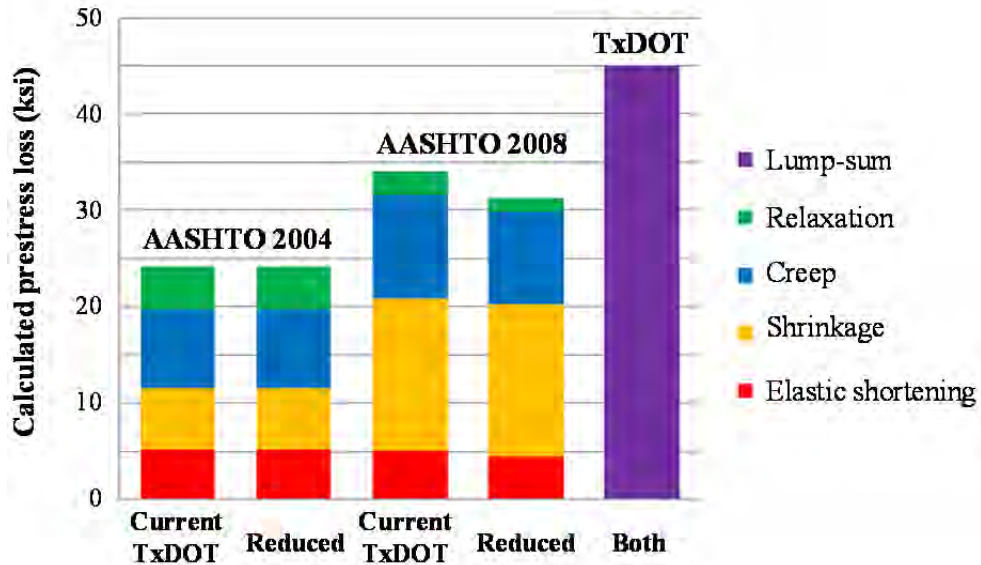


Figure 6-14: Calculations of prestress losses using AASHTO and TxDOT procedures

6.5 Results from Monitoring of Panel Strains

6.5.1 Concrete Tensile Stress and Strain during Release

Three testing methods are commonly used for measuring concrete tensile strength: i) DTTs; ii) splitting tensile tests; and iii) modulus of rupture tests. Upper and lower limits for the range of tensile strain values at concrete cracking are determined by empirical equations from DTTs and modulus of rupture tests.

Table 6-6 shows tensile strength and the corresponding tensile strain. The tensile strength is determined by the empirical equations of DTTs and modulus of rupture tests, and the equations are shown in the first column of Table 5-6. The corresponding tensile strain is calculated by dividing the tensile strength by the elastic modulus of concrete at release. The elastic modulus was taken as 4,225 ksi using Equation 6-1. In the calculation, the concrete compressive strength at release was assumed as 6,500 psi. This compressive strength at release is average value of test results from both plants.

Table 6-6: Typical tensile strengths and corresponding strains using two different tensile test methods

Test methods	Tensile strength	Tensile strain
Direct tensile strength ($4.0\sqrt{f'_c}$)	320 psi	75 $\mu\epsilon$
Modulus of rupture ($7.5\sqrt{f'_c}$)	600 psi	140 $\mu\epsilon$

$$E_c = 1265 \sqrt{f_{ci}'} + 1000$$

Equation 6-1

Where, f_{ci}' = compressive strength of concrete at release (ksi)

The measured concrete strains are shown in Figure 6-15. In the figure, “C” designates panels whose reinforcement was arranged according to TxDOT current design specification, and “M” designates panels with additional transverse bars at edges. In some panels (C01 and C07), tensile strains at release were not detected due to a malfunction of the data logger. The panels that are not included in Figure 6-15 (C03, C06, C09, C11, M06, M08 and M12) were not instrumented.

Tensile strains were in Figure 6-15 were determined by choosing the maximum strains from gages installed on the transverse reinforcement in each panel at release. Gages 1 to 3 and 8 to 10 in Figure 6-1, and Gages 1 to 3 and 16 to 18 in Figure 6-2, were used for the Current TxDOT initial prestressed panels. Gages 1 to 3 and 8 to 10 in Figure 6-3 were used for the Reduced initial prestressed panels.

The measured tensile stresses of all panels during release (Figure 6-15) are smaller than the expected tensile strengths (Table 5-6). Therefore, no cracking would be expected in the panels during release. This expectation was confirmed by field inspection before and after release. Therefore, it can be expected that additional transverse reinforcement is unnecessary to prevent collinear cracking at release. This result is consistent with the fact that reinforcement is not effective until concrete cracks, because its transformed area is generally small compared to that of the concrete.

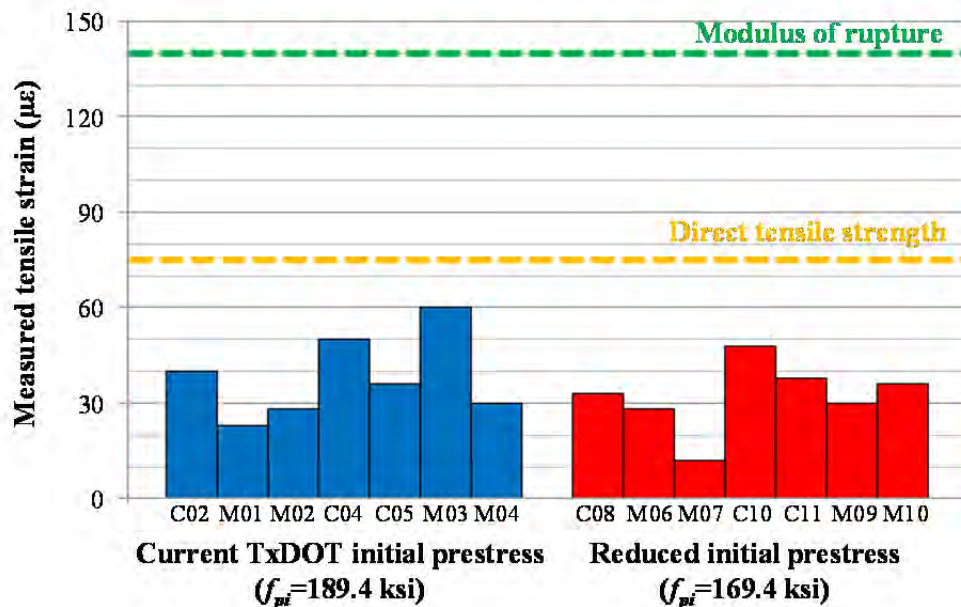


Figure 6-15: Measured tensile strains in all test panels in transverse direction (Foreman 2010, Azimov 2012)

Table 6-7 shows average tensile strains and stresses depending on initial prestress level, presence of additional transverse edge bars, and type of coarse aggregate. Stresses were calculated by multiplying measured tensile strain values by the elastic modulus of concrete used in Table 6-6.

Table 6-7: Average measured tensile strain and stress depending on existence of additional transverse edge bar and type of coarse aggregate

	Current TxDOT initial prestress $f_{pi}=189.4$ ksi				Reduced initial prestress $f_{pi}=169.4$ ksi			
	Plant A (limestone)		Plant B (river gravel)		Plant A (limestone)		Plant B (river gravel)	
	Strain [$\mu\epsilon$]	Stress [psi]	Strain [$\mu\epsilon$]	Stress [psi]	Strain [$\mu\epsilon$]	Stress [psi]	Strain [$\mu\epsilon$]	Stress [psi]
C-panels	40	184	43	198	33	152	43	198
M-panels	26	118	45	207	20	92	33	152
Average	30	140	44	202	24	112	38	175

The average tensile stress in the transverse direction for the Current TxDOT initial prestressed panels (175 psi) is higher than that for the Reduced initial prestressed panels (147 psi). The average tensile stress of the panels made using limestone aggregate (126 psi) is smaller than that of the panels made using river-gravel aggregate (188 psi).

Based on the result from Table 6-7, the transverse tensile stress in PCPs were reduced by applying reduced initial prestress, and using limestone instead of river gravel.

It is impossible to determine whether initial prestress or aggregate type is more critical in reducing collinear cracking, because this result is based on a small number of specimens and there is no specified procedure regarding the time of release or the manner in which the release is carried out.

6.5.2 Concrete Tensile Stress and Strain during the First Week after Release

In Figure 6-16 and Figure 6-17 are shown the strain variation in the gages, instrumented along transverse reinforcement at edges of panels, during the first week after release. Each figure is based on the results from one panel. The yellow shaded areas in both figures refer to the strain range where cracks would be expected. The upper limit of the area is calculated tensile strain from modulus of rupture tests, and its lower limit is calculated tensile strain from DTTs. The compressive strength and elastic modulus of concrete for calculating both limits had different values depending on the age of the concrete.

The range of tensile strain measured in the Current TxDOT initial prestressed panels is 150 to 200 $\mu\epsilon$, and the range measured in the Reduced initial prestressed panels is 100 to 150 $\mu\epsilon$. Peak tensile strain in the Reduced initial prestressed panels ($\approx 140 \mu\epsilon$) is 25% lower than the strain in the Current TxDOT initial prestressed panels ($\approx 180 \mu\epsilon$).

Peak tensile strain values in most panels were greater than expected cracking strains. However, only one Current TxDOT initial prestressed panel had a collinear crack. The length and the width of that crack were very small and the crack did not propagate further during the entire monitoring period. There are two possible reasons for this. The first reason is that actual

concrete strength of the panels at specific time is greater than the expected strength. The second reason is that the data used for developing tensile strengths was scattered broadly.

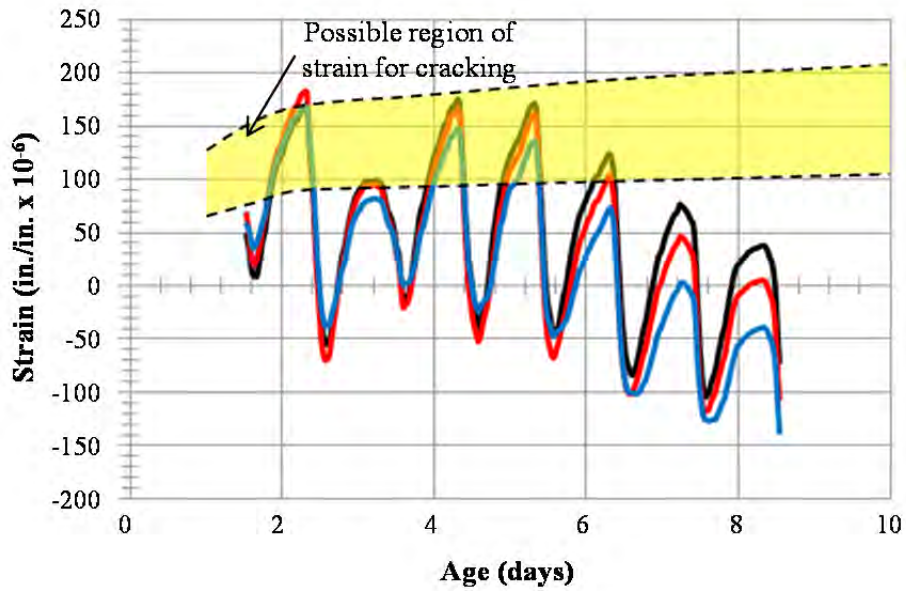


Figure 6-16: Strain variation in current TxDOT initial prestressed panel during first week after release

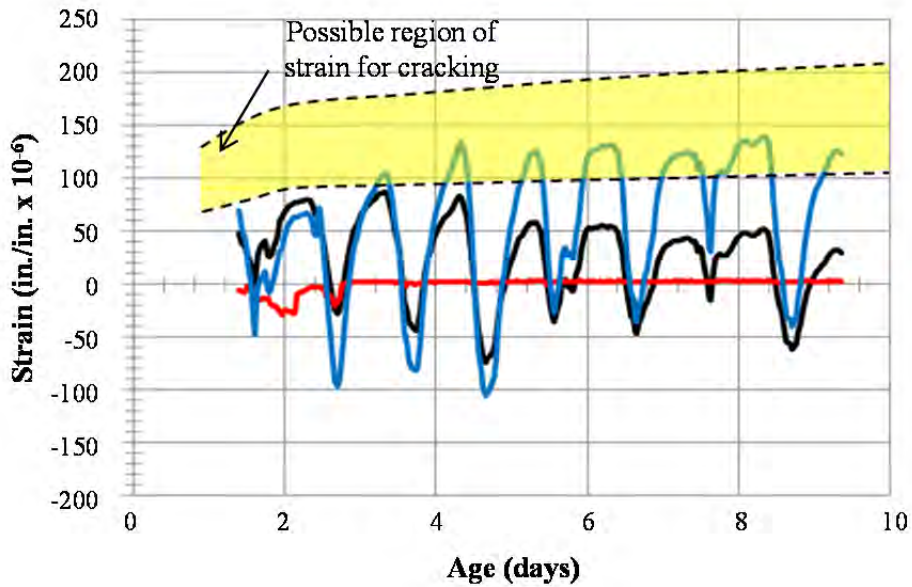


Figure 6-17: Strain variation in reduced initial prestressed panel during first week after release

6.5.3 Measured versus Predicted Prestress Losses

In Figure 6-18 and Figure 6-19, measured and predicted prestress are compared over time. The predicted values were calculated using AASHTO 2004, AASHTO 2008 and the TxDOT specification. Their values are shown using horizontal dashed lines. The yellow dashed line refers to AASHTO 2004, the purple dashed line refers to AASHTO 2008, and the green dashed line refers to the TxDOT specification. TxDOT design specification required consideration of the largest prestress loss (45 ksi) and AASHTO 2004 predicted smallest prestress loss (24 ksi). The measured prestress losses were smaller than the losses predicted using all three design specifications. The results indicate that initial prestress level may be reduced because the required initial prestress is determined as the prestress level required for serviceability plus expected prestress losses.

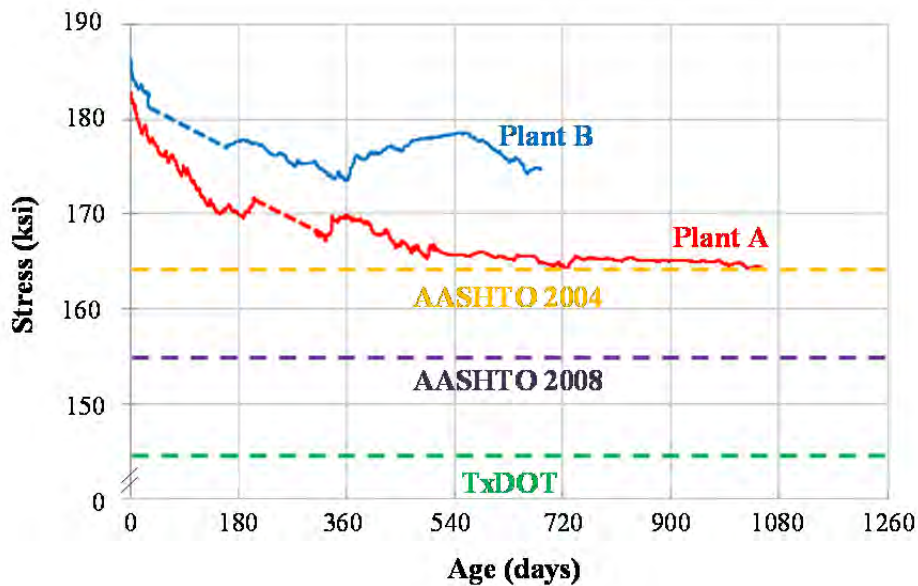


Figure 6-18: Long-term prestress in the current TxDOT initial prestressed panels

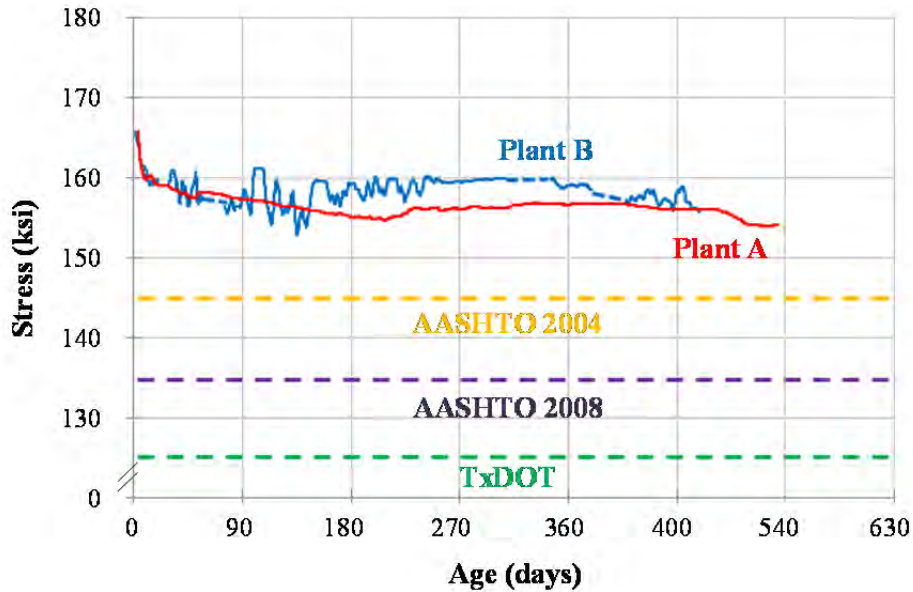


Figure 6-19: Long-term prestress losses in the reduced initial prestressed panels

In Figure 6-20, the monitoring results for all panels are plotted. The residual remaining prestress in the Reduced initial prestressed panels (green and yellow lines) are larger than the expected effective prestress by TxDOT specifications for the Current TxDOT initial prestressed panels (purple dashed line). The value for the purple dashed line was 149.4 ksi, calculated by subtracting lump-sum value of prestress loss in TxDOT specifications (45 ksi) from the current TxDOT initial prestress (189.4 ksi). This means that although reduced initial prestress is applied, the remaining stress is still larger than the value currently assumed by TxDOT for the panels with the current initial prestress. In other words, the serviceability requirements assumed in current TxDOT design can be satisfied even though the initial prestress is reduced.

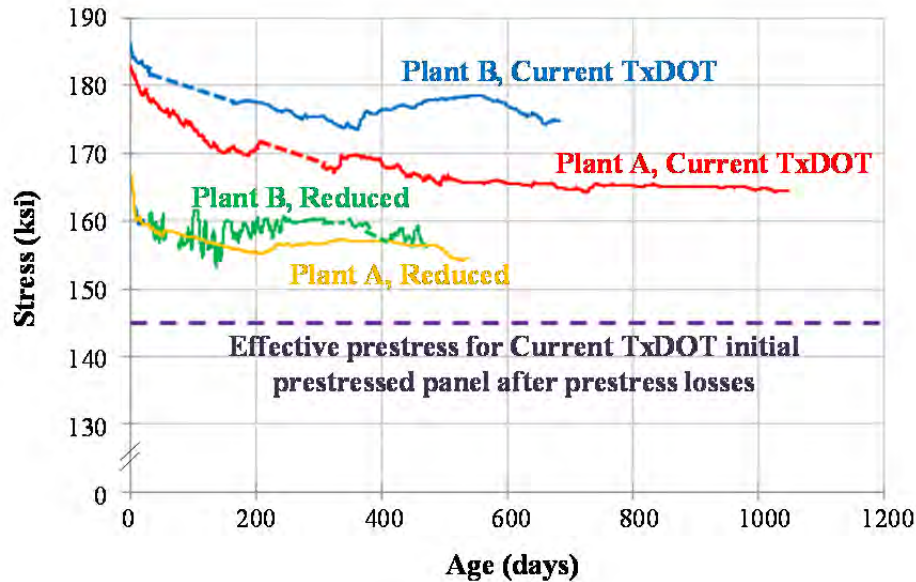


Figure 6-20: Long-term monitoring results of the current TxDOT and the Reduced initial prestressed panels

6.6 Conclusions of Study on Control of Cracking in PCPs

Long-term monitoring of prestress loss in PCPs was conducted to determine if collinear cracking in PCPs could be controlled. The variables that could be controlled were the coarse aggregate used in concrete, the season of fabrication, and initial prestress. It was observed that the current TxDOT design procedure overestimates prestress loss in PCPs. Moreover, although initial prestress was reduced from current initial prestress of 189.4 ksi to 169.4 ksi, the remaining prestress after stabilization was greater than the currently assumed prestress level after losses are considered (144.4 ksi).

The lump-sum prestress loss assumed in TxDOT procedure (45 ksi) is much larger than that observed. Therefore, a new lump-sum value of 25 ksi is proposed for prestress loss in PCPs. This value gives conservative results for the panels with the current TxDOT initial prestress (189.4 ksi) and the reduced initial prestress (169.4 ksi).

Using the measured losses in PCPs in this research, a new equation for prestress loss in the panels was developed. AASHTO 2008 was used as the basic form of the model. Terms in the AASHTO model were simplified using new constants that were introduced. The constants were derived through numerical analysis of the monitoring data. The constants have different values depending on types of aggregates. The proposed equation includes effects of aggregate types on prestress loss.

Prestress losses due to relaxation were not included in the proposed equation because they are very small for low-relaxation tendons which were used in this research. Total prestress loss predicted by the proposed equation is smaller than that by current design codes. As a result, the level of initial prestressing force could be reduced, and the occurrence of collinear cracking in the PCPs would be reduced as well by using the proposed equation in design of PCPs.

However, the proposed equation has several limitations. Since the data are limited to the project reported here, the testing method, equipment, material properties and geometrical

properties do not vary. Therefore, the proposed equation needs to be verified by different research groups. Moreover, the number of the panels which were used in this research is not sufficient and composite action between PCPs and the CIP slab is not considered. To overcome these limitations and develop a more general prediction model, additional tests by different research groups would be very useful.

Chapter 7. Summary, Conclusions, and Recommendations

7.1 Summary and Conclusions on Top-Mat Reinforcement and PCP Cracking

Bridge decks composed of precast, prestressed panels (PCPs) overlain by cast-in-place (CIP) are popular in many states of the US, including Texas. Because PCPs placed between adjacent girders serve as stay-in-place formwork for CIP slabs, construction cost and time can be saved. Moreover, the system uses precast panels as the bottom portion of the deck, so it is much easier to control quality of the bridge deck than when full-depth CIP concrete decks are used. The following requirements to current TxDOT designs were studied in this project.

- i) Ways to reduce top-mat reinforcement; and
- ii) Ways to reduce cracking in PCPs during fabrication and transportation to the job sites.

Foster (2010), who worked in the same project, suggested possible top-mat reinforcement options based on crack-width calculations, and conducted laboratory tests, including bending tests and DTTs. Based on his study, three conclusions were obtained:

- i) Longitudinal top-mat reinforcement specified by TxDOT (No. 4 bars at 9-in. spacing) could not be reduced.
- ii) To find optimized top-mat reinforcement in the transverse direction, field conditions (CIP-PCP interaction, boundary conditions) should be simulated as closely as possible.
- iii) Large test specimens were too complex to test in the laboratory.

To overcome the limitations noted in previous exploratory studies by Foster (2010), two sets of field applications and large-scale restrained-shrinkage test were conducted in this study. Moreover, the optimization of transverse reinforcement was the focus of this study because the longitudinal reinforcement is already optimized.

Transverse reinforcement controls longitudinal cracks. Cracks are the result of creep deformation of PCPs and shrinkage deformation of the CIP deck. Therefore, it is important to simulate proper CIP-PCP interactions and boundary conditions in evaluating the performance of various top-mat reinforcement options in the transverse direction. A large-scale restrained-shrinkage test and field instrumentation of two bridges (Wharton-Weems Overpass and Lampasas River Bridge) under construction were carried out. Current TxDOT design for the transverse reinforcement is No. 5 bars at 6-in. spacing. Two alternatives were considered: reducing bar size (No. 4 bars at 6-in. spacing) and welded-wire reinforcement (D 20 wires at 6-in. spacing) which would provide the same area as No. 4 bars at 6-in. spacing. Use of No. 4 bars or D 20 wire results in a 30% reduction in the transverse steel, and represents a significant cost saving considering the area of bridge deck constructed annually in Texas.

To control collinear cracking in PCPs, two approaches were considered: placing additional transverse bars at ends of the panel; and reducing initial prestressing force.

To evaluate the effects of additional transverse bars on control crack width, knife-edge test was conducted by Foreman (2010). In the test, collinear cracks were made by applying negative moment along strands. Through the test, it was observed that width and spacing of

collinear cracks can be reduced by placing additional transverse reinforcement near the edge of the panel, and strands did not slip although the crack was quite wide. However, his tests did not simulate load and boundary conditions of real bridges, so it is still unclear whether the additional bars help control cracks under real field conditions.

Based on long-term monitoring of prestress loss in PCPs, Foreman (2010) and Azimov (2012) propose reducing initial prestressing force. They also suggest that prestress loss in PCPs be estimated using a lump-sum value of 25 ksi.

7.2 Recommendations on Top-Mat Reinforcement and PCP Cracking

Through the tests and data analyses of this study, the following conclusions were derived:

- i) Field applications and restrained-shrinkage test
 - a. Current longitudinal reinforcement (No. 4 @ 9 in.) is already optimized.
 - b. Current transverse reinforcement (No. 5 @ 6 in.) can be reduced by using a smaller bar (No. 4 @ 6 in.) or welded-wire reinforcement (D 20 @ 6 in.).
- ii) Long-term monitoring of prestress loss in PCPs
 - a. Initial applied prestress level can be adjusted from current TxDOT specified value (189.4 ksi) to a reduced value (169.4 ksi). By reducing the level of initial prestress, the possibility of cracking in panels can be reduced, and the panels will still meet the serviceability criteria implied by current TxDOT specifications.
 - b. The lump-sum prestress losses assumed in current TxDOT specifications of 45 ksi can be decreased to 25 ksi. That new lump-sum value (25 ksi) gives conservative result for the panels with Current TxDOT initial prestress (189.4 ksi) and Reduced initial prestress (169.4 ksi).
 - c. A new equation for predicting prestress loss in PCP was proposed that takes into account the types of aggregate and the levels of initial prestress.

7.3 Summary and Conclusions on Double-Punch Test

A series of DPTs were conducted at the University of Texas at Arlington and the University of Texas at Austin. In this project, DPT was organized to produce sufficient intra-laboratory and inter-laboratory data to draw conclusions and provide recommendations regarding the simplicity, reliability, and reproducibility of the DPT for evaluating the performance of concrete reinforced with high-performance steel fibers.

7.4 Conclusions regarding DPT

The DPT can reliably distinguish between the effects of different fiber types and volume fractions on steel fiber-reinforced concrete (SFRC), indicating that the DPT is useful for comparing SFRC mixtures. Statistical analysis (derived data), substantiates the validity of the DPT for such comparisons. The DPT can also be used to characterize other aspects of the mechanical performance of SFRC, such as resistance to cracking, residual strength, and toughness.

The following conclusions are based on the results of the DPT Research and Testing Program and statistical analysis described in this report. Conclusions are categorized based on their relation to the simplicity, reliability, and reproducibility of the DPT.

7.4.1 Simplicity of the DPT

- The *specimens* required to conduct the DPT can be fabricated using basic cylinder molds, are lightweight, and can be placed into the testing apparatus without the need for special fixtures.
 - a) The specimens can be prepared using the same type of cylinder molds used to determine the compressive strength of concrete (ASTM C39/C39M).
 - b) Because DPT specimens are cylindrical, cores from existing structures can easily be extracted and tested using the DPT to determine in-place properties. This can be useful in forensic investigations involving fiber-reinforced concrete.
- The *test setup* and *support conditions* are simple and it is very easy to ensure concentric load is applied to the specimen through the steel punches by using dimensional guides and masking tape.
- As for *test machine*, any Universal Testing Machine can be used to conduct the DPT; a closed-loop, servo-controlled machine is not required as is the case for other tests to determine FRC characteristics.
- The *test procedure* is quick and simple; the average DPT takes less than 20 minutes to perform.

7.4.2 Reliability of the DPT

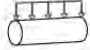
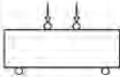
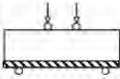

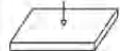


- The *test results* show that the DPT is an effective way to compare the post-cracking ductility and performance of mixtures containing different fiber types (manufacturer and geometry) as well as different fiber volume fractions (% fiber).
- The *failure mechanism* produced by the DPT occurs along multiple planes; typical damage is concentrated along three or four radial planes, thus test results represent an averaged mechanical behavior.
- The *within-batch, single-laboratory precision (COV)* for key test parameters is generally low and comparable to or better than other current test methods for FRC: $\pm 10\%$ Initial Slope; $\pm 5\%$ Peak Load; and $\pm 20\%$ Residual Strength at 0.1 in. deflection.
 - a) The test setup can have some effect on the measured initial stiffness depending on the stiffness of the machine. For this reason, specimens should be tested on the same test machine if compared directly.
 - b) The measured initial stiffness is tabulated to provide further evidence of the repeatability of the DPT on the same machine; it should not be used as an estimate of the actual stiffness of the DPT test specimen due to flexibilities observed in the DPT setup.

7.4.3 Reproducibility of the DPT

- The *inter-laboratory precision (COV)* for key test parameters was not determined in this study.

In Table 7-1, the DPT is compared with the complexity, reliability, and reproducibility of other current test methods for FRC. It is clear that the DPT can be extended to SFRC with similar precision and less complexity compared to other tests.

Table 7-1: Simplicity, reliability, and reproducibility of current FRC testing procedures vs. DPT

TEST INFORMATION ¹		SIMPLICITY ²				RELIABILITY ³		REPRODUCIBILITY ³
Designation	Layout	Specimen Fabrication & Handling	Test Setup & Support Fixtures	Test Procedure	Test Machine	Failure Mechanism	Within-Batch Precision (COV)	Inter-Laboratory Precision (COV)
ASTM C496		Easy	Easy	Easy	Standard	Single Major Crack	± 5% PL	Not Available
ASTM C1609		Moderate	Difficult	Moderate	Closed-Loop	Single Major Crack	± 8% PL ± 20% RS	Not Available
ASTM C1399		Moderate	Difficult	Difficult	Standard	Single Major Crack	± 20% RS	± 40% RS
ASTM C1550		Difficult	Difficult	Difficult	Closed-Loop	Multiple Cracks	± 6% PL ± 10% RS	± 9% PL ± 9% RS
EFNARC Panel Test		Difficult	Difficult	Moderate	Closed-Loop	Multiple Cracks	Not Available	Not Available
Uniaxial Direct Tensile Test		Difficult	Moderate	Moderate	Closed-Loop	Single Major Crack	Not Available	Not Available
Double-Punch Test		Easy	Easy	Easy	Standard	Multiple Cracks	± 10% Initial Slope ± 5% Peak Load ± 20% Residual Strength	Not Available

¹ Test layouts modified from (Molins 2006).

² Complexity levels assigned based on literature and personal communication with researchers who conducted these and other similar tests (S. Chao 2012).

³ Reliability and reproducibility data obtained from industry standards and research literature (ASTM C496 2011, ASTM C1609 2010, ASTM C1550 2010, ASTM C1399 2010, S.-H. Chao 2011, Bernard 2002). COVs for peak load and residual strength (toughness) are denoted (PL) and (RS), respectively.

7.5 Recommendations regarding Double-Punch Test

7.5.1 Recommended DPT Protocols for Effective Application to FRC

After conducting more than 240 tests on steel fiber-reinforced concrete specimens, it has been determined that the DPT is effective for evaluating the performance of SFRC. For optimal results, the following protocols are recommended:

Calibration

- 1) LVDTs of appropriate stroke (2 in. or less) should be used and calibrated with gage blocks to ensure that small deflections are recorded accurately.

Specimen Size

- 2) The top or bottom 6 x 6-in. portion of a 6 x 12-in. cylinder specimen can be used for testing.
- 3) Top and bottom specimens should not be compared directly, as bottom portions have a greater fiber density for a given fiber volume fraction due to segregation during casting.

Specimen Surface Preparation

- 4) Specimen surfaces should be smooth so that the steel punches make uniform (flat) contact with the top and bottom faces of the specimen.
- 5) End grinding cylinders is the preferred method of obtaining a smooth surface; however, a thin layer of Hydro-Stone can be used to provide an even surface beneath the steel punches if grinding equipment is unavailable.
- 6) Results obtained from specimens with different surface finishes should not be compared directly.

Punch Alignment

- 7) To avoid eccentric loading, use a dimensional guide and masking tape to center the punches and secure them to the cylinder specimen.

Shakedown Procedure

- 8) Follow shakedown procedure and corresponding load rates presented in Chapter 5 to obtain the DPT Performance Curve (load-deflection plot).

7.5.2 Recommendations for Future Research

In this report, fundamental data was reported that showed the DPT is useful for evaluating SFRC. However, the fiber types and volume fractions needed for specific performance requirements have not been quantified in this study. Research that correlates field stresses in bridge decks (or other applications of interest) with stresses from a DPT will be useful for determining if the DPT can be used in this way. Other applications of interest may include using steel fibers as a replacement of secondary reinforcement in the end regions of reinforced concrete beams and girders.

The DPT appears to be less complex and at least or more reliable than current test methods for FRC. However, additional intra- and inter-laboratory studies are needed before this method can be widely accepted by researchers or standardized by testing agencies. In anticipation of future experiments that verify the DPT for FRC, a proposal for standardization has been drafted and is included in Appendix C.

References

- AASHTO (2004). *LRFD Design Specifications*, 3rd Edition, American Association of State Highway and Transportation Officials, Washington, D.C.
- AASHTO (2008). *LRFD Design Specifications*, 4th Edition, American Association of State Highway and Transportation Officials, Washington, D.C.
- ACI 209 (1997): *Prediction of Creep, Shrinkage, and Temperature Effects in Concrete Structures* (ACI 209r-97), American Concrete Institute, Farmington Hills, Michigan.
- ACI 318 (2011). *Building Code Requirements for Structural Concrete* (ACI 318-11) and *Commentary* (ACI 318R-11), American Concrete Institute, Farmington Hills, MI.
- ASTM C1399. *Standard Test Method for Obtaining Average Residual-Strength of Fiber-Reinforced Concrete*. American Society of Testing and Materials, 2010.
- ASTM C1550. *Standard Test Method for Flexural Toughness of Fiber Reinforced Concrete (Using Centrally Loaded Round Panel)*. American Society of Testing and Materials, 2010.
- ASTM C1609. *Standard Test Method for Flexural Performance of Fiber-Reinforced Concrete (Using Beam with Third-Point Loading)*. American Society of Testing and Materials, 2010.
- ASTM C496. *Standard Test Method for Splitting Tensile Strength of Cylindrical Concrete Specimens*. American Society of Testing and Materials, 2011.
- Al-Manaseer, A. & J.-P. Lam (2005). "Statistical Evaluation of Shrinkage and Creep models," *ACI Materials Journal*, 102, 170-176.
- Ayyub, B. M., P. C. Chang & N. A. Al-Mutairi (1994). "Welded wire fabric for bridges. I: ultimate strength and ductility," *ASCE Journal of Structural Engineering*, 120, 1866-1881.
- Azimov, U. (2012). "Controlling Cracking in Precast Prestressed Concrete Panels," Masters Thesis, The University of Texas at Austin.
- Banthia, N., and A. Dubey. "Measurement of Flexural Toughness of Fiber Reinforced Concrete Using a Novel Technique, Part I: Assessment and Calibration." *Materials Journal* (American Concrete Institute), 1999: 651-656.
- Barker, J. M. (1975). "Research, Application, and Experience with Precast Prestressed Bridge Deck Panels," *PCI Journal*, 20, 66-85.
- Batchelor, B. D. & B. E. Hewitt (1976). "Tests of model composite bridge decks," *ACI Journal*, 73, 340-343.
- Bazant, Z. P. (1972). "Prediction of Concrete Creep Effects Using Age-Adjusted Effective Modulus Method," *ACI Journal*, 69, 212-217.
- Bentur, A., and S. Mindess. "Cracking Process in Steel Fiber Reinforced Cement Paste." *Cement Concrete Research* 15 (1985): 331-342.

- Bentur, A., and S. Mindess. *Fibre Reinforced Cementitious Composites*. 2nd. New York, NY: Taylor & Francis, 2007.
- Bernard, E. S. "Correlations in the Behaviour of Fibre Reinforced Shotcrete Beam and Panel Specimens." *Materials and Structures (RILEM)* 35 (April 2002): 156-164.
- Bernold, L., P. Chang & B. M. Ayyub. (1989). "Feasibility of Using Welded Steel Mesh in Bridge Decks," *Report No. FHWA/MD-89/14*, Maryland Department of Transportation.
- Bortolotti, Lionello. "Double-Punch Test for Tensile and Compressive Strengths in Concrete." *ACI Materials Journal* (American Concrete Institute), January-February 1988: 26-32.
- Buth, E., H. L. Furr & H. L. Jones (1972). "Evaluation of a Prestressed Panel, Cast-in-Place Concrete Bridge," *Research Report 145-3*, Texas Transportation Institute, College Station, Texas.
- Carrasquillo, R. L., A. H. Nilson & F. Slate (1981). "Microcracking and Behavior of High Strength Concrete Subject to Short-Term Loading," *ACI Journal*, 78, 179-186.
- Chao, Shih-Ho. "FRC Performance Comparison: Uniaxial Direct Tensile Test, Third-Point Bending Test, and Round Panel Test." *ACI Special Publication 276: Durability Enhancements in Concrete with Fiber Reinforcement*, 2011: 5.1-5.20.
- Chen, L., and S. Mindess. "Comparative Toughness Testing of Fiber Reinforced Concrete." *ACI SP-155* (American Concrete Institute), 1995: 45, 59.
- Chen, W.F. "Bearing Capacity of Concrete Blocks or Rock." *ASCE Proceedings*. American Society of Civil Engineers, 1969. 955-978.
- Chen, W.F. "Double Punch Test for Tensile Strength of Concrete." *ACI Journal* (American Concrete Institute), December 1970: 993-995.
- Cho, J.-S., "Shear Behavior of Steel Fiber Reinforced Prestressed Concrete Beams without Shear Reinforcement," Ph.D. Dissertation, The University of Texas at Arlington, December 2011, 373 pages.
- Collins, M. P. & D. Mitchell (1991). *Prestressed Concrete Structures*, Prentice-Hall, New Jersey.
- Coselli, C. J. (2004). "Behavior of Bridge Deck with Precast Panels at Expansion Joints," Master Thesis, The University of Texas at Austin, Austin, TX.
- Coselli, C. J., E. M. Griffith, J. L. Ryan, O. Bayrak, J. O. Jirsa & J. E. Breen. (2006). "Bridge Slab Behavior at Expansion Joints," *Research Report 0-4418-1*, Center for Transportation Research, The University of Texas at Austin.
- Corley, W. & M. Sozen (1966). "Time Dependent Deflection of Reinforced Concrete Beams," *ACI Journal*, 63, 373-386.
- De Vekey, R.C, and A.J. Majumdar. "Determining Bond Strength in Fiber Reinforced Composites." *Magazing of Concrete Research*, 1968: 229-234.
- Dilger, W. H. (1982). "Creep Analysis of Prestressed Concrete Structures using Creep Transformed Section Properties," *PCI Journal*, 27, 89-117.

- EFNARC. *European Specification for Sprayed Concrete*. European Federation of National Associations of Specialist Representing Concrete, 1996.
- Fang, I.-K., J. Worley, R. E. Klingner & N. H. Burns (1986). "Behavior of Ontario-Type Bridge Decks on Steel Girders," *Report 350-1*, Center for Transportation Research, The University of Texas at Austin.
- Fang, I.-K., J. Worley, R. E. Klingner & N. H. Burns (1990). "Behavior of Isotropic Concrete Bridge Decks on Steel Girders," *ASCE Structures Journal*, 116, 659-679.
- Fang, I.-K., C. K.-T. Tsui, N. H. Burns & R. E. Klingner (1990). "Fatigue Behavior of Cast-in-Place and Precast Panel Bridge Decks with Isotropic Reinforcement," *PCI Journal*, 35, 28-39.
- Folliard, K., C. Smith, G. Sellers, M. Brown & J. E. Breen. (2003). "Evaluation of Alternative Materials to Control Drying-Shrinkage Cracking in Concrete Bridge Decks," *Report 0-4098-4*, Center for Transportation Research, The University of Texas at Austin.
- Foreman, J. M. (2010). "Controlling Cracking in Prestressed Concrete Panels," Master Thesis, The University of Texas at Austin.
- Foster, S. W. (2010). "Reducing Top Mat Reinforcement in Bridge Decks," Master Thesis, The University of Texas at Austin.
- Gilbert, R. I. & Z. I. Sakka (2007). "Effect of Reinforcement Type on the Ductility of Suspended Reinforced Concrete Slabs," *ASCE Journal of Structural Engineering*, 133, 834-843.
- Goldberg, D. (1987). "Precast Prestressed Concrete Bridge Deck Panels," *PCI Journal*, 32, 26-45.
- Graddy, J. C., N. H. Burns & R. E. Klingner (1995). "Factors Affecting the Design Thickness of Bridge Slabs," *Report 0-1305-3F*, Center for Transportation Research, The University of Texas at Austin.
- Graddy, J. C., J. Kim, J. H. Whitt, N. H. Burns & R. E. Klingner (2002). "Punching-Shear Behavior of Bridge Decks under Fatigue Loading," *ACI Structures Journal*, 99, 257-266.
- Johnston, C. D. "Deflection Measurement Considerations in Evaluating FRC Performance Using ASTM C1018." *ACI SP-155* (American Concrete Institute), 1995: 1-11.
- Karki, N. B., "Flexural Behavior of Steel Fiber Reinforced Prestressed Concrete Beams and Double Punch Test for Fiber Reinforced Concrete," Ph.D. Dissertation, The University of Texas at Arlington, December 2011, 420 pages.
- Kim, J., N. H. Burns & R. E. Klingner (1994). "Factors Affecting the Design Thickness of Bridge Slabs: Results of Static and Fatigue Tests," *Report 1305-2*, Center for Transportation Research, The University of Texas at Austin.
- Klingner, R. E., I.-K. Fang, C. K.-T. Tsui & N. H. Burns (1990). "Load Capacity of Isotropically Reinforced, Cast-in-Place and Precast Panel Bridge Decks," *PCI Journal*, 35, 104-114
- Krauss, P. D. & E. A. Rogalla. (1996). "Transverse Cracking in Newly Constructed Bridge Decks," *NCHRP Report 380*, Transportation Research Board, Washington, D.C.

- Krishnamurthy, D. (1971). "A Method of Determining the Tensile Stresses in the End Zones of Pre-tensioned Beams," *The Indian Concrete Journal*, 45, 286-297.
- Krishnamurthy, D. (1973). "Design of End Zone Reinforcement to Control Horizontal Cracking in Pre-Tensioned Concrete Members at Transfer," *The Indian Concrete Journal*, 47, 346-349.
- Kwon, K., "Design Recommendations for CIP-PCP Bridge Decks," PhD dissertation, Department of Civil Engineering, the University of Texas at Austin, December 2012.
- Lukefahr, E. & L. Du (2010). "Coefficients of Thermal Expansion of Concrete with Different Coarse Aggregates-Texas Data," *Journal of Testing and Evaluation*, 38, 1-8.
- Marti, Peter. "Size Effect in Double-Punch Tests on Concrete Cylinders." *ACI Materials Journal* (American Concrete Institute), November-December 1989: 597-601.
- Merrill, B. D. (2002). "Texas' Use of Precast Concrete Stay-In-Place Forms for Bridge Decks," *Proceedings*, Concrete Bridge Conference, National Concrete Bridge Council, Skokie, IL.
- Molins, C. "Quality Control Test for SFRC to be used in Precast Segments." *Tunneling and Underground Space Technology* 21, 2006: 423-424.
- Molins, Climent, and A. Aguado. "Double Punch Test to Control the Energy Dissipation in Tension of FRC (Barcelona Test)." *Materials and Structures* , 2009: 415-425.
- Muller, H. S. & H. K. Hilsdorf (1990). "Evaluation of the Time-Dependent Behavior of Concrete," *CEB Bulletin d'Information*, 199.
- Naaman, A. E., et al., "Measurement of Tensile Properties of Fiber Reinforced Concrete: Draft Submitted to ACI Committee 544." High Performance Fiber Reinforced Cement Composites (HPFRCC5), Mainz, Germany, 2007, 3-12.
- Neville, A. M., W. H. Dilger & J. J. Brooks. (1983). *Creep of Plain and Structural Concrete*. Construction Press, London and New York.
- Ockleston, A. J., "Arching Action in Reinforced Concrete Slabs," *The Structural Engineer*, Vol. 36, No. 6, June 1958, pp. 197-201.
- PCI (2004). *Manual for the Evaluation and Repair of Precast, Prestressed Concrete Bridge Products*, Precast/Prestressed Concrete Institute, Chicago, IL.
- Peterman, R. J. & J. A. Ramirez (1998). "Restraint Moments in Bridges with Full-Span Prestressed Concrete Panels," *PCI Journal*, January-February, 54-73.
- Pros, Alba, Pedro Diez, and Climent Molins. "Numerical Modeling of the Double Punch Test for Plain Concrete." *Internation Journal of Solids and Structures*, November 2010: 1-32.
- Ramakrishnan, V. "Flexural Fatigue Strength of Steel Fiber Reinforced Concrete." *ACI-SP 105-13: Fiber Reinforced Concrete Properties and Applications* (American Concrete Institute), 1987: 225-245.
- Riding, K. A., J. L. Poole, A. K. Schindler, M. C. G. Juenger & K. J. Folliard (2009). "Effects of Construction Time and Coarse Aggregate on Bridge Deck Cracking," *ACI Materials Journal*, 106, 448-454.

- Roberts, C. L., J. E. Breen & M. E. Kreger. (1993). "Measurement based Revisions for Segmental Bridge Design and Construction Criteria," *Report 1234-3F*, Center for Transportation Research, The University of Texas at Austin.
- Russo, S. (1999). "Structural Behavior of Double-T Prestressed Slabs with High Quality Welded Wire Mesh," *ACI Structural Journal*, 96, 972-980.
- Shrestha, K. M. & B. Chen (2011). "Aging Coefficient, Creep Coefficient and Extrapolating Aging Coefficient from Short Term Test for Sealed Concrete," *Journal of Wuhan University of Technology-Mater*, 26, 154-159.
- Sneed, L., A. Belarbi & Y. M. You. (2010). "Spalling Solution of Precast-Prestressed Bridge Deck Panels," *Report TRyy0912*, Missouri Department of Transportation.
- Soltani, M., X. An & K. Maekawa (2004). "Cracking response and local stress characteristics of RC membrane elements reinforced with welded wire mesh. Cement and Concrete Composites," *Cement and Concrete Composites*, 26, 389-404.
- Sprinkel, M. M. (1985). "Prefabricated Bridge Elements and Systems," *NCHRP Synthesis of Highway Practice 119*, Transportation Research Board, Washington D.C.
- Stroeven, P., and S.P. Shah. "Use of Radiography-Image Analysis for Steel Fibre Reinforced Concrete." In *Testing and Test Methods for Fibre Cement Composites*, by R.N. Swamy, 275-288. Lancaster, England: The Construction Press, 1978.
- Tadros, M. K., A. Ghali & W. H. Dilger (1975). "Time-Dependent Prestress Loss and Deflection in Prestressed Concrete Members," *PCI Journal*, 20, 86-98.
- Tadros, M. K., A. Nabil, A. J. Seguirant, & J. G Gallt (2003). "Prestress Losses in Pretensioned High-Strength Concrete Bridge Girders," *NCHRP Report 496*, Transportation Research Board, Washington, D.C.
- TxDOT (2004). *Standard Specifications for Construction and Maintenance of Highways, Streets, and Bridges*, Texas Department of Transportation, Austin, TX.
- TxDOT (2008). *Standard Specifications for Construction and Maintenance of Highways, Streets, and Bridges*, Texas Department of Transportation, Austin, TX.
- Waweru, R. N., "The Effect of Fiber Corrosion on Shear Capacity of Steel Fiber Reinforced Concrete Beams and Initial Investigation on Alkali-Silica Reaction in Steel Fiber Reinforced Concrete," Master Thesis, The University of Texas at Arlington, August 2011, 177 pages.
- Woods, Aaron, Double-Punch Test for Evaluating the Performance of Steel Fiber-Reinforced Concrete, MS thesis, Department of Civil Engineering, the University of Texas at Austin, August 2012.

Appendix A. Development Length Calculation

In this appendix, the detailed calculation procedures for the development length for Chapter 3 are introduced. For considering worst case, it is assumed that rebar and wire are coated with epoxy. Development length in the section where two different types of reinforcement used, longer one is governed. Some sections have the same development length, so representative cases are only shown in here. Following things were assumed for calculating development length in Chapter 3:

- Specified concrete strength = 4,000 psi
- Specified yield strength of deformed bar = 60,000 psi
- Specified yield strength of welded wire = 75,000 psi

A.1. Section A-A (No. 4 bar at 9 in.)

Equation 3-1 can be transformed as follows:

$$l_d = \left[\frac{3}{40} \times \frac{f_y}{\lambda \times \sqrt{f'_c}} \times \frac{\psi_t \times \psi_e \times \psi_s}{\left(\frac{c_b + K_{tr}}{d_b} \right)} \right] \times d_b$$

where,

$$d_b = \frac{4}{8} \text{ in.}$$

$$f_y = 60,000 \text{ psi}$$

$$f'_c = 4,000 \text{ psi}$$

$$\psi_t = 1.0 \text{ (for less than 12 in. of concrete is cast below the rebar)}$$

$$\psi_e = 1.5 \text{ (for epoxy coated bar)}$$

$$\psi_s = 0.8 \text{ (for No. 6 and smaller bar)}$$

$$\lambda = 1.0 \text{ (for normal weight concrete)}$$

$$c_b = \left[\begin{array}{l} 2 + \frac{14}{28} = 2.5 \\ \frac{1}{2} \times 9 = 4.5 \end{array} \right]_{\text{min.}} = 2.25$$

$$K_{tr} = 0$$

$$\frac{c_b + K_{tr}}{d_b} = \frac{2.25 + 0}{4/8} = 4.5 \geq 2.5 \rightarrow \text{Use } 2.5$$

Therefore,

$$l_d = \left(\frac{3}{40} \frac{60,000}{1.0 \times \sqrt{4,000}} \frac{1.0 \times 1.5 \times 0.8}{2.5} \right) \times \frac{4}{8} = 17.1 \text{ in.} \geq 12.0$$

→ Required development length = **17.1 in.**

→ Actual development length = **18.0 in.**

A.2. Section E-E (D 20 wire at 9 in.)

Equation 3-2 can be transformed as follows

$$l_d = \left[\psi_w \times \frac{3}{40} \frac{f_y}{\lambda \times \sqrt{f_c'}} \frac{\psi_t \times \psi_e \times \psi_s}{\left(\frac{c_b + K_{tr}}{d_b} \right)} \right] \times d_b$$

where,

$$\psi_w = \left[\begin{array}{l} \frac{f_y - 35,000}{f_y} = \frac{75,000 - 35,000}{75,000} = 0.53 \\ \frac{5d_b}{s} = \frac{5 \times 0.504}{9} = 0.28 \end{array} \right]_{\max.} = 0.53 \leq 1.0 \rightarrow \text{Use } 0.53$$

$$s = 9 \text{ in.}$$

$$d_b = 0.504 \text{ in.}$$

$$f_y = 75,000 \text{ psi}$$

$$\lambda = 1.0$$

$$f_c' = 4,000 \text{ psi}$$

$$\psi_t = 1.0$$

$$\psi_e = 1.0 \text{ (for epoxy coated welded wire reinforcement)}$$

$$\psi_s = 0.8$$

$$\frac{c_b + K_{tr}}{d_b} = \frac{2.252 + 0}{0.504} = 4.683 \geq 2.5 \rightarrow \text{Use } 2.5$$

Therefore,

$$l_d = \left[0.53 \times \frac{3}{40} \frac{75,000}{1.0 \times \sqrt{4,000}} \frac{1.0 \times 1.0 \times 0.8}{2.5} \right] \times 0.504 = 7.6 \leq 8.0$$

→ Required development length = **8.0 in.**

→ Actual development length = **16.0 in.**

A.3. Section M-M (No. 5 bar at 6 in.)

$$l_d = \left[\frac{3}{40} \frac{f_y}{\lambda \times \sqrt{f'_c}} \frac{\psi_t \times \psi_e \times \psi_s}{\left(\frac{c_b + K_{tr}}{d_b} \right)} \right] \times d_b$$

where,

$$d_b = \frac{5}{8} \text{ in.}$$

$$f_y = 6,000 \text{ psi}$$

$$f'_c = 4,000 \text{ psi}$$

$$\psi_t = 1.0$$

$$\psi_e = 1.5$$

$$\psi_s = 0.8$$

$$\lambda = 1.0$$

$$c_b = \left[\begin{array}{l} 2 + \frac{15}{28} = 2.3125 \\ \frac{1}{2} \times 9 = 4.5 \end{array} \right]_{\text{min.}} = 2.3125$$

$$K_{tr} = 0$$

$$\frac{c_b + K_{tr}}{d_b} = \frac{2.3125 + 0}{5/8} = 3.7 \geq 2.5 \rightarrow \text{Use } 2.5$$

Therefore,

$$l_d = \left(\frac{3}{40} \frac{6,000}{1.0 \times \sqrt{4,000}} \frac{1.0 \times 1.5 \times 0.8}{2.5} \right) \times \frac{5}{8} = 21.3 \text{ in.} \geq 12.0$$

→ Required development length = **21.3 in.**

→ Actual development length = **24.0 in.**

A.4. Section O-O (D 20 wire at 6 in.)

$$l_d = \left[\psi_w \times \frac{3}{40} \frac{f_y}{\lambda \times \sqrt{f'_c}} \frac{\psi_t \times \psi_e \times \psi_s}{\left(\frac{c_b + K_{tr}}{d_b} \right)} \right] \times d_b$$

where,

$$\psi_w = \left[\begin{array}{l} \frac{f_y - 3,500}{f_y} = \frac{75,000 - 35,000}{75,000} = 0.53 \\ \frac{5d_b}{s} = \frac{5 \times 0.504}{6} = 0.42 \end{array} \right]_{\max.} = 0.53 \leq 4.0 \rightarrow \text{Use } 0.53$$

$$s = 6 \text{ in.}$$

$$d_b = 0.504 \text{ in.}$$

$$f_y = 75,000 \text{ psi}$$

$$\lambda = 1.0$$

$$f'_c = 4,000 \text{ psi}$$

$$\psi_t = 1.0$$

$$\psi_e = 1.0 \text{ (for epoxy coated welded wire reinforcement)}$$

$$\psi_s = 0.8$$

$$\frac{c_b + K_{tr}}{d_b} = \frac{2.252 + 0}{0.504} = 4.683 \geq 2.5 \rightarrow \text{Use } 2.5$$

Therefore,

$$l_d = \left[0.53 \times \frac{3}{40} \frac{75,000}{1.0 \times \sqrt{4,000}} \frac{1.0 \times 1.0 \times 0.8}{2.5} \right] \times 0.504 = 7.6 \leq 8.0$$

→ Required development length = **8.0 in.**

→ Actual development length = **16.0 in.**

A.5. Section R-R (No. 4 bar at 6 in.)

$$l_d = \left[\frac{3}{40} \frac{f_y}{\lambda \times \sqrt{f'_c}} \frac{\psi_t \times \psi_e \times \psi_s}{\left(\frac{c_b + K_{tr}}{d_b} \right)} \right] \times d_b$$

where,

$$d_b = \frac{4}{8} \text{ in.}$$

$$f_y = 6,000 \text{ psi}$$

$$f'_c = 4,000 \text{ psi}$$

$$\psi_t = 1.0$$

$$\psi_e = 1.5$$

$$\psi_s = 0.8$$

$$\lambda = 1.0$$

$$c_b = \left[\begin{array}{l} 2 + \frac{14}{28} = 2.25 \\ \frac{1}{2} \times 9 = 4.5 \end{array} \right]_{\text{min.}} = 2.25$$

$$K_{tr} = 0$$

$$\frac{c_b + K_{tr}}{d_b} = \frac{2.25 + 0}{4/8} = 4.5 \geq 2.5 \rightarrow \text{Use } 2.5$$

Therefore,

$$l_d = \left(\frac{3}{40} \frac{6,000}{1.0 \times \sqrt{4,000}} \frac{1.0 \times 1.5 \times 0.8}{2.5} \right) \times \frac{4}{8} = 17.1 \text{ in.} \geq 12.0$$

→ Required development length = **17.1 in.**

→ Actual development length = **18.0 in.**

Appendix B. Sample Restraint Moment Calculation Using P-method Wharton-Weems Overpass

The restraint moments of the Wharton-Weems overpass in both directions were calculated using Excel and the results were shown in Chapter 3. This appendix shows the detailed calculation procedure of the restraint moment in the Wharton-Weems Overpass 14 days after casting of the CIP topping slabs. In the calculation, following conditions and assumptions are used:

B.1. Conditions and assumptions for calculation

B.1.a: Precast concrete panels:

Design strength (f'_c)_{precast}: 9000 psi

Elastic modulus of strand (E_s): 29000 ksi

Unit weight concrete (w_c): 150 lb/ft³

Use eight 3/8 in. low-relaxation strand per panel

Strands are located 2 in. from top of precast panel

Remaining prestress during a month after CIP concrete casting: 175 ksi.

Ultimate shrinkage strain of PCPs: 600×10^{-6}

Ultimate creep coefficient of the PCPs: 3.42

B.1.b: CIP concrete slabs:

Design strength (f'_c)_{CIP}: 4000 psi

Compressive strength at 14 days after casting using Equation 4-5:

$$f_c(14) = 4000 \times \frac{14}{2.3 + (0.92 \times 14)} = 3689 \text{ psi}$$

Elastic modulus of top-mat reinforcement (E_s): 29000 ksi

Current TxDOT standard reinforcement was used:

No. 5 bar at 6 in (transverse dir.) / No. 4 bar at 6 in (longitudinal dir.)

Unit weight concrete (w_c): 150 lb/ft³

CIP concrete was cast when the precast panels was 55 days old

Ultimate shrinkage strain of CIP slabs: 613×10^{-6}

Ultimate creep coefficient of the CIP slabs: 3.40

B.2. Calculations of components for longitudinal restraint moment

A.I.a Dimension of specimen:

Width: 111.6 in. (=9.3 ft)

Length of main span (L_m): 600 in. (=50 ft)

Length of diaphragm (L_d): 1 in.

Thickness: 8 in. (4 in. precast panel and 4 in. CIP topping)

B.2.a: Composite section properties:

$y_b = 3.56$ in.

$$y_t = 4.44 \text{ in.}$$

$$I_g = 5879.4 \text{ in.}^4$$

$$I_{cr} = 371.0 \text{ in.}^4$$

B.2.b: Calculate the moment due to eccentric prestressing, M_p :

$$M_p = f_p \times A_p \times (y_b - 2) = 175 \times 0 \times (3.54 - 2) = 0 \text{ kip-in.}$$

$$f_p = 175 \text{ kips}$$

$$A_p = 0 \text{ in.}^2$$

$$y_b = 3.56 \text{ in.}$$

B.2.c: Calculate the dead load moment, $(M_d)_{\text{precast}}$, $(M_d)_{\text{CIP}}$:

$$(M_d)_{\text{precast}} = \frac{wl^2}{8} = \frac{4 \times 111.6}{144} \times 150 \times \frac{50^2}{8} \times 10^{-3} \times 12 = 1743.8 \text{ kip-in.}$$

$$(M_d)_{\text{CIP}} = \frac{wl^2}{8} = \frac{4 \times 111.6}{144} \times 150 \times \frac{50^2}{8} \times 10^{-3} \times 12 = 1743.8 \text{ kip-in.}$$

B.2.d: Calculate the uniform shrinkage moment, M_s :

$$M_s = \varepsilon_s E_d A_d \left(e_s - \frac{h}{2} \right) \left(\frac{1}{1 + \frac{E_p A_p}{E_d A_d}} \right) \left(\frac{1}{1 + \frac{E_s A_s}{E_d A_d}} \right)$$

$$E_d = 57 \sqrt{3689} = 3462 \text{ ksi}$$

$$E_p = 57 \sqrt{9000} = 5408 \text{ ksi}$$

$$E_s = 29000 \text{ ksi}$$

$$A_d = A_p = 111.6 \times 4 = 446.4 \text{ in.}^2$$

$$A_s = 12.4 \times 0.2 = 2.48 \text{ in.}^2 \text{ (No. 4 bar at 9 in. in 111.6 in. width deck)}$$

$$e_c = y_t = 4.44 \text{ in.}$$

$$h = 4 \text{ in.}$$

Therefore,

$$M_s = \varepsilon_s \times 3462 \times 192 \left(4.44 - \frac{4}{2} \right) \left(\frac{1}{1 + \frac{5408 \times 446.4}{3462 \times 446.4}} \right) \left(\frac{1}{1 + \frac{29000 \times 2.48}{3462 \times 446.8}} \right)$$

$$= 3,711,346.5 \times \varepsilon_s \text{ kips-in.}$$

B.2.e: Shrinkage strains in precast panels and CIP concrete slabs for calculating M_s :

B.2.e.(1) Precast concrete panels

Shrinkage strain in the panels at time t using Equation 4-4

$$\varepsilon_{sh, \text{precast}}(t) = 600 \times 10^{-6} \times 0.13 \times \ln(t+1)$$

Shrinkage in the panels when the CIP topping is cast ($t=55$ days)

$$\varepsilon_{sh, \text{precast}}(55) = 600 \times 10^{-6} \times 0.13 \times \ln(55+1) = 314 \times 10^{-6}$$

Shrinkage in the panels when CIP topping is 14 days old ($t=55+14=69$ days)

$$\varepsilon_{sh,precast}(69)=600 \times 10^{-6} \times 0.13 \times \ln(55+14+1) = 331 \times 10^{-6}$$

Shrinkage strain in precast panel during 14 days after CIP topping is cast

$$\varepsilon_{sh,precast} = (331 \times 10^{-6}) - (314 \times 10^{-6}) = 17 \times 10^{-6}$$

B.2.e.(2) CIP concrete slabs

Shrinkage strain in CIP concrete slabs at time t

$$\varepsilon_{sh,CIP}(t) = 613 \times 10^{-6} \times 0.13 \times \ln(t+1)$$

Shrinkage in CIP topping during the first 14 days ($t=14$ days)

$$\varepsilon_{sh,CIP}(14) = 613 \times 10^{-6} \times 0.13 \times \ln(14+1) = 216 \times 10^{-6}$$

Differential shrinkage between precast concrete panels and CIP slabs

$$\varepsilon_{sh} = (216 \times 10^{-6}) - (17 \times 10^{-6}) = 199 \times 10^{-6}$$

Therefore

$$M_s = 3,711,346.5 \times (199 \times 10^{-6}) = 736.3 \text{ kip-in.}$$

B.2.f: Creep effects on M_p and $(M_d)_{precast}$:

$$[\Delta(1-e^{-\phi_1})] = (1-e^{-1.889}) - (1-e^{-1.790}) = 0.01577$$

$$(\phi_1)_{initial} = 3.42 \times 0.13 \times \ln(55+1) = 1.790$$

$$(\phi_1)_{14 \text{ days}} = 3.42 \times 0.13 \times \ln(55+14+1) = 1.889$$

B.2.g: Creep effects on $(M_d)_{CIP}$ and M_s :

$$\phi_2 = 3.40 \times 0.13 \times \ln(14+1) = 1.197$$

$$(1-e^{-\phi_2}) = (1-e^{-1.197}) = 0.698$$

$$\frac{(1-e^{-\phi_2})}{\phi_2} = \frac{(1-e^{-1.197})}{1.197} = 0.583$$

B.3. Calculate longitudinal restraint moment

α can be calculated using moment distribution method, and it is assumed that the specimen has not been cracked ($I_d = I_m = I_g$). Resultant restraint moments due to fixed-ends moment M_s and M_d are shown in Figure B-1 and Figure B-2.

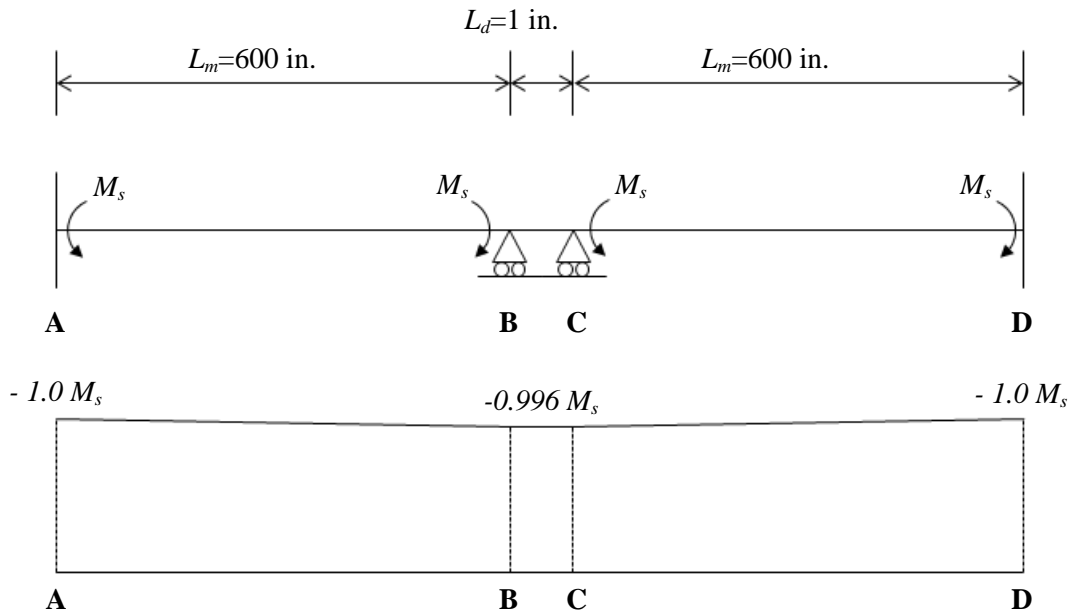


Figure B-1: Longitudinal restraint moment due to M_s

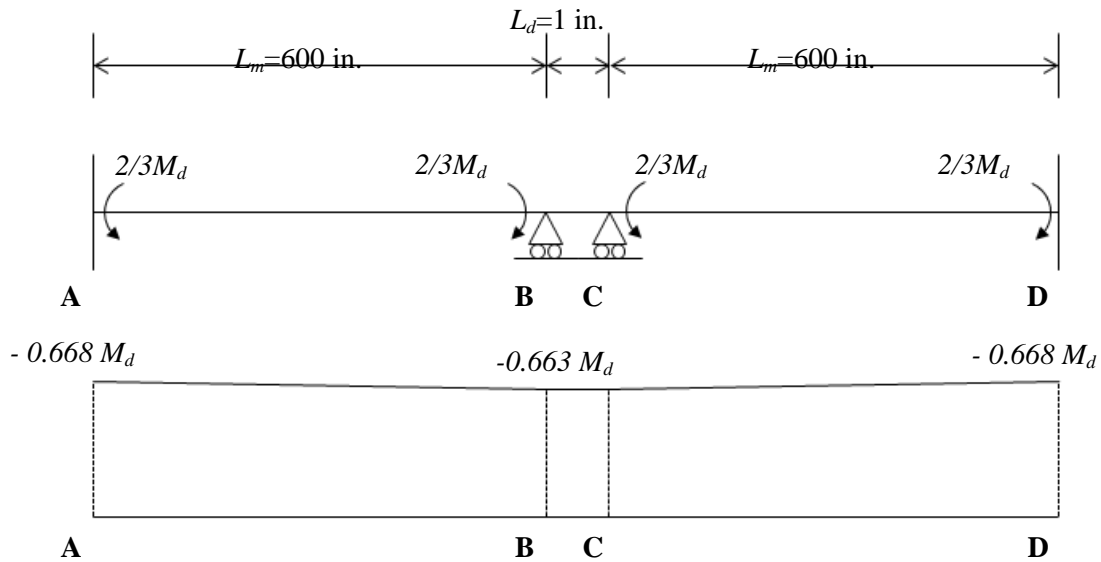


Figure B-2: Longitudinal restraint moment due to M_d

Therefore

$M_r =$ Equation 3-2

$$\begin{aligned}
 &= [\alpha M_p - \alpha (M_d)_{\text{precast}}] [\Delta (1 - e^{-\phi_1})] - \alpha (M_d)_{\text{CIP}} (1 - e^{-\phi_2}) - \alpha M_s \left(\frac{1 - e^{-\phi_2}}{\phi_2} \right) \\
 &= [(0.996 \times 0 - 0.663 \times 1743.75) \times 0.01577] - (0.663 \times 1743.75 \times 0.698) \\
 &\quad - (0.996 \times 736.3 \times 0.583) \\
 &= -1253.9 \text{ kip-in.}
 \end{aligned}$$

Cracking moment at 14 days after CIP topping is cast:

$$M_{cr} = -\frac{7.5\sqrt{3689}}{1000} \times \frac{111.6 \times 8^2}{6} = -542.3 \text{ kip-in.}$$

The restraint moment is greater than the cracking moment ($|M_r| > |M_{cr}|$), so it can be concluded that cracks are formed in the specimen.

B.4. Calculations of components for transverse restraint moment

B.4.a: Dimension of specimen:

Width: 1,200 in. (=100 ft)

Length of main span (L_m): 92 in. (=7.67 ft)

Length of diaphragm (L_d): 36 in.

Thickness: 8 in. (4 in. precast panel and 4 in. CIP topping)

B.4.b: Composite section properties:

$$y_b = 3.56 \text{ in.}$$

$$y_t = 4.44 \text{ in.}$$

$$I_g = 63219.0 \text{ in.}^4$$

$$I_{cr} = 8118.4 \text{ in.}^4$$

B.4.c: Calculate the moment due to eccentric prestressing, M_p :

$$M_p = f_p \times A_p \times (y_b - 2) = 175 \times 16 \times (3.56 - 2) = 4371.7 \text{ kip-in.}$$

$$f_p = 175 \text{ kips}$$

$$A_p = 200 \times 0.08 = 16 \text{ in.}^2$$

$$y_b = 3.56 \text{ in.}$$

B.4.d: Calculate the dead load moment, $(M_d)_{\text{precast}}$, $(M_d)_{\text{CIP}}$:

$$(M_d)_{\text{precast}} = \frac{wl^2}{8} = \frac{4 \times 1200}{144} \times 150 \times \frac{7.67^2}{8} \times 10^{-3} \times 12 = 440.8 \text{ kip-in.}$$

$$(M_d)_{\text{CIP}} = \frac{wl^2}{8} = \frac{4 \times 1200}{144} \times 150 \times \frac{7.67^2}{8} \times 10^{-3} \times 12 = 440.8 \text{ kip-in.}$$

B.4.e: Calculate the uniform shrinkage moment, M_s :

$$M_s = \varepsilon_s E_d A_d \left(e_s - \frac{h}{2} \right) \left(\frac{1}{1 + \frac{E_p A_p}{E_d A_d}} \right) \left(\frac{1}{1 + \frac{E_s A_s}{E_d A_d}} \right)$$

$$E_d = 57\sqrt{3689} = 3462 \text{ ksi}$$

$$E_p = 57\sqrt{9000} = 5408 \text{ ksi}$$

$$E_s = 29000 \text{ ksi}$$

$$A_d = A_p = 1200 \times 4 = 4800 \text{ in.}^2$$

$$A_s = 200 \times 0.31 = 62 \text{ in.}^2 \text{ (No. 5 bar at 6 in. in 1200 in. width deck)}$$

$$e_c = y_t = 4.44 \text{ in.}$$

$$h = 4 \text{ in.}$$

Therefore,

$$M_s = \varepsilon_s \times 3462 \times 192 \left(4.44 - \frac{4}{2} \right) \left(\frac{1}{1 + \frac{5408 \times 4800}{3462 \times 4800}} \right) \left(\frac{1}{1 + \frac{29000 \times 62}{3462 \times 4800}} \right)$$

$$= 37,686,507.5 \times \varepsilon_s \text{ kips-in.}$$

B.4.f: Shrinkage strains in precast panels and CIP concrete slabs for calculating M_s :

B.4.f.(1) Precast concrete panels

Shrinkage strain in the panels at time t using Equation 4-4

$$\varepsilon_{sh,precast}(t) = 600 \times 10^{-6} \times 0.13 \times \ln(t+1)$$

Shrinkage in the panels when the CIP topping is cast ($t=55$ days)

$$\varepsilon_{sh,precast}(55) = 600 \times 10^{-6} \times 0.13 \times \ln(55+1) = 314 \times 10^{-6}$$

Shrinkage in the panels when CIP topping is 14 days old ($t=55+14=69$ days)

$$\varepsilon_{sh,precast}(69) = 600 \times 10^{-6} \times 0.13 \times \ln(55+14+1) = 331 \times 10^{-6}$$

Shrinkage strain in precast panel during 14 days after CIP topping is cast

$$\varepsilon_{sh,precast} = (331 \times 10^{-6}) - (314 \times 10^{-6}) = 17 \times 10^{-6}$$

B.4.f.(2) CIP concrete slabs

Shrinkage strain in CIP concrete slabs at time t

$$\varepsilon_{sh,CIP}(t) = 613 \times 10^{-6} \times 0.13 \times \ln(t+1)$$

Shrinkage in CIP topping during the first 14 days ($t=14$ days)

$$\varepsilon_{sh,CIP}(14) = 613 \times 10^{-6} \times 0.13 \times \ln(14+1) = 216 \times 10^{-6}$$

Differential shrinkage between precast concrete panels and CIP slabs

$$\varepsilon_{sh} = (216 \times 10^{-6}) - (17 \times 10^{-6}) = 199 \times 10^{-6}$$

Therefore

$$M_s = 37,686,507.5 \times (199 \times 10^{-6}) = 7477.0 \text{ kip-in.}$$

B.4.g: Creep effects on M_p and $(M_d)_{precast}$:

$$[\Delta(1-e^{-\varphi_1})] = (1-e^{-1.889}) - (1-e^{-1.790}) = 0.01577$$

$$(\varphi_1)_{initial} = 3.42 \times 0.13 \times \ln(55+1) = 1.790$$

$$(\varphi_1)_{14 \text{ days}} = 3.42 \times 0.13 \times \ln(55+14+1) = 1.889$$

B.4.h: Creep effects on $(M_d)_{CIP}$ and M_s :

$$\varphi_2 = 3.40 \times 0.13 \times \ln(14+1) = 1.197$$

$$(1-e^{-\varphi_2}) = (1-e^{-1.197}) = 0.698$$

$$\frac{(1-e^{-\phi_2})}{\phi_2} = \frac{(1-e^{-1.197})}{1.197} = 0.583$$

B.5. Calculate transverse restraint moment

α can be calculated using moment distribution method, and it is assumed that the specimen has not been cracked ($I_d=I_m=I_g$). Resultant restraint moments due to fixed-ends moment M_p , M_s and M_d are shown in Figure B-3 to Figure B-5.

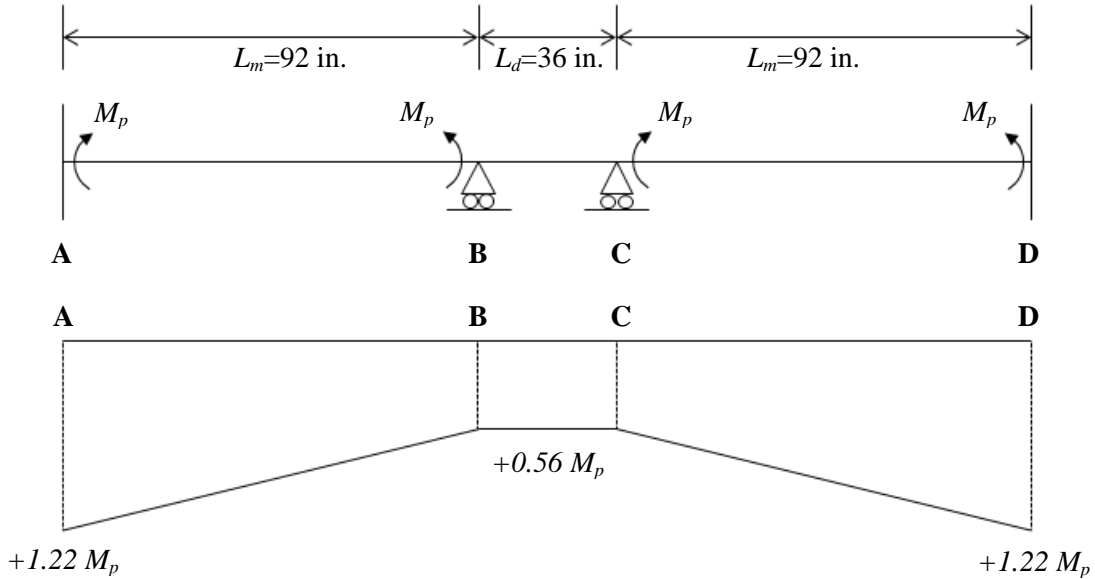


Figure B-3: Transverse restraint moment due to M_p

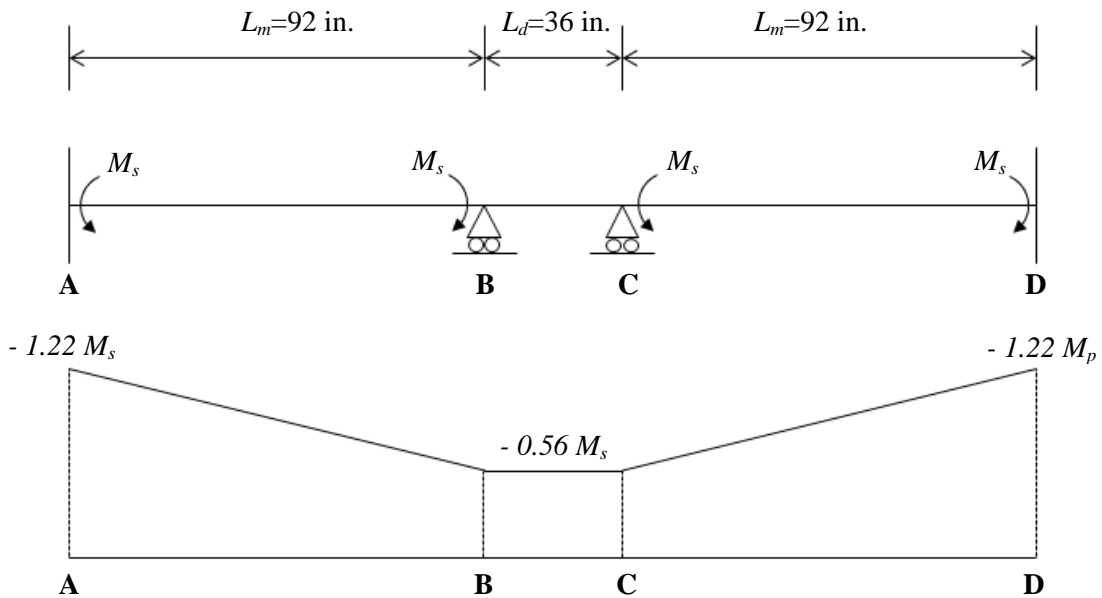


Figure B-4: Transverse restraint moment due to M_s

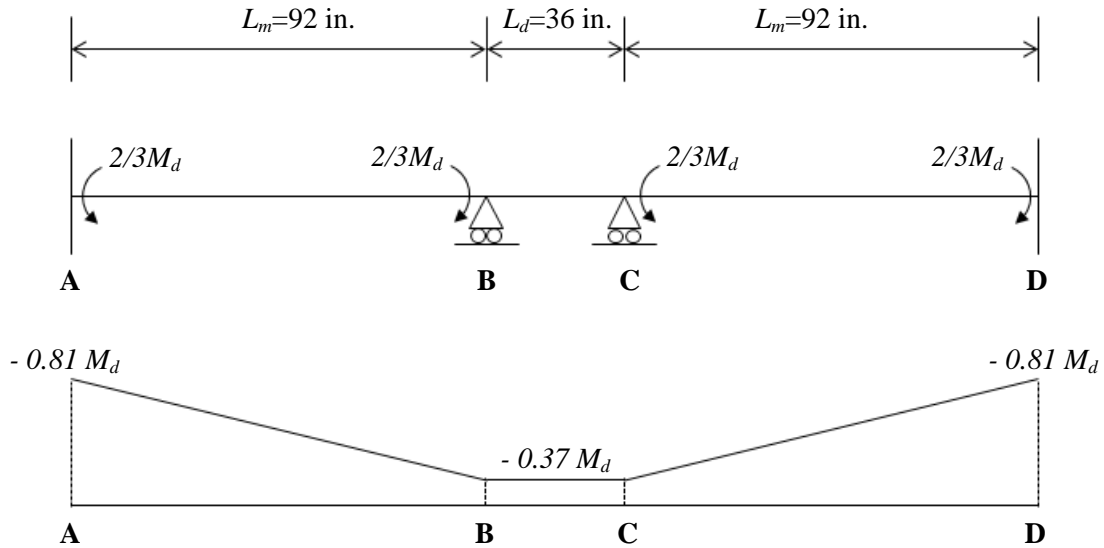


Figure B-5: Transverse restraint moment due to M_d

Therefore

$$\begin{aligned}
 M_r &= \text{Equation 3-2} \\
 &= [\alpha M_p - \alpha (M_d)_{\text{precast}}] [\Delta (1 - e^{-\phi_1})] - \alpha (M_d)_{\text{CIP}} (1 - e^{-\phi_2}) - \alpha M_s \left(\frac{1 - e^{-\phi_2}}{\phi_2} \right) \\
 &= [(0.56 \times 4371.7 - 0.37 \times 440.8) \times 0.01577] - (0.37 \times 440.8 \times 0.698) \\
 &\quad - (0.56 \times 7477.0 \times 0.583) \\
 &= -2519.1 \text{ kip-in.}
 \end{aligned}$$

Cracking moment at 14 days after CIP topping is cast

$$M_{cr} = - \frac{7.5 \sqrt{3689}}{1000} \times \frac{1200 \times 8^2}{6} = -5830.8 \text{ kip-in.}$$

The restraint moment is greater than the cracking moment ($|M_r| < |M_{cr}|$), so it can be concluded that cracks are not formed in the specimen.

Appendix C. Sample Restraint Moment Calculation Using the P-method Restrained Shrinkage Test

The restraint moment of the test specimen was calculated using P-method in Chapter 4, and the results were shown in Figure 4-25. This appendix shows the detailed calculation procedure of the restraint moment in the specimen 14 days after casting of the CIP topping slabs. In the calculation, following conditions and assumptions are used:

C.1. Conditions and assumptions for calculation

C.1.a: Precast concrete panels:

Design strength (f_c')_{precast}: 9000 psi

Elastic modulus of strand (E_s): 29000 ksi

Unit weight concrete (w_c): 150 lb/ft³

Use eight 3/8 in. low-relaxation strand per panel

Strands are located 2 in. from top of precast panel

Remaining prestress during a month after CIP concrete casting: 175 ksi.

Ultimate shrinkage strain of PCPs: 600×10^{-6}

Ultimate creep coefficient of the PCPs: 3.42

C.1.b: CIP concrete slabs:

Design strength (f_c')_{CIP}: 4000 psi

Compressive strength at 14 days after casting using Equation 4-5:

$$f_c(14) = 4000 \times \frac{14}{2.3 + (0.92 \times 14)} = 3689 \text{ psi}$$

Elastic modulus of top-mat reinforcement (E_s): 29000 ksi

Current TxDOT standard reinforcement was used: No. 5 at 6 in.

Unit weight concrete (w_c): 150 lb/ft³

CIP concrete was cast when the precast panels was 55 days old

Ultimate shrinkage strain of CIP slabs: 613×10^{-6}

Ultimate creep coefficient of the CIP slabs: 3.40

C.1.c: Dimension of specimen:

Width: 48 in.

Length of main span (L_m): 8 ft

Length of diaphragm (L_d): 10 in.

Thickness: 8 in. (4 in. precast panel and 4 in. CIP topping)

C.1.d: Composite section properties:

$y_b = 3.56$ in.

$y_t = 4.44$ in.

$$I_g = 2528.8 \text{ in.}^4$$

$$I_{cr} = 324.7 \text{ in.}^4$$

C.2. Calculations of each component for calculating restraint moment

C.2.a: Calculate the moment due to eccentric prestressing, M_p :

$$M_p = f_p \times A_p \times (y_b - 2) = 175 \times 0.64 \times (3.56 - 2) = 174.7 \text{ kip-in.}$$

$$f_p = 175 \text{ kips}$$

$$A_p = 8 \times 0.08 = 0.64 \text{ in.}^2$$

$$y_b = 3.56 \text{ in.}$$

C.2.b: Calculate the dead load moment, $(M_d)_{\text{precast}}$, $(M_d)_{\text{CIP}}$:

$$(M_d)_{\text{precast}} = \frac{wl^2}{8} = \frac{4 \times 48}{144} \times 150 \times \frac{8^2}{8} \times 10^{-3} \times 12 = 19.2 \text{ kip-in.}$$

$$(M_d)_{\text{CIP}} = \frac{wl^2}{8} = \frac{4 \times 48}{144} \times 150 \times \frac{8^2}{8} \times 10^{-3} \times 12 = 19.2 \text{ kip-in.}$$

C.2.c: Calculate the uniform shrinkage moment, M_s :

$$M_s = \varepsilon_s E_d A_d \left(e_s - \frac{h}{2} \right) \left(\frac{1}{1 + \frac{E_p A_p}{E_d A_d}} \right) \left(\frac{1}{1 + \frac{E_s A_s}{E_d A_d}} \right)$$

$$E_d = 57 \sqrt{3689} = 3462 \text{ ksi}$$

$$E_p = 57 \sqrt{9000} = 5408 \text{ ksi}$$

$$E_s = 29000 \text{ ksi}$$

$$A_d = A_p = 48 \times 4 = 192 \text{ in.}^2$$

$$A_s = 8 \times 0.31 = 2.48 \text{ in.}^2$$

$$e_c = y_t = 4.44 \text{ in.}$$

$$h = 4 \text{ in.}$$

Therefore,

$$M_s = \varepsilon_s \times 3462 \times 192 \left(4.44 - \frac{4}{2} \right) \left(\frac{1}{1 + \frac{5408 \times 192}{3462 \times 192}} \right) \left(\frac{1}{1 + \frac{29000 \times 2.48}{3462 \times 192}} \right)$$

$$= 1,507,460.3 \times \varepsilon_s \text{ kips-in.}$$

C.2.d: Shrinkage strains in precast panels and CIP concrete slabs for calculating M_s :

C.2.d.(1) Precast concrete panels

Shrinkage strain in the panels at time t using Equation 4-4

$$\varepsilon_{sh,precast}(t)=600 \times 10^{-6} \times 0.13 \times \ln(t+1)$$

Shrinkage in the panels when the CIP topping is cast ($t=55$ days)

$$\varepsilon_{sh,precast}(55)=600 \times 10^{-6} \times 0.13 \times \ln(55+1)=314 \times 10^{-6}$$

Shrinkage in the panels when CIP topping is 14 days old ($t=55+14=69$ days)

$$\varepsilon_{sh,precast}(69)=600 \times 10^{-6} \times 0.13 \times \ln(55+14+1)=331 \times 10^{-6}$$

Shrinkage strain in precast panel during 14 days after CIP topping is cast

$$\varepsilon_{sh,precast}=(331 \times 10^{-6})-(314 \times 10^{-6})=17 \times 10^{-6}$$

C.2.d.(2) CIP concrete slabs

Shrinkage strain in CIP concrete slabs at time t

$$\varepsilon_{sh,CIP}(t)=613 \times 10^{-6} \times 0.13 \times \ln(t+1)$$

Shrinkage in CIP topping during the first 14 days ($t=14$ days)

$$\varepsilon_{sh,CIP}(14)=613 \times 10^{-6} \times 0.13 \times \ln(14+1)=216 \times 10^{-6}$$

Differential shrinkage between precast concrete panels and CIP slabs

$$\varepsilon_{sh}=(216 \times 10^{-6})-(17 \times 10^{-6})=199 \times 10^{-6}$$

Therefore

$$M_s=1,507,460.3 \times (199 \times 10^{-6})=300 \text{ kip-in.}$$

C.2.e: Creep effects on M_p and $(M_d)_{precast}$:

$$[\Delta(1-e^{-\varphi_1})]=(1-e^{-1.889})-(1-e^{-1.790})=0.01577$$

$$(\varphi_1)_{initial}=3.42 \times 0.13 \times \ln(55+1)=1.790$$

$$(\varphi_1)_{14 \text{ days}}=3.42 \times 0.13 \times \ln(55+14+1)=1.889$$

C.2.f: Creep effects on $(M_d)_{CIP}$ and M_s :

$$\varphi_2=3.40 \times 0.13 \times \ln(14+1)=1.197$$

$$(1-e^{-\varphi_2})=(1-e^{-1.197})=0.698$$

$$\frac{(1-e^{-\varphi_2})}{\varphi_2}=\frac{(1-e^{-1.197})}{1.197}=0.583$$

C.3. Calculate restraint moment

Assume that the specimen has not been cracked ($I_d=I_m=I_g$)

$$\alpha = \frac{\frac{2I_d}{L_d}}{\frac{2I_d}{L_d} + \frac{3I_m}{L_m}} = \frac{\frac{2I_g}{L_d}}{\frac{2I_g}{L_d} + \frac{3I_g}{L_m}} = \frac{\frac{2 \times 2528.8}{10/12}}{\frac{2 \times 2528.8}{10/12} + \frac{3 \times 2528.8}{8}} = 0.865$$

Therefore

$$\begin{aligned} M_r &= \text{Equation 3-2} \\ &= \left[\frac{3}{2} \alpha M_p - \alpha (M_d)_{\text{precast}} \right] [\Delta(1 - e^{-\phi_1})] - \alpha (M_d)_{\text{CIP}} (1 - e^{-\phi_2}) - \frac{3}{2} \alpha M_s \left(\frac{1 - e^{-\phi_2}}{\phi_2} \right) \\ &= \left[\left(\frac{3}{2} \times 0.865 \times 174.72 - 0.865 \times 19.2 \right) \times 0.01577 \right] - (0.865 \times 19.2 \times 0.698) \\ &\quad - \left(\frac{3}{2} \times 0.865 \times 300 \times 0.583 \right) \\ &= -234.80 \text{ kip-in.} \end{aligned}$$

Cracking moment at 14 days after CIP topping is cast

$$M_{cr} = -\frac{7.5\sqrt{3689}}{1000} \times \frac{48 \times 8^2}{6} = -233.23 \text{ kip-in.}$$

The restraint moment is greater than the cracking moment ($|M_r| > |M_{cr}|$), so it can be concluded that cracks are formed in the specimen. The restraint moment should be re-calculated considering reduction of stiffness in diaphragm region ($I_d=I_{cr}$). The stiffness of main span is not changed ($I_m=I_g$).

$$\alpha = \frac{\frac{2I_d}{L_d}}{\frac{2I_d}{L_d} + \frac{3I_m}{L_m}} = \frac{\frac{2I_{cr}}{L_d}}{\frac{2I_{cr}}{L_d} + \frac{3I_g}{L_m}} = \frac{\frac{2 \times 324.7}{10/12}}{\frac{2 \times 324.7}{10/12} + \frac{3 \times 2528.8}{8}} = 0.451$$

Then

$$\begin{aligned} M_r &= \left[\left(\frac{3}{2} \times 0.451 \times 174.72 - 0.451 \times 19.2 \right) \times 0.01577 \right] - (0.451 \times 19.2 \times 0.698) \\ &\quad - \left(\frac{3}{2} \times 0.451 \times 300 \times 0.583 \right) \\ &= -122.64 \text{ kip-in.} \end{aligned}$$

Appendix D. Model for Prestress Loss in PC Panels

D.1. Introduction

Data from monitoring prestress loss in precast, prestressed concrete panels (PCPs) shows that actual prestress losses in PCPs are much smaller than the values predicted by most current models or assumed in TxDOT procedures for PCP design. Most current models overestimate prestress loss in PCPs, because those models were developed from test results of prestressed girders or beams. Prestressed girders or beams have geometric conditions (ratio of surface area to volume), initial prestress force levels, and strand profiles different than those for prestressed panels. Therefore, patterns and amounts of prestress losses in prestressed girders or beams can be different from those in prestressed panels. Some current models, such as the PCI model, can accurately predict prestress losses in PCPs, probably because they were developed based on widely scattered data. Because they also do not consider the characteristics of PCPs, they may not give consistently accurate predictions. If expected prestress loss is larger than the measured values, the initial prestressing force may be higher than required to account for losses. Increasing initial prestressing force may increase the likelihood of cracking. Therefore, a model for predicting prestress loss specifically for PCPs is proposed.

D.2. Current prediction models for prestress loss

D.2.a: AASHTO 2008

AASHTO 2008 equations for calculating prestress losses are presented in Equation D-1 to Equation D-14. A lump-sum prestress loss of 45 ksi is suggested as a conservative estimate.

D.2.a.(1) Total prestress loss by AASHTO 2008

The total prestress loss can be calculated using Equation D-1. The total prestress loss is the sum of the loss due to elastic shortening (Δf_{pES}) and the long-term loss (Δf_{pLT}). The long-term prestress loss, as shown in Equation D-2, consists of losses due to shrinkage ($\Delta f_{pSR,id}$), creep ($\Delta f_{pCR,id}$), and relaxation ($\Delta f_{pRI,id}$). The subscript 'id' was added in all components of long-term prestress loss to indicate all components were occurred between transfer and deck placement, and this subscript was the same used in AASHTO 2008 and NCHRP Report 496. Each term for Equation D-1 and Equation D-2 is introduced in Sections D.2.a.(2) to D.2.a.(5).

$$\Delta f_{pT} = \Delta f_{pES} + \Delta f_{pLT} \quad \text{Equation D-1}$$

$$\Delta f_{pLT} = \left(\Delta f_{pSR} + \Delta f_{pCR} + \Delta f_{pRI} \right)_{id} \quad \text{Equation D-2}$$

Where,

Δf_{pT}	= total loss in prestressing steel stress (ksi)
Δf_{pES}	= loss in prestressing steel due to elastic shortening (ksi)
Δf_{pLT}	= loss in prestressing steel due to long-term deformations (ksi)

$\Delta f_{pSR,id}$	= prestress loss due to shrinkage between transfer and deck placement (ksi)
$\Delta f_{pCR,id}$	= prestress loss due to creep between transfer and deck placement (ksi)
$\Delta f_{pRI,id}$	= prestress loss due to relaxation of prestressing strands between transfer and deck placement (ksi)

D.2.a.(2) Elastic shortening by AASHTO 2008

Prestress loss due to elastic shortening is evaluated using Equation D-3.

$$\Delta f_{pES} = \frac{A_{ps} f_{pbt} (I_g + e_{cl}^2 A_g) - e_{cl} M_g A_g}{A_{ps} (I_g + e_{cl}^2 A_g) + \frac{A_g I_g E_{ci}}{E_p}} \quad \text{Equation D-3}$$

(Eq. C5.9.5.2.3a-1, AASHTO 2008)

Where,	A_{ps}	= area of prestressing steel (in. ²)
	f_{pbt}	= stress in prestressing steel immediately prior to transfer (ksi)
	I_g	= moment of inertia of the gross cross section (in. ⁴)
	e_{cl}	= eccentricity of strand (in.)
	A_g	= gross area of section (in. ²)
	M_g	= maximum moment due to member self-weight (kip-in.)
	E_{ci}	= modulus of elasticity of concrete at transfer (ksi)

D.2.a.(3) Shrinkage deformation by AASHTO 2008

Prestress loss due to shrinkage deformation is calculated using Equation D-4. All components of the equation are deformed by equations from Eqs. D-6 to D-13. The values of 480×10^{-6} in Equation D-5 and 1.9 in Equation D-7 represent ultimate shrinkage strain and constant for creep coefficient respectively. These two constants were determined based on results reported by previous researchers (Tadros *et al.* 2003). The tests were mostly conducted using rectangular parallelepiped concrete specimens without any reinforcement under controlled environmental conditions (constant temperature and humidity).

$$\Delta f_{pSR} = \varepsilon_{bid} E_p K_{id} \quad \text{Equation D-4}$$

(Eq. 5.9.5.4.3a-1, AASHTO 2008)

$$\varepsilon_{bid} = k_s k_{hs} k_f k_{td} (480 \times 10^{-6}) \quad \text{Equation D-5}$$

$$K_{id} = \frac{1}{1 + \frac{E_p A_{ps}}{E_{ci} A_g} \left(1 + \frac{A_g e_{cl}^2}{I_g} \right) [1 + 0.7 \phi_B (t_f, t_i)]} \quad \text{Equation D-6}$$

(Eq. 5.9.5.4.2a-2, AASHTO 2008)

$$\varphi_B(t_f, t_i) = 1.9k_s k_{hc} k_{td} t_i^{-0.118} \quad \text{Equation D-7}$$

$$k_s = 1.45 - 0.13 \frac{V}{S} \quad \text{Equation D-8}$$

$$k_{hs} = 2.00 - 0.014H \quad \text{Equation D-9}$$

$$k_{hc} = 1.56 - 0.008H \quad \text{Equation D-10}$$

$$k_f = \frac{5}{1 + f_{ci}} \quad \text{Equation D-11}$$

$$k_{td} = \frac{(t_f - t_i)}{61 - 4f_{ci}' + (t_f - t_i)} \quad \text{Equation D-12}$$

Where,	ε_{bid}	= shrinkage strain between transfer to placement of CIP deck (in./in.)
	E_p	= modulus of elasticity of prestressing steel (ksi)
	K_{id}	= transformed section age-adjusted effective modulus of elasticity factor, for adjustment between the time of transfer and deck placement
	$\varphi_B(t_f, t_i)$	= creep coefficient minus the ratio of the strain that exists t_f days after casting to the elastic strain caused when load is applied t_i days after casting
	k_s	= volume-to-surface ratio shrinkage correction factor
	k_{hc}	= humidity correction factor for creep
	k_{td}	= time-development correction factor
	t_i	= age at transfer after casting (days)
	k_{hs}	= humidity correction factor for shrinkage
	k_f	= concrete strength correction factor for creep
	t_f	= final age after casting (days)

D.2.a.(4) Creep deformation by AASHTO 2008

The prestress loss due to creep deformation can be obtained using Equation D-13. Equation D-6 and Equation D-7 can be used for obtaining K_{id} and $\varphi_B(t_f, t_i)$ in Equation D-13.

$$\Delta f_{pCR} = \frac{E_p}{E_{ci}} f_{cgp} \varphi_B(t_f, t_i) K_{id} \quad \text{Equation D-13}$$

(Eq. 5.9.5.4.2b-1, AASHTO 2008)

Where,	f_{cgp}	= average concrete stress at the center of gravity of the prestressing steel at time of release
--------	-----------	---

D.2.a.(5) Relaxation by AASHTO 2008

Prestress loss due to relaxation can be calculated using Equation D-14.

$$\Delta f_{pRI} = \frac{f_{pt}}{K_L} \left(\frac{f_{pt}}{f_{py}} - 0.55 \right)$$

Equation D-14
(Eq. 5.9.5.4.2c-1, AASHTO 2008)

Where, f_{pt} = stress in prestressing steel immediately after transfer (ksi)
 K_L = 30 for low relaxation steel
 f_{py} = yield strength of strands (ksi)

D.2.b: TxDOT 2004 Design Specification

A lump-sum value of 45 ksi is recommended for total prestress loss in PCPs designed by TxDOT 2004.

D.2.c: PCI Design Handbook, 6th edition

The PCI Design Handbook (PCI 2004) provides a procedure for calculating total prestress losses, presented in Eqs. D-16 to D-23.

D.2.c.(1) Total prestress loss by PCI 2004

As similar with AASHTO 2008, total prestress loss using the PCI Design Handbook can be calculated by adding prestress losses due to elastic shortening (*ES*), shrinkage (*SH*) creep (*CR*), and relaxation (*RE*) as shown in Equation D-15. All components of the equation are explained in the following sections.

$$TL = ES + CR + SH + RE$$

Equation D-15
(Eq. 4.7.3.1, PCI 2004)

Where, TL = total prestress loss
 ES = loss of prestress due to elastic shortening
 CR = loss of prestress due to creep of concrete
 SH = loss of prestress due to shrinkage of concrete
 RE = loss of prestress due to relaxation of steel

D.2.c.(2) Elastic shortening by PCI 2004

Prestress loss due to elastic shortening is calculated using Equation D-16. The value of f_{cir} in the equation can be calculated using Equation D-17.

$$ES = \frac{K_{es} E_{ps} f_{cir}}{E_{ci}}$$

Equation D-16
(Eq. 4.7.3.2, PCI 2004)

$$f_{cir} = K_{cir} \left(\frac{P_i}{A_g} + \frac{P_i e^2}{I_g} \right) - \frac{M_g e}{I_g}$$

Equation D-17
(Eq. 4.7.3.3, PCI 2004)

Where,	K_{es}	= 1.0 for pretensioned members
	E_{ps}	= modulus of elasticity of prestressing tendons
	f_{cir}	= net compressive stress in concrete at center of gravity of prestressing force immediately after the prestress has been applied to the concrete
	K_{cir}	= 0.9 for pretensioned members
	P_i	= initial prestress force (after anchorage seating loss)
	A_g	= gross sectional area (in. ²)
	e	= eccentricity of center of gravity of tendons with respect to center of gravity of concrete at the cross section considered
	I_g	= moment of inertia of the gross section (in. ⁴)
	M_g	= bending moment due to dead weight of prestressed member and any other permanent loads in place at time of prestressing

D.2.c.(3) Shrinkage deformation, by PCI 2004

Prestress loss due to shrinkage deformation can be calculated using Equation D-18.

$$SH = (8.2 \times 10^{-6}) K_{sh} E_{ps} \left(1 - 0.06 \frac{V}{S} \right) (100 - RH)$$

Equation D-18
(Eq. 4.7.3.6, PCI 2004)

Where,	K_{sh}	= 1.0 for pretensioned members
	V/S	= volume to surface ratio (in.)
	RH	= average ambient relative humidity (%)

D.2.c.(4) Creep deformation by PCI 2004

Prestress loss due to creep deformation can be evaluated using Equation D-19. Equation D-17 and Equation D-20 can be used for f_{cir} and f_{cds} in Equation D-19.

$$CR = K_{cr} \frac{E_{ps}}{E_c} (f_{cir} - f_{cds})$$

Equation D-19
(Eq. 4.7.3.4, PCI 2004)

$$f_{cds} = \frac{M_{sd} e_{cl}}{I_g}$$

Equation D-20
(Eq. 4.7.3.5, PCI 2004)

Where,

K_{cr}	= 2.0 for normal weight concrete = 1.6 for light weight concrete
E_c	= modulus of elasticity of concrete at 28 days
M_{sd}	= moment due to all superimposed permanent dead and sustained loads applied after prestressing

D.2.c.(5) Relaxation by PCI 2004

Prestress loss due to relaxation can be obtained using Equation D-21 and the constant C is determined using Equation D-22.

$$RE = [K_{re} - J(SH + CR + ES)]C$$

Equation D-21
(Eq. 4.7.3.7, PCI 2004)

$$C = \frac{\left(\frac{f_{pi}}{f_{pu}}\right)}{0.21} \left[\frac{\left(\frac{f_{pi}}{f_{pu}}\right)}{0.9} - 0.55 \right] \text{ for } \left(\frac{f_{pi}}{f_{pu}}\right) \geq 0.54$$

Equation D-22
(Eq. 4.7.3.11, PCI 2004)

Where,

K_{re}	= 5,000 for 270 Grade low-relaxation strand
J	= 0.040 for 270 Grade low-relaxation strand
f_{pi}	= P_i/A_{ps}
f_{pu}	= ultimate strength of prestressing steel

D.3. Proposed equation for prestress loss in PC panels

Long-term prestress loss monitoring data, described in Chapter 5.4, were used to develop a model for prestress loss in PC panels. Fourteen instrumented panels were used. Among the fourteen panels, six panels had an initial prestress of 189.4 ksi. Eight panels had an initial prestress of 169.4 ksi.

General conditions were used to develop a simple and user-friendly model. The model can be used to predict prestress losses from time of transfer to time of CIP slab placement, because all monitored panels used for developing the model did not have a CIP slab. CIP topping slabs change the shrinkage and creep deformations in PCPs by restraining these deformations and changing exposure conditions of PCPs. Assumed conditions used for developing the model are stated below:

- i) Concrete strength at release (f_{ci}): 4,000 psi
- ii) Concrete strength at 28 days (f_c): 5,000 psi
- iii) Volume-to-surface ratio (V/S): 1.92
- iv) Time of releasing (t_i): 1 day after casting
- v) Average ambient relative humidity (RH): 60%

The concrete strengths at release and at 28 days were determined using the values in the TxDOT design specification. The width and length of the panel are assumed to be 8 ft, and a 4-in. thickness is assumed based on dimensions of the test panels in this study. Exposed surface area is calculated adding top and bottom faces (2×8 ft×8 ft) and two-side faces parallel to prestress strands (2×8 ft×4 in.). The faces in which prestressing strands were projected are excluded. The date for release is set at 1 day because strands were usually cut one or two days after casting at both Plant A and Plant B. Average humidity is calculated using measured humidity data during the monitoring period.

Figure D-1 shows the sequence for developing new model of prestress loss in PCPs, and the following sections are organized according to the sequence shown in this chart. Number and kinds of the panels used in each step were presented in the chart.

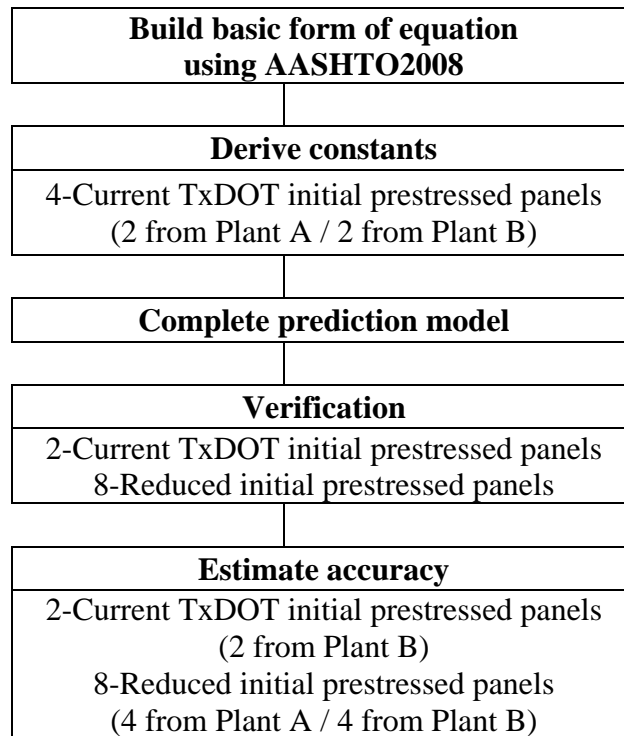


Figure D-1: Flow chart for proposing new equation for predicting prestress loss in PCPs

D.3.a: Development of basic form for proposed equation

AASHTO 2008 was used for developing the basic form of the loss model. Because TxDOT design specifications give only a lump-sum value of prestress loss, TxDOT specifications were not used.

D.3.a.(1) Elastic shortening, proposed equation

Equation D-3 can be simplified by considering layout of strands and sectional properties of PCPs. The eccentricity of strand (e_{cl}) is zero in the panel, and the area of prestress strands (A_{ps}) is much smaller than the gross area of the section (A_g), and can be neglected in Equation D-23. The simplified result is shown in Equation D-23.

The prestress loss due to elastic shortening in PCPs can be calculated using Equation D-24, whose calculated value using Equation D-24 is 5.0 ksi for an initial prestress of 189.4 ksi, and 4.5 ksi for an initial prestress of 169.4 ksi. The calculated values are consistent with the measured values as shown in Table D-2. By using constant values depending on initial prestress, the model can be further simplified.

$\Delta f_{pES} = \text{Equation 5-4} = \frac{A_{ps}f_{pbt}}{A_{ps} + \frac{A_g E_{ci}}{E_p}} = \frac{E_p}{E_{ci}} \times \frac{A_{ps}f_{pbt}}{\frac{A_{ps}E_p}{E_{ci}} + A_g}$	Equation D-23
$\Delta f_{pES} = \frac{E_p}{E_{ci}} \times \frac{A_{ps}f_{pbt}}{A_g}$	Equation D-24

D.3.a.(2) Shrinkage deformation, proposed equation

The prestress loss due to shrinkage deformation can be calculated using Equation D-4. All components for that equation are obtained using Equation D-25 to Equation D-32, and the assumed conditions in Section D.3.a. The prestress due to shrinkage deformation in PCPs becomes Equation D-33.

As stated, 480×10^{-6} is used as ultimate shrinkage strain (C_{SH}). Based on previous research, this value is a common assumption for predicting prestress loss in prestressed girders or beams, but there is no evidence that it is also adequate for predicting prestress loss in PCPs. Therefore, ultimate shrinkage strain is left as an unknown value in Equation D-33 and it will be derived through a numerical analysis of data. Moreover, a constant of 1.39 in Equation 5-4 was rounded to 1.50 for simplicity.

$\Delta f_{pSR} = 1.39 \times C_{SH} \times \frac{(t_f - t_i)}{45 + (t_f - t_i)} \times E_p \times 1.00$	<i>Equation 5-4</i>
$\begin{aligned} \epsilon_{bid} &= k_s k_{hs} k_f k_{td} \times C_{SH} = 1.20 \times 1.16 \times 1.00 \times \frac{(t_f - t_i)}{45 + (t_f - t_i)} \times C_{SH} \\ &= 1.39 \times C_{SH} \times \frac{(t_f - t_i)}{45 + (t_f - t_i)} \end{aligned}$	Equation D-25
$K_{id} = \frac{1}{1 + \frac{E_p A_{ps}}{E_{ci} A_g} \left(1 + \frac{A_g e_{cl}^2}{I_g} \right) [1 + 0.7 \varphi_B(t_f, t_i)]} \cong 1.00$	Equation D-26
$\varphi_B(t_f, t_i) = C_{CR} \times k_s k_{hc} k_{td} t_i^{-0.118}$	Equation D-27
$k_s = 1.45 - 0.13 \frac{V}{S} = 1.45 - 0.13 \times 1.92 = 1.20$	Equation D-28

$k_{hs} = 2.00 - 0.014H = 2.00 - 0.014 \times 60 = 1.16$	Equation D-29
$k_{hc} = 1.56 - 0.008H = 1.56 - 0.008 \times 60 = 1.08$	Equation D-30
$k_f = \frac{5}{1+f_{ci}} = \frac{5}{1+4} = 1.00$	Equation D-31
$k_{td} = \frac{(t_f - t_i)}{61 - 4f_{ci}' + (t_f - t_i)} = \frac{(t_f - t_i)}{61 - 4 \times 4 + (t_f - t_i)} = \frac{(t_f - t_i)}{45 + (t_f - t_i)}$	Equation D-32
$\Delta f'_{pSR} = 1.50 \times C_{SH} \times \frac{(t_f - t_i)}{45 + (t_f - t_i)} \times E_p$	Equation D-33

D.3.a.(3) Creep deformation, proposed equation

All components calculated using Equation D-34 to Equation D-41, and the assumed conditions in Section D.3.a are applied to Equation D-13 to obtain Equation D-42.

In AASHTO 2008, 1.9 is used as the constant (C_{CR}) for creep coefficient (ϕ_B). However, in Equation D-42, the constant C_{CR} is left unknown, and will be derived through numerical analysis of monitoring data. Moreover, a constant of 10.4 in Equation D-12 is rounded to 10.5 in Equation D-42 for simplicity.

$\Delta f_{pCR} = 10.4 \times \frac{f_{pr} A_{ps}}{A_g} \times C_{CR} \times \frac{(t_f - t_i)}{45 + (t_f - t_i)} \times 1.0$	<i>Equation 5-13</i>
$\frac{E_p}{E_{ci}} = \frac{2,8500}{(57,000 \sqrt{4,000}) \times 10^{-3}} \cong 8.0$	Equation D-34
$f_{cgp} = \frac{f_{pr} A_{ps}}{A_g}$	Equation D-35
$\begin{aligned} \phi_B(t_f, t_i) &= C_{CR} \times k_s k_{hc} k_{td} t_i^{-0.118} \\ &= C_{CR} \times 1.20 \times 1.08 \times \frac{(t_f - t_i)}{45 + (t_f - t_i)} \times 1^{-0.118} \\ &= 1.30 \times C_{CR} \times \frac{(t_f - t_i)}{45 + (t_f - t_i)} \end{aligned}$	Equation D-36
$k_s = 1.45 - 0.13 \frac{V}{S} = 1.45 - 0.13 \times 1.92 = 1.20$	Equation D-37
$\frac{V}{S} = \frac{8 \times 12 \times 4 \times 8 \times 12}{(8 \times 12 + 4) \times 2 \times 8 \times 12} = 1.92$	Equation D-38

$k_{hc} = 1.56 - 0.008H = 1.56 - 0.008 \times 60 = 1.08$	Equation D-39
$k_f = \frac{5}{1+f_{ci}} = \frac{5}{1+4} = 1.00$	Equation D-40
$k_{id} = \frac{(t_f - t_i)}{61 - 4f_{ci}' + (t_f - t_i)} = \frac{(t_f - t_i)}{61 - 4 \times 4 + (t_f - t_i)} = \frac{(t_f - t_i)}{45 + (t_f - t_i)}$	Equation D-41
$\Delta f'_{pCR} = 10.5 \times C_{CR} \times \frac{f_{pr} A_{ps}}{A_g} \times \frac{(t_f - t_i)}{45 + (t_f - t_i)}$	Equation D-42

D.3.a.(4) Relaxation, proposed equation

AASHTO 2008 and PCI design Handbook suggest calculating prestress loss due to relaxation by using Equation D-14 and Equation D-21. In these two design specifications, the loss due to relaxation is considered as constant. In the proposed equation, the prestress loss due to relaxation is ignored, because relaxation effects are generally very small and can be ignored in calculation of prestress losses. Total prestress loss, proposed equation

By combining all components explained in Section in Section D.3.a, the final form of an equation for predicting prestress loss in PCPs is shown in Equation D-43. The first term refers to prestress loss due to shrinkage, and the second term refers to prestress loss due to creep. In the equation, it is assumed that the stress in strands immediately after transfer (f_{pt}) has the same value as the initial applied prestress (f_{pi}) because no change was observed in prestress value right after transfer in the tests of this study. The third term refers to prestress loss due to elastic shortening. Its value is 5.0 ksi when initial prestress is 189.4 ksi and 4.5 ksi when initial prestress is 169.4 ksi.

$\Delta f'_{pT} = (\Delta f'_{pSR} + \Delta f'_{pCR})_{id} + \Delta f'_{pES}$ $= 1.50 C_{SH} \frac{(t_f - t_i)}{45 + (t_f - t_i)} E_p + 10.5 C_{CR} \frac{f_{pr} A_{ps}}{A_g} \frac{(t_f - t_i)}{45 + (t_f - t_i)} + \Delta f'_{pES}$	Equation D-43
---	----------------------

D.3.b: Derivation of constants, proposed equation

Values of the constants C_{SH} and C_{CR} for PCPs in Equation D-43 were derived by numerical analysis (curve fitting), conducted using the software, IGOR Pro 6.11 (<http://www.wavemetrics.com>).

Two panels from Plant A (limestone) and two panels from Plant B (river gravel) were used to obtain constant values, C_{SH} and C_{CR} . All four panels had an initial prestress of 189.4 ksi.

Figure D-2 and Figure D-3 show results of curve-fitting for panels from both plants. The x-axis is based on $t/(45+t)$, and the y-axis is the prestress loss, where t equals to $t_f - t_i$, t_f is the age after casting, and t_i is the age at transfer after casting. Panels from Plant B were monitored for almost two years. However, the data were not measured from about 1 month to 5 months after casting, so the data for 1 month was used for deriving constant values C_{SH} and C_{CR} of Plant B.

Black-dashed lines in Figure D-2 and Figure D-3 indicate that the best curves for Panel 1 of Plants A and B. Red-dashed lines in both figures indicate the best-fit curves for Panel 2 of both plants. As shown in Figure D-2, the best-fit curves of the panels from Plant A are almost identical. The resultant values of C_{SH} and C_{CR} for Panel are shown in the top box, and the values for Panel 2 are shown in the bottom box in both figures.

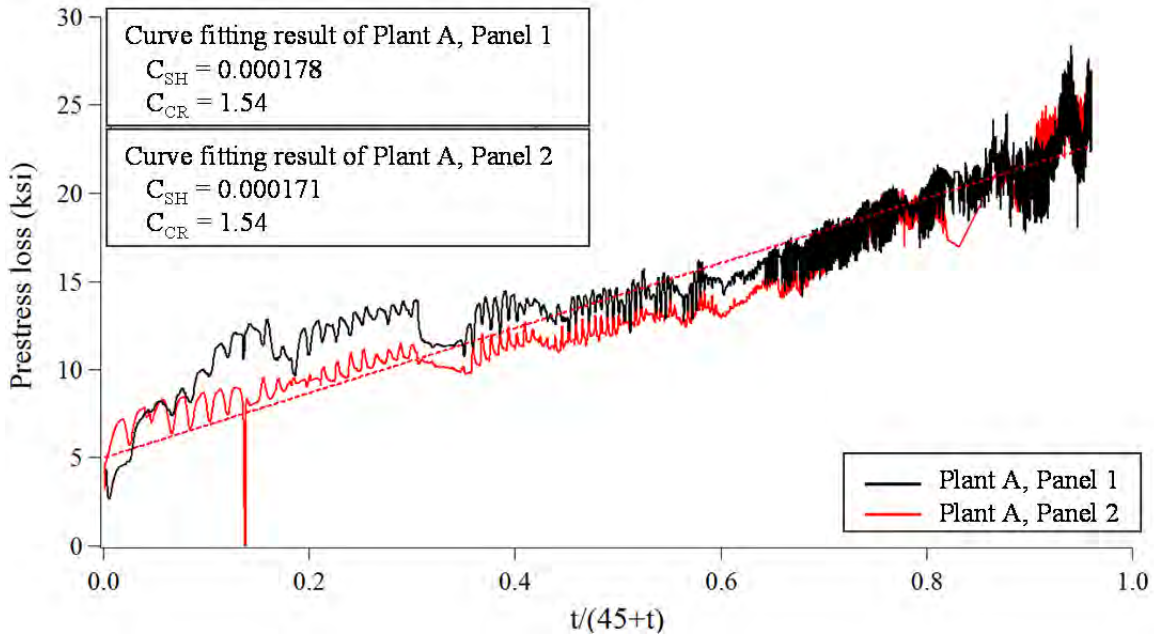


Figure D-2: Curve fitting result for Plant A

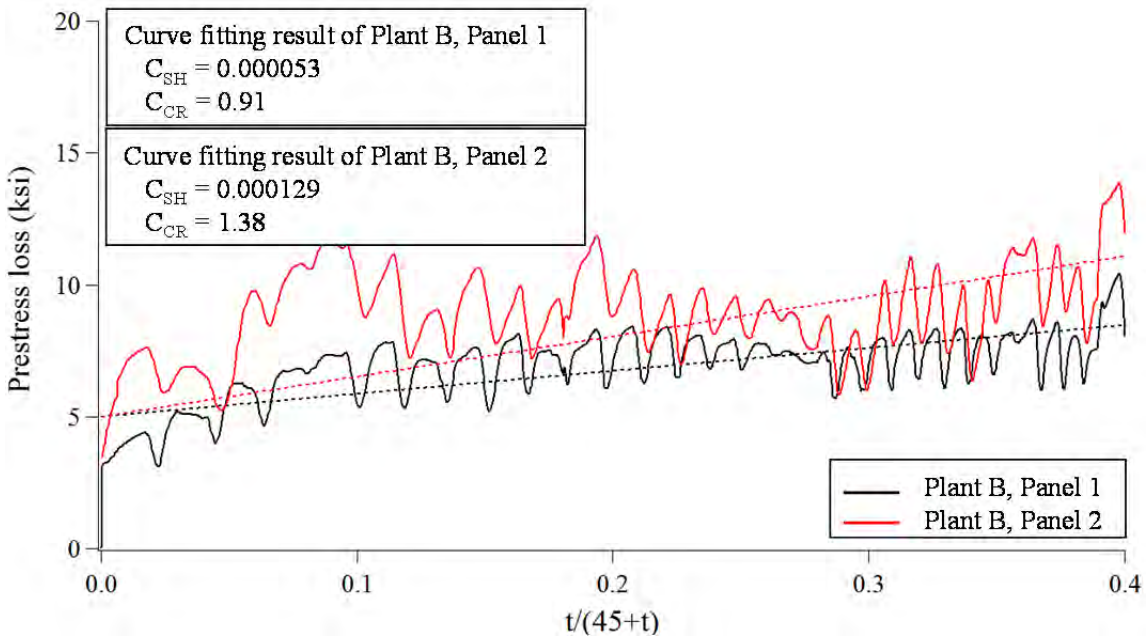


Figure D-3: Curve fitting result for Plant B

Table D-1: Resultant values for constants C_{SH} and C_{CR}

Constants	Values
C_{SH}	180 x 10 ⁻⁶ for limestone, Plant A 90 x 10 ⁻⁶ for river gravel, Plant B
C_{CR}	1.55 for limestone, Plant A 1.15 for river gravel, Plant B

The resultant values for the constants C_{SH} and C_{CR} are shown in Table D-1. Those values were obtained by calculating average values of two panels from each plant. Therefore the best-fit curves for each plant using the values in Table D-1 will be located between two dashed lines shown in Figure D-2 and Figure D-3.

D.3.c: Propose new equation for predicting prestress loss in PCPs

Based on the results from Section D.3.a and Section D.3.b, a new equation for predicting prestress loss in PCPs is proposed. The final form for the proposed equation is shown in Equation D-44. All constant values and parameters for the proposed equation are listed in Table D-2.

$$\Delta f_{pT} = 1.50C_{SH} \frac{(t_f - t_i)}{45 + (t_f - t_i)} E_p + 10.5C_{CR} \frac{f_{pt} A_{ps}}{A_g} \frac{(t_f - t_i)}{45 + (t_f - t_i)} + C_{ES} \quad \text{Equation D-44}$$

Table D-2: Constant values and parameters for Equation 5-45

Constants & Parameters	Values & Definitions
C_{SH}	180 × 10 ⁻⁶ for limestone 90 × 10 ⁻⁶ for river gravel
C_{CR}	1.55 for limestone 1.15 for river gravel
C_{ES}	5.0 ksi for $f_{pi}=189.4$ ksi (Current TxDOT initial prestress) 4.5 ksi for $f_{pi}=169.4$ ksi (Reduced initial prestress)
t_f	final age at transfer after casting (days)
t_i	age at transfer after casting (days)
E_p	modulus of elasticity of prestressing steel (ksi)
f_{pt}	stress in prestressing steel immediately after transfer (ksi)
A_{ps}	area of prestressing steel (in. ²)
A_g	gross area of section (in. ²)

D.3.d: Verification of proposed equation

To verify the proposed equation, measured and predicted values were compared using four Current TxDOT initial prestressed panels and eight Reduced initial prestressed panels. All

Current TxDOT initial prestressed panel from Plant A were used for derivation of C_{SH} and C_{CR} , so the same panels were used for deriving constants and for verifying the proposed equation in this case. However, the panels used for verifying the model and the panels for the derivation were different for the Current TxDOT initial prestressed panel from Plant B. Results of all twelve panels are similar; the result of one panel for each case is shown in Figure D-4 to Figure D-7. In those figures, the purple solid lines represent a new lump-sum prestress loss of 25 ksi as proposed by Foreman (2010). The results obtained from Figure D-4 to Figure D-7 are as follows:

- i) The proposed equation gives better estimates than the others.
- ii) As shown in Figure D-4 and Figure D-6, the PCI design code and the proposed equation give similar prediction result for the panels cast in Plant A (limestone).
- iii) The TxDOT design specifications and the AASHTO code predict prestress losses much greater than those observed in this study.
- iv) A new lump-sum value of 25 ksi is conservative for the panels with current TxDOT initial prestress (189.4 ksi) and reduced initial prestress (169.4 ksi).

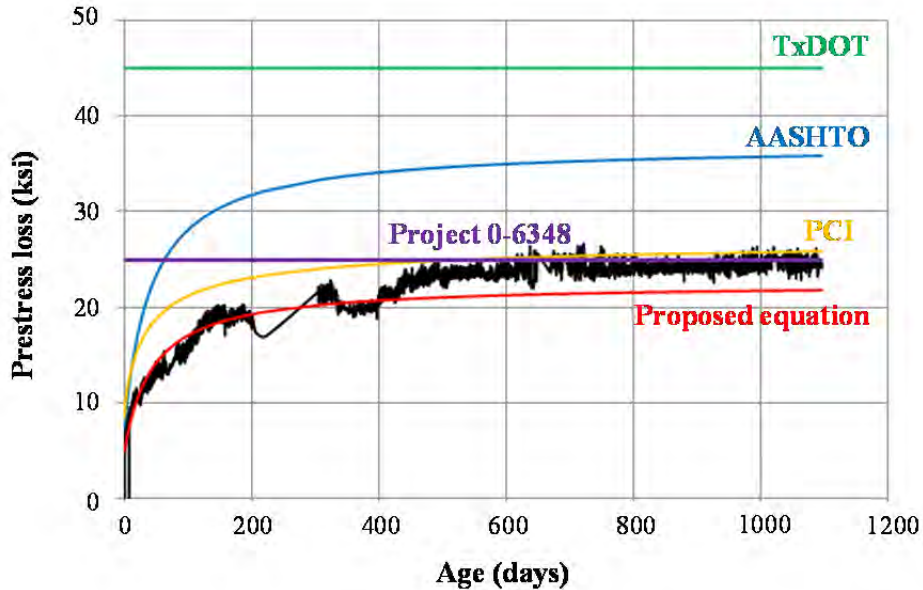


Figure D-4: Measured and predicted prestress losses, current TxDOT initial prestress, Plant A

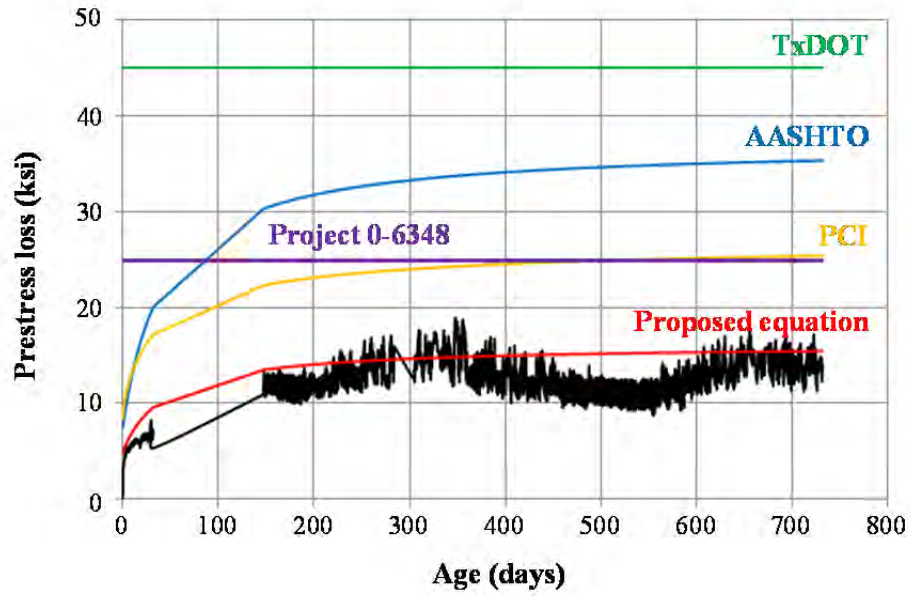


Figure D-5: Measured and predicted prestress losses, current TxDOT initial prestress, Plant B

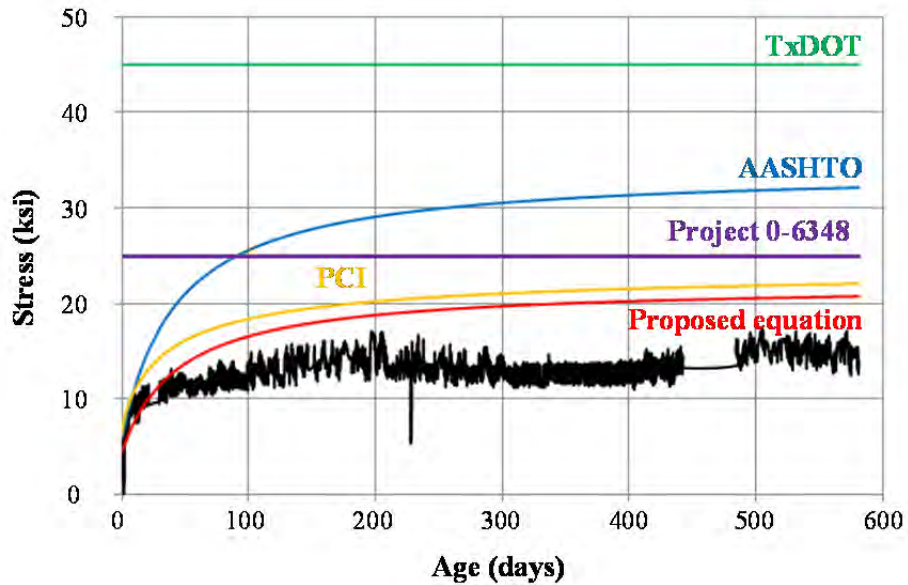


Figure D-6: Measured and predicted prestress losses, reduced initial prestress, Plant A

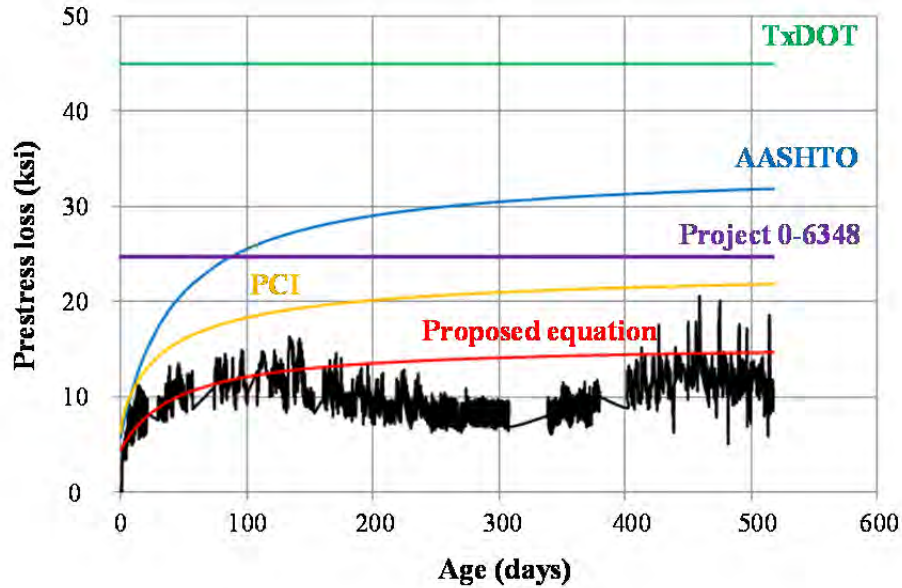


Figure D-7: Measured and predicted prestress losses, reduced initial prestress, Plant B

D.3.e: Accuracy of proposed equation

The accuracy of the proposed equation is evaluated and compared with that of the AASHTO 2008, PCI, and TxDOT methods, using four statistical methods:

- i) Residual method
- ii) CEB coefficient of variation (V_{CEB} %) method
- iii) CEB mean square error (F_{CEB} %) method
- iv) CEB mean deviation (M_{CEB}) method

D.3.e.(1) Residual method

The residual method is one of the simplest methods for determining accuracy of a model. Residual values are calculated by subtracting predicted values from measured values. If the calculated residual values are negative, predicted values are smaller than measured values, so the model underestimates the values. If the residual values are positive, predicted values are bigger than measured values, so the model overestimates the values (Al-Manaseer and Lam 2005).

D.3.e.(2) CEB coefficient of variation (V_{CEB} %) method

The CEB coefficient of variation method was suggested by Muller and Hilsdorf (1990). Equations for the method are stated below:

$$Y_i = \frac{\sum_{i=1}^n Y_{ij}}{n}$$

Equation D-45

$$S_i = \sqrt{\frac{1}{n-1} \sum_{j=1}^n (\Delta Y_{ij})^2}$$

Equation D-46

$$V_i = \frac{S_i}{Y_i} \times 100$$

Equation D-47

$$V_{CEB} = \sqrt{\frac{1}{N} \sum_{i=1}^N V_i^2}$$

Equation D-48

Where,

n	= number of differences (data points) taken in each set, j
N	= total number of data sets considered
S_i	= standard error determined from ΔY_{ij} for experiment i
V_i	= COV of experiment i
V_{CEB}	= mean COV
Y_i	= mean value from experiment
Y_{ij}	= measured value at time j of experiment i
ΔY_{ij}	= difference between observed and predicted values at time j of experiment i

D.3.e.(3) CEB mean square error (F_{CEB} %) method

This method was proposed by Muller and Hilsdorf (1990). Smaller values of F_{CEB} denote more accurate results. By using the following equations, F_{CEB} could be calculated.

$$f_j = \frac{(Cal X_{ij} - Obs X_{ij})}{Obs X_{ij}} \times 100$$

Equation D-49

$$F_i = \sqrt{\frac{1}{n-1} \sum_{j=1}^n f_j^2}$$

Equation D-50

$$F_{CEB} = \sqrt{\frac{1}{N} \sum_{i=1}^N F_i^2}$$

Equation D-51

Where,

$Cal X_{ij}$	= predicted value of time j of experiment i
$Obs X_{ij}$	= experimental value of time j of experiment i
f_j	= percent difference between calculated and observed data

	point j
F_i	= mean square of residuals, %
F_{CEB}	= mean square of error, %
n	= total number of values j of experiment i considered at a fixed time
N	= total number of data sets considered

D.3.e.(4) CEB mean deviation (M_{CEB}) method

This method was also suggested by Muller and Hilsdorf (1990). If the value of M_{CEB} is less than 1.0, the model underestimates values. If the value of M_{CEB} is bigger than 1.0, the model overestimates values.

$$M_i = \frac{1}{n} \sum_{j=1}^n \frac{Cal X_{ij}}{Obs X_{ij}} \quad \text{Equation D-52}$$

$$M_{CEB} = \frac{\sum_{i=1}^N M_i}{N} \quad \text{Equation D-53}$$

Where,	$Cal X_{ij}$	= predicted value of time j of experiment i
	$Obs X_{ij}$	= experimental value of time j of experiment i
	M_i	= deviation between predicted values and experimental values of experiment i
	M_{CEB}	= mean deviation
	n	= total number of values j of experiment i considered at a fixed time
	N	= total number of data sets considered

D.3.e.(5) Results for accuracy of proposed equation

Two Current TxDOT initial prestressed panels and eight Reduced initial prestressed panels were used for estimating the accuracy of the proposed equation. Two Current TxDOT initial prestressed panels were made in Plant B. Among the eight Reduced initial prestressed panels, four were made in Plant A, and four panels were made in Plant B. The initial prestress level of the Current TxDOT initial prestressed panel is 189.4 ksi, and that of the Reduced initial prestressed panel is 169.4 ksi. Plant A used limestone and Plant B used river gravel as coarse aggregate. All Current TxDOT initial prestressed panels made in Plant A were used in the derivation of the constants in the proposed equation, so those panels were not included in the analysis of accuracy.

Table D-3 shows a summary of the residual method, and Table D-4 shows a summary of other statistical analysis results including CEB coefficient of variation (V_{CEB} %), CEB mean square error (F_{CEB} %) and CEB mean deviation (M_{CEB}) method.

As shown in Table D-4, all statistical values of the proposed equation are smaller than that of any other existing models: AASHTO, PCI, and TxDOT. It means that the proposed equation has less variability and more accuracy than those other models.

Plant A shows less variability (V_{CEB} , F_{CEB} , and M_{CEB}) than Plant B. This indicates that the concrete properties of Plant A are more uniform than the properties of Plant B. This result is caused by different type of aggregate. Carrasquillo, Nilsson, and Slate (1981) observe that the concrete with limestone has more uniform material properties than the concrete with river gravel because of smaller micro-cracks caused by higher bond strength between aggregate and mortar.

Table D-3: Comparative accuracy by residual method

	Plant	Specification	Range of values		Percentage of negative values	Percentage of positive values
			Min.	Max.		
Current TxDOT (189.4 ksi)	B (river gravel)	Proposed	-5.0	12.5	11.2	88.9
		PCI	0.0	22.5	0.0	100.0
		AASHTO	0.0	27.5	0.0	100.0
		TxDOT	25.0	45.0	0.0	100.0
Reduced (169.4 ksi)	A (limestone)	Proposed	-6.5	15.0	24.1	75.9
		PCI	-5.0	15.0	2.6	97.4
		AASHTO	-3.8	25.0	1.4	98.6
		TxDOT	22.5	45.0	0.0	100.0
	B (river gravel)	Proposed	-5.0	13.8	15.8	84.2
		PCI	0.0	21.3	0.0	100.0
		AASHTO	0.0	30.0	0.0	100.0
		TxDOT	26.3	45.0	0.0	100.0

Table D-4: Summary of statistical analysis results for accuracy

Method	Specification	Current TxDOT (189.4 ksi)	Reduced (169.4 ksi)	
		Plant B (river gravel)	Plant A (limestone)	Plant B (river gravel)
V_{CEB} %	Proposed equation	30.80	32.77	56.68
	PCI	93.07	42.62	123.14
	AASHTO 2008	185.51	97.60	211.78
	TxDOT	322.61	257.07	423.26
F_{CEB} %	Proposed equation	60.10	402.80	895.71
	PCI	145.30	614.87	1382.90
	AASHTO 2008	196.64	546.49	1243.85
	TxDOT	144606.32	3660.45	8576.78
M_{CEB}	Proposed equation	1.28	1.00	1.56
	PCI	2.16	1.46	2.36
	AASHTO 2008	2.80	1.90	3.23
	TxDOT	4.78	4.31	6.13

Appendix E. Standard Test Methods for Fiber-Reinforced Concrete

E.1. Overview

The evaluation of the properties of fiber-reinforced concrete (FRC) composites is essential to the effective and economical use of these materials in design and construction practice. Some properties, such as compressive strength and freeze-thaw resistance, are largely matrix-dependent, and can be measured by methods commonly used for conventional concrete mixtures. However, the properties of the composite are much more dependent on the presence, proportion, and properties of the fiber phase as well as the fiber-matrix interactions. It is the *composite properties* that are of greatest interest for FRC materials and engineering purposes, because they can be used to quantify the effectiveness of fibers, the ductility of the composite, and the resistance offered by the material against crack propagation. These characteristics are generally undetectable by methods intended for standard concrete mix designs, and must be evaluated by test methods sensitive to the addition of fibers and capable of reflecting the composite behavior. It has been recommended that such processes used to describe key parameters of FRC should ideally satisfy the following criteria (Mindess, Young and Darwin 2003):

- i. It should have a physical meaning that is both understandable and of fundamental significance if it is to be used for the specification or quality control of FRC.
- ii. The “end-point” used in the calculation of the toughness parameters should reflect the most severe serviceability conditions anticipated for the particular application.
- iii. The variability inherent in any measurement of concrete properties should be low enough to give acceptable levels of both within-batch and between-laboratory precision.
- iv. It should be able to quantify at least one important aspect of FRC behavior such as tensile strength, toughness (residual strength), and crack resistance; and reflect some characteristics of the load-deflection curve.
- v. It should be as independent as possible of the specimen size and geometry.

Various test methods exist to evaluate the performance characteristics of FRC in a way that satisfies the above criteria. Most are used privately by fiber producers or in research fields, but a select minority have been refined and published by national and international agencies such as the American Society for Testing and Materials (ASTM), the European Federation of National Associations of Specialist Representing Concrete (EFNARC), the Japan Society of Civil Engineers (JSCE), and the International Union of Laboratories and Experts in Construction Materials, Systems, and Structures (RILEM). Several attempts have been made over the years to quantify the behavior of FRC in terms of parameters that can be used for comparing different fiber types and contents, as well as for specifications and quality control. The test methods presented in this chapter represent those most commonly used to achieve this result. The general scope, significance, and use of these methods are summarized, followed by a discussion of their limitations that are of particular importance to this research.

E.1.a: ASTM C496: Standard Test Method for Splitting Tensile Strength of Cylindrical Concrete Specimens

This test method is used to determine the splitting tensile strength of cylindrical concrete specimens, such as molded cylinders and drilled cores (ASTM C496 2011). The *Splitting Tensile Test*, as it is commonly called, consists of applying a compressive force along the diametrical length of a 4 x 8-in. [100 x 200-mm] cylindrical concrete specimen until failure occurs due to indirect tension.

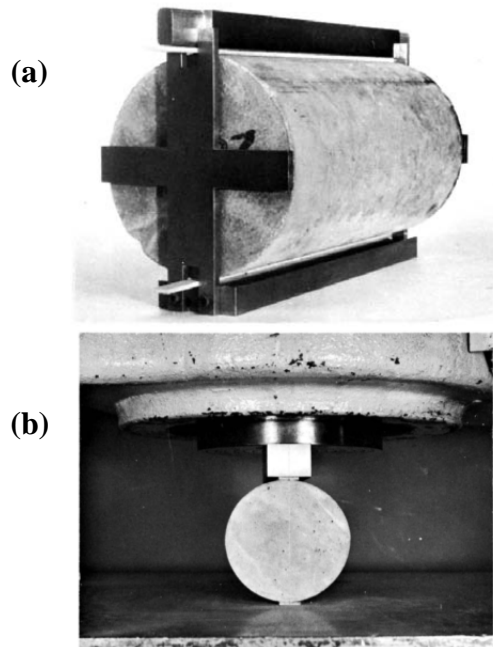


Figure E-1: Test specimen positioned in (a) jig for aligning cylinder and bearing strips and in testing machine for determination of splitting tensile strength (ASTM C496 2011)

Failure occurs in tension rather than compression because the areas of load application are in a state of tri-axial compression, thereby allowing them to withstand much higher compressive stress than a uniaxial compressive stress state. As shown in Figure E-1, thin plywood bearing strips are used to distribute the load applied along the length of the cylinder. The maximum sustained load is divided by the appropriate geometrical factors in Equation E-1 to obtain the splitting tensile strength (ASTM C496 2011).

$$T = 2P/\pi ld$$

Equation E-1

Where:

T = splitting tensile strength, psi [MPa]

P = maximum applied load indicated by the testing machine, lbf [N]

l = length, in. [mm]

d = diameter, in. [mm]

Traditionally, the splitting tensile strength obtained from this test method is used in the design of structural concrete members to evaluate the shear resistance provided by concrete and to determine the required development length of reinforcement. Although less frequently utilized

for fiber-reinforced concrete, some researchers have also used ASTM C496 as an indicator of the tensile capacity of FRC (Folliard and Smith 2003).

The Splitting Tensile Test is reliable and gives consistent results for both in-batch and inter-laboratory tests. Available research data suggests that the within-batch coefficient of variation is 5% for 6 x 12-in. [150 x 300-mm] cylindrical specimens with an average splitting tensile strength of 405 psi [2.8 MPa]. This test uses commonly available equipment, relatively small specimens, and a simple test setup and procedure. Splitting tensile strength is a good indicator of tensile capacity, and correlates well with the performance of conventional concrete structures stressed in tension (ASTM C496 2011).

However, when this test method is extended to FRC, some limitations arise. ASTM C496 concentrates the loading along the diameter of the cylinder, and forces failure to occur along a single, pre-determined plane. This type of loading does not favor fiber-reinforced concrete mixtures. Since fibers are randomly distributed within a given concrete specimen, forcing failure to a single, pre-determined plane reduces the probability that the crack plane will coincide with a plane containing fibers. Moreover, should the crack plane coincide with a plane containing a representative sample of the particular fiber content, there is no guarantee that the fibers will be oriented perpendicular to the crack plane, where they would be most effective.

Also, based on the test arrangement, procedure, and calculations, one is unable to determine the post-cracking behavior which is of greatest concern for FRC composites. ASTM C496 does not provide a means of obtaining the load-deflection curve, and cannot be used to measure or compare the performance of different fiber types and volume fractions except in terms of ultimate tensile capacity.

E.1.b: ASTM C1609: Standard Test Method for Flexural Performance of Fiber-Reinforced Concrete (Using Beam with Third-Point Loading)

This test method evaluates the flexural performance of FRC using parameters derived from the load-deflection curve obtained by testing a simply supported beam using a closed-loop, servo-controlled testing system. Molded or sawn beam specimens having a square cross-section are tested in flexure using a third-point loading arrangement as shown in Figure E-2. Preferred specimen sizes include 4 x 4 x 14-in. [100 x 100 x 350-mm] beam tested on a 12-in. [300-mm] span, or 6 x 6 x 20-in. [150 x 150 x 500-mm] beam tested on an 18-in. [450-mm] span. In this method, the first-peak and the peak loads are determined and the corresponding stresses calculated using the provided formulas. Residual strengths at specified deflections can be calculated similarly. Additionally, ASTM C1609 provides for determination of specimen toughness based on the area under the load-deflection curve up to a prescribed deflection (ASTM C1609 2010).

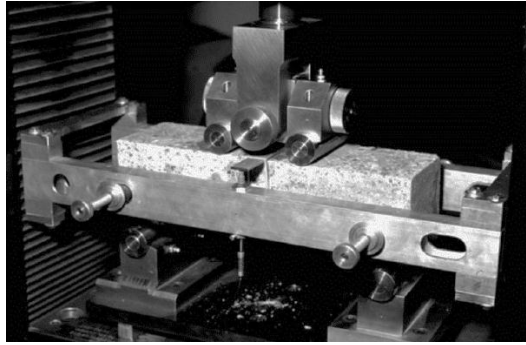


Figure E-2: Beam with three-point loading test setup (ASTM C1609 2010)

Previously denoted as ASTM C1018, and now as ASTM C1609, this test has evolved over the years to address its potential errors and complications. The most prevalent complication is accounting for extraneous deflections that occur due to machine deformations and seating and twisting of the specimen on the supports (Johnston 1995). Currently, testing laboratories can address this complication as they choose (ASTM C1609 2010). One acceptable technique, known as the “Japanese Yoke,” was introduced in the mid-90s by the JSCE, and is widely used for this test method (Chen and Mindess 1995). A schematic of this arrangement and its application is provided in Figures E-3 and E-4.

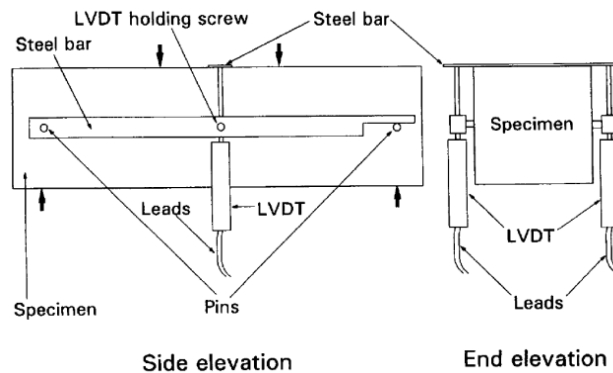


Figure E-3: Schematic of Japanese yoke loading system (Chen and Mindess 1995)

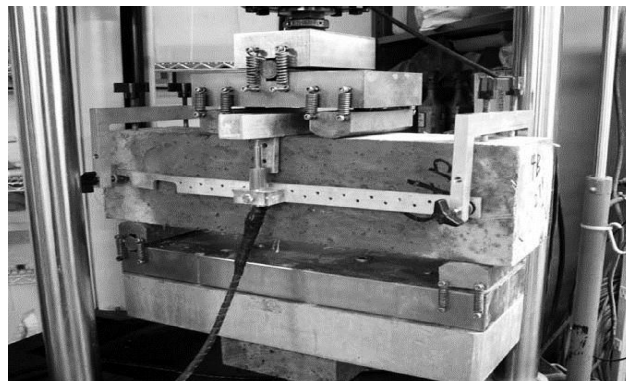


Figure E-4: Test arrangement to obtain net deflection via Japanese yoke loading system (ASTM C1609 2010)

ASTM C1609 provides an advantage over ASTM C496 (Splitting Tensile Test) in that it is useful for describing post-peak behavior of FRC. The experimental results may be used for comparing the performance of various fiber-reinforced concrete mixtures or in research and development work. They may also be used to monitor concrete quality, to verify compliance with construction specifications, to obtain flexural strength data on fiber-reinforced concrete members subject to pure bending, or to evaluate the quality of concrete in service (ASTM C1609 2010).

Although ASTM C1609 can be used for several purposes, it has many disadvantages. For one, although the preferred specimen dimensions result in manageable size test samples, the test method depends on the specimen dimensions. Note (5) of the standard specification clearly states:

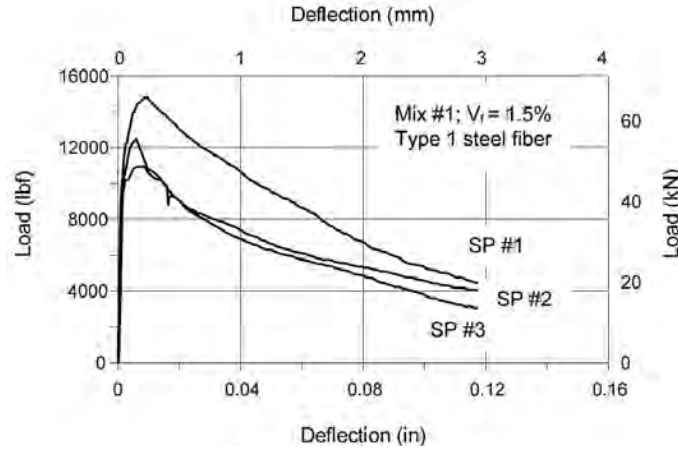
The results obtained from using one size of molded specimen may not correspond to the performance of larger or smaller molded specimens, concrete in large structural units, or specimens sawn from such units (ASTM C1609 2010).

Variations in results may occur due to the degree of preferential fiber alignment within different specimens, but this random orientation is to be expected and should be accounted for in an adequate test method. Similar to the limitations of the Splitting Tensile Test, the random fiber distribution and orientation is unaccounted for due to the failure mechanism inherent in the test. In ASTM C1609, failure of the specimen is also dominated by a *single large crack* in a *well-defined plane*. In fact, if the fracture occurs outside of the middle third of the span, the results are required to be discarded (ASTM C1609 2010). Again, because the fibers are randomly distributed and oriented, the effects that they produce are not well represented by a test in which the failure location is constrained.

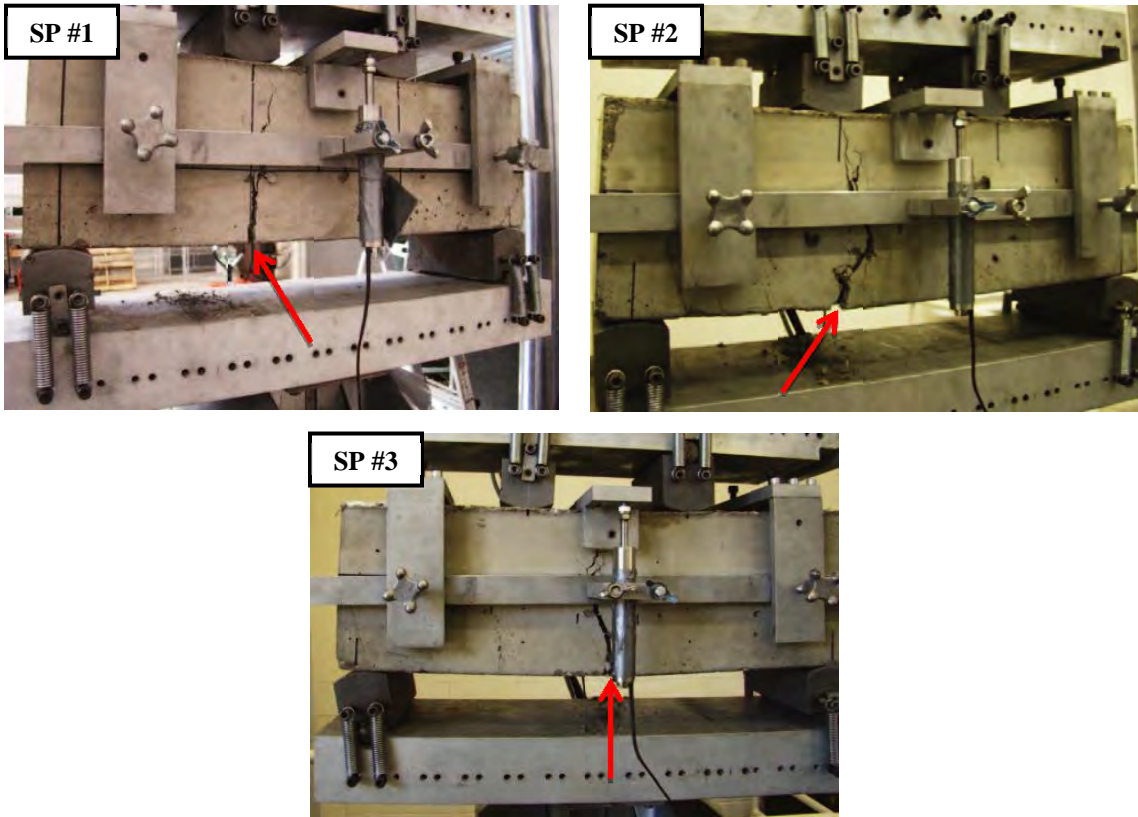
Secondly, the calculated toughness parameters greatly depend on how the point of “first crack” is defined. Thus it is important to determine the load vs. deflection curve very precisely. As a result, a number of difficulties arise (Bentur and Mindess 2007):

1. It is essential to correct for the “extraneous” deflections that occur due to seating of the specimen on the supports and machine deformations. Different laboratories may make these corrections differently, and hence may report different results (Chen and Mindess 1995, ASTM C1609 2010).
2. Because some micro-cracking begins almost immediately upon loading, it is difficult to define the point of first cracking unambiguously.
3. An *instability* often occurs in the measured load vs. deflection curve immediately after the first significant crack, particularly for low toughness FRC, and a servo-controlled operation is required to control the rate of increase of deflection. Closed-loop testing equipment is not always available, and different loading systems can result in quite different calculated toughness values.
4. Due to the uncertainty in determining the point of first cracking and difficulties introduced by the instability previously mentioned, toughness and residual strength parameters are sometimes insensitive to different fiber types or geometries.

Due to these and other factors, toughness and residual strength parameters show considerable scatter. The within-batch coefficient of variation (COV) has been reported from 15% to greater than 20% (ASTM C1609 2010, Bernard 2002, S.-H. Chao 2011). Moreover, reproducibility has yet to be determined (ASTM C1609 2010). Experimental evidence indicated that the high variability is due to the lack of control over the position of the cracks, as well as fiber orientation relative to the major crack plane (S.-H. Chao 2011). The effect of non-uniform fiber distribution on the variation in the load-deflection curves and crack location for replicate specimens can be seen in Figure E-5 (a) and (b), respectively.



(a) Replicate Specimen P- δ



(b) Location of Major Cracks

Figure E-5: Variability of ASTM C1609 for replicate specimens in the (a) load vs. deflection curves and (b) location of major cracks (S.-H. Chao 2011)

Despite the considerable improvements that have been made in ASTM C1609 over the years, this testing procedure still presents major difficulties in accurately describing the behavior of FRC.

E.1.c: ASTM C1399: Standard Test Method for Obtaining Average Residual Strength of Fiber-Reinforced Concrete

This test method covers the determination of the residual strength of a fiber-reinforced concrete test beam. The average residual strength is computed using specified beam deflections that are obtained from the load-deflection curve of a beam that has been cracked in a standard manner (ASTM C1399 2010). Cast or sawed FRC beams having dimensions of 4 x 4 x 14-in. [100 x 100 x 350-mm] are cracked using a third-point loading apparatus similar to that described ASTM C1609, but modified by a steel plate used to support the concrete beam during the initial loading cycle (Figure E-6).

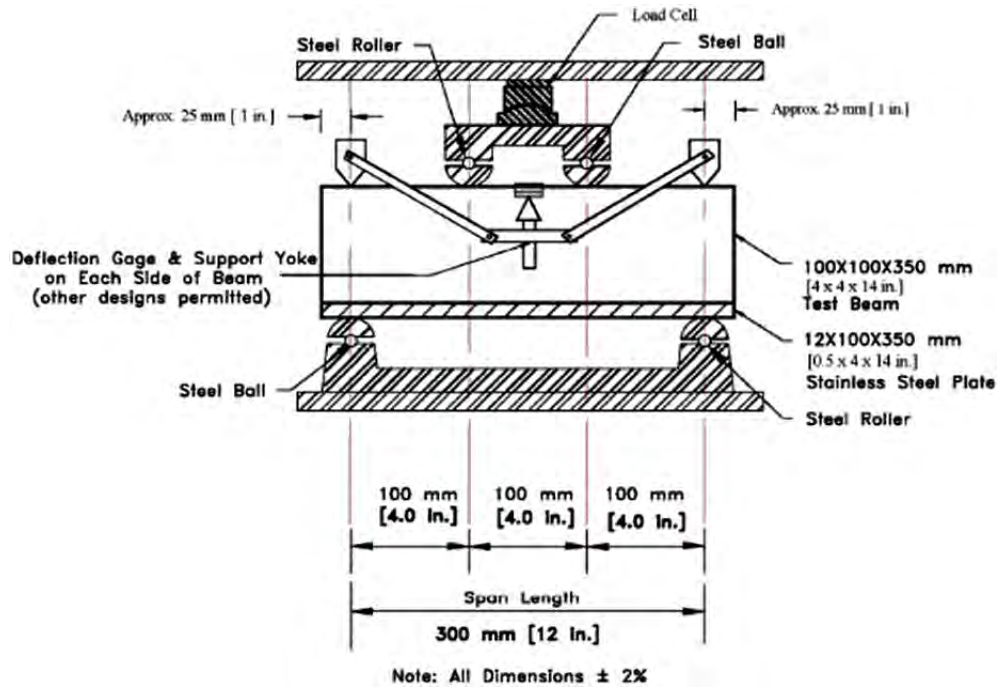


Figure E-6: Schematic of apparatus with stainless steel plate and suitable support frame (ASTM C1399 2010)

As mentioned previously, for low-toughness FRC composites, an unstable condition often occurs in the load-deflection curve after the first major crack forms and begins to open. The steel plate is used in this method to help control the rate of deflection when the beam cracks, thereby eliminating the need for a servo-controlled operation as required by ASTM C1609. After the beam is cracked in the specified manner, the steel plate is removed and the cracked specimen is reloaded to obtain data and plot a reloading load-deflection curve. Load values at specified deflection values on the reloading curve (Figure E-7) are averaged and used to calculate the average residual strength of the beam by Equation E-2 (ASTM C1399 2010).

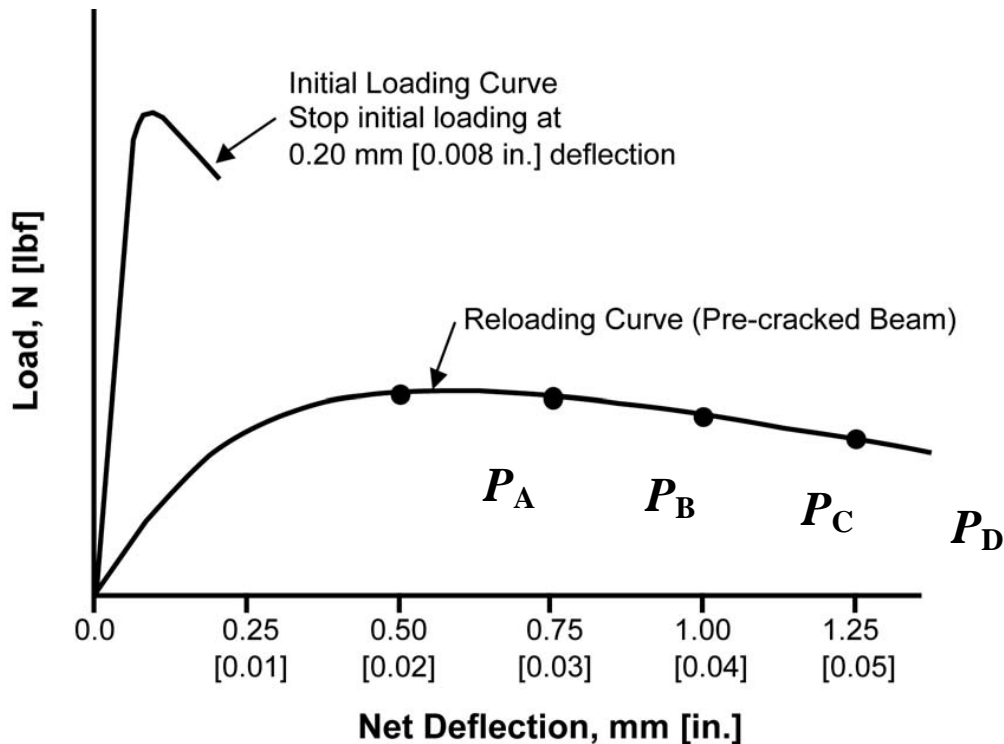


Figure E-7: Typical load-deflection curve (ASTM C1399 2010)

$$ARS = \left(\frac{P_A + P_B + P_C + P_D}{4} \right) * k$$

Equation E-2

Where:

k	= L/bd^2 , in ⁻² [mm ⁻²]
ARS	= average residual strength, psi [MPa]
$P_A + P_B + P_C + P_D$	= sum of recorded loads at specified deflections, lbf [N]
L	= span length, in. [mm]
b	= average width of beam, in. [mm]
d	= average depth of beam, in. [mm]

This test method provides a quantitative measure useful in the evaluation of the performance of fiber-reinforced concrete. Results are intended for comparative analyses of FRC beams and to reflect consistencies or differences among variables used in proportioning the fiber-reinforced concrete to be tested, such as fiber type, fiber size and shape, fiber amount, beam preparation (sawed or molded), and beam conditioning. Results can be used to optimize the proportions of FRC mixtures, to determine compliance with construction specifications, to evaluate FRC which has been in service, and as a research tool. For tests based on studies at ten laboratories on sets of three replicates of four different mixtures, the single-operator coefficient of variation ranged between 13% to 20%, and the multi-laboratory precision was 16% to 44% depending on the fiber content (ASTM C1399 2010).

ASTM C1399 has some advantages over other tests for FRC. Unlike ASTM C496, it is useful for comparing mixtures containing different fiber types and amounts. Also, it uses commonly available equipment, and does not require a servo-controlled machine. In contrast to ASTM 1609, the load-deflection curves that it produces, using the modified steel plate

arrangement, agree closely with those obtained using a displacement-controlled, closed-loop setup (Banthia and Dubey 1999). Therefore, testing can be accomplished using an ordinary universal testing machine. Another benefit of this test method is that preferential fiber alignment is taken into account in a meaningful way. The previously mentioned test methods did not take fiber alignment into account. In ASTM C1399, it is recognized that for molded beams fiber orientation near formed surfaces will be affected by the process of molding. For FRC containing relatively rigid or stiff fibers of length greater than 1.4 in. [35 mm], the use of sawed beams cut from samples with an initial width and depth of at least 3 times the length of the fiber is required to minimize the effects of fiber orientation. When sawed beams are employed, the flexural tensile surface of the beam is required to be a *sawed surface* to avoid the effects of fiber orientation (ASTM C1399 2010). This test condition is shown in the schematic provided in Figure E-8.

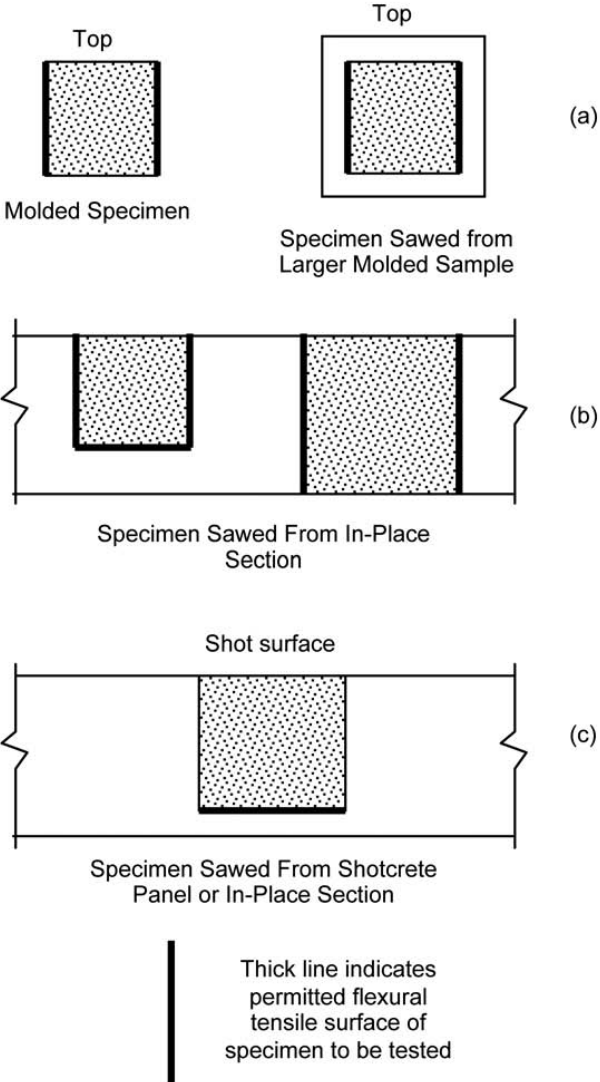


Figure E-8: Schematic of specimen cross sections to indicate permitted flexural tensile surfaces during testing (ASTM C1399 2010)

Although ASTM C1399 addresses some of the difficulties of similar test methods, it has limitations of its own, many of which stem from the application of the steel plate. First, the steel plate adds stiffness to the specimen prior to cracking, which makes it more difficult to estimate the modulus of elasticity (initial slope). Second, the length of the pre-crack obtained prior to the removal of the steel plate is unknown. Thus, for different types of FRC composites, the pre-cracks obtained with this loading system may be of different lengths, making comparisons of the residual capacities between different specimens more complicated since conditions prior to reloading the specimen could vary considerably. Third, the test is useful only for describing a portion of the load-deflection curve: Because the steel plate is removed and the test is stopped after the “first crack” appears, the effect of the fibers on the performance immediately after the first crack is ignored (Bentur and Mindess 2007). As shown in Figure E-9, this lack of data means that a strain-softening composite cannot be distinguished from one that exhibits highly ductile, strain hardening behavior (ASTM C1399 2010).

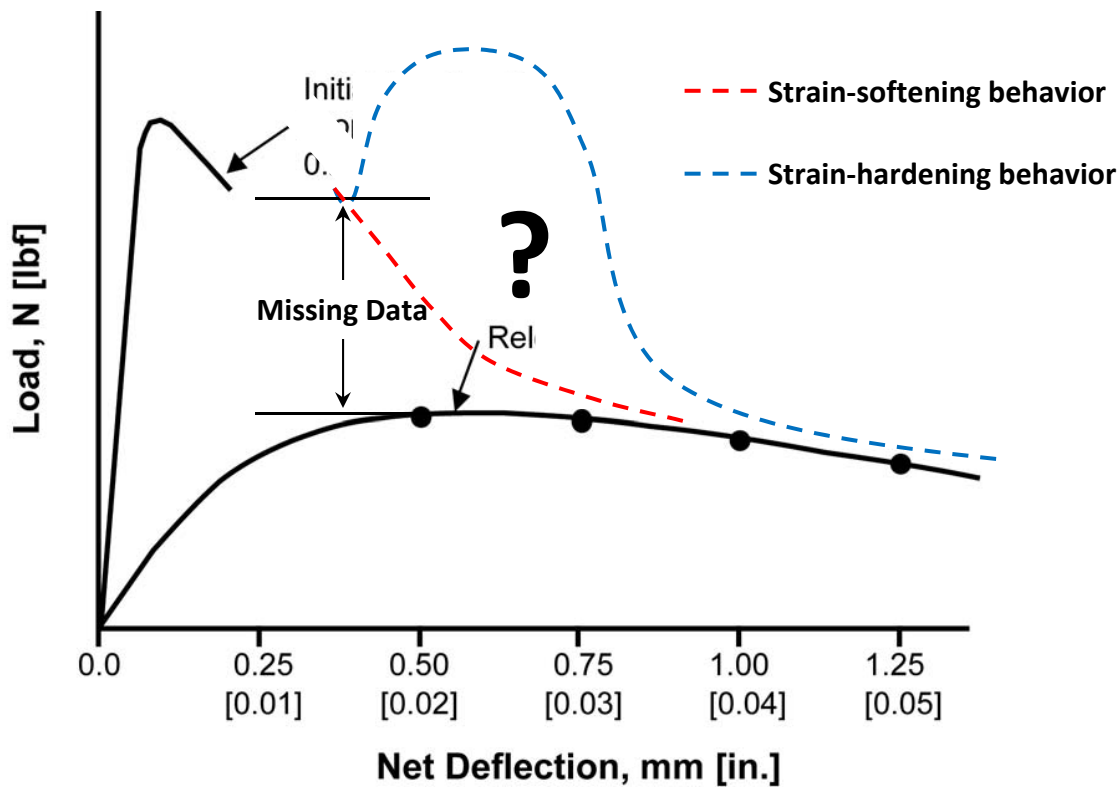


Figure E-9: Effect of steel plate on determining performance immediately after first crack—adapted from (ASTM C1399 2010)

In addition to complexities involving the test arrangement, ASTM C1399 is based on questionable theory related to the determination of the residual strength. Simple beam theory (as required in this method) cannot be used to calculate the strength of a cracked system, so it is unclear what the calculated “residual strengths” mean (Bentur and Mindess 2007). Although sawing the tested surface of the specimen may reduce the effects of fiber orientation, failure is still governed by a *single crack* in a *well-defined* plane, which does not favor any remaining random fiber distribution or alignment.

Although ASTM C1399 is better than its predecessors, the modified test setup (which was originally designed to reduce complexity by eliminating the need for closed-loop operation) presents new drawbacks. The test gives similar precision compared to other bending tests, but does not completely describe the load-deflection behavior of FRC.

E.1.d: ASTM C1550: Standard Test Method for Flexural Toughness of Fiber Reinforced Concrete (Using Centrally Loaded Round Panel)

ASTM C1550 is intended for determination of the flexural toughness of FRC, expressed as energy absorption in the post-cracking range. Molded round panels of cast fiber-reinforced concrete or fiber-reinforced shotcrete are subjected to a central-point load while supported on three symmetrically arranged pivots. The load is applied through a hemispherical-ended steel piston advanced at a prescribed rate of displacement. Load and deflection are recorded simultaneously up to a specified central deflection. The suggested panel support fixture and test arrangement are shown in Figure E-10. The nominal dimensions of the panel are 3-in. [75-mm] in thickness and 31.5-in. [800-mm] in diameter. Molded and shotcrete specimens are cast using steel forms. The use of round panels eliminates the sawing that is required to prepare shotcrete beam specimens. Typical molded and shotcrete construction is shown in Figures E-11 and E-12, respectively (ASTM C1550 2010).

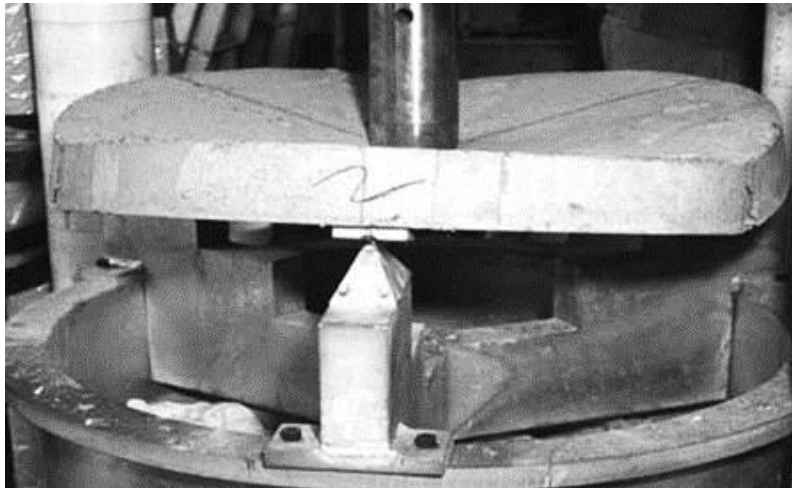


Figure E-10: Testing arrangement using suggested round panel support fixture (ASTM C1550 2010)



Figure E-11: Rolling steel form after molded specimen has gained sufficient strength (ASTM C1550 2010)



Figure E-12: Manual spraying of shotcrete panels (ASTM C1550 2010)

The central deflection of the specimen relative to the support points must be determined in a manner that excludes extraneous deformations of the testing machine and support fixture. This is achieved by one of two methods. As shown in Figure E-13 (a) and (b), if the displacement of the tensile surface at the center of the panel is measured relative to the pivot supports, then the recorded deflections do not need to be corrected. However, if the movement of the loading piston relative to the crosshead of the testing machine is used to measure deflection, the deflection record must be adjusted to discount extraneous deformations. Regardless of the

method of deflection measurement selected, the method requires a servo-controlled testing machine and a displacement transducer with a precision of ± 0.05 -mm (ASTM C1550 2010).

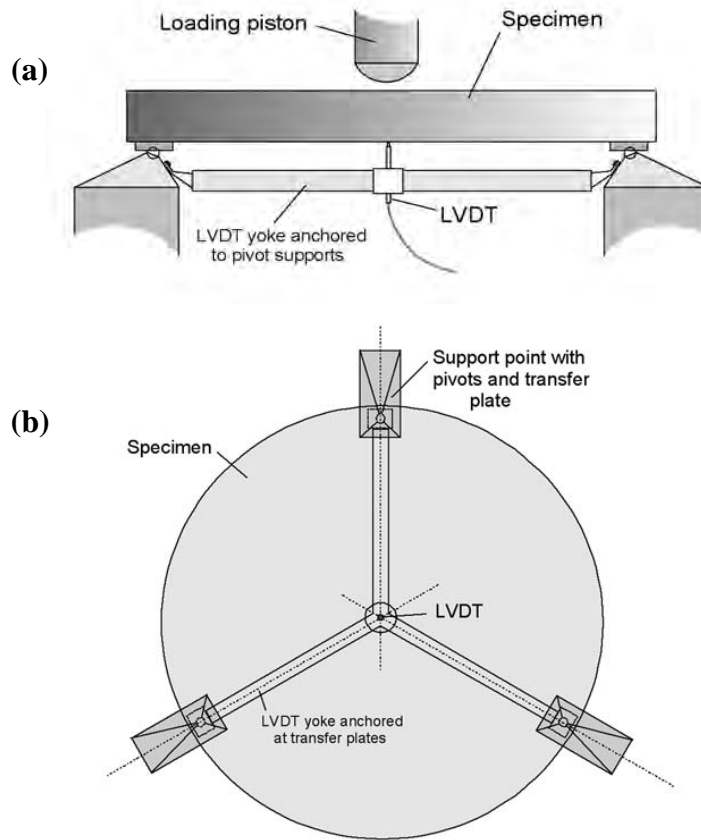


Figure E-13: (a) Profile and (b) plan views of suggested method of deflection measurement to exclude load-train deformations using an LVDT (ASTM C1550 2010)

The performance of specimens tested by ASTM C1555 is quantified in terms of the energy absorbed between the onset of loading and selected values of central deflection of the fiber-reinforced concrete panel. Test panels experience bi-axial bending in response to the central point load and exhibit a mode of failure that can be related to the in-situ behavior of structures. The energy absorbed is taken to represent the ability of an FRC to redistribute stress following cracking (ASTM C1550 2010). The single-operator coefficient of variation for peak load and energy absorption are reported as 6.2% and 10.1%, respectively; the multi-laboratory precision is approximately 9% for the same test parameters (ASTM C1550 2010).

The main advantage of ASTM C1550 over other test methods for FRC is that it appears to discriminate reasonably well between different fiber types and volumes, and does so with a higher degree of precision than other tests. Previous studies indicated that the variation in cracking load, peak load, or energy absorbed up to a specified central deflection from this test is generally lower than bending tests, with a COV between 5% and 13% (Bernard 2002, S.-H. Chao 2011). The reduced scatter in the results could be attributed to the following (S.-H. Chao 2011):

1. Location of cracks as well as crack patterns are less constrained: As seen in Figure E-14 (a) and (b), panels tested by this method almost always split into three segments upon failure, at angles of about 120° .
2. Increased cracked area: the three major cracks give a somewhat average mechanical behavior of the reinforcement that minimizes the influence of non-uniform fiber distribution as well as random fiber orientation.

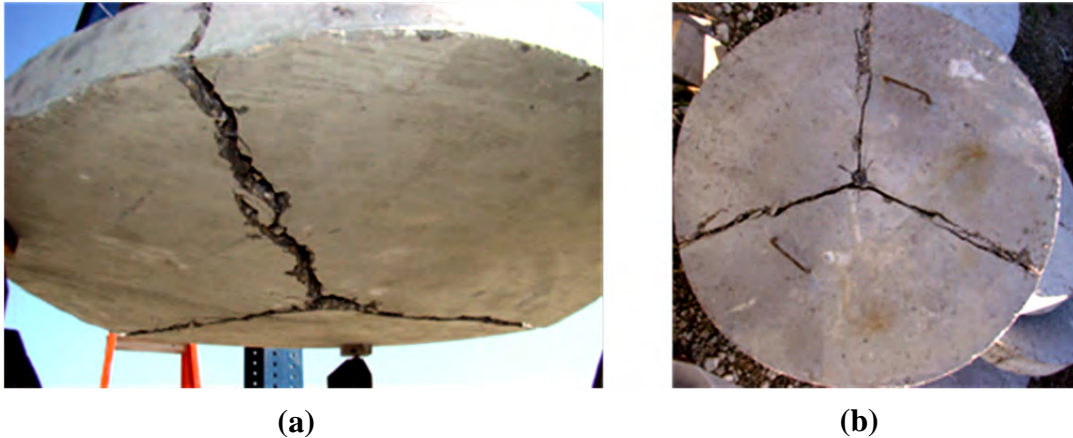


Figure E-14: View from (a) below and (b) above tested round panel specimen showing location of major cracks (S.-H. Chao 2011)

The chief disadvantage of ASTM C1550 is that the specimen itself is too large and too heavy to be easily handled, and does not fit into commonly used test machines (Bentur and Mindess 2007). Each specimen weighs about 200-lb [888-N], and as a result some previous tests were reportedly carried out at 80% scale of the specimen dimensions (S.-H. Chao 2011). Additionally, due to the size of the panel and nature of the test, a closed-loop servo-controlled test machine is required to avoid unstable behavior after cracking (ASTM C1550 2010).

As seen in Figure E-15, another complication can occur if the crack opening at the center of the panel near the location of the LVDT exceeds the probe width of the LVDT (S.-H. Chao 2011). The probe can slip into the crack, resulting in errors in deflection measurements.



Figure E-15: View of underside of ASTM C1550 test specimen showing crack width vs. LVDT probe width at location of LVDT (S.-H. Chao 2011)

In ASTM C1550, it is suggested that using an LVDT with a maximum probe width of 0.8-in. [20-mm] can alleviate this problem. Greater probe widths are not recommended because off-center cracks may induce exaggerated apparent deflections if they occur adjacent to a wide probe (ASTM C1550 2010). However, even if the maximum probe width is used, the opening at the center could be greater than 0.8-in. [20-mm] at large deflections, which may lead to incorrect measurements of displacement (S.-H. Chao 2011).

The size of the specimen, the need for a servo-controlled machine, and the intricate support fixtures required by ASTM C1550 combine to make this test method difficult. More effort is required to achieve the same results (with slightly better accuracy) as with other less complicated procedures.

E.1.e: Other Test Methods Proposed for Determination of the Toughness of FRC

Among the many other test methods that have been proposed for the determination of the toughness of FRC, two are worth mentioning here.

E.1.e.(1) EFNARC Panel Tests (Using Square Panel)

The EFNARC square panel test is possibly the most widely known panel-based assessment procedure. Though often used in Europe as an alternative to beam-based toughness testing, it is rarely used in North America. ASTM C1550, the US alternative, correlates well with results from the EFNARC test (Bernard 2002, Bentur and Mindess 2007). Because shotcrete linings are often required to resist point loads, it is rational in some situations to quantify the performance of competing mix designs by applying a point load to a panel that represents a portion of a continuous lining (Bernard 2002). The EFNARC test involves the application of a central point load to a 4 x 24 x 24-in. [100 x 600 x 600-mm] square panel simply supported on a 20 x 20-in. [500 x 500-mm] flat square base (EFNARC 1996). The test specimen alone weighs about 200-lb. A simple schematic of this test is shown in Figure E-16.

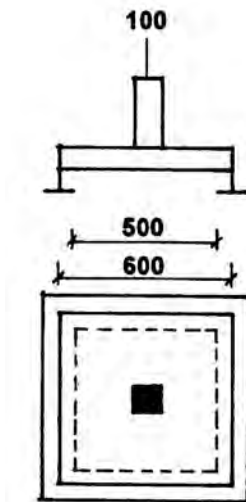


Figure E-16: Setup for EFNARC panel test (EFNARC 1996)

Although this test is widely accepted in Europe and elsewhere, it suffers from a number of shortcomings. The most significant is the difficulty entailed in trying to produce a specimen

with a perfectly planar base, so that the specimen will have simple and uniform support around the perimeter of the test fixture. Such a flat specimen typically produces a load-displacement curve with a single peak, and maximum possible performance is quantified in terms of energy absorption between the start of loading and a total central deflection of 1-in. [25-mm]. A specimen that is not flat will deform unpredictably, and will often display multiple peaks in load capacity as stress is redistributed around the progressively failing panel. This compromises the usefulness of the test (Bernard 2002).

E.1.e.(2) Uniaxial Direct Tensile Test

A uniaxial DTT can identify the key properties of FRC, such as strain-hardening or strain-softening, elastic modulus, and tensile stress-strain relationships, which are useful for modeling and design of FRC structural members (Naaman 2007). Currently, there is no standard method for this test in the U.S., in part because it is difficult to provide a gripping arrangement that precludes specimen cracking at the grips (S.-H. Chao 2011). Test specimens have “dog-bone” geometry (Figure E-17) with an overall length of 23-in. [584-mm], a uniform thickness of 4-in. [102-mm], a flange width of 8-in. [203-mm], and a web width of 4-in. [102-mm].

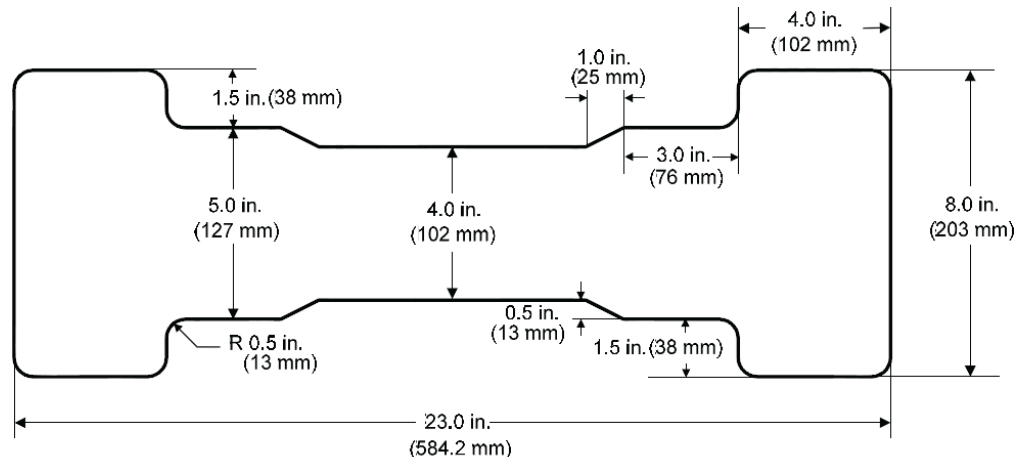


Figure E-17: Uniaxial DTT specimen dimensions (S.-H. Chao 2011)

Specimens evaluated by this test method are specifically designed to create a pinned-pinned loading condition at the ends. The advantages of this end condition and specimen geometry are (S.-H. Chao 2011):

1. A pure axial load is applied in tension;
2. No specific treatment such as adhesives is needed to fix the ends to the test setup;
3. Both ends of the specimen are strengthened by steel meshes to ensure that cracking will occur only within the central portion.

Strains are measured by a pair of LVDTs with gauge lengths of about 7-in. [178-mm]. Tests can be facilitated using closed-loop, servo-controlled machine with a loading rate of approximately 0.002 inches per minute [0.05 mm/min] (S.-H. Chao 2011).

Figure E-18 (a) and (b) show the dog-bone mold and typical test arrangement for specimens.

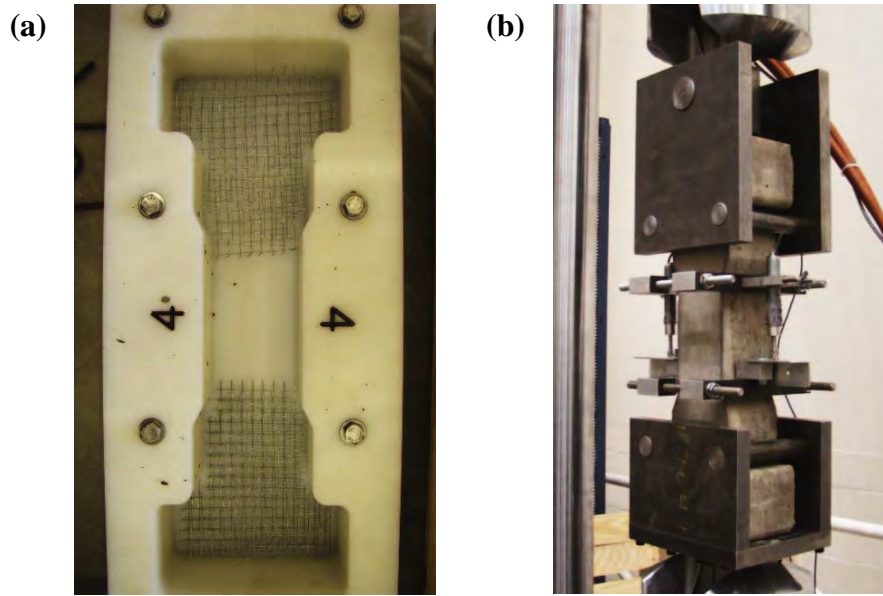


Figure E-18: Uniaxial DTT: (a) mold and (b) testing arrangement (S.-H. Chao 2011)

Unfortunately, the major drawback of this test (like others that constrain failure to a single major crack in a well-defined plane) is that it provides only a localized description of the FRC behavior, rather than an average or broad description. Figure E-19 displays the typical response of two replicate tensile test specimens with 1.5% fiber content. Figure E-20 shows the various locations of the major cracks in four replicate specimens. These images confirm that the dog-bone geometry and steel-mesh reinforcement at the ends generally do confine the major cracks to the narrow portion of the specimen. Crack locations are inconsistent, however, and crack-propagation paths are not controlled. As shown in Figure E-19, this results in variable post-cracking response (S.-H. Chao 2011).

The Uniaxial DTT may become a more useful method with future improvements, but currently the large specimen size, requirement for a servo-controlled machine, and variability of crack location are complications.

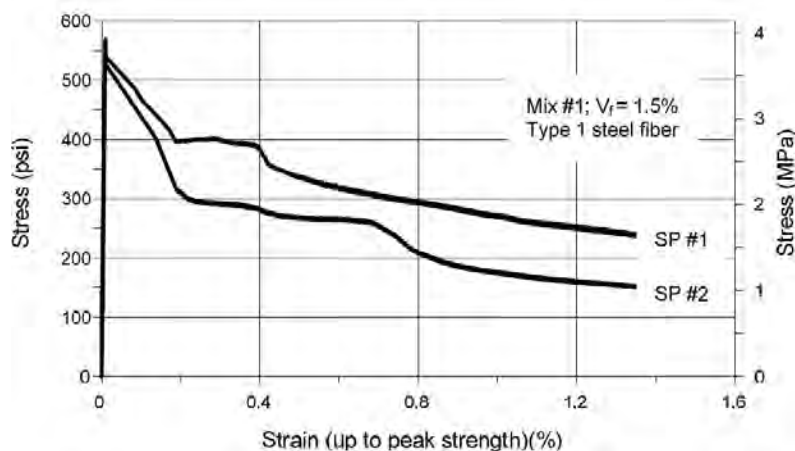


Figure E-19: Replicate specimen results for uniaxial DTT (S.-H. Chao 2011)

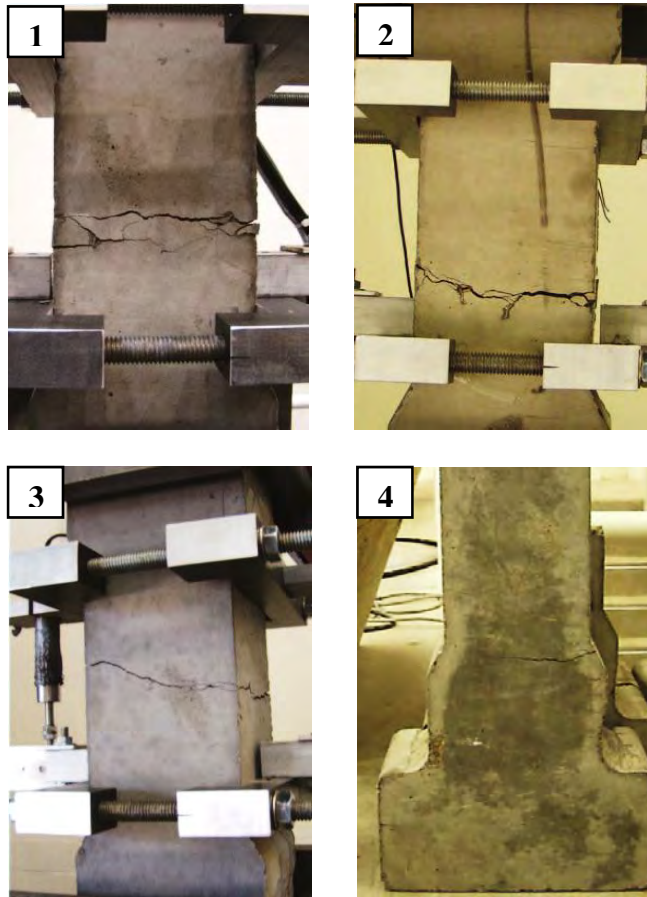


Figure E-20: Variability of uniaxial tensile test in location of major cracks for four replicate specimens with 1.5% fiber content (S.-H. Chao 2011)

Appendix F. Details of Double-Punch Testing

Double-punch testing (DPT) at the University of Texas at Arlington was organized into four phases, each of which is described below.

F.1. Phase 1 Experimental Program at UT Arlington

F.1.a: Overview of Phase 1 Experimental Program at UT Arlington

In the first phase of the experimental program at UT Arlington, the DPT was used to investigate the load-deformation response and the equivalent tensile strength of plain concrete and of concrete reinforced with high-performance steel fibers. Three different types of steel fibers were used, with volume fractions ranging from 0.5% (67 pounds of steel fibers per cubic yard of concrete) to 2.0% (268 pounds of steel fibers per cubic yard of concrete). Each set (with one fiber type and one volume fraction of fiber) had 10 replicate specimens, for a total of 126 specimens. Tests were performed when the compressive strength was about 4 ksi to represent a typical early-age strength of prestressed concrete members (especially prestressed concrete panels), achieved within of 24 to 48 hours after release.

F.1.b: Steel Fibers Used in Phase 1 at UT Arlington

In the first phase, three types of steel fibers were used, including US-made and foreign-made fibers. Properties of the fibers are presented in Table F-1. As shown in Figure F-1, Type 1 fiber (Royal, US-made) has a single-bend hooked shape at the ends and Type 2 (Bekaert short, foreign-made) and Type 3 (Bekaert long, foreign-made) fibers have double-bend hooked shapes at the ends. Type 1 has an aspect ratio (L/D) of 40 and Type 2 and Type 3 fibers have an aspect ratio of 53 and 83, respectively. All steel fibers have a tensile strength of approximately 150 ksi.

Table F-1: Properties of steel fibers used in Phase 1 at UT Arlington

Fiber Type	Shape	Length (L) ^[1]	Diameter (D) ^[1]	Aspect ratio (L/D) ^[1]	Tensile strength ^[2]
Type 1 (Royal)	Hooked-end (single-bend)	1.525 in. (38.7 mm)	0.038 in. (0.97 mm)	40	150 ksi (1034 MPa)
Type 2 (Bekaert, short)	Hooked-end (double-bend)	1.171 in. (29.8 mm)	0.022 in. (0.56 mm)	53	152.3 ksi (1050 MPa)
Type 3 (Bekaert, long)	Hooked-end (double-bend)	2.427 in. (61.6 mm)	0.029 in. (0.74 mm)	83	152.3 ksi (1050 MPa)

[1] Measured; [2] Provided by manufacturers

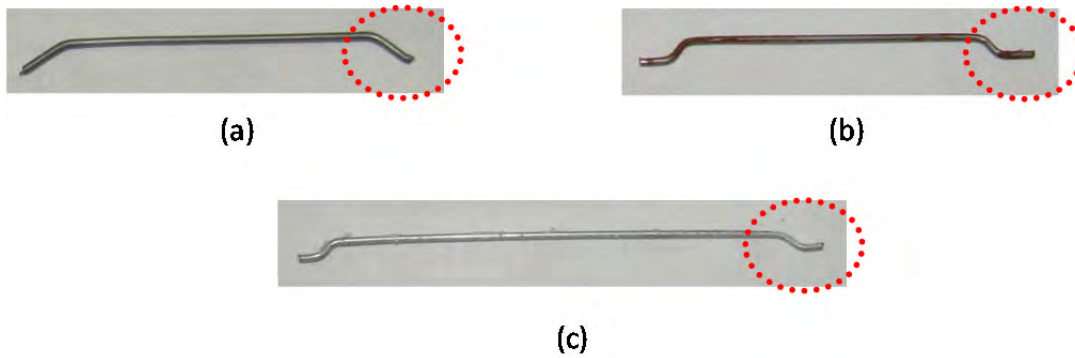


Figure F-1: Types of fiber used in first phase of study for DPT: (a) Type 1 (royal, single-bend hooked at end); (b) Type 2 (Bekaert short, double-bend hooked at end); (c) Type 3 (Bekaert long, double-bend hooked at end)

F.1.c: Concrete Mixtures Used in Phase 1 at UT Arlington

As shown in Table F-2, the concrete mixture design used for Phase 1 at UT Arlington was provided by the Texas Department of Transportation (TxDOT). The trial mix was generally feasible for the steel fiber-reinforced concrete.

Table F-2: Mixture proportions by weight used in Phase 1 at UT Arlington

Specimens	Cement (Type-I)	Sand	Coarse aggregate ^[1]	Water	Steel fiber	Super plasticizer ^[7]
PC (control)	1.00	1.96	2.72	0.34	0	0.013
SFRC-X*-050					0.101 ^[2]	
SFRC-X-075					0.152 ^[3]	
SFRC-X-100					0.204 ^[4]	
SFRC-X-150					0.311 ^[5]	
SFRC-X-200					0.422 ^[6]	

[1] Maximum size = $\frac{3}{4}$ in.; [2] 0.50% of volume fraction; [3] 0.75% of volume fraction; [4] 1.00% of volume fraction; [5] 1.50% of volume fraction; [6] 2.00% of volume fraction; [7] GRACE ADVA® Cast 530.

* X: R for Type 1 fiber, BS for Type 2 fiber, and BL for Type 3 fiber

Cement, sand, and coarse aggregate were obtained from a local precast concrete plant (Hanson Precast and Pipe, Grand Prairie). ASTM Natural River sand (fineness modulus 2.57), crushed limestone aggregate with a maximum size of $\frac{3}{4}$ in., and Type I cement were used. The concrete was mixed by a drum mixer at the Civil Engineering Lab (CELB). During mixing, the sand and cement were first mixed for about 1–2 minutes. Then water (initially with superplasticizer) was gradually added to achieve a workable paste. Then coarse aggregate was added and mixed again. When the concrete mix was ready, the steel fibers were gradually added and mixed again for a few minutes. The steps for mixing the concrete are illustrated in Figures F-2 and F-3.



(a)

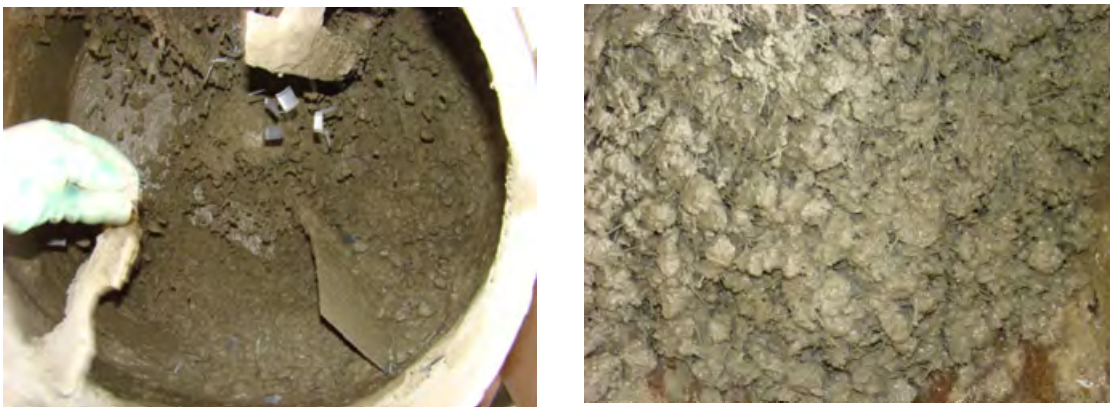


(b)

Figure F-2: Typical procedure for mixing concrete: (a) batching of materials; (b) gradual addition of water to prepare workable paste



(c)



(d)

Figure F-3: Typical procedure for mixing concrete (continued): (c) adding coarse aggregate; (d) adding steel fibers

F.1.d: Preparation of Phase 1 Specimens at UT Arlington

Phase 1 specimens were named as shown in Table F-3:

- 1) PC: plain concrete; SFRC: steel fiber reinforced concrete;
- 2) the letter (s) after SFRC represents type of fiber: R represents Royal fiber (Type 1), BS represents Bekaert short fiber (Type 2) and BL represents Bekaert long fiber (Type 3) ;
- 3) the subsequent number represents the volume fraction of fiber, 050 means 0.50% and 075 means 0.75% volume fraction of fibers, and so on.

Each group of specimens consisted of 10 replicates, except for SFRC BL-150 which had only six replicates. In all, Phase 1 comprised 126 specimens.

Table F-3: Specimens for Phase 1 at UT Arlington

Specimens name	Steel fiber type	Volume of fraction	Number of specimens
PC	-	-	10 for each set, total 120
SFRC-R-050	Type 1 (Royal)	0.50 %	
SFRC-R-075		0.75 %	
SFRC-R-100		1.00 %	
SFRC-R-150		1.50 %	
SFRC-R-200		2.00 %	
SFRC-BS-050	Type 2 (Bekaert short)	0.50 %	
SFRC-BS-075		0.75 %	
SFRC-BS-100		1.00 %	
SFRC-BL-050	Type 3 (Bekaert long)	0.50 %	
SFRC-BL-075		0.75 %	
SFRC-BL-100		1.00 %	
SFRC-BL-150		1.50 %	
Total numbers of specimens			
			126

Plastic molds measuring 6 × 12 in. were used to cast the specimens. Each mold produced two specimens. Molds that bulged at the bottom were not used, to ensure the even loading surfaces that are essential for DPT specimens. Specimens were cast in three layers and compacted with a table vibrator (Figure F-4 (a)). Three 4×8 inches cylinders were also prepared for determining the compressive strength. After casting all specimens were then moved to the curing room with a controlled environment (27°C (80°F) and 100% RH), as shown in Figure F-3 (b).



(a) 6- x 12-in. specimens



(b) plate vibrator



(c) casting and curing space

Figure F-4: Preparation of Phase 1 specimens at UT Arlington

To prepare the specimens for the DPT, the 6- × 12-in. cylinders were cut in half with a concrete saw to form two 6- × 6-in. cylindrical specimens, as shown in Figure F-5. The top and bottom surfaces of the resulting specimens were smoothed with a sanding stone, and their centers were marked.

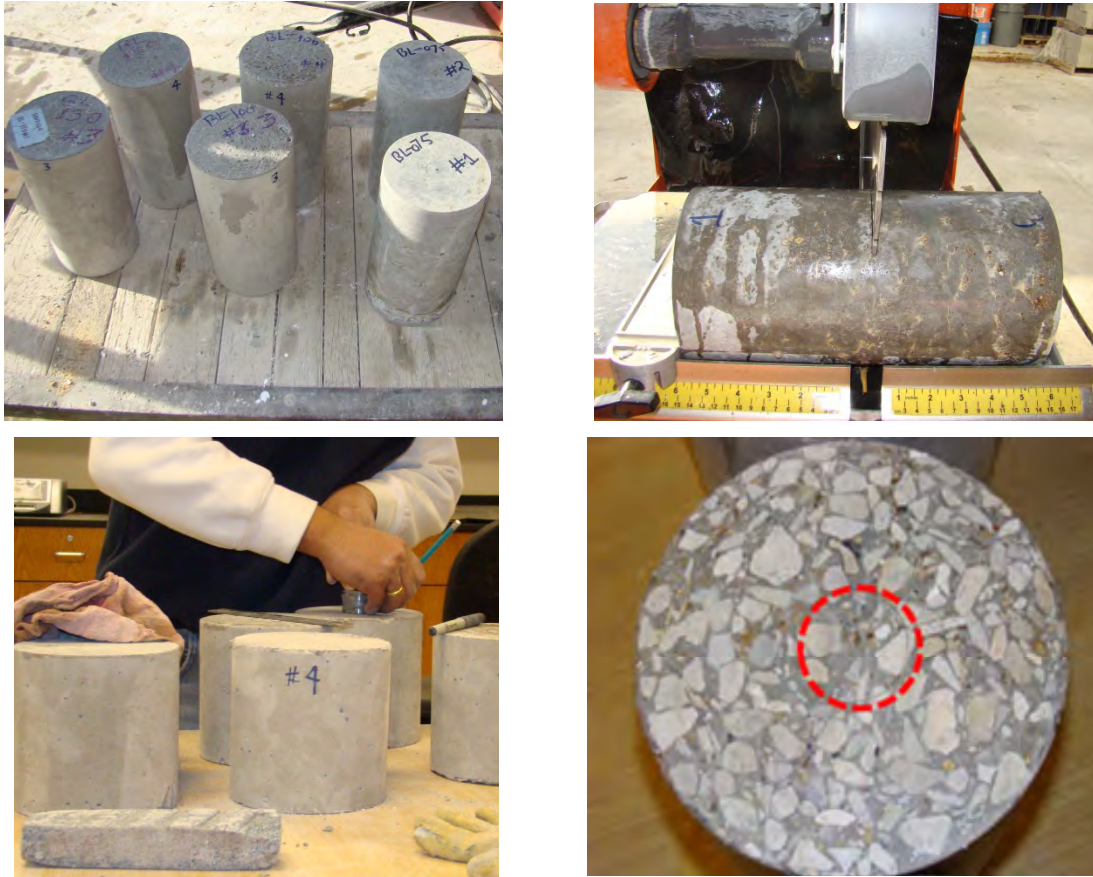


Figure F-5: Preparation of 6-in. × 6-in. DPT specimens, Phase 1 at UT Arlington

F.1.e: Test Setup and Instrumentation, Phase 1 at UT Arlington

As shown in Figure F-6, the simple apparatus suggested by Chen (1970) was used to test the specimens. The test setup consisted of a 60-kip Baldwin universal testing machine (Baldwin), LVDTs (Linear Variable Differential Transformers), a 50-kip load cell, and two steel punches measuring 1.5 in. in diameter by 1 in. in height. The punches were centered on the top and bottom surfaces of the specimen, and secured using tape. A steel plate was placed between the bottom punch and the load cell to distribute the load. Two LVDTs were used to measure the vertical deformation of the specimens. The LVDTs and the load cell were connected to data acquisition box to record the data during the test. The overall view of the test setup is shown in Figure F-6.

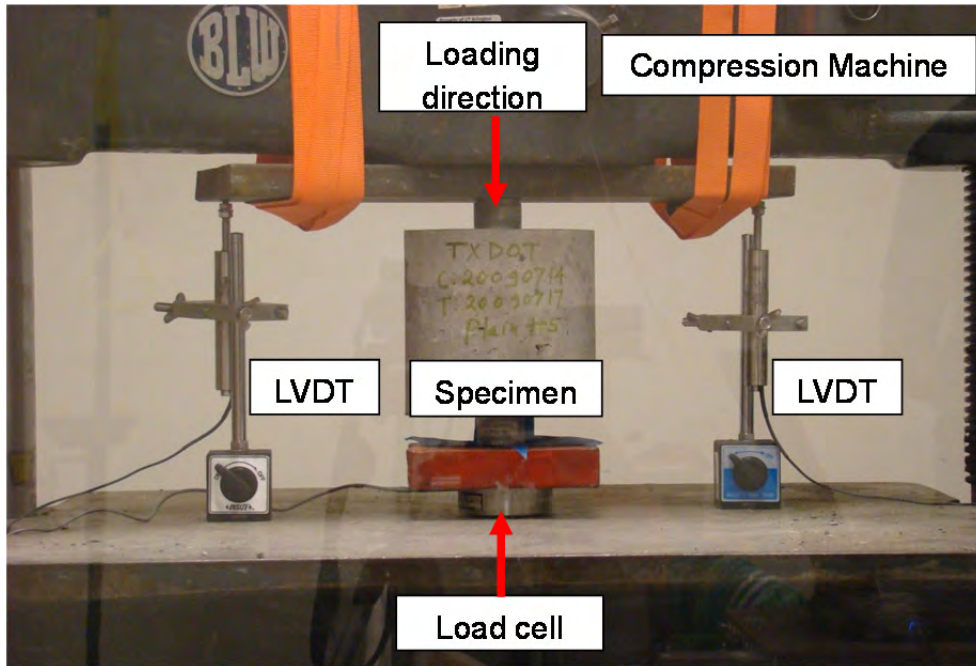


Figure F-6: Setup for DPT, Phase 1 at UT Arlington

F.1.f: Testing of Phase 1 Specimens at UT Arlington

The Phase 1 specimens at UT Arlington were tested at an age of 24 to 48 hours, at a compressive strength of about 4 ksi, corresponding to a typical expected compressive strength at release. The compressive strength of the concrete was determined by testing three 4- \times 8-in. cylinders.

Compressive force was applied by 60-kips Baldwin testing machine at a manually controlled loading rate of 100 lb/sec or the corresponding deformation rate of 0.002 in./sec, up to peak load, after which a deformation rate of about 0.006 inches/sec was used. In general the deformation rate is easier to control than the loading rate. Photographs were taken at different stages. The test was stopped when the residual load reached approximately one-fourth of the peak load. Typical stages of testing for the Phase 1 DPTs and for the corresponding compression test are shown in of the first phase of the DPT and compressive strength test are shown in Figure F-7.



Figure F-7: Typical stages of testing for Phase 1 at UT Arlington (DPT and compressive-strength tests)

F.2. Phase 2 of Experimental Program at UT Arlington

As reported later in this chapter, typical coefficients of variation among the 10 replicates of each set in Phase 1 at UT Arlington were low. As a result, the number of replicate specimens in each set was reduced from ten to four. This was convenient for several reasons. In Phase 1, because 10 replicates had to be prepared in each set (one fiber type and volume fraction), only one set could be cast at a time. To reduce variability in concrete properties due to casting different sets on different days, in Phase 2, several groups of specimens (one fiber type and multiple volume fractions) were prepared on the same day and tested after 48 hours, using the same specimen matrix as in Phase 1 shown in Table F-3). For example, SFRC-R-X series specimens (all specimens with Royal fibers with different volume fractions) were prepared on the same day and tested after 48 hours.

Phase 1 included trial mixes with high volume fractions of steel fibers were prepared. As shown in Figure F-8, mixing of such specimens was problematic. High volume fractions of fibers

normally require more cement paste, less coarse aggregate, and a high dosages of water-reducing admixtures. Based on prior experiences, the mix design used in the first phase experimental program was not suitable for volume fractions greater than about 1.5%, except for the Royal fiber, which has a small aspect ratio (40) and relatively little deformation (a single bend at the ends). Hence, series SFRC-BS-200 and SFRC-BL-200 series were removed from Phase 2 and subsequent phases. Also, in Phase 1 the R-050 specimen showed nearly the same peak loads as plain concrete. This series was also removed from subsequent testing.



Figure F-8: Examples of mixing difficulties in Phase 1 with high fiber-volume fractions

F.2.a: Fabrication and Testing of Phase 2 Specimens at UT Arlington

Details of Phase 2 specimens at UT Arlington are shown in Table F-4. Specimen preparation and testing were the same as for Phase 1.

Table F-4: Phase 2 specimens tested at UT Arlington

Specimens name	Steel fiber type	Fiber volume fraction	Number of specimens
PC	-	-	3
SFRC-R-075	Type 1 (Royal)	0.75 %	4 for each set, total 28
SFRC-R-100		1.00 %	
SFRC-R-150		1.50 %	
SFRC-R-200		2.00 %	
SFRC-BS-075	Type 2 (Bekaert)	0.75 %	
SFRC-BS-100		1.00 %	
SFRC-BS-150		1.50 %	
SFRC-BL-075	Type 3 (Bekaert)	0.75 %	
SFRC-BL-100		1.00 %	
SFRC-BL-150		1.50 %	
Total numbers of specimens			40

F.3. Phase 3 Experimental Program at UT Arlington

Phase 3 at UT Arlington was carried out to: 1) verify reduction in the variability in specimens with the same type of fibers by casting and testing all of them on the same days; 2) investigate if fewer replicates would still give a reasonably small coefficient of variation; and 3) obtain more consistent initial ascending curves by slightly modifying the testing procedure. In the modified procedure, the specimen was loaded up to 2 kips and unloaded to 0.5 kips, after which the test was started. This revised procedure was successful in producing a consistent initial stiffness of replicate specimens.

Materials used in Phase 3 were the same as in the first two phases. The mixture design was changed slightly, however. The dosage of superplasticizer was reduced from 0.013 to 0.0015 in order to reduce segregation and bleeding, giving the mixture proportions shown in Table F-5.

Table F-5: Mixture proportions by weight for Phase 3 at UT Arlington

Specimens	Cement (Type-1)	Sand	Coarse aggregate ^[1]	Water	Steel fiber	Super plasticizer
PC (control)	1.00	1.96	2.72	0.34	0	0.0015
SFRC-X*-050					0.101 ^[2]	
SFRC-X-075					0.152 ^[3]	
SFRC-X-100					0.204 ^[4]	
SFRC-X-150					0.311 ^[5]	
SFRC-X-200					0.422 ^[6]	

[1] Maximum size = $\frac{3}{4}$ in.; [2] 0.50% of volume fraction; [3] 0.75% of volume fraction; [4] 1.0% of volume fraction; [5] 1.5% of volume fraction; [6] 2.0% of volume fraction;

* X: R for Type 1 fiber, BS for Type 2 fiber and BL for Type 3 fiber

F.4. Preparation and Testing of Phase 3 Specimens at UT Arlington

Detailed information on Phase 3 specimens tested at UT Arlington is provided in Table F-6. The casting procedure in Phase 3 is similar to that of Phase 2. All specimens in specimen group (for example, all specimens with Type 1 fibers) were tested on the same day. In Phases 1 and 2, the bottom faces of the some plastic cylinder molds bulged out, so that some cylinders did not have smooth bottom surface. In Phase 3, this was corrected by using steel molds, as shown in Figure F-9. Other aspects of specimen preparation were the same as in previous phases. Specimen testing was also the same, with the exception of the initial seating load discussed above.

Table F-6: Specimens tested in Phase 3 at UT Arlington

Specimen name	Steel fiber type	Fiber volume fraction	Number of specimens
SFRC-R-075	Type 1 (Royal)	0.75 %	4 for each set, total 16
SFRC-R-100		1.00 %	
SFRC-R-150		1.50 %	
SFRC-R-200		2.00 %	
SFRC-BS-050	Type 2 (Bekaert, short)	0.50 %	4 for each set, total 16
SFRC-BS-075		0.75 %	
SFRC-BS-100		1.00 %	
SFRC-BS-150		1.50 %	
SFRC-BL-050	Type 3 (Bekaert, long)	0.50%	4 for each set, total 16
SFRC-BL-075		0.75 %	
SFRC-BL-100		1.00 %	
SFRC-BL-150		1.50 %	
Total numbers of specimens			48



Figure F-9: Steel molds used to prepare specimens in Phase 3 at UT Arlington

F.5. Phase 4 Experimental Program at UT Arlington

Phase 4 of the experimental program at UT Arlington was carried out to: 1) see if replicate specimens tested at an age of 28 days would have less variability than specimens tested at an early age; 2) see if fewer replicates, tested at 28 days, would still have a reasonably small coefficient of variation; and 3) see if the DPT could identify strain-hardening behavior and toughness SFRC.

F.6. Preparation and Testing of Phase 4 Specimens at UT Arlington

Materials and mixture proportions in Phase 4 at UT Arlington were the same as for Phase 3. Mixture proportions are shown in Table F-7. In Phase 4, the Helix 5-25 twisted fiber was

added (Figure F-10). One new additional type of steel fiber was added, as shown in Figure F-10 and Table F-8. Information for all Phase 4 specimens at UT Arlington is shown in Table F-9.

Table F-7: Mixture proportions used in Phase 4 at UT Arlington

Specimens	Cement (Type-1)	Sand	Coarse aggregate ^[1]	Water	Steel fiber	Super plasticizer
PC (control)	1.00	1.96	2.72	0.34	0	0.0015
SFRC-X*-050					0.101 ^[2]	
SFRC-X-075					0.152 ^[3]	
SFRC-X-100					0.204 ^[4]	
SFRC-X-150					0.311 ^[5]	
SFRC-X-200					0.422 ^[6]	

[1] Maximum size = ¾ in.; [2] 0.50% of volume fraction; [3] 0.75% of volume fraction; [4] 1.0% of volume fraction; [5] 1.5% of volume fraction; [6] 2.0% of volume fraction;

* X: R for Type 1 fiber, BS for Type 2 fiber, BL for Type 3 fiber and H for Type 4 (Helix)

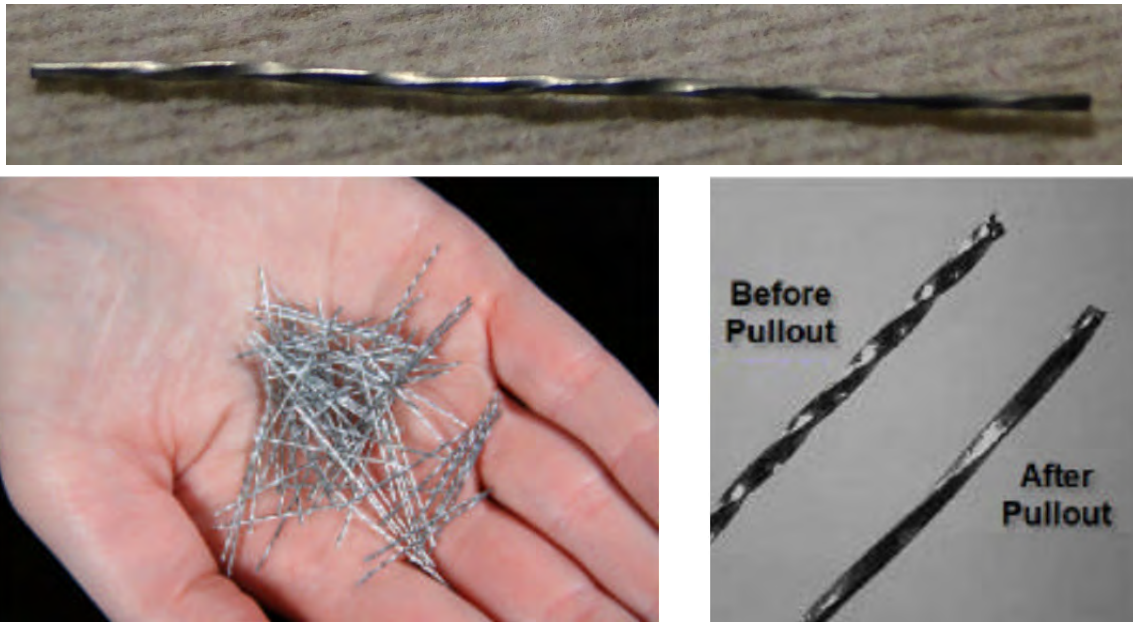


Figure F-10: Helix (twisted fiber) added in Phase 4 at UT Arlington

Table F-8: Properties of Helix fiber added in Phase 4 at UT Arlington

Fiber Type	Shape	Length (L) ^[1]	Diameter (D) ^[1]	Aspect ratio (L/D) ^[1]	Tensile strength ^[1]
Type 4 (Helix 5-25)	Twisted	1.0 in. (25 mm)	0.02 in. (0.50 mm)	50	304 ksi (2000 MPa)

[1]: From manufacturer's profile

Table F-9: Phase 4 specimens tested at UT Arlington

Specimen name	Steel fiber type	Fiber volume fraction	Number of specimens
PC	-	-	4
SFRC-R-075	Type 1 (Royal)	0.75 %	4 for each set, total 16
SFRC-R-100		1.00 %	
SFRC-R-150		1.50 %	
SFRC-R-200		2.00 %	
SFRC-BS-050	Type 2 (Short Bekaert)	0.50 %	4 for each set, total 16
SFRC-BS-075		0.75 %	
SFRC-BS-100		1.00 %	
SFRC-BS-150		1.50 %	
SFRC-BL-050	Type 3 (Long Bekaert)	0.50 %	4 for each set, total 16
SFRC-BL-075		0.75 %	
SFRC-BL-100		1.00 %	
SFRC-BL-150		1.50 %	
SFRC-H-075	Type 4 (Helix, twisted)	0.75 %	4 for each set, total 12
SFRC-H-150		1.50 %	
SFRC-H-200		2.00 %	
Total numbers of specimens			64

As shown in Table F-9, the specimens with Helix steel fiber were named SFRC H-075, SFRC H-150, and SFRC H-200. As in Phases 2 and 3, all specimens in one group (for example, with Type 1 fibers) were prepared on the same day and tested on the same day.

In Phase 4, specimens were tested at an age of 55 to 58 days. Some specimens (for example, BL-150) had a peak strength higher than 50 kips, requiring a higher-capacity testing machine (a 400-kip Tinius Olsen SuperL) and a higher-capacity load cell (200 kips). As shown in Figure F-11, the upper steel plate was bolted to the testing machine to provide a more uniform loading plane.

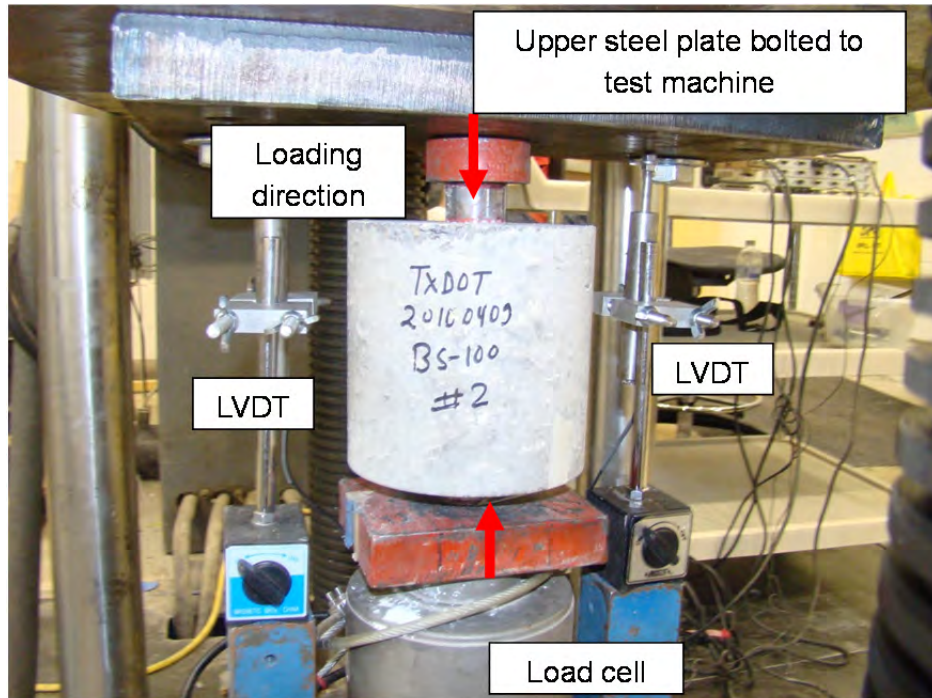


Figure F-11: Test setup used for Phase 4 testing at UT Arlington

Figure F-12 shows the photographs of some tested specimens. As shown in Figure F-12, while the plain concrete specimens broke into 4 pieces upon peak load, the SFRC specimens maintained their integrity due to the fiber bridging effect and produced more radial cracks.

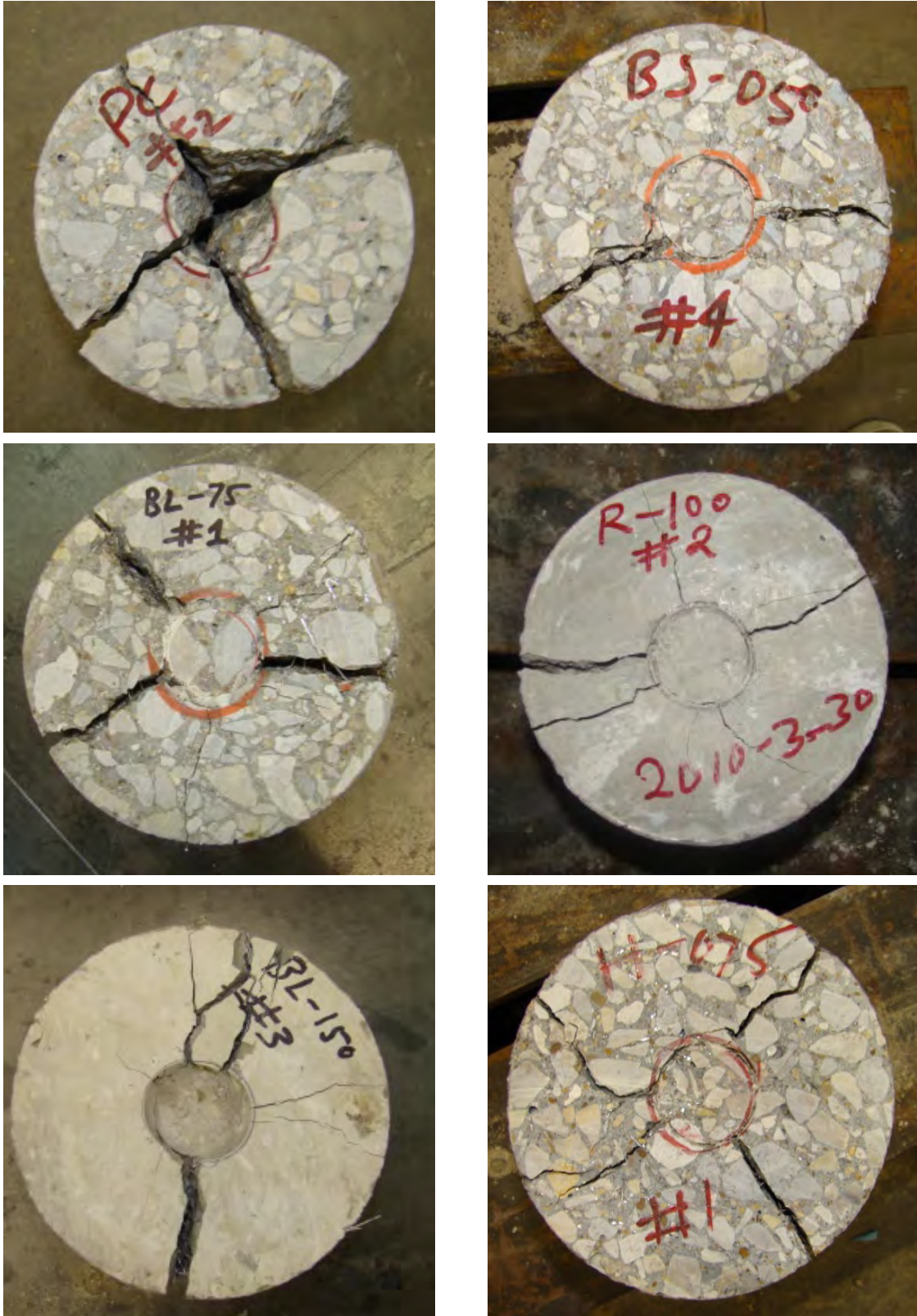


Figure F-12: Typical test specimens with various fiber volume fractions (Phase 4, UT Arlington)

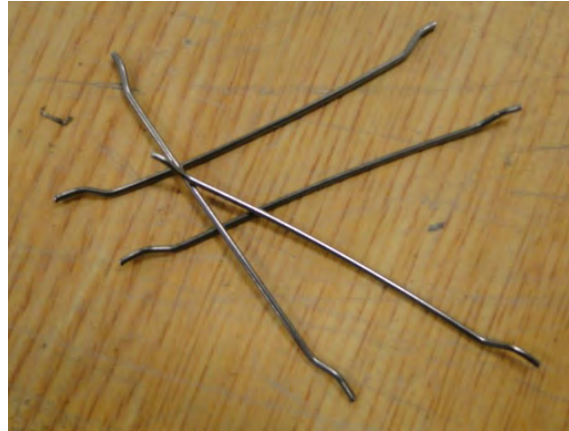
F.7. Phase 5: Comparison of DPT Method with Other Material Test Methods and Post-Crack Investigation

F.7.a: General Aspects of Phase 5 (UT Arlington)

In Phase 5 of double-punch research at UT Arlington, the DPT was compared with the third-point bending test (ASTM C1609) and the direct tensile test (DTT). Similarly, the post-cracking behavior of the SFRC tested by DPT was also studied. Twisted fibers, micro steel fibers, and a mix of these two types of fibers (hybrid) were used to evaluate the strain-hardening and post-cracking behavior SFRC using the DPT.

F.7.b: Materials and Specimen Preparation for Phase 5, UT Arlington

As shown in Figure F-13 and Table F-10, three additional types of steel fibers and combinations of those fibers (hybrid) were used in Phase 5. Volume fractions of 0.75%, 1.5%, and 1.5% were used. Six DPT specimens, six ASTM beams, and six DTT specimens were prepared with three different mixtures. Three compressive-strength cylinders (4 × 8 in.) were prepared with each concrete mixture.



a) Type 5: Maccaferri Long Steel Fiber (Double Bend Hook at End, FF 3)



b) Type 6: Twisted Steel Fiber



c) Type 7: Maccaferri Micro Steel Fiber

Figure F-13: Steel fibers used in Phase 5 at UT Arlington

Table F-10: Steel fibers used in Phase 5 at UT Arlington

Fiber Type	Shape	Length (L) ^[1]	Diameter (D) ^[1]	Aspect ratio (L/D)	Tensile strength ^[2]
Type 5	Maccaferri Long (FF3)	1.87 in. (47.5 mm)	0.031 in. (0.76 mm)	60	166 ksi (1100 MPa)
Type 6	Twisted	1 in. (25.4 mm)	0.008 in. (0.20 mm)	125	304 ksi (2000 MPa)
Type 7	Maccaferri micro	0.5 in. ^[1] (12.7 mm)	0.007 in. ^[2] (0.175 mm)	71	328 ksi (2200 MPa)

[1]: measured; [2]: provided by manufacturer;

Concrete mixtures used in previous phases of DPT testing at UT Arlington contained high percentages of coarse aggregate relative to cement and sand, and also used ¾-in. coarse aggregate. This often led to non-uniform distribution of fibers, and sometimes to segregation. In view of this, the percentage and maximum size of coarse aggregate were decreased in that portion of Phase 5 dealing with comparison of test methods (Table F-11). One group of specimens (with one mixture from Table F-11) was prepared on the same day with two batches due to the capacity limitation of the drum mixer used. All specimens were then moved to the curing room under controlled environment at 80°F (27°C) and 100% RH. Tests were conducted 21 to 30 days after casting.

Table F-11: Mixture proportions by weight used in Phase 5 at UT Arlington (comparison of test methods)

Mix type	Cement Type 1	Fly ash (class C)	Sand ^[1]	Coarse Aggregate ^[2]	Water	SP ^[3]	Steel Fiber	f_c ^[4] ksi
ML-075	1.00	0.50	1.7	1.0	0.35	0.001	0.114	9.23
ML-150	1.00	0.50	1.7	1.0	0.35	-	0.232	7.75
Hybrid	1.00	0.50	1.7	1.0	0.35	0.001	0.232	9.72

[1] ASTM natural river sand (Fineness Modulus = 2.57); [2] ASTM C33 Size Number 8), 95% of mass finer than 3/8 in., nominal maximum size = 3/8 in.; [3] Super Plasticizer: High Range Water Reducing Admixture; [4] compressive strength average of three 4 × 8 in. cylinders, tested on the same day when the specimen was tested;

* Note: with 0.75% Type 5 (Maccaferri long steel fiber) and 0.75 % Type 6 (twisted steel fiber)

As shown in Table F-12, six other mixtures were used to prepare additional DPT specimens to study post-cracking behavior and strain-hardening. In part of Phase 5, hybrid combinations of macro and micro fibers were used to study if DPT could identify high-performance mechanical behavior due to the synergistic effects from the two fibers. It was expected that a cement mortar mix with a 3% volume fraction of twisted and micro fibers would be able to achieve high-performance fiber-reinforced concrete. For these six mixtures, specimens were prepared using manual compaction (tamping rod) rather than vibrators, to reduce the

settlement of fibers, which could lead to inconsistent properties of the upper and bottom halves of the cylinders.

Table F-12: Mixture proportions by weight used for Phase 5 at UT Arlington (post-cracking behavior and strain-hardening)

Mixture	Cement Type 1	Fly ash (Class C)	Sand ^[1]	Coarse Aggregate ^[2]	Water	SP ^[3]	Steel Fiber	$f_c^{[4]}$ ksi
HYB1	1.00	0.50	1.7	-	0.32	0.002	0.312	12.14
HYB 2	1.00	0.50	1.7	1.0	0.35	0.001	0.232	7.38
HYB 3	1.00	0.50	1.7	1.0	0.35	0.001	0.232	7.85
HYB 4	1.00	-	1.3	0.67	0.40	0.001	0.165	6.03
ML-075	1.00	0.50	1.7	1.0	0.35	0.001	0.114	7.05
R-075	1.00	0.50	1.7	1.0	0.35	0.001	0.114	7.52

[1] ASTM natural river sand (Fineness Modulus = 2.57); [2] ASTM C33 Size Number 8, 95% of mass finer than 3/8 in., nominal maximum size = 3/8; [3] Super Plasticizer: High Range Water Reducing Admixture; [4] compressive strength average of three 4 × 8 in. cylinders, tested on the same day when the specimen was tested.

F.7.c: Specimens Used for Phase 5 of DPT (UT Arlington)

Specimens in Phase 5 of DPT at UT Arlington were named as follows: 1) The first word denotes the material test method (bending, tensile, or DPT); 2) the second set of characters represents the type of fiber (ML means Maccaferri long fibers; the mixed-fiber Maccaferri and twisted-fiber specimen was named as *hybrid*.; and 3) the third number represents the volume fraction of fibers (075 corresponds to a 0.75% volume fraction and 150 corresponds to a 1.5% volume fraction). For example, Bending: ML-150 means the specimen was tested in third-point bending (ASTM C1609), and had Maccaferri fibers with a 1.5% volume fraction of fibers. Each set had 6 replicates (Table F-13).

Table F-13: Specimens in Phase 5 of DPT (UT Arlington)

Specimen	Steel fiber type	Fiber volume fraction	Number of replicates
Bending: M-075	Type 5	0.75%	6
Tensile: ML-075			6
DPT: ML-075			6
Bending: ML-150		1.50%	6
Tensile: ML-150			6
DPT: ML-150			6
Bending: Hybrid	Type 5 + Type 6	(0.75%+0.75%)	6
Tensile: Hybrid			6
DPT: Hybrid			6
Total number of specimens			60

Specimens with hybrid steel fibers are named as follows (Table F-14):

- HYB1 represents a combination of 2% Type 6 fiber (twisted steel fiber) and 1.0% Type 7 fiber (micro Maccaferri fiber),
- HYB2 represents a combination of 1% Type 6 fiber (twisted steel fiber) and 0.50% Type 5 fiber (Maccaferri long (FF3)) fiber,
- HYB3 represents combination of 0.75% Type 5 fiber (Maccaferri long steel fiber) and 0.75% Type 7 fiber (Maccaferri micro fiber) (mixed with 3/8 in. aggregate).
- HYB4 is the same as HYB3, again with a combination of 0.75% Type 5 fiber (Maccaferri long fiber) and Type 7 fiber (0.75% Maccaferri micro fiber). However, this mixture used larger aggregate sizes (3/4-in. coarse aggregate) and more water to purposely create a lower-quality SFRC mixture.

Table F-14: Hybrid-fiber specimens in Phase 5 of DPT (UT Arlington)

Specimen	Steel fiber type	Fiber volume fraction	Number of specimens
HYB 1	Type 6 + Type 7	(2%+1%)	4
HYB 2	Type 5 + Type 6	(0.50%+1.0%)	4
HYB 3	Type 5 + Type 7	(0.75%+0.75%)	4
HYB 4	Type 5 + Type 7	(0.75%+0.75%)	4
ML-075	Type 5, FF3	0.75%	4
R-075	Type 1, Royal	0.75%	4
Total numbers of specimens			24

Note: FF3 represents for, Maccaferri long, double-bend hooked at fiber ends

F.7.d: Testing of Specimens in Phase 5 of Double-Punch Research at UT Arlington

The specimens shown in Table F-13 were tested between 21 to 28 days using a servo-controlled, closed-loop MTS machine for the third-point bending test (ASTM C1609) and the DTT (dogbone-shaped specimens). A 60-kip compression machine was used for the DPT. The specimens shown in Table F-14 were tested with the DPT in a 400-kip compression machine after 28 days.

Previous experimental investigation of DPT with hybrid (mixed fibers), especially with large quantities of short and micro fibers, has shown strain-hardening after first cracking, along with higher variation in post-peak strength. To investigate ways of reducing that variation, six more DPT mortar specimens were cast, with the mixture proportions shown in Table F-41. A viscosity-modifying agent (VMA) was added to reduce the possibility of segregation of fibers.

Table F-15: Mixture proportions by weight used for mortar specimens in Phase 5 of DPT (UT Arlington)

Mix type	Cement Type 1	Fly ash (class C)	Sand ^[1]	CA ^[2]	Water	VMA ^[3]	SP ^[4]	Steel Fiber	f'_c ^[5] ksi
HYB5*	1.00	0.50	1.7	-	0.40	0.002	0.023	0.312	10.47

[1] ASTM natural river sand (Fineness Modulus = 2.57); [2] Coarse aggregate ASTM C33 Size Number (8), 95% of mass finer than 3/8 in., nominal maximum size = 3/8 in.; [3] RHEOMAC® VMA 362; [4] Super Plasticizer: GRACE ADVA® Cast 530; [5] compressive strength average of three 4 × 8 in. cylinders, tested on the same day when the specimen was tested;

* Note: HYB5 represents a combination of 2% Type 6 fiber (twisted steel fiber) and 1.0% of Type 7 fiber (Maccaferri micro fiber),

F.8. Results from DPT at UT Arlington

The main parameters evaluated in the DPT were peak equivalent tensile strength, residual strength at 0.10-in. deformation, coefficient of variation of these properties, deflection hardening and deflection softening, stiffness, crack widths, and total energy dissipation (toughness). In this section, the results obtained are presented and discussed.

F.8.a: Experimental Results from Phase 1 of DPT

Equivalent tensile strength was calculated from the ultimate load based on Equation (1) as developed by Chen (1970). As shown in Table 2.1, SFRC specimens showed higher tensile strength compared to PC except SFRC BL-075. This might be due to the fact that the compressive strength of SFRC BL-075 was about 17% less than that of PC, because ultimate tensile strength is related to compressive strength. SFRC BL-075 was tested after 24 hours, while PC was tested at 48 hours. The compressive strength of SFRC-BL was slightly lower than 4 ksi and far lower than that of PC. However, SFRC BL-075 showed higher residual strength at 0.10-in. deformation. This is discussed further in the next section. SFRC BL-150, with 1.5% Type 3 (Bekaert long, BL) steel fiber, had the highest equivalent tensile strength, 18.5% higher than that of PC. Results are presented in Table F-16 and Figure F-14.

Table F-16: Results from Phase 1 of DPT at UT Arlington

Specimen	Compressive strength (ksi)	Peak load (kips)	Equivalent tensile strength (psi)	Comparison with PC	Coefficient of variation	Tested hours after casting
PC	4.7	27.1	410	-	5.2 %	48
SFRC-R-050	4.5	27.4	414	1.0 %	7.5 %	48
SFRC-R-075	5.9	32.4	491	16.4 %	6.2 %	48
SFRC-R-100	4.4	28.0	423	3.1 %	4.2 %	24
SFRC-R-150	5.6	33.2	502	18.2 %	3.8 %	24
SFRC-R-200	5.6	30.9	467	12.2 %	6.9 %	24
SFRC-BS-050	5.5	32.8	496	17.3 %	3.9 %	48
SFRC-BS-075	5.1	31.2	472	13.1 %	8.5 %	42
SFRC-BS-100	4.9	32.4	490	16.3 %	3.1 %	24
SFRC-BL-050	5.8	29.3	444	7.5 %	7.2 %	48
SFRC-BL-075	3.9	23.8	361	-13.7 %	4.7 %	24
SFRC-BL-100	4.9	33.7	509	19.5 %	8.2 %	24
SFRC-BL-150	4.6	36.9	559	26.6 %	18.5 %	24

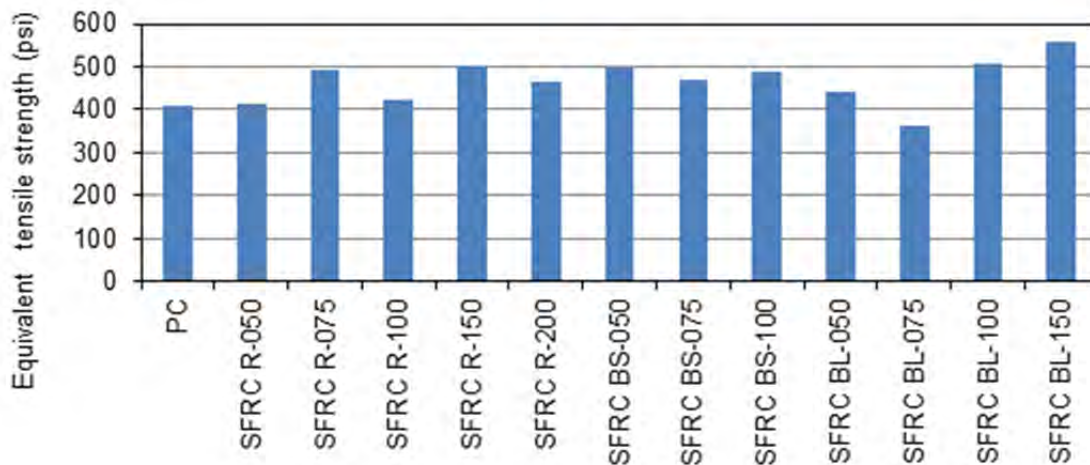


Figure F-14: Equivalent tensile strengths from Phase 1 DPT at UT Arlington

Specimens with Type 1 (Royal, SFRC-R) and Type 2 (Bekaert short, SFRC-BS) were compared to those with Type 3 fiber (Bekaert long, SFRC-BL). As shown in Table F-17, the SFRC-BL specimens had higher average equivalent tensile strength for each volume fraction of fibers except for the 0.75% volume fraction, . SFRC-BL specimens have higher equivalent tensile strength than SFRC-R specimens by 7.3%, 20.3%, and 11.4% for fiber volume fractions of 0.5%, 1.00%, and 1.50%, respectively.

For SFRC-BS, equivalent tensile strength increased by 3.9% for a fiber volume fraction of 1.50%. The equivalent tensile strength decreased by 10.5% and 23.5% for fiber volume fraction of 0.50% and 0.75%, respectively. As mentioned previously, that Type 3 steel fiber is 2.4 inches long and was a little difficult to mix with this particular concrete mixture. Even though the Type 2 fiber is shorter than the Type 1 fiber, Type 2 fibers resulted in higher strength than Type 1 because of the double hook at the ends of the Type 2 fibers, which provides better mechanical bond.

Table F-17: Peak strength of specimens using Type 3 fibers (SFRC-BL) versus specimens using Type 1 fibers (SFRC-R) and specimens using Type 2 fiber (SFRC-BS) (First Phase)

Volume fraction	Equivalent tensile strength of SFRC-BL (ksi)	Equivalent tensile strength of SFRC-R (ksi)	Difference with SFRC-R (ksi)	Equivalent tensile strength of SFRC-BS (ksi)	Difference with SFRC-BS (ksi)
0.50%	444	414	30 (7.3% ↑)	496	-52 (10.5% ↓)
0.75%	361	491	-130 (26.5% ↓)	472	-111 (23.5% ↓)
1.00%	509	423	86 (20.3% ↑)	490	19 (3.9% ↑)
1.50%	559	502	57 (11.4% ↑)	-	-

F.8.b: Residual Strength at 0.1-in. Deformation, Phase 1 of DPT at UT Arlington

Plain concrete (PC) specimens failed immediately after cracking load, and therefore had no residual strength. For SFRC specimens, the peak strength and the residual strength at a deformation of 0.1 in. were selected as key criteria to differentiate the performance of different FRC mixtures. As shown in Figure F-15 and as explained immediately below, the characteristics of the descending branch of the load-deformation response can be quickly identified based on those two points. To capture residual strength accurately, tests were continued until the residual strength reduced to about 25% of the peak strength.

1. If the descending curve does not reach 0.1 in., this means that the ductility beyond peak strength (or first cracking) is generally not significant;
2. A straight line connecting these two points can approximate the descending branch;
3. FRC mixtures with higher strengths at these two points generally have higher strengths throughout the entire load-deformation curve.

- Comparison between residual strengths at 0.1-in. deformation generally gives the relative toughness (energy absorption ability) beyond first cracking for different SFRC mixtures.

However, if a mixture has a relatively flat ascending branch (smaller modulus of elasticity), using the 0.1-in. deformation might lead to unconservative results and an unfair comparison with an FRC having relatively steep ascending branch. In such a case, the second point can be taken at 0.05 in. beyond the deformation at peak strength. This criterion could also be applied to ultra-high performance FRC mixtures for which the 0.1-in. deformation is still within the ascending branch of the load-deformation curve.

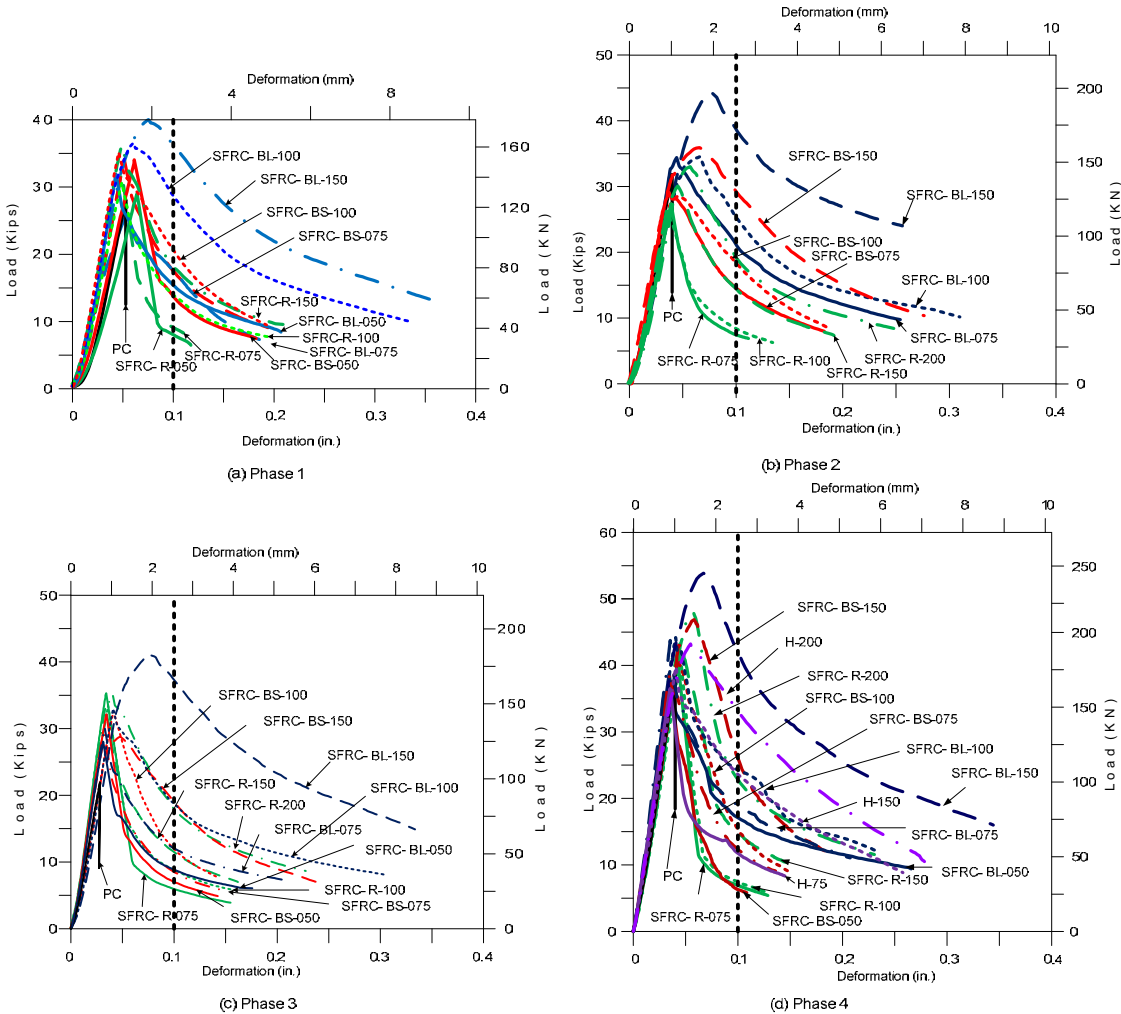


Figure F-15: Selection of 0.1-in deformation to determine residual strength

A few other things can also be observed from Figure F-15:

- Peak loads generally occurred at deformations of 0.045 to 0.055 in.. This value could be increased by strain hardening.

- Some SFRC specimens with low fiber volume fractions (0.50%) exhibited very low residual loads at 0.1-in. deformation. SFRC specimens with high volume fractions (>1.5%), residual loads at 0.1-in. deformation could exceed 75% of peak load.

Residual strengths are summarized in Table F-18 and Figure F-16. In Table F-19, residual strengths are compared between Type 3 fiber and Type 1 and 2 fibers. SFRC-BL specimens with Type 3 fiber showed residual strengths from 70% to 120% higher residual strengths than SFRC-R specimens with Type 1 fiber, for different volume fractions.

Table F-18: Residual strengths at 0.1-in. deformation, Phase 1 of DPT at UT Arlington

Specimens	Residual load at 0.1 in. deformation (kips)	Coefficient of variation
PC	-	-
SFRC-R-050	6.5	13%
SFRC-R-075	7.4	17%
SFRC-R-100	11.5	22%
SFRC-R-150	15.2	20%
SFRC-R-200	17.6	25%
SFRC-BS-050	11.2	24%
SFRC-BS-075	14.8	8%
SFRC-BS-100	17.3	16%
SFRC-BL-050	12.9	16%
SFRC-BL-075	12.5	20%
SFRC-BL-100	25.2	20%
SFRC-BL-150	32.1	36%

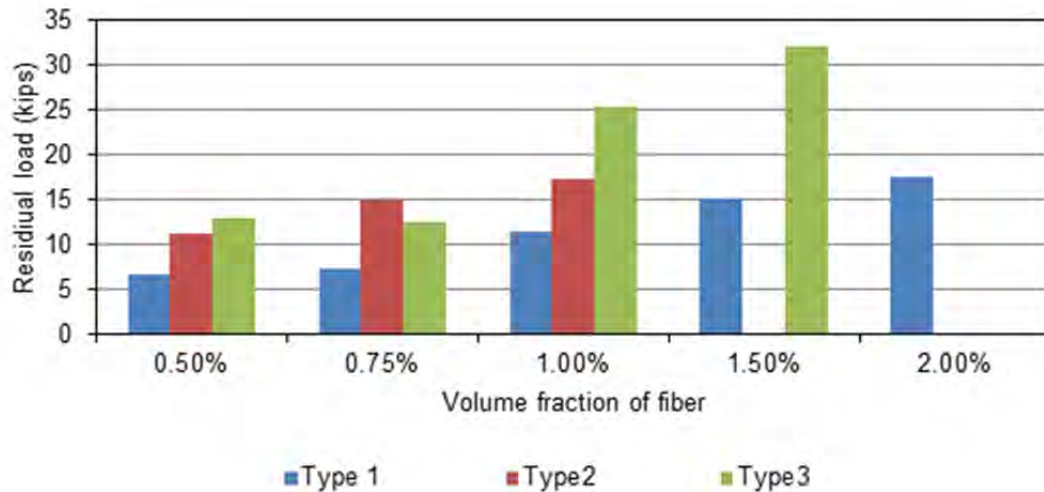


Figure F-16: Comparison of residual strengths at 0.1-in. deformation, Phase 1 of DPT at UT Arlington

Table F-19: Comparison of residual strengths at 0.1-in. deformation for specimens with Type 3 fibers (SFRC-BL) and specimens with Type 2 fibers (SFRC-BS), Phase 1 of DPT, UT Arlington

Volume fraction	Corresponding load at deformation 0.1 in. for SFRC-BL (kips)	Corresponding load at deformation 0.1 in. for SFRC-R (kips)	Difference with SFRC-R (kips)	Corresponding load at deformation 0.1 in. for SFRC-BS (kips)	Difference with SFRC-BS (kips)
0.50%	12.9	6.5	6.4 (98.2% ↑)	11.2	1.8 (16% ↑)
0.75%	12.5	7.4	5.1 (69.3% ↑)	14.8	-2.4 (15.9% ↓)
1.00%	25.2	11.5	13.7 (119.5% ↑)	17.3	8.0 (46.1% ↑)
1.50 %	32.1	15.2	16.95 (111.0% ↑)	-	-

F.8.c: Coefficients of Variation, Phase 1 of DPT, UT Arlington

The coefficients of variation (COV) for peak and residual strengths are the principal measures of reliability of a test method. As shown in Table F-16, for all SFRC specimens except SFRC BL-150, COVs for peak load are less than 10%. These COVs are lower than the 20% or higher typically shown by the third-point flexural test (ASTM C1609). This point is discussed in more detail later in this appendix. Similarly, as shown in Table F-18, COVs for residual strength at 0.10-in. deformation varied from 8% to 36%.

In Figure F-17 are compared the average load-deformation curves for plain concrete specimens and SFRC specimens with the same type but different volume fractions of fibers. In Figure F-18 are compared the same values for specimens with different types of fibers but the same volume fraction of fibers.

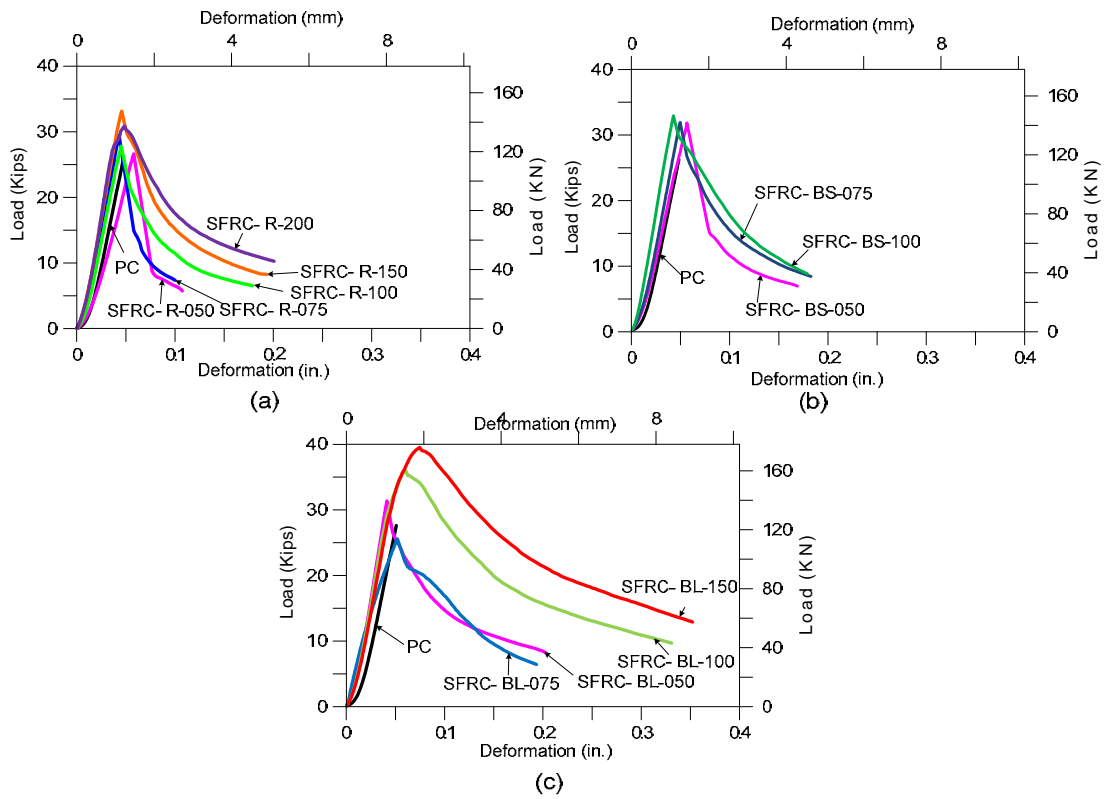


Figure F-17: Average DPT curves for plain concrete versus SFRC specimens, Phase 1 of DPT at UT Arlington: (a) SFRC-R, (b) SFRC-BS, and (c) SFRC-BL

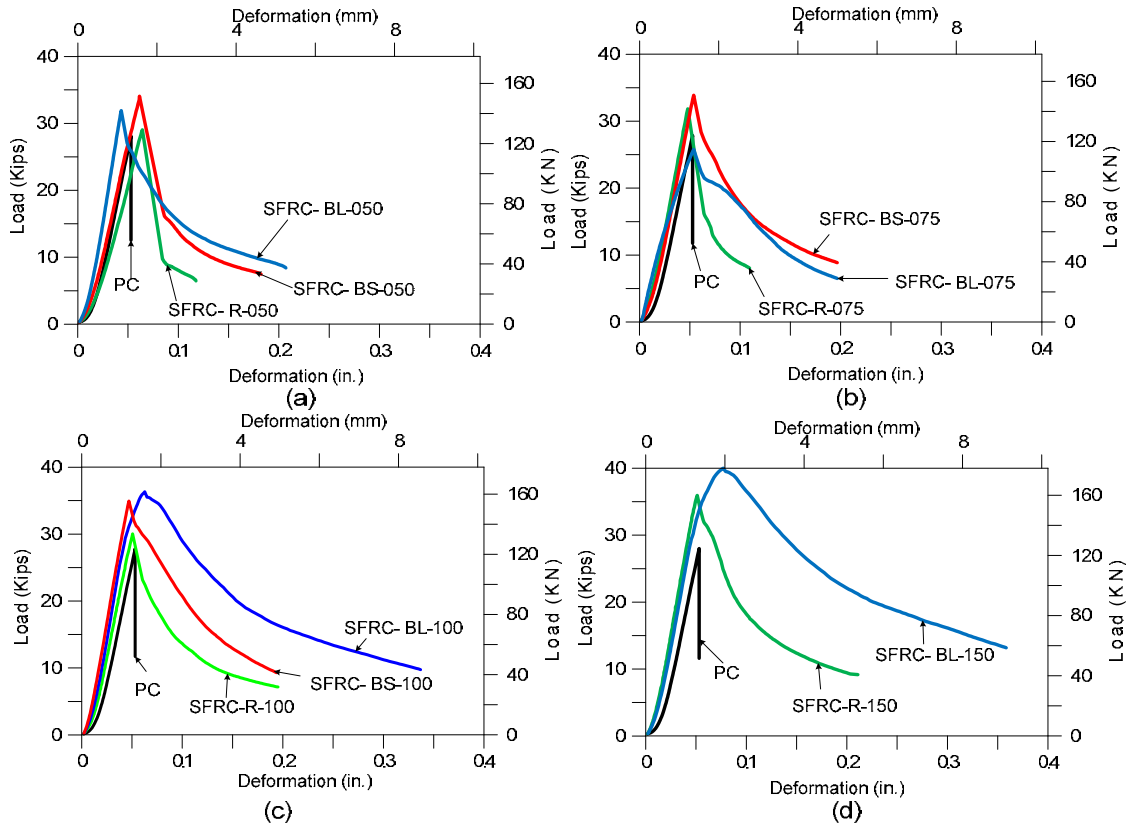


Figure F-18: Average load-deformation curves for DPT for plain concrete versus SFRC specimens, Phase 1 of DPT at UT Arlington: volume fraction of (a) 0.50%, (b) 0.75%, (c) 1.0%, and (d) 1.5%

F.9. Results from Phase 2 of DPT, UT Arlington

Similar to Phase 1, DPTs were performed when the compressive strength reached approximately 4 ksi. Based on results of Phase 1 (low COV for peak strengths), the number of replicate specimens was reduced to from 10 to four. One set of specimens was prepared at same time and also tested after 42 hours, so that all specimens would have compressive strength greater than or equal to 4 ksi.

F.9.a: Equivalent Tensile Strength of Phase 2 DPT Specimens, UT Arlington

Test results for Phase 2 of DPT at UT Arlington are shown in Table F-20, and equivalent tensile strengths are shown graphically in Figure F-19. SFRC specimens had higher peak equivalent tensile strengths than plain concrete, except for SFRC-R-100. As the volume fraction of fiber increased the equivalent tensile strength increased as well. For SFRC-BL-150 specimens, the ultimate strength increased up to 39.5% as compared to PC specimens. As in Phase 1, specimens with Type 3 fibers were compared with specimens with Type 1 and Type 2 fibers (Table F-21). Specimens with Type 3 fiber were up to 27% stronger than those with Type 1 or Type 2 fiber.

Table F-20: Average peak load and equivalent tensile strength, Phase 2 of DPT, UT Arlington

Specimens	Compressive strength (ksi)	Peak load (kips)	Equivalent tensile strength (psi)	Comparison with PC	Coefficient of variation	Age at testing (hours)
PC	4.24	26.97	408	-	12.67	42
SFRC-R-075	6.77	27.91	422	+ 3.4%	9.01	
SFRC-R-100	6.65	26.20	396	- 2.9%	10.47	
SFRC-R-150	6.71	29.55	447	+ 9.6%	15.17	
SFRC-R-200	6.65	32.42	491	+ 20.3%	4.94	
SFRC-BS-075	5.60	28.08	425	+ 4.2%	4.18	
SFRC-BS-100	5.10	28.29	428	+ 4.9%	8.53	
SFRC-BS-150	5.10	34.66	524	+ 28.4	9.32	
SFRC-BL-075	6.53	27.64	418	+ 2.5%	4.39	
SFRC-BL-100	5.73	28.02	424	+ 3.9%	4.80	
SFRC-BL-150	6.81	37.62	569	+ 39.5%	9.03	

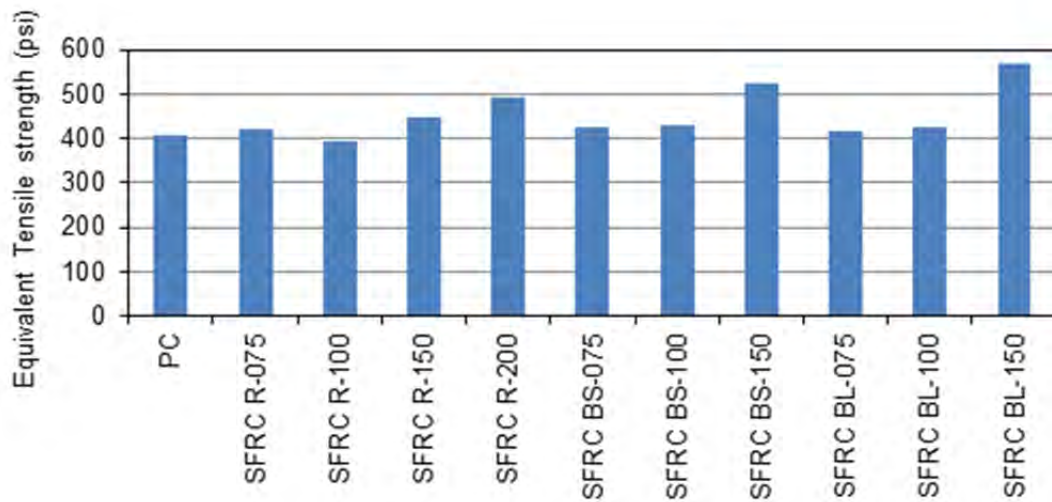


Figure F-19: Comparison of Equivalent Tensile Strengths, Phase 2 of DPT, UT Arlington

Table F-21: Peak strengths of specimens with Type 3 fiber versus specimens with Type 1 and Type 2 fiber, Phase 2, UT Arlington

Volume fraction	Equivalent tensile strength of SFRC-BL (ksi)	Equivalent tensile strength of SFRC-R (ksi)	Difference with SFRC-R (ksi)	Equivalent tensile strength of SFRC-BS (ksi)	Difference with SFRC-BS (ksi)
0.75%	418	422	-4 (0.95% ↓)	425	-3 (0.7% ↓)
1.00%	424	396	28 (7.1% ↑)	428	-4 (0.9% ↓)
1.50%	569	447	122 (27.3% ↑)	524	45 (8.6% ↑)

F.9.b: Residual Strength at 0.1-in. Deformation, Phase 2, UT Arlington

Results for residual strength in Phase 2 of DPT at UT Arlington are shown in Table F-22 and Figure F-20, and were similar to those from Phase 1. SFRC-BL specimens showed higher residual strength than SFRC-R and SFRC-BS, and SFRC-BL has 100% more residual strength than SFRC-R. Table 2.8 and Figure 2.7 show the comparison of residual strength of specimens with different types and volumes fractions of fibers.

Table F-22: Residual strength at 0.1-in. deformation, Phase 2, UT Arlington

Specimen	Corresponding load at 0.1 in. deformation (kips)	Coefficient of variation at 0.10-in. deformation
PC	-	-
SFRC-R-075	7.5	7%
SFRC-R-100	6.9	3%
SFRC-R-150	13.9	13%
SFRC-R-200	19.4	25%
SFRC-BS-075	14.3	2%
SFRC-BS-100	17.6	19%
SFRC-BS-150	27.6	29%
SFRC-BL-075	16.2	11%
SFRC-BL-100	20.4	34%
SFRC-BL-150	31.1	39%

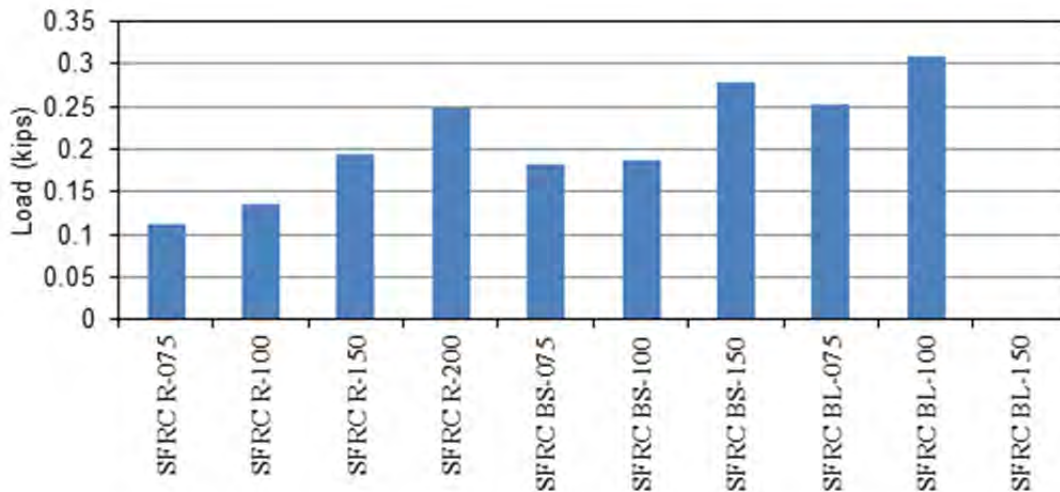


Figure F-20: Comparison of residual strengths at 0.1-in. deformation, Phase 2, UT Arlington

In Table F-23, residual strengths of Phase 2 specimens with Type 3 fibers are compared with those of specimens with Type 1 and Type 2 fibers. Results show that residual strengths of specimens with Type 3 fibers are up to 166% of those for specimens with Type 1 and Type 3 fibers. Even though the peak load of SFRC-BL-075 is slightly lower than that of SFRC-R-075 and SFRC-BS-075, its residual strength was quite high.

Table F-23: Residual strength of specimens with Type 3 fibers versus specimens with Type 1 and Type 2 fibers, Phase 2, UT Arlington

Volume fraction	Corresponding load at deformation 0.1 in. for SFRC-BL (kips)	Corresponding load at deformation 0.1 in. for SFRC-R (kips)	Difference with SFRC-R (kips)	Corresponding load at deformation 0.1 in. for SFRC-BS (kips)	Difference with SFRC-BS (kips)
0.75%	16.9	6.3	10.5 (166% ↑)	14.4	2.4 (16.7% ↑)
1.00%	16.7	8.2	8.7 (103% ↑)	18.1	-1.4 (7.6% ↓)
1.50%	29.8	14.5	15.5 (106% ↑)	28.4	1.4 (5.0% ↑)

F.9.c: Coefficients of Variation for Results of Phase 2 DPTs, UT Arlington

In Table F-20 and Table F-22, coefficients of variation for peak and residual strengths are compared for the Phase 2 specimens. Even though only 4 replicates were used rather than the 10 used in the first phase, the coefficients of variation for peak strength for most specimens were less than 10% except for PC (12.7%) and R-100 (15.2%). Similarly, coefficients of variation for residual strengths were similar to those in the first phase. The COVs for some specimens were slightly higher.

F.9.d: Load-Deformation Curves

In Figure F-21 the equivalent tensile strengths of plain concrete specimens are compared with SFRC specimens with different volume fractions of fibers. In Figure F-22, load-deformation curves are compared for different fibers, with the same volume fractions of fibers. These figures indicate that the initial stiffnesses of the load-deformation curves were very consistent for all specimens, including plain concrete. The post-cracking curves, in contrast, showed quite behavior for changes in types or volume fractions of fibers. Long fibers with higher volume fractions typically gave greater toughness.

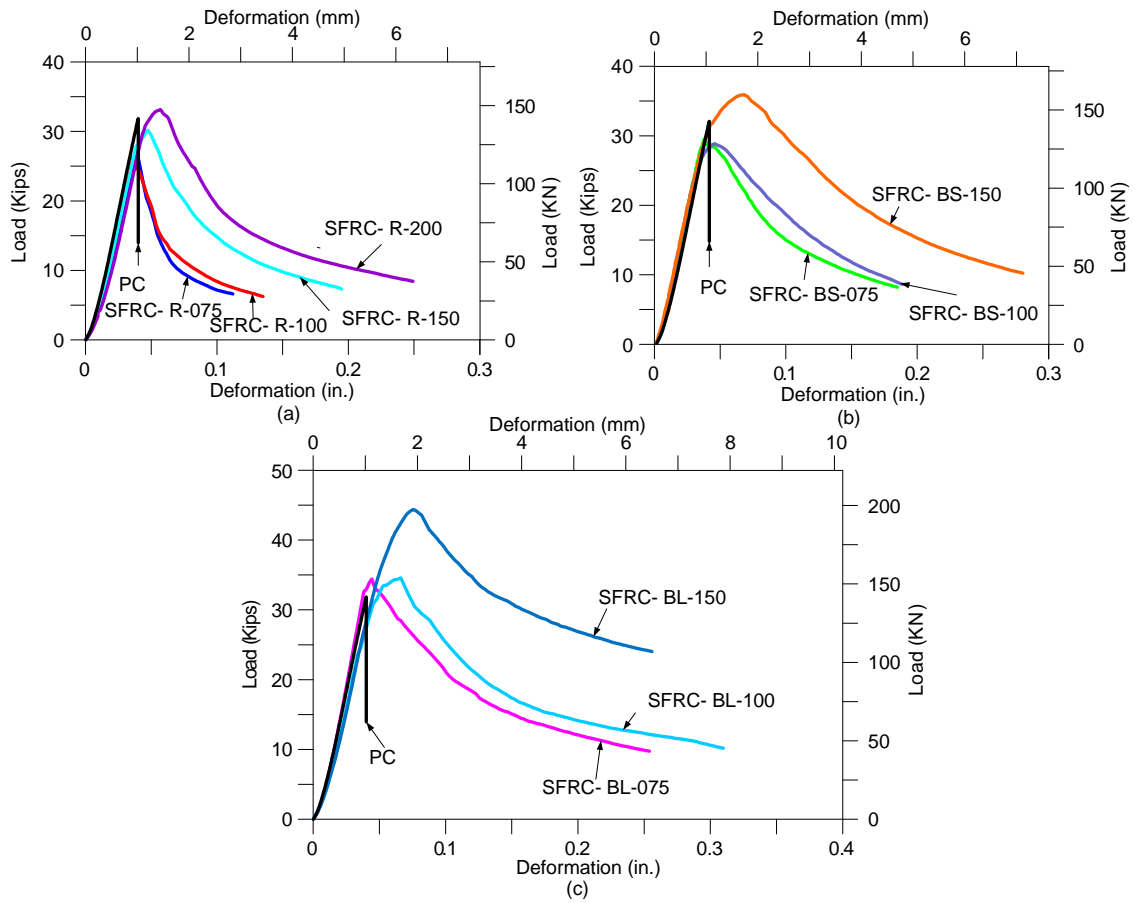


Figure F-21: Average load-deformation curves for plain concrete and SFRC specimens, Phase 2, UT Arlington: (a) SFRC-R, (b) SFRC-BS, and (c) SFRC-BL

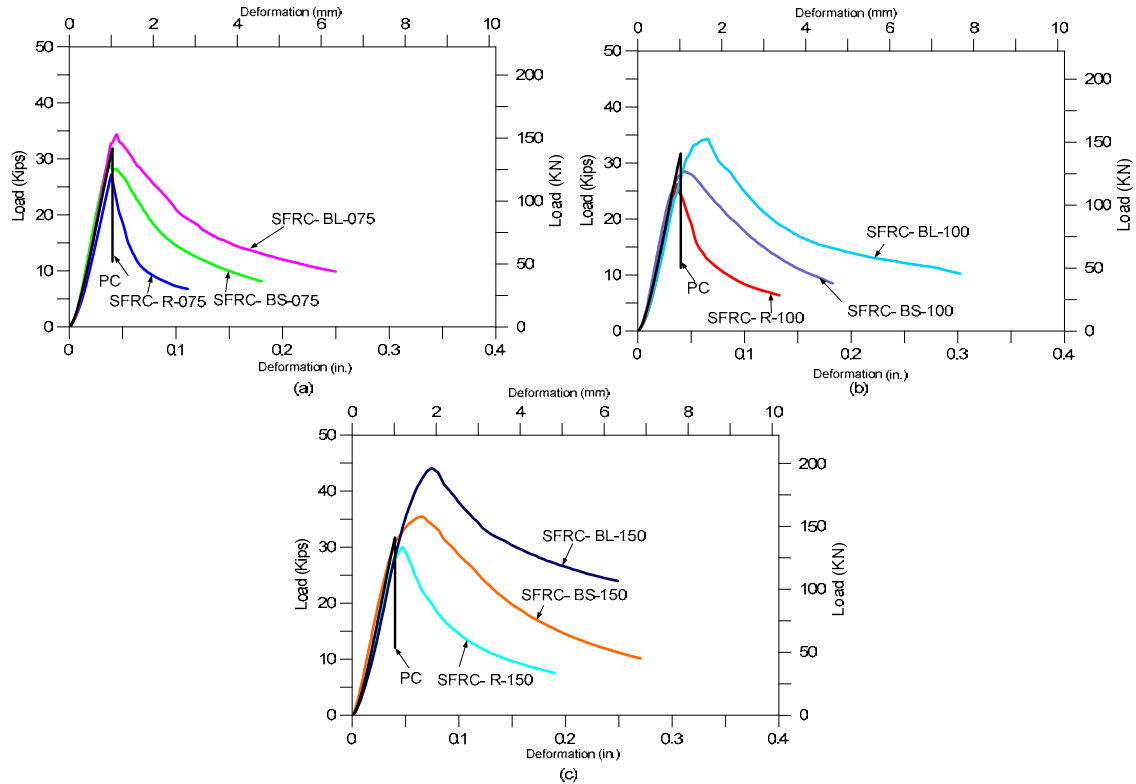


Figure F-22: Average load-deformation curves for plain concrete and SFRC specimens, Phase 2, UT Arlington: (a) 0.75%, (b) 1.0%, and (c) 1.50%

F.9.e: Crack Patterns for DPT, Phase 2, UT Arlington

In Figure F-23 are shown photographs of typical cracking patterns from DPT of plain and SFRC specimens with 0.5% and 1.0% volume fractions of fibers. The plain concrete specimens broke into four pieces at peak load, while the SFRC specimens had several radial cracks, and the integrity of the specimen was maintained by fibers bridging across those cracks. Cracks generally developed from top of the specimens and propagated to the bottom, parallel to the applied load.

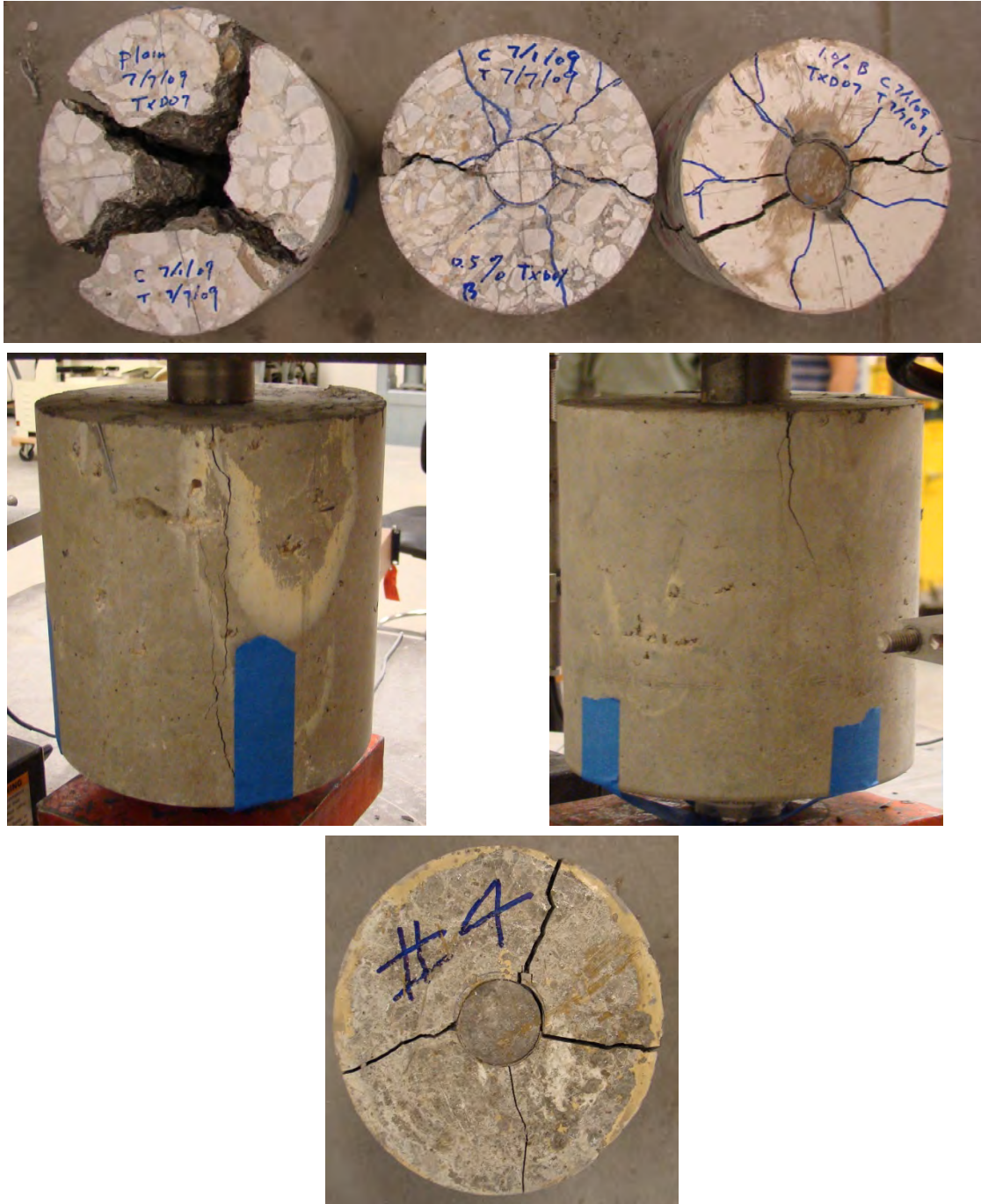


Figure F-23: Typical cracking patterns, DPT, Phase 2, UT Arlington

F.10. Results of Phase 3 DPT, UT Arlington

As in Phases 1 and 2, DPTs were performed in Phase 3 at a compressive strength of about 4 ksi. In Phase 3, sets of specimens were cast on one day and tested the next day, within about 24 hours after casting.

F.10.a: Equivalent Tensile Strength of Double-Punch Specimens, Phase 3, UT Arlington

As shown in Table F-24 and Figure F-24, in Phase 3 all SFRC specimens except BS-150 showed higher equivalent tensile strength than the plain concrete specimens. Equivalent tensile strength increased with increasing fiber volume fractions. Specimens with Type 2 fibers (Double bend hooks: Bekaert short) showed no or little increase in maximum tensile strength as compared to PC. This result was unexpected, and is partly attributable to the compressive strength of concrete, which can hardly be the same at early ages. As in Phases 1 and 2, specimens with longer fiber generally showed better performance.

Table F-24: Average peak load and equivalent tensile strength, Phase 3, UT Arlington

Specimen Type	Compressive strength (ksi)	Peak Load (kips)	Equivalent tensile strength (psi)	Increased strength compared to PC	Coefficient of Variation (COV)	Time of test after casting (hrs)
PC	4.7	27.1	410		5.2 %	24
SFRC-R-075	5.1	32.7	495	20.7 %	4.4 %	
SFRC-R-100	4.7	31.4	476	16.1 %	2.0 %	
SFRC-R-150	6.5	31.4	476	16.1 %	6.8 %	
SFRC-R-200	5.8	33.0	499	21.7 %	2.9 %	
SFRC-BS-050	5.3	30.1	456	11.2 %	4.2 %	
SFRC-BS-075	4.5	27.2	412	0.5 %	7.0 %	
SFRC-BS-100	4.9	30.2	457	11.5 %	4.4 %	
SFRC-BS-150	4.1	26.9	407	-0.7 %	2.4 %	
SFRC-BL-050	4.9	27.9	422	2.9 %	4.2%	
SFRC-BL-075	5.2	30.3	458	11.7 %	4.9 %	
SFRC-BL-100	6.1	33.1	501	22.2 %	6.7 %	
SFRC-BL-150	6.0	41.7	631	53.90 %	10.64 %	

As in Phases 1 and 2, ultimate equivalent tensile strengths for Type 1 and Type 2 fibers were compared to Type 3 fiber as shown in Table F-25. Type 3 fibers have a larger diameter, which gives higher stiffness as well as mechanical bonding strength due to the higher elastic modulus of the hooks. This in turn leads to higher ultimate strength of the SFRC. As mentioned earlier, however, the greater aspect ratio of the long fibers as well as the larger diameter and amount of coarse aggregate limited the fiber volume fraction to 1.5%. As shown in Table F-25, specimens with Type 3 fibers generally showed higher peak strengths.

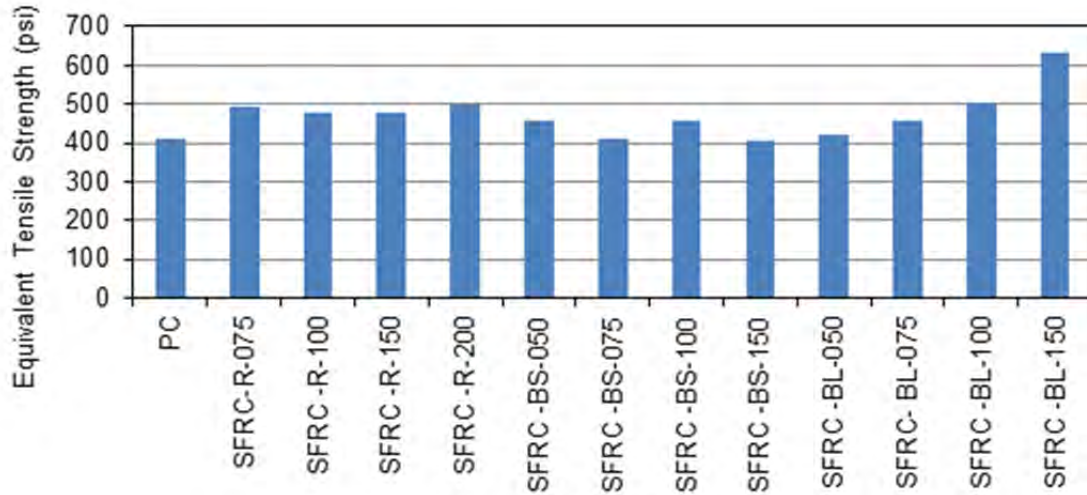


Figure F-24: Peak equivalent tensile strengths, Phase 3, UT Arlington

Table F-25: Peak strengths of specimens with Type 3 fibers and specimens with Type 1 or Type 2 fibers, Phase 3, UT Arlington

Volume fraction	Equivalent tensile strength of SFRC-BL (ksi)	Equivalent tensile strength of SFRC-R (ksi)	Difference with SFRC-R (ksi)	Equivalent tensile strength of SFRC-BS (ksi)	Difference with SFRC-BS (ksi)
0.50%	422	-	-	455	-33 (7.8% ↓)
0.75%	458	495	-37 (8.1% ↓)	412	46 (10.0% ↑)
1.00%	501	475	26 (5.2% ↑)	457	44 (8.8% ↑)
1.50%	631	475	156 (24.7% ↑)	407	224 (35.5% ↑)

R: Type 1 fiber, BS: Type 2 fiber, BL: Type 3 fiber

F.10.b: Residual Strengths at 0.1-in. Deformation, Phase 3, UT Arlington

As shown in Table F-26, residual strengths for specimens with steel fibers are between 6 and 38 kips at 0.10-in. deformation. Residual strengths obtained in Phase 3 were similar to those of Phases 1 and 2. Specimens with Type 3 fiber showed higher residual strength than specimens with Type 2 fibers and Type 1 fibers. As shown in Figure F-25, long fibers with larger volume fractions gave higher residual strengths.

Table F-26: Residual strengths at 0.1-in. deformation, Phase 3, UT Arlington

Specimen Type	Residual Strength at 0.1 in. Deformation		
	Coefficient Of Variation (COV)	Ultimate load (kips)	Equivalent tensile strength (psi)
SFRC-R-075	6.8	5.6	85
SFRC-R-100	19.5	8.3	126
SFRC-R-150	7.3	10.9	165
SFRC-R-200	17.1	16.6	251
SFRC-BS-050	10.8	6.6	100
SFRC-BS-075	22.8	7.9	120
SFRC-BS-100	3.0	11.5	174
SFRC-BS-150	17.2	17.0	257
SFRC-BL-050	24.5	9.0	136
SFRC-BL-075	33.9	8.6	130
SFRC-BL-100	15.1	18.5	280
SFRC-BL-150	30.2	38.8	587

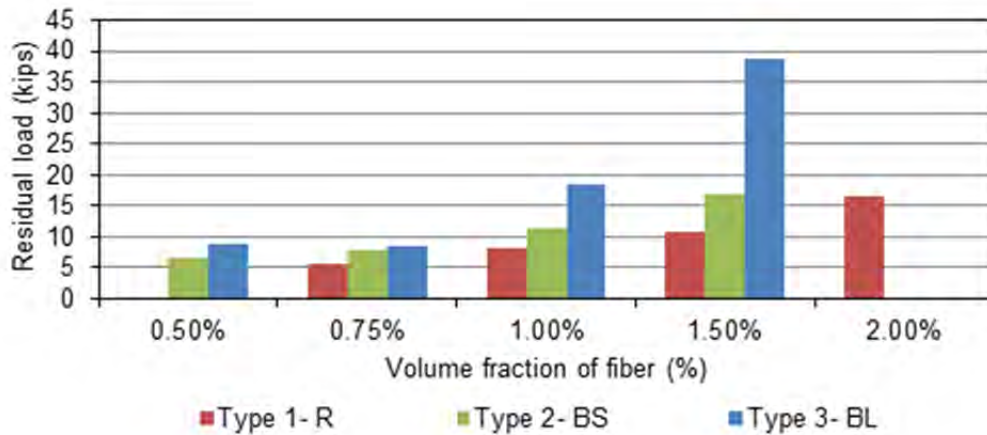


Figure F-25: Residual strengths at 0.1-in. deformation, Phase 3, UT Arlington

Table F-27 compares Type 3 residual strength specimens with Type 1 or Type 2 specimens. Type 3 specimens generally had the higher residual strengths.

Table F-27: Residual strengths of specimens with Type 3 fibers versus specimens with Type 1 or Type 2 fibers, Phase 3, UT Arlington

Volume fraction	Corresponding load at deformation 0.1 in. for SFRC-BL (kips)	Corresponding load at deformation 0.1 in. for SFRC-R (kips)	Difference with SFRC-R (kips)	Corresponding load at deformation 0.1 in. for SFRC-BS (kips)	Difference with SFRC-BS (kips)
0.50%	9.0	-	-	6.6	2.4 (26.7% ↑)
0.75%	8.6	5.6	3.0 (34.9% ↑)	7.9	0.7 (8.1% ↑)
1.00%	18.5	10.2	11.6 (62.7% ↑)	11.5	7.0 (37.8% ↑)
1.50%	38.8	10.9	27.9 (28.1% ↑)	17.0	21.8 (56.2% ↑)

R: Type 1 fiber, BS: Type 2 fiber, BL: Type 3 fiber

F.10.c: Coefficients of Variation, Phase 3, UT Arlington

In Table F-24 and Table F-26 are shown the coefficients of variations for peak strengths and residual strengths for Phase 3. The COV for peak strength in Phase 3 is about 5%, less than that obtained in Phases 1 and 2. Even though the number of replicate specimens was reduced to four, the double-punch is still reliable. The COVs of residual strengths were less than 20% for most specimens.

F.10.d: Load-Deformation Responses for DPT, Phase 3, UT Arlington

In Figure F-26, load-deformation curves for specimens with different types of fibers are compared at the same volume fractions. In Figure F-27, load-deformation curves are compared for specimens with different fibers across the complete range of volume fractions.. The initial stiffnesses (slope of curves before first crack load or peak load) are very close for all specimens, including plain concrete. The post-cracking response, in contrast, is quite different, and depends on the type of fiber and the volume fraction of fiber. Specimens with longer fibers and higher volume fractions typically showed greater toughness.

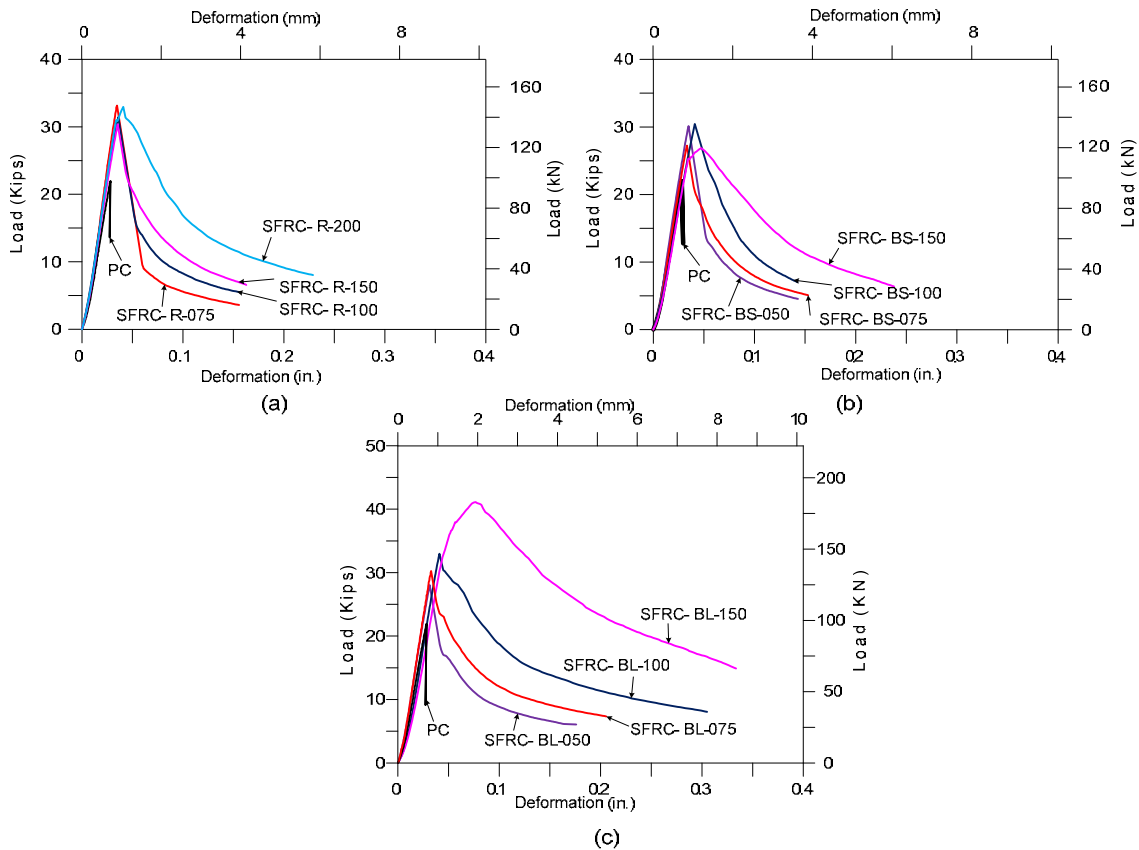


Figure F-26: Load-deformation curves for plain concrete and SFRC specimens with different types of fibers, Phase 3, UT Arlington: (a) SFRC-R, (b) SFRC-BS, and (c) SFRC-BL

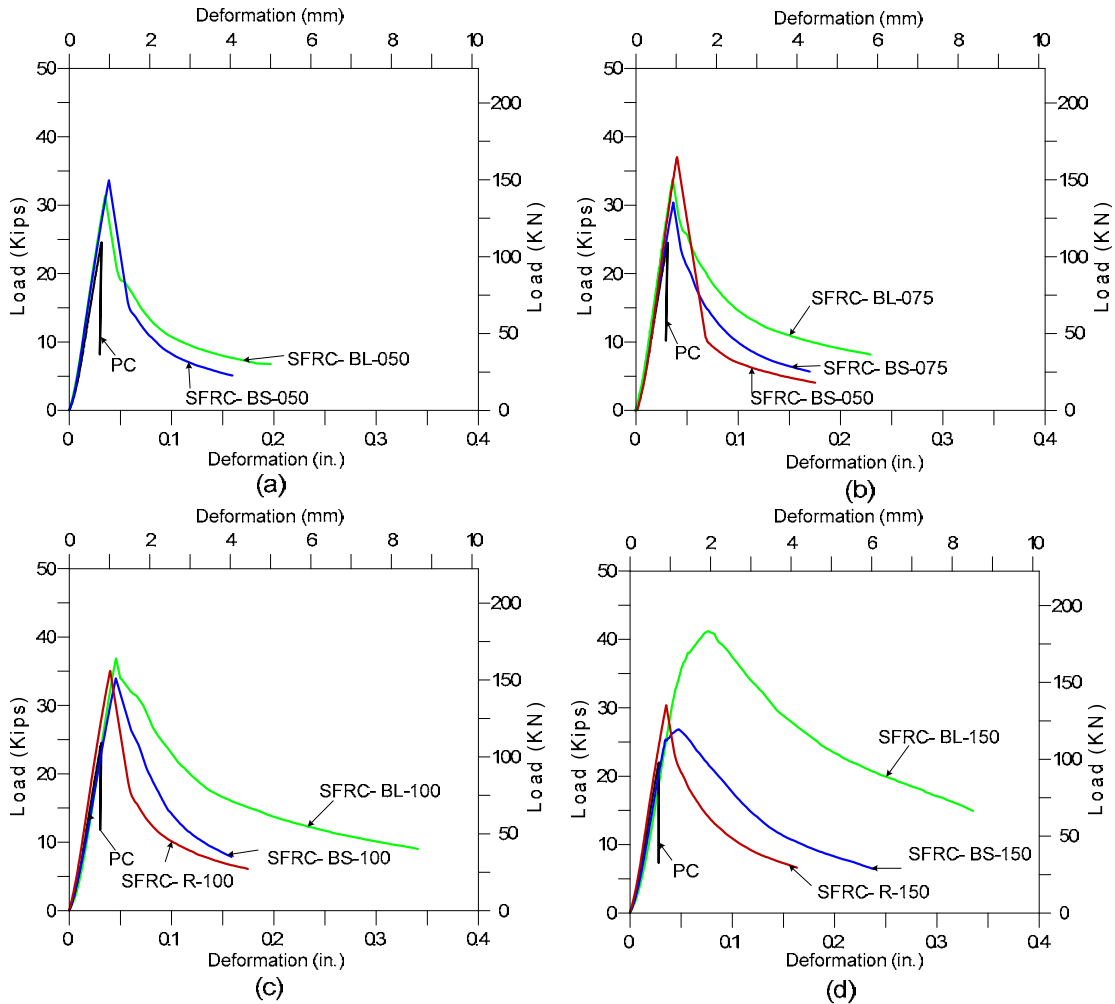


Figure F-27: Load-deformation curves for plain concrete and SFRC specimens with different volume fractions of fibers, Phase 3, UT Arlington: (a) 0.50%, (b) 0.75%, (c) 1.0%, and (d) 1.50%

In Figure F-28, load-deformation curves for Phase 1 and Phase 3 are compared. Phase 1 had large variations in ascending-branch response and descending-branch response. In Phase 3, in contrast, those variations were significantly reduced. This was due primarily to the improvement in testing technique by the introduction of a “shakedown” load.

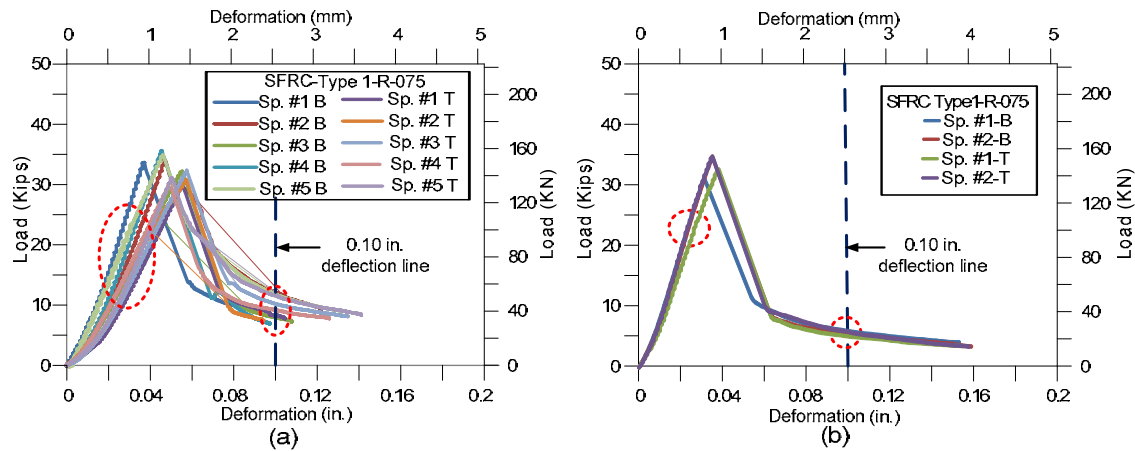


Figure F-28: Load-deformation curves for (a) Phase 1 with SFRC-R-075 (Type 1 fiber 0.75%) and (b) Phase 3 with SFRC-R-075 (Type 1 fiber 0.75%)

F.11. Results for Phase 4 of DPT, UT Arlington

In previous phases of study it had been seen that some of the specimens showed uncontrolled results. Some SFRC with higher volume content showed lower ultimate strength. Some of them also showed high COV especially for residual strengths. It was mainly due to the difficulty in controlling the early age of strength of concrete. In this phase of experimental investigation all tests were carried out when concrete achieved its longer term compressive strength. All specimens were tested after 28 days. In general the specimens were tested at age of 55–58 days after casting.

F.11.a: Equivalent Tensile Strength

As shown in Table F-28 and Figure F-29, almost all SFRC specimens showed higher equivalent tensile strength than that of PC specimens. Except SFRC-BS-050 and SFRC-H-075, they showed slightly lower peak strength as compared to PC. It was seen that increasing fiber contents normally increased the ultimate equivalent tensile strength. Nevertheless, SFRC, in general, showed better performance in equivalent ultimate tensile strength compared to PC. In the case of SFRC-BL-150 specimens, the ultimate tensile strength was 39.4% higher than that of the PC ones.

Table F-28: Average peak load and equivalent tensile strength, Phase 4, UT Arlington

S.N.	Specimen Type	Peak Load	Equivalent Tensile strength	Coefficient of Variation	Compressive strength	Time of Testing
		kips	psi	%	ksi	Days
1	PC	38.6	585	5.2	7.1	55-58
2	SFRC-BL-050	38.7	586	4.3	6.5	
3	SFRC-BL-075	43.5	659	6.6	7.4	
4	SFRC-BL-100	44.1	667	3.2	7.7	
5	SFRC-BL-150	53.8	815	5.0	8.2	
6	SFRC-BS-050	37.7	571	4.7	7.0	
7	SFRC-BS-075	39	590	3.2	7.6	
8	SFRC-BS-100	40.9	618	2.9	7.8	
9	SFRC-BS-150	47.1	713	3.6	8.0	
10	SFRC-R-075	40.9	618	3.7	7.5	
11	SFRC-R-100	42.8	646	5.3	7.9	
12	SFRC-R-150	43.6	659	2.5	8.0	
13	SFRC-R-200	48.0	727	5.2	8.2	
14	SFRC-H-075	36.5	552	4.6	6.3	
15	SFRC-H-150	39.8	601	5.5	7.1	
16	SFRC-H-200	43.2	654	6.1	7.5	

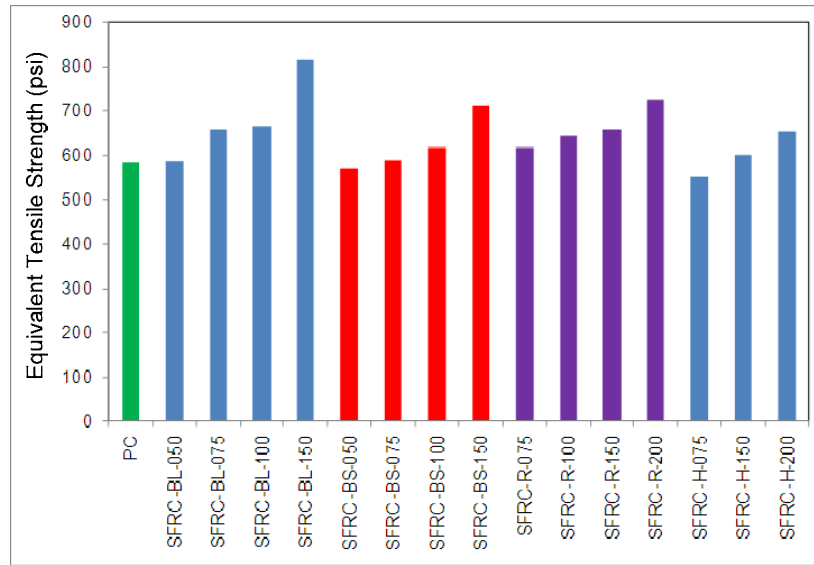


Figure F-29: Peak equivalent tensile strengths, Phase 4, UT Arlington

As in the previous phases, ultimate equivalent tensile strengths of Type 1 and Type 2 fibers specimens were compared to Type 3 fiber specimens as shown in Table F-29. The comparison was also made for specimens with Type 4 (Helix) fibers. The test results agreed with the results from the previous phases of the experimental program as the specimens with Type 3 fiber showed better performance.

Table F-29: Peak strengths of SFRC specimens with Type 3 fibers versus specimens with Type 1, Type 2, or Type 4 (Helix) fibers, Phase 4, UT Arlington

Volume fraction	Equivalent tensile strength SFRC-BL	Equivalent tensile strength SFRC-R	Compared to SFRC-R	Equivalent tensile strength SFRC-BS	Compared to SFRC-BS	Equivalent tensile strength SFRC-H	Compared to SFRC-H
	(psi)	(psi)	(psi)	(psi)	(psi)	(psi)	(psi)
0.50%	586	-	-	571	15 (2.5% ↑)	-	-
0.75 %	659	618	41 (6.3% ↑)	590	69 (10.5% ↑)	552	106 (16.1% ↑)
1.00%	667	646	21 (3.2% ↑)	618	49 (7.3% ↑)	-	-
1.50%	815	659	156 (19.1% ↑)	713	102 (12.5% ↑)	601	213 (26.1% ↑)

F.11.b: Residual Strengths at 0.10-in. Deformation, Phase 4, UT Arlington

As shown in Figure F-30 and Table F-30, residual strengths of SFRC specimens at 0.10-in. deformation were between 6.9 and 41.6 kips. As shown in Table F-31, SFRC-BL specimens showed higher residual strengths than SFRC-BS and SFRC-R specimens. SFRC-BL specimens showed higher residual strengths than SFRC-H specimens for all volume fractions.

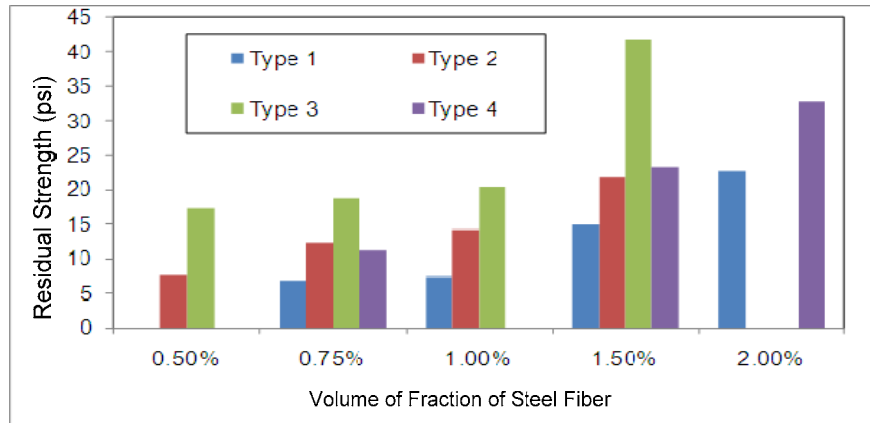


Figure F-30: Comparison of residual strengths at 0.1-in. deformation for different fiber types, Phase 4, UT Arlington

Table F-30: Comparisons of residual strength at 0.1-in. deformation, Phase 4, UT Arlington

Specimen type	Residual strength at 0.1 in. Deformation		
	Coefficient of variation (COV)	Load (kips)	Equivalent tensile strength (psi)
SFRC-BL-050	16.8	17.4	263
SFRC-BL-075	21.8	18.8	284
SFRC-BL-100	11.1	20.5	309
SFRC-BL-150	9.0	41.6	630
SFRC-BS-050	13.2	7.7	116
SFRC-BS-075	14.4	12.3	186
SFRC-BS-100	14.4	14.2	214
SFRC-BS-150	7.8	21.9	331
SFRC-R-075	17.3	6.9	104
SFRC-R-100	21.4	7.4	112
SFRC-R-150	11.7	14.9	226
SFRC-R-200	12.7	22.7	344
SFRC-H-075	10.3	11.3	170
SFRC-H-150	16.1	23.4	354
SFRC-H-200	10.4	32.8	496

Table F-31: Comparison of residual strengths of specimens with Type 3 fibers versus specimens with Type 1, 2, or 4 fibers, Phase 4, UT Arlington

Volume fraction	Equivalent tensile strength SFRC-BL	Equivalent tensile strength SFRC-R	Compared to SFRC-R	Equivalent tensile strength to SFRC-BS	Compared to SFRC-BS	Equivalent tensile strength SFRC-H	Compared to SFRC-H
	(psi)	(psi)	(psi)	(psi)	(psi)	(psi)	(psi)
0.50%	263	-	-	116	147 (44.1% ↑)	-	-
0.75 %	284	104	180 (26.6% ↑)	186	98 (34.5% ↑)	170	114 (40.1% ↑)
1.00%	309	112	197 (63.8% ↑)	214	95 (30.7% ↑)	-	-
1.50%	630	226	404 (64.1% ↑)	331	299 (40.7% ↑)	496	134 (21.1% ↑)

F.11.c: Coefficients of Variation, Phase 4, UT Arlington

For the Phase 4 DPTs at UT Arlington, the average COV is 4.5%, lower than for previous phases, and much less than that typically produced by ASTM C1609 tests. Average COVs for residual strengths were also lower than in previous phases.

F.11.d: Load-Deformation Responses for Phase 4 Double-Punch Specimens, Phase 4, UT Arlington

In Figure F-31, equivalent tensile strengths of plain concrete are compared with those of SFRC with one type of fiber and different volume fractions. In Figure F-32, load-deformation curves are compared for different types of fiber with the same volume fraction. Longer fibers with higher volume fractions led to larger toughness (greater area under the load-deformation curves).

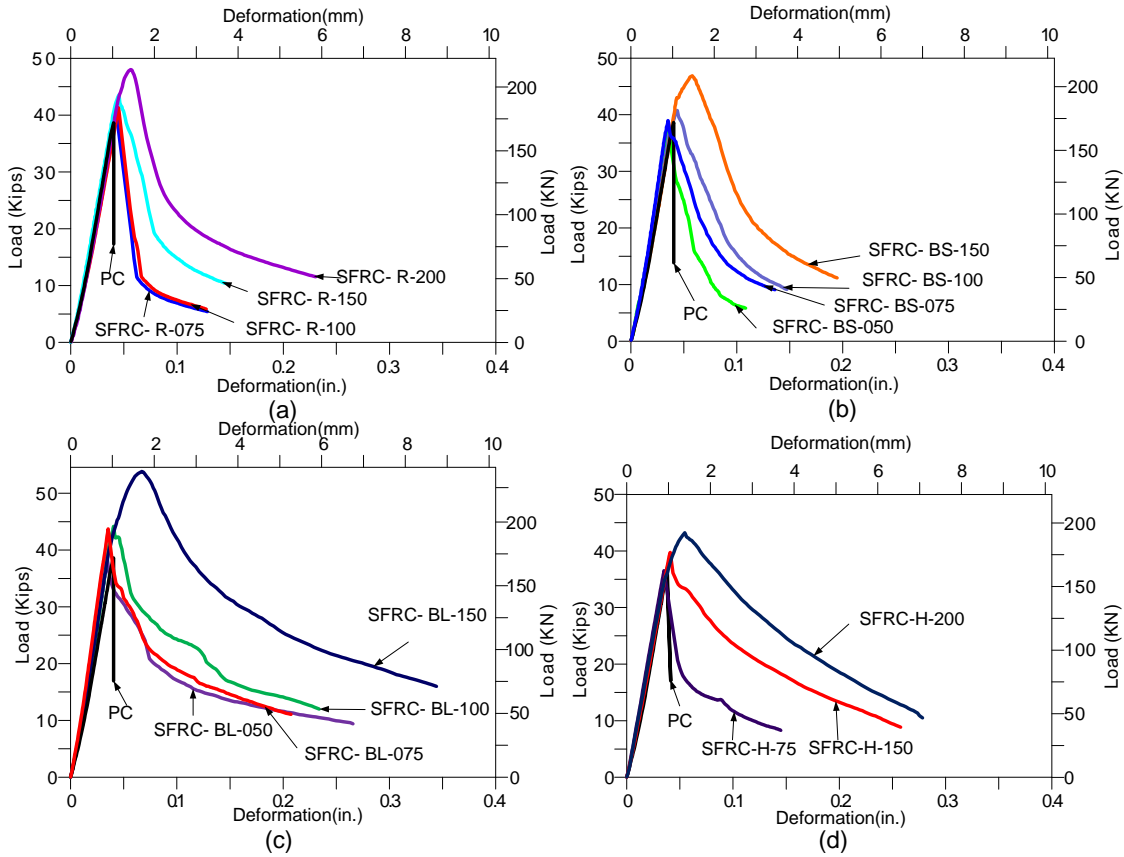


Figure F-31: Comparisons of plain concrete and SFRC specimens with different types of fibers, Phase 4, UT Arlington: (a) SFRC-R, (b) SFRC-BS, (c) SFRC-BL, and (d) SFRC-H

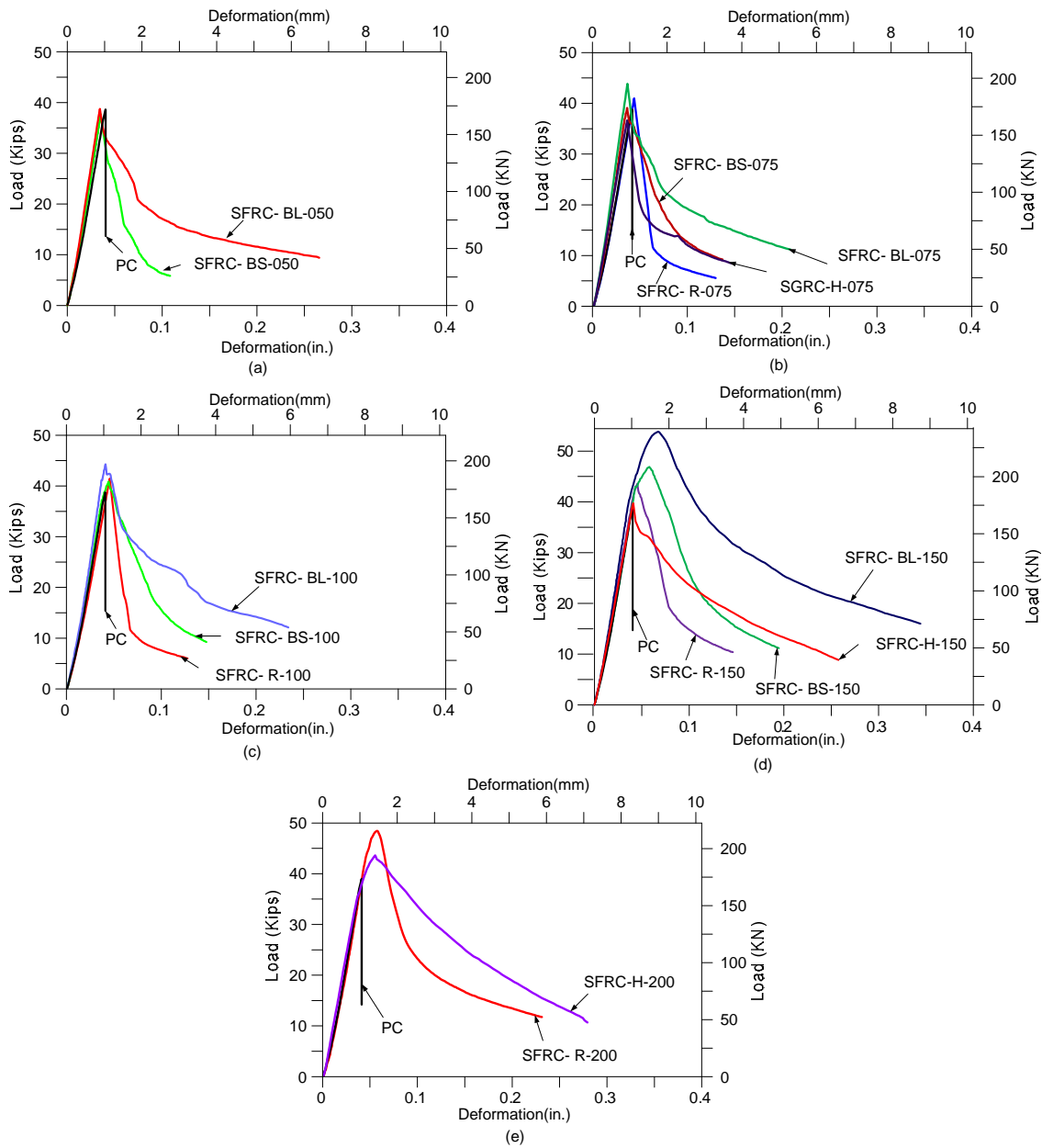


Figure F-32: Comparisons of plain concrete and SFRC specimens with different volume fractions, Phase 4, UT Arlington: (a) 0.50%, (b) 0.75 %, (c) 1.0%, (d) 1.5%, and (e) 2.0%

In Table F-32 are shown the toughnesses for Phase 4 specimens. Specimens SFRC-BL-150, with Type 3 fiber (long fiber) showed the highest toughness (3845.8 lb-in). Coefficients of variation for toughness were about 10% for most of specimens. Specimens with higher fiber contents (R-200, H-200, and BL-150) showed strain-hardening. This is investigated further in the next section.

Table F-32: Average toughness at 0.10-in. deformation, Phase 4, UT Arlington

S.N.	Specimen type	Average toughness at 0.10 in. deformation	Coefficient of variation
		lb-in	%
1	PC	752*	18.0
3	SFRC-BL-050	2246.5	9.9
4	SFRC-BL-075	2343.0	22.7
5	SFRC-BL-100	2598.0	8.6
6	SFRC-BL-150	3845.8	8.4
7	SFRC-BS-050	1437.5	11.7
8	SFRC-BS-075	2081.0	2.4
9	SFRC-BS-100	2318.3	4.3
10	SFRC-BS-150	3047.0	2.5
11	SFRC-R-075	1330.5	14.0
12	SFRC-R-100	1500.3	9.8
13	SFRC-R-150	2819.8	3.6
14	SFRC-R-200	2246.8	9.9
15	SFRC-H-075	1652.0	12.0
16	SFRC-H-150	2823.3	10.4
17	SFRC-H-200	3115.3	5.2

*Note : Toughness value for PC specimen is at end of test (at deflection of 0.05 inches)

F.11.e: Crack Patterns from DPT, Phase 4, UT Arlington

In Figure F-33 are shown typical photographs from DPT for plain concrete specimens, and for specimens with different types of fibers with different volume fractions (0.5% to 2%). As shown in the figure, the plain concrete specimen broke into four pieces at peak load, while the SFRC specimens showed several radial cracks until the test was stopped at one-quarter the peak load. Most cracks propagated along the entire depth of the specimens.

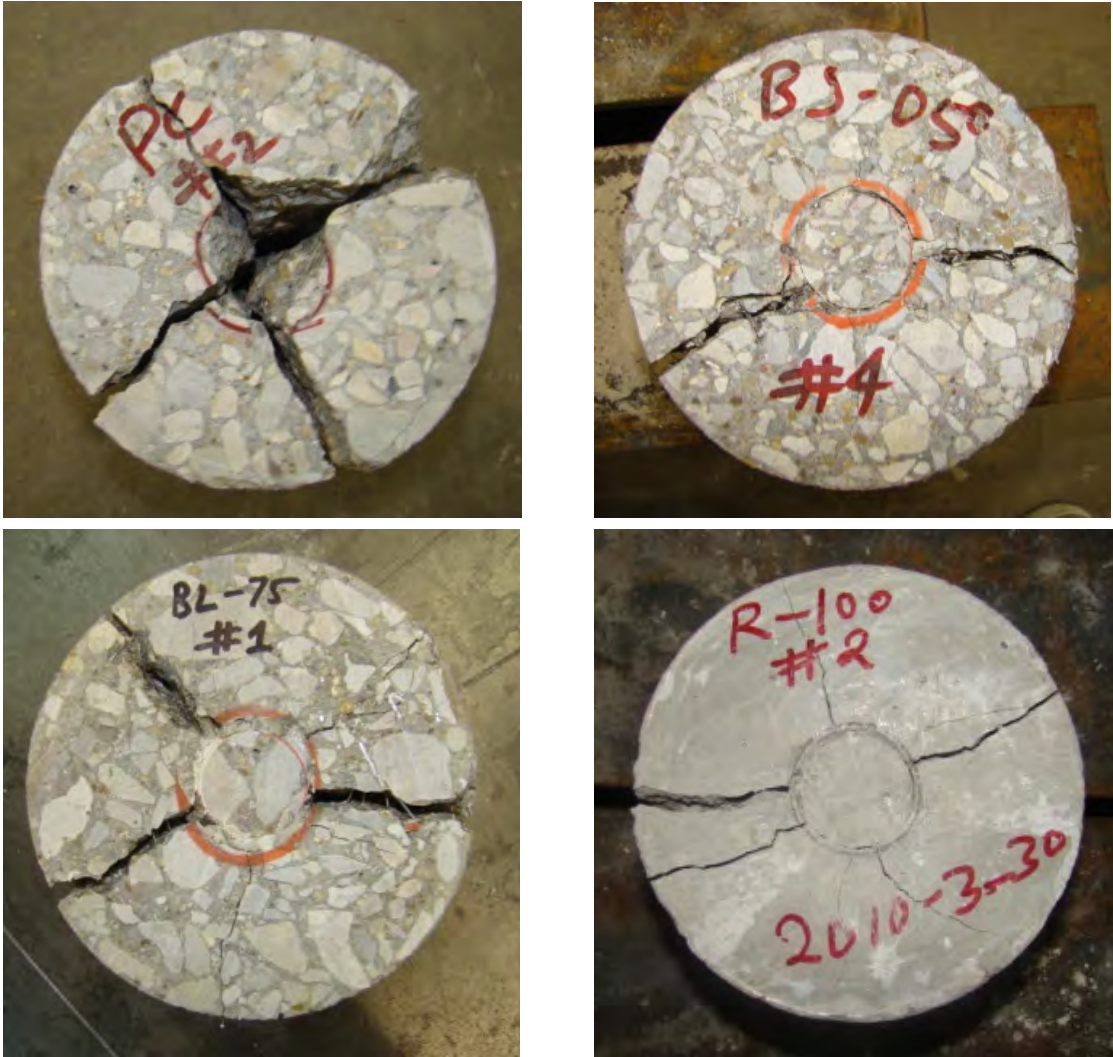
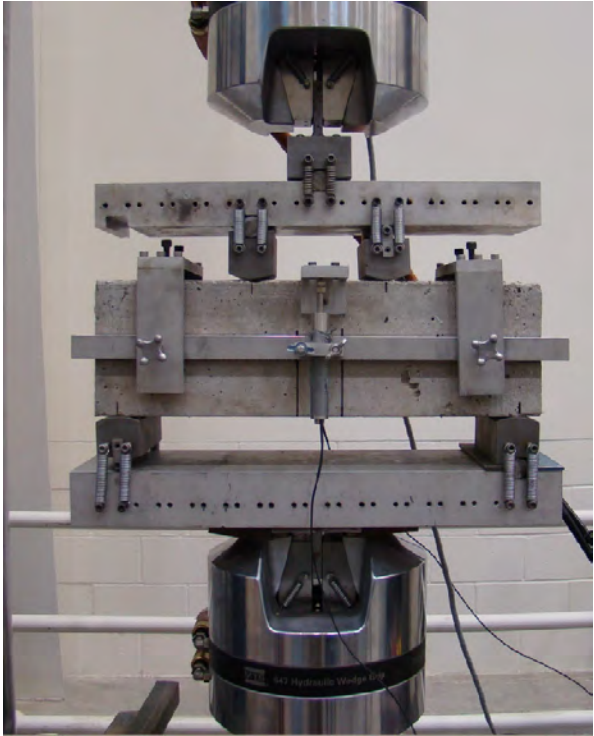


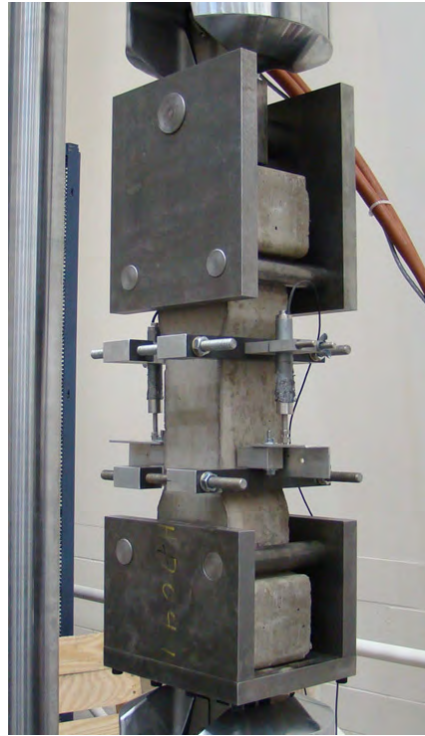
Figure F-33: Photographs of typical double-punch specimens, Phase 4, UT Arlington

F.12. Comparison of DPT with Other Material Test Methods for SFRC

Results from the DPT were compared with other material test methods such as third-point bending test (ASTM C1609) and DTT, whose test setups are shown in Figure F-34.



(a) ASTM C1609 third-point test



(b) Uniaxial direct tension test (DTT)

Figure F-34: Other material test setups for SFRC

In Table F-33, peak loads and their corresponding COVs are compared for the DPT, the ASTM C1609 third-point test, and the uniaxial direct tension test. For all three mixtures, COVs for the DPT are much lower (5-7%) than those for the third-point bending test and the DTT, which are typically more than 10% and sometimes as high as 26% (ML-075 bending).

Table F-33: Comparison of peak loads and COVs between DPT and other material test methods for SFRC

Specimen	At peak load		Compressive strength ksi
	Deformation in.	Load kips/COV	
Tensile: ML 150	0.01	8.5	7.75
		12.8%	
Bending: ML150	0.014	15.4	
		13%	
DPT: ML150	0.05	41.6	
		4.6%	
Tensile: ML075	0.001	9.0	9.23
		14.3%	
Bending: ML075	0.004	11.0	
		26.2%	
DPT: ML075	0.04	39.0	
		6.9%	
Tensile: Hybrid	0.002	9.4	9.72
		24%	
Bending: Hybrid	0.018	17.0	
		11.4%	
DPT: Hybrid	0.06	43.9	
		5.7%	

In Table F-34, residual strengths and toughnesses, along with their corresponding COVs, are compared for all three test methods at specified deformation levels. The second and third columns of the table present average residual strengths, toughnesses, and COVs at a 0.12-in. deformation, which is the deformation at which the third-point bending test was typically stopped. As seen in the table, COVs for residual strength and for toughness are lower for the DPT than for the bending test and the DTT. COVs for the bending and DTTs are as high as 77.5%. For the DPT, in contrast, COVs are much lower, even for the relatively scatter associated with Specimens ML-075.

Table F-34: Comparison of residual strengths and toughnesses (and corresponding COVs) for DPT versus other material test methods for SFRC

Specimen	At same deformation		At various selected deformations	
	Load/COV	Toughness/COV	Load/COV	Toughness/COV
	kips/%	(k-in)/%	kips/%	(k-in)/%
	At of 0.12 in. deformation (within the gauge length)		At of 0.04 in. deformation	
Tensile: ML-150	2.2	496.6	5.0	242.8
	23.4%	23.4%	17.8%	9.9%
Tensile: ML-075	2.4	391.0	3.8	176.7
	68.9%	28.2%	39.5%	29.2%
Tensile: Hybrid	2.0	417.5	4.8	214.2
	64.5%	35.5%	38.8%	35.2%
	At of 0.12 in. deformation		At of 0.06 in. deformation	
Bending: ML-150	3.8	1063.7	8.3	715.7
	23.6%	12.8%	15.7%	12.1%
Bending: ML-075	3.5	741.4	6.3	490.8
	41.4%	45.5%	43.4%	43.1%
Bending: Hybrid	3.8	1175.0	9.7	801.0
	77.5%	25.6%	31.2%	17.3%
	At of 0.12 in. deformation		At of 0.10 in. deformation	
DPT: ML-150	21.5	3045.2	24.3	2629.2
	6.9%	4.5%	6.8%	5.2%
DPT: ML-075	10.7	2042.4	12.5	1814.4
	22.1%	15.9%	25.8%	15.0%
DPT: Hybrid	26.3	3337.8	30.9	2750.8
	14.1%	8.7%	11.7%	7.4%

In Figure F-35 are compared the individual and average load-deformation curves from DPT for three different mixtures (ML-075, ML-150, and hybrid). For all specimens, up to peak load the slopes of the curves are similar, but after peak load the curves are quite different. These differences are greater for Specimen ML-075 than for Specimen ML-150 and the hybrid specimens. As shown in Figure F-35(d), the descending branch of the load-deformation curve falls more gradually with increasing volume fractions. Hence, the DPT can easily differentiate between different fibers and different volume fractions.

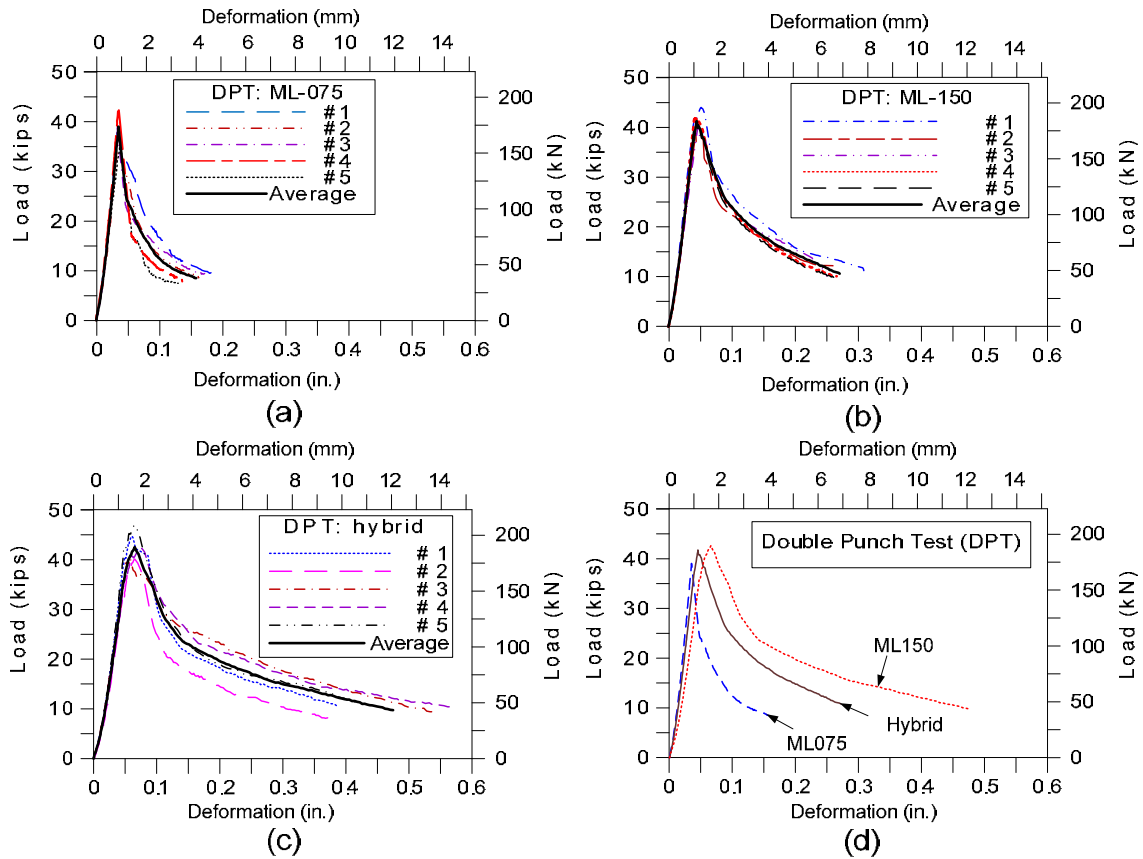


Figure F-35: Load-deformation curves from DPT

In Figure F-36 and Figure F-37, respectively, are shown individual and average load versus deformation curves from the third-point bending test and the DTT. Those results show considerable scatter. In Figure F-36(d), for the bending test, the residual loads at 0.12 in. deformation for all type of specimens appear very close to each other. This is probably the result of averaging very scattered data, and not a reflection of the true behavior. In Figure F-37(d), for the DTT, even though the peak loads were quite close, a specimen with a higher volume fraction of steel fiber (hybrid) had a lower residual strength than a specimen with a lower volume fraction (ML-075). Hence using average results for this test does not reflect the true properties of SFRC.

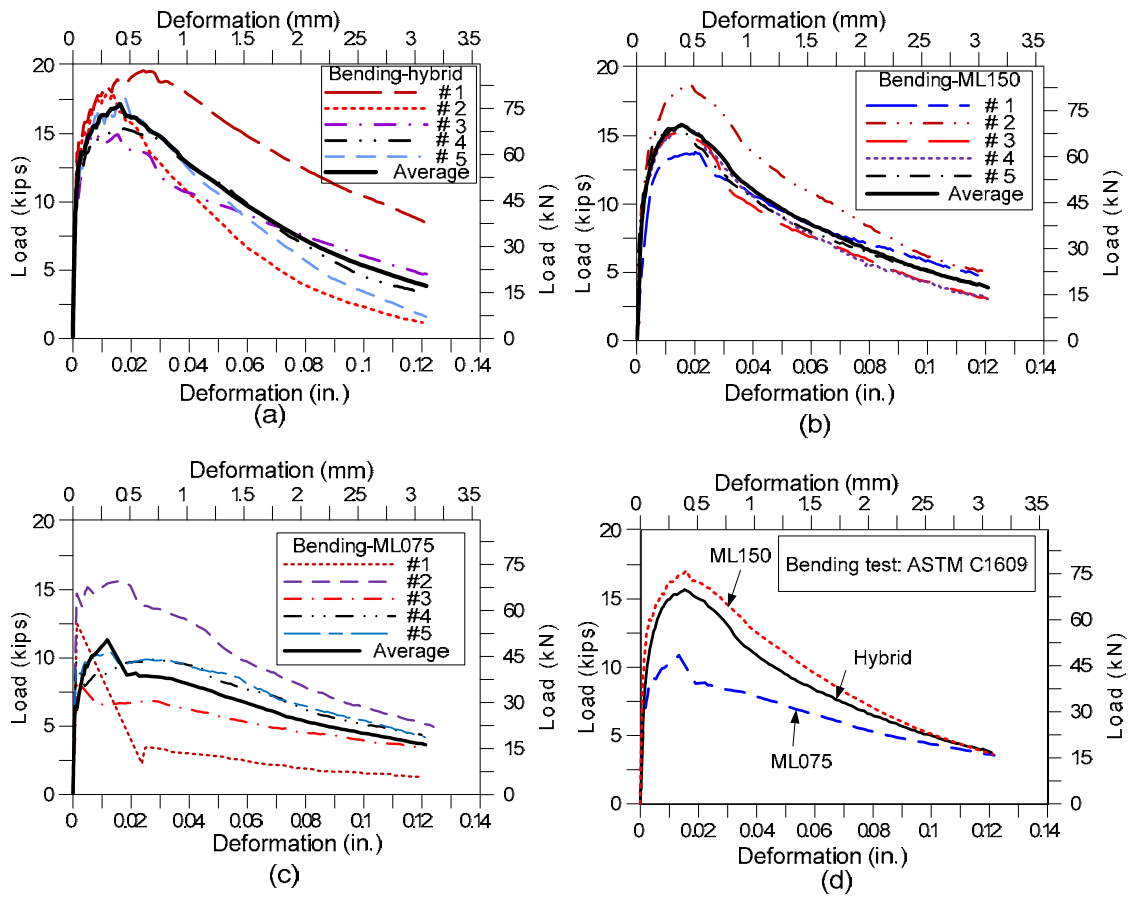


Figure F-36: Load-deflection curves from third-point bending test (ASTM C1609)

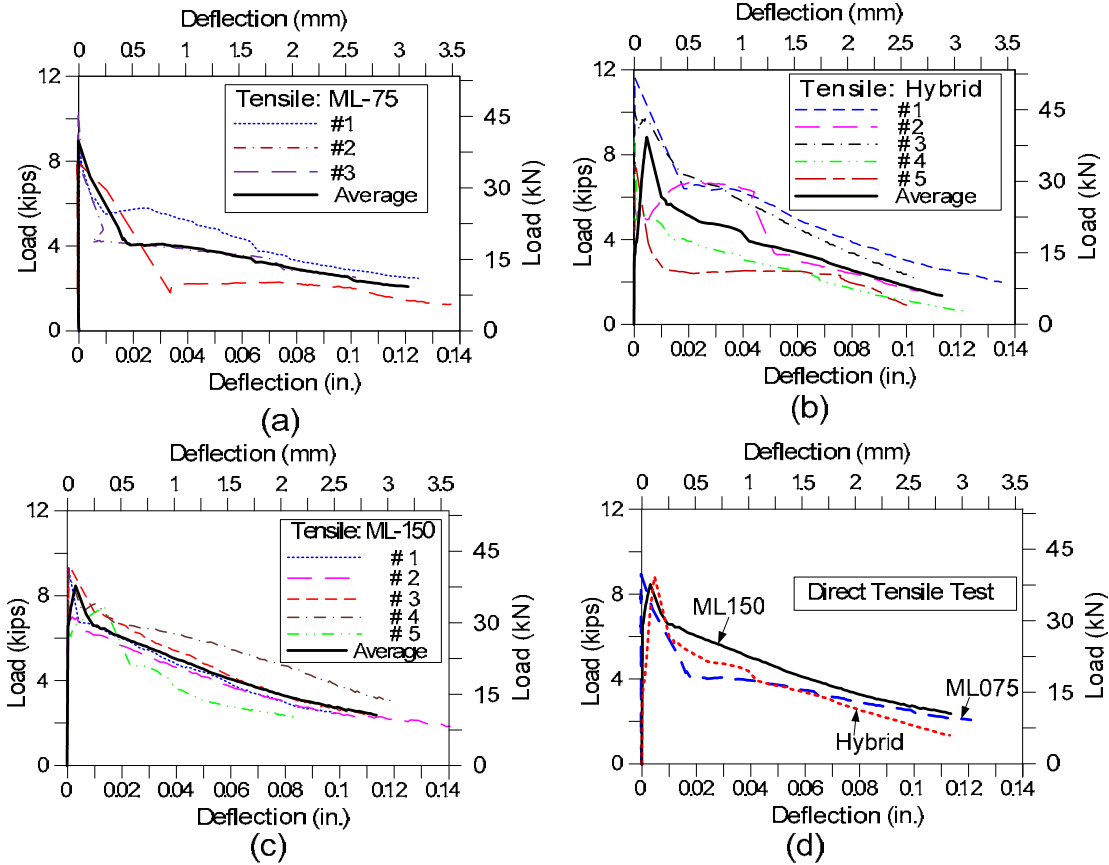


Figure F-37: Load-deflection curves from direct tension test

Section 5.6.6.2 of ACI 318-11 requires that for steel-fiber reinforced concrete to be acceptable for shear resistance, the residual loads at a midspan deflection of 1/300 the span length and at 1/150 the span length shall exceed 90% and 75%, respectively, of the peak load from the third-point bending test. In this case, those deflections correspond to 0.06 in. and 0.12 in. The capacities at those deflections are less than those required by ACI 318-11. The corresponding residual loads at these deflections are much less than 90% and 75% of the peak load, respectively.

**Table F-35: Residual strengths for third-point bending test (ASTM C1609)
as per ACI 318-11**

Specimen	Load at 0.06 in. (L/300) Deflection	Load at 0.12 in. (L/150) Deflection	90% of 1st peak load	75% of 1st peak load	Check for ACI 318-11 Section 5.6.6.2	
	(kips)	(kips)	(kips)	(kips)		
ML-150						
ASTM#1	8.2	4.7	12.2	10.2	Not pass	Not pass
ASTM#2	10.6	4.8	16.8	14.0	Not pass	Not pass
ASTM#3	7.5	3.0	12.5	10.4	Not pass	Not pass
ASTM#4	7.5	3.0	14.1	11.7	Not pass	Not pass
ASTM#5	7.8	3.7	13.8	11.5	Not pass	Not pass
Mean	8.3	3.8	13.9	11.6	Not pass	Not pass
ML-075						
ASTM#1	7.5	4.3	10.1	8.4	Not pass	Not pass
ASTM#2	2.3	1.2	11.6	9.7	Not pass	Not pass
ASTM#3	9.3	5.0	13.4	11.2	Not pass	Not pass
ASTM#4	5.0	3.2	7.1	5.9	Not pass	Not pass
ASTM#5	7.3	4.1	8.3	6.9	Not pass	Not pass
Mean	8.6	3.6	10.1	8.4	Not pass	Not pass
Hybrid						
ASTM#1	14.7	8.4	16.9	14.1	Not pass	Not pass
ASTM#2	6.5	1.1	15.9	13.3	Not pass	Not pass
ASTM#3	6.7	3.4	15.8	13.2	Not pass	Not pass
ASTM#4	8.9	4.6	13.4	11.1	Not pass	Not pass
ASTM#5	8.9	3.2	13.7	11.4	Not pass	Not pass
Mean	9.1	4.1	15.1	12.6	Not pass	Not pass

In Figure F-38, strengths from each of the three test methods are compared. For all three mixtures, the bending strength is higher than the direct tensile strength and the equivalent tensile strength, and the direct tensile strength and the equivalent tensile strength are quite close to each other.

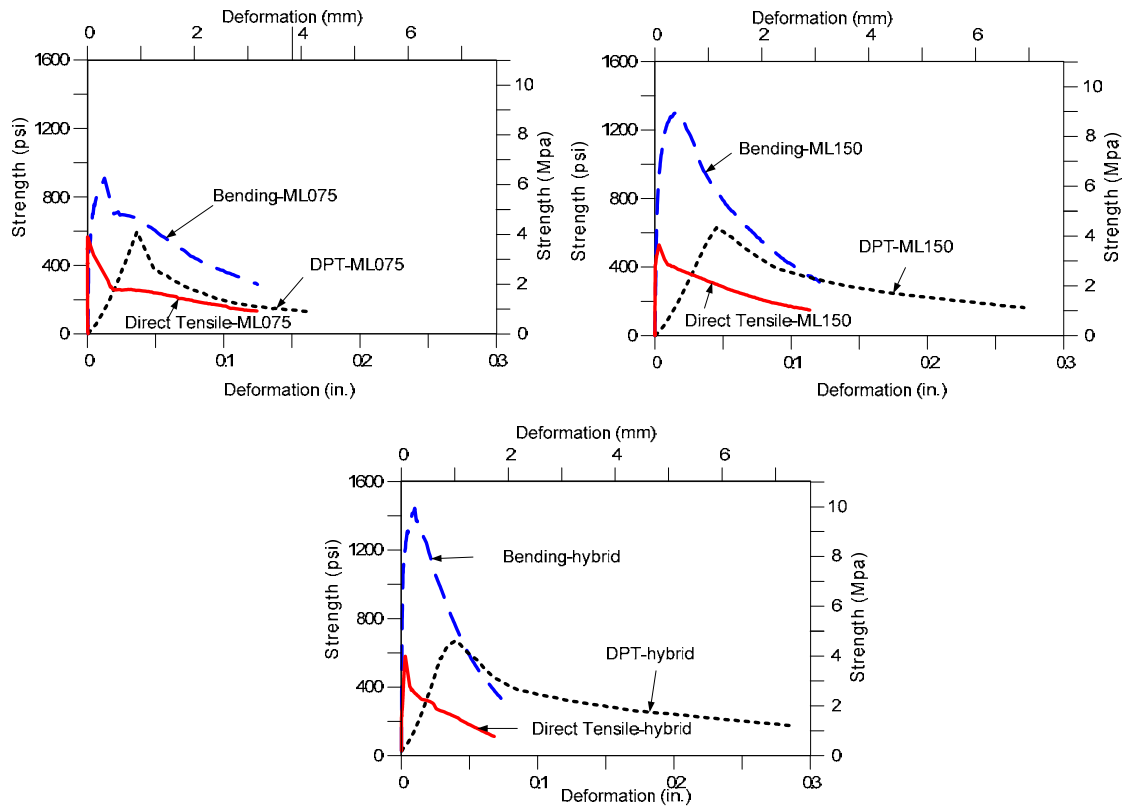


Figure F-38: Comparative strengths of three test methods (DPT, bending, DTT)

In Figure F-39, load-deformation curves are compared for DPT specimens made from the top and the bottom halves of 6- x 12-in. cylinders. The curves for the top halves show more scatter than the curves for the bottom halves. COVs of peak strength, residual strength, and toughness are 4.7%, 12.3% and 9.0%, respectively, for the bottom halves, and 7.3%, 14.9%, and 11.1%, respectively, for the top halves. This could be attributed to the tendency of fibers to settle toward the bottoms of the cylinder molds during vibration.

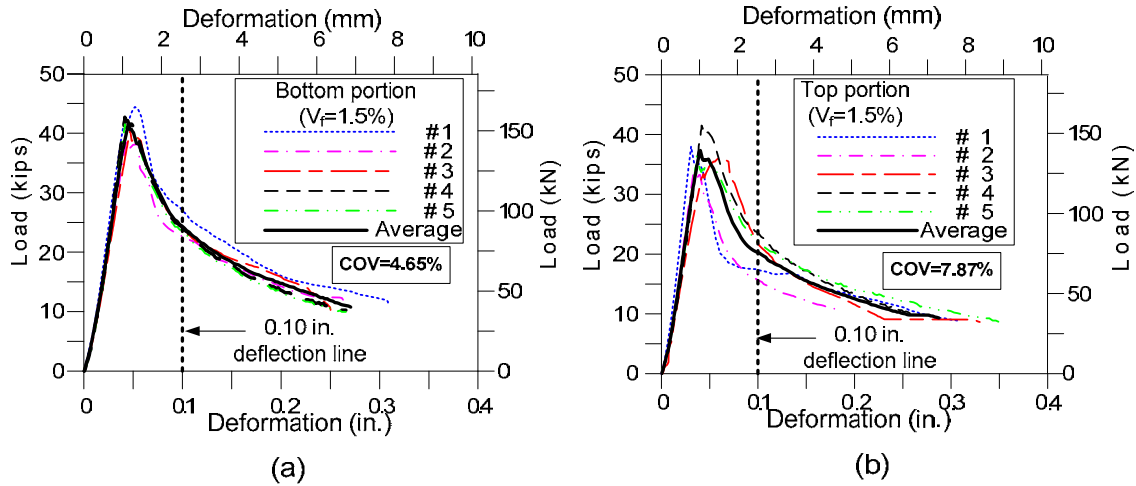


Figure F-39: Load-deflection curves for top versus bottom portions of cylinders used in DPTs, UT Arlington

F.13. Results from Phase 5 (Post-Cracking Investigation of DPT Specimens), UT Arlington

Each phase of the preceding study shows that DPT gives lower COVs for peak load and residual load than other material test methods such as the third-point bending test and the DTT. To further evaluate post-cracking performance, additional DPT specimens were prepared and tested. Peak strengths, residual strengths, and COVs are presented in Table F-36. COVs are about 6% for peak strength and 10% for residual strength, except for Specimens HYB4 and R-075. COVs for toughness are very low for all specimens.

Table F-36: Summary results for Phase 5 (post-cracking evaluation of DPT), UT Arlington

Specimen	Compressive strength	At peak load			At 0.1 in. deformation		
		Load	Deflection	Tensile strength	Load	Tensile strength	Toughness
		COV	COV	COV	COV	COV	COV
	(ksi)	(Kips)	(in.)	(psi)	(Kips)	(psi)	lb-in
HYB1	12.1	110.3	0.2	1668.4	84.8	1282.6	4110.3
		6.6%	28.1%	6.64%	5.0%	5.0%	3.2%
HYB2	7.4	46.4	0.1	702.8	42.3	640.2	2731.8
		5.5%	4.8%	5.48%	7.8%	7.8%	4.7%
HYB3	7.9	44.5	0.07	673.4	34.1	515.5	2395.5
		5.6%	9.0%	5.58%	8.9%	8.9%	10.2%
HYB4	6.0	38.2	0.08	578.6	26.6	402.1	2180.8
		4.8%	9.7%	4.77%	20.8%	20.8%	3.14%
ML-075	7.1	38	0.06	574.9	17.0	405.8	1821.8
		6.2%	2.6%	6.24%	10.9%	10.9%	3.99%
R-075	7.5	36.9	0.07	558.7	10.8	470.7	1594.1
		8.5%	9.3%	8.48%	15.0%	15.0%	7.3%

In Figure F-40, the load-deformation curves for mortar specimen (HYB1) with 3% hybrid steel fibers (2% Type 6: twisted and 1% Type 7: micro Maccaferri). Strain-hardening behavior is clearly evident after first cracking. Larger numbers of small cracks developed during the test. Also due to the ultra-high performance of the HYB1 specimens, first cracking occurred at about 0.1-in. deformation, and peak load occurred at about 0.2-in. deformation.

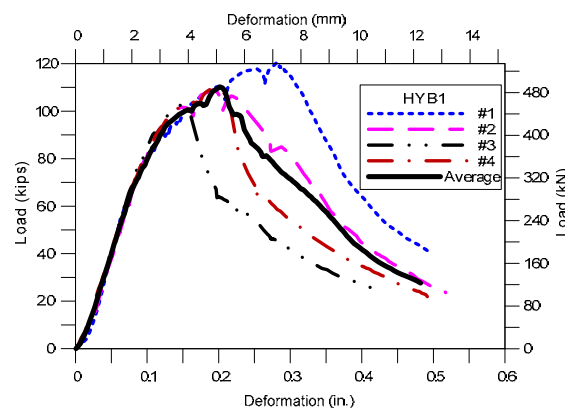


Figure F-40: Load-deformation curves from DPT with HYB1, UT Arlington

In Figure F-41, results for two hybrid SFRC mixtures are compared. The first (Hybrid) is consists of specimens with equal volume fractions (0.75% Type 5+0.75% Type 6) of both types of fibers, while the second one (HYB2) consists of specimens with a higher percentage of

twisted steel fibers (0.5% Type 5+1% Type 6). Both types of specimens used the same mixture. As shown in the figure, the load-deformation curves of HYB2 showed higher peak strength and residual strength, and less scatter. Both types of specimens showed similar strain-hardening behavior.

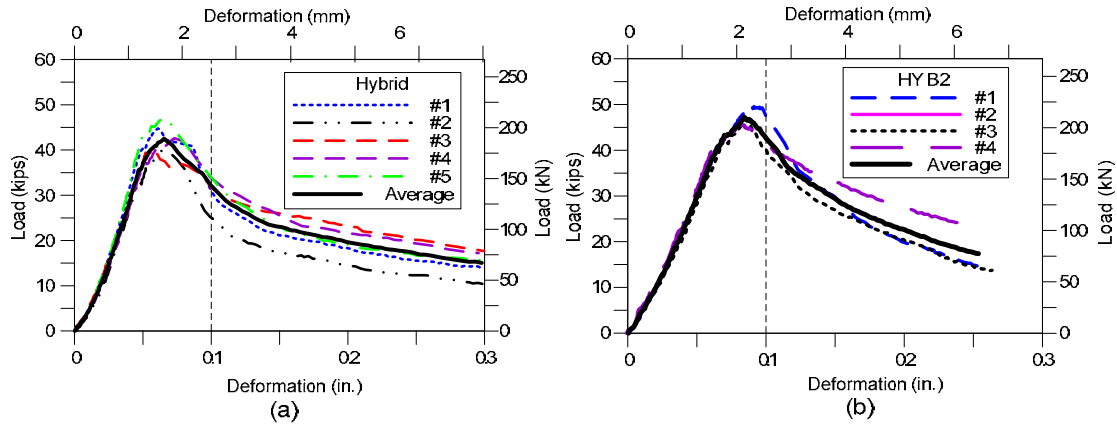


Figure F-41: Comparison of load-deformation curves for two SFRC specimens: (a) Hybrid (0.75% Type 5 fiber + 0.75 Type 6 fiber) and (b) HYB2 (0.50% Type 5 fiber + 1% Type 6 fiber) (Phase 5, UT Arlington)

In Figure F-42, load-deformation curves are compared for two specimens with the same type and volume fraction of steel fibers (mixed fiber), but with different concrete mixtures. The first (HYB3) was a good mixture (lower water-cement ratio and smaller aggregate size) with $f'_c = 7.9$ ksi. The second (HYB4) was a lower-quality mixture (higher water-cement ratio and larger aggregate size) with $f'_c = 6$ ksi. As shown in the figure, HYB3 had better peak strength and residual strength, with less variability. This test series shows that the DPT can distinguish between mixtures with different qualities.

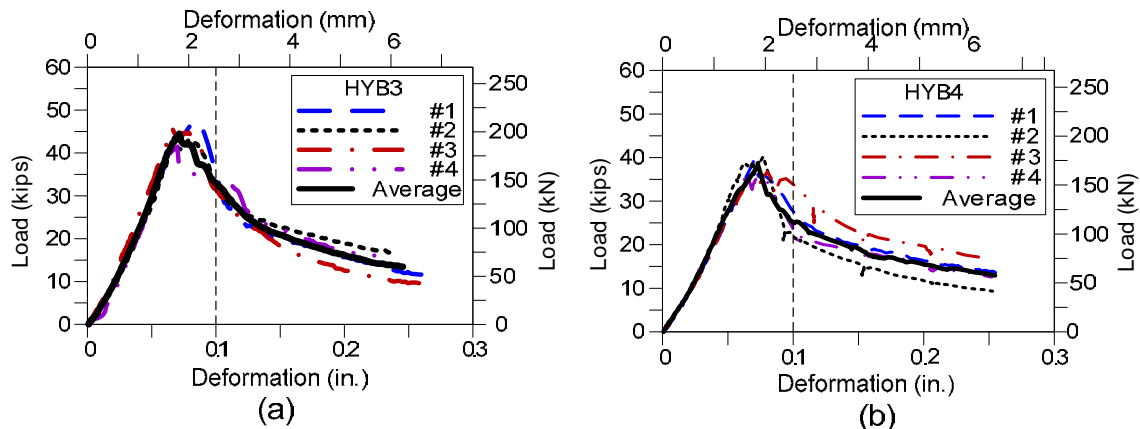


Figure F-42: Comparison of load-deformation curves for two hybrid specimens with the same type of steel fibers and the same volume fraction, but different concrete mixtures: (a) HYB3 and (b) HYB4 (Phase 5, UT Arlington)

In Figure F-43, load-deformation curves are prepared for two specimens with the same type of fibers, the same fiber volume fraction, and the same concrete mixture, but with different methods of preparing that mixture. The first group of specimens was compacted using a table vibrator, which led to a less-uniform distribution of fibers. The second group of specimens was compacted only with a tamping rod. As shown in the figure, the second group of specimens (ML-075(2)) showed much more consistent post-cracking behavior. This suggests that over-vibration should be avoided in order to have consistent DPT specimens cut from the 6- x 12-in. cylinders.

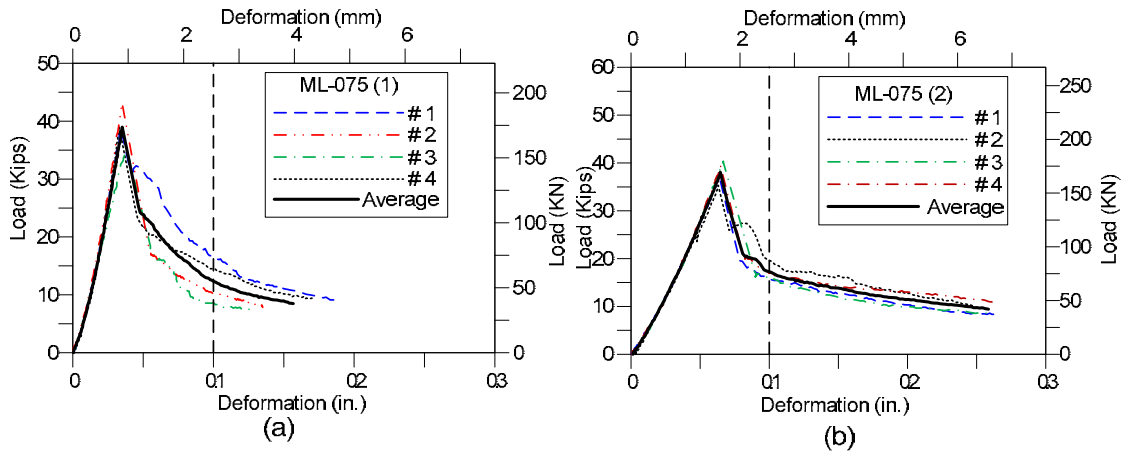


Figure F-43: Comparison of load-deflection curves for two specimens with the same concrete mix but with different methods of preparation: (a) ML-075(1) and (b) ML-075(2) (Phase 5, UT Arlington)

In Figure F-44, the pre-peak (pre-crack) stiffnesses of two different mixtures are compared. A mixture with high compressive strength (HYB1, a SFRC mortar mix) showed larger stiffness than the other mixtures. The initial stiffnesses for those other mixtures are very close to each other, though depending to some degree on the type of mixture and fibers used in each.

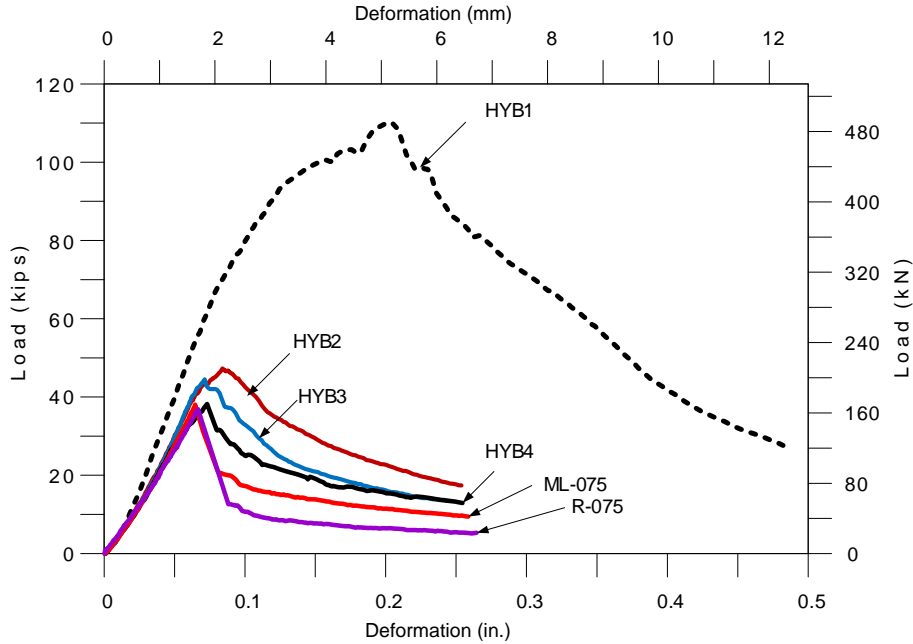


Figure F-44: Comparison of stiffness between different concrete mixtures with different types of fibers (Phase 5, UT Arlington)

In Figure F-45, deformations versus average crack width are compared for different specimens. Specimen HYB1 (3% volume fraction of steel fibers and strain-hardening behavior) showed the smallest crack widths at all levels of load. Specimens HYB2, HYB3, and HYB4, all with a volume fraction of 1.5%, showed crack widths that were larger than those of HYB1, but smaller than those of Specimens ML-075 and R-075, which had low volume fraction of 0.75%. Among Specimens HYB2, HYB3, and HYB4, Specimen HYB2 showed slightly smaller crack widths, because it had a slightly higher volume fraction of twisted fiber (1%) than Specimens HYB3 and HYB4, each of which had 0.75% twisted fiber. Specimens ML-075 and R-075 also showed larger crack widths but are similar to each other. This study suggests a second criterion (besides the residual strength at 0.1 in. deformation) of using specified maximum average crack width at certain deformations to evaluate the performance of FRC by using DPT.

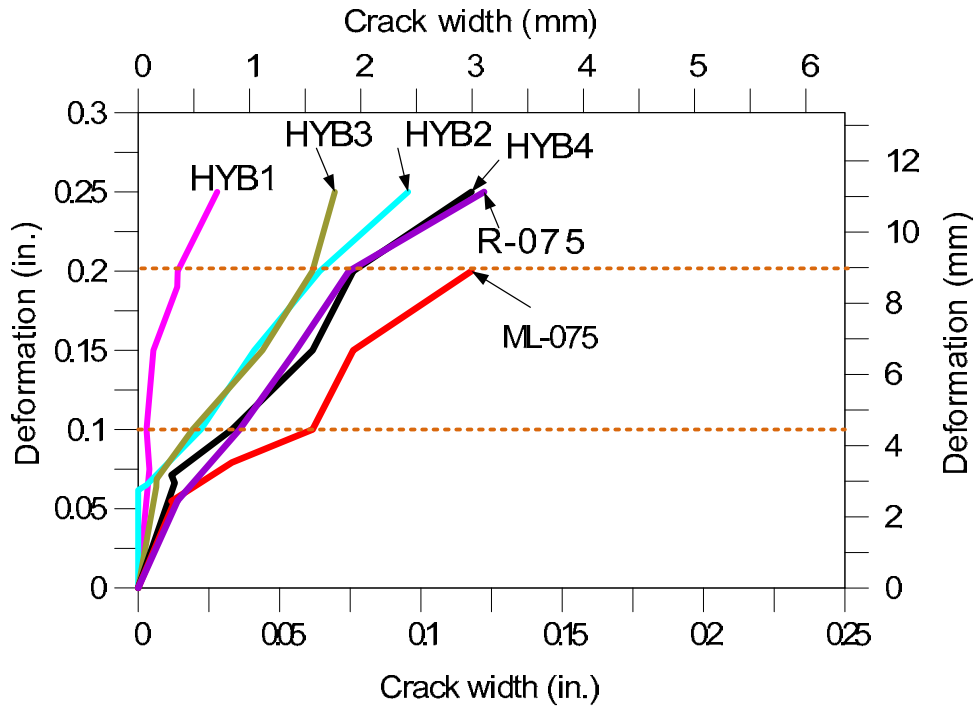


Figure F-45: Comparison of average total crack widths at different deformations for different DPT specimens (Phase 5, UT Arlington)

Finally, as discussed previously, six more cylinders were tested by DPT, and the results are shown in Table F-37. Because the peak loads occurred beyond 0.1-in. deformation, residual loads were compared at 0.2-in. deformation. The top and bottom halves of the cylinders were compared separately. COVs for both halves were 3% to 6% for peak loads and 9% to 12% for residual loads, both of which are quite reasonable compared to the results of previous phases. Average response curves for the top and bottom halves of cylinders show little scatter (Figure F-46). The improvement may be due to the use of hand compaction instead of a plate vibrator. Use of a viscous modifying agent (VMA) could also have minimized the segregation of fibers.

Table F-37: Summary of results from additional DPTs (Phase 5, UT Arlington)

Specimen	At peak load			At 0.2 in. deformation	
	Load	Deformation	Tensile strength	Load	Tensile strength
	(Kips)	in.	(psi)	(Kips)	(psi)
#1 Bottom	65.6	0.12	992.2	40.2	608.5
#3 Bottom	65.8	0.13	996.3	44.2	668.4
#4 Bottom	69.3	0.13	1048.6	48.5	733.6
Mean	66.9	0.13	1012.4	44.3	670.2
STDEV	2.1	0.01	31.5	4.1	62.6
COV	3.1%	5.7%	3.1%	9.3%	9.3%
#2 Top	64.1	0.12	969.6	25.9	391.5
#4 Top	63.0	0.12	953.1	29.7	450.0
#6 Top	59.4	0.11	898.4	23.5	355.5
Mean	62.1	0.11	940.4	26.4	399.0
STDEV	2.5	0.01	37.3	3.2	47.7
COV	4.0%	6.3%	4.0%	12.0%	12.0%

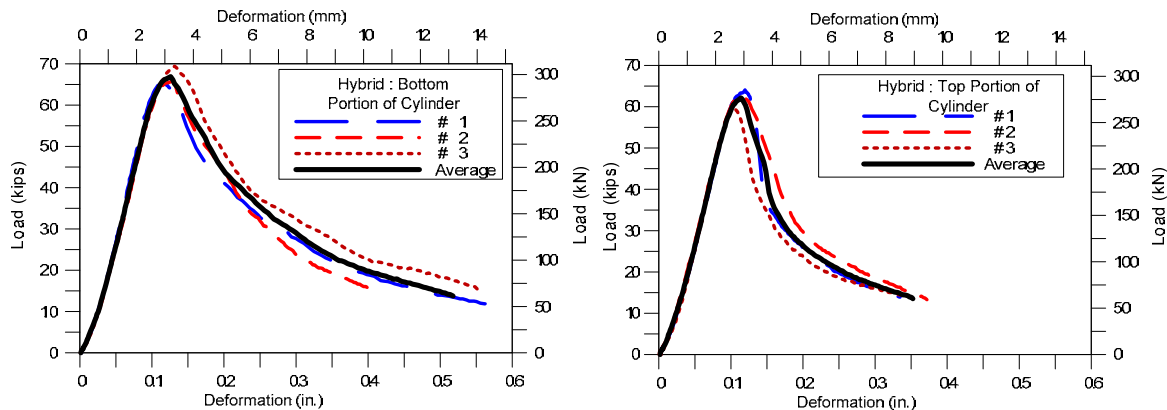


Figure F-46: Load-deflection curve for hybrid mortar specimens (2% Type 6 and 1% Type 7 Steel Fibers) (Phase 5, UT Arlington)

F.14. Discussion of Results from DPTs, UT Arlington

F.14.a: Discussion of Results from Phases 1 through 3 of DPT, UT Arlington

The first three phases of DPT at UT Arlington were concentrated on validation of DPT methods in terms of peak strengths and residual strengths. Tests were carried out with three types of high-performance steel fibers, in volume fractions from 0 to 2%. A simple 60-kip universal testing machine was successfully used for DPT. Volume fractions of fibers less than 0.50% did not enhance the performance of concrete significantly. Volume fractions greater than 1.5% caused mixing problems in the early phases of the study, particularly for long fibers (Type 3).

The specimen size used (halves of a 6- × 12-in. cylinder) may not be adequate to ensure uniform distribution of fibers, particularly long fibers. Additionally, the amount and the size of coarse aggregates can significantly affect fiber distribution, particular with longer fibers. Results from the first three phases of study at UT Arlington were based on early-age specimens (24 to 48 hours), whose strength was difficult to control.

Fibers with double-bend hooks at the ends performed better than fibers with single-bend hooks. Specimens with longer fibers (Type 3) generally performed better than specimens with short fibers (Type 1 and Type 2). Increased volume fractions of fibers enhanced the performance of SFRC, particular for BL-150 (with Type 3 fiber), which showed higher peak load and residual load.

Applying the criteria of equal peak strength and equal residual strength at 0.1-in. deformation, the volume fractions necessary to achieve equivalent performance is approximately (Royal: Short Bekaert: Long Bekaert) = (2.4: 1.55: 1.0). For example, a mixture with a volume fraction of 1% Long Bekaert fibers will have the same performance as a mixture with 1.55% short Bekaert fibers, and as a mixture with 2.4% Royal fibers.

Phase 1 of DPT at UT Arlington showed significant variability in elastic stiffness and post-peak behavior, even though 10 replicates were used. In contrast, this variability was much lower in Phase 3, even though the number of replicates was reduced to four. This was due to the introduction of an initial “shakedown” loading. Plain concrete specimens usually broke into 3 or 4 pieces once the first cracking load was reached. In contrast, SFRC specimens formed several radial cracks, and maintained their integrity after peak load due to the bridging of fibers across the cracks. Cracks generally developed near the top of the specimen (near loading point), and propagated towards the bottom of the specimen.

F.14.b: Discussion of Results from Phase 4 of DPT, UT Arlington

In Phase 4 of DPT at UT Arlington, the variability in residual strength at 0.1-in. deformation was further reduced by carrying out tests at 28 days rather than at early ages. As shown in Table F-38, COVs for peak strength and for residual strength at 0.10-in. deformation were less than 15%, lower than those for other material test methods. Specimens BL-150 and H-200 showed moderate strain-hardening (or deformation-hardening) behavior.

Table F-38: Comparison of average COVs for Phases 1 through 4 of DPT (UT Arlington)

Type of Specimen	Peak Load				Residual Load (at 0.1 in. Deformation)			
	Phase 1	Phase 2	Phase 3	Phase 4	Phase 1	Phase 2	Phase 3	Phase 4
PC	5.2%	12.7%	5.2%	5.2%	-	-	-	-
SFRC-R-Type 1	5.7%	9.9%	4.1%	4.2%	11.6%	11.9%	13.7%	15.8%
SFRC-BS-Type 2	5.2%	7.3%	4.5%	3.7%	14.8%	19.8%	16.9%	14.9%
SFRC-BL-Type 3	8.3%	6.2%	4.5%	4.5%	20.0%	21.4%	25.9%	14.4%
SFRC-HX-Type 4	-	-	-	5.4%	-	-	-	12.3%

F.14.c: DPT versus Other Material Test Methods

In this work at UT Arlington, the DPT method was compared with the third point bending test (ASTM C1609) and the DTT. Test results clearly show that peak strengths obtained from the DPT have a much lower COV (about 5%) than do peak strengths from the bending test and the DTT. As shown in Table F-39, although COVs for residual strength and toughness from the DPT were greater than 10%, these values still were less than half the corresponding COVs from bending and DTTs. Similarly, individual load-deformation curves from bending tests and DTTs show more scatter around their average curves.

Table F-39: Comparison of average COVs for DPT, bending test, and DTT (UT Arlington)

Type of test	Peak load	Residual Strength	Toughness
DPT	5.7%	14.8%	9.2%
Bending test (ASTM C1609)	16.8%	32.0%	24.2%
DTT	17.8%	32.0%	24.8%

The bending test results (Table F-40) clearly show that none of the specimens satisfied the residual-strength criteria set by Section 5.6.6.2 of ACI 318-11 for the use of steel fiber for shear resistance of concrete. This may be due partly to the relatively high scatter in residual-strength values from the third-point bending test (ASTM C1609) that is required for evaluation of residual strengths.

Table F-40: Verification of average residual strengths to meet requirements of ACI 318-11 for use of steel fibers for shear resistance

Specimen	Load at 0.06 in. (L/300) Deflection	Load at 0.12 in. (L/150) Deflection	90% of 1st peak load	75 % of 1st peak load	Check for ACI 318-11 Section 5.6.6.2	
	(kips)	(kips)	(kips)	(kips)		
ML-150	8.33	3.77	13.87	11.56	Not pass	Not pass
ML-075	8.57	3.63	9.7254	8.1045	Not pass	Not pass
Hybrid	2.98	2.69	15.11	12.59	Not pass	Not pass

An additional disadvantage of the third-point bending test and the DTT is that each must be carried out with a closed-loop, servo-controlled machine. This always requires more time and effort than the DPT, for which only a simple universal testing machine is required. Finally, double-punch specimens (halves of a 6-× 12-in. cylinder) were much easier to prepare than the specimens required for the other two methods.

F.14.d: Post-Cracking Behavior of Double-Punch Specimens (UT Arlington)

From Phase 5 of the experimental studies conducted at UT Arlington, it can be concluded that the DPT is a reliable way of determining various aspects of the post-cracking behavior of SFRC, such as strain-hardening, strain-softening, and toughness. Concrete mixtures with mixed fibers (hybrid combinations of long fibers with twisted and micro fibers) effectively controlled crack widening, and also increased strength and toughness. SFRC with larger volume fractions of twisted and micro fibers showed high equivalent tensile strengths and more significant strain-hardening behavior, as observed in DPTs. Test results from Phase 5 at UT Arlington show the ability of DPT to distinguish between good and poor mixtures of SFRC.

F.15. DPT at the University of Texas at Austin

The main objectives of *this portion* of Study 6348, previously stated in Chapter 1, include the following:

1. Quantify the influence of mix compositions, fiber types, and fiber volume fractions on the mechanical characteristics of FRC;
2. Develop test protocols for comparing the effectiveness of steel fiber-reinforced concrete mixtures with different fiber types and volume fractions;
3. Supply intra- and inter-laboratory data and observations useful for comparing the DPT with current test methods for FRC.

Again, the central focus of the DPT Research and Testing Program at UT Austin is to produce sufficient within-batch, intra-laboratory data to make conclusions and recommendations regarding the simplicity, reliability, and reproducibility of the DPT when applied to steel fiber-reinforced concrete.

F.16. Organization of DPT Program at UT Austin

The experimental program was conducted in two phases. Test variables include fiber manufacturer and type, fiber volume fraction, specimen surface preparation, and testing machine. As shown in the testing matrix provided in Figure F-47, the most significant difference between **PHASE 1** and **PHASE 2** is the fiber manufacturer. Royal™ (domestic) steel fibers are used in the first series of tests, whereas Bekaert Dramix® (foreign) steel fibers are used in the second round of testing. Also, in **PHASE 2**, the specimen surface preparation variable was eliminated based on results obtained from **PHASE 1** which indicated that surface preparation was not a distinguishing factor in the experiment. Thirty 6 x 12-in. cylinders were cast in each phase.

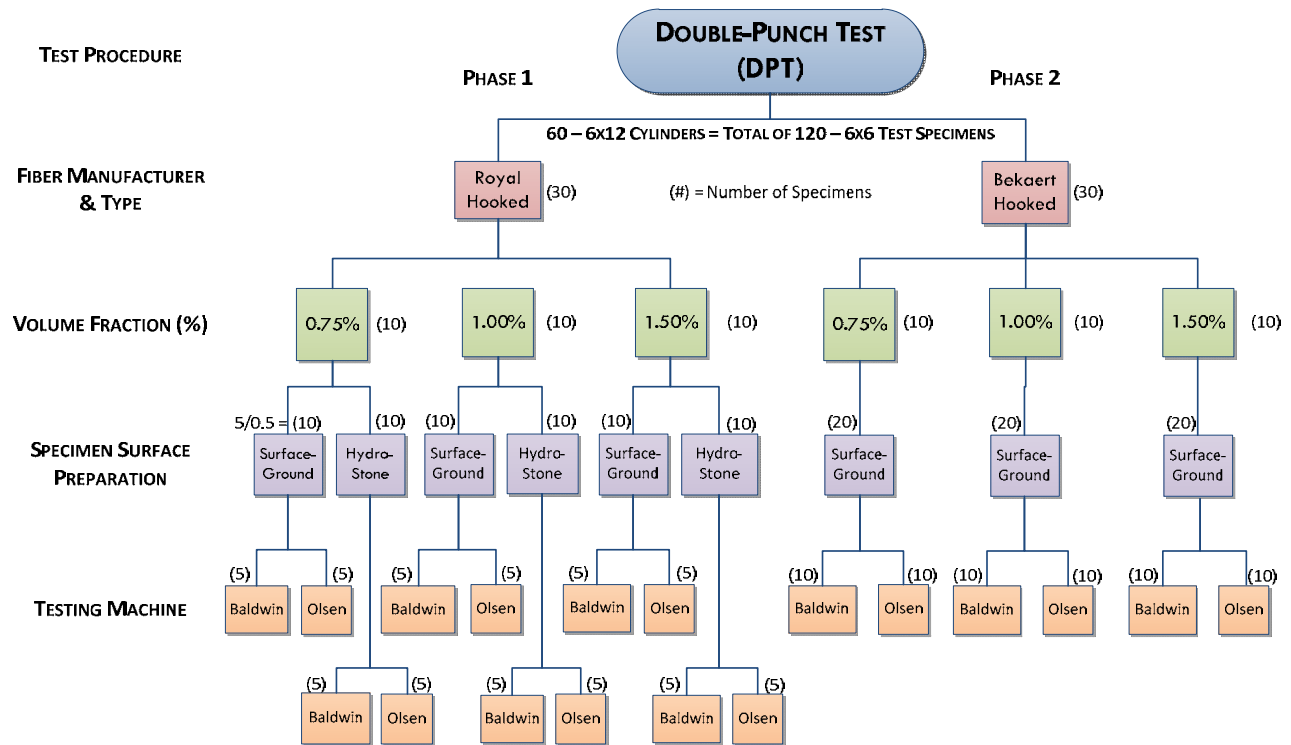


Figure F-47: Testing matrix for DPT research and testing program

F.16.a: Nomenclature Used to Identify Test Specimens at UT Austin

The thirty 6 x 12-in. steel fiber-reinforced concrete cylinders that were cast in each phase were cut in half to obtain 120, 6 x 6-in. specimens for the DPT Research and Testing Program. Because of the large number of test variables, each 6 x 6-in. test specimen was uniquely identified according to the nomenclature provided in Figure F-48.

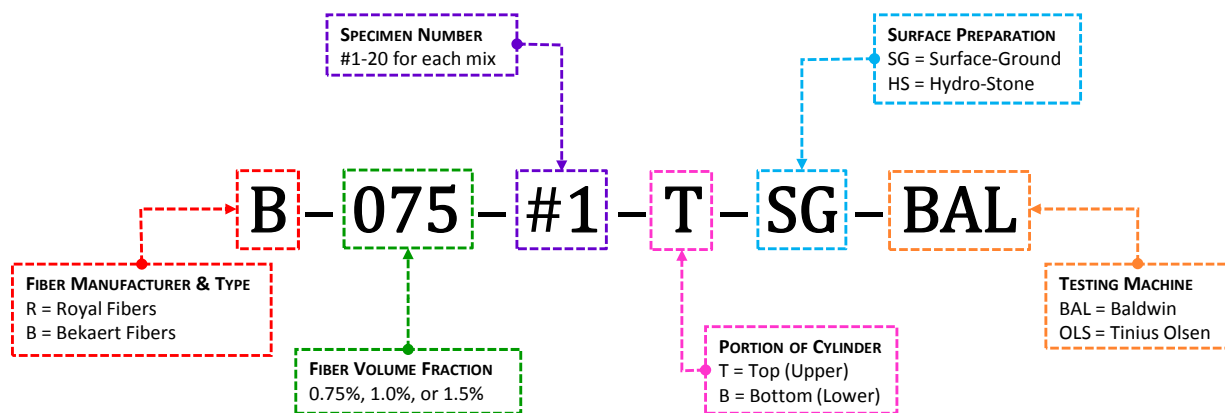


Figure F-48: Nomenclature used to identify specimens for DPT research and testing program

F.17. DPT Program Materials at UT Austin

F.17.a: Steel Fibers Used at UT Austin

Both US-made (domestic) and foreign steel fibers were used in the testing program. Royal™ fibers are commonly used in SFRC applications in the United States and were selected as the domestic fiber in **PHASE 1** of this study. These fibers are manufactured from cold-drawn, low-carbon steel wire, and are designed to enhance concrete performance such as average residual strength, toughness, and impact resistance. As shown in Figure F-49, the Royal™ fibers have a hooked geometry, are 1.2-in. [30-mm] long, and have an aspect ratio of 38.

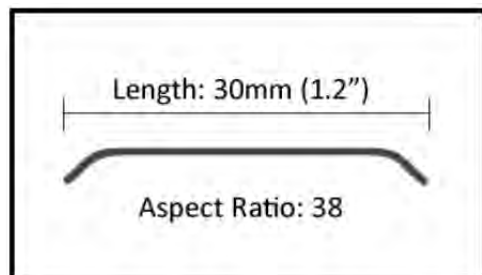


Figure F-49: Royal™ steel fibers

Bekaert is a major international fiber manufacturer, and is recognized as a leader in fiber technology. Bekaert Dramix® fibers were employed in **PHASE 2** of the current study. Similar to the Royal™ fibers, Bekaert Dramix® fibers are cold-drawn steel wire with hooked ends for optimum anchorage. As shown in Figure F-50, these fibers are approximately 1.37-in. [35-mm] long, and have an aspect ratio of 65.



Figure F-50: Bekaert Dramix® steel fibers

Figure F-51 provides a side-by-side visual comparison of the two fiber types used in this study.



Figure F-51: Royal vs. Bekaert fiber type

The fiber volume fraction, or fiber content, is denoted as a percentage of the total volume of freshly mixed concrete. The weight of fibers added to the concrete mix was calculated using the given fiber content, total volume of concrete, and the unit weight of steel as shown in Equation 5-1:

$$\text{Steel Fiber (lb)} = \frac{\text{Fiber VF (\%)}}{100} * \text{Total Volume of Concrete (ft}^3\text{)} * 490 \frac{\text{lb}}{\text{ft}^3} \quad \text{Equation 5-1}$$

*Note: The DPT Research and Testing Program is meant to evaluate the DPT method. It is **not intended** to compare the performance of the different fibers used in this study. Royal™ and Bekaert Dramix® fibers were chosen arbitrarily to determine the ability of the DPT to distinguish between FRC composed of different fiber types and volume fractions.*

F.17.b: Concrete Mix Design & Procedure for DPT at UT Austin

To produce the number of specimens required for the DPT Research and Testing Program, six separate concrete mixtures were batched and mixed using a standard drum mixer. Although batches varied by fiber type and fiber content, the mixture proportions shown in Table F-41 were used throughout. The cement, sand, and coarse aggregate used were Alamo Type I/II, Colorado River Sand, and Martin Marietta crushed limestone, respectively. Prior to mixing, the sand and coarse aggregate were lightly coated with water in the drum mixer. Samples were removed from these constituents and oven dried. The moisture content was determined, and adjustments were made to the mix quantities to satisfy saturated-surface-dry (SSD) conditions.

Table F-41: Concrete mixture proportions

Cement	Sand	Coarse Aggregate	Water	Total
1.00	2.00	2.25	0.50	5.75

* Proportions based on 2.5 ft³ of concrete.

Mixture proportions and mixing procedure affect the microstructure of the final SFRC produced. Fiber performance can be maximized by using well-graded aggregates and high fines

content; however this was not done in the DPT Research and Testing Program because this research is focused on evaluating the test method itself. In this case, the aggregate gradation is not important as long as each batch is proportioned identically. To ensure consistency between mixes, quantities were corrected based on SSD and the concrete was mixed using the following sequence recommended by researchers at UT Arlington.

- **Step 1:** Calculate weight of materials based on concrete mix proportions and correct for SSD conditions.
- **Step 2:** Place cement and sand into mixer. Mix for about 3 minutes.



Figure F-52: SFRC mixing sequence, Step 2

- **Step 3:** Add water in phases, mixing for about 30 seconds between each addition.

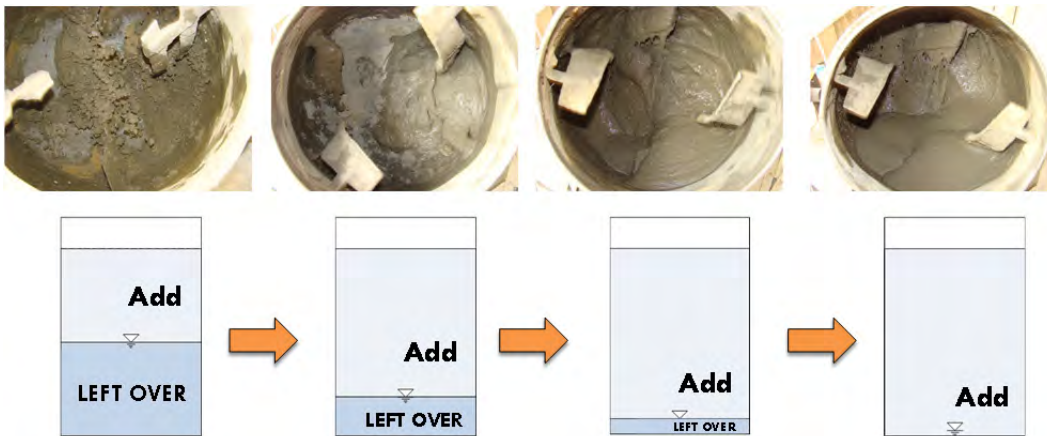


Figure F-53: SFRC mixing sequence, Step 3

- **Step 4:** Add coarse aggregate. Mix for about 3 minutes and visually inspect mixing status.



Figure F-54: SFRC mixing sequence, Step 4

- **Step 5:** Add steel fibers. Mix for about 3 minutes and visually inspect mixing status. Ensure uniform mixing by breaking up “clumped” or “balled” fibers (Figure F-55).



Figure F-55: SFRC mixing sequence, Step 5



Figure F-56: Example of “clumping” and “balling” of fibers observed during mixing

- **Step 6:** Measure concrete fresh properties (slump and unit weight).



Figure F-57: SFRC mixing sequence, Step 6

- **Step 7:** Place concrete into 6 x 12-in. cylinder molds, consolidate concrete by tapping with steel rod and placing on vibrating table for 1 to 2 minutes.



Figure F-58: SFRC mixing sequence, Step 7

- **Step 8:** Cap cylinder specimens. Cure in mixing room at 73°F for first 24 hours, strip cylinder molds, and place in curing chamber (fog room) at 73°F and 100% relative humidity until testing date.



Figure F-59: SFRC mixing sequence, Step 8

Table F-42 (a) and (b) provides the batch quantities and fresh and hardened concrete properties of the SFRC mixtures used to create the DPT test specimens.

Table F-42: (a) Batch quantities and (b) fresh and hardened concrete properties of SFRC mixtures used in DPT experiments

(a)

Mix Number	Mix ID	Cement (lbs/ft ³)	Coarse Aggregate (lbs/ft ³)	Sand (lbs/ft ³)	Water ¹ (lbs/ft ³)	Steel Fiber (lbs/ft ³)
1	R-075	67.3	154.5	138.0	31.8	9.2
2	R-100	67.3	154.8	137.0	26.3	12.6
3	R-150	67.3	156.2	139.9	28.6	18.9
4	B-075	94.7	218.7	194.7	43.8	11.4
5	B-100	90.8	209.2	185.7	43.2	14.4
6	B-150	90.8	208.7	186.7	42.7	21.6

¹ Water content was adjusted for SSD conditions

(b)

Mix Number	Mix ID	w/cm	Slump (in)	Unit Weight (lbs/ft ³)	28-Day Strength ² (psi)	Modulus of Elasticity (psi)
1	R-075	0.47	10.50	147	5531	4.38E+06
2	R-100	0.39	3.25	149	6635	4.88E+06
3	R-150	0.42	5.00	150	6439	4.85E+06
4	B-075	0.46	8.25	146	5634	4.37E+06
5	B-100	0.48	7.50	146	5164	4.20E+06
6	B-150	0.47	5.50	147	4753	4.05E+06

² Avg. 28-day Compressive Strength reported was back-calculated using ACI-209 equations for mix-IDs R-075, R-100, and R-150. Actual cylinders were tested at 35-days for these mixes.

F.17.c: Specimen Preparation for DPT at UT Austin

In the DPT, specimens are loaded in concentric axial compression through two steel punches. It is important that the steel punches lay flat against the test machine and concrete cylinder surfaces, because smooth contact between these surfaces will generate the most uniform loading possible.



Figure F-60: Using wet-saw to cut 6 x 12-in. cylinder in half

As seen in Figure F-60, 6 x 6-in. test specimens were prepared by cutting the cast 6 x 12-in. cylinders in half using a heavy-duty concrete wet-saw. Once cut in half, only the cut face of the specimen is guaranteed to be smooth in the area where the steel punch will be located. As shown in Figure F-61, the top and bottom faces of the cast 6 x 12-in. concrete cylinder have uneven surfaces due to the cylinder cap and cylinder mold, respectively.

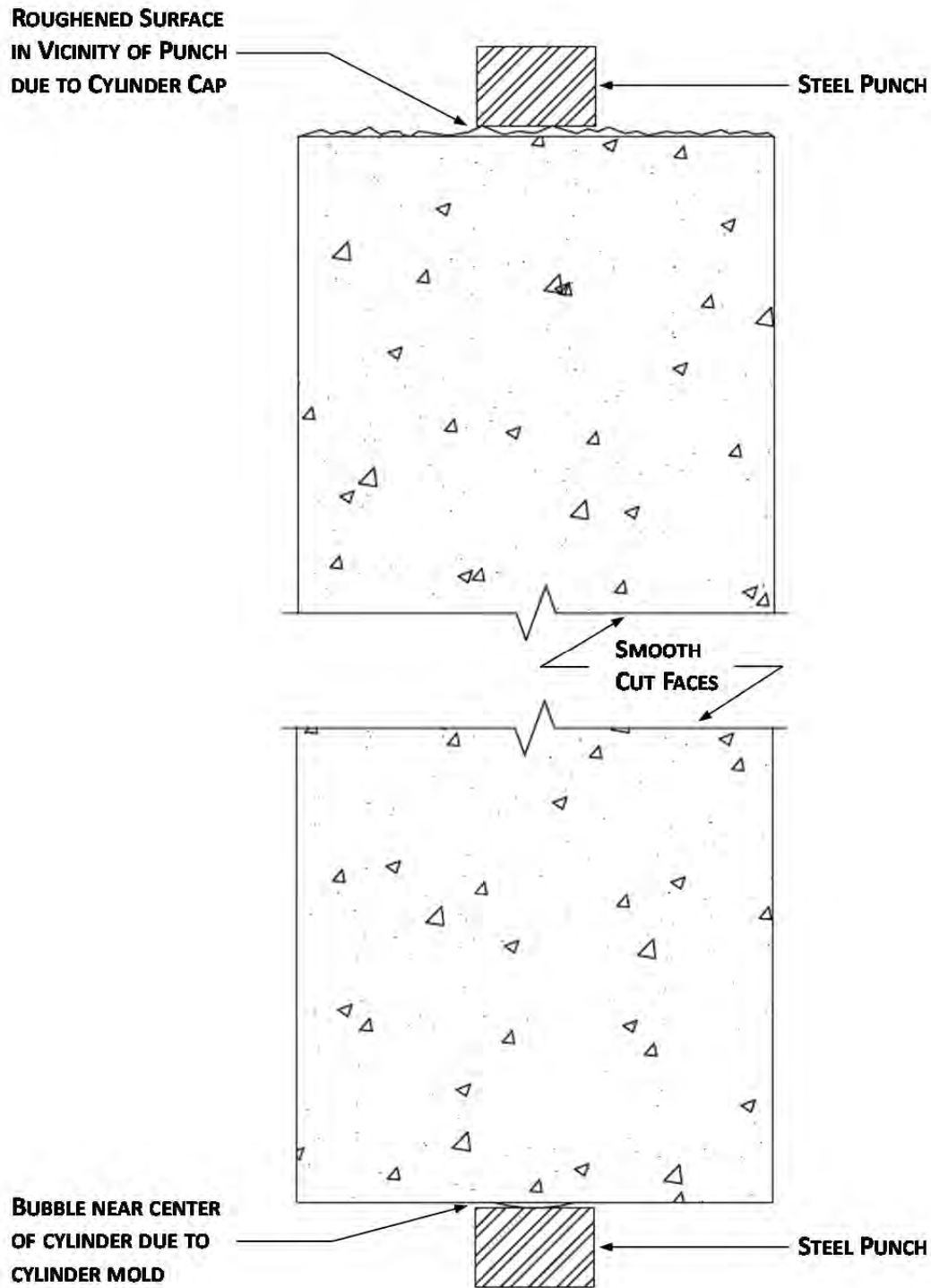


Figure F-61: Schematic showing surface roughness on top and bottom surfaces of cylinder due to mold

This can cause an uneven distribution of stress under the area of the punch. Furthermore, the net effect of the defect on the stress distribution could vary between specimens, and result in increased variation in experimental measurements. For this reason, the surfaces of the test

specimens were refinished to provide a smooth contact area in the vicinity of the steel punches. Two methods were employed: (1) surface grinding the top and bottom faces, and (2) applying a thin layer of Hydro-Stone to the rough faces prior to testing. The latter was selected to determine if satisfactory results could be obtained without grinding, since some laboratories may not have equipment capable of surface grinding the ends of 6-in. diameter cylinders.

Specimens refinished by surface grinding were milled using a Gilson Concrete Cylinder End Grinding machine. As shown in Figure F-62, this machine is capable of producing a smooth testing surface for cylinders up to 6 in. in diameter.



Figure F-62: Surface-grinding (SG) uneven faces of test specimens

Other specimens were refinished by applying Hydro-Stone to the uneven area under the punch location as illustrated in Figure F-63. A small amount of Hydro-Stone was placed on the steel punch and the cylinder was carefully placed on top using a guide. Upon hardening, the Hydro-Stone produces a smooth layer that allows for uniform contact with the steel punches.

1. Hydro-Stone mixture placed on steel punch surface area.



2. Cylinder gently placed on steel punch using constructed guide to ensure punch location coincides with centroidal axis of test specimen.



3. Cylinder removed from guide and set aside to allow thin layer of Hydro-Stone to solidify. Process repeated for other side of test specimen.



Figure F-63: Process of applying hydro-stone to rough faces of test specimen

F.18. DPT Program Testing at UT Austin

F.18.a: Test Setup and Equipment for DPT at UT Austin

After the test specimens were cut to size and refinished using Hydro-Stone or surface grinding, they were ready to be placed in the test frame for the DPT. To assess the reliability of the DPT for different testing equipment, two universal test machines (UTM) were used: (1) 60-kip capacity Baldwin UTM and (2) 120-kip capacity Tinius Olsen UTM. Half of the test

specimens from each batch were tested using the Baldwin machine, and the other half were tested on the Olsen machine. The same basic setup was used in each arrangement. Each setup consisted of the following:

- *Spherical Head* - to compensate for any unevenness of the specimen cut, ground, or Hydro-Stone faces;
- *Steel Punches* - two 1.0 x 1.5-in. diameter steel punches cut from a section of 75 ksi tool steel;
- *LVDTs* - two linear variable differential transducers (LVDTs) of 2.0-in. stroke to measure vertical displacement of the DPT test specimen. Displacement was taken as the average of the two measurements;
- *PDAQ* - load and deflection data was recorded using a data acquisition system and LabView software.

Schematics and photographs of the testing arrangements used on the Baldwin and Olsen UTMs are provided in the following figures.

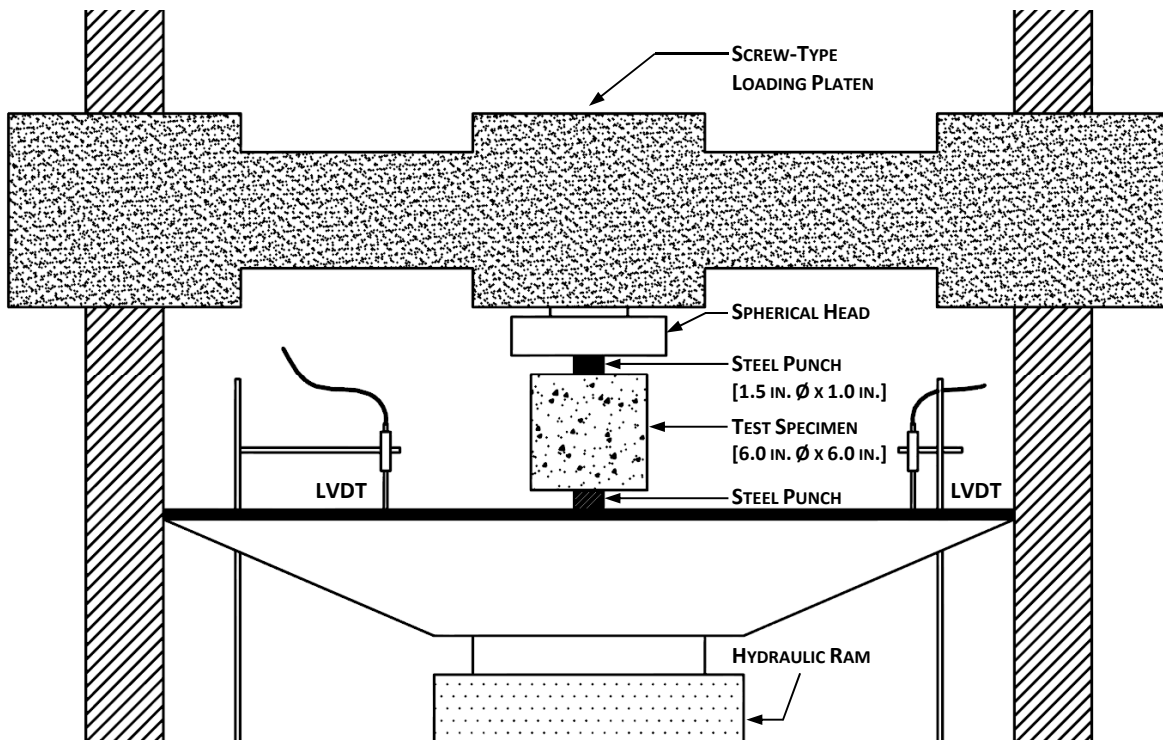


Figure F-64: Schematic of DPT arrangement on 60-kip Baldwin UTM (hydraulic)



Figure F-65: DPT setup on 60-kip Baldwin UTM (hydraulic)

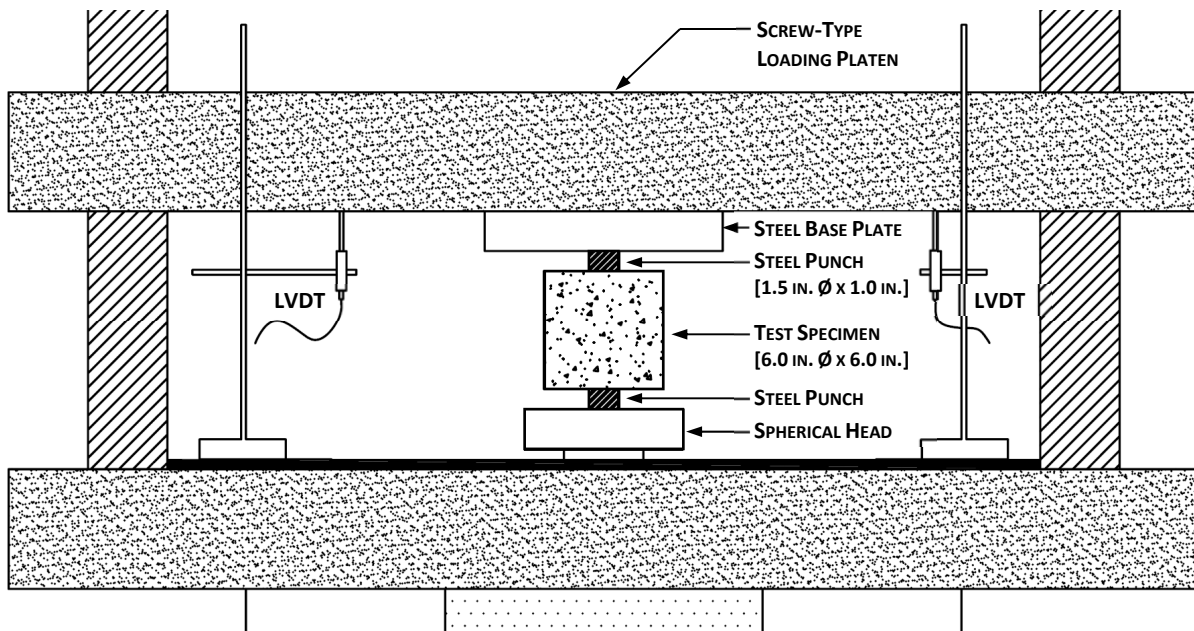


Figure F-66: Schematic of DPT arrangement on 120-kip Olsen UTM (screw-type)



Figure F-67: DPT setup on 120-kip Olsen UTM (screw-type)

F.18.b: Testing Procedure for DPT at UT Austin

In the DPT, a 6 x 6-in. cylindrical concrete specimen is placed vertically between the loading platens of the test machine and compressed by two steel punches located concentrically on the top and bottom surfaces of the specimen. This loading produces radial transverse tension in the specimen. Although the DPT is simple, centering and seating of the steel punches prior to taking load-deflection measurements is critical. Centering of the punches is necessary to avoid placing a moment on the specimen due to eccentric load. As shown in Figure F-68, if the punches are misaligned, the specimen can topple during loading due to the overturning force. Results obtained under these conditions are meaningless, and are disregarded.

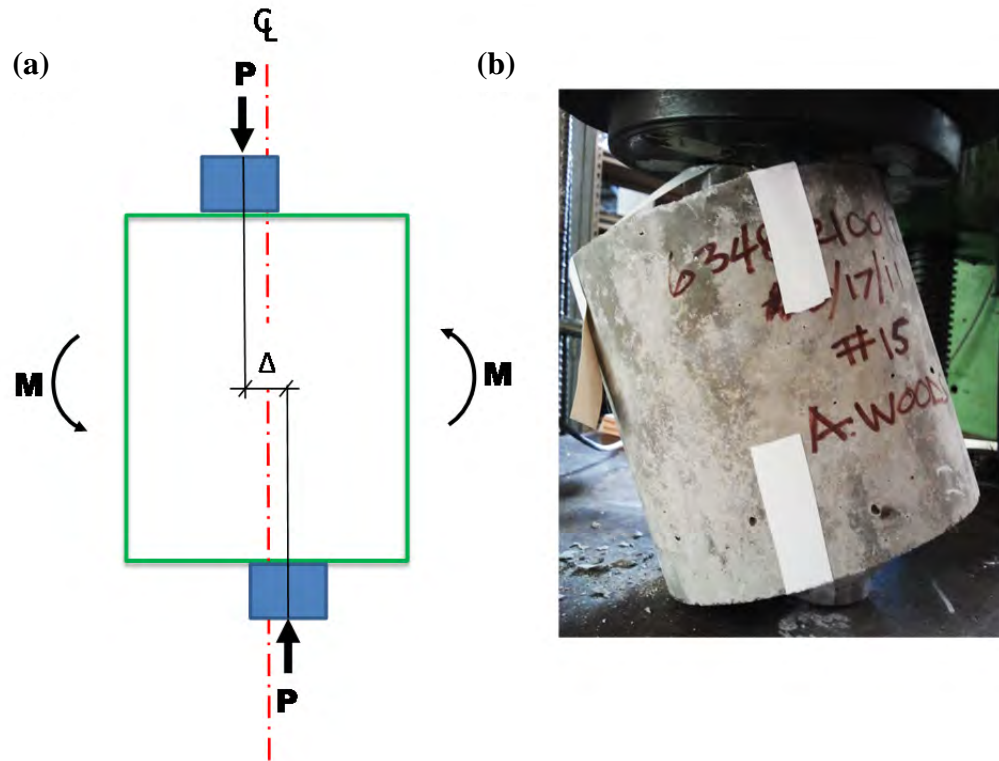


Figure F-68: Effect of misaligned steel punches in DPT shown (a) schematically and (b) for trial specimen

Even a small degree of misalignment can result in this behavior, and simple measures were used to guard against the effects of eccentric loading. For one, a punch centering guide was constructed to ensure adequate placement of the punches on the DPT specimen. Secondly, the punches were strapped to the specimen using masking tape for additional security against slipping or sliding of the steel punches during placement and loading. Finally, a spherical loading head was used to compensate for any unevenness of the DPT specimen produced from cutting, grinding, or Hydro-Stone.



Figure F-69: Steel punch centering guide and masking tape used to secure against eccentric loading effects

In addition to alignment, the steel punches must be seated into the specimen. As shown in Figure F-70, during the initial loading stage, the effect of the steel punches seating into the concrete can be seen in the curved ascending branch of the load-deflection plot. This initial non-linearity indicates the *seating process*. To correct for the seating of the punches, a “shakedown” loading sequence was employed: DPT specimens were loaded up to 10 kips, unloaded, and then reloaded to failure. In this way, the steel punches are set into the concrete and the appropriate *linear-elastic* behavior up to first crack was obtained by using a corrected zero reading corresponding to the end of the shakedown.

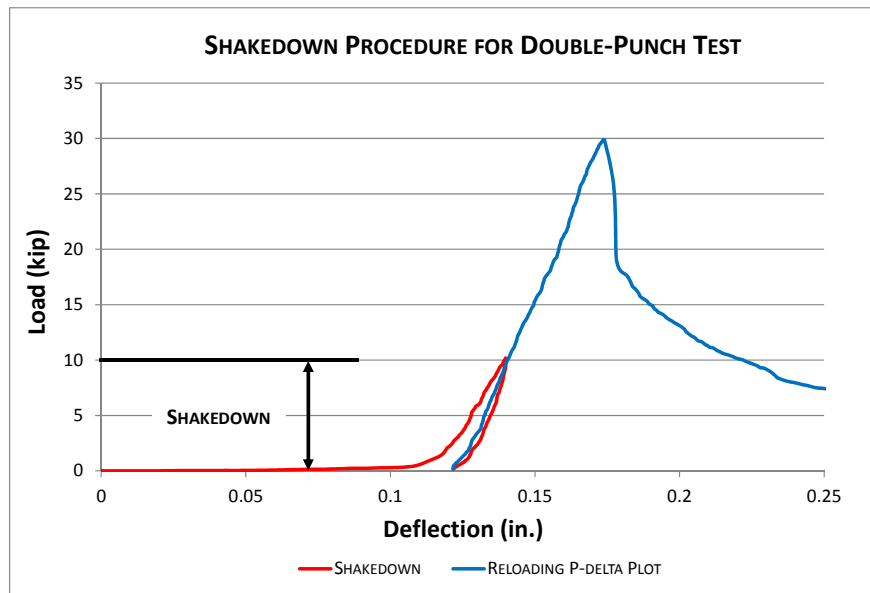


Figure F-70: Schematic of shakedown procedure for DPT experiments

All specimens were carefully prepared and placed into the loading apparatus. Once positioned, each DPT specimen was tested according to the following sequence:

- 1) *Shakedown (Initial Loading and Unloading to Seat Punches)*
 - Load the specimen at a rate of 100 lb/sec [445 N/sec] \pm 25 lb/sec [\pm 111 N/sec] up to a load of 10 kips [44.5 kN].
 - Unload the specimen at a rate between 100 and 300 lb/sec [445 and 1334 N/sec] to a load between 100 lb [445 N] and 200 lb [890 N].
 - The deflection at that final load is termed the “initial deflection offset.”
- 2) *Reloading*
 - Load the specimen at a rate of 100 lb/sec [445 N/sec] \pm 25 lb/sec [\pm 111 N/sec].
 - Note the corresponding rate of applied deformation.
 - Load at that deformation rate until the first radial crack appears in the top or bottom face of the specimen.

3) *End Point*

- Continue loading at a rate between 1.0 and 3.0 times the pre-cracking deformation rate until the deformation reaches or exceeds 0.5 in. [13 mm], or the steel punches are almost fully penetrated into the specimen.
- Do not permit the loading head of the testing machine to contact the specimen.

4) *Data Recording*

- Record the applied load and the deflection of the loading head at approximately 1-second time intervals.

F.18.c: Calculation of Key Test Parameters for DPT at UT Austin

The corrected load-deflection plot was obtained, and key test parameters were assigned in order to determine how the fiber type, volume fraction, surface preparation, and test machine affect the DPT results. This was done by the following process:

1) *Correct Deflections*

- Subtract the “initial deflection offset” from each deflection reading during the reloading phase. The resulting deflections are termed “corrected deflections.”

2) *Calculate Key Test Parameters*

Using the recorded loads and the corrected deflections, calculate and report the initial slope, peak load, and residual strength, as follows:

- **Initial Slope:** Evaluate the initial slope as the slope between applied loads of approximately 5 kips [22 kN] and 15 kips [67 kN].
- **Peak Load:** Evaluate the maximum load directly.
- **Residual Strength:** Evaluate the residual load at a corrected deflection of 0.1 in. ± 0.01 in. [2.5 mm \pm 0.025 mm].

The key parameters are shown graphically in Figure F-71: (1) initial slope, (2) peak load, and (3) the residual strength at a deflection of 0.1 in. With these values, the elastic modulus, ultimate tensile strength, and toughness can be calculated, respectively, and the performance of mixtures with different fiber types and volume fractions can be compared. Ultimately, these parameters summarize the behavior of steel fiber-reinforced concrete.

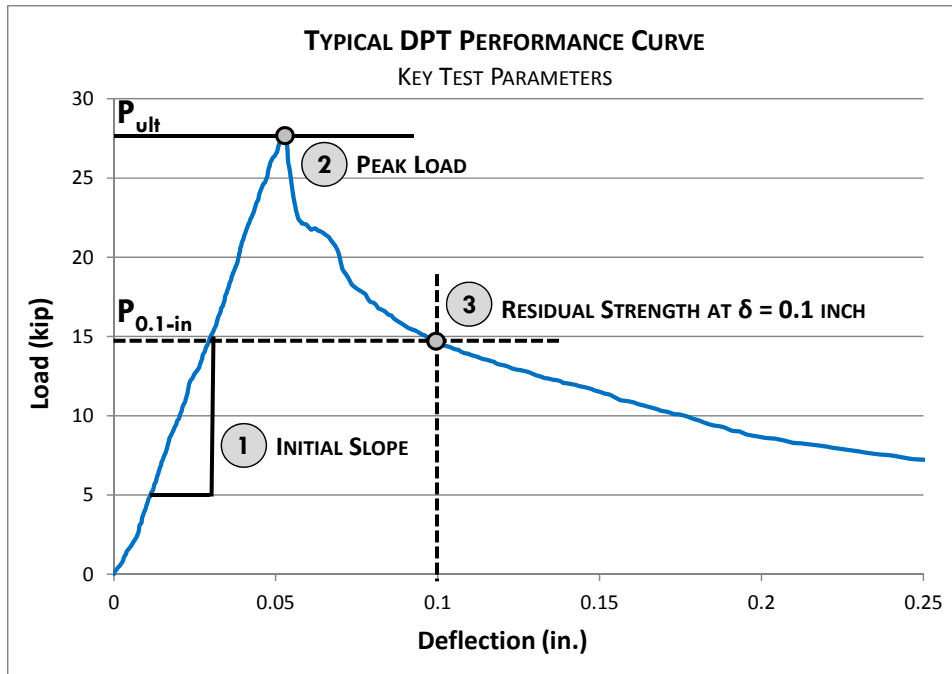


Figure F-71: Typical DPT performance curve showing key test parameters

The initial slope was calculated between 5 and 15 kips because this range represents the most stable portion of the ascending branch. It was very difficult to control the rate of loading up to 5 kips and beyond about 20 kips due to sensitive dials on the testing equipment. The initial slope represents a tangent stiffness, and was taken in the specified region to avoid potential errors introduced by variations in loading rate.

The key test parameters were evaluated statistically to assess the reliability and reproducibility of the DPT, as well as its ability to accurately describe the performance of steel fiber-reinforced concrete. This information is presented in the following chapter.

Appendix G. Statistical Evaluation of DPT Results At UT Austin

G.1. DPT Statistical Analysis

The DPT performance curves and cracking patterns are useful for comparing general trends and performance, but cannot be strictly relied upon to make conclusions and recommendations regarding the potential of the DPT to replace current test methods for FRC. Thus, the data from the two-phase study was combined and a pivot table was constructed to analyze the effects of several variables. A statistical analysis was conducted to evaluate the reliability and reproducibility of the DPT, as well as its ability to accurately describe the performance of steel fiber-reinforced concrete. Each variable was analyzed in terms of how it affected the key test parameters: initial slope, peak load, and residual strength at 0.1 inch deflection.

In the following sections, Phase 1 (Royal fibers) and Phase 2 (Bekaert fibers) analysis results will be shown for the investigation of fiber type and volume fraction. Only Phase 1 analysis results will be shown for the surface preparation variable since this variable was eliminated in Phase 2. Statistics for all other test variables in Phase 1 and Phase 2 were similar, and only results from Phase 2 will be discussed. Comprehensive statistical analysis results for Royal and Bekaert fibers are provided in Appendix B.

The analysis results presented in this thesis are “irrespective of cylinder portion.” This means that specimens from both the top and the bottom of cast cylinders were used to calculate the averages and coefficient of variations of key test parameters. Although the cylinder portion (top versus bottom) is technically another variable in the experiment, results for top and bottom specimens were fairly similar and were grouped for simplification. A separate analysis of the effects of cylinder portion (casting) was conducted to identify any key differences between the results from top and bottom specimens.

G.1.a: Analyzing the Effects of Fiber Type & Volume Fraction

As shown in the selected DPT Performance Curves, it is evident that the DPT is sensitive to both fiber type and volume fraction. In order to determine to what extent the DPT is able to detect changes in fiber geometry and content, a statistical analysis was conducted. Figure G-1, Figure G-2, and Figure G-3 show the effects of fiber type and volume fraction on the (a) coefficient of variation and (b) average value of key parameters of the DPT. These statistics are based on ten tests.

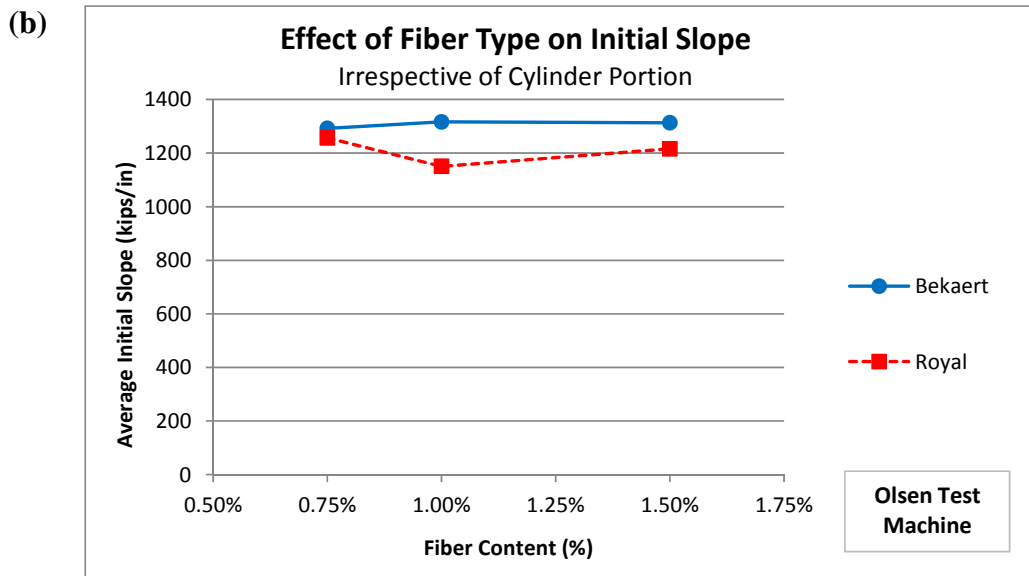
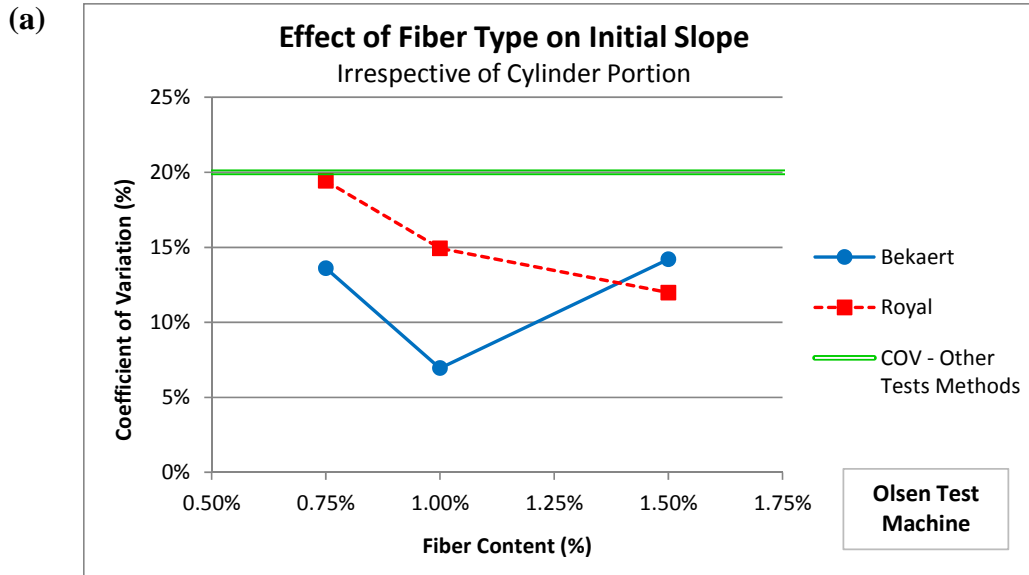


Figure G-1: Effect of fiber type and volume fraction on (a) coefficient of variation and (b) average value of initial slope

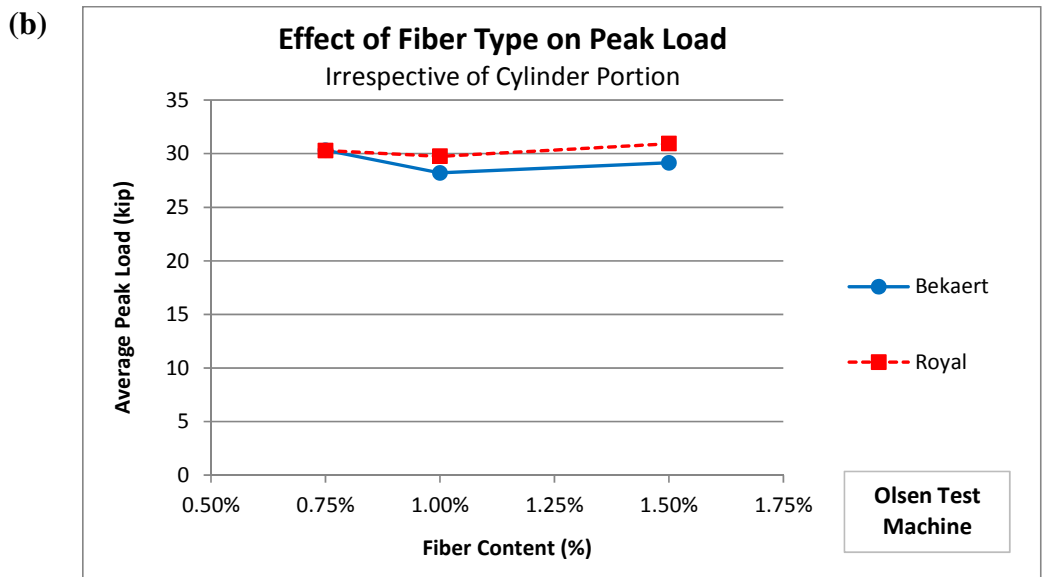
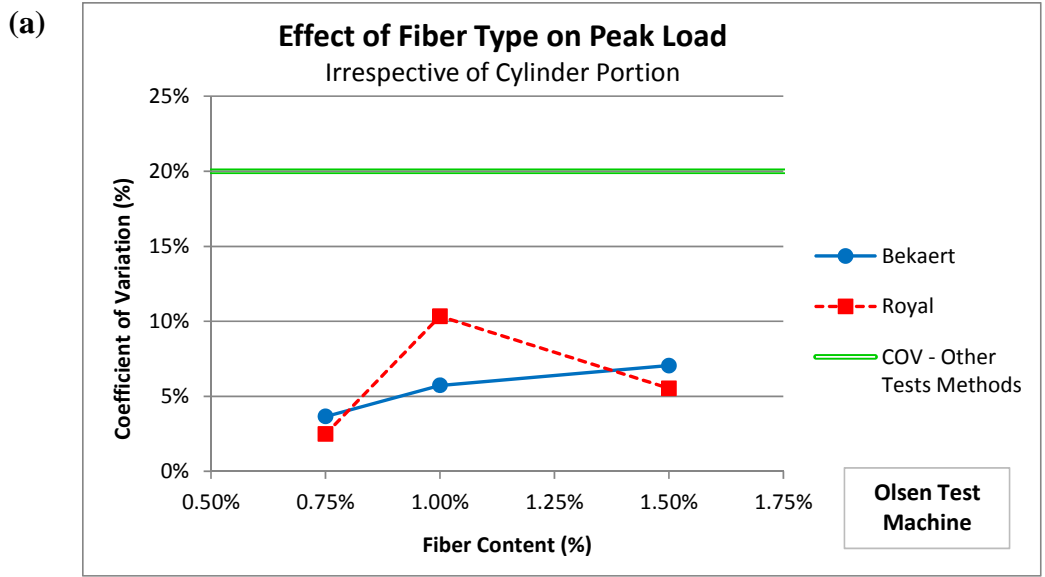


Figure G-2: Effect of fiber type and volume fraction on (a) coefficient of variation and (b) average value of peak load

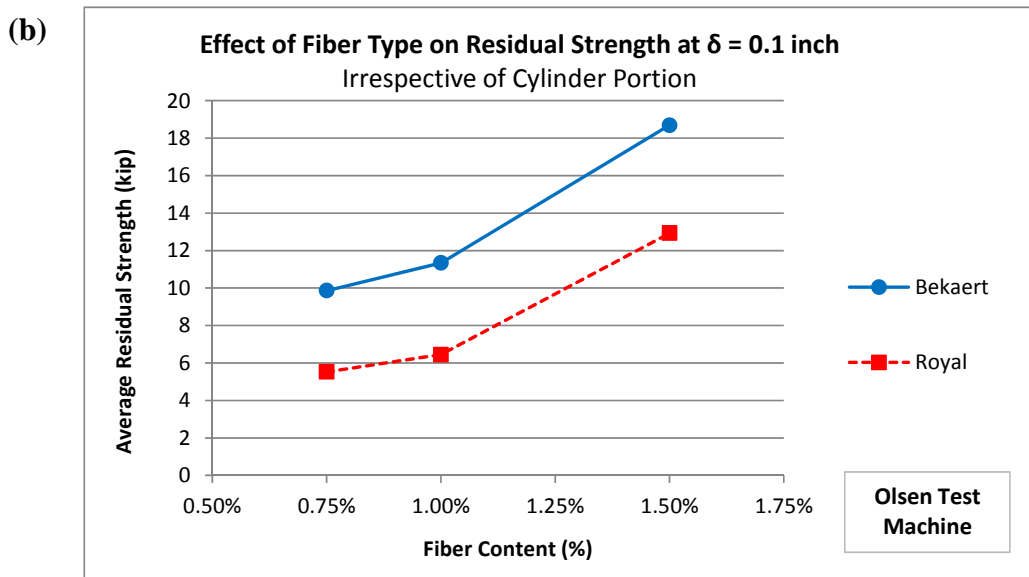
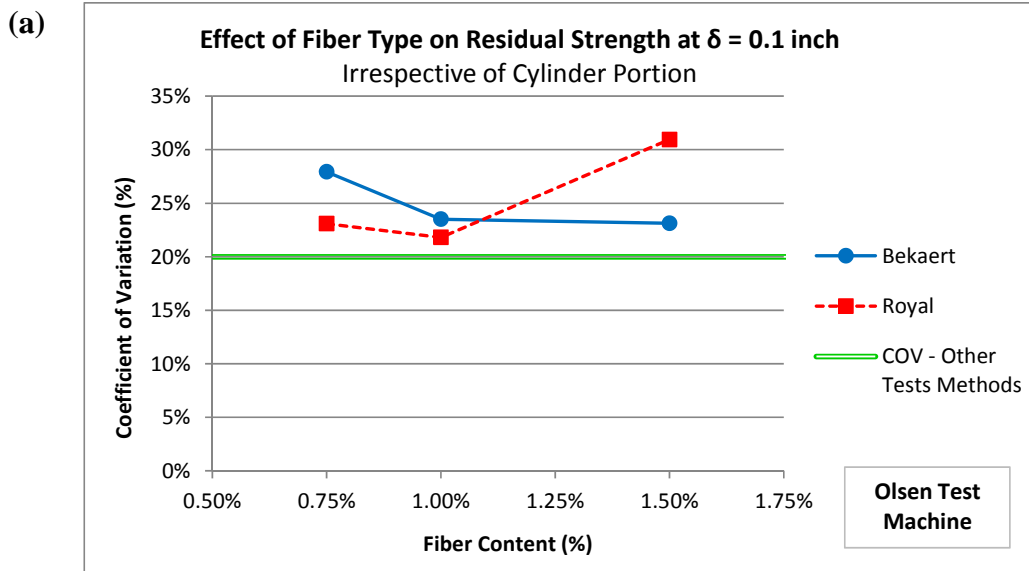


Figure G-3: Effect of fiber type and volume fraction on (a) coefficient of variation and (b) average value of residual strength

G.1.a.(1) Analysis Summary

The coefficient of variation is generally low for key test parameters (less than 20%), but variation in the residual strength parameter is high compared to the initial slope and peak load variation. The coefficients of variation are similar for Royal and Bekaert fiber types; results from both fiber types have similar statistical dispersions.

The average value of initial slope and peak load are independent of fiber type and content. With increasing fiber volume fraction, or different fiber type, the initial slope and peak load do not change. This agrees with the expected behavior of steel fiber-reinforced concrete, because reinforcement in general is not effective until the concrete cracks.

On the other hand, the residual strength is highly dependent on the fiber volume fraction and fiber type. Increased fiber content means an increased number of fibers potentially crossing crack planes, and hence increased strength after cracking. As shown in Figure G-3 (b), this aspect of SFRC behavior is adequately captured by the DPT, in that the residual strength increases as the fiber volume fraction increases.

It is also clear from Figure G-3 (b) that the DPT is able to distinguish between different fiber types. For instance, the average value of the residual strength is 20-50% higher for Bekaert specimens than for Royal specimens. This superiority in reserve capacity indicates that the Bekaert Dramix® fibers perform better than the Royal™ fibers. Thus, information obtained from the DPT can be useful for comparing different fiber-reinforcement options, and determining the appropriate fiber type(s) and relative volume fraction(s) needed for SFRC applications.

This analysis confirms the trends obtained from DPT performance curves and verifies that the DPT is effective at comparing post-cracking ductility and fiber performance.

G.1.b: Analyzing the Effects of Surface Preparation

Figure G-4, Figure G-5, and Figure G-6 show the effects of surface preparation on the (a) coefficient of variation and (b) average value of key parameters of the DPT. These statistics are based on five tests.

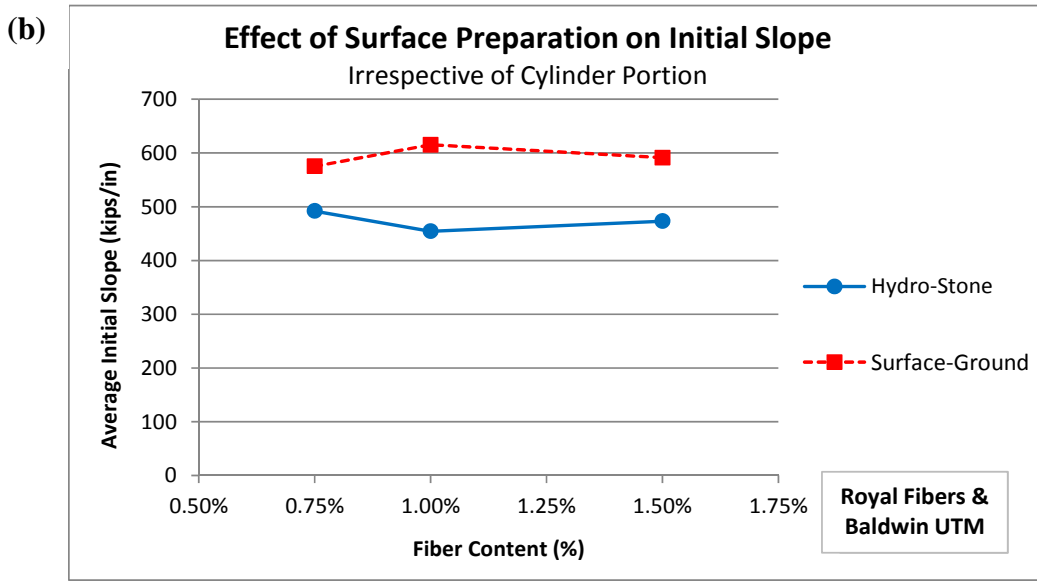
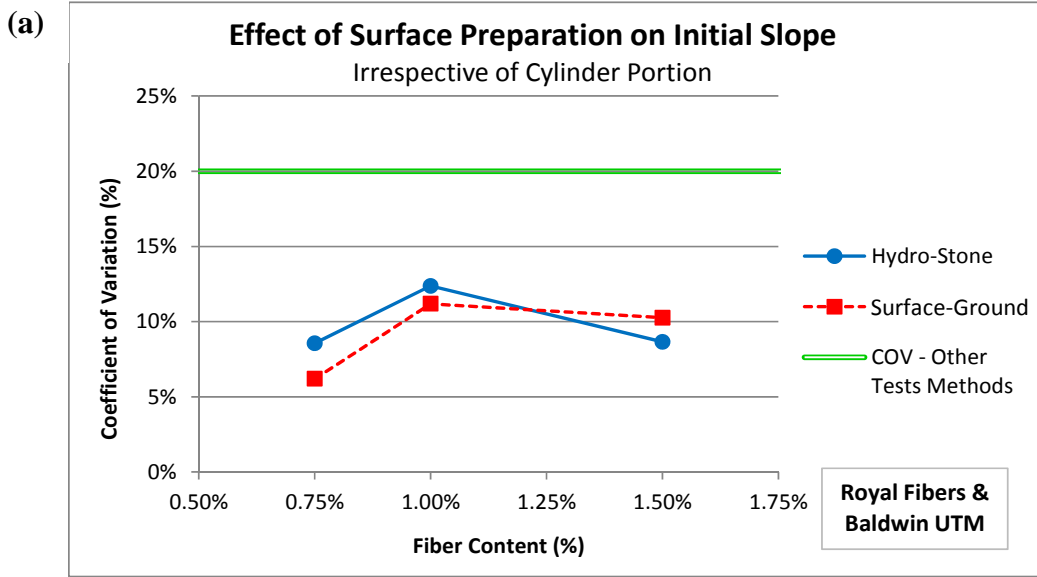


Figure G-4: Effect of surface preparation on (a) coefficient of variation and (b) average value of initial slope for royal fiber type

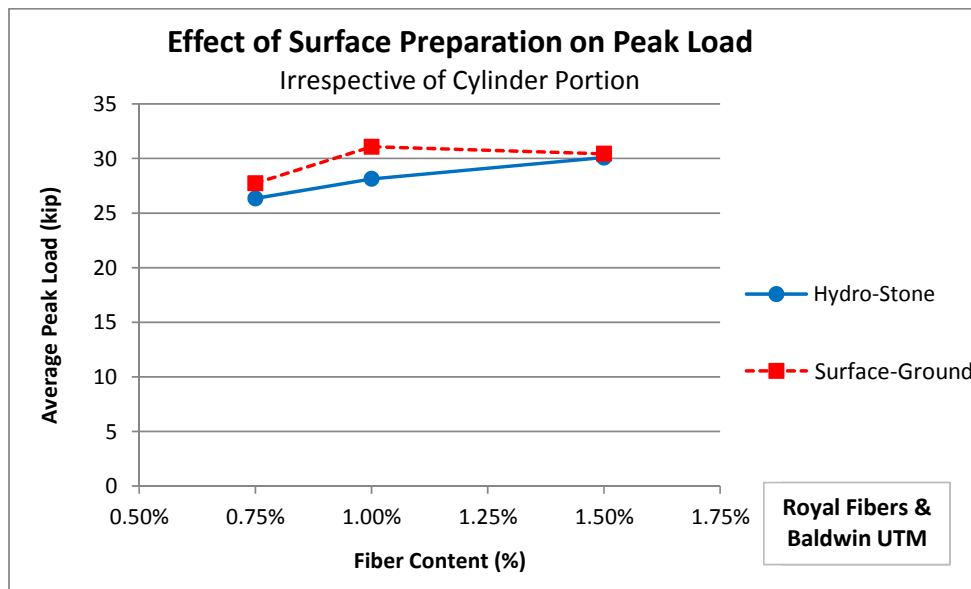
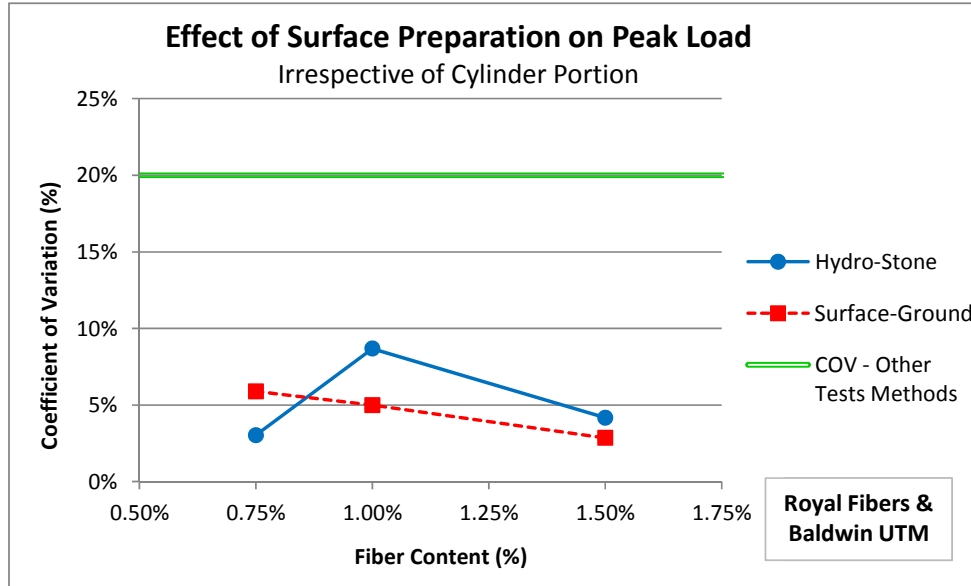


Figure G-5: Effect of surface preparation on (a) coefficient of variation and (b) average value of peak load for royal fiber type

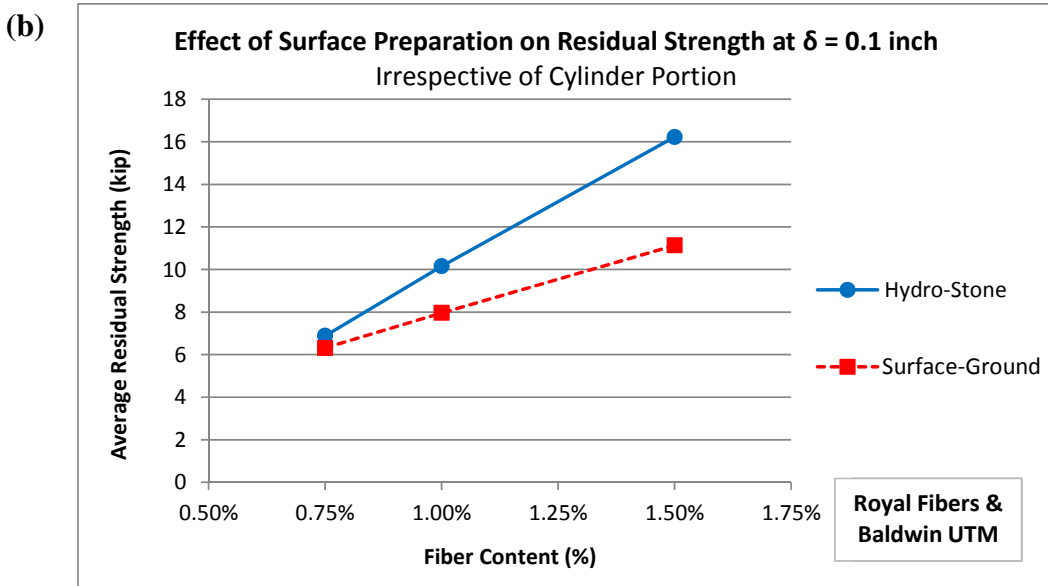
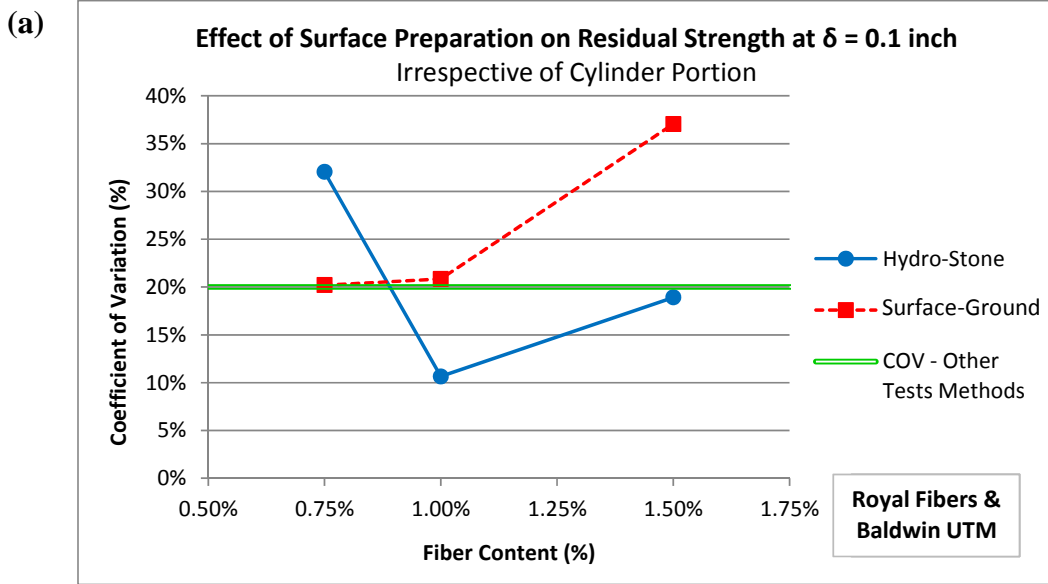


Figure G-6: Effect of surface preparation on (a) coefficient of variation and (b) average value of residual strength for royal fiber type

G.1.b.(1) Analysis Summary

The coefficient of variation is generally low for key test parameters (less than 20%), but variation in residual strength parameter is high compared to initial slope and peak load variation. Surface-ground and Hydro-Stone specimens exhibited similar COV. On average, Hydro-Stone specimens had a smaller initial slope (less stiff) and higher residual strength than Surface-Ground specimens, probably due to stress concentrations under the steel punches. As shown in Figure G-7, this is most noticeable at loads beyond about 10 kips, as the brittle layer of Hydro-Stone fails and the steel punches flatten the roughened concrete surface underneath prior to rupture of the specimen.

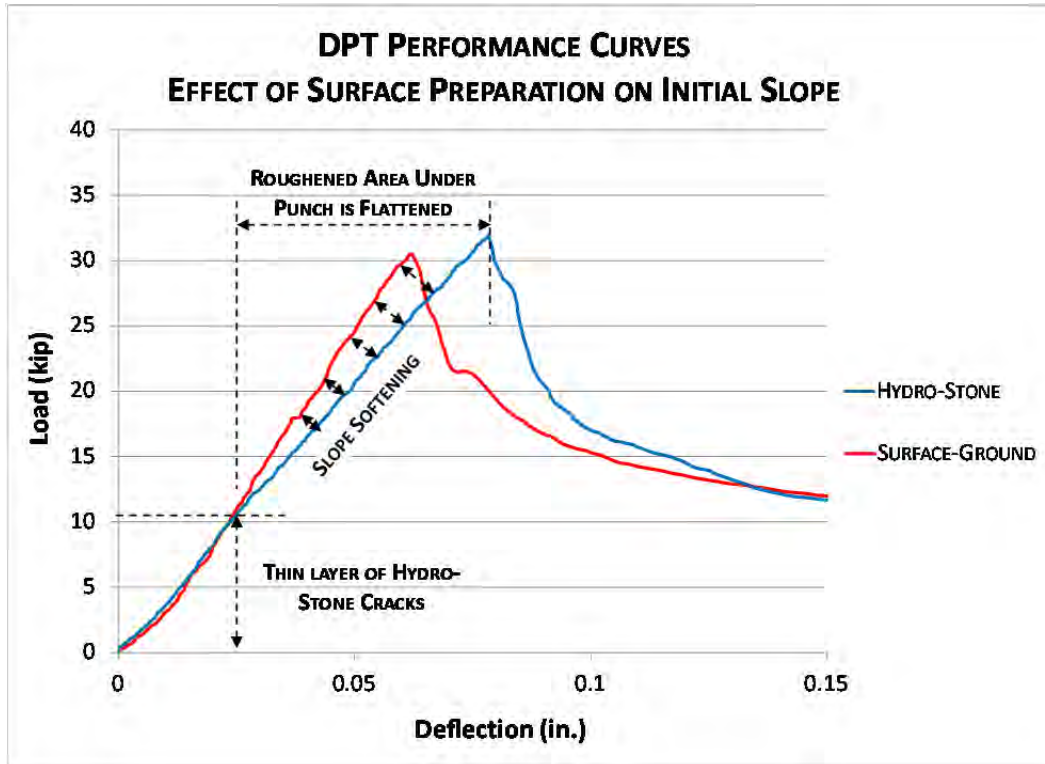


Figure G-7: DPT performance curves showing effect of surface preparation on initial slope parameter

In general, end grinding the surfaces of specimens is preferred over using Hydro-Stone for two reasons: (1) surface grinding specimens provides a smoother surface between the punch and concrete, and does not produce stress concentrations; and (2) the reduction in initial stiffness resulting from Hydro-Stone application may result in an error in the value of residual strength at a specified deflection, leading to a perceived increase in performance. Because Hydro-Stone is a surface application only, it would be unreasonable to conclude that it is able to increase the residual strength or ductility of the specimen. When the peak load is reached, the Hydro-Stone and surface concrete crack, and do not provide additional internal resistance. It is evident from other results that improved *post-peak* performance is only related to the fiber type, content, and distribution.

Although refinishing the DPT specimen by end grinding is preferred, it is possible that some laboratories may not have the necessary equipment to grind 6-in. diameter cylinders. In this case, a thin layer of Hydro-Stone can be applied to the area beneath the punch location to provide a relatively smooth contact surface between the steel punches and DPT specimen. However, specimens with different surface finishes should not be compared directly.

Similar results are obtained for surface-ground and Hydro-Stone finishes, and either method is acceptable for the DPT for means of comparing mixtures with different fiber types and volume fractions.

G.1.c: Analyzing the Effects of Test Machine

The data from test conducted in Phase 1 and Phase 2 indicate that some results from the DPT may be dependent on the test machine. Figure G-8, Figure G-9, and Figure G-10 show the

effects of test machine on the (a) coefficient of variation and (b) average value of key parameters of the DPT. These statistics are based on ten DPTs.

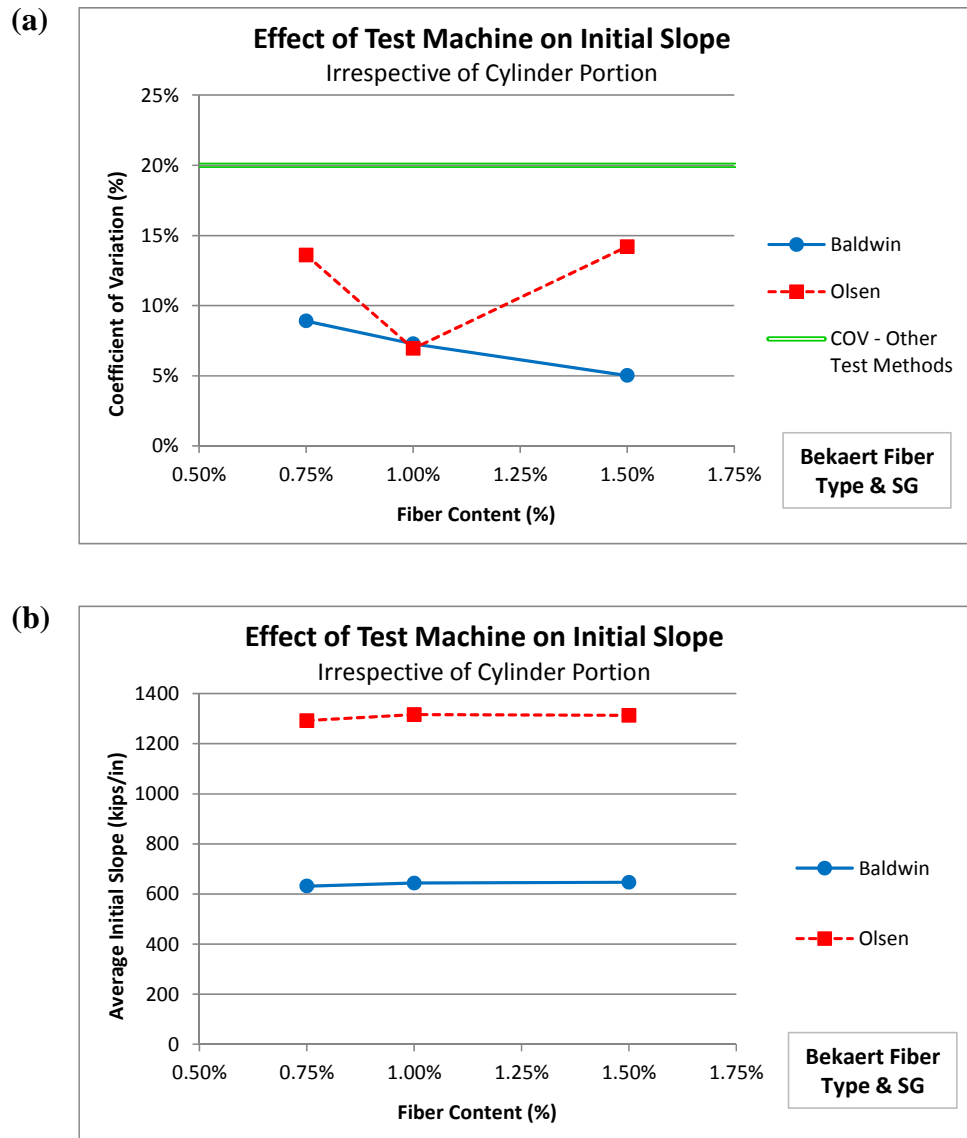


Figure G-8: Effect of test machine on (a) coefficient of variation and (b) average value of initial slope for Bekaert fiber type

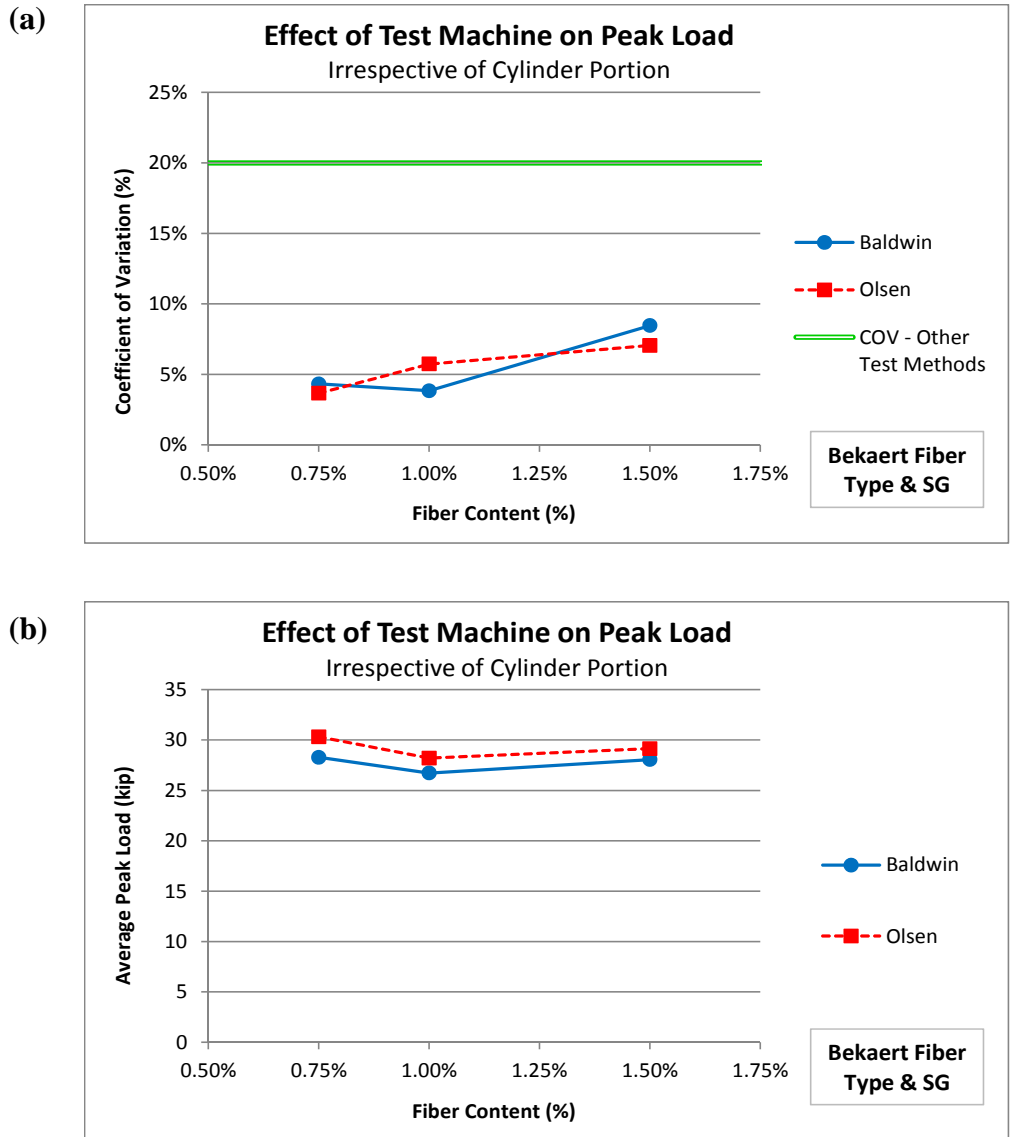


Figure G-9: Effect of test machine on (a) coefficient of variation and (b) average value of peak load for Bekaert fiber type

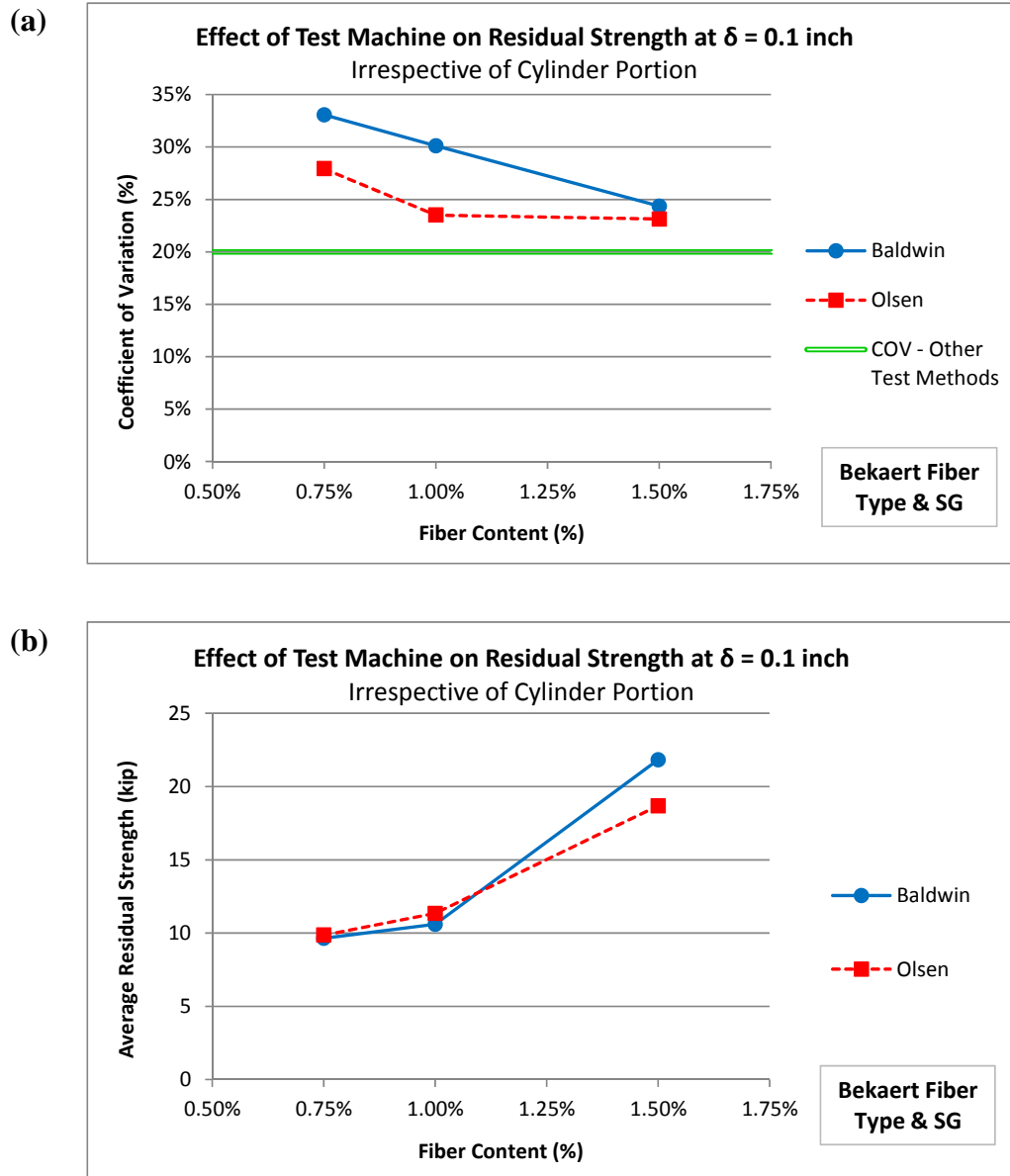


Figure G-10: Effect of test machine on (a) coefficient of variation and (b) average value of residual strength for Bekaert fiber type

As shown in the previous figures, the effect of the test machine is significant only for the initial slope parameter for both Royal and Bekaert fibers. The average value of the initial slope of specimens tested on the Olsen UTM is about 1½ to 2 times that of otherwise identical specimens tested on the Baldwin UTM. This difference was unexpected, because the specimens tested on the two machines were from identical batches of concrete and tested beyond 28 days (concrete strength has leveled off). The elastic modulus of the specimens should not differ by a factor of 2. Thus, a calibration, independent of DPT specimens and measuring devices, was conducted to determine the stiffness of the two test machines in order to evaluate the effects of the test machine on DPT results.

The machines were checked simply, using a dial gage and load cell. The load cell was used to confirm the load displayed by the UTMs was correct. Next, readings of load (from machine) and displacement (from dial gage) were taken for a concrete cylinder loaded in compression. The calibration setups are shown in Figure G-11.



Figure G-11: Calibration setup for Baldwin (left) and Olsen (right) UTMs

Finally, a small portion of the initial loading curve was constructed to determine the tangent stiffness of the same cylinder tested on the Baldwin and Olsen UTMs. In

Table G-1, this data is compared to the averages for initial slope found in the DPT. The tangent stiffness calibration curves for the Baldwin and Olsen are shown in Figure G-12.

Table G-1: Comparison between initial slopes from DPT and calibration test

Machine	Avg. Initial Slope from DPT Data	Measured Initial Slope from Calibration
<i>Baldwin</i>	587	781
<i>Olsen</i>	1187	1087
Olsen/Baldwin	2.02	1.39

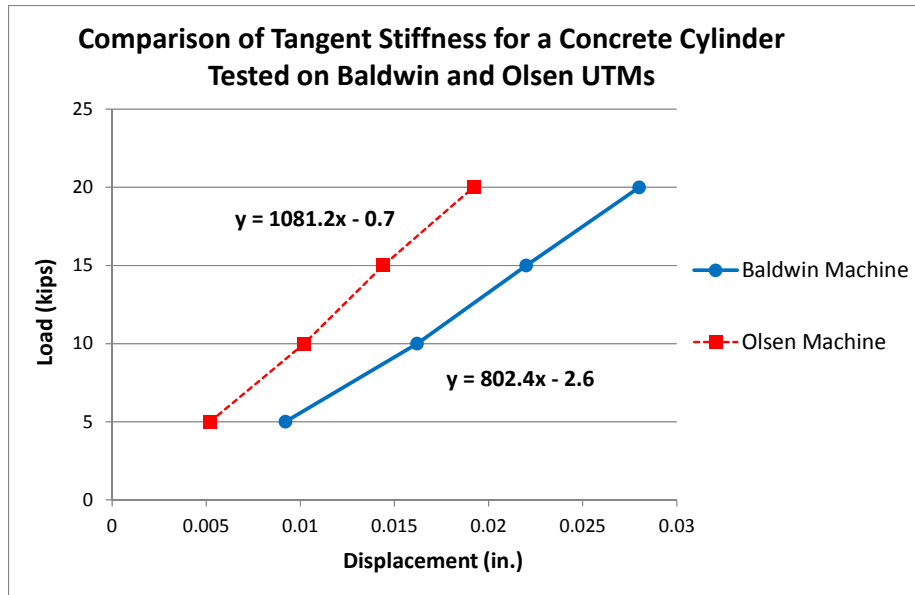


Figure G-12: Tangent stiffness calibration curves

The calibration curves and test data show that the test setup can have some effect on the measured initial stiffness. Similar to DPT data, the calibration experiment suggests the Olsen machine is about twice as stiff as the Baldwin machine. This is explained by the fact that the Olsen UTM (120-kip) has twice the load capacity as the Baldwin UTM (60-kip); thus, the stiffness of the connecting rods on the Olsen UTM are twice that of the Baldwin UTM.

Due to these effects, the initial stiffness of the test specimen itself does not correspond to the measured stiffness from the DPT. The actual stiffness of the specimen can only be determined if strains are measured directly on the test cylinder using an extensometer, strain gauge, or other methods. Thus, the measured initial stiffness from the DPT should only be used to provide further evidence of the repeatability of the DPT on the same machine; it should not be used as an estimate of the actual stiffness of the DPT test specimen due to flexibilities observed in the DPT setup.

G.I.c.(1) Analysis Summary

The coefficient of variation is generally low for key test parameters (less than 20%), but variation in the residual strength parameter is high compared to initial slope and peak load variation. Results did not show that the test machine has an effect on the coefficients of variation for the key test parameters. However, the test machine was found to effect the average values (or performance) of DPT specimens. These effects varied based on the test parameter:

1. Initial Slope

The value of the initial slope differed by a factor of approximately 2 between the two test machines used in this study. This difference can be attributed to the differences in the stiffness of the *testing equipment* used and not the DPT *specimens* themselves;

The measured initial slope is only valuable for analyzing the statistical variation of DPT results obtained on a single test machine.

2. Peak Load

The peak load is not influenced by the stiffness of the machine;

3. Residual Strength at 0.1 inch Deflection

The measure of ductility may be slightly influenced, but because the specimens are sufficiently less stiff after cracking, the differences in machine stiffness are not as apparent in results for the residual strength. Also, the shallow slope of the post-peak curve is much flatter so the net effect of machine stiffness is not as significant.

Nevertheless, since many test methods for FRC require the use of closed-looped, servo-controlled test machines, the DPT presents an immediate advantage over current tests since any common universal test machine can be used to conduct the test.

G.1.d: Analyzing the Effects of Cylinder Portion (Casting)

Figure G-13, Figure G-14, and Figure G-15 show the effects of cylinder portion (casting) on the (a) coefficient of variation and (b) average value of key parameters of the DPT. These statistics are based on ten DPTs.

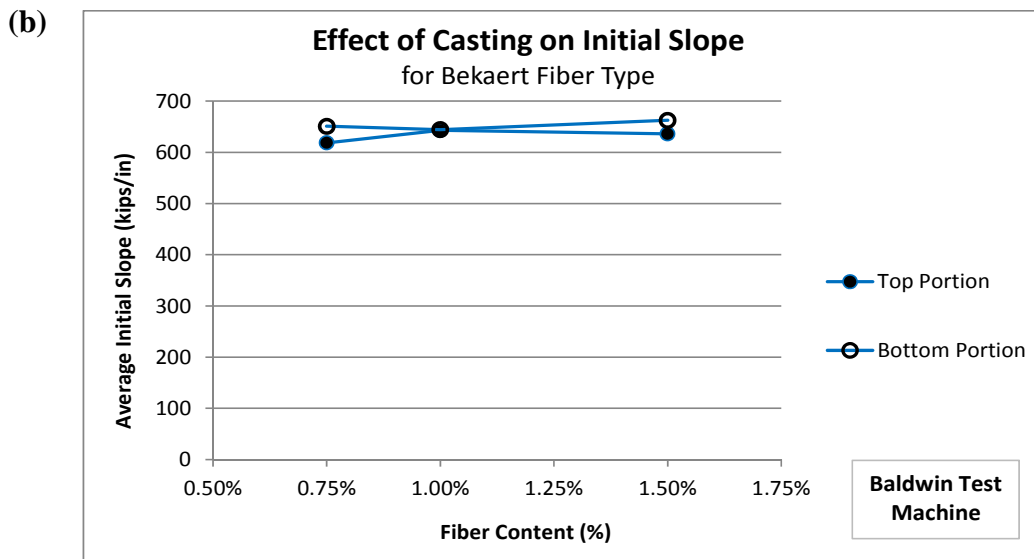
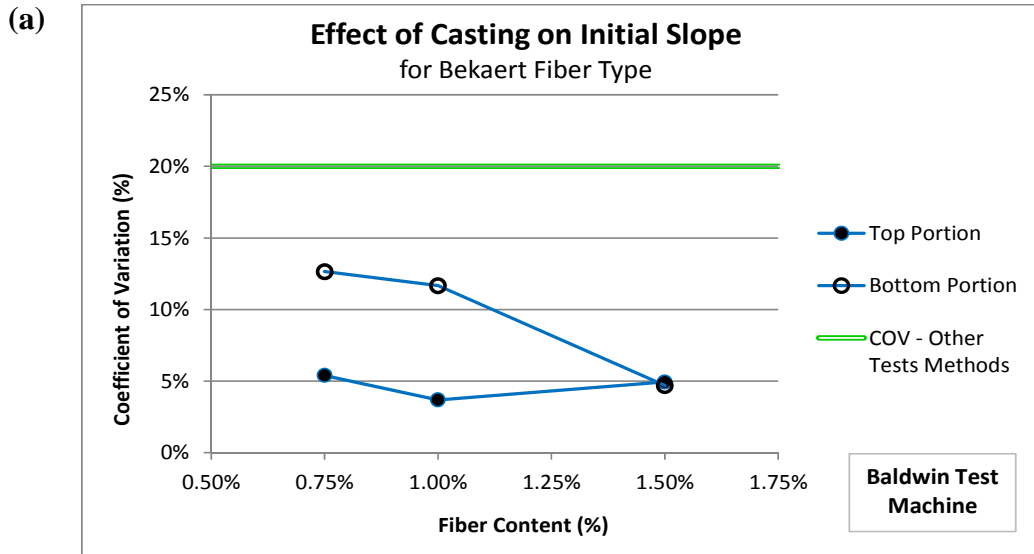


Figure G-13: Effect of cylinder portion (casting) on (a) coefficient of variation and (b) average value of initial slope for Bekaert fiber type

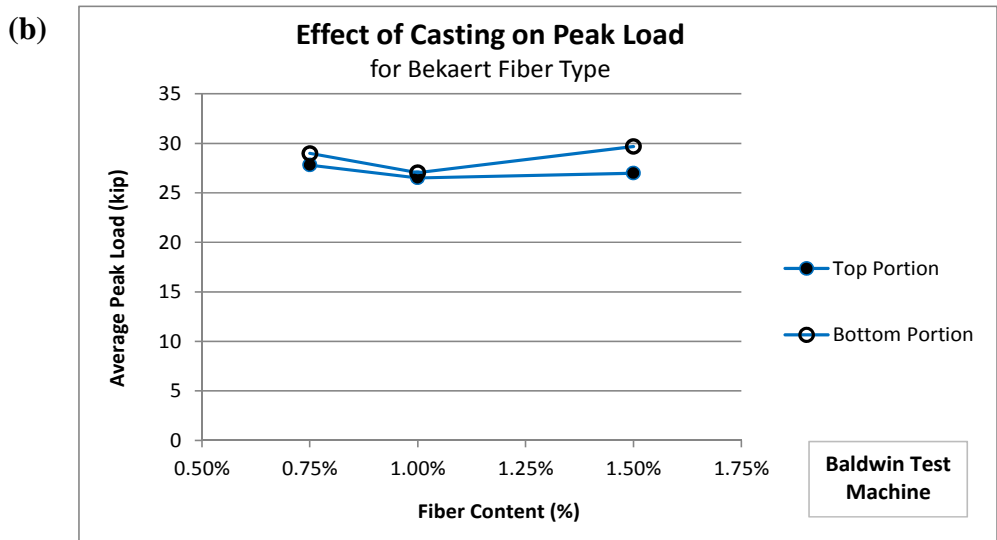
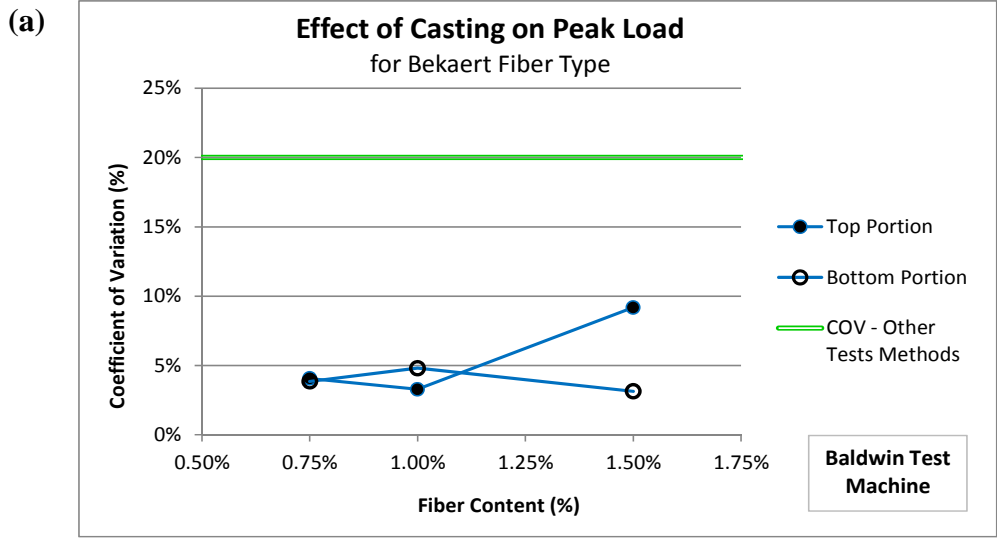


Figure G-14: Effect of cylinder portion (casting) on (a) coefficient of variation and (b) average value of peak load for Bekaert fiber type

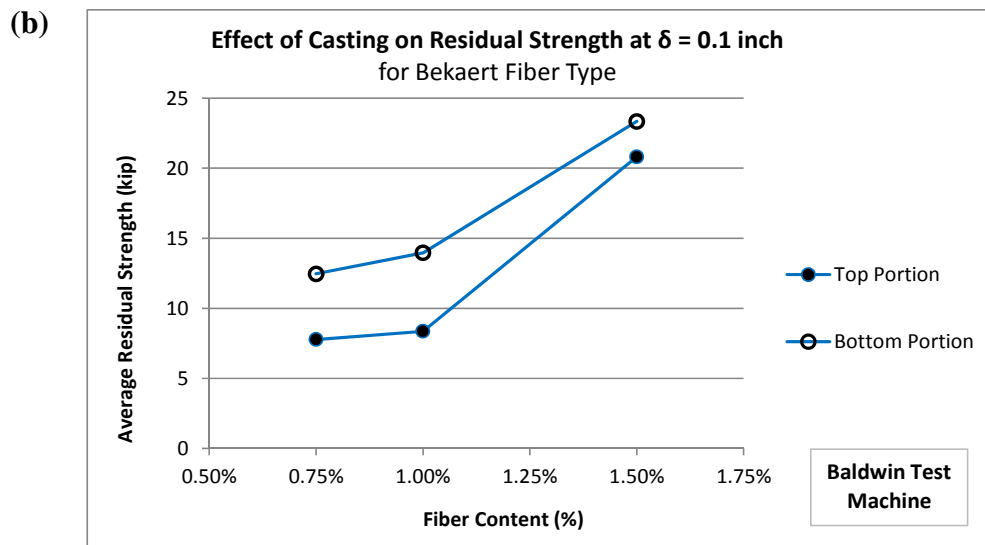
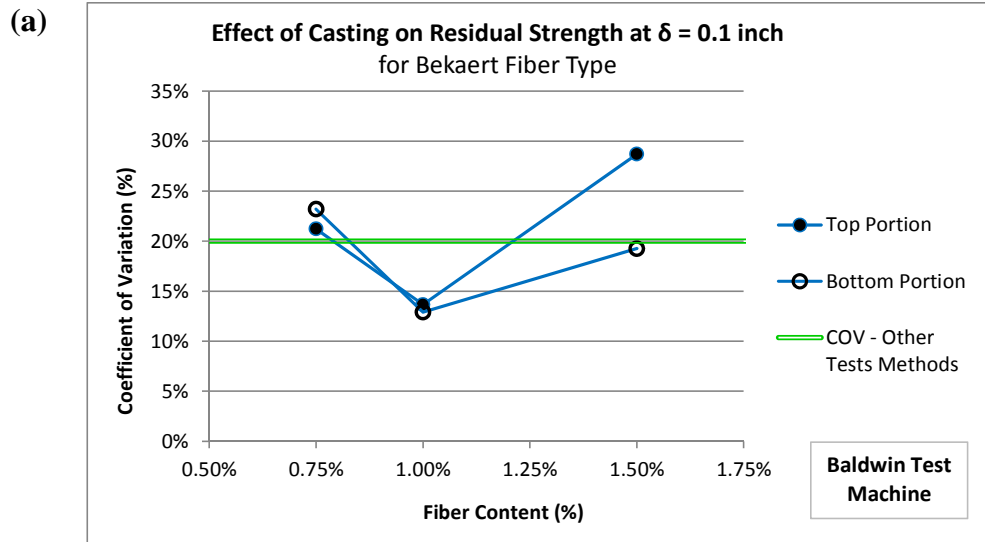


Figure G-15: Effect of cylinder portion (casting) on (a) coefficient of variation and (b) average value of residual strength for Bekaert fiber type

G.I.d.(1) Analysis Summary

The coefficient of variation is generally low for key test parameters (less than 20%), but the variation in the residual strength is higher than that of the initial slope and peak load. The coefficients of variation for are similar for Top and Bottom specimens, indicating that the scatter is not dependent on the portion of cylinder used in the DPT. The average values of initial slope and peak load are also independent of the cylinder portion.

However, the average value of residual strength is greatly dependent on the cylinder portion. As shown in Figure G-15 (b), the bottom portion of the cylinder has additional reserve capacity for a given fiber content. This is directly associated with the distribution of fibers. As shown in Figure G-16 (a), the distribution of fibers in the bottom portion of the cylinder is denser

due to segregation during casting. This is corroborated by the appearance of the cracked specimens from DPT experiments as seen in Figure G-16 (b).

The number of fibers bridging the cracks of failed specimens was much greater for specimens taken from the bottom portion of the original 6 x 12-in. cylinders. Thus, residual strengths are generally higher for bottom specimens because they have more fibers crossing the radial cracks.

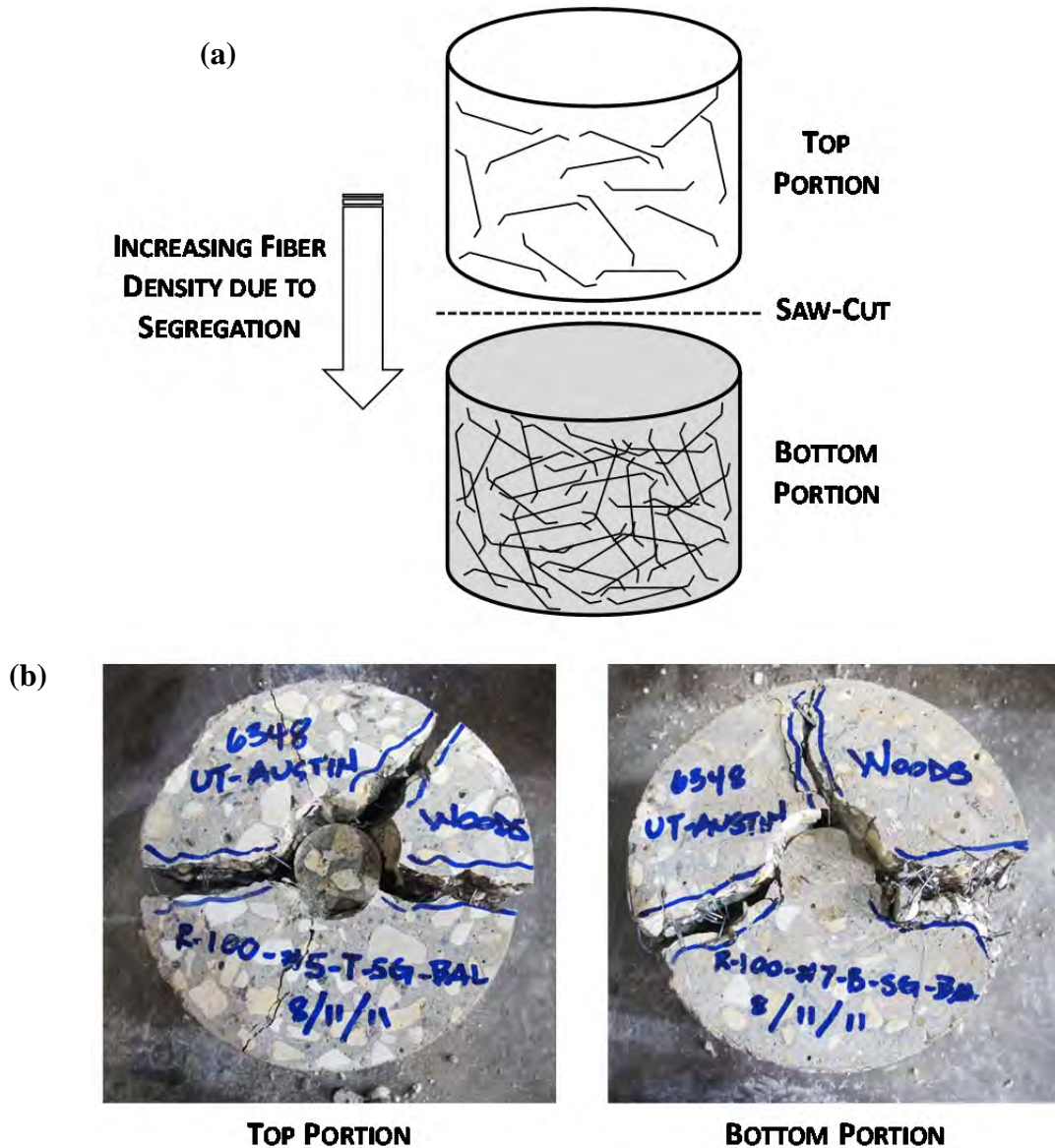


Figure G-16: Effect of casting on (a) the fiber distribution and (b) the number of fibers crossing crack planes in top and bottom test specimens

Appendix H. ASTM Draft Ballot for Standardization of Double-Punch Test



C.2 ASTM DRAFT BALLOT FOR STANDARDIZATION OF DOUBLE-PUNCH TEST

1 **Standard Test Method for**
2 **Evaluating the Performance of Fiber-Reinforced Concrete (Using**
3 **Cylindrical Specimens with Double-Punch Loading)¹**

4 This standard is issued under the fixed designation X XXXX; the number immediately following the
5 designation indicates the year of original adoption or, in the case of revision, the year of last revision. A
6 number in parentheses indicates the year of last reapproval. A superscript epsilon (ϵ) indicates an editorial
7 change since the last revision or reapproval.

8
9 **1. Scope**

10 1.1 This test method can be applied to plain concrete or fiber-reinforced concrete (FRC)
11 cylindrical specimens, such as molded cylinders and drilled cores.

12 1.2 This test method covers the determination of the ultimate tensile strength and residual
13 capacity (toughness) up to a specified deflection. In this test, commonly referred to as the
14 “Double-Punch Test (DPT),” a concrete cylinder is placed vertically between the loading platens
15 of a universal test machine and compressed by two steel punches located concentrically on the
16 top and bottom surfaces of the cylinder. The applied compression results in uniformly
17 distributed, indirect tension along radial planes of the cylindrical specimen. The performance of
18 specimens tested by this method is quantified in terms of the initial stiffness, peak load, and
19 residual strength at a specified deflection.

20 *1.3 The values stated in either SI units or inch-pound units are to be regarded separately as*
21 *standard. The values stated in each system may not be exact equivalents; therefore, each system*
22 *shall be used independently of the other. Combining values from the two systems may result in*
23 *non-conformance with the standard.*

¹ This test method is under the jurisdiction of ASTM Committee and is the direct responsibility of Subcommittee.
Current edition approved XXX. XX, XXXX. Published XX XXXX. DOI:10.1520/XXXXX-XX

24 1.4 *This standard does not purport to address all of the safety concerns, if any, associated*
25 *with its use. It is the responsibility of the user of this standard to establish appropriate safety and*
26 *health practices and determine the applicability of regulatory limitations prior to use.*

27 **2. Referenced Documents**

28 2.1 *ASTM Standards:*

29 **C31/C31M Practice for Making and Curing Concrete Test Specimens in the Field**

30 **C39/C39M Test Method for Compressive Strength of Cylindrical Concrete Specimens**

31 **C42/C42M Test Method for Obtaining and Testing Drilled Cores and Sawed Beams of**
32 **Concrete**

33 **C172 Practice for Sampling Freshly Mixed Concrete**

34 **C192/C192M Practice for Making and Curing Concrete Test Specimens in the Laboratory**

35 **C496/C496M Test Method for Splitting Tensile Strength of Cylindrical Concrete Specimens**

36 **C823 Practice for Examination and Sampling of Hardened Concrete in Constructions**

37 **C1609/C1609M Test Method for Flexural Performance of Fiber-Reinforced Concrete (Using**
38 **Beam with Third-Point Loading)**

39 **C1399/C1399M Test Method for Obtaining Average Residual-Strength of Fiber-Reinforced**
40 **Concrete**

41 **3. Terminology**

42 3.1 *Definitions:* This test method has no definitions unique to this standard.

43 **4. Summary of Test Method**

44 4.1 This test method consists of loading molded cylinders or cores, at a rate that is within a
45 prescribed range, through cylindrical steel punches at each end, until a prescribed deflection is
46 reached. Test results are the initial stiffness of the specimen, its maximum strength, and its
47 residual strength at a deflection of 0.1 in. (2.5 mm).

48 **5. Significance and Use**

49 5.1 The test provides the entire load-deflection curve, before and after cracking, for a
50 concrete or fiber-reinforced concrete cylinder specimen loaded axially through cylindrical steel
51 punches at each end. Key parameters (initial stiffness, peak load, and residual strength at 0.1 in.

52 [2.5 mm] deflection) are obtained from the load-deflection curve, and are useful for evaluating
53 the elastic and plastic behavior of FRC with different fiber types and volume fractions (% fiber
54 content). The test is particularly appropriate for comparing the behavior of concrete reinforced
55 with high-performance steel fibers.

56 5.2 The motivation for using the “Double-Punch Test (DPT)” setup is based on the within-
57 batch, intra-laboratory repeatability and consistency of the failure mode that arises through the
58 use of steel punches.²

59 **6. Apparatus**

60 6.1 *Testing Machine* -- The testing machine shall meet the requirements of Sections 5.1
61 through 5.4 of Specification C 39.

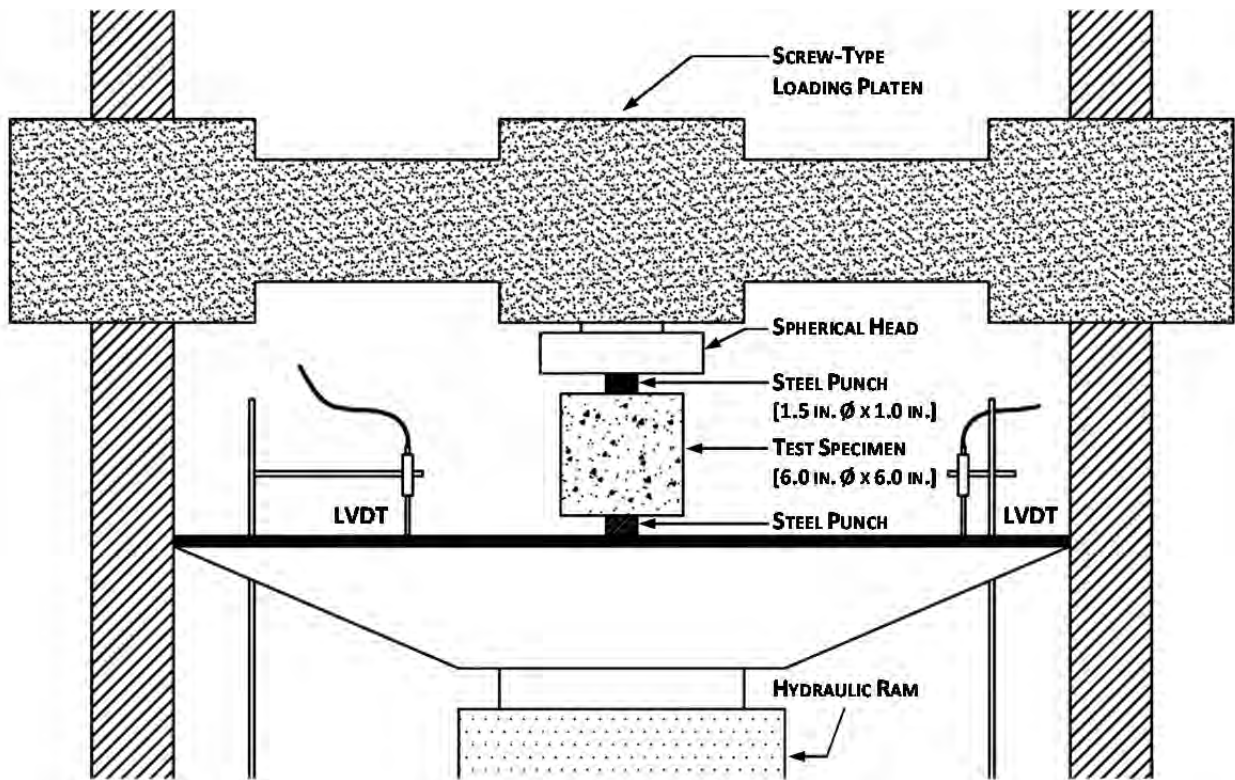
62 6.2 *Steel Punches* -- The steel punches shall be cylindrical in shape, with a diameter of 1.5
63 in. (38 mm) \pm 0.1 in. (\pm 2.5 mm) and a height of 1.0 in. (25 mm) \pm 0.1 in. (\pm 2.5 mm). The
64 punches shall be cut from tool steel with a yield strength between 75 ksi [517 MPa] and 90 ksi
65 [620 MPa].

66 6.3 *Instrumentation for Measuring Deflections* -- Measure the deflection of the loading head
67 using a dial indicator or linear potentiometer with a range of at least 1 in. (25 mm) and a
68 precision of at least 1% of that range.

69
70
71
72
73
74
75
76
77
78

79 ² Woods, A.P. “Double-Punch Test for Evaluating the Performance of Steel Fiber-Reinforced Concrete.” MS Thesis,
80 Department of Civil Engineering, University of Texas at Austin, 2012.

81



82

83

Figure 6-1: Schematic of Double-Punch Test Arrangement

84 **7. Specimens**

85 7.1 Specimens shall be prepared by cutting molded concrete cylinders having a nominal
 86 diameter of 6 in. (150 mm) and a nominal height of 12 in. (300 mm), into two cylinders, each
 87 having a nominal diameter of 6 in. (150 mm) and a nominal height of 6 in. (150 mm).

88 7.2 The top or bottom 6 x 6 in. portion can be used for testing. However, specimens obtained
 89 from the bottom portion have a greater fiber density than those from the top portion, due to
 90 segregation during casting. Thus, top and bottom specimens should not be compared directly.

91 7.3 Specimen surfaces shall be smoothed so that the steel punches make uniform (flat)
 92 contact with the top and bottom faces of the specimen. Smooth contact surfaces can be obtained
 93 by grinding the ends of the cylinder using a milling machine, or by applying a thin layer of
 94 Hydro-Stone to the rough concrete at the location of the steel punches. End grinding is preferred;

95 however, Hydro-Stone application is acceptable should grinding equipment be unavailable.
96 Results obtained from specimens with different surface finishes should not be compared directly.

97 **8. Procedure**

98 8.1 Using masking tape, affix steel punches concentrically to the top and bottom of the
99 specimen. To avoid eccentricity of load, the centroid of each steel punch should align with the
100 centroid of the cylinder surface within ± 0.1 in. [± 2.5 mm]. A plywood dimensional guide may
101 be used to help ensure this.

102 8.2 Place the specimen concentrically in the testing machine.

103 8.3 Load the specimen using the following sequence:

104 8.3.1 *Shakedown (Initial Loading and Unloading to Seat Punches)* -- Load the specimen at a
105 rate of 100 lb/sec (445 N/sec) \pm 25 lb/sec (\pm 111 N/sec) up to a load of 10 kips (44.5 kN).
106 Unload the specimen at a rate between 100 and 300 lb/sec (445 and 1334 N/sec) to a load
107 between 100 lb (445 N) and 200 lb (890 N). The deflection at that final load is termed the
108 “initial deflection offset.”

109 8.3.2 *Reloading* -- Load the specimen at a rate of 100 lb/sec (445 N/sec) \pm 25 lb/sec (\pm 111
110 N/sec). Note the corresponding rate of applied deflection. Load at that deflection rate until the
111 first radial crack appears in the top or bottom face of the specimen. Continue loading at a rate
112 between 1.0 and 3.0 times that deflection rate until the deflection reaches or exceeds 0.5 in. (13
113 mm), or the steel punches are almost fully seated into the specimen. Do not permit the loading
114 head of the testing machine to contact the specimen.

115 8.4 *Data Recording* -- Record the applied load and the deflection of the loading head at 1-
116 second time intervals.

117 **9. Evaluation and Reporting of Results**

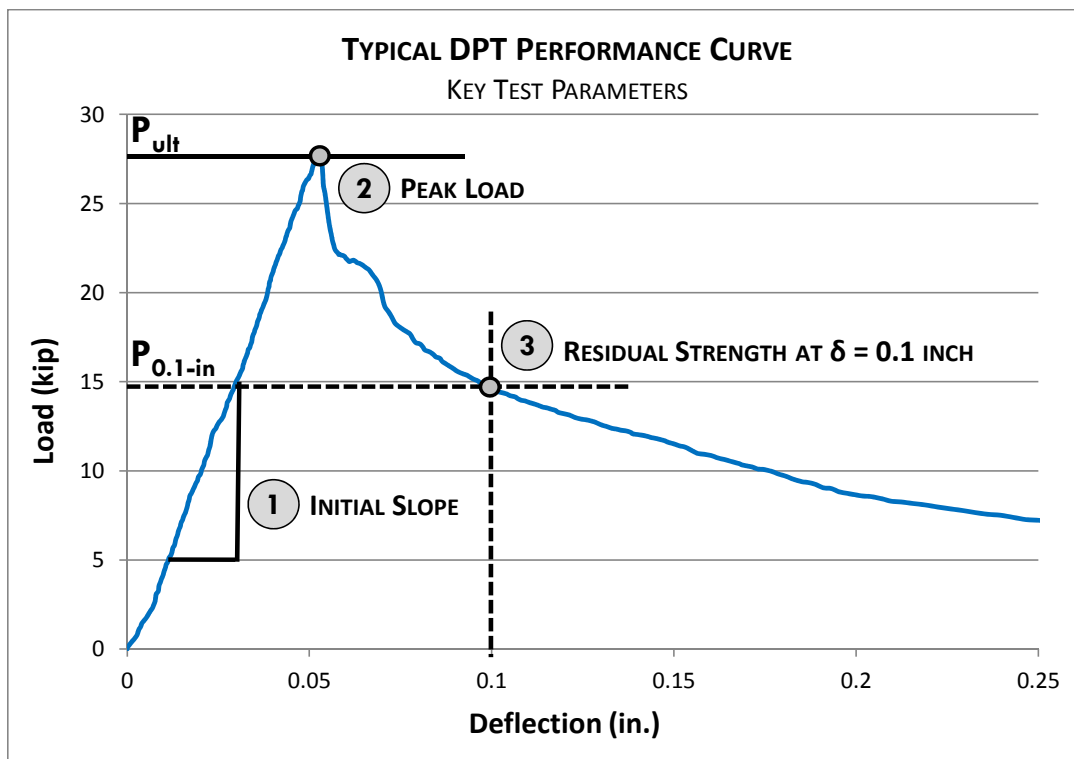
118 9.1 Subtract the initial deflection offset from each deflection reading during the reloading
 119 phase. The resulting deflections are termed “corrected deflections.”

120 9.2 Using the recorded loads and the corrected deflections, calculate and report the initial
 121 slope, maximum load, and residual load, as follows:

122 9.2.1 Evaluate the initial slope as the slope between applied loads of approximately 5 kips
 123 (22 kN) and 15 kips (67 kN).

124 9.2.2 Evaluate the maximum load directly.

125 9.2.3 Evaluate the residual load at a corrected deflection of 0.1 in. ± 0.01 in. (2.5 mm \pm 0.025
 126 mm).



127

Figure 9-1: Typical Double-Punch Test (DPT) Load-Deflection Plot (Performance Curve) showing Key Test Parameters

128

129

130

131 **10. Precision and Bias**

132 10.1 Because the specific testing protocol of this standard is relatively new, an inter-
133 laboratory study of this test method has not been performed to quantify its precision and bias.
134 Available research data, however, suggests that the within-batch, intra-laboratory coefficients of
135 variation for key test parameters is generally low and comparable to other current test methods
136 for FRC: $\pm 10\%$ Initial Slope; $\pm 5\%$ Peak Load; and $\pm 20\%$ Residual Strength at 0.1 in.
137 deflection.² A precision and bias statement will be prepared as more data becomes available.

138 **11. Keywords**

139 11.1 double-punch test; cylindrical concrete specimens; fiber-reinforced concrete; peak
140 tensile strength; residual strength; toughness

141

142 ² Woods, A.P. "Double-Punch Test for Evaluating the Performance of Steel Fiber-Reinforced Concrete." MS Thesis,
143 Department of Civil Engineering, University of Texas at Austin, 2012.